Developing Strategies for Improving Our Understanding of the Air Quality Impacts of Dust Heterogeneous Chemistry

by

Maya Abou-Ghanem

A thesis submitted in partial fulfillment of the requirements for the degree of

Doctor of Philosophy

Department of Chemistry
University of Alberta

Abstract

Dust is one of the leading contributors to particulate matter (PM) in the atmosphere and can be natural (*i.e.*, mineral dust) and anthropogenic (*i.e.*, road and industrial dust) in origin. Natural and anthropogenic dusts provide a reactive surface for the chemical transformation of pollutant gases, which can influence both the composition of the atmosphere and dust PM. To date, most heterogeneous chemistry studies exploring dust–pollutant interactions have used commercially available, single-component metal oxides as a proxy for mineral dust, and no studies have investigated the heterogeneous chemistry of anthropogenic dust. Together, this limits our ability to predict the air quality (AQ) impacts of dust PM, which will become increasingly important in the future as a result of: a) an increase in mineral dust emissions due to increasing aridity and desertification as a result of climate change and land modification, respectively and b) road dust dominating traffic-related PM as countries move towards net-zero fleet emissions. The goal of this thesis is to advance dust–pollutant interaction studies by investigating the uptake of ozone, an important atmospheric oxidant, by natural, road, and atmospherically aged dust substrates.

In my first project, I found that the photoreactivity of a suite of natural titanium (Ti)-containing minerals commonly found in mineral dust display vastly different photoreactivity with ozone, even within the same mineral phase sampled from different locations. In addition, I found that the photoreactivity of natural titanium dioxide (TiO_2) minerals is orders of magnitude lower than commercial TiO_2, which is typically used as a photoactive proxy in

studies of dust photochemistry. This work highlights the importance of considering mineral phase when assessing dust photoreactivity and provided motivation for me to explore the photochemical drivers of Icelandic volcanic dust in my second project. Here, I observed modest photochemistry of a Ti-rich sample from the Mýrdalssandur dust source region with ozone and found that most of the elemental Ti is contained in the non-photoactive glass fraction of the sample, with minor amounts present in moderately photoactive Ti-containing mineral phases. This project demonstrated the advantages of using elemental speciation for predicting and understanding the photochemistry of glass-rich volcanic dusts.

In my third project, I investigated the reactivity of ozone with road dust and commercial anti-icer, a saline solution applied to roads in cold-climate regions. Interestingly, I found that ozone is more reactive towards road dust than mineral dust. In addition, I demonstrated that the interaction of ozone with anti-icer leads to production of inorganic chlorine gas, an important precursor for the reactive chlorine radical. This work demonstrates that the interaction of ozone with road dust PM and the road surface has the potential to influence the oxidative power of the urban atmosphere, and that this heterogeneous chemistry should be considered in future when making road maintenance decisions in high-latitude urban regions.

My fourth project focused on the influence of atmospheric aging on dust photochemistry by exploring the photochemistry of internally mixed dusts. In this work, I discuss the design and construction of a custom-built photochemical aerosol flow tube reactor that is used to investigate the photochemical uptake ozone by organic-coated TiO_2, which I used as a simple

model system for atmospherically aged mineral dust. Here, I demonstrated the suppression of ozone uptake by organic coatings and observed decreasing ozone uptake with increasing coating thickness. This work is the first to demonstrate the evolution of mineral dust photochemistry during atmospheric aging, which may require us to consider the influence of organic coatings on the inherent photoreactivity of dust.

This thesis provides significant advancements in dust heterogeneous chemistry studies by exploring the reactivity of naturally sourced mineral and road dust, as well as the influence of atmospheric aging on dust photochemistry. Together, this will ultimately allow us to better predict the AQ impacts of dust in the urban atmosphere.

Preface

My research contributions for each chapter of this thesis are summarized below. Chapter 1, 5, and 6 contain unpublished material, Chapter 2 and 3 include published material, and Chapter 4 has been submitted for publication and is under peer review.

Chapter 1
Introduction
Contributions
The manuscript was written by Maya Abou-Ghanem with critical comments from Dr. Sarah A. Styler.

Chapter 2
Significant variability in the photocatalytic activity of natural Titanium-containing minerals: implications for understanding and predicting atmospheric mineral dust photochemistry
Published as:
Abou-Ghanem, M.; Oliynyk, A.O.; Chen, Z.; Matchett, L.C; McGrath, D.T.; Katz, M.J.; Locock, A.J.; and Styler, S.A. "Significant Variability in the Photocatalytic Activity of Natural Titanium-Containing Minerals: Implications for Understanding and Predicting Atmospheric Mineral Dust Photochemistry" in *Environmental Science and Technology* 2020, 54, 21, 13509–13516.
Contributions
All experiments were carried out by Maya Abou-Ghanem. Mineralogical and elemental and mineralogical characterization of samples were performed by Dr. Andrew J. Locock and Dr. Anton O. Oliynyk, respectively. The manuscript was written by Maya Abou-Ghanem, with critical comments from Dr. Sarah A. Styler, Dr. Andrew J. Locock, and Dr. Anton O. Oliynyk.

Chapter 3
Ozone chemistry and photochemistry at the surface of Icelandic volcanic dust: insights from elemental speciation analysis
Published as:
Abou-Ghanem, M.; Jensen, B.J.L.; Romanías, M.N.; and Styler, S.A. "Ozone Chemistry and Photochemistry at the Surface of Icelandic Volcanic Dust: Insights from Elemental Speciation Analysis" in *ACS Earth and Space Chemistry* 2021,
doi-org./10.1021/acsearthspacechem.0c00363
Contributions
Coated-wall flow tube experiments were carried out by Dr. Sarah A. Styler and Dr. Manolis N. Romanías. Sample preparation for electron microprobe analysis was performed by Maya Abou-Ghanem, which were analyzed Dr. Britta J. L. Jensen with help from Maya Abou-Ghanem. The manuscript was written by Maya Abou-Ghanem, with critical comments from Dr. Sarah A. Styler.

Chapter 4

Ozone uptake and halogen activation by road dust and anti-icing solution: implications for wintertime air quality in high-latitude urban environments

Submitted as:

Abou-Ghanem, M.; Nodeh-Farahani, D.; McGrath, D.T.; VandenBoer, T.C.; and Styler, S.A. "Ozone uptake and halogen activation by road dust and anti-icing solution: implications for wintertime air quality in high-latitude urban environments" in *Environmental Science: Processes & Impacts*. Submitted September 18th, 2021.

Contributions

All coated-wall flow tube and halogen activation experiments were carried out by Maya Abou-Ghanem. Anion quantification was performed by Danial Nodeh-Farahani under the supervision of Dr. Trevor C. Vandenboer. The manuscript was written by Maya Abou-Ghanem, with critical comments from Dr. Sarah A. Styler and Dr. Trevor C. VandenBoer.

Chapter 5

Design and first experiments of an aerosol flow tube reactor

Contributions

All experiments were carried out by Maya Abou-Ghanem. The manuscript was written by Maya Abou-Ghanem, with critical comments from Dr. Sarah A. Styler.

Chapter 6

Conclusions and future research directions

Contributions

The manuscript was written by Maya Abou-Ghanem, with critical comments from Dr. Sarah A. Styler.

I dedicate my PhD thesis to my mother, Julia Abou Ghanem.

Acknowledgments

First, I would like to express my deepest gratitude to my supervisor, Dr. Sarah Styler, for her endless support and wisdom over the past five years. As a member of Sarah's first cohort of graduate students, I vividly recall my first tour of the Styler Research Group laboratory in 2016, which at the time, only contained a few pieces of glassware and a solar simulator. It has been a privilege to help grow your laboratory from the ground up and see it become the success it is today–even if I had to witness first-hand how expensive laboratory instrumentation and equipment can be. I could not have chosen a supervisor more supportive of my curiosity for science, independence as a researcher, and future career aspirations. Lastly, I would like to thank Sarah for cultivating a research group based on equity, diversity, and inclusivity. Sarah's advocacy for the representation of marginalized groups in academia has helped me overcome my own challenges of being a minority in STEM, which has given me the confidence to continue to pursue scientific research while working towards dismantling the systematic biases in science.

I would like to thank Ming, Mario, and Patrick for being amazing colleagues and making my graduate school experience enjoyable. I am grateful for our discussions about science and life while sipping beers at RAT and Dewey's. Furthermore, I would like to thank Brett Wickware, Zhihao Chen, Yi Cai, Amanda Aantjes, Lisa Michelat, Katica Naude, and Luxiga Thanabalachandra for being such an excellent group of mentees. My research projects would not have been possible without your hard work and dedication. Finally, I am thankful for my supervisory committee, Dr. Wolfgang Jäger and Dr. Jason Olfert, as well as Dr. Ran Zhao for their advice and support.

The design and construction of my flow tube systems would not have been possible without the Department of Chemistry machine shop. Thank you, Vincent Bizon, Dirk Kelm, Dieter Starke, and Paul Crothers for your brilliant ideas and innovations, which have helped me design some of the most aesthetic flow tubes my field has ever seen. Thank you to Jason Dibbs at the glass blowing shop who was always able to perfect my glass apparati, regardless of abstract they were. Thank you to Andrew Hillier, who was formerly at the electronics shop, for helping me wire UV-lights and relative humidity sensors. Thank you to Wayne Moffat and Jennifer Jones at the Analytical Services Laboratory for letting me use your analytical balance about a million times and for offering your expert advice whenever I was faced with technical difficulties.

During my graduate degree, I was fortunate enough to attend two international conferences, which lead me to meet inspirational researchers in my field. In particular, Dr. Manolis Romanías, whom I met at the DUST 2018 conference in Bari, Italy, and later had the privilege of working for during a Mitacs Globalink Research Award in Lille, France. Thank you, Manolis, for spending the time to train me on new instrumentation and experimental set-ups, regardless of how many U-shaped sample holders I broke. I am also grateful for the opportunity

to participate in the INVOC CESAM campaign in Paris, where I learned about the many experimental challenges of conducting smog chamber experiments. Thank you to everyone at LISA, including Edouard Pangui, Mathieu Cazaunau, Dr. Joel de Brito, Dr. Paola Formenti, and Dr. Jean-François Doussin.

Thank you to my family for their constant love and support. My mother, Julia, for always believing in me and helping through the tough times. My brother, Rami, who would often refer to himself as my "tech support" whenever I needed to bug him for his programming skills. My father, Issmat, whose optimism is contagious and kept me in good spirit. Finally, I don't think I could have survived graduate school without my amazing friends, Jade, Mariam, Carol, Ghazal, Tokunbo, and Kristen. Whether we were binge watching a new TV series, trying out new food spots, having Rock Band nights, camping, travelling, or video chatting, I've truly cherished all our moments and am eternally grateful for each one of you.

Table of Contents

List of Figures

List of Tables

List of abbreviations

Abbreviation	Phrase
AAS	Atomic absorption spectroscopy
AMS	Aerosol mass spectrometer
ATD	Arizona test dust
ATOFMS	Aerosol time of flight mass spectrometer
APS	Aerodynamic particle sizer
AQ	Air quality
ATD	Arizona test dust
BET	Brunauer-Emmett-Teller
BVOCs	Biogenic volatile organic compounds
CIMS	Chemical ionization mass spectrometer
CCN	Cloud condensation nuclei
CPC	Condensation particle counter
DRIFTS	Diffuse reflectance infrared Fourier transform spectroscopy
EDS	Energy dispersive spectroscopy
EDXRF	Energy dispersive X-ray fluorescence
EMPA	Electron microprobe analysis
FTIR	Fourier transform infrared spectroscopy
IC	Ion chromatography
ICP-AES	Inductively coupled plasma atomic emission spectroscopy
ICP-MS	Inductively coupled plasma mass spectrometry
IN	Ice nuclei
INAA	Instrumental neutron activation analysis
HPLC	High performance liquid chromatography
MFC	Mass flow controller
OPC	Optical particle counter
PAHs	Polycyclic aromatic hydrocarbons
PALMS	Particle analysis by laser mass spectrometry
PIXE	Particle induced X-ray emission
PM	Particulate matter
$PM_{2.5}$	Particulate matter (<2.5 μm in diameter)
PM_{10}	Particulate matter (<10 μm in diameter)
RH	Relative humidity
SEM	Scanning electron microscope
SEMS	Scanning electrical mobility spectrometer
SMPS	Scanning mobility particle sizer
TC	Total carbon
TD-GC/MS	Thermal desorption gas chromatography mass spectrometry

TOC	Total organic carbon
VOCs	Volatile organic compounds
WDS	Wavelength dispersive spectroscopy
WDXRF	Wavelength dispersive X-ray fluorescence
XPS	X-ray photoelectron spectroscopy
XRD	X-ray diffraction
XRF	X-ray fluorescence

Chapter 1

Introduction

Contributions:
This manuscript was written by Maya Abou-Ghanem with critical comments from Dr. Sarah A. Styler.

1.1 Atmospheric dust

Earth's chemically complex atmosphere is comprised of gases and suspended liquid or solid particles in air, known as particulate matter (PM). Atmospheric dust is a large contributor to PM mass loadings with global model emission estimates ranging from 500–4400 Tg yr^{-1}.[1] On average, the residence time of dust in the atmosphere ranges from 1.6 to 7.1 days[1] but can be over two weeks during transatlantic transport.[2] During its atmosphere lifetime, dust can influence climate, air quality (AQ), and health; for example, dust can directly impact climate by scattering and absorbing light, and indirectly by influencing the formation of clouds.[3] Furthermore, because atmospheric dust particles span a large size range (<0.5 to >75 μm in diameter)[4,5], they contribute to particulate matter less than 10 μm in diameter (PM_{10}) and particulate matter less than 2.5 μm in diameter ($PM_{2.5}$), both of which can be inhaled and lead to respiratory and cardiovascular health issues.[6] Finally, atmospheric dust provides a reactive surface in the atmosphere for chemical transformation of pollutant species,[7,8] which can impact regional AQ during periods of high dust loadings by changing the chemical composition of both the troposphere[9] and dust particles themselves.[10] The influence of atmospheric dust on climate, AQ, and health is complicated by the fact that its physicochemical properties are governed by its composition, which is dependent on its source[11,12] and chemical evolution during its atmospheric lifetime.[10]

1.1.1 Natural dust: source regions, chemical composition, and transport

Earth's crust is the thinnest, most-outer layer of Earth and contains, on average, Si (28.2%), Al (8.2%), Fe (5.6%), Ca (4.2%), Na (2.4%), Mg (2.3%), K (2.1%), and Ti (0.6%).[13] Geothermal and geochemical processes lead to the transformation of crustal elements into minerals, which are inorganic solids that contain an ordered and repeating arrangement of atoms (*i.e.*, crystalline).[14] Most minerals that exist on Earth are oxidized because of the oxygen-rich environment;[14] as a result, elemental quantification of crustal material is often reported in oxide form.[15] Approximately 90% of minerals on Earth belong to the silicate mineral group, which contain silica tetrahedrons (SiO_4^-) as their basic building blocks for crystal lattices;

however, Al substitution for Si is common and can lead to the formation of Al-rich silicates.[16] Other mineral groups found on Earth include native elements,[17] sulfides, oxides, halides, carbonates, sulfates, and phosphates.[18,19]

Minerals that comprise the uppermost layer of Earth's crust are the most susceptible to physical, chemical, and biological weathering, which can result in their breakdown to smaller particles that can become airborne when surface winds are sufficient for suspension.[14] The atmospheric residence time of mineral dust is highly dependent on particle size, as larger particles are more likely to experience gravitational settling[20], which is governed by the Stokes equation.[21] Evidence for this settling has been observed in a number of field studies;[22–24] however, turbulence, strong convective clouds, and triboelectric effects can result in long-range transport of giant mineral dust particles (>75 μm in diameter).[25] Transport-related changes in mineral dust size distributions are also often associated with changes in dust mineralogy and morphology;[26,27] for example, Glaccum et al. attributed decreasing quartz:clay content with increasing atmospheric transport time in Saharan dust to the settling of quartz particles, which have a larger mass median diameter compared to clays.[26]

Aeolian dust can be transported thousands of kilometers; one classic example of this phenomenon is the Saharan air layer (SAL), a warm, dry air mass, which transports billions of tons of Saharan dust each year from the west coast of Africa to the Atlantic Ocean, Europe, North America, and South America (Figure 1.1).[28] The deposition of this dust into the Atlantic Ocean and South America provides an important source of micronutrients for oceanic phytoplankton[29] and soil in the Amazon rainforest,[30] respectively. Asian mineral dust, which originates from deserts in China and Mongolia, can also undergo long-range transport and reduce AQ in Japan[31] and Taiwan.[32]

1.1.1.1 Mineral dust from warm desert regions

Low-latitude deserts are by far the largest contributors to natural dust in the atmosphere with ~ 50, 40, and 10 % of global dust loadings (20 μm in diameter) from North Africa, Asia, and

North American and Southern Hemisphere regions, respectively.[33] These areas can be further divided into nine source regions, which include (1) western North Africa, (2) eastern North Africa, (3) the southern Sahara and Sahel, (4) the Middle East and central Asia (which includes the Horn of Africa), (5) East Asia, (6) North America, (7) Australia, (8) South America, and (9) southern Africa.[33]

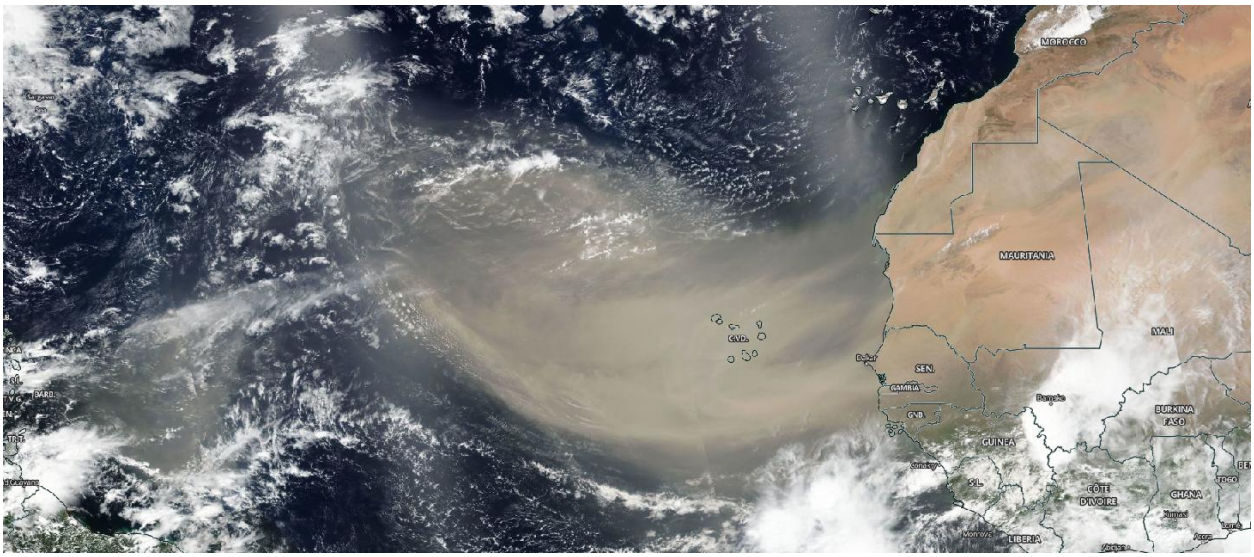

Figure 1.1: A satellite image of a Saharan dust plume captured by the National Aeronautics and Space Administration (NASA)-National Oceanic and Atmospheric Administration (NOAA) Suomi National Polar-orbiting Partnership on June 18th, 2020. The dust plume, shown in light brown, is being transported off the west coast of Africa into the Atlantic Ocean. Image (with adapted caption) obtained from NASA Worldview.[34]

Despite the fact that mineral dust is generally composed of quartz, clay, feldspar, gypsum, calcite, hematite, and goethite minerals,[11] its chemical and mineralogical composition is still source dependent.[11,35–37] For example, illite/kaolinite ratios in the clay fraction of mineral dust have been used to identify dust source regions[38] because dust from northern Africa is known to contain a lower illite/kaolinite ratio (<2) compared to Asian dust (>5).[36] Calcite content in mineral dust also varies with source location,[36] as calcite content in dust source regions decreases with increasing annual rainfall.[11] However, the identification of dust source regions based off the mineralogical analysis of collected samples is not always conclusive; instead,

satellite imagery and air mass back trajectory models are also used to predict the original sources of atmospheric dust.[39]

1.1.1.2 High-latitude glaciogenic and volcanic dust

Although warm desert regions are the largest source for natural atmospheric dust,[33] high-latitude regions contribute up to ~ 5% of global dust loadings[40] and ~ 27% of dust loadings in the Arctic.[41] In the Northern Hemisphere, high-latitude dust regions include Alaska, Canada, Iceland, and Greenland, and in the Southern Hemisphere, they include Antarctica, New Zealand, and Patagonia.[40] In contrast to warm deserts, high-latitude dust is often formed by the frictional movement of glaciers, which can displace, break-down, and expose sediments that can become subject to atmospheric transport by surface winds.[42] While high-latitude dust source regions cover a significantly smaller land area compared to lower-latitude deserts, their cold, dense air results in some of the strongest winds on Earth, which allows for more efficient dust transport.[43,44]

The chemical composition of high-latitude dust is significantly less studied than mineral dust from desert regions; however, studies have shown it contains similar mineral classes to desert dust.[45–47] For example, Bachelder and coworkers found that mineral dust emitted from a retreating glacier area in Yukon, Canada contained ~45% clay with lesser amounts of feldspar, quartz, calcite, amphiboles, gypsum, and dolomite minerals.[45] Similarly, topsoil from Patagonia and aeolian dust collected in the Argentinian Pampas was also found to be high in clay content.[46,47] In addition to its dominant clay fraction, dust from these South American regions can also contain materials of volcanic origin.[47]

In regions with high volcanic activity, magma is cooled too rapidly to form minerals, and instead, leads to the production of glass, which is amorphous (*i.e.*, non-crystalline).[48] This glassy composition is also reflected in volcanic dust;[49,50] for example, dust from Iceland, the most volcanically active region in the world and largest source for high-latitude dust,[42] is predominantly composed of glass rich in Fe, Ti, Mg, and Ca.[49] In addition, unlike mineral dust,

which is abundant in clay and quartz minerals,[51,52] the mineral component of Icelandic volcanic dust contains pyroxene, olivine, and plagioclase minerals.[49] These minerals are often embedded in the glass fraction or exist as individual micron-sized grains.

1.1.2 Anthropogenic dust: source regions, chemical composition, and transport

Although anthropogenic dust, which is emitted from human activities, has existed since the Industrial Revolution,[53] its contribution to atmospheric dust loadings was neglected until the mid-1990s.[54] Humans are responsible for both indirect and direct anthropogenic dust emissions;[55] for example, indirect emissions have been attributed to the exposure of fresh soils from land modification by deforestation and agriculture.[54] Direct dust emissions can arise from vehicular traffic,[56] mining operations,[57] farming,[58] fossil fuel extraction,[59] and construction activities.[60] The chemical composition of anthropogenic dusts can be much more complex than mineral dust because they often contain significant components of non-crustal material.[57,59,61] To date, only dust emissions from land modification have been included in global dust models,[33,62,63] which will result in underestimations of ambient dust loadings.

1.1.2.1 Industrial dust

Industrial areas are a significant source for fugitive dusts (*i.e.*, dust generated by open air operations), which can be emitted by wind,[64,65] vehicular traffic,[64] mining operations,[66] and construction activities[60]. According to one study, surface disturbances by traffic on unpaved roads in the Athabasca oil sands region in northeastern Alberta can increase PM_{10} emissions by a factor of 9 to 160 compared to background levels.[64] Likewise, haul and transport roads in mining areas are also a significant source for local PM emissions.[66]

Often, industrial dusts are more harmful to human health than mineral dust because of their enrichment of toxic, heavy metals,[57,67] and carcinogenic organic species (*e.g.*, polycyclic aromatic hydrocarbons (PAHs))[59]. For example, Brotons and coworkers detected high concentrations of Pb and Zn (~75 and 65 ppm, respectively) in wind-blown dusts from a mining waste area in southeast Spain.[65] Similar to mineral dust, fugitive dust from the

Athabasca oil sands region is abundant in Al, Si, K, Ca, and Fe; however, the organic content of this dust is much higher (9–11%), which is reflective of local combustion emissions and bitumen.[59] Together, industrial dusts can pose a serious human health hazard for frontline workers and residents of nearby communities;[57,58,60] as a result, much research has focused on dust suppressant techniques to mitigate industrial dust emissions.[68–70]

1.1.2.2 Urban road dust

In an effort to reduce traffic-related PM, stricter regulations on vehicular exhaust emissions over the last several decades have been imposed in many locations;[71] however, in many urban centers, road dust resuspension still remains a dominant source of PM.[56] Road dust is a complex mixture of non-exhaust emissions (*e.g.*, brake and tire wear particles), road abrasion, road salts, plant debris, and stormwater/meltwater runoff.[56,61,72] Like mineral and industrial dusts, the chemical composition of urban road dust is location specific; for example, in regions with mild winters, non-exhaust emissions are the dominant source of road dust PM,[73] which are known to contain heavy metals (*e.g.*, Pb, Zn, Cu, Cd, Ba, Sb and Ni),[74] whereas in cold-climate areas, road dust composition is dominated by salts[72] and crustal material[75] due to the application of road salts and sand, respectively.

Urban road dust can have local environmental and health effects;[76–78] for example, in Edmonton, Canada, the application of road salts has been found to induce stress in urban trees by increasing soil salinity.[76] Furthermore, Yu and coworkers determined higher than baseline cancer risks from PAHs in road dust samples collected from Tianjin, China for city residents using the Incremental Lifetime Cancer Risk model.[79] In addition to local effects, road dust components can also distributed globally.[80] Recently, brake and tire wear particles have been found to be a dominant source of atmospheric microplastics,[81] with an estimated 140 and 86 kt deposited into the ocean and on snow/ice surfaces (in polar and mountain regions), respectively, each year.[80] This demonstrates that like mineral dust, road dust can also undergo long-range transport to remote regions.

1.2 Chemical characterization techniques for atmospheric dust

The chemical and mineralogical composition of atmospheric dust has been characterized by a variety of sampling and analytical techniques,[82] which each offer their own advantages and disadvantages. In this section, these techniques will be described, in addition to their strengths and weaknesses.

1.2.1 Offline measurements

Offline sampling of atmospheric dust is typically carried out in two ways: 1) filter collection[45,83] and 2) grab sampling.[84] For filter collection, ambient dust is either sampled passively (*i.e.*, without flow control)[83] or actively (*i.e.*, by a vacuum pump).[45] The latter technique can allow for particle size selection; for example, cascade impactors can be placed prior to the inlet of the sampler to control the transmission of particles within a given size range.[85] Depending on the atmospheric dust loadings in the sampling area of interest, dust mass may be limited and require collection over long periods of time. On the other hand, grab sampling from a source region is not sample-limited but requires sieving to obtain the smaller fractions that can become airborne.[84,86] This sampling method involves manual collection by sweeping (*e.g.*, dust pan and brush) or scooping;[86] however, in the case of road dust, vacuums and street sweepers have also been employed for collection.[56] Most studies use offline sampling techniques because they are less costly and simpler to operate; however, offline sampling techniques come with several caveats; for example, the temporal data collected during offline analysis is weakly resolved. In addition, semi-volatile components of dust,[87] may partition to the gas phase prior to characterization.

1.2.1.1 Bulk elemental analysis

Bulk elemental analysis is the most common approach for the chemical characterization atmospheric dust and includes analysis by inductively coupled plasma mass spectrometry (ICP-MS),[59,88–90] inductively coupled plasma atomic emission spectroscopy (ICP-AES),[91–93] and atomic absorption spectroscopy (AAS),[94] all of which require acid digestion (*e.g.*, HNO_3, HF,

or HCl) for metal dissolution prior to analysis.[82] In ICP-MS, a plasma is used to atomize/ionize the sample and individual ions are detected by a mass spectrometer based on their mass to charge ratio; whereas, in ICP-AES, the sample is atomized/excited by a plasma and the emitted characteristic electromagnetic radiation of an excited state atom is detected by an optical spectrometer.[95] In contrast, AAS uses a flame/graphite furnace to atomize the sample and the characteristic wavelengths absorbed from a set of hollow cathode lamps is detected by an optical spectrometer; however, compared to ICP-OES/ICP-MS, AAS has a slower analysis time because it is a single element technique.[95] Since ICP-MS, ICP-OES, and AAS are sample destructive, they do not provide insight on elemental speciation; however, they can detect elements at trace levels (ppb and sub-pbb levels). Together, these methods have been successfully used to determine elemental abundances of mineral dust[90,92] and volcanic dust[89,91] (*e.g.*, Si, Al, Ca, K, Na, Mg, Fe, K, and P), as well as heavy metals in road dust[74,88,93] and industrial dust[59,88] (*e.g.*, Ba, Cu, Zn, Pb, Sb, Ni, V, Cd).

Non-destructive bulk elemental analysis for dust is typically performed by X-ray spectroscopy,[82] with the most common technique being X-ray fluorescence (XRF).[27,65,96,97] In this technique, a dust sample is excited by an incident X-ray beam and the emitted characteristic fluorescent wavelengths from individual atoms are dispersed by wavelength [wavelength dispersive X-ray fluorescence (WDXRF)] or by energy [energy dispersive X-ray fluorescence (EDXRF)] and detected.[98] Despite the ability of XRF to sample within a given area, it is still considered a bulk analysis technique because the incident X-ray beams are large (μm to mm range) and able to represent the chemical composition of an entire dust sample.[99] Other non-destructive techniques, including particle induced X-ray emission (PIXE)[100–103] and instrumental neutron activation analysis (INAA)[102,104] have also been used for bulk elemental analysis of dust. In contrast to XRF, PIXE uses a proton beam to excite the sample;[98] whereas in INAA, radioactive isotopes of elements within the sample are formed from the bombardment of an incident neutron beam and their subsequent radioactive emissions are measured.[105] Compared to PIXE and INAA, XRF offers the greatest sampling depth, as X-rays

penetrate deeper (μm to mm range) than electron, proton, and neutron beams.[98] Finally, since the emitted X-rays from lighter elements have longer wavelengths, they can be easily absorbed by the sample; as a result, XRF and PIXE are not suitable for the detection of lighter elements (atomic number <11).[98]

1.2.1.2 Spot-selected elemental analysis

X-ray spectroscopy is also used for instances of individual particle analysis or elemental speciation of dust particles; [45,106,107] however, it is often coupled to electron microscopy to spot-select regions for chemical characterization. Electron microscopy involves bombardment of a sample by a high energy electron beam, which produces electron images through the detection of transmitted electrons [transmission electron microscopy (TEM)] or reflected/secondary electrons [scanning electron microscopy (SEM)].[108] While both imaging techniques provide information on particle size and morphology (Figure 1.2),[109] SEM and TEM images offer greater surface details and inner structural details, respectively.[108] Like XRF, SEM and TEM are commonly coupled to energy dispersive spectrometers (EDS) to detect X-ray emissions.[98] Electron microprobe analysis (EMPA) uses a similar operating principle as SEM-EDS; however, it provides more quantitative elemental analysis because emitted X-rays are detected by a wavelength dispersive spectrometer (WDS), which has a greater wavelength resolution.[98] In contrast to XRF, these techniques use a narrow electron beam for surface excitation,[98] which makes them capable of spot-selected elemental analysis within individual particles.[106,107,109] However, since many components of dust are non-conducting, surface charging can be a problem during imaging, which usually requires samples to be coated with a conductive film (*e.g.*, carbon, gold, etc.).[45,106]

The greatest advantage of spot-selected elemental analysis is that it can be used to predict the elemental speciation in dust samples based on elemental abundance ratios. For example, as I outline in Chapter 3 of this thesis, EMPA has been used to show that Ti in Icelandic volcanic dust is mainly found in the glass fraction.[110] In addition, elemental abundance ratios have been used for putative qualitative and semi-quantitative mineralogical identification in natural

dusts.[45,106,107,111,112] Finally, spot-selected techniques have also been used to look for chemical tracers to differentiate between tire, brake, and road wear related components in road dust particles.[86]

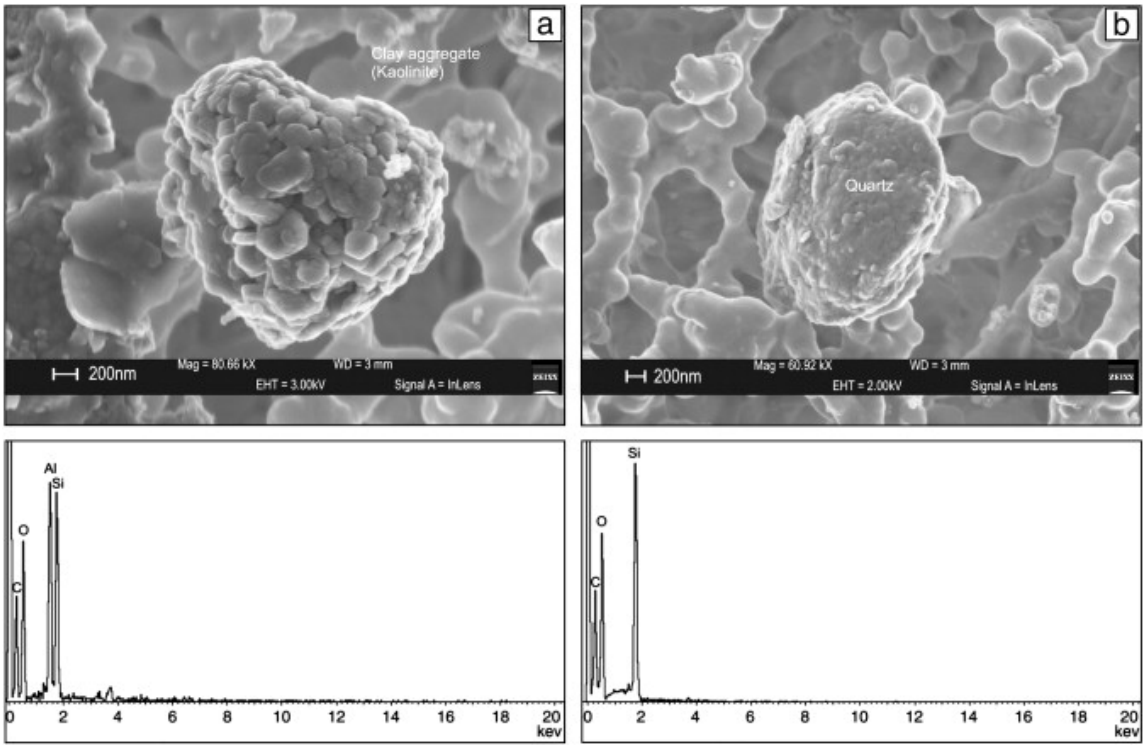

Figure 1.2: SEM-EDS analysis of mineral dust particles sampled from Potenza, Italy: a) an agglomerate kaolinite particles and b) a rounded quartz particle. Image reprinted from *Atmos. Res.* 102, (1-2), Caggiano et al. $PM_{2.5}$ measurements in a Mediterranean site: Two typical cases. 157–166, **2011**,[112] with permission from Elsevier.

1.2.1.3 Surface elemental analysis

Since many dust properties, including heterogeneous chemistry and cloud condensation nuclei (CCN) efficiency are governed by the chemical composition of the particle surface,[113] some studies have used X-ray photoelectron spectroscopy (XPS) for elemental surface analysis.[91,110,114–116] In this technique, an incident X-ray beam is focused onto a dust substrate and the number and kinetic energy of generated photoelectrons is measured to determine both the elemental abundances at the surface (1-100 nm) and the binding energy of electrons.[117] These binding energies can be used to predict the chemical speciation of atoms in dust; for

example, the carbon binding energy for industrial dust from an open pit mining area in northern Colombia has been shown to be consistent with that of graphite.[115] Furthermore, XPS has been used to identify the chemical speciation of Hg, a harmful neurotoxin,[118] in anthropogenic dusts to better understand its binding affinity towards individual components of dust.[116,119]

1.2.1.4 Mineralogical analysis by X-ray diffraction

Qualitative mineralogical analysis is achieved using X-ray diffraction (XRD), which involves the illumination of a dust sample by an incident X-ray and detection of the diffracted X-rays.[120] The obtained diffractograms contain unique X-ray signatures for individual mineral phases, which can be fit to geological standards from mineralogical databases.[106] XRD has been successfully applied to determine the mineral phases in mineral dust,[84] volcanic dust,[49] and road dust.[121] In addition, XRD has been used to track mineralogical changes in mineral dust during atmospheric transport[37] and identify dust source regions.[49] Finally, XRD is not only limited to mineralogical analysis of dust; for example, this technique has been used to identify 5-(4-methoxyphenyl)tetrazole, a crystalline organic material in ground brake pad material.[122]

Although more challenging, quantitative mineralogical analysis can be achieved by XRD using Rietveld refinement, which fits the entire diffractogram to multiple phases.[123] This has recently been demonstrated by Nowak and coworkers, who used Rietveld refinement to quantify the clay, quartz, calcite, dolomite, and microcline mineral mass fractions in Niger and Tunisian dust samples.[124] Furthermore, Rietveld refinement has also been used to identify mineralogical impurities in natural Ti-containing minerals relevant to mineral dust.[106]

1.2.1.5 Biological, ionic, and organic/elemental carbon analysis

It is well established that mineral dust serves as an important transport vector for biological agents (*e.g.,* bacteria, viruses, and fungi) in the atmosphere.[125–127] Not only are these biological agents a human health concern,[128] but they can also significantly increase the ice nucleation (IN) efficiency of mineral dust particles, thereby influencing the formation of clouds.[129]

Typically, biological materials in airborne dust are characterized using gel electrophoresis,[130] fluorescence,[126] DNA sequencing,[131] and staining[127,131] techniques. Furthermore, morphological features of dust particles provided by microscopy (*e.g.*, SEM-EDS) can be used to identify biological material in mineral dust.[132]

Atmospheric dust can also contain water-soluble inorganic (e.g., Cl^-, Br^-, NO_3^-, SO_4^{2-}, PO_4^{3-}, Na^+, Mg^{2+}, NH_4^+) and organic (*e.g.*, formate, acetate, oxalate) salts.[102,133,134] Although some of these ions can be measured directly in dust by Fourier transform infrared spectroscopy (FTIR),[135] they are often extracted from dust using water and analyzed by ion chromatography (IC),[102,133,134] which separates molecules based on their ionic interactions with an ion-exchange resin.[95] In addition, as I will show Chapter 4, IC analysis has been used to quantify significant amounts of chloride content in Edmonton road dust leachate induced by winter road salting.[136] Furthermore, inorganic and organic ions have been measured by IC in collected samples during Saharan[102,133] and southern Asian dust events,[137] as well as in fugitive dust from the Athabasca oil sands region.[59] However, one major limitation of this technique is that the degree of leaching depends highly on the extraction method used,[138] which may underestimate the soluble ion content of a given dust sample.

Additional organic analysis techniques for dust include thermal desorption gas chromatography mass spectrometry (TD-GC/MS), which is used to measure the semi-volatile organic components of dust.[59,87] For example, Wang and colleagues used TD-GC/MS to identify PAHs, *n*-alkanes, branched alkanes, and cyclic alkanes in fugitive dust from the Athabasca oil sands region.[59] In addition, fluorescence has been used to measure humic-like substances in road dust.[139] Furthermore, other spectroscopic techniques, including FTIR and Raman have also been employed to detect organics in mineral dust.[140] Finally, total mass fractions of organic carbon and elemental carbon in natural and anthropogenic dusts have been determined using dry combustion,[136] thermogravimetric,[122,141] and loss-on-ignition[142] techniques.

1.2.2 Online Measurements

Studies that require high temporal and spatial resolution turn to online instrumentation for the chemical characterization of atmospheric dust. Although online measurements are most used in field studies,[143–148] laboratory studies of dust heterogeneous chemistry have also coupled online measurement techniques to atmospheric reaction chambers and flow tubes to monitor changes in the chemical composition of dust particles over time.[149–151]

1.2.2.1 Bulk analysis

Aerosol mass spectrometry (AMS) is the most common online bulk analysis technique, which uses thermal evaporation to vaporize components of dust PM that are then measured by mass spectrometry.[152] In addition, these instruments contain an a time-of-flight region upstream of the heated impactor, which is used to estimate the size of individual particles. Despite the inability of AMS to detect refractory (non-vaporizable at 600°C; *e.g.*, minerals, soot, sea salt) components of dust, it is useful for measuring non-refractory components (vaporizable at 600°C; *e.g.*, organics, nitrates, and sulfates).[152] For example, AMS has been used to measure organic[149] and sulfate[150] mass fractions of laboratory generated internally mixed mineral dust particles to explore the role of these species on the IN efficiency of mineral dust. Finally, it is worth noting that AMS uses electron impact, a hard ionization technique that leads to significant molecular fragmentation, which greatly prevents the identification of parent organic molecules.[152]

1.2.2.2 Single-particle analysis

Over the last two decades, advancements in mass spectrometry have resulted in increased usage of single-particle mass spectrometry (SPMS) for individual dust analysis.[143–148,151] These SPMS instruments include particle analysis by laser mass spectrometry (PALMS)[153] and aerosol time of flight mass spectrometry (ATOFMS).[154] Unlike other dust characterization techniques, SPMS instruments use lasers to ablate and ionize both refractory and non-refractory components, which are then measured in positive and negative ion mode using a time of flight mass spectrometer.[153,154] As a result, SPMS is very advantageous for determining the internal

mixing state of individual dust particles.[145,151] However, the identified individual components are in their fragmented form because laser ionization leads to molecular fragmentation.[153,154]

Similar to AMS, ATOFMS determines particle size using aerosol time of flight,[154] whereas particle size in PALMS is measured by light scattering.[153] The identification of individual, size-resolved dust particles are based on chemical signatures provided by single-particle mass spectra and can include Al^+, Si^+, K^+, Fe^+, Ca^+, Ba^+, Rb^+, and Li^+ for mineral dust,[143] Pb^+ and Fe^+ for industrial dust,[146] Fe^+ FeO_2^-, Ba^+, and BaO^- for brake wear,[147] and unique mass to charge ratios for organic material (*e.g.*, m/z 41, 43, and 69) in tire dust.[148]

1.3 Evidence for dust–pollutant interactions observed in the field

In the mid 1990s, Dentener and colleagues used a global three-dimensional model to propose that mineral dust heterogeneous chemistry has the potential to influence the gaseous composition of the troposphere.[155] Since the time of this study, fluctuations in pollutant gas mixing ratios during major dust events have been observed in the field,[9,156–160] as well as changes in the chemical composition of dust itself.[145,161] These dust–pollutant interactions result in formation of internally mixed mineral dust particles, which can have different optical,[162] CCN[163]/IN,[149] reactive,[164,165] and toxicological[166] properties than the parent material.

1.3.1 Evidence for changes in tropospheric gas composition

Numerous field studies have reported correlations between gas mixing ratios and dust loadings;[9,156–160] for example, reductions in HNO_3 mixing ratios during major mineral dust events have been observed near the Canary Islands[156,158] and in the northeast Pacific.[157] Furthermore, de Reus and coworkers observed reductions in ozone mixing ratios of up to 40% during mineral dust episodes near the Canary Islands, which they attributed to both dust scavenging of HNO_3 (a precursor for ozone) and ozone.[156] Similarly, ozone depletion has also been observed during dust events in northern China.[9] Finally, dust events can suppress photochemical oxidant cycles by reducing the transmission of sunlight to Earth's surface.[167,168]

For example, Li et al. observed reductions in the photochemical production of ozone by 5–20% and OH radicals by ~9% during dust episodes in Mexico City.[168]

Only recently have researchers started to consider the implications of anthropogenic dust–pollutant interactions on the troposphere.[96,169,170] Although most of these studies have been conducted in laboratory settings,[96,170] McNamara and colleagues attributed 80–100% of $ClNO_2$, an important precursor gas for the reactive chlorine atom,[171] to N_2O_5 uptake by road salts in Ann Arbor, Michigan.[169] Finally, elevated levels of $ClNO_2$ during early spring in Calgary, Alberta have also been attributed to reactive N_2O_5 uptake by road salts.[172,173]

1.3.2 Evidence for changes in dust composition

Dust–pollutant interactions can lead to the formation of internally mixed particles, often referred to as "atmospherically aged" or "atmospherically processed" dust. Changes in dust composition have been observed in several field studies;[10,114,169] for example, Goel and coworkers observed the transformation of calcite to calcium chloride, calcium nitrate, and calcium sulfate in mineral dust analyzed after a dust storm in Delhi, India.[114] Similarly, during the ACE-Asia campaign, Sullivan et al. observed high amounts of nitrates and sulfates on Ca-rich and aluminosilicate-rich mineral dust, respectively.[10] The formation of surface nitrates, sulfates, and chloride on mineral dust is thought to occur from mineral reactions with NO_y (*e.g.*, NO_2,[174,175] HNO_3,[175] and N_2O_5[176]), SO_2,[174,177] and HCl,[178] respectively. Sulfate and nitrate enrichment from atmospheric processing has also been observed in aged road salt, as well as chloride depletion, which was attributed to $ClNO_2$ release during N_2O_5 uptake by road salt.[169]

Aged dust can also be internally mixed with organics;[64,87,144,179–181] for example, during the Atlanta SuperSite Project, Lee and colleagues identified the presence of organic material in individual mineral dust particles using PALMS (Figure 1.3).[144] Furthermore, Falkovich and colleagues used TD-GC/MS to identify PAHs, pesticides, and biocides in mineral dust transported from the Sahara Desert to Tel Aviv, Israel.[87] In addition, these authors used SEM-EDS analysis to determine that the organics in these internal dust mixtures take on the form

of coatings. Finally, organic acids, including formate[180,181] and acetate[180] have been found to be internally mixed with mineral dust, which is likely a result of mineral reactions with acetic and formic acid, respectively.[182]

Changes in dust composition are not only limited to its reaction with pollutant gases but also from internal mixing with other PM classes; for example, mixed sea salt and mineral dust particles have been observed in the marine boundary layer off the east coast of Asia during Taklimakan and Gobi desert dust events.[183] In addition, Paris and coworkers found that Fe speciation in biomass burning particles in Niamey, Niger, was of mineral dust origin,[134] , which suggests internal mixing between dust and biomass burning PM. Similarly, internal mixing of biomass burning PM and sea salt with mineral dust has been observed during transatlantic transport of Saharan dust.[184] Finally, Smith and coworkers observed higher than background levels of microbial mass in PM during transpacific dust plume events in Oregon, United States, which suggests that internal mixing between dust and biological agents persists during long-range transport.[185]

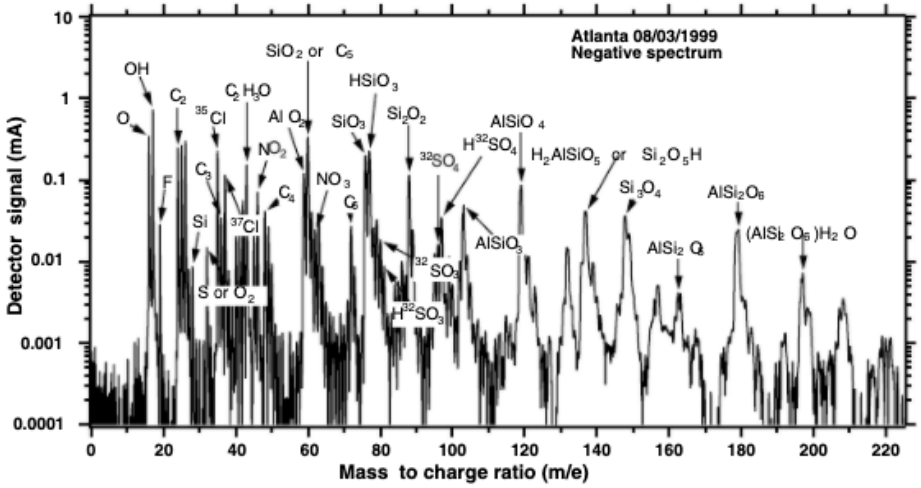

Figure 1.3: A mass spectrum of an individual mineral dust particle sampled by the PALMS in negative ion mode during the Atlanta SuperSite Project. Al and Si-containing chemical signatures indicate the mineral components of the particle whereas carbon-containing signatures signify the presence of organic material (image and caption adapted from Lee et al.).[144]

1.4 Laboratory dust heterogeneous chemistry studies

1.4.1 Determination of pollutant gas uptake by dust substrates

To quantify the reactivity of dust PM towards a pollutant gas, atmospheric scientists use an uptake coefficient (γ), which is defined as the number of gas molecules taken up by a surface divided by the total number of gas molecule collisions with the surface.[113] The uptake of a pollutant gas by a given dust substrate can involve both reactive (via chemical transformation) and non-reactive (via adsorption) processes at the dust surface.[7] Although uptake coefficients do not provide any mechanistic details regarding these reactive and non-reactive processes, they can be incorporated into atmospheric models to estimate the quantitative impacts of dust–pollutant interactions on the chemical composition of the surrounding atmosphere.[186]

1.4.1.1 Initial and steady-state uptake coefficients

Often, the uptake of a pollutant gas by a dust substrate is time-dependent due to surface deactivation with increasing pollutant exposure time.[106,187–189] For example, as shown in Figure 1.4, ozone uptake by Gobi Desert dust is greatest during its initial exposure and slowly decreases over time until a plateau mixing ratio is reached (*i.e.*, steady-state).[187] As a result of this time dependent uptake, uptake coefficients are reported as either initial uptake (γ_0) or steady-state uptake (γ_{ss}).[7] Initial uptake coefficients are generally calculated seconds after a pollutant exposure to a dust substrate and include contributions from both reactive and non-reactive processes;[189–191] whereas the steady-state uptake coefficient captures the reactivity of dust over longer time periods and reflects only sustained uptake by reactive, regenerative surface sites.[106,188,189,192]

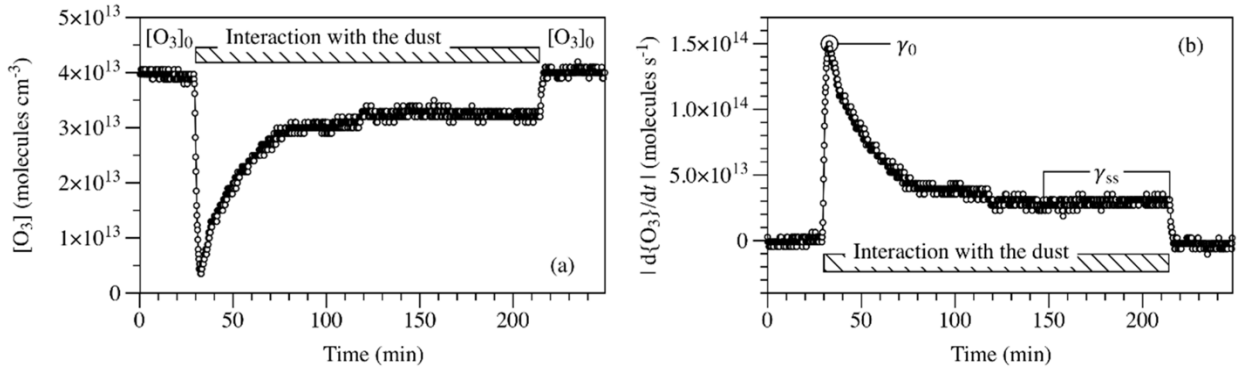

Figure 1.4: a) Reaction profile of ozone with Gobi Desert dust as a function of time. $[O_3]_0$ indicates the initial ozone mixing ratio in the absence of dust; and b) the total number of ozone molecules taken up by the dust surface as a function of exposure time (image and caption adapted from Wang et al.).[187]

1.4.2 Experimental techniques

Although the use of initial and steady-state uptake coefficients can be used to capture the heterogeneous reactivity of dust over time, these values can vary depending on the experimental technique used to study dust–pollutant interactions. For example, uptake differs with temperature, pressure, and relative humidity (RH),[7] which are often sensitive to the specific technique.[193] Together, this makes it difficult to use representative uptake coefficients in atmospheric models. A list of reported uptake coefficients from mineral dust–pollutant interaction studies have been summarized in a 2010 Gas Kinetic Data Evaluation for Atmospheric Chemistry by the IUPAC Task Group,[194] which is continuously updated on an online database (https://iupac-aeris.ipsl.fr/). In the following section, the determination of these uptake coefficients for each laboratory technique will be discussed.

1.4.2.1 Knudsen cells

In the early 1970s, Golden and colleagues used a Knudsen cell to investigate the rate of surface reactions for the first time.[195] Shortly after, Knudsen cells gained wide-spread popularity for dust heterogeneous chemistry studies.[97,189,196,197] In this technique, a dust substrate is placed in a sample holder, which contains an isolation plate to control the exposure of a pollutant gas of interest diluted in a carrier gas (*e.g.*, nitrogen, zero air) to a dust sample.[189] The sample holder

is also connected to an exit orifice, which is connected to a mass spectrometer for the measurement of the pollutant mixing ratio prior to and during exposure to dust (Figure 1.5).

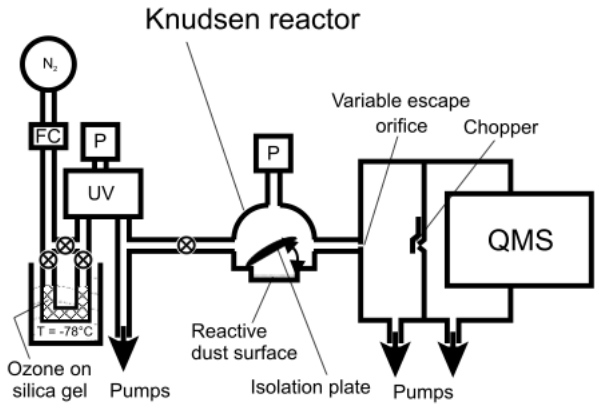

Figure 1.5: A schematic of a Knudsen cell used by Hanisch and Crowley to investigate ozone uptake by Cape Verde depositional dust from the Sahara Desert. Here, ozone is generated by a commercial ozone generator and stored on silica gel prior to being carried by a gas flow to the sample holder and detected by mass spectrometry (image adapted with permission from Dr. John N. Crowley).[189]

Knudsen cells operate under extremely low pressures (< 10 mTorr), so that the mean free path of the gas molecules is greater than the dimensions of the sample holder.[193] This results in a molecular flow regime, in which gas molecule collisions with the surface outnumber collisions in the gas-phase; as a result, the effusion of a pollutant gas is only driven by its heterogeneous reaction with the sample or its escape through the exit orifice. The uptake coefficient for Knudsen cell studies is determined as follows:[193]

$$\gamma_{eff} = \frac{A_h}{A_s}\left(\frac{N_0 - N_t}{N_t}\right) \tag{1.1}$$

Here, γ_{eff} is the effective uptake (*i.e.*, observed uptake), A_h and A_s are the geometric surface area of the exit orifice and dust, respectively, and N_0 and N_t are the measured mass spectral signals when the sampled holder is closed and open, respectively. In this calculation, the

uptake is scaled to the geometric surface area of the dust which neglects its porosity; as a result, obtained effective uptake coefficient values are often scaled to the total surface area, which is determined using the Brunauer–Emmett–Teller (BET) specific surface area and dust sample mass (γ_{BET}).[189,198]

Knudsen cells have been successfully used to investigate the uptake of ozone[177,189,196] and N_2O_5[199] by mineral dust; however, most Knudsen cell studies have been conducted on single-component mineral dust proxies.[196,200,201] In addition, Styler and coworkers developed the first photochemical Knudsen cell reactor,[198] which has been used to investigate the photochemical transformations of organic gases on mineral dust[97] and mineral dust proxies.[198] However, because of the low operating pressures required for Knudsen cell studies, gas uptake is measured in the absence of water vapour, which may bias reactivity parameters with respect to those obtained under ambient conditions.

1.4.2.2 Coated-wall flow tubes

In coated-wall flow tube experiments, a dust substrate is coated on the inner surface of a glass insert tube, which is housed in a horizontal reactor with an inlet and outlet for gas flow (Figure 1.6).[202] A movable injector is used to introduce the pollutant gas into the flow tube system, while also controlling the exposure time of the dust-coated tube to the pollutant gas. In addition, coated-wall flow tubes can be equipped with lights to investigate the photoreactivity of a dust substrate.[106,192] Unlike Knudsen cells, coated-wall flow tubes can operate at atmospheric pressure, which allows for investigations of gas uptake as a function of RH; however, for heterogeneous reactions that proceed quickly, coated-wall flow tubes have been operated under vacuum to reduce gas-phase diffusion limitations.[203]

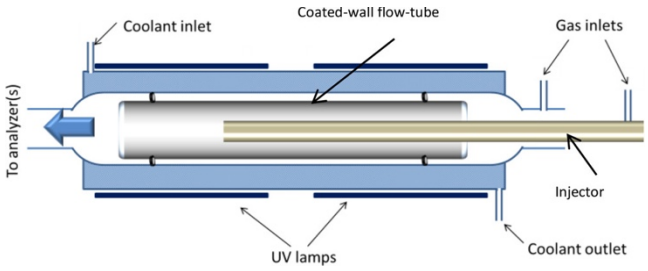

Figure 1.6: A schematic of a coated-wall flow tube used to investigate the uptake of ozone by commercial clays, kaolinite and montmorillonite. Here, ozone is introduced into the system via a movable injector and the difference in ozone mixing ratio is measured by a commercial ozone analyzer in both the absence (with the movable injector fully pushed in) and presence (with the movable injector retracted) of the dust-coated tube. Image (adapted) with permission from Lasne et al. Ozone Uptake by Clay Dusts under Environmental Conditions. *ACS Earth & Space Chem.* **2018**, 2, (9), 904–914.[202] Copyright 2018 American Chemical Society.

The removal rate of a pollutant gas by dust is generally assumed to proceed via a pseudo-first-order reaction. The pseudo-first-order rate constant (k_{obs}) for the removal of a pollutant, X, from the gas phase to the condensed phase is calculated using the following equation:

$$k_{obs} = \frac{\ln\left(\frac{[X]_t}{[X]_0}\right)}{-t} \tag{1.2}$$

Here, $[X]_t$ is the mixing ratio of pollutant X in the presence of dust, $[X]_0$ is the initial mixing ratio of pollutant X in the absence of dust, and t is the interaction time of pollutant X with dust. In coated-wall flow tube studies, k_{obs} is used to determine an effective uptake coefficient, which is scaled to the geometric surface area of the coated section of the tube. This uptake coefficient is calculated as follows:[193]

$$\gamma_{eff} = \frac{k_{obs} D_{tube}}{< c >} \tag{1.3}$$

Here, k_{obs} is the pseudo-first-order rate constant for the loss of a pollutant gas of interest, D_{tube} is the internal diameter of the Pyrex insert tube, $< c >$ is the mean molecular speed of the pollutant gas of interest. In many dust–pollutant laboratory studies, k_{obs} decreases with increasing pollutant mixing ratio, which implies a Langmuir–Hinshelwood reaction mechanism that results in saturation of surface sites at higher pollutant mixing ratios.[106,187,192] For example, Langmuir–Hinshelwood reaction mechanisms have been proposed for ozone uptake by both road dust[136] and mineral dusts.[187,192] In addition, this mechanism has been suggested for NO_2 uptake by Saharan dust[188,192] and volatile organic compounds (VOCs) uptake by Gobi Desert dust.[204–206]

In coated-wall flow tube studies, if the uptake of a pollutant is large, then the pollutant mixing ratio near the dust surface becomes depleted and may not be replenished quickly enough via diffusive processes, which can result in an underestimation in the measured uptake coefficient. To correct for these diffusion limitations, both the Cooney–Kim–Davis (CKD)[207] and Knopf–Pöschl–Shiraiwa (KPS)[208] methods have been used. In addition, similar to Knudsen cells, the calculation shown above assumes the geometric surface area of the dust; therefore, uptake coefficients are often scaled to their total (BET) surface area using the following equation:[106]

$$\gamma_{BET} = \gamma_{eff} \times \frac{S_{geo}}{S_{BET} \times m} \tag{1.4}$$

Here, S_{geo} is the geometric surface area of the dust-coated section of the tube, S_{BET} is the BET specific surface area of the dust, and m is the dust mass.

Coated-wall flow tubes have been used to investigate the photochemical uptake of ozone[106] by NO_2[188,192] by mineral dusts, as well as the uptake of SO_2 by mineral dusts.[89,191] In addition, I present the first investigation of road dust heterogeneous chemistry with ozone using a coated-wall flow tube apparatus in Chapter 4 of this thesis.[136]

1.4.2.3 Aerosol flow tubes

Aerosol flow tubes offer the most realistic conditions for atmospheric dust–pollutant interactions, as gas uptake is measured with suspended dust particles.[193] Aerosol flow tubes are equipped with a movable injector, which can be used for the introduction of a pollutant gas or dust aerosol (Figure 1.7). A variety of techniques have been used for the generation of dust aerosol, including rotating brush generators,[209] magnetic stirrers,[210,211] fluidized bed reactors,[212] and nebulizers.[213] The dust particle size distribution, along with the pollutant mixing ratio, are measured at the exit of the flow tube.

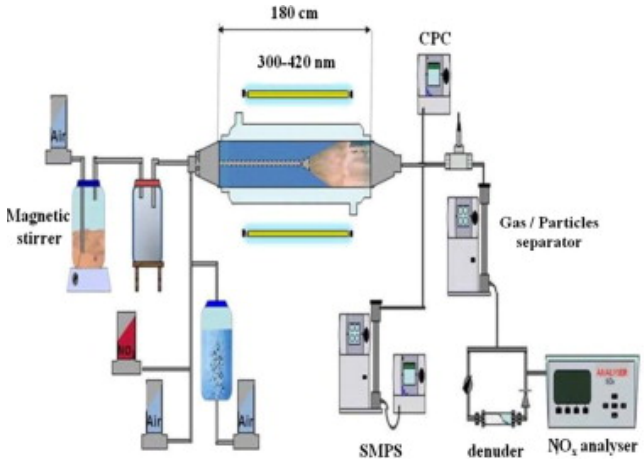

Figure 1.7: A schematic of an aerosol flow tube used to study the photoenhanced uptake of NO_2 by Arizona Test Dust (ATD). Particle size and number are measured by a scanning mobility particle sizer (SMPS) and NO_2 mixing ratio is measured by a NO_x analyzer. Image reprinted from *Aeolian. Res.* 15, Dupart et al. Heterogeneous uptake of NO_2 on Arizona Test Dust under UV-A irradiation: An aerosol flow tube study. 45–51, **2014**,[210] with permission from Elsevier.

The following equation is used to calculate the uptake coefficient for aerosol flow tube studies:[193]

$$\gamma = \frac{4k_s}{< c > S_a} \tag{1.5}$$

Here, k_s is the pseudo-first-order rate constant for loss of a pollutant gas, corrected for gas wall losses, $< c >$ is the mean molecular speed of the pollutant gas of interest, and S_a is the aerosol surface area per unit volume of gas determined using a particle sizing instrument.

Aerosol flow tubes offer several advantages over Knudsen cells and coated-wall flow tubes. For example, they can operate at atmospherically relevant pressures but unlike coated-wall flow tubes, they do not require radial diffusion corrections since dust is carried in the gas flow. In addition, particle size and number can be measured in real-time using particle sizers, including SMPS[210,211] and aerodynamic particle sizers (APS),[176,209,211] which provide more accurate estimates for total particle surface area compared to offline BET analysis. Furthermore, aerosol flow tubes can be used in tandem with online particle characterization equipment, including ATOFMS[214] and continuous flow diffusion chambers[212] to monitor the compositional and IN efficiency changes of dust, respectively, as a result of pollutant uptake.

1.4.2.4 Atmospheric simulation chambers

Similar to aerosol flow tubes, atmospheric simulation chambers (Figure 1.8) also measure pollutant gas uptake in the presence of suspended dust particles; however, compared to aerosol flow tubes, the residence time of both the pollutant gas and dust PM is longer in simulation chambers, which allow dust–pollutant interactions to be measured over longer exposure times.[215] In this technique, the experimental protocol typically proceeds as follows: first, the chamber is filled with a carrier gas until a desired pressure is reached; second, a pollutant gas of interest is introduced into the chamber and adjusted to its desired mixing ratio; and third, the pollutant inlet is closed and dust is pumped into the chamber.

Uptake coefficients for aerosol simulation chambers are determined using the same equation for aerosol flow tubes and similarly require corrections for gas-phase wall loss.[215] Finally, to date, dust heterogeneous chemistry studies have solely used mineral dust proxies in aerosol simulation chambers[215–217,217] because authentic dust particles are larger in size, and require generation of much higher dust mass loadings to observe pollutant uptake, which can be difficult to achieve.

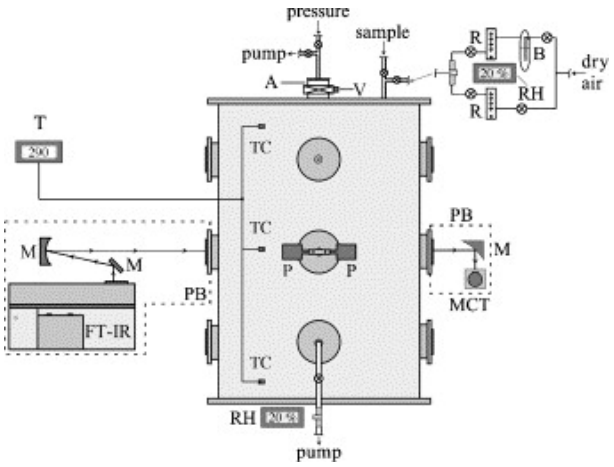

Figure 1.8: A schematic of a 151 L environmental aerosol reaction chamber used to investigate N_2O_5 uptake on kaolinite, montmorillonite, hematite, calcite, and quartz mineral dust proxies. Image reprinted from *Atmos. Environ.* 40, (38), Mogili et al. N_2O_5 Hydrolysis on the Components of Mineral Dust and Sea Salt Aerosol: Comparison Study in an Environmental Aerosol Reaction Chamber. 7401–7408, **2006**,[215] with permission from Elsevier.

1.4.2.5 Spectroscopic techniques

Diffuse reflectance infrared Fourier transform spectroscopy (DRIFTS) is a surface analysis technique that has been used to investigate the uptake of VOCs,[218] N_2O_5,[199] HNO_3/NO_2,[219] and ozone[220] by mineral dust and mineral dust proxies. In this technique, an incident infrared beam is directed towards a sample holder containing a dust substrate, and the reflected infrared beams from the surface and inner layers of the dust sample are measured during exposure to a pollutant gas (Figure 1.9).[218] This enables the detection and quantification of IR-active surface adsorbed pollutants formed during heterogeneous uptake.

The obtained DRIFTS spectra are dependent on dust particle size, dust packing density in the sample holder, and refractive index, which varies from sample to sample;[221] as a result, there is no linear correlation between infrared band intensity and concentration in DRIFTS. However, quantitative analysis is possible via the application of the Kubelka–Munk equation, which

converts the diffuse reflectance to the transmittance of the surface absorbing species.[222] From here, an uptake coefficient can be calculated as follows:[219]

$$\gamma = \frac{d[P]}{dt\, Z} \tag{1.6}$$

Here, [P] is the concentration of the IR-active surface adsorbed product measured by DRIFTS and Z is the total number of reactive surface collisions.

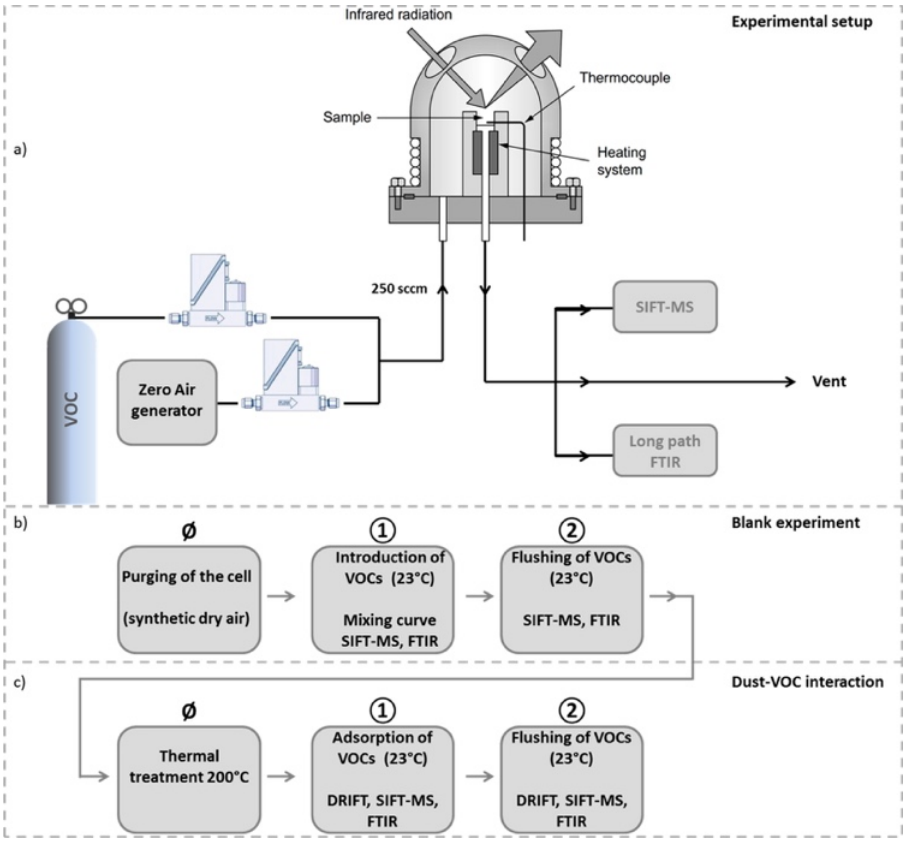

Figure 1.9: A schematic of a DRIFTS set-up used to investigate the uptake of limonene and toluene by Saharan dust and consequent reaction products. The adsorbed-phase and gas-phase species were measured using infrared spectroscopy and selected-ion flow-tube mass spectrometry (SIFT–MS), respectively. Image (adapted) with permission from Romanías et al. Investigating the Heterogeneous Interaction of VOCs with Natural Atmospheric Particles: Adsorption of Limonene and Toluene on Saharan Mineral Dusts. *J. Phys. Chem A* **2016**, 120, (8), 1197–1212.[218] Copyright 2016 American Chemical Society.

The greatest advantage of DRIFTS is that it can be used to make inferences on chemical reaction mechanisms during pollutant gas uptake by identifying surface products formed in real-time. For example, Börensen and colleagues used DRIFTS to measure the uptake of HNO_3 and NO_2 by Al_2O_3, a mineral dust proxy, as well as detect the formation of surface-sorbed nitrate.[219] Finally, Romanías et al. used DRIFTS to compare the reversible (weakly bound) and irreversible (strongly bound) adsorption of VOCs by mineral dust samples collected from different regions in the Sahara Desert.[218]

1.4.3 Limitations, considerations, and challenges of laboratory studies

1.4.3.1 Influence of relative humidity

Like pollutant gases, water vapor can also be taken up at the surface of dust.[223] For example, studies of water adsorption by mineral dust proxies (*i.e.*, metal oxides) have shown that water dissociates at the particle surface at low RH (< 1%), which results in the formation of surface hydroxyl groups.[224,225] These hydroxyl groups can act as hydrogen bonding sites for the subsequent non-dissociative uptake of water. However, under ambient RH conditions it is assumed that the dust surface is fully hydroxylated and that the uptake of water by mineral dust proxies proceeds by non-reactive mechanisms.[223] In fact, Joshi and coworkers used DRIFTS to show that monolayer water coverage at the surface of mineral dusts occurs between 15–25% RH (assuming even surface coverage), with multilayer coverage formed at higher RH.[226]

The presence of water at the dust surface can influence dust–pollutant interactions;[7,8] as a result, dust heterogeneous chemistry laboratory studies often investigate pollutant uptake as a function of RH. For example, N_2O_5 uptake by mineral dust and mineral dust proxies is mediated by its hydrolysis at the particle surface,[199,215] which leads to the formation of surface nitrates and release of gas-phase HNO_3.[215] For this reason, N_2O_5 uptake by mineral dust is found to increase with increasing relative humidity.[209] Furthermore, although NO_2 uptake by mineral dust proxies decreases with increasing RH,[227,228] the gas-phase HONO product yield is found to increase under elevated RH, as its formation requires surface sorbed water.[228] Finally, ozone

uptake by mineral dust[110,190] and mineral dust proxies[106,202,216] generally decreases with increasing RH due to the competitive adsorption between water vapor and ozone.

Although water uptake by anthropogenic dusts has not yet been explored, similar to mineral dust, the metal oxides in the crustal fraction of road dust are likely hydroxylated and may also participate in hydrogen bonding with water.[223] However, as I will show in Chapter 4, unlike mineral dust and mineral dust proxies,[190,216] ozone uptake by road dust increases with increasing RH.[136] Instead, the observed RH trend is similar to that of ozone uptake by humic acid films,[229] which suggests that the organic fraction of road dust may be responsible for its reactivity with ozone at higher RH.

1.4.3.2 Available surface area assumptions for pollutant gas uptake

One of the greatest experimental challenges for dust heterogeneous chemistry studies is scaling the measured uptake coefficients to appropriate dust particle surface areas.[230] For example, in Knudsen cell and coated-wall flow tube studies both effective (scaled to the geometric surface area) and BET (scaled to the BET specific surface area and mass of the sample) uptake coefficients have been reported,[7,8] which represent the upper and lower limits of dust reactivity, respectively. Furthermore, in coated-wall flow tube studies, the BET specific surface area, which is typically measured via nitrogen adsorption from a powdered dust sample,[106] may not be representative of the specific surface area of the dust when present as a coating. For example, the preparation of dust-coated tubes involves the addition of water to form dust slurries, which are then dried to form coatings; however, the available surface area for gas uptake by these coatings may be overestimated by using the BET specific surface area, as the coating process may lead to particle agglomeration.[165] In fact, Aubin and Abbatt performed *in-situ* BET specific surface area analysis on soot-coated tubes[231,232] and reported smaller values compared to those obtained by powdered soot samples.[233] Furthermore, since BET specific surface area is determined under vacuum,[234] the removal of surface-sorbed water and organics is possible, which could influence the measured surface area of the sample. Finally, BET

specific surface area determination via nitrogen adsorption may also underestimate the available surface area for uptake of larger pollutant gas molecules.

For aerosol flow tubes and atmospheric simulation chambers, the surface area of mineral dust can be measured directly by particle sizing/counting instruments. For example, the mineral dust surface area has been estimated using optical particle counters (OPCs),[235] which determine particle size based on light scattering. Although OPCs are useful for measuring coarser PM (*e.g.*, mineral dust), these instruments are usually calibrated with polystyrene spheres, which have different refractive index to that of mineral dust. This difference can be corrected for by Mie theory, however, particle sphericity assumptions still result in surface area uncertainties.[236] APS, which use time-of-flight to obtain particle size, have been employed for surface area determination of mineral dust in flow tube studies,[209,237] which uses time-of-flight to obtain aerodynamic particle diameters. To correct for particle non-unity density and asphericity, aerodynamic diameters are converted to a Stokes equivalent diameter and a particle shape factor correction (χ) is applied.[209] In addition, SMPS has been used in dust heterogeneous chemistry studies to measure the surface area of finer PM (*e.g.*, mineral dust proxies).[213,238,239] Although SMPS does not require optical or density corrections because particle size is detected using a differential mobility analyzer (DMA), a particle shape factor correction is still needed if particles are aspherical. Finally, since each individual dust particle is unique in morphology, the application of a particle shape factor correction may also lead to differences in the "measured" vs "true" sample surface area.

1.5 Application of mineral dust proxies in laboratory studies

1.5.1 Mineral dust proxies used in heterogeneous chemistry studies

In an effort to understand the individual chemical drivers and reaction mechanisms of mineral dust heterogeneous chemistry, most studies to date have investigated dust interactions using commercially purchased, single-component mineral dust proxies.[7,8] These commercial proxies include metal oxides (*e.g.*, SiO_2, Al_2O_3, Fe_2O_3, and TiO_2, CaO, and MgO),[175,196,200] calcite

($CaCO_3$),[214,240] and clays (*e.g.*, kaolinite, illite, and montmorillonite).[202,241] For example, Michel et al. used a Knudsen cell to demonstrate that the initial uptake of ozone by mineral dust proxies increases in the following order: SiO_2<Al_2O_3<Fe_2O_3,[200] which also is also similar to its steady-state uptake.[196] The uptake of ozone by metal oxides has been suggested to occur by its decomposition on Lewis acid sites at the surface of metal oxides, which results in the release of molecular oxygen.[220,242] This mechanism has similarly been proposed to occur with commercial clays during ozone uptake.[202]

In many cases, the interactions between mineral dust proxies and pollutant gases lead to the formation of surface-sorbed species.[7,8] For example, Börensen and colleagues observed the formation of surface nitrates and nitrites on Al_2O_3 during NO_2 uptake using DRIFTS, which they attributed to NO_2 reaction with surface hydroxyl groups.[219] These authors also demonstrated that in the presence of water, surface nitrates and nitrites lead to the formation of surface-sorbed HNO_3 and gas-phase release of HONO. In addition, surface nitrate formation have been observed during reaction of NO_2 with $CaCO_3$.[243] The formation of surface nitrates has also been demonstrated during HNO_3 uptake by Al_2O_3[219,244] and $CaCO_3$.[240] Finally, the production of other inorganic surface species, including chloride and sulfites, can occur from HCl and SO_2 reaction with $CaCO_3$, respectively.[240]

The interactions between organic pollutants and mineral dust proxies have also been well documented.[201,245–247] For example, Tang et al. demonstrated that acetic acid uptake by metal oxides results in molecularly adsorbed acetic acid and acetate under wet and dry conditions, respectively.[245] Furthermore, adsorbed formaldehyde on Al_2O_3 surfaces from formaldehyde uptake can be oxidized by molecular oxygen to form dioxymethylene, which can undergo further oxidation to form surface formate.[246] Lastly, Al-Hosney and coworkers demonstrated that heterogeneous uptake formic acid by $CaCO_3$ leads to the formation of calcium formate, and under dry conditions (RH <1%), carbonic acid.[201] Many of these reactions, as well as additional mineral dust proxy–pollutant gas interactions, have been summarized in several major reviews on mineral dust heterogeneous chemistry.[7,8,194]

1.5.2 Mineral dust proxies used in heterogeneous photochemistry studies

Until recently, the heterogeneous photochemistry of dust was thought to be primarily driven by semi-conducting metal oxides, Fe_2O_3 and TiO_2,[248,249] which upon illumination at wavelengths equal to or greater than their band gap, lead to the formation of electron–hole pairs (e^-/h^+) (Figure 1.10).[250] These e^-/h^+ pairs can participate in both oxidative and reductive reactions in dust–pollutant interactions; as a result, studies have predominantly employed the use of commercial TiO_2 and Fe_2O_3 as photoactive proxies for mineral dust. For example, the photoenhanced uptake of ozone by TiO_2 has been attributed to ozone reduction via e^- and/or superoxide radicals formed by the reaction of molecular oxygen with e^-.[106,217,251] This mechanism has also been proposed for the photochemical uptake of ozone by Fe_2O_3.[217] In addition, ozone can be reduced by OH radicals formed by h^+ reaction with surface-sorbed water.[106] Finally, the photoenhanced uptake of NO_2 by TiO_2 has also been attributed to both direct and indirect reactions of NO_2 with photogenerated e^-/h^+ pairs.[192]

The photochemical transformation of pollutants has also been demonstrated using mineral dust proxies. For example, Styler and colleagues observed the production of gas-phase acetone and propionaldehyde during the photoenhanced uptake of isopropanol and *n*-propanol, respectively, by TiO_2.[198] In addition, a recent study by Wang et al. demonstrated the photochemical transformation of surface nitrates to gas phase NO_x during NO uptake by TiO_2.[252] Lastly, surface-sorbed sulfite formed during the heterogeneous uptake of SO_2 by TiO_2 is oxidized to sulfate upon illumination.[253] In summary, the use of semi-conducting metal oxides in heterogeneous chemistry studies have suggested that many dust–pollutant interactions can be promoted in the presence of light.

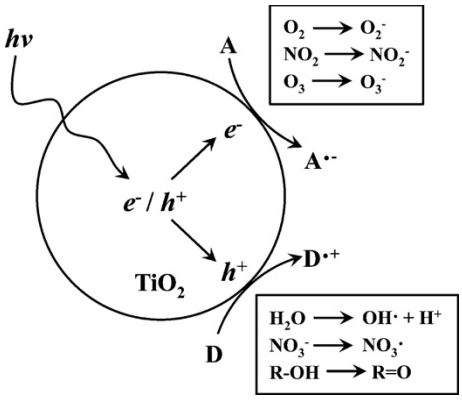

Figure 1.10: Schematic of the formation of e^-/h^+ at the surface of illuminated TiO_2. Examples of pollutant species that can serve as e^- and h^+ acceptors are shown in (A) and (D), respectively. Image (adapted) with permission from Chen et al. Titanium Dioxide Photocatalysis in Atmospheric Chemistry. *Chem Rev.* **2012**, 112, (11), 5919–5948.[248] Copyright 2012 American Chemical Society.

1.5.3 Limitations of using mineral dust proxies

1.5.3.1 Importance of elemental speciation

Although the use of single-component mineral dust proxies has provided insight into potential dust heterogeneous chemistry mechanisms and pathways, these proxies are not always reflective of ambient dust. For example, the use of commercially sourced metal oxides as a mineral dust substitute assumes that the metals in dust exist in their individual oxide form, which oversimplifies the chemical composition of mineral dust in several ways: first, metal oxides can exist as polymorphs (*i.e.*, minerals with the same chemical formula but different crystalline structures);[18] second, metals in dust can be present in other mineral forms besides their individual oxide phase;[16,18,19] third, mineral phases in ambient dust may contain unique elemental impurities and different crystalline structure parameters[16] compared to commercially synthesized materials; fourth, dust substrates which contain non-crustal material, including volcanic dust[89,110] and anthropogenic dusts,[59,61,139] cannot be accurately represented using traditional mineral dust proxies. Together, this makes it challenging to correlate the heterogeneous chemistry observed for mineral dust proxies to that of dust in the natural environment.

1.5.3.2 Considerations for atmospheric aging

To date, mineral heterogeneous chemistry studies have primarily used fresh mineral dust and mineral dust proxy surfaces when determining uptake coefficients for pollutant gases; however, this approach neglects the chemical evolution of dust as it undergoes atmospheric aging.[87,145,151] The implications of atmospheric aging on dust heterogeneous chemistry were first explored in the early 2000s by Usher and colleagues, who found that ozone uptake by Al_2O_3 decreased by 70% when Al_2O_3 was processed by HNO_3, which they attributed to the blockage of surface sites by adsorbed nitrate.[197] In contrast, these authors also observed a 33% increase in ozone uptake after Al_2O_3 exposure to SO_2, which they attributed to ozone oxidation of surface-sorbed sulfite. More recently, Lederer et al. demonstrated that the rate of formation of surface products during limonene uptake by mineral dust is 2–5× faster in presence of nitrate coatings.[164] Finally, Coates Fuentes observed an increase in ozone uptake by up to two orders of magnitude when kaolinite was pretreated with limonene or α-pinene, which they attributed to ozone oxidation of alkene functional groups at the particle surface.[165] Together, these studies have highlighted that atmospheric processing can influence the inherent reactivity of atmospheric dust and should be considered when conducting future studies on dust heterogeneous chemistry.

1.6 Introduction to thesis work

As discussed in the preceding sections, most studies of dust heterogenous chemistry have been conducted using commercially purchased, single-component mineral dust proxies or unprocessed mineral dust, which limits our ability to predict the climate, AQ, and health implications of atmospheric dust. The goal of this thesis is to improve our understanding of dust heterogeneous chemistry by exploring: 1) the photoreactivity of naturally sourced minerals, 2) the importance of elemental speciation in predicting dust reactivity, 3) the reactivity of pollutant gases with urban road dust and anti-icing road maintenance materials, and 4) the influence of atmospheric aging on mineral dust photochemistry.

Chapter 2 explores the photochemical uptake of ozone by a suite of naturally sourced Ti-containing minerals using a coated-wall flow tube. In addition, this chapter provides comprehensive chemical characterization of each mineral as an attempt to understand its photoreactivity and address the following questions:

- Is the photoreactivity of commercial TiO_2 different than naturally sourced TiO_2?
- Does the photochemical uptake of ozone change with different TiO_2 polymorphs?
- Does the photochemical uptake of ozone change with the same mineral phase sampled from different geographical locations?

Chapter 3 uses a coated-wall flow tube to report the photochemical uptake of ozone by Ti-rich volcanic dust obtained from the Mýrdalssandur source region in southern Iceland. In this chapter, the elemental speciation of Ti is explored using EMPA to address the following questions:

- Where does the elemental Ti reside in volcanic dusts?
- Can the elemental speciation of Ti be used to predict the photoreactivity of mineral dust?

Chapter 4 provides the first investigation of pollutant gas uptake by urban road dust and a commonly used anti-icing solution in high-latitude regions. Specifically, I explore the uptake of ozone by urban road dust and halogen activation during ozone uptake by anti-icer to address the following questions:

- Can road dust participate in heterogeneous chemistry with ozone?
- How does the reactivity of road dust compare to mineral dust?
- Does the heterogenous uptake of ozone by anti-icer result in the release of gas-phase chlorine species?

Chapter 5 reports the design and construction of a new custom-built photochemical aerosol flow tube reactor used to explore the AQ implications of atmospheric aging on dust photochemistry. In particular, this chapter includes preliminary experiments on the

influence of organic coatings on the photochemical uptake of ozone by TiO_2 to address the following questions:

- Do organic coatings influence the photochemical uptake of ozone by TiO_2?
- Does ozone uptake change with increasing coating thickness?

Chapter 6 is the concluding chapter of this thesis, which highlights the importance of these results in an AQ context. In addition, this chapter discusses the future implications of climate change and human activities on natural and anthropogenic dust emissions, respectively, as well as the impacts of these emissions on dust heterogeneous chemistry. Finally, it provides recommendations for future studies in this field.

1.7 References

(1) Huneeus, N.; Schulz, M.; Balkanski, Y.; Griesfeller, J.; Prospero, J.; Kinne, S.; Bauer, S.; Boucher, O.; Chin, M.; Dentener, F.; Diehl, T.; Easter, R.; Fillmore, D.; Ghan, S.; Ginoux, P.; Grini, A.; Horowitz, L.; Koch, D.; Krol, M. C.; Landing, W.; Liu, X.; Mahowald, N.; Miller, R.; Morcrette, J.-J.; Myhre, G.; Penner, J.; Perlwitz, J.; Stier, P.; Takemura, T.; Zender, C. S. Global Dust Model Intercomparison in AeroCom Phase I. *Atmospheric Chem. Phys.* **2011**, *11* (15), 7781–7816.

(2) Perry, K. D.; Cahill, T. A.; Eldred, R. A.; Dutcher, D. D.; Gill, T. E. Long-Range Transport of North African Dust to the Eastern United States. *J. Geophys. Res. Atmospheres* **1997**, *102* (D10), 11225–11238.

(3) Choobari, O. A.; Zawar-Reza, P.; Sturman, A. The Global Distribution of Mineral Dust and Its Impacts on the Climate System: A Review. *Atmospheric Res.* **2014**, *138*, 152–165.

(4) Betzer, P. R.; Carder, K. L.; Duce, R. A.; Merrill, J. T.; Tindale, N. W.; Uematsu, M.; Costello, D. K.; Young, R. W.; Feely, R. A.; Breland, J. A.; Bernstein, R. E.; Greco, A. M. Long–Range Transport of Giant Mineral Aerosol Particles. *Nature* **1988**, *336* (6199), 568–571.

(5) Jaenicke, R.; Schütz, L. Comprehensive Study of Physical and Chemical Properties of the Surface Aerosols in the Cape Verde Islands Region. *J. Geophys. Res. Oceans* **1978**, *83* (C7), 3585–3599.

(6) Cook, A. G.; Weinstein, P.; Centeno, J. A. Health Effects of Natural Dust: Role of Trace Elements and Compounds. *Biol. Trace Elem. Res.* **2005**, *103* (1), 001–016.

(7) Tang, M.; Huang, X.; Lu, K.; Ge, M.; Li, Y.; Cheng, P.; Zhu, T.; Ding, A.; Zhang, Y.; Gligorovski, S.; Song, W.; Ding, X.; Bi, X.; Wang, X. Heterogeneous Reactions of Mineral Dust Aerosol: Implications for Tropospheric Oxidation Capacity. *Atmospheric Chem. Phys.* **2017**, *17* (19), 11727–11777.

(8) Usher, C. R.; Michel, A. E.; Grassian, V. H. Reactions on Mineral Dust. *Chem. Rev.* **2003**, *103* (12), 4883–4940.

(9) Nan, Y.; Wang, Y. Observational Evidence for Direct Uptake of Ozone in China by Asian Dust in Springtime. *Atmos. Environ.* **2018**, *186*, 45–55.
(10) Sullivan, R. C.; Guazzotti, S. A.; Sodeman, D. A.; Prather, K. A. Direct Observations of the Atmospheric Processing of Asian Mineral Dust. *Atmospheric Chem. Phys.* **2007**, *7* (5), 1213–1236.
(11) Journet, E.; Balkanski, Y.; Harrison, S. P. A New Data Set of Soil Mineralogy for Dust-Cycle Modeling. *Atmospheric Chem. Phys.* **2014**, *14* (8), 3801–3816.
(12) Amato, F.; Pandolfi, M.; Moreno, T.; Furger, M.; Pey, J.; Alastuey, A.; Bukowiecki, N.; Prevot, A. S. H.; Baltensperger, U.; Querol, X. Sources and Variability of Inhalable Road Dust Particles in Three European Cities. *Atmos. Environ.* **2011**, *45* (37), 6777–6787.
(13) Haynes, W. M. *CRC Handbook of Chemistry and Physics*; CRC Press, 2016.
(14) Christiansen, E. H.; Hamblin, W. K. *Dynamic Earth: An Introduction to Physical Geology*; Jones & Bartlett Publishers, 2014.
(15) Nicol, A. *Physicochemical Methods of Mineral Analysis*; Springer Science & Business Media, 2012.
(16) Deer, W. A.; Howie, R. A.; Zussman, J. *An Introduction to the Rock-Forming Minerals*; Mineralogical Society, 2013.
(17) Hefferan, K.; O'Brien, J. *Earth Materials*; John Wiley & Sons, 2010.
(18) Bowles, J. F. W.; Howie, R. A.; Vaughan, D. J.; Zussman, J. *Rock-Forming Minerals*; Geological Society of London, 2011.
(19) Chang, L. L. Y.; Deer, W. A.; Howie, R. A.; Zussman, J. *Rock-Forming Minerals*; Geological Society of London, 1998.
(20) Tegen, I.; Fung, I. Modeling of Mineral Dust in the Atmosphere: Sources, Transport, and Optical Thickness. *J. Geophys. Res. Atmospheres* **1994**, *99* (D11), 22897–22914.
(21) Stokes, G. G. On the Effect of Internal Friction of Fluids on the Motion of Pendulums. *Trans. Camb. Philos. Soc.* **1850**, *9*, 8–106.
(22) Maring, H.; Savoie, D. L.; Izaguirre, M. A.; Custals, L.; Reid, J. S. Mineral Dust Aerosol Size Distribution Change during Atmospheric Transport. *J. Geophys. Res. Atmospheres* **2003**, *108* (D19).
(23) Ryder, C. L.; Highwood, E. J.; Lai, T. M.; Sodemann, H.; Marsham, J. H. Impact of Atmospheric Transport on the Evolution of Microphysical and Optical Properties of Saharan Dust. *Geophys. Res. Lett.* **2013**, *40* (10), 2433–2438.
(24) Denjean, C.; Cassola, F.; Mazzino, A.; Triquet, S.; Chevaillier, S.; Grand, N.; Bourrianne, T.; Momboisse, G.; Sellegri, K.; Schwarzenbock, A.; Freney, E.; Mallet, M.; Formenti, P. Size Distribution and Optical Properties of Mineral Dust Aerosols Transported in the Western Mediterranean. *Atmospheric Chem. Phys.* **2016**, *16* (2), 1081–1104.
(25) Does, M. van der; Knippertz, P.; Zschenderlein, P.; Harrison, R. G.; Stuut, J.-B. W. The Mysterious Long-Range Transport of Giant Mineral Dust Particles. *Sci. Adv.* **2018**, *4* (12), eaau2768.
(26) Glaccum, R. A.; Prospero, J. M. Saharan Aerosols over the Tropical North Atlantic — Mineralogy. *Mar. Geol.* **1980**, *37* (3), 295–321.
(27) Reid, J. S.; Jonsson, H. H.; Maring, H. B.; Smirnov, A.; Savoie, D. L.; Cliff, S. S.; Reid, E. A.; Livingston, J. M.; Meier, M. M.; Dubovik, O.; Tsay, S.-C. Comparison of Size and Morphological Measurements of Coarse Mode Dust Particles from Africa. *J. Geophys. Res. Atmospheres* **2003**, *108* (D19).

(28) Tsamalis, C.; Chédin, A.; Pelon, J.; Capelle, V. The Seasonal Vertical Distribution of the Saharan Air Layer and Its Modulation by the Wind. *Atmospheric Chem. Phys.* **2013**, *13* (22), 11235–11257.
(29) Jickells, T. D.; An, Z. S.; Andersen, K. K.; Baker, A. R.; Bergametti, G.; Brooks, N.; Cao, J. J.; Boyd, P. W.; Duce, R. A.; Hunter, K. A.; Kawahata, H.; Kubilay, N.; laRoche, J.; Liss, P. S.; Mahowald, N.; Prospero, J. M.; Ridgwell, A. J.; Tegen, I.; Torres, R. Global Iron Connections Between Desert Dust, Ocean Biogeochemistry, and Climate. *Science* **2005**, *308* (5718), 67–71.
(30) Bristow, C. S.; Hudson-Edwards, K. A.; Chappell, A. Fertilizing the Amazon and Equatorial Atlantic with West African Dust. *Geophys. Res. Lett.* **2010**, *37* (14).
(31) Onishi, K.; Otani, S.; Yoshida, A.; Mu, H.; Kurozawa, Y. Adverse Health Effects of Asian Dust Particles and Heavy Metals in Japan. *Asia Pac. J. Public Health* **2015**, *27* (2), NP1719–NP1726.
(32) Liu, C.-M.; Young, C.-Y.; Lee, Y.-C. Influence of Asian Dust Storms on Air Quality in Taiwan. *Sci. Total Environ.* **2006**, *368* (2), 884–897.
(33) Kok, J. F.; Adebiyi, A. A.; Albani, S.; Balkanski, Y.; Checa-Garcia, R.; Chin, M.; Colarco, P. R.; Hamilton, D. S.; Huang, Y.; Ito, A.; Klose, M.; Li, L.; Mahowald, N. M.; Miller, R. L.; Obiso, V.; Pérez García-Pando, C.; Rocha-Lima, A.; Wan, J. S. Contribution of the World's Main Dust Source Regions to the Global Cycle of Desert Dust. *Atmospheric Chem. Phys.* **2021**, *21* (10), 8169–8193.
(34) NASA Worldview https://worldview.earthdata.nasa.gov (accessed 2021 -06 -23).
(35) Claquin, T.; Schulz, M.; Balkanski, Y. J. Modeling the Mineralogy of Atmospheric Dust Sources. *J. Geophys. Res. Atmospheres* **1999**, *104* (D18), 22243–22256.
(36) Formenti, P.; Schütz, L.; Balkanski, Y.; Desboeufs, K.; Ebert, M.; Kandler, K.; Petzold, A.; Scheuvens, D.; Weinbruch, S.; Zhang, D. Recent Progress in Understanding Physical and Chemical Properties of African and Asian Mineral Dust. *Atmospheric Chem. Phys.* **2011**, *11* (16), 8231–8256.
(37) Caquineau, S.; Gaudichet, A.; Gomes, L.; Legrand, M. Mineralogy of Saharan Dust Transported over Northwestern Tropical Atlantic Ocean in Relation to Source Regions. *J. Geophys. Res. Atmospheres* **2002**, *107* (D15), AAC 4-1-AAC 4-12.
(38) Caquineau, S.; Gaudichet, A.; Gomes, L.; Magonthier, M.-C.; Chatenet, B. Saharan Dust: Clay Ratio as a Relevant Tracer to Assess the Origin of Soil-Derived Aerosols. *Geophys. Res. Lett.* **1998**, *25* (7), 983–986.
(39) Muhs, D. R.; Prospero, J. M.; Baddock, M. C.; Gill, T. E. Identifying Sources of Aeolian Mineral Dust: Present and Past. In *Mineral Dust: A Key Player in the Earth System*; Knippertz, P., Stuut, J.-B. W., Eds.; Springer Netherlands: Dordrecht, 2014; pp 51–74.
(40) Bullard, J. E.; Baddock, M.; Bradwell, T.; Crusius, J.; Darlington, E.; Gaiero, D.; Gasso, S.; Gisladottir, G.; Hodgkins, R.; McCulloch, R.; McKenna-Neuman, C.; Mockford, T.; Stewart, H.; Thorsteinsson, T. High-Latitude Dust in the Earth System. *Rev. Geophys.* **2016**, *54* (2), 447–485.
(41) Zwaaftink, C. D. G.; Grythe, H.; Skov, H.; Stohl, A. Substantial Contribution of Northern High-Latitude Sources to Mineral Dust in the Arctic. *J. Geophys. Res. Atmospheres* **2016**, *121* (22), 13,678-13,697.
(42) Bullard, J. E. Contemporary Glacigenic Inputs to the Dust Cycle. *Earth Surf. Process. Landf.* **2013**, *38* (1), 71–89.

(43) McKenna Neuman, C. A Review of Aeolian Transport Processes in Cold Environments. *Prog. Phys. Geogr. Earth Environ.* **1993**, *17* (2), 137–155.
(44) Mckenna Neuman, C. Effects of Temperature and Humidity upon the Entrainment of Sedimentary Particles by Wind. *Bound.-Layer Meteorol.* **2003**, *108* (1), 61–89.
(45) Bachelder, J.; Cadieux, M.; Liu-Kang, C.; Lambert, P.; Filoche, A.; Galhardi, J. A.; Hadioui, M.; Chaput, A.; Bastien-Thibault, M.-P.; Wilkinson, K. J.; King, J.; Hayes, P. L. Chemical and Microphysical Properties of Wind-Blown Dust near an Actively Retreating Glacier in Yukon, Canada. *Aerosol Sci. Technol.* **2020**, *54* (1), 2–20.
(46) Gaiero, D. M.; Depetris, P. J.; Probst, J.-L.; Bidart, S. M.; Leleyter, L. The Signature of River- and Wind-Borne Materials Exported from Patagonia to the Southern Latitudes: A View from REEs and Implications for Paleoclimatic Interpretations. *Earth Planet. Sci. Lett.* **2004**, *219* (3), 357–376.
(47) Ramsperger, B.; Peinemann, N.; Stahr, K. Deposition Rates and Characteristics of Aeolian Dust in the Semi-Arid and Sub-Humid Regions of the Argentinean Pampa. *J. Arid Environ.* **1998**, *39* (3), 467–476.
(48) Friedman, I.; Long, W. Volcanic Glasses, Their Origins and Alteration Processes. *J. Non-Cryst. Solids* **1984**, *67* (1), 127–133.
(49) Baldo, C.; Formenti, P.; Nowak, S.; Chevaillier, S.; Cazaunau, M.; Pangui, E.; Di Biagio, C.; Doussin, J.-F.; Ignatyev, K.; Dagsson-Waldhauserova, P.; Arnalds, O.; MacKenzie, A. R.; Shi, Z. Distinct Chemical and Mineralogical Composition of Icelandic Dust Compared to Northern African and Asian Dust. *Atmospheric Chem. Phys.* **2020**, *20* (21), 13521–13539.
(50) Arnalds, O.; Gisladottir, F.; Sigurjonsson, H. Sandy Deserts of Iceland: An Overview. *J. Arid Environ.* **2001**, *47* (3), 359–371.
(51) Jeong, G. Y. Bulk and Single-Particle Mineralogy of Asian Dust and a Comparison with Its Source Soils. *J. Geophys. Res. Atmospheres* **2008**, *113* (D2).
(52) Shi, Z.; Krom, M. D.; Bonneville, S.; Baker, A. R.; Bristow, C.; Drake, N.; Mann, G.; Carslaw, K.; McQuaid, J. B.; Jickells, T.; Benning, L. G. Influence of Chemical Weathering and Aging of Iron Oxides on the Potential Iron Solubility of Saharan Dust during Simulated Atmospheric Processing. *Glob. Biogeochem. Cycles* **2011**, *25* (2).
(53) Hooper, J.; Marx, S. A Global Doubling of Dust Emissions during the Anthropocene? *Glob. Planet. Change* **2018**, *169*, 70–91.
(54) Tegen, I.; Fung, I. Contribution to the Atmospheric Mineral Aerosol Load from Land Surface Modification. *J. Geophys. Res. Atmospheres* **1995**, *100* (D9), 18707–18726.
(55) Chen, S.; Jiang, N.; Huang, J.; Zang, Z.; Guan, X.; Ma, X.; Luo, Y.; Li, J.; Zhang, X.; Zhang, Y. Estimations of Indirect and Direct Anthropogenic Dust Emission at the Global Scale. *Atmos. Environ.* **2019**, *200*, 50–60.
(56) Casotti Rienda, I.; Alves, C. A. Road Dust Resuspension: A Review. *Atmospheric Res.* **2021**, *261*, 105740.
(57) Csavina, J.; Field, J.; Taylor, M. P.; Gao, S.; Landázuri, A.; Betterton, E. A.; Sáez, A. E. A Review on the Importance of Metals and Metalloids in Atmospheric Dust and Aerosol from Mining Operations. *Sci. Total Environ.* **2012**, *433*, 58–73.
(58) Hiscox, A. L.; Miller, D. R.; Holmén, B. A.; Yang, W.; Wang, J. Near-Field Dust Exposure from Cotton Field Tilling and Harvesting. *J. Environ. Qual.* **2008**, *37* (2), 551–556.

(59) Wang, X.; Chow, J. C.; Kohl, S. D.; Percy, K. E.; Legge, A. H.; Watson, J. G. Characterization of PM2.5 and PM10 Fugitive Dust Source Profiles in the Athabasca Oil Sands Region. *J. Air Waste Manag. Assoc.* **2015**, *65* (12), 1421–1433.
(60) Flanagan, M. E.; Seixas, N.; Majar, M.; Camp, J.; Morgan, M. Silica Dust Exposures During Selected Construction Activities. *AIHA J.* **2003**, *64* (3), 319–328.
(61) Thorpe, A.; Harrison, R. M. Sources and Properties of Non-Exhaust Particulate Matter from Road Traffic: A Review. *Sci. Total Environ.* **2008**, *400* (1–3), 270–282.
(62) Kok, J. F.; Adebiyi, A. A.; Albani, S.; Balkanski, Y.; Checa-Garcia, R.; Chin, M.; Colarco, P. R.; Hamilton, D. S.; Huang, Y.; Ito, A.; Klose, M.; Leung, D. M.; Li, L.; Mahowald, N. M.; Miller, R. L.; Obiso, V.; Pérez García-Pando, C.; Rocha-Lima, A.; Wan, J. S.; Whicker, C. A. Improved Representation of the Global Dust Cycle Using Observational Constraints on Dust Properties and Abundance. *Atmospheric Chem. Phys.* **2021**, *21* (10), 8127–8167.
(63) Ginoux, P.; Prospero, J. M.; Gill, T. E.; Hsu, N. C.; Zhao, M. Global-Scale Attribution of Anthropogenic and Natural Dust Sources and Their Emission Rates Based on MODIS Deep Blue Aerosol Products. *Rev. Geophys.* **2012**, *50* (3).
(64) Wang, X.; Chow, J. C.; Kohl, S. D.; Yatavelli, L. N. R.; Percy, K. E.; Legge, A. H.; Watson, J. G. Wind Erosion Potential for Fugitive Dust Sources in the Athabasca Oil Sands Region. *Aeolian Res.* **2015**, *18*, 121–134.
(65) Brotons, J. M.; Díaz, A. R.; Sarría, F. A.; Serrato, F. B. Wind Erosion on Mining Waste in Southeast Spain. *Land Degrad. Dev.* **2010**, *21* (2), 196–209.
(66) Chakraborty, M. K.; Ahmad, M.; Singh, R. S.; Pal, D.; Bandopadhyay, C.; Chaulya, S. K. Determination of the Emission Rate from Various Opencast Mining Operations. *Environ. Model. Softw.* **2002**, *17* (5), 467–480.
(67) Al-Khashman, Omar. A. Heavy Metal Distribution in Dust, Street Dust and Soils from the Work Place in Karak Industrial Estate, Jordan. *Atmos. Environ.* **2004**, *38* (39), 6803–6812.
(68) Xu, G.; Chen, Y.; Eksteen, J.; Xu, J. Surfactant-Aided Coal Dust Suppression: A Review of Evaluation Methods and Influencing Factors. *Sci. Total Environ.* **2018**, *639*, 1060–1076.
(69) Parvej, S.; Naik, D. L.; Sajid, H. U.; Kiran, R.; Huang, Y.; Thanki, N. Fugitive Dust Suppression in Unpaved Roads: State of the Art Research Review. *Sustainability* **2021**, *13* (4), 2399.
(70) Wu, Z.; Zhang, X.; Wu, M. Mitigating Construction Dust Pollution: State of the Art and the Way Forward. *J. Clean. Prod.* **2016**, *112*, 1658–1666.
(71) Belton, D. N.; Taylor, K. C. Automobile Exhaust Emission Control by Catalysts. *Curr. Opin. Solid State Mater. Sci.* **1999**, *4* (1), 97–102.
(72) Kolesar, K. R.; Mattson, C. N.; Peterson, P. K.; May, N. W.; Prendergast, R. K.; Pratt, K. A. Increases in Wintertime PM2.5 Sodium and Chloride Linked to Snowfall and Road Salt Application. *Atmos. Environ.* **2018**, *177*, 195–202.
(73) Harrison, R. M.; Jones, A. M.; Gietl, J.; Yin, J.; Green, D. C. Estimation of the Contributions of Brake Dust, Tire Wear, and Resuspension to Nonexhaust Traffic Particles Derived from Atmospheric Measurements. *Environ. Sci. Technol.* **2012**, *46* (12), 6523–6529.

(74) Lin, C.-C.; Chen, S.-J.; Huang, K.-L.; Hwang, W.-I.; Chang-Chien, G.-P.; Lin, W.-Y. Characteristics of Metals in Nano/Ultrafine/Fine/Coarse Particles Collected Beside a Heavily Trafficked Road. *Environ. Sci. Technol.* **2005**, *39* (21), 8113–8122.
(75) Kupiainen, K. J.; Tervahattu, H.; Räisänen, M.; Mäkelä, T.; Aurela, M.; Hillamo, R. Size and Composition of Airborne Particles from Pavement Wear, Tires, and Traction Sanding. *Environ. Sci. Technol.* **2005**, *39* (3), 699–706.
(76) Equiza, M. A.; Calvo-Polanco, M.; Cirelli, D.; Señorans, J.; Wartenbe, M.; Saunders, C.; Zwiazek, J. J. Long-Term Impact of Road Salt (NaCl) on Soil and Urban Trees in Edmonton, Canada. *Urban For. Urban Green.* **2017**, *21*, 16–28.
(77) Khan, R. K.; Strand, M. A. Road Dust and Its Effect on Human Health: A Literature Review. *Epidemiol. Health* **2018**, *40*, e2018013.
(78) Shi, G.; Chen, Z.; Bi, C.; Wang, L.; Teng, J.; Li, Y.; Xu, S. A Comparative Study of Health Risk of Potentially Toxic Metals in Urban and Suburban Road Dust in the Most Populated City of China. *Atmos. Environ.* **2011**, *45* (3), 764–771.
(79) Yu, B.; Xie, X.; Ma, L. Q.; Kan, H.; Zhou, Q. Source, Distribution, and Health Risk Assessment of Polycyclic Aromatic Hydrocarbons in Urban Street Dust from Tianjin, China. *Environ. Sci. Pollut. Res.* **2014**, *21* (4), 2817–2825.
(80) Evangeliou, N.; Grythe, H.; Klimont, Z.; Heyes, C.; Eckhardt, S.; Lopez-Aparicio, S.; Stohl, A. Atmospheric Transport Is a Major Pathway of Microplastics to Remote Regions. *Nat. Commun.* **2020**, *11* (1), 3381.
(81) Brahney, J.; Mahowald, N.; Prank, M.; Cornwell, G.; Klimont, Z.; Matsui, H.; Prather, K. A. Constraining the Atmospheric Limb of the Plastic Cycle. *Proc. Natl. Acad. Sci.* **2021**, *118* (16).
(82) Rodríguez, S.; Alastuey, A.; Querol, X. A Review of Methods for Long Term in Situ Characterization of Aerosol Dust. *Aeolian Res.* **2012**, *6*, 55–74.
(83) Waza, A.; Schneiders, K.; May, J.; Rodríguez, S.; Epple, B.; Kandler, K. Field Comparison of Dry Deposition Samplers for Collection of Atmospheric Mineral Dust: Results from Single-Particle Characterization. *Atmospheric Meas. Tech.* **2019**, *12* (12), 6647–6665.
(84) Engelbrecht, J. P.; Moosmüller, H.; Pincock, S.; Jayanty, R. K. M.; Lersch, T.; Casuccio, G. Technical Note: Mineralogical, Chemical, Morphological, and Opticalinterrelationships of Mineral Dust Re-Suspensions. *Atmospheric Chem. Phys.* **2016**, *16* (17), 10809–10830.
(85) May, K. R. The Cascade Impactor: An Instrument for Sampling Coarse Aerosols. *J. Sci. Instrum.* **1945**, *22* (10), 187–195.
(86) Adachi, K.; Tainosho, Y. Characterization of Heavy Metal Particles Embedded in Tire Dust. *Environ. Int.* **2004**, *30* (8), 1009–1017.
(87) Falkovich, A. H.; Schkolnik, G.; Ganor, E.; Rudich, Y. Adsorption of Organic Compounds Pertinent to Urban Environments onto Mineral Dust Particles. *J. Geophys. Res. Atmospheres* **2004**, *109* (D2), D02208.
(88) Manno, E.; Varrica, D.; Dongarrà, G. Metal Distribution in Road Dust Samples Collected in an Urban Area Close to a Petrochemical Plant at Gela, Sicily. *Atmos. Environ.* **2006**, *40* (30), 5929–5941.
(89) Urupina, D.; Lasne, J.; Romanias, M. N.; Thiery, V.; Dagsson-Waldhauserova, P.; Thevenet, F. Uptake and Surface Chemistry of SO2 on Natural Volcanic Dusts. *Atmos. Environ.* **2019**, *217*, 116942.

(90) Ahmady-Birgani, H.; McQueen, K. G.; Mirnejad, H. Characteristics of Mineral Dust Impacting the Persian Gulf. *Aeolian Res.* **2018**, *30*, 11–19.
(91) Maters, E. C.; Delmelle, P.; Rossi, M. J.; Ayris, P. M. Reactive Uptake of Sulfur Dioxide and Ozone on Volcanic Glass and Ash at Ambient Temperature. *J. Geophys. Res. Atmospheres* **2017**, *122* (18), 10,077-10,088.
(92) Guieu, C.; Loÿe-Pilot, M.-D.; Ridame, C.; Thomas, C. Chemical Characterization of the Saharan Dust End-Member: Some Biogeochemical Implications for the Western Mediterranean Sea. *J. Geophys. Res. Atmospheres* **2002**, *107* (D15), ACH 5-1-ACH 5-11.
(93) Rajaram, B. S.; Suryawanshi, P. V.; Bhanarkar, A. D.; Rao, C. V. C. Heavy Metals Contamination in Road Dust in Delhi City, India. *Environ. Earth Sci.* **2014**, *72* (10), 3929–3938.
(94) Khairy, M. A.; Barakat, A. O.; Mostafa, A. R.; Wade, T. L. Multielement Determination by Flame Atomic Absorption of Road Dust Samples in Delta Region, Egypt. *Microchem. J.* **2011**, *97* (2), 234–242.
(95) Harris, D. C.; Lucy, C. A. *Quantitative Chemical Analysis*; W. H. Freeman, 2019.
(96) Cote, C. D.; Schneider, S. R.; Lyu, M.; Gao, S.; Gan, L.; Holod, A. J.; Chou, T. H. H.; Styler, S. A. Photochemical Production of Singlet Oxygen by Urban Road Dust. *Environ. Sci. Technol. Lett.* **2018**, *5* (2), 92–97.
(97) Styler, S. A.; Donaldson, D. J. Heterogeneous Photochemistry of Oxalic Acid on Mauritanian Sand and Icelandic Volcanic Ash. *Environ. Sci. Technol.* **2012**, *46* (16), 8756–8763.
(98) Margui, E.; Grieken, R. V. *X-Ray Fluorescence Spectrometry and Related Techniques: An Introduction*; Momentum Press, 2013.
(99) Beckhoff, B.; Kanngießer, B.; Langhoff, N.; Wedell, R.; Wolff, H. *Handbook of Practical X-Ray Fluorescence Analysis*; Springer Science & Business Media: Berlin Heidelberg, 2007.
(100) Formenti, P.; Rajot, J. L.; Desboeufs, K.; Caquineau, S.; Chevaillier, S.; Nava, S.; Gaudichet, A.; Journet, E.; Triquet, S.; Alfaro, S.; Chiari, M.; Haywood, J.; Coe, H.; Highwood, E. Regional Variability of the Composition of Mineral Dust from Western Africa: Results from the AMMA SOP0/DABEX and DODO Field Campaigns. *J. Geophys. Res. Atmospheres* **2008**, *113* (D23).
(101) Formenti, P.; Nava, S.; Prati, P.; Chevaillier, S.; Klaver, A.; Lafon, S.; Mazzei, F.; Calzolai, G.; Chiari, M. Self-Attenuation Artifacts and Correction Factors of Light Element Measurements by X-Ray Analysis: Implication for Mineral Dust Composition Studies. *J. Geophys. Res. Atmospheres* **2010**, *115* (D1).
(102) Formenti, P.; Elbert, W.; Maenhaut, W.; Haywood, J.; Andreae, M. O. Chemical Composition of Mineral Dust Aerosol during the Saharan Dust Experiment (SHADE) Airborne Campaign in the Cape Verde Region, September 2000. *J. Geophys. Res. Atmospheres* **2003**, *108* (D18).
(103) Zhang, R.; Han, Z.; Cheng, T.; Tao, J. Chemical Properties and Origin of Dust Aerosols in Beijing during Springtime. *Particuology* **2009**, *7* (1), 61–67.
(104) Faiz, Y.; Siddique, N.; Tufail, M. Pollution Level and Health Risk Assessment of Road Dust from an Expressway. *J. Environ. Sci. Health Part A* **2012**, *47* (6), 818–829.
(105) Guinn, V. P.; Wagner, C. D. Instrumental Neutron Activation Analysis. *Anal. Chem.* **1960**, *32* (3), 317–323.

(106) Abou-Ghanem, M.; Oliynyk, A. O.; Chen, Z.; Matchett, L. C.; McGrath, D. T.; Katz, M. J.; Locock, A. J.; Styler, S. A. Significant Variability in the Photocatalytic Activity of Natural Titanium-Containing Minerals: Implications for Understanding and Predicting Atmospheric Mineral Dust Photochemistry. *Environ. Sci. Technol.* **2020**, *54* (21), 13509–13516.
(107) Falkovich, A. H.; Ganor, E.; Levin, Z.; Formenti, P.; Rudich, Y. Chemical and Mineralogical Analysis of Individual Mineral Dust Particles. *J. Geophys. Res. Atmospheres* **2001**, *106* (D16), 18029–18036.
(108) Egerton, R. F. *Physical Principles of Electron Microscopy: An Introduction to TEM, SEM, and AEM*; Springer: Germany, 2016.
(109) Jabłońska, M.; Janeczek, J. Identification of Industrial Point Sources of Airborne Dust Particles in an Urban Environment by a Combined Mineralogical and Meteorological Analyses: A Case Study from the Upper Silesian Conurbation, Poland. *Atmospheric Pollut. Res.* **2019**, *10* (3), 980–988.
(110) Abou-Ghanem, M.; Jensen, B. J. L.; Styler, S. A.; Romanias, M. N. Accepted. Ozone Chemistry and Photochemistry at the Surface of Icelandic Volcanic Dust: Insights from Elemental Speciation Analysis. *ACS Earth Space Chem.* **2021**.
(111) Coz, E.; Gómez-Moreno, F. J.; Casuccio, G. S.; Artíñano, B. Variations on Morphology and Elemental Composition of Mineral Dust Particles from Local, Regional, and Long-Range Transport Meteorological Scenarios. *J. Geophys. Res. Atmospheres* **2010**, *115* (D12).
(112) Caggiano, R.; Fiore, S.; Lettino, A.; Macchiato, M.; Sabia, S.; Trippetta, S. PM2.5 Measurements in a Mediterranean Site: Two Typical Cases. *Atmospheric Res.* **2011**, *102* (1), 157–166.
(113) Pöschl, U.; Rudich, Y.; Ammann, M. Kinetic Model Framework for Aerosol and Cloud Surface Chemistry and Gas-Particle Interactions–Part 1: General Equations, Parameters, and Terminology. *Atmospheric Chem. Phys.* **2007**, *7* (23), 5989–6023.
(114) Goel, V.; Mishra, S. K.; Pal, P.; Ahlawat, A.; Vijayan, N.; Jain, S.; Sharma, C. Influence of Chemical Aging on Physico-Chemical Properties of Mineral Dust Particles: A Case Study of 2016 Dust Storms over Delhi. *Environ. Pollut.* **2020**, *267*, 115338.
(115) Huertas, J. I.; Huertas, M. E.; Solís, D. A. Characterization of Airborne Particles in an Open Pit Mining Region. *Sci. Total Environ.* **2012**, *423*, 39–46.
(116) Lin, H.; Zhu, X.; Feng, Q.; Guo, J.; Sun, X.; Liang, Y. Pollution, Sources, and Bonding Mechanism of Mercury in Street Dust of a Subtropical City, Southern China. *Hum. Ecol. Risk Assess. Int. J.* **2019**, *25* (1–2), 393–409.
(117) Heide, P. van der. *X-Ray Photoelectron Spectroscopy: An Introduction to Principles and Practices*; John Wiley & Sons: Hoboken, New Jersey, 2011.
(118) Chang, L. W. Neurotoxic Effects of Mercury—A Review. *Environ. Res.* **1977**, *14* (3), 329–373.
(119) Liu, Y.; Liu, G.; Yousaf, B.; Zhou, C.; Shen, X. Identification of the Featured-Element in Fine Road Dust of Cities with Coal Contamination by Geochemical Investigation and Isotopic Monitoring. *Environ. Int.* **2021**, *152*, 106499.
(120) Waseda, Y.; Matsubara, E.; Shinoda, K. *X-Ray Diffraction Crystallography: Introduction, Examples and Solved Problems*; Springer Science & Business Media: Germany, 2011.

(121) Fujiwara, F.; Rebagliati, R. J.; Dawidowski, L.; Gómez, D.; Polla, G.; Pereyra, V.; Smichowski, P. Spatial and Chemical Patterns of Size Fractionated Road Dust Collected in a Megacitiy. *Atmos. Environ.* **2011**, *45* (8), 1497–1505.
(122) Matchett, L. C.; Abou-Ghanem, M.; Stix, K. A. R.; McGrath, D. T.; Styler, S. A. Accepted. Ozone Uptake by Commercial Brake Pads: Assessing the Potential Indirect Air Quality Impacts of Non-Exhaust Emissions. *Environ. Sci. Atmospheres* **2021**.
(123) Rietveld, H. M. Line Profiles of Neutron Powder-Diffraction Peaks for Structure Refinement. *Acta Crystallogr.* **1967**, *22* (1), 151–152.
(124) Nowak, S.; Lafon, S.; Caquineau, S.; Journet, E.; Laurent, B. Quantitative Study of the Mineralogical Composition of Mineral Dust Aerosols by X-Ray Diffraction. *Talanta* **2018**, *186*, 133–139.
(125) Soleimani, Z.; Teymouri, P.; Darvishi Boloorani, A.; Mesdaghinia, A.; Middleton, N.; Griffin, D. W. An Overview of Bioaerosol Load and Health Impacts Associated with Dust Storms: A Focus on the Middle East. *Atmos. Environ.* **2020**, *223*, 117187.
(126) Hallar, A. G.; Chirokova, G.; McCubbin, I.; Painter, T. H.; Wiedinmyer, C.; Dodson, C. Atmospheric Bioaerosols Transported via Dust Storms in the Western United States. *Geophys. Res. Lett.* **2011**, *38* (17).
(127) Prospero, J. M.; Blades, E.; Mathison, G.; Naidu, R. Interhemispheric Transport of Viable Fungi and Bacteria from Africa to the Caribbean with Soil Dust. *Aerobiologia* **2005**, *21* (1), 1–19.
(128) Chen, P.-S.; Tsai, F. T.; Lin, C. K.; Yang, C.-Y.; Chan, C.-C.; Young, C.-Y.; Lee, C.-H. Ambient Influenza and Avian Influenza Virus during Dust Storm Days and Background Days. *Environ. Health Perspect.* **2010**, *118* (9), 1211–1216.
(129) Conen, F.; Morris, C. E.; Leifeld, J.; Yakutin, M. V.; Alewell, C. Biological Residues Define the Ice Nucleation Properties of Soil Dust. *Atmospheric Chem. Phys.* **2011**, *11* (18), 9643–9648.
(130) Jeon, E. M.; Kim, H. J.; Jung, K.; Kim, J. H.; Kim, M. Y.; Kim, Y. P.; Ka, J.-O. Impact of Asian Dust Events on Airborne Bacterial Community Assessed by Molecular Analyses. *Atmos. Environ.* **2011**, *45* (25), 4313–4321.
(131) Tang, K.; Huang, Z.; Huang, J.; Maki, T.; Zhang, S.; Shimizu, A.; Ma, X.; Shi, J.; Bi, J.; Zhou, T.; Wang, G.; Zhang, L. Characterization of Atmospheric Bioaerosols along the Transport Pathway of Asian Dust during the Dust-Bioaerosol 2016 Campaign. *Atmospheric Chem. Phys.* **2018**, *18* (10), 7131–7148.
(132) Bora, J.; Deka, P.; Bhuyan, P.; Sarma, K. P.; Hoque, R. R. Morphology and Mineralogy of Ambient Particulate Matter over Mid-Brahmaputra Valley: Application of SEM–EDX, XRD, and FTIR Techniques. *SN Appl. Sci.* **2021**, *3* (1), 137.
(133) Müller, K.; Lehmann, S.; van Pinxteren, D.; Gnauk, T.; Niedermeier, N.; Wiedensohler, A.; Herrmann, H. Particle Characterization at the Cape Verde Atmospheric Observatory during the 2007 RHaMBLe Intensive. *Atmospheric Chem. Phys.* **2010**, *10* (6), 2709–2721.
(134) Paris, R.; Desboeufs, K. V.; Formenti, P.; Nava, S.; Chou, C. Chemical Characterisation of Iron in Dust and Biomass Burning Aerosols during AMMA-SOP0/DABEX: Implication for Iron Solubility. *Atmospheric Chem. Phys.* **2010**, *10* (9), 4273–4282.
(135) Song, Y.-C.; Eom, H.-J.; Jung, H.-J.; Malek, M. A.; Kim, H. K.; Geng, H.; Ro, C.-U. Investigation of Aged Asian Dust Particles by the Combined Use of Quantitative ED-EPMA and ATR-FTIR Imaging. *Atmospheric Chem. Phys.* **2013**, *13* (6), 3463–3480.

(136) Abou-Ghanem, M.; Nodeh-Farahani, D.; McGrath, D. T.; VandenBoer, T. C.; Styler, S. A. Submitted. Ozone Uptake and Halogen Activation by Road Dust and Anti-Icing Solution: Implications for Wintertime Air Quality in High-Latitude Urban Environments. *Environ. Sci. Process. Impacts* **2021**.

(137) Lee, Y.-N.; Weber, R.; Ma, Y.; Orsini, D.; Maxwell-Meier, K.; Blake, D.; Meinardi, S.; Sachse, G.; Harward, C.; Chen, T.-Y.; Thornton, D.; Tu, F.-H.; Bandy, A. Airborne Measurement of Inorganic Ionic Components of Fine Aerosol Particles Using the Particle-into-Liquid Sampler Coupled to Ion Chromatography Technique during ACE-Asia and TRACE-P. *J. Geophys. Res. Atmospheres* **2003**, *108* (D23).

(138) Witham, C. S.; Oppenheimer, C.; Horwell, C. J. Volcanic Ash-Leachates: A Review and Recommendations for Sampling Methods. *J. Volcanol. Geotherm. Res.* **2005**, *141* (3), 299–326.

(139) Aryal, R.; Lee, B.-K.; Beecham, S.; Kandasamy, J.; Aryal, N.; Parajuli, K. Characterisation of Road Dust Organic Matter as a Function of Particle Size: A PARAFAC Approach. *Water. Air. Soil Pollut.* **2015**, *226* (2), 24.

(140) Laskina, O.; Young, M. A.; Kleiber, P. D.; Grassian, V. H. Infrared Extinction Spectroscopy and Micro-Raman Spectroscopy of Select Components of Mineral Dust Mixed with Organic Compounds. *J. Geophys. Res. Atmospheres* **2013**, *118* (12), 6593–6606.

(141) Youn, J.-S.; Kim, Y.-M.; Siddiqui, M. Z.; Watanabe, A.; Han, S.; Jeong, S.; Jung, Y.-W.; Jeon, K.-J. Quantification of Tire Wear Particles in Road Dust from Industrial and Residential Areas in Seoul, Korea. *Sci. Total Environ.* **2021**, *784*, 147177.

(142) Xu, J.; Bergin, M. H.; Greenwald, R.; Schauer, J. J.; Shafer, M. M.; Jaffrezo, J. L.; Aymoz, G. Aerosol Chemical, Physical, and Radiative Characteristics near a Desert Source Region of Northwest China during ACE-Asia. *J. Geophys. Res. Atmospheres* **2004**, *109* (D19).

(143) Froyd, K. D.; Murphy, D. M.; Brock, C. A.; Campuzano-Jost, P.; Dibb, J. E.; Jimenez, J.-L.; Kupc, A.; Middlebrook, A. M.; Schill, G. P.; Thornhill, K. L.; Williamson, C. J.; Wilson, J. C.; Ziemba, L. D. A New Method to Quantify Mineral Dust and Other Aerosol Species from Aircraft Platforms Using Single-Particle Mass Spectrometry. *Atmospheric Meas. Tech.* **2019**, *12* (11), 6209–6239.

(144) Lee, S.-H.; Murphy, D. M.; Thomson, D. S.; Middlebrook, A. M. Chemical Components of Single Particles Measured with Particle Analysis by Laser Mass Spectrometry (PALMS) during the Atlanta SuperSite Project: Focus on Organic/Sulfate, Lead, Soot, and Mineral Particles. *J. Geophys. Res. Atmospheres* **2002**, *107* (D1), AAC 1-1-AAC 1-13.

(145) Li, W.; Shao, L.; Zhang, D.; Ro, C.-U.; Hu, M.; Bi, X.; Geng, H.; Matsuki, A.; Niu, H.; Chen, J. A Review of Single Aerosol Particle Studies in the Atmosphere of East Asia: Morphology, Mixing State, Source, and Heterogeneous Reactions. *J. Clean. Prod.* **2016**, *112, Part 2*, 1330–1349.

(146) Dall'Osto, M.; Beddows, D. C. S.; McGillicuddy, E. J.; Esser-Gietl, J. K.; Harrison, R. M.; Wenger, J. C. On the Simultaneous Deployment of Two Single-Particle Mass Spectrometers Atan Urban Background and a Roadside Site during SAPUSS. *Atmospheric Chem. Phys.* **2016**, *16* (15), 9693–9710.

(147) Beddows, D. C. S.; Dall'Osto, M.; Olatunbosun, O. A.; Harrison, R. M. Detection of Brake Wear Aerosols by Aerosol Time-of-Flight Mass Spectrometry. *Atmos. Environ.* **2016**, *129*, 167–175.
(148) Dall'Osto, M.; Beddows, D. C. S.; Gietl, J. K.; Olatunbosun, O. A.; Yang, X.; Harrison, R. M. Characteristics of Tyre Dust in Polluted Air: Studies by Single Particle Mass Spectrometry (ATOFMS). *Atmos. Environ.* **2014**, *94*, 224–230.
(149) Möhler, O.; Benz, S.; Saathoff, H.; Schnaiter, M.; Wagner, R.; Schneider, J.; Walter, S.; Ebert, V.; Wagner, S. The Effect of Organic Coating on the Heterogeneous Ice Nucleation Efficiency of Mineral Dust Aerosols. *Environ. Res. Lett.* **2008**, *3* (2), 025007.
(150) Reitz, P.; Spindler, C.; Mentel, T. F.; Poulain, L.; Wex, H.; Mildenberger, K.; Niedermeier, D.; Hartmann, S.; Clauss, T.; Stratmann, F.; Sullivan, R. C.; DeMott, P. J.; Petters, M. D.; Sierau, B.; Schneider, J. Surface Modification of Mineral Dust Particles by Sulphuric Acid Processing: Implications for Ice Nucleation Abilities. *Atmospheric Chem. Phys.* **2011**, *11* (15), 7839–7858.
(151) Marsden, N. A.; Ullrich, R.; Möhler, O.; Eriksen Hammer, S.; Kandler, K.; Cui, Z.; Williams, P. I.; Flynn, M. J.; Liu, D.; Allan, J. D.; Coe, H. Mineralogy and Mixing State of North African Mineral Dust by Online Single-Particle Mass Spectrometry. *Atmospheric Chem. Phys.* **2019**, *19* (4), 2259–2281.
(152) Jayne, J. T.; Leard, D. C.; Zhang, X.; Davidovits, P.; Smith, K. A.; Kolb, C. E.; Worsnop, D. R. Development of an Aerosol Mass Spectrometer for Size and Composition Analysis of Submicron Particles. *Aerosol Sci. Technol.* **2000**, *33* (1–2), 49–70.
(153) Murphy, D. M.; Thomson, D. S. Laser Ionization Mass Spectroscopy of Single Aerosol Particles. *Aerosol Sci. Technol.* **1995**, *22* (3), 237–249.
(154) Gard, E.; Mayer, J. E.; Morrical, B. D.; Dienes, T.; Fergenson, D. P.; Prather, K. A. Real-Time Analysis of Individual Atmospheric Aerosol Particles: Design and Performance of a Portable ATOFMS. *Anal. Chem.* **1997**, *69* (20), 4083–4091.
(155) Dentener, F. J.; Carmichael, G. R.; Zhang, Y.; Lelieveld, J.; Crutzen, P. J. Role of Mineral Aerosol as a Reactive Surface in the Global Troposphere. *J. Geophys. Res. Atmospheres* **1996**, *101* (D17), 22869–22889.
(156) de Reus, M.; Dentener, F.; Thomas, A.; Borrmann, S.; Ström, J.; Lelieveld, J. Airborne Observations of Dust Aerosol over the North Atlantic Ocean during ACE 2: Indications for Heterogeneous Ozone Destruction. *J. Geophys. Res. Atmospheres* **2000**, *105* (D12), 15263–15275.
(157) Fairlie, T. D.; Jacob, D. J.; Dibb, J. E.; Alexander, B.; Avery, M. A.; van Donkelaar, A.; Zhang, L. Impact of Mineral Dust on Nitrate, Sulfate, and Ozone in Transpacific Asian Pollution Plumes. *Atmospheric Chem. Phys.* **2010**, *10* (8), 3999–4012.
(158) Umann, B.; Arnold, F.; Schaal, C.; Hanke, M.; Uecker, J.; Aufmhoff, H.; Balkanski, Y.; Dingenen, R. V. Interaction of Mineral Dust with Gas Phase Nitric Acid and Sulfur Dioxide during the MINATROC II Field Campaign: First Estimate of the Uptake Coefficient from Atmospheric Data. *J. Geophys. Res. Atmospheres* **2005**, *110* (D22).
(159) Matsumoto, J.; Takahashi, K.; Matsumi, Y.; Yabushita, A.; Shimizu, A.; Matsui, I.; Sugimoto, N. Scavenging of Pollutant Acid Substances by Asian Mineral Dust Particles. *Geophys. Res. Lett.* **2006**, *33* (7).
(160) Bonasoni, P.; Cristofanelli, P.; Calzolari, F.; Bonafè, U.; Evangelisti, F.; Stohl, A.; Zauli Sajani, S.; van Dingenen, R.; Colombo, T.; Balkanski, Y. Aerosol-Ozone Correlations during Dust Transport Episodes. *Atmospheric Chem. Phys.* **2004**, *4* (5), 1201–1215.

(161) Kandler, K.; Lieke, K.; Benker, N.; Emmel, C.; Küpper, M.; Müller-Ebert, D.; Ebert, M.; Scheuvens, D.; Schladitz, A.; Schütz, L.; Weinbruch, S. Electron Microscopy of Particles Collected at Praia, Cape Verde, during the Saharan Mineral Dust Experiment: Particle Chemistry, Shape, Mixing State and Complex Refractive Index. *Tellus B Chem. Phys. Meteorol.* **2011**, *63* (4), 475–496.
(162) Scarnato, B. V.; China, S.; Nielsen, K.; Mazzoleni, C. Perturbations of the Optical Properties of Mineral Dust Particles by Mixing with Black Carbon: A Numerical Simulation Study. *Atmospheric Chem. Phys.* **2015**, *15* (12), 6913–6928.
(163) Gibson, E. R.; Gierlus, K. M.; Hudson, P. K.; Grassian, V. H. Generation of Internally Mixed Insoluble and Soluble Aerosol Particles to Investigate the Impact of Atmospheric Aging and Heterogeneous Processing on the CCN Activity of Mineral Dust Aerosol. *Aerosol Sci. Technol.* **2007**, *41* (10), 914–924.
(164) Lederer, M. R.; Staniec, A. R.; Coates Fuentes, Z. L.; Van Ry, D. A.; Hinrichs, R. Z. Heterogeneous Reactions of Limonene on Mineral Dust: Impacts of Adsorbed Water and Nitric Acid. *J. Phys. Chem. A* **2016**, *120* (48), 9545–9556.
(165) Coates Fuentes, Z. L.; Kucinski, T. M.; Hinrichs, R. Z. Ozone Decomposition on Kaolinite as a Function of Monoterpene Exposure and Relative Humidity. *ACS Earth Space Chem.* **2018**, *2* (1), 21–30.
(166) Kameda, T.; Azumi, E.; Fukushima, A.; Tang, N.; Matsuki, A.; Kamiya, Y.; Toriba, A.; Hayakawa, K. Mineral Dust Aerosols Promote the Formation of Toxic Nitropolycyclic Aromatic Compounds. *Sci. Rep.* **2016**, *6*, 24427.
(167) Bian, H.; Zender, C. S. Mineral Dust and Global Tropospheric Chemistry: Relative Roles of Photolysis and Heterogeneous Uptake. *J. Geophys. Res. Atmospheres* **2003**, *108* (D21).
(168) Li, G.; Bei, N.; Tie, X.; Molina, L. T. Aerosol Effects on the Photochemistry in Mexico City during MCMA-2006/MILAGRO Campaign. *Atmospheric Chem. Phys.* **2011**, *11* (11), 5169–5182.
(169) McNamara, S. M.; Kolesar, K. R.; Wang, S.; Kirpes, R. M.; May, N. W.; Gunsch, M. J.; Cook, R. D.; Fuentes, J. D.; Hornbrook, R. S.; Apel, E. C.; China, S.; Laskin, A.; Pratt, K. A. Observation of Road Salt Aerosol Driving Inland Wintertime Atmospheric Chlorine Chemistry. *ACS Cent. Sci.* **2020**, *6* (5), 684–694.
(170) Schmidt, M.; Jansen van Beek, S. M.; Abou-Ghanem, M.; Oliynyk, A. O.; Locock, A. J.; Styler, S. A. Production of Atmospheric Organosulfates via Mineral-Mediated Photochemistry. *ACS Earth Space Chem.* **2019**, *3* (3), 424–431.
(171) Finlayson-Pitts, B. J.; Jr, J. N. P. *Chemistry of the Upper and Lower Atmosphere: Theory, Experiments, and Applications*; Academic Press, 1999.
(172) Mielke, L. H.; Furgeson, A.; Odame-Ankrah, C. A.; Osthoff, H. D. Ubiquity of ClNO2 in the Urban Boundary Layer of Calgary, Alberta, Canada. *Can. J. Chem.* **2015**, *94* (4), 414–423.
(173) Mielke, L. H.; Furgeson, A.; Osthoff, H. D. Observation of ClNO2 in a Mid-Continental Urban Environment. *Environ. Sci. Technol.* **2011**, *45* (20), 8889–8896.
(174) Ullerstam, M.; Johnson, M. S.; Vogt, R.; Ljungström, E. DRIFTS and Knudsen Cell Study of the Heterogeneous Reactivity of SO_2 and NO_2 on Mineral Dust. *Atmospheric Chem. Phys.* **2003**, *3* (6), 2043–2051.
(175) Underwood, G. M.; Song, C. H.; Phadnis, M.; Carmichael, G. R.; Grassian, V. H. Heterogeneous Reactions of NO_2 and HNO_3 on Oxides and Mineral Dust: A Combined

Laboratory and Modeling Study. *J. Geophys. Res. Atmospheres* **2001**, *106* (D16), 18055–18066.

(176) J. Tang, M.; Thieser, J.; Schuster, G.; N. Crowley, J. Kinetics and Mechanism of the Heterogeneous Reaction of N_2O_5 with Mineral Dust Particles. *Phys. Chem. Chem. Phys.* **2012**, *14* (24), 8551–8561.

(177) Usher, C. R.; Al-Hosney, H.; Carlos-Cuellar, S.; Grassian, V. H. A Laboratory Study of the Heterogeneous Uptake and Oxidation of Sulfur Dioxide on Mineral Dust Particles. *J. Geophys. Res. Atmospheres* **2002**, *107* (D23), 4713.

(178) Sullivan, R. C.; Guazzotti, S. A.; Sodeman, D. A.; Tang, Y.; Carmichael, G. R.; Prather, K. A. Mineral Dust Is a Sink for Chlorine in the Marine Boundary Layer. *Atmos. Environ.* **2007**, *41* (34), 7166–7179.

(179) Koulouri, E.; Saarikoski, S.; Theodosi, C.; Markaki, Z.; Gerasopoulos, E.; Kouvarakis, G.; Mäkelä, T.; Hillamo, R.; Mihalopoulos, N. Chemical Composition and Sources of Fine and Coarse Aerosol Particles in the Eastern Mediterranean. *Atmos. Environ.* **2008**, *42* (26), 6542–6550.

(180) Collaud Coen, M.; Weingartner, E.; Schaub, D.; Hueglin, C.; Corrigan, C.; Henning, S.; Schwikowski, M.; Baltensperger, U. Saharan Dust Events at the Jungfraujoch: Detection by Wavelength Dependence of the Single Scattering Albedo and First Climatology Analysis. *Atmospheric Chem. Phys.* **2004**, *4* (11/12), 2465–2480.

(181) Aymoz, G.; Jaffrezo, J.-L.; Jacob, V.; Colomb, A.; George, C. Evolution of Organic and Inorganic Components of Aerosol during a Saharan Dust Episode Observed in the French Alps. *Atmospheric Chem. Phys.* **2004**, *4* (11/12), 2499–2512.

(182) Wang, Y.; Zhou, L.; Wang, W.; Ge, M. Heterogeneous Uptake of Formic Acid and Acetic Acid on Mineral Dust and Coal Fly Ash. *ACS Earth Space Chem.* **2020**, *4* (2), 202–210.

(183) Bates, T. S.; Quinn, P. K.; Coffman, D. J.; Covert, D. S.; Miller, T. L.; Johnson, J. E.; Carmichael, G. R.; Uno, I.; Guazzotti, S. A.; Sodeman, D. A.; Prather, K. A.; Rivera, M.; Russell, L. M.; Merrill, J. T. Marine Boundary Layer Dust and Pollutant Transport Associated with the Passage of a Frontal System over Eastern Asia. *J. Geophys. Res. Atmospheres* **2004**, *109* (D19).

(184) Groß, S.; Tesche, M.; Freudenthaler, V.; Toledano, C.; Wiegner, M.; Ansmann, A.; Althausen, D.; Seefeldner, M. Characterization of Saharan Dust, Marine Aerosols and Mixtures of Biomass-Burning Aerosols and Dust by Means of Multi-Wavelength Depolarization and Raman Lidar Measurements during SAMUM 2. *Tellus B Chem. Phys. Meteorol.* **2011**, *63* (4), 706–724.

(185) Smith, D. J.; Timonen, H. J.; Jaffe, D. A.; Griffin, D. W.; Birmele, M. N.; Perry, K. D.; Ward, P. D.; Roberts, M. S. Intercontinental Dispersal of Bacteria and Archaea by Transpacific Winds. *Appl. Environ. Microbiol.* **2013**, *79* (4), 1134–1139.

(186) Li, M.; Su, H.; Li, G.; Ma, N.; Pöschl, U.; Cheng, Y. Relative Importance of Gas Uptake on Aerosol and Ground Surfaces Characterized by Equivalent Uptake Coefficients. *Atmospheric Chem. Phys.* **2019**, *19* (16), 10981–11011.

(187) Wang, X.; Romanias, M. N.; Thévenet, F.; Rousseau, A. Geocatalytic Uptake of Ozone onto Natural Mineral Dust. *Catalysts* **2018**, *8* (7), 263.

(188) Ndour, M.; Nicolas, M.; D'Anna, B.; Ka, O.; George, C. Photoreactivity of NO 2 on Mineral Dusts Originating from Different Locations of the Sahara Desert. *Phys. Chem. Chem. Phys.* **2009**, *11* (9), 1312–1319.

(189) Hanisch, F.; Crowley, J. N. Ozone Decomposition on Saharan Dust: An Experimental Investigation. *Atmos Chem Phys* **2003**, *3* (1), 119–130.
(190) Chang, R. Y.-W.; Sullivan, R. C.; Abbatt, J. P. D. Initial Uptake of Ozone on Saharan Dust at Atmospheric Relative Humidities. *Geophys. Res. Lett.* **2005**, *32* (14).
(191) Adams, J. W.; Rodriguez, D.; Cox, R. A. The Uptake of SO2 on Saharan Dust: A Flow Tube Study. *Atmospheric Chem. Phys.* **2005**, *5* (10), 2679–2689.
(192) Ndour, M.; D'Anna, B.; George, C.; Ka, O.; Balkanski, Y.; Kleffmann, J.; Stemmler, K.; Ammann, M. Photoenhanced Uptake of NO_2 on Mineral Dust: Laboratory Experiments and Model Simulations. *Geophys. Res. Lett.* **2008**, *35* (5).
(193) Kolb, C. E.; Cox, R. A.; Abbatt, J. P. D.; Ammann, M.; Davis, E. J.; Donaldson, D. J.; Garrett, B. C.; George, C.; Griffiths, P. T.; Hanson, D. R.; Kulmala, M.; McFiggans, G.; Pöschl, U.; Riipinen, I.; Rossi, M. J.; Rudich, Y.; Wagner, P. E.; Winkler, P. M.; Worsnop, D. R.; O' Dowd, C. D. An Overview of Current Issues in the Uptake of Atmospheric Trace Gases by Aerosols and Clouds. *Atmospheric Chem. Phys.* **2010**, *10* (21), 10561–10605.
(194) Crowley, J. N.; Ammann, M.; Cox, R. A.; Hynes, R. G.; Jenkin, M. E.; Mellouki, A.; Rossi, M. J.; Troe, J.; Wallington, T. J. Evaluated Kinetic and Photochemical Data for Atmospheric Chemistry: Volume V – Heterogeneous Reactions on Solid Substrates. *Atmospheric Chem. Phys.* **2010**, *10* (18), 9059–9223.
(195) Golden, D. M.; Spokes, G. N.; Benson, S. W. Very Low-Pressure Pyrolysis (VLPP); A Versatile Kinetic Tool. *Angew. Chem. Int. Ed. Engl.* **1973**, *12* (7), 534–546.
(196) Michel A. E.; Usher C. R.; Grassian V. H. Heterogeneous and Catalytic Uptake of Ozone on Mineral Oxides and Dusts: A Knudsen Cell Investigation. *Geophys. Res. Lett.* **2002**, *29* (14), 10–11.
(197) Usher, C. R.; Michel, A. E.; Stec, D.; Grassian, V. H. Laboratory Studies of Ozone Uptake on Processed Mineral Dust. *Atmos. Environ.* **2003**, *37* (38), 5337–5347.
(198) Styler, S. A.; Donaldson, D. J. Photooxidation of Atmospheric Alcohols on Laboratory Proxies for Mineral Dust. *Environ. Sci. Technol.* **2011**, *45* (23), 10004–10012.
(199) Seisel, S.; Börensen, C.; Vogt, R.; Zellner, R. Kinetics and Mechanism of the Uptake of N_2O_5 on Mineral Dust at 298 K. *Atmospheric Chem. Phys.* **2005**, *5* (12), 3423–3432.
(200) Michel, A. E.; Usher, C. R.; Grassian, V. H. Reactive Uptake of Ozone on Mineral Oxides and Mineral Dusts. *Atmos. Environ.* **2003**, *37* (23), 3201–3211.
(201) Al-Hosney, H. A.; Carlos-Cuellar, S.; Baltrusaitis, J.; Grassian, V. H. Heterogeneous Uptake and Reactivity of Formic Acid on Calcium Carbonate Particles: A Knudsen Cell Reactor, FTIR and SEM Study. *Phys. Chem. Chem. Phys.* **2005**, *7* (20), 3587–3595.
(202) Lasne, J.; Romanias, M. N.; Thevenet, F. Ozone Uptake by Clay Dusts under Environmental Conditions. *ACS Earth Space Chem.* **2018**, *2* (9), 904–914.
(203) Bedjanian, Y.; Romanias, M. N.; El Zein, A. Interaction of OH Radicals with Arizona Test Dust: Uptake and Products. *J. Phys. Chem. A* **2013**, *117* (2), 393–400.
(204) Wang, X.; Romanias, M. N.; Pei, Z.; Rousseau, A.; Thévenet, F. Uptake Mechanism of Acetic Acid onto Natural Gobi Dust. *ACS Earth Space Chem.* **2020**, *4* (9), 1650–1662.
(205) Romanias, M. N.; Zeineddine, M. N.; Gaudion, V.; Lun, X.; Thevenet, F.; Riffault, V. Heterogeneous Interaction of Isopropanol with Natural Gobi Dust. *Environ. Sci. Technol.* **2016**, *50* (21), 11714–11722.

(206) Zeineddine, M. N.; Romanias, M. N.; Gaudion, V.; Riffault, V.; Thévenet, F. Heterogeneous Interaction of Isoprene with Natural Gobi Dust. *ACS Earth Space Chem.* **2017**, *1* (5), 236–243.
(207) Cooney, D. O.; Kim, S.-S.; James Davis, E. Analyses of Mass Transfer in Hemodialyzers for Laminar Blood Flow and Homogeneous Dialysate. *Chem. Eng. Sci.* **1974**, *29* (8), 1731–1738.
(208) Knopf, D. A.; Pöschl, U.; Shiraiwa, M. Radial Diffusion and Penetration of Gas Molecules and Aerosol Particles through Laminar Flow Reactors, Denuders, and Sampling Tubes. *Anal. Chem.* **2015**, *87* (7), 3746–3754.
(209) Wagner, C.; Hanisch, F.; Holmes, N.; de Coninck, H.; Schuster, G.; Crowley, J. N. The Interaction of N_2O_5 with Mineral Dust: Aerosol Flow Tube and Knudsen Reactor Studies. *Atmospheric Chem. Phys.* **2008**, *8* (1), 91–109.
(210) Dupart, Y.; Fine, L.; D'Anna, B.; George, C. Heterogeneous Uptake of NO2 on Arizona Test Dust under UV-A Irradiation: An Aerosol Flow Tube Study. *Aeolian Res.* **2014**, *15*, 45–51.
(211) Matthews, P. S. J.; Baeza-Romero, M. T.; Whalley, L. K.; Heard, D. E. Uptake of HO_2 Radicals onto Arizona Test Dust Particles Using an Aerosol Flow Tube. *Atmospheric Chem. Phys.* **2014**, *14* (14), 7397–7408.
(212) Sullivan, R. C.; Miñambres, L.; DeMott, P. J.; Prenni, A. J.; Carrico, C. M.; Levin, E. J. T.; Kreidenweis, S. M. Chemical Processing Does Not Always Impair Heterogeneous Ice Nucleation of Mineral Dust Particles. *Geophys. Res. Lett.* **2010**, *37* (24).
(213) Moon, D. R.; Taverna, G. S.; Anduix-Canto, C.; Ingham, T.; Chipperfield, M. P.; Seakins, P. W.; Baeza-Romero, M.-T.; Heard, D. E. Heterogeneous Reaction of HO_2 with Airborne TiO_2 Particles and Its Implication for Climate Change Mitigation Strategies. *Atmospheric Chem. Phys.* **2018**, *18* (1), 327–338.
(214) C. Sullivan, R.; K. Moore, M. J.; D. Petters, M.; M. Kreidenweis, S.; C. Roberts, G.; A. Prather, K. Timescale for Hygroscopic Conversion of Calcite Mineral Particles through Heterogeneous Reaction with Nitric Acid. *Phys. Chem. Chem. Phys.* **2009**, *11* (36), 7826–7837.
(215) Mogili, P. K.; Kleiber, P. D.; Young, M. A.; Grassian, V. H. N_2O_5 Hydrolysis on the Components of Mineral Dust and Sea Salt Aerosol: Comparison Study in an Environmental Aerosol Reaction Chamber. *Atmos. Environ.* **2006**, *40* (38), 7401–7408.
(216) Mogili, P. K.; Kleiber, P. D.; Young, M. A.; Grassian, V. H. Heterogeneous Uptake of Ozone on Reactive Components of Mineral Dust Aerosol: An Environmental Aerosol Reaction Chamber Study. *J. Phys. Chem. A* **2006**, *110* (51), 13799–13807.
(217) Chen, H.; Stanier, C. O.; Young, M. A.; Grassian, V. H. A Kinetic Study of Ozone Decomposition on Illuminated Oxide Surfaces. *J. Phys. Chem. A* **2011**, *115* (43), 11979–11987.
(218) Romanías, M. N.; Ourrad, H.; Thévenet, F.; Riffault, V. Investigating the Heterogeneous Interaction of VOCs with Natural Atmospheric Particles: Adsorption of Limonene and Toluene on Saharan Mineral Dusts. *J. Phys. Chem. A* **2016**, *120* (8), 1197–1212.
(219) Börensen, C.; Kirchner, U.; Scheer, V.; Vogt, R.; Zellner, R. Mechanism and Kinetics of the Reactions of NO_2 or HNO_3 with Alumina as a Mineral Dust Model Compound. *J. Phys. Chem. A* **2000**, *104* (21), 5036–5045.

(220) Roscoe, J. M.; Abbatt, J. P. D. Diffuse Reflectance FTIR Study of the Interaction of Alumina Surfaces with Ozone and Water Vapor. *J. Phys. Chem. A* **2005**, *109* (40), 9028–9034.
(221) Armaroli, T.; Bécue, T.; Gautier, S. Diffuse Reflection Infrared Spectroscopy (Drifts): Application to the in Situ Analysis of Catalysts. *Oil Gas Sci. Technol.* **2004**, *59* (2), 215–237.
(222) Kortüm, G. *Reflectance Spectroscopy: Principles, Methods, Applications*; Springer Science & Business Media, 2012.
(223) Rubasinghege, G.; H. Grassian, V. Role(s) of Adsorbed Water in the Surface Chemistry of Environmental Interfaces. *Chem. Commun.* **2013**, *49* (30), 3071–3094.
(224) Newberg, J. T.; Starr, D. E.; Yamamoto, S.; Kaya, S.; Kendelewicz, T.; Mysak, E. R.; Porsgaard, S.; Salmeron, M. B.; Brown, G. E.; Nilsson, A.; Bluhm, H. Formation of Hydroxyl and Water Layers on MgO Films Studied with Ambient Pressure XPS. *Surf. Sci.* **2011**, *605* (1), 89–94.
(225) Ketteler, G.; Yamamoto, S.; Bluhm, H.; Andersson, K.; Starr, D. E.; Ogletree, D. F.; Ogasawara, H.; Nilsson, A.; Salmeron, M. The Nature of Water Nucleation Sites on TiO2(110) Surfaces Revealed by Ambient Pressure X-Ray Photoelectron Spectroscopy. *J. Phys. Chem. C* **2007**, *111* (23), 8278–8282.
(226) Joshi, N.; Romanias, M. N.; Riffault, V.; Thevenet, F. Investigating Water Adsorption onto Natural Mineral Dust Particles: Linking DRIFTS Experiments and BET Theory. *Aeolian Res.* **2017**, *27*, 35–45.
(227) Wang, L.; Wang, W.; Ge, M. Heterogeneous Uptake of NO_2 on Soils under Variable Temperature and Relative Humidity Conditions. *J. Environ. Sci.* **2012**, *24* (10), 1759–1766.
(228) Liu, Y.; Han, C.; Ma, J.; Bao, X.; He, H. Influence of Relative Humidity on Heterogeneous Kinetics of NO_2 on Kaolin and Hematite. *Phys. Chem. Chem. Phys.* **2015**, *17* (29), 19424–19431.
(229) D'Anna, B.; Jammoul, A.; George, C.; Stemmler, K.; Fahrni, S.; Ammann, M.; Wisthaler, A. Light-Induced Ozone Depletion by Humic Acid Films and Submicron Aerosol Particles. *J. Geophys. Res. Atmospheres* **2009**, *114* (D12), D12301.
(230) Abbatt, J. P. D.; Lee, A. K. Y.; Thornton, J. A. Quantifying Trace Gas Uptake to Tropospheric Aerosol: Recent Advances and Remaining Challenges. *Chem. Soc. Rev.* **2012**, *41* (19), 6555–6581.
(231) Aubin, D. G.; Abbatt, J. P. Adsorption of Gas-Phase Nitric Acid to n-Hexane Soot: Thermodynamics and Mechanism. *J. Phys. Chem. A* **2003**, *107* (50), 11030–11037.
(232) Aubin, D. G.; Abbatt, J. P. D. Interaction of NO_2 with Hydrocarbon Soot: Focus on HONO Yield, Surface Modification, and Mechanism. *J. Phys. Chem. A* **2007**, *111* (28), 6263–6273.
(233) Lelièvre, S.; Bedjanian, Y.; Pouvesle, N.; Delfau, J.-L.; Vovelle, C.; Bras, G. L. Heterogeneous Reaction of Ozone with Hydrocarbon Flame Soot. *Phys. Chem. Chem. Phys.* **2004**, *6* (6), 1181–1191.
(234) Underwood, G. M.; Li, P.; Usher, C. R.; Grassian, V. H. Determining Accurate Kinetic Parameters of Potentially Important Heterogeneous Atmospheric Reactions on Solid Particle Surfaces with a Knudsen Cell Reactor. *J. Phys. Chem. A* **2000**, *104* (4), 819–829.

(235) Park, J.; Jang, M.; Yu, Z. Heterogeneous Photo-Oxidation of SO_2 in the Presence of Two Different Mineral Dust Particles: Gobi and Arizona Dust. *Environ. Sci. Technol.* **2017**, *51* (17), 9605–9613.
(236) Di Biagio, C.; Formenti, P.; Balkanski, Y.; Caponi, L.; Cazaunau, M.; Pangui, E.; Journet, E.; Nowak, S.; Andreae, M. O.; Kandler, K.; Saeed, T.; Piketh, S.; Seibert, D.; Williams, E.; Doussin, J.-F. Complex Refractive Indices and Single-Scattering Albedo of Global Dust Aerosols in the Shortwave Spectrum and Relationship to Size and Iron Content. *Atmospheric Chem. Phys.* **2019**, *19* (24), 15503–15531.
(237) Wagner, C.; Schuster, G.; Crowley, J. N. An Aerosol Flow Tube Study of the Interaction of N_2O_5 with Calcite, Arizona Dust and Quartz. *Atmos. Environ.* **2009**, *43* (32), 5001–5008.
(238) Tang, M. J.; Camp, J. C. J.; Rkiouak, L.; McGregor, J.; Watson, I. M.; Cox, R. A.; Kalberer, M.; Ward, A. D.; Pope, F. D. Heterogeneous Interaction of SiO_2 with N_2O_5: Aerosol Flow Tube and Single Particle Optical Levitation–Raman Spectroscopy Studies. *J. Phys. Chem. A* **2014**, *118* (38), 8817–8827.
(239) Vlasenko, A.; Huthwelker, T.; W. Gäggeler, H.; Ammann, M. Kinetics of the Heterogeneous Reaction of Nitric Acid with Mineral Dust Particles: An Aerosol Flowtube Study. *Phys. Chem. Chem. Phys.* **2009**, *11* (36), 7921–7930.
(240) Santschi, Ch.; Rossi, M. J. Uptake of CO_2, SO_2, HNO_3 and HCl on Calcite ($CaCO_3$) at 300 K: Mechanism and the Role of Adsorbed Water. *J. Phys. Chem. A* **2006**, *110* (21), 6789–6802.
(241) Tang, M. J.; Schuster, G.; Crowley, J. N. Heterogeneous Reaction of N_2O_5 with Illite and Arizona Test Dust Particles. *Atmospheric Chem. Phys.* **2014**, *14* (1), 245–254.
(242) Li, W.; Oyama, S. T. Mechanism of Ozone Decomposition on a Manganese Oxide Catalyst. 2. Steady-State and Transient Kinetic Studies. *J. Am. Chem. Soc.* **1998**, *120* (35), 9047–9052.
(243) Jia, X.; Gu, W.; Peng, C.; Li, R.; Chen, L.; Wang, H.; Wang, H.; Wang, X.; Tang, M. Heterogeneous Reaction of $CaCO_3$ With NO_2 at Different Relative Humidities: Kinetics, Mechanisms, and Impacts on Aerosol Hygroscopicity. *J. Geophys. Res. Atmospheres* **2021**, *126* (11), e2021JD034826.
(244) Seisel, S.; Börensen, C.; Vogt, R.; Zellner, R. The Heterogeneous Reaction of HNO_3 on Mineral Dust and γ-Alumina Surfaces: A Combined Knudsen Cell and DRIFTS Study. *Phys. Chem. Chem. Phys.* **2004**, *6* (24), 5498–5508.
(245) Tang, M.; Larish, W. A.; Fang, Y.; Gankanda, A.; Grassian, V. H. Heterogeneous Reactions of Acetic Acid with Oxide Surfaces: Effects of Mineralogy and Relative Humidity. *J. Phys. Chem. A* **2016**, *120* (28), 5609–5616.
(246) Xu, B.; Shang, J.; Zhu, T.; Tang, X. Heterogeneous Reaction of Formaldehyde on the Surface of γ-Al_2O_3 Particles. *Atmos. Environ.* **2011**, *45* (21), 3569–3575.
(247) Carlos-Cuellar, S.; Li, P.; Christensen, A. P.; Krueger, B. J.; Burrichter, C.; Grassian, V. H. Heterogeneous Uptake Kinetics of Volatile Organic Compounds on Oxide Surfaces Using a Knudsen Cell Reactor: Adsorption of Acetic Acid, Formaldehyde, and Methanol on α-Fe_2O_3, α-Al_2O_3, and SiO_2. *J. Phys. Chem. A* **2003**, *107* (21), 4250–4261.
(248) Chen, H.; Nanayakkara, C. E.; Grassian, V. H. Titanium Dioxide Photocatalysis in Atmospheric Chemistry. *Chem. Rev.* **2012**, *112* (11), 5919–5948.
(249) George, C.; D'Anna, B.; Herrmann, H.; Weller, C.; Vaida, V.; Donaldson, D. J.; Bartels-Rausch, T.; Ammann, M. Emerging Areas in Atmospheric Photochemistry. In

Atmospheric and Aerosol Chemistry; Topics in Current Chemistry; Springer, Berlin, Heidelberg, 2012; pp 1–53.

(250) Hoffmann, M. R.; Martin, S. T.; Choi, W.; Bahnemann, D. W. Environmental Applications of Semiconductor Photocatalysis. *Chem. Rev.* **1995**, *95* (1), 69–96.

(251) Nicolas, M.; Ndour, M.; Ka, O.; D'Anna, B.; George, C. Photochemistry of Atmospheric Dust: Ozone Decomposition on Illuminated Titanium Dioxide. *Environ. Sci. Technol.* **2009**, *43* (19), 7437–7442.

(252) Wang, H.; Li, K.; Li, J.; Sun, Y.; Dong, F. Photochemical Transformation Pathways of Nitrates from Photocatalytic NO_x Oxidation: Implications for Controlling Secondary Pollutants. *Environ. Sci. Technol. Lett.* **2021**.

(253) Ma, Q.; Wang, L.; Chu, B.; Ma, J.; He, H. Contrary Role of H_2O and O_2 in the Kinetics of Heterogeneous Photochemical Reactions of SO_2 on TiO_2. *J. Phys. Chem. A* **2019**, *123* (7), 1311–1318.

Chapter 2

Significant Variability in the Photocatalytic Activity of Natural Titanium-Containing Minerals: Implications for Understanding and Predicting Atmospheric Mineral Dust Photochemistry

Maya Abou-Ghanem, Anton O. Oliynyk, Zhihao Chen, Laura C. Matchett, Devon T. McGrath, Michael J. Katz, Andrew J. Locock, and Sarah A. Styler

Published in *Environmental Science & Technology*, 2020, 54 (21), 13509-13516, DOI: 10.1021/acs.est.0c05861; reproduced with minor edits.

2.1 Introduction

Although each cubic meter of air contains only microgram quantities of particulate matter,[1] these particles have an outsize influence on climate[2] and human health.[3] Mineral dust is one of the most abundant types of atmospheric particulate matter, with over a billion tons emitted into the atmosphere each year from remote arid regions in North Africa, East Asia, and Australia.[4] Once aloft, dust can be transported to urban areas, where it can interact with locally emitted pollutants[5] and thereby influence the composition of the urban atmosphere: for example, observed reductions in mixing ratios of ozone, an important component of urban smog,[6] during periods of elevated dust loadings have been attributed to the scavenging of ozone and its precursor gases (*e.g.*, HNO_3).[7] These interactions can also influence the properties of the dust itself: for example, the reaction of dust with pollutants can change its toxicity,[8] optical properties,[9] cloud condensation nuclei (CCN)[10] and ice nuclei (IN)[11] activity, and its ability to act as a depositional source of soluble iron to marine ecosystems.[12]

Motivated by these diverse impacts, many laboratory studies have examined the kinetics and products of the reaction of mineral dust and mineral dust proxies with both inorganic[13] and organic[14,15] pollutant gases; in many cases, researchers have found these reactions to be enhanced by light.[16] Because mineral dust contains Ti, which is a well-known semiconductor photocatalyst in its oxide form,[17] the atmospheric chemistry community has extensively studied the TiO_2-catalyzed photochemistry of many urban pollutants.[18]

Although the use of TiO_2 enables detailed mechanistic analysis that is challenging for natural dust, the composition of which is complex and variable, it is not without its weaknesses: for example, although the Ti content of mineral dust determined using elemental analysis is typically reported as TiO_2, Ti is also a component of many other minerals detected in atmospheric dust.[19,20] In addition, even in cases where mineralogical analysis has specifically identified TiO_2 in dust samples,[21] there is no guarantee that the reactivity of this TiO_2 is identical across all natural samples or comparable to that of commercially sourced samples,

since the surface and band structures of TiO_2 are influenced by many sample-specific properties, including crystal structure,[22] degree of hydration,[23] presence of dopants,[24] and particle size.[25]

To improve our understanding of natural mineral photochemistry, we investigated the uptake of ozone by 10 natural Ti-containing minerals, which we chose based on both their Ti content and their environmental abundance. We find that all of these minerals display photoenhanced uptake of ozone, that ozone uptake varies both between and within mineral phases, that ozone uptake does not increase linearly with elemental Ti content, and that commercial TiO_2 is significantly more reactive toward ozone than all of the natural samples studied here. Further, we discuss these observations in the context of comprehensive characterization data, including particle size, morphology, crystallographic structure, band structure, and elemental impurity identification. This approach, which brings together both atmospheric and materials chemistry perspectives, will ultimately enable us to better predict the influence of dust–pollutant interactions on atmospheric composition.

2.2 Materials and methods

Experiments were conducted using a set of 10 natural Ti-containing minerals, which we sourced from www.minfind.com and purchased through contact with individual vendors. Details regarding sample purification, preparation, grinding, and characterization via X-ray diffraction (XRD; phase identification), electron microprobe analysis (EMPA; Ti content of the dominant mineral phase present in each sample), nitrogen adsorption analysis (specific surface area determination), ultraviolet–visible (UV–vis) diffuse reflectance spectroscopy (optical properties and, where possible, band gap determination), and scanning electron microscopy (SEM; particle size and morphology) are presented in Appendix A.

Mineral-coated Pyrex insert tubes were exposed to ozone in a coated-wall atmospheric pressure flow tube reactor, which was mounted in the center of a black plastic box and surrounded by four UV-A lamps (4.13–3.02 eV, eV_{max}: 3.48; 300–410 nm, λ_{max}: 356 nm). With

four lamps turned on, the NO_2 photolysis frequency (JNO_2)[26] inside the reactor was 0.0045 ± 0.0001 s^{-1}, which is in the range of noontime photolysis frequencies measured at a northern midlatitude site.[27] We note, however, that this comparison does not take into account the spectral mismatch between our lamp emission profiles and the solar radiation spectrum at this location. Further details regarding the flow tube reactor, NO_2 actinometry, insert tube preparation, and experimental protocols are presented in Appendix A.1.

Ozone was introduced to the flow tube by a movable injector; the ozone–surface interaction time was calculated using the volumetric gas flow and the flow tube dimensions, and the pseudo-first-order rate constant for the reaction, k_{obs}, was determined using the following equation[28]

$$[O_3] = [O_3]_0 \times e^{-k_{obs}t} \quad (2.1)$$

Here, $[O_3]$ is the average steady-state ozone concentration at the exit of the flow tube upon exposure to the mineral substrate under either light or dark conditions, $[O_3]_0$ is the average ozone concentration with the movable injector entirely pushed in (*i.e.*, with no exposure to the mineral substrate), and t is the residence time of ozone inside the mineral-coated section of the flow tube. The obtained k_{obs} values were then used to calculate effective uptake coefficients, γ_{eff}, as follows[28]

$$\gamma_{eff} = \frac{D_{tube} \times k_{obs}}{\omega_{O_3}} \quad (2.2)$$

Here, D_{tube} is the flow tube diameter and ω_{O_3} is the mean thermal velocity of ozone under our experimental conditions. Finally, γ_{eff} was corrected for gas-phase diffusion limitations[29] and sample-specific surface area scaling (Brunauer–Emmett– Teller; BET) was applied to yield γ_{BET}, which is the value reported in this work[30]

$$\gamma_{corr} = \frac{\gamma_{eff}}{1 - \gamma_{eff} \frac{3}{2N_{Shw}^{eff} Kn}} \quad (2.3)$$

$$\gamma_{BET} = \gamma_{corr} \times \frac{S_{geo}}{S_{BET}{}' \, m} \quad (2.4)$$

Here, N_{Shw}^{eff} is the effective Sherwood number, Kn is the Knudsen number, S_{geo} is the geometric surface area of the mineral-coated section of the coated-wall flow tube (m^2), m is the sample mass (g), and S_{BET} is the specific BET surface area ($m^2\ g^{-1}$) of the sample; these values, which are specific for our experimental conditions and the geometry of the coated-wall flow tube, are presented in Table A.4.

For both the commercial and natural TiO_2 samples, almost complete depletion of ozone was observed upon illumination; therefore, to minimize diffusion limitations for these samples, we performed experiments using TiO_2/SiO_2 mixtures. This approach required additional considerations for the γ_{BET} calculations, which we present in Appendix A.1.3.3.1. To verify that uptake of ozone was insignificant in the absence of minerals, we conducted blank experiments using empty Pyrex insert tubes ($n = 3$). In all cases except for one trial of titanite 2 under dark conditions, the loss of ozone in these blank tubes was significantly lower than the loss observed for mineral-coated tubes. For this reason, the γ_{BET} values presented here are not blank-corrected and γ_{BET} values for titanite 2 under dark conditions are not reported.

2.3 Results and discussion

2.3.1 Selection and characterization of Ti-containing minerals relevant to mineral dust

Our sample set consists of anatase and rutile, two of the three naturally occurring TiO_2 polymorphs (the third, brookite, is uncommon);[31] ilmenite, an iron–titanium oxide commonly found in igneous and metamorphic rocks;[32] titanite, the most abundant titanosilicate;[33] and the titanium-bearing minerals phlogopite, hastingsite, augite, and epidote, which are commonly found members of the mica, amphibole, pyroxene, and epidote supergroups, respectively.[20,34] To assess the extent to which photochemistry varies within a single mineral class, we studied two samples of both anatase and titanite. The mineral names, simplified chemical formulas, geographic origins, and elemental Ti contents of our sample set are displayed in Table 2.1.

Mineral	Simplified Chemical Formula	Origin	Ti content (mass %)[a]
anatase (commercial)	TiO_2	Sigma Aldrich	99.8[b]
anatase 1	TiO_2	Pakistan	99.5 ± 0.3
anatase 2	TiO_2	Brazil	99.8 ± 0.2
rutile	TiO_2	Brazil	98.8 ± 0.1
ilmenite	$FeTiO_3$	United States	51.0 ± 1.2
titanite 1	$CaTiSiO_5$	Canada	34.7 ± 0.2
titanite 2	$CaTiSiO_5$	Brazil	38.5 ± 0.2
phlogopite	$KMg_3(AlSi_3O_{10})(F,OH)_2$	Canada	1.02 ± 0.05
hastingsite	$NaCa_2(Mg_4Fe^{3+})(Si_6Al_2)O_{22}(OH)_2$	United States	0.79 ± 0.03
augite	$(Ca,Na)(Mg,Fe,Al,Ti)(Si,Al)_2O_6$	United States	0.71 ± 0.08
epidote	$Ca_2(Al,Fe)_2Si_3O_{12}(OH)$	Norway	0.21 ± 0.02

[a] reported as TiO_2 by mass; in all cases except commercial anatase, the dominant mineral phase was selected for spot analysis

[b] reported as TiO_2 by the supplier (Sigma Aldrich)

Table 2.1: Ti and Ti-bearing minerals under study.

2.3.2 Photoenhanced ozone uptake by Ti-containing minerals varies by several orders of magnitude

We investigated the uptake of ozone by Ti-containing minerals using a custom-built coated-wall photochemical flow tube reactor (Figure A.1), in which ozone passes through a Pyrex tube coated with the mineral sample of interest and the loss of ozone measured at the outlet of the tube reflects the degree of surface reaction. All mineral samples were exposed to ozone under both dark and illuminated conditions; a representative ozone reaction profile is shown in Figure 2.1 for titanite 1, and reaction profiles for all other minerals are shown in Figures A.3 and A.4. In all cases, ozone loss was higher upon illumination and higher than in the absence of mineral samples, which implies the existence of a light-mediated pathway for ozone loss at

the surface of all samples. To our knowledge, these results are the first demonstration of photoenhanced trace gas uptake by natural Ti-containing minerals.

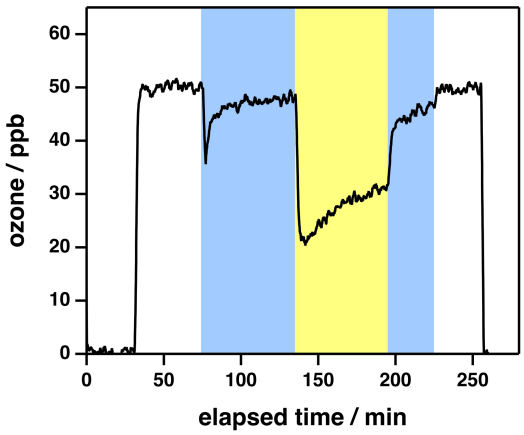

Figure 2.1: Reaction profile of ozone with titanite 1 at 25% RH. The unshaded regions of the profile denote time periods in which ozone was not exposed to titanite 1. The blue and yellow regions of the profile denote the exposure of ozone to titanite 1 under dark and illuminated conditions, respectively.

For each mineral sample, the γ_{BET} values under illumination are higher than those under dark conditions; these values are presented in Figures 2.2 (illuminated conditions) and S14 (dark conditions). As illustrated in Figure 2.2, γ_{BET} values for illuminated samples span four orders of magnitude, ranging from $(1.8 \pm 0.3) \times 10^{-4}$ for commercial TiO_2 to $(1.2 \pm 0.5) \times 10^{-7}$ for epidote. It is not surprising that the TiO_2 minerals (anatase 1, anatase 2, and rutile) are the natural samples with the highest γ_{BET} values, given that TiO_2 is a well-known semiconductor photocatalyst with band gaps in the near-UV for both its anatase and rutile phases.[35] In their study of ozone decomposition at the surface of mixed TiO_2–SiO_2 films, Nicolas et al. drew from studies of the behavior of ozone in aqueous systems (see *e.g.*, Staehelin and Hoigné[36]) to propose a mechanism for the TiO_2-catalyzed uptake of ozone.[37] In this mechanism, which is described in detail in Appendix A.2.2.1, absorption of light with energy equal to or greater than the band gap of TiO_2 leads to the release of molecular oxygen.

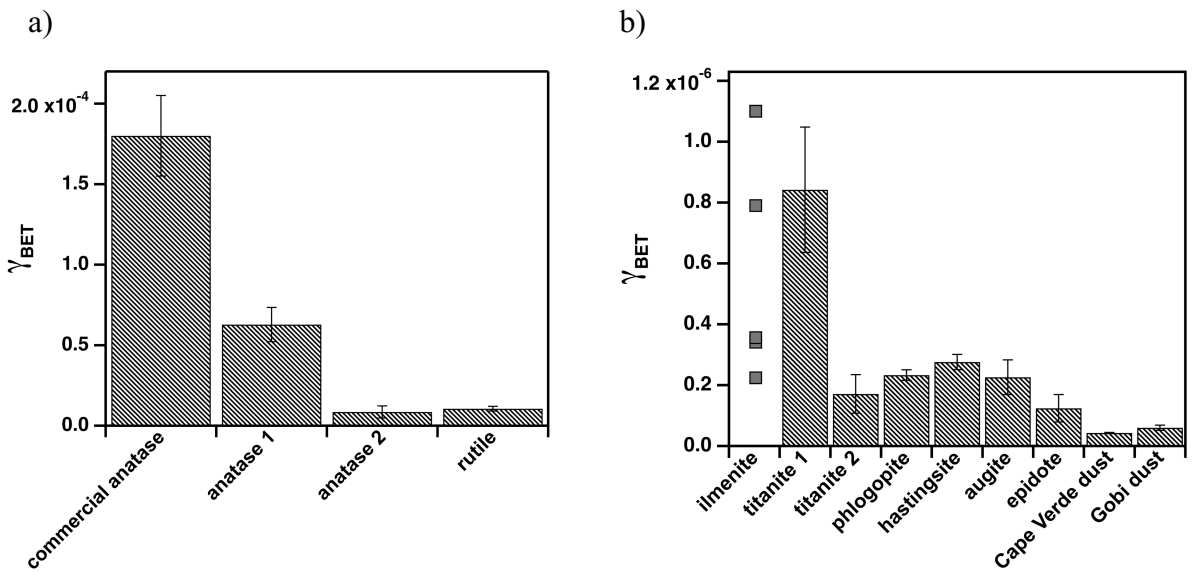

Figure 2.2: BET uptake coefficients (γ_{BET}) for ozone at RH 25% at the surface of illuminated (JNO_2 = 0.0045 ± 0.0001 s^{-1}; see Appendix A.1): a) commercial and natural TiO_2 and b) other Ti minerals, Ti-bearing minerals, and desert dust samples (Cape Verde depositional dust and Gobi dust). For all samples except ilmenite, each data point represents the mean of three trials, with 1σ error bars; for ilmenite, which appeared to display bimodal reactivity (see Appendix A.2.1), each trial (n = 6) is displayed individually.

Since the light-enhanced uptake of ozone has not been previously explored for Ti-containing minerals other than TiO_2, no specific mechanisms currently exist to explain the reactivity of the remaining minerals in our sample set. To assess if these minerals have the potential to be semiconductor photocatalysts, we obtained diffuse reflectance spectra for each sample, which we then transformed using the Kubelka–Munk function as described in Appendix A.1.4.5. As shown in Figures 2.3 and A.11, all of the mineral samples investigated in this study absorb light in the emission range of the UV-A lamps used in the photoreactor and many have band gaps that lie within this emission range. Therefore, the non-TiO_2 minerals in our sample set can, in principle, catalyze the photoreduction of ozone *via* the mechanism proposed for TiO_2. However, as shown in Figure 2.2, these samples are significantly less photoactive than the TiO_2 minerals, which for a given mineral sample may reflect considerations such as the extent of its band gap overlap with the emission range of the UV-A lamps; the absolute position of its

conduction/valence band edges in comparison to the redox potential of the relevant adsorbed species (i.e., oxygen and/or ozone);[38] and its interfacial charge transfer efficiency, which in turn reflects the competition between electron–hole recombination and charge transfer to adsorbed species.[17]

As described in Appendix A.2.1, the catalytic uptake of ozone by metal oxides under dark conditions is thought to be mediated by reactive Lewis acid surface sites (SS).[39] In particular, the interaction of ozone with these sites has been proposed to lead to the formation of gas-phase molecular oxygen and adsorbed atomic oxygen (SS–O), the latter of which can subsequently react with ozone or another adsorbed oxygen atom to regenerate the surface sites.[40,41] In this context, we propose that the photocatalytic loss of ozone in our experiments may also occur *via* photocleavage of the SS–O bond, which would also regenerate reactive surface sites and thus enable sustained ozone uptake. Since the photocleavage potential of this bond would depend on the strength of the SS–O interaction, and thus be sample-specific,[39] this mechanism would also explain the sample-to-sample variability in ozone uptake coefficients apparent in Figure 2.2. Although we expect the semiconductor photocatalysis mechanism described in Appendix A.2.2 to dominate for the TiO_2 minerals, we note that if these minerals also possess strong SS–O bonds, which would limit surface site regeneration, then SS–O photocleavage would also lead to enhanced ozone uptake upon illumination for these samples. We suggest that further studies of the mechanism of ozone photochemistry at mineral surfaces would benefit from surface spectroscopic measurements of ozone binding frequencies,[39,42] which have previously been shown to provide insight into the influence of molecular geometry and symmetry on the photochemistry of adsorbed species.[43]

2.3.3 Samples of the same mineral phase exhibit significantly different photoreactivities

Interestingly, as shown in Figure 2.2, we find significantly different photoreactivities for two titanite samples originating from different locations. These observations may reflect differences in the optical properties of the two samples: as shown in Figure 2.3, the band gap of titanite 1 (3.49 eV; 355 nm) is smaller than that of titanite 2 (3.66 eV; 339 nm), and in

particular overlaps the maximum emission wavelength of the UV lamps used in this study (3.48 eV; 356 nm), which enables it to absorb a greater fraction of emitted light in the flow tube reactor.

As shown in Tables A.9 and A.10, the primary compositional difference between the two titanite samples is that the Fe content of titanite 1 is considerably higher than that of titanite 2. Although no studies have investigated the influence of Fe content on titanite photocatalysis, Fe doping of TiO_2 nanoparticles has been shown to result in band gap energy reductions.[44] In this context, we tentatively attribute the red shift in the band gap of titanite 1 to substitution of Ti by Fe in its crystal structure. Fe doping has also been found to reduce the charge-carrier recombination rate for TiO_2 nanoparticles and thereby increase the probability that photogenerated electrons and holes will react with adsorbed species.[45] If Fe doping affects titanite similarly, then this mechanism would also explain the elevated reactivity observed for titanite 1 with respect to titanite 2.

We also observe significant differences in photoreactivity for the two anatase samples employed in this study: as shown in Figure 2.2, γ_{BET} for illuminated anatase 1 is more than 7× larger than that of anatase 2. In this case, the explanations employed for the titanite samples do not suffice: despite their different photoreactivities, the two anatase samples have similar band gaps (Figure 2.3), elemental compositions (Tables A.5 and A.6), and X-ray diffractogram peak positions (Figure A.9). Because we identified only the dominant phase for each mineral using EMPA and XRD, we cannot assess the extent to which dopants[24] (*e.g.*, trace Nb and Fe, the quantities of which vary for these two samples) and/or intergrown mineral phases[46] present at trace levels may have influenced the photoreactivity of these samples. In the following paragraphs, we consider several additional factors that may have contributed to the observed differences in reactivity.

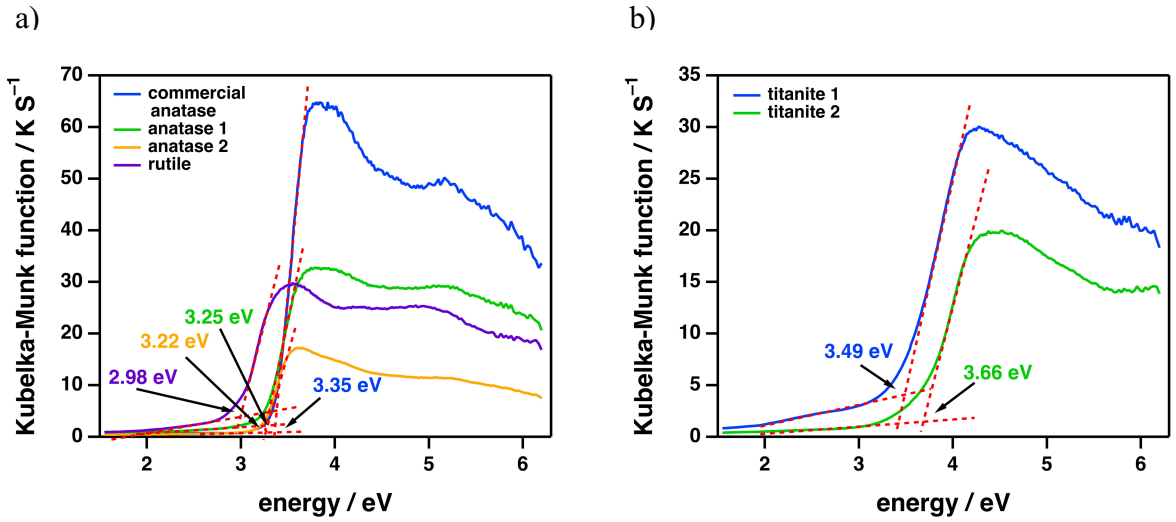

Figure 2.3: Diffuse reflectance UV-Vis spectra (displayed in Kubelka–Munk units) for a) titanite samples and b) TiO_2 minerals. The intersection of the dashed red lines for each sample indicates the position of the band gap.

The photocatalytic potential of TiO_2 is influenced by particle size, which controls the available surface area for reactions to occur. In this context, as noted above, we scaled all uptake coefficients to the BET surface area of each mineral. Particle size can also influence the surface acidity[47] and inherent photoreactivity of semiconductors (*e.g.*, by changing the charge-carrier recombination rate[25] and mechanism of electron transport[48]); for these reasons, we used field emission scanning electron microscopy (FESEM) to image a subset of the samples (all TiO_2 samples and both titanite samples). As illustrated in Figure A.12, although we found commercial TiO_2 particles to be much smaller and more spherical than the natural mineral samples, we did not see any obvious size distribution differences for the natural samples, which implies that the photoreactivity differences observed for our anatase samples did not arise from sample preparation (*i.e.*, hand grinding) artifacts.

The photoreactivity of TiO_2 can be influenced by many additional factors, including crystal facet[49]; electron mobility[50]; interfacial charge-carrier dynamics[24]; amorphous/crystalline content[51]; exposure of fresh, active surfaces upon grinding[52]; and the amount of surface-sorbed

water, which can alter the symmetry of adsorbed species and thereby modify the relative importance of subsequent surface photochemical pathways.[43] As a result of this complexity, predicting and understanding differences in photocatalytic activity is challenging even for synthesized TiO_2 samples.[53] In the natural environment, where a given mineral phase can exhibit a range of elemental substitutions and crystal lattice parameters,[32] the situation is even more complex; nevertheless, we suggest that some/all of these factors may have also been in operation for our samples.

2.3.4 Implications for the study of atmospheric mineral dust photochemistry

Studies of mineral dust photochemistry performed to date have largely assumed that Ti present in mineral dust exists solely as TiO_2, and therefore that the photoactive potential of a given dust sample can be predicted using elemental analysis.[18,37,54] To assess the validity of this approach, we first plotted the ozone photoreactivity (γ_{BET}) of our mineral samples as a function of the Ti content of their dominant mineral phase. As illustrated in Figure 2.4, although γ_{BET} generally increases with Ti content, this increase is not linear; in addition, we observe substantial variability in γ_{BET} values for all mineral types (*i.e.*, TiO_2 minerals, non-TiO_2 Ti minerals with intermediate Ti content, and Ti-bearing minerals with low Ti content). To explicitly test the validity of elemental analysis-based predictions of dust photoreactivity, we also investigated the uptake of ozone at the surface of two natural mineral dust samples: Cape Verde depositional dust (4.5% Ti)[55] and Gobi dust (1.3% Ti).[14] If the Ti in these samples were present exclusively as TiO_2, with an assumed γ_{BET} range of 6.2×10^{-6} –7.4×10^{-5} (the γ_{BET} values for all replicates of the three natural TiO_2 samples shown in Figure 2.2), then we would expect γ_{eff} values in the range of 1.8×10^{-6} –5.3×10^{-5} and 5.6×10^{-7} –1.7×10^{-5} for Cape Verde and Gobi dusts, respectively. Although the γ_{eff} values for Cape Verde and Gobi dusts obtained in this work ($(6.4 \pm 0.7) \times 10^{-6}$ and $(2.7 \pm 0.4) \times 10^{-6}$, respectively) fall within the lower bound of these broad ranges, this approach also assumes that the Ti in these samples is present in grains with specific surface areas identical to those of the hand-ground TiO_2 samples studied here, which may not be the case. In addition, these γ_{eff} values are much smaller than those

predicted from the results obtained for commercial anatase ((2.9–3.8) × 10^{-4} and (0.9– 1.2) × 10^{-4} for Cape Verde and Gobi dusts, respectively). Together, these results highlight the limitations of both elemental and mineralogical analyses in predicting mineral dust photoreactivity and provide the first direct evidence that the use of commercial TiO_2 as a proxy for the photoactive component of mineral dust can lead to overestimates in the magnitude of light-mediated processes at the surface of ambient dust.

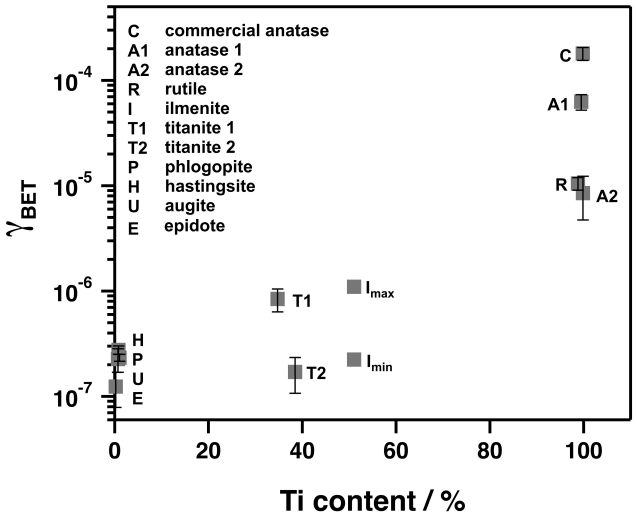

Figure 2.4: BET uptake coefficients (γ_{BET}) for ozone at the surface of all Ti-containing minerals as a function of the Ti content of each mineral, with the latter obtained as described in Table 2.1. For all samples except ilmenite, each data point represents the mean of three trials, with 1σ error bars; for ilmenite, which appeared to display bimodal reactivity (see Appendix A.2.1), the minimum and maximum γ_{BET} values are shown.

Climate change is predicted to exacerbate mineral dust emissions;[56] in this context, it is increasingly important to understand the influence of dust on climate, air quality, and health. The atmospheric chemistry community has employed elemental and/or mineralogical analysis to quantify dust nutrient inputs to oceanic ecosystems,[57] determine source regions of ambient dust aerosol,[58] and identify mineral phases important for ice nucleation[59] and trace gas chemistry at the soil surface.[60] Our results highlight for the first time that dust photochemistry

does not easily lend itself to these types of bottom-up approaches: specifically, we show that Ti-containing minerals other than TiO_2 photocatalyze trace gas uptake, that dust photochemistry does not scale linearly with elemental Ti content, and that samples of the same mineral phase can exhibit significantly different photoreactivity. To address these limitations, we propose instead a top-down approach, in which the photoactive potential of dust is assessed using samples collected from global source regions representing a diverse range of mineralogical compositions.[61] Because this expanded approach does not make assumptions regarding the components of dust that drive its reactivity, it has the added benefit of considering contributions from both known (*e.g.*, iron oxides[62,63]) and as-yet unidentified photoactive species present in mineral dust.

2.4 References

(1) Hand, J. L.; Gill, T. E.; Schichtel, B. A. Urban and Rural Coarse Aerosol Mass across the United States: Spatial and Seasonal Variability and Long-Term Trends. *Atmospheric Environment* **2019**, *218*, 117025. https://doi.org/10.1016/j.atmosenv.2019.117025.

(2) IPCC. AR5 Climate Change 2013: The Physical Science Basis.

(3) World Health Organization. *Ambient Air Pollution: A Global Assessment of Exposure and Burden of Disease*; World Health Organization, 2016.

(4) Tanaka, T. Y.; Chiba, M. A Numerical Study of the Contributions of Dust Source Regions to the Global Dust Budget. *Global Planet. Change* **2006**, *52* (1), 88–104. https://doi.org/10.1016/j.gloplacha.2006.02.002.

(5) Pan, X.; Uno, I.; Wang, Z.; Nishizawa, T.; Sugimoto, N.; Yamamoto, S.; Kobayashi, H.; Sun, Y.; Fu, P.; Tang, X.; Wang, Z. Real-Time Observational Evidence of Changing Asian Dust Morphology with the Mixing of Heavy Anthropogenic Pollution. *Sci. Rep.* **2017**, *7* (1), 335. https://doi.org/10.1038/s41598-017-00444-w.

(6) Sillman, S. *"Tropospheric Ozone and Photochemical Smog" Environmental Geochemistry*; Elsevier, 2003; Vol. 9.

(7) de Reus, M.; Dentener, F.; Thomas, A.; Borrmann, S.; Ström, J.; Lelieveld, J. Airborne Observations of Dust Aerosol over the North Atlantic Ocean during ACE 2: Indications for Heterogeneous Ozone Destruction. *J. Geophys. Res. Atmos.* **2000**, *105* (D12), 15263–15275. https://doi.org/10.1029/2000JD900164.

(8) Kameda, T.; Azumi, E.; Fukushima, A.; Tang, N.; Matsuki, A.; Kamiya, Y.; Toriba, A.; Hayakawa, K. Mineral Dust Aerosols Promote the Formation of Toxic Nitropolycyclic Aromatic Compounds. *Sci. Rep.* **2016**, *6*, 24427. https://doi.org/10.1038/srep24427.

(9) Alexander, J. M.; Grassian, V. H.; Young, M. A.; Kleiber, P. D. Optical Properties of Selected Components of Mineral Dust Aerosol Processed with Organic Acids and Humic Material. *J. Geophys. Res. Atmos.* **2015**, *120* (6). https://doi.org/10.1002/2014JD022782.

(10) Sullivan, R. C.; Moore, M. J. K.; Petters, M. D.; Kreidenweis, S. M.; Roberts, G. C.; Prather, K. A. Effect of Chemical Mixing State on the Hygroscopicity and Cloud Nucleation Properties of Calcium Mineral Dust Particles. *Atmos. Chem. Phys.* **2009**, *9* (10), 3303–3316. https://doi.org/10.5194/acp-9-3303-2009.

(11) Möhler, O.; Benz, S.; Saathoff, H.; Schnaiter, M.; Wagner, R.; Schneider, J.; Walter, S.; Ebert, V.; Wagner, S. The Effect of Organic Coating on the Heterogeneous Ice Nucleation Efficiency of Mineral Dust Aerosols. *Environ. Res. Lett.* **2008**, *3* (2), 025007. https://doi.org/10.1088/1748-9326/3/2/025007.

(12) Shi, Z.; Krom, M. D.; Jickells, T. D.; Bonneville, S.; Carslaw, K. S.; Mihalopoulos, N.; Baker, A. R.; Benning, L. G. Impacts on Iron Solubility in the Mineral Dust by Processes in the Source Region and the Atmosphere: A Review. *Aeolian Res.* **2012**, *5*, 21–42. https://doi.org/10.1016/j.aeolia.2012.03.001.

(13) Tang, M.; Huang, X.; Lu, K.; Ge, M.; Li, Y.; Cheng, P.; Zhu, T.; Ding, A.; Zhang, Y.; Gligorovski, S.; Song, W.; Ding, X.; Bi, X.; Wang, X. Heterogeneous Reactions of Mineral Dust Aerosol: Implications for Tropospheric Oxidation Capacity. *Atmos. Chem. Phys.* **2017**, *17* (19), 11727–11777. https://doi.org/10.5194/acp-17-11727-2017.

(14) Romanías, M. N.; Ourrad, H.; Thévenet, F.; Riffault, V. Investigating the Heterogeneous Interaction of VOCs with Natural Atmospheric Particles: Adsorption of Limonene and Toluene on Saharan Mineral Dusts. *J. Phys. Chem. A* **2016**, *120* (8), 1197–1212. https://doi.org/10.1021/acs.jpca.5b10323.

(15) Carlos-Cuellar, S.; Li, P.; Christensen, A. P.; Krueger, B. J.; Burrichter, C.; Grassian, V. H. Heterogeneous Uptake Kinetics of Volatile Organic Compounds on Oxide Surfaces Using a Knudsen Cell Reactor: Adsorption of Acetic Acid, Formaldehyde, and Methanol on α-Fe_2O_3, α-Al_2O_3, and SiO_2. *J. Phys. Chem. A* **2003**, *107* (21), 4250–4261. https://doi.org/10.1021/jp0267609.

(16) George, C.; Ammann, M.; D'Anna, B.; Donaldson, D. J.; Nizkorodov, S. A. Heterogeneous Photochemistry in the Atmosphere. *Chem. Rev.* **2015**, *115* (10), 4218–4258. https://doi.org/10.1021/cr500648z.

(17) Hoffmann, M. R.; Martin, S. T.; Choi, W.; Bahnemann, D. W. Environmental Applications of Semiconductor Photocatalysis. *Chem. Rev.* **1995**, *95* (1), 69–96. https://doi.org/10.1021/cr00033a004.

(18) Chen, H.; Nanayakkara, C. E.; Grassian, V. H. Titanium Dioxide Photocatalysis in Atmospheric Chemistry. *Chem. Rev.* **2012**, *112* (11), 5919–5948. https://doi.org/10.1021/cr3002092.

(19) Guthrie, G. D.; Mossman, B. T. *Health Effects of Mineral Dusts*; Reviews in Mineralogy; Walter de Gruyter GmbH & Co KG, 2018; Vol. 28.

(20) Fitzpatrick, R. W.; Chittleborough, D. J. Titanium and Zirconium Minerals. In *Soil Mineralogy with Environmental Applications*; John Wiley & Sons, Ltd, 2002; pp 667–690. https://doi.org/10.2136/sssabookser7.c22.

(21) Engelbrecht, J. P.; McDonald, E. V.; Gillies, J. A.; Jayanty, R. K. M. "Jay"; Casuccio, G.; Gertler, A. W. Characterizing Mineral Dusts and Other Aerosols from the Middle East—Part 2: Grab Samples and Re-Suspensions. *Inhal. Toxicol.* **2009**, *21* (4), 327–336. https://doi.org/10.1080/08958370802464299.

(22) Zhang, J.; Zhou, P.; Liu, J.; Yu, J. New Understanding of the Difference of Photocatalytic Activity among Anatase, Rutile and Brookite TiO_2. *Phys. Chem. Chem. Phys.* **2014**, *16* (38), 20382–20386. https://doi.org/10.1039/C4CP02201G.

(23) Folli, A.; Campbell, S. B.; Anderson, J. A.; Macphee, D. E. Role of TiO2 Surface Hydration on NO Oxidation Photo-Activity. *J .Photoch. Photobio. A* **2011**, *220* (2), 85–93. https://doi.org/10.1016/j.jphotochem.2011.03.017.

(24) Kumar, S. G.; Devi, L. G. Review on Modified TiO_2 Photocatalysis under UV/Visible Light: Selected Results and Related Mechanisms on Interfacial Charge Carrier Transfer Dynamics. *J. Phys. Chem. A* **2011**, *115* (46), 13211–13241. https://doi.org/10.1021/jp204364a.

(25) Sieland, F.; Schneider, J.; W. Bahnemann, D. Photocatalytic Activity and Charge Carrier Dynamics of TiO_2 Powders with a Binary Particle Size Distribution. *Phys. Chem. Chem. Phys.* **2018**, *20* (12), 8119–8132. https://doi.org/10.1039/C8CP00398J.

(26) Zafonte, L.; Rieger, P. L.; Holmes, J. R. Nitrogen Dioxide Photolysis in the Los Angeles Atmosphere. *Environ. Sci. Technol.* **1977**, *11* (5), 483–487.

(27) Michoud, V.; Colomb, A.; Borbon, A.; Miet, K.; Beekmann, M.; Camredon, M.; Aumont, B.; Perrier, S.; Zapf, P.; Siour, G.; Ait-Helal, W.; Afif, C.; Kukui, A.; Furger, M.; Dupont, J. C.; Haeffelin, M.; Doussin, J. F. Study of the Unknown HONO Daytime Source at a European Suburban Site during the MEGAPOLI Summer and Winter Field Campaigns. *Atmos. Chem. Phys.* **2014**, *14* (6), 2805–2822. https://doi.org/10.5194/acp-14-2805-2014.

(28) Pöschl, U.; Rudich, Y.; Ammann, M. Kinetic Model Framework for Aerosol and Cloud Surface Chemistry and Gas-Particle Interactions–Part 1: General Equations, Parameters, and Terminology. *Atmos. Chem. Phys.* **2007**, *7* (23), 5989–6023.

(29) Knopf, D. A.; Pöschl, U.; Shiraiwa, M. Radial Diffusion and Penetration of Gas Molecules and Aerosol Particles through Laminar Flow Reactors, Denuders, and Sampling Tubes. *Analytical Chemistry* **2015**, *87* (7), 3746–3754. https://doi.org/10.1021/ac5042395.

(30) Michel, A. E.; Usher, C. R.; Grassian, V. H. Reactive Uptake of Ozone on Mineral Oxides and Mineral Dusts. *Atmos. Environ.* **2003**, *37* (23), 3201–3211. https://doi.org/10.1016/S1352-2310(03)00319-4.

(31) Jaffe, H. W. *Crystal Chemistry and Refractivity*; Courier Corporation, 1996.

(32) Bowles, J. F. W.; Howie, R. A.; Vaughan, D. J.; Zussman, J. *Rock-Forming Minerals*; Geological Society of London, 2011.

(33) Clarke, F. W.; Washington, H. S. *The Composition of the Earth's Crust*; U.S. Government Printing Office, 1924.

(34) Franz, G.; Liebscher, A. Physical and Chemical Properties of the Epidote Minerals–an Introduction. *Rev. Mineral Geochem.* **2004**, *56* (1), 1–81. https://doi.org/10.2138/gsrmg.56.1.1.

(35) Reyes-Coronado, D.; Rodríguez-Gattorno, G.; Espinosa-Pesqueira, M. E.; Cab, C.; Coss, R. de; Oskam, G. Phase-Pure TiO_2 Nanoparticles: Anatase, Brookite and Rutile. *Nanotechnology* **2008**, *19* (14), 145605. https://doi.org/10.1088/0957-4484/19/14/145605.

(36) Staehelin, J.; Hoigne, J. Decomposition of Ozone in Water in the Presence of Organic Solutes Acting as Promoters and Inhibitors of Radical Chain Reactions. *Environ. Sci. Technol.* **1985**, *19* (12), 1206–1213. https://doi.org/10.1021/es00142a012.

(37) Nicolas, M.; Ndour, M.; Ka, O.; D'Anna, B.; George, C. Photochemistry of Atmospheric Dust: Ozone Decomposition on Illuminated Titanium Dioxide. *Environ. Sci. Technol.* **2009**, *43* (19), 7437–7442. https://doi.org/10.1021/es901569d.

(38) Xu, Y.; Schoonen, M. A. A. The Absolute Energy Positions of Conduction and Valence Bands of Selected Semiconducting Minerals. *Am. Mineral.* **2000**, *85* (3–4), 543–556. https://doi.org/10.2138/am-2000-0416.

(39) Bulanin, K. M.; Lavalley, J. C.; Tsyganenko, A. A. IR Spectra of Adsorbed Ozone. *Colloids Surf. A Physicochem. Eng. Asp.* **1995**, *101* (2), 153–158. https://doi.org/10.1016/0927-7757(95)03130-6.

(40) Li, W.; Gibbs, G. V.; Oyama, S. T. Mechanism of Ozone Decomposition on a Manganese Oxide Catalyst. 1. In Situ Raman Spectroscopy and Ab Initio Molecular Orbital Calculations. *J. Am. Chem. Soc.* **1998**, *120* (35), 9041–9046. https://doi.org/10.1021/ja981441+.

(41) Li, W.; Oyama, S. T. Mechanism of Ozone Decomposition on a Manganese Oxide Catalyst. 2. Steady-State and Transient Kinetic Studies. *J. Am. Chem. Soc.* **1998**, *120* (35), 9047–9052. https://doi.org/10.1021/ja9814422.

(42) Bulanin, K. M.; Lavalley, J. C.; Tsyganenko, A. A. Infrared Study of Ozone Adsorption on TiO2 (Anatase). *The Journal of Physical Chemistry* **1995**, *99* (25), 10294–10298. https://doi.org/10.1021/j100025a034.

(43) Ostaszewski, C. J.; Stuart, N. M.; Lesko, D. M. B.; Kim, D.; Lueckheide, M. J.; Navea, J. G. Effects of Coadsorbed Water on the Heterogeneous Photochemistry of Nitrates Adsorbed on TiO2. *J. Phys. Chem. A* **2018**, *122* (31), 6360–6371. https://doi.org/10.1021/acs.jpca.8b04979.

(44) George, S.; Pokhrel, S.; Ji, Z.; Henderson, B. L.; Xia, T.; Li, L.; Zink, J. I.; Nel, A. E.; Mädler, L. Role of Fe Doping in Tuning the Band Gap of TiO_2 for the Photo-Oxidation-Induced Cytotoxicity Paradigm. *J. Am. Chem. Soc.* **2011**, *133* (29), 11270–11278. https://doi.org/10.1021/ja202836s.

(45) Zhou, M.; Yu, J.; Cheng, B. Effects of Fe-Doping on the Photocatalytic Activity of Mesoporous TiO_2 Powders Prepared by an Ultrasonic Method. *J. Hazard. Mater.* **2006**, *137* (3), 1838–1847. https://doi.org/10.1016/j.jhazmat.2006.05.028.

(46) Hurum, D. C.; Agrios, A. G.; Gray, K. A.; Rajh, T.; Thurnauer, M. C. Explaining the Enhanced Photocatalytic Activity of Degussa P25 Mixed-Phase TiO_2 Using EPR. *J. Phys. Chem. B* **2003**, *107* (19), 4545–4549. https://doi.org/10.1021/jp0273934.

(47) Zaki, M. I.; Fouad, N. E.; Mekhemer, G. A. H.; Jagadale, T. C.; Ogale, S. B. TiO2 Nanoparticle Size Dependence of Porosity, Adsorption and Catalytic Activity. *Colloids and Surfaces A: Physicochemical and Engineering Aspects* **2011**, *385* (1), 195–200. https://doi.org/10.1016/j.colsurfa.2011.06.010.

(48) Schneider, J.; Matsuoka, M.; Takeuchi, M.; Zhang, J.; Horiuchi, Y.; Anpo, M.; Bahnemann, D. W. Understanding TiO_2 Photocatalysis: Mechanisms and Materials. *Chem. Rev.* **2014**, *114* (19), 9919–9986. https://doi.org/10.1021/cr5001892.

(49) Pan, J.; Liu, G.; Lu, G. Q. (Max); Cheng, H.-M. On the True Photoreactivity Order of 001, 010, and 101 Facets of Anatase TiO_2 Crystals. *Angew. Chem. Int. Ed.* **2011**, *50* (9), 2133–2137. https://doi.org/10.1002/anie.201006057.

(50) Luttrell, T.; Halpegamage, S.; Tao, J.; Kramer, A.; Sutter, E.; Batzill, M. Why Is Anatase a Better Photocatalyst than Rutile? - Model Studies on Epitaxial TiO_2 Films. *Sci. Rep.* **2014**, *4* (1), 1–8. https://doi.org/10.1038/srep04043.

(51) Gao, L.; Zhang, Q. Effects of Amorphous Contents and Particle Size on the Photocatalytic Properties of TiO_2 Nanoparticles. *Scr. Mater.* **2001**, *44* (8), 1195–1198. https://doi.org/10.1016/S1359-6462(01)00681-9.

(52) Miao, J.; Zhang, R.; Zhang, L. Photocatalytic Degradations of Three Dyes with Different Chemical Structures Using Ball-Milled TiO_2. *Mater. Res. Bull.* **2018**, *97*, 109–114. https://doi.org/10.1016/j.materresbull.2017.08.032.

(53) Ohtani, B.; Mahaney, O. O. P.; Amano, F.; Murakami, N.; Abe, R. What Are Titania Photocatalysts?—An Exploratory Correlation of Photocatalytic Activity with Structural and Physical Properties. *J. Adv. Oxid. Technol.* **2016**, *13* (3), 247–261. https://doi.org/10.1515/jaots-2010-0303.

(54) Ndour, M.; D'Anna, B.; George, C.; Ka, O.; Balkanski, Y.; Kleffmann, J.; Stemmler, K.; Ammann, M. Photoenhanced Uptake of NO_2 on Mineral Dust: Laboratory Experiments and Model Simulations. *Geophys. Res. Lett.* **2008**, *35* (5), L05812. https://doi.org/10.1029/2007GL032006.

(55) Hanisch, F.; Crowley, J. N. Ozone Decomposition on Saharan Dust: An Experimental Investigation. *Atmos. Chem. Phys.* **2003**, *3* (1), 119–130. https://doi.org/10.5194/acp-3-119-2003.

(56) Ji, Z.; Wang, G.; Yu, M.; Pal, J. S. Potential Climate Effect of Mineral Aerosols over West Africa: Part II—Contribution of Dust and Land Cover to Future Climate Change. *Clim. Dyn.* **2018**, *50* (7), 2335–2353. https://doi.org/10.1007/s00382-015-2792-x.

(57) Journet, E.; Desboeufs, K. V.; Caquineau, S.; Colin, J.-L. Mineralogy as a Critical Factor of Dust Iron Solubility. *Geophys. Res. Lett.* **2008**, *35* (7), L07805. https://doi.org/10.1029/2007GL031589.

(58) Caquineau, S.; Gaudichet, A.; Gomes, L.; Magonthier, M.-C.; Chatenet, B. Saharan Dust: Clay Ratio as a Relevant Tracer to Assess the Origin of Soil-Derived Aerosols. *Geophys. Res. Lett.* **1998**, *25* (7), 983–986. https://doi.org/10.1029/98GL00569.

(59) Atkinson, J. D.; Murray, B. J.; Woodhouse, M. T.; Whale, T. F.; Baustian, K. J.; Carslaw, K. S.; Dobbie, S.; O'Sullivan, D.; Malkin, T. L. The Importance of Feldspar for Ice Nucleation by Mineral Dust in Mixed-Phase Clouds. *Nature* **2013**, *498* (7454), 355–358. https://doi.org/10.1038/nature12278.

(60) Kebede, M. A.; Bish, D. L.; Losovyj, Y.; Engelhard, M. H.; Raff, J. D. The Role of Iron-Bearing Minerals in NO_2 to HONO Conversion on Soil Surfaces. *Environ. Sci. Technol.* **2016**, *50* (16), 8649–8660. https://doi.org/10.1021/acs.est.6b01915.

(61) Engelbrecht, J. P.; Moosmüller, H.; Pincock, S.; Jayanty, R. K. M.; Lersch, T.; Casuccio, G. Technical Note: Mineralogical, Chemical, Morphological, and Optical Interrelationships of Mineral Dust Re-Suspensions. *Atmos. Chem. Phys.* **2016**, *16* (17), 10809–10830. https://doi.org/10.5194/acp-16-10809-2016.

(62) Mishra, M.; Chun, D.-M. α-Fe_2O_3 as a Photocatalytic Material: A Review. *Appl. Catal. A Gen.* **2015**, *498*, 126–141. https://doi.org/10.1016/j.apcata.2015.03.023.

(63) Chen, H.; Navea, J. G.; Young, M. A.; Grassian, V. H. Heterogeneous Photochemistry of Trace Atmospheric Gases with Components of Mineral Dust Aerosol. *J. Phys. Chem. A* **2011**, *115* (4), 490–499. https://doi.org/10.1021/jp110164j.

Chapter 3

Ozone Chemistry and Photochemistry at the Surface of Icelandic Volcanic Dust: Insights from Elemental Speciation Analysis

Maya Abou-Ghanem, Britta J. L. Jensen, Sarah A. Styler, and Manolis N. Romanias

Published in *ACS Earth and Space Chemistry*, 2021, 5, 11, 3065–3074, DOI: 10.1021/acsearthspacechem.0c00363; reproduced with minor edits.

3.1 Introduction

Although the majority of atmospheric dust is released from desert regions in North Africa, Central Asia, and Australia,[1] high-latitude environments are also productive dust sources: as a result of their extreme winds and low absolute humidities,[2] high-latitude dust sources contribute ~3–5% of global dust emissions despite their relatively modest geographical area (~500,000 km^2).[2,3] On a more local scale, northern sources are the dominant contributor to Arctic surface dust loadings[3] and can deliver nutrients to surrounding marine and terrestrial ecosystems.[4]

Iceland, arguably the most important of the high-latitude source regions, emits 30–40 million tons of dust each year,[5] with these emissions reflecting both glacial and volcanic processes. Approximately 10% of Iceland is covered by glaciers,[6] which sit above the basaltic material that comprises most of the island.[7] Glacial and wind erosion of this material has resulted in over 20,000 km^2 of sandy deserts,[8] which in turn contain a number of highly active dust source areas;[5] according to one report, the deposition rate of glaciogenic volcanic dust is higher in Iceland than in any other location.[9] Particulate matter (PM) concentrations in Iceland are also influenced by resuspension of deposited volcanic ash:[10–12] for example, resuspension of ash from the 2010 Eyjafjallajökull eruption[13] led to major dust events even years later.[14,15]

According to one long-term observational data set, Iceland experiences an average of 135 dust days each year.[16] These dust events, which are highly dependent on meteorological conditions (e.g., wind speed and humidity),[10,17–19] can result in episodic air quality reductions in populated areas.[20] To date, most investigations of the health impacts of volcanic PM have focused on its direct inhalation effects;[21–23] fewer, in contrast, have explored potential indirect air quality impacts arising from the interaction of this PM class with gas-phase pollutants.[24,25]

The short-term impacts of volcanic eruptions on the gas-phase composition of the troposphere are comparatively well documented: in particular, many field studies have reported ozone

depletion within and downwind of volcanic plumes.[26] This depletion is believed to arise from catalytic destruction of ozone by halogen radicals formed from coemitted volcanic gases,[26–28] rather than from ozone loss at the surface of volcanic PM. However, this may not be the case after eruptions, when the mixing ratios of halogen-containing gases have returned to background levels, but volcanic dust emissions persist. Ozone depletion has also been observed within Saharan[29] and Gobi[30] dust plumes; here, in contrast, ozone loss has been attributed to the direct uptake of ozone (as observed in the laboratory[31–33]) and/or the scavenging of its precursors (i.e., nitrogen oxides[34]) by mineral dust. Although the composition of lower-latitude dusts differs significantly from that of Icelandic dust,[35] these observations nonetheless suggest that the interaction of ozone with high-latitude dust may also be important.

To date, laboratory investigations of ozone–volcanic PM interactions have been performed at low pressure and in the absence of water vapor and have focused exclusively on volcanic ash.[36,37] However, the reactivity of ozone with mineral surfaces typically displays a strong relative humidity (RH) dependence;[38] in addition, the reactivity of volcanic dust produced via erosion of surface volcanic material may differ from that of freshly emitted ash. The situation is further complicated by the fact that both Icelandic PM[25,39,40] and lower-latitude mineral dust[31,41] are photochemically active. In the case of lower-latitude mineral dust, we have suggested that this photoenhancement may be mediated by Ti-containing minerals;[31] however, the potential drivers of this chemistry in Icelandic volcanic dust remain unexplored. Together, these gaps in our knowledge limit our ability to predict the atmospheric reactivity of volcanic dust toward ozone and, more broadly, to quantify the overall air quality impacts of volcanic dust emissions.

Here, we report ozone uptake by volcanic dust obtained from Mýrdalssandur, a major dust source region located in southern Iceland,[5,9] which we characterized using bulk, surface, and spatially resolved compositional analysis. To better understand the mechanism and environmental relevance of this reaction, we performed experiments under both dark and light conditions and at a range of ozone concentrations and RHs. Based on the kinetic

parameters we obtain here, we conclude that this chemistry will influence ozone concentrations in volcanically active regions only during extreme dust events.

3.2 Experimental

3.2.1 Experimental apparatus

Experiments were conducted in a coated-wall flow tube reactor (Figure B.1), which has previously been used to investigate the uptake of NO_2 and SO_2 by volcanic dust[24,25] and the uptake of ozone by clays.[42] The reactor consists of a Pyrex reaction tube (length = 20 cm; internal diameter = 0.975 cm) housed within a larger Pyrex flow cell, the latter of which is equipped with a water jacket for temperature control. All experiments were performed at 295 K and at atmospheric pressure.

Illumination of the flow tube is accomplished using two UV-A lamps (Philips PL-L 18W/10/4P), which are positioned ~10 cm from the tube. The photon flux in the flow tube was estimated using the photolysis frequency for NO_2, J_{NO2}, as determined in a nitrogen flow.[43] Under our experimental conditions, J_{NO2} in the flow tube was $(3.0 \pm 0.3) \times 10^{-3}$ s^{-1}, which is lower than spring clear-sky photon fluxes measured in the SAPHIR atmospheric simulation chamber (Jülich, Germany)[44] but higher than expected under typical Icelandic weather conditions. This difference, coupled with the spectral mismatch between the UV-A lamps and the solar radiation spectrum, may lead to corresponding differences between sample photoreactivity observed in the laboratory and in the ambient Icelandic environment.

All experiments were conducted using zero air as bath gas (total volatile organic compounds (VOCs) < 0.1 ppb, CO_2 < 10 ppb, CO < 80 ppb, and H_2O < 2 ppm). Ozone was generated in a dry air flow (~200 cm^3 min^{-1}) using a UV ozone generator (Model 165, Thermo Environmental Instruments Ltd.). The output of the ozone generator was diluted into a second flow of dry air and subsequently mixed with a flow of wet air from a water bubbler. Both dilution flows were controlled using mass flow controllers (MKS) connected to a four-channel readout unit (Type 247, MKS). The ozone-containing air flow was introduced to the reactor using a Pyrex movable

injector (internal diameter = 0.49 cm), the position of which determines the gas–surface interaction time. Ozone mixing ratios were measured at the outlet of the flow tube using a commercial ozone analyzer (O342e, Envea; optical detection at 254 nm). Experiments were performed at environmentally relevant ozone concentrations (10–200 ppb in the combined flow) and RHs (<5–50%).

In these experiments, the total volumetric flow through the flow tube was ~900 $cm^3\ min^{-1}$, which corresponds to a Reynolds number of ~130 (i.e., laminar flow). Under these experimental conditions, the ratio of the mean free path of ozone to the flow reactor radius (i.e., the Knudsen number, *Kn*) is $\sim 2.2 \times 10^{-5}$, which implies that experiments were conducted in the continuum regime.[45] Additional details regarding the flow tube dimensions and flow parameters are provided in Lasne et al.[42]

3.2.2 Reaction tube preparation

Pyrex reaction tubes were rinsed with ethanol and deionized water prior to use. Then, one end of the tube was stoppered, and volcanic dust (~30–450 mg) and a small amount of water (0.5–2 mL; to facilitate tube coating while minimizing potential loss/redistribution of any water-soluble material) were added. The tube was then shaken by hand until the water/dust suspension evenly coated its inner walls. Finally, the tube was slowly rotated for several minutes under a heat gun held at 393 K to ensure that the sample dried in a uniform manner. The tube was then stored in an oven at 373 K overnight prior to use.

3.2.3 Experimental procedure

At the beginning of each experiment, a dust-coated reaction tube was placed in the coated-wall flow tube reactor and the movable injector was retracted to expose the sample to a flow of air at the RH employed in the experiment. After ~30 min, the injector was fully pushed in and the ozone generator was turned on. Once the measured ozone mixing ratio reached a constant baseline value, the injector was completely retracted such that the ozone-containing gas flow could interact with the entire dust sample. After 2 h, at which point the ozone mixing

ratio had approached a plateau (i.e., steady state) value, the sample was illuminated for 1 h; then, the sample was exposed to ozone for a further 1 h under dark conditions; finally, the injector was again pushed in and baseline measurements were taken for an additional 30 min.

3.2.4 Data analysis

Since the reactivity of the Mýrdalssandur dust sample decreased rapidly with increasing ozone exposure (Figure 3.1), its integrated influence on ambient ozone mixing ratios is best captured using its steady-state uptake coefficient. These values were obtained by first calculating the pseudo-first-order loss rates for ozone, k_{obs}, for each experiment as follows

$$k_{obs} = \frac{ln\left(\frac{[O_3]_t}{[O_3]_0}\right)}{-t} \tag{3.1}$$

Here, $[O_3]_t$ is the steady-state ozone mixing ratio under dark or light conditions, $[O_3]_0$ is the baseline ozone mixing ratio, and t is the gas–surface interaction time (at the volumetric flow rates employed here, $t = 0.8$ s). The values of k_{obs} thus obtained were used to calculate effective uptake coefficients, γ_{eff}, using the following equation[46]

$$\gamma_{eff} = \frac{k_{obs} D_{tube}}{< c >} \tag{3.2}$$

Here, D_{tube} is the internal diameter of the flow tube and $\langle c \rangle$ is the mean thermal velocity of ozone under our experimental conditions. To correct for the influence of radial ozone diffusion limitations on calculated γ_{eff} values, the KPS method was employed[47]

$$\gamma_{corr} = \frac{\gamma_{eff}}{1 - \gamma_{eff} \frac{3}{N_{Shw}^{eff} Kn}} \tag{3.3}$$

Here, Sh^{eff} is the effective Sherwood number, as estimated for the flow tube parameters and experimental conditions in the present study.

As described in Lasne et al.,[42] errors associated with the uptake coefficients reported here are estimated as <15%; this estimation takes into account the precision of the ozone analyzer and the mass flow controllers employed here, as well as errors associated with Mýrdalssandur dust mass measurement, tube coating length, and specific surface area.

3.2.5 Sample provenance, preparation, and characterization

3.2.5.1 Sample collection and preparation

Recently, our group reported the uptake of SO_2 and NO_2 by volcanic dust samples obtained from four main source regions in Iceland.[24,25] As the photochemical activity of natural mineral dusts and volcanic ash has previously been attributed to photoactive titanium[39,48,49] and iron[39,49] oxides, we selected from this set the sample with the highest bulk Ti content for this study. This sample was obtained from the Mýrdalssandur region of southern Iceland (63°26′50.1″N 18°48′52.8″W)[24] and grinded in a mortar and pestle prior to use. Importantly, we note that the vesicular morphology of this sample (see Figure 3.4) renders it less dense than typical lower-latitude dust and, consequently, more susceptible to atmospheric transport than expected based on its size.[50]

3.2.5.2 Surface area analysis

The Brunauer–Emmett–Teller (BET) specific surface area for the sample, S_{BET} (1.8 ± 0.2 m^2 g^{-1}),[24,25] was determined in a custom-built BET apparatus[51] using nitrogen gas as the adsorbate. The sample was degassed at 523 K to remove any surface-sorbed water prior to collecting nitrogen adsorption isotherms ($n = 3$).

3.2.5.3 Bulk elemental analysis

The bulk elemental composition of the sample was determined by inductively coupled plasma mass spectrometry (ICP–MS; NexION 300×, PerkinElmer). Sample aliquots (2–7 mg, $n = 6$) were prepared for analysis using microwave acid digestion (Milestone Ultrawave;

$HF/HNO_3/H_2O_2$; 500 K, 35 bar, 15 min). The method was evaluated by repeated measurements on acid blanks, quality control standard solutions, and standard reference materials (NIST SRM 1648a and SRM 2584).[24] The results of this analysis, which were previously published in Urupina et al.,[24] are shown here in Table B.1.

3.2.5.4 Surface elemental analysis

The surface (uppermost 2–10 nm)[52] elemental composition of the sample was analyzed using X-ray photoelectron spectroscopy (XPS; Kratos Axis Ultra). High-resolution scans at a pass energy of 40 eV were acquired for C_{1s}, O_{1s}, Si_{2p}, Al_{2p}, Fe_{2p}, Mg_{2p}, Ca_{2p}, Na_{1s}, K_{2p}, Ti_{2p}, and Mn_{2p} using a monochromatic Al X-ray beam centered at 1486.6 eV; data processing was performed using the CasaXPS software program. The binding energy scale was calibrated by fixing the C_{1s} peak for adventitious carbon at 284.8 eV. The results of this analysis are presented in Table B.1.

3.2.5.5 Elemental speciation analysis

3.2.5.5.1 Sieving

The sample was dry sieved by hand using 8 in. stainless-steel sieves into >150, 150–75, and 75–45 μm size fractions. The <45 μm fraction was wet sieved with deionized water into 45–20 and <20 μm size fractions, both of which were collected on cellulose acetate filters (1005-110 Grade 5 qualitative filter paper, Whatman) via vacuum filtration. Sample-laden filters were dried in a gravity oven at 363 K prior to further processing.

3.2.5.5.2 Density fractionation

In an attempt to isolate the glass and mineral components of each size fraction (except the <20 μm fraction, which did not contain sufficient mass), samples were subjected to density separation using lithium heteropolytungstate (LST), a heavy liquid (2.85 g cm^{-3}) commonly used in soil and volcanic ash density separations,[53,54] with density (2.85 g cm^{-3}) intermediate between that of Icelandic volcanic glass (1–3 g cm^{-3})[9] and the predicted mineral phases in the sample (olivine, ilmenite, and plagioclase; 2.6–4.7 g cm^{-3}).[55] In this procedure, each size

fraction was transferred into 15 mL centrifuge tubes; then, ~3 mL of LST was added and the suspension was centrifuged twice at 3500 rpm for 5 min (5804, Eppendorf). After centrifugation, the floating (putative glass) and settled (putative mineral) subfractions were separated and collected as described in Section 3.2.5.5.1.

3.2.5.5.3 Light microscopy

Preliminary information regarding the morphology, composition, and size distribution of the volcanic dust particles was obtained by imaging the 150–75 μm fraction using polarized light microscopy (Axio Scope.A1, Zeiss). As shown in Figure 3.4, the sample contains both glass (vesicular, transparent/semi-transparent) and mineral (opaque) components. Mineral components may be free (i.e., phenocrysts) or lightly coated in glass, but are often microlites within a glass matrix (Figure 3.5).

3.2.5.5.4 Electron microprobe analysis

Size- and density-fractionated samples were transferred into predrilled holes on acrylic pucks, which were then backfilled with epoxy. Once cured, samples were polished and carbon-coated for analysis. Glass and mineral components were analyzed separately by wavelength-dispersive spectroscopy using an electron microprobe (JXA-8900R electron probe microanalyzer, JEOL), which was calibrated using either glass or mineral standards. For the glass fraction, a 10 μm beam size was used, with a 15 keV accelerating voltage and a 6 nA beam current. The Kα lines of 11 elements were measured in each selected spot (Na, Ca, Si, Fe, Mn, K, Ti, Mg, Al, Cl, and P). For the mineral fraction, a 2 μm beam size was used, with a 20 keV accelerating voltage and a 20 nA beam current. The Kα lines of 10 elements were measured in each selected spot (Na, Ca, Si, Fe, Mn, K, Ti, Mg, Al, and Cr).

Because preliminary electron microprobe analysis (EMPA) data indicated that the five size fractions displayed similar composition, we collected detailed EMPA data for only the 75–45 μm density-separated sample. A total of 78 spots were selected for analysis of the light and heavy separated fractions; to capture the sample's compositional heterogeneity, grains with

different morphologies and back scattering electron (BSE) reflectivity were chosen for both the glass and mineral fractions, as brighter and darker shades on BSE images indicate higher and lower atomic numbers, respectively.[56] The geochemical composition and predicted mineral phase for each spot analyzed are presented in Tables B.2–7.

3.3 Results and discussion

As shown in Figure 3.1, the ozone mixing ratio measured at the exit of the coated-wall flow tube decreased substantially upon exposure to Mýrdalssandur dust and subsequently increased gradually toward a steady-state value; in the presence of light, the ozone mixing ratio decreased further. In the following sections, we report the influence of sample mass, ozone mixing ratio, and RH on ozone uptake by this sample.

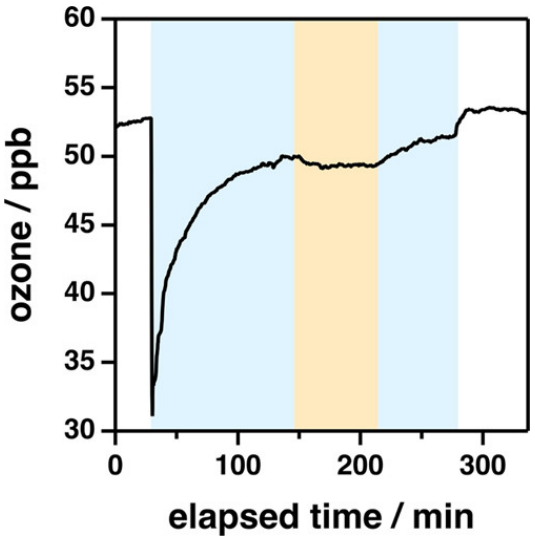

Figure 3.1: Reaction profile of Mýrdalssandur dust with ozone at 0% RH. The unshaded regions of the profile denote time periods when ozone was not exposed to the sample. The blue and yellow regions of the profile denote the exposure of ozone to the sample under dark and illuminated conditions, respectively.

3.3.1 Ozone uptake by Mýrdalssandur dust

3.3.1.1 Influence of sample mass

The steady-state uptake coefficient for ozone by Mýrdalssandur dust (γ_{corr}) increases as a function of dust mass under dark and light conditions (Figure B.2; experiments performed under dry conditions and 50 ppb ozone). These results imply that the dust surface area available for reaction with ozone was larger than the geometric surface area of the dust-coated section of the Pyrex reaction tube (S_{geo}). In all subsequent sections, therefore, we report γ_{BET}, which accounts for the interaction of ozone with the entire coating volume

$$\gamma_{BET} = \gamma_{corr} \times \frac{S_{geo}}{S_{BET} \times m} \quad (3.4)$$

Here, m is the dust mass (g) and S_{BET} is the specific surface area of the dust (BET; $m^2\ g^{-1}$), as determined for bulk samples. Importantly, because this approach may overestimate the surface area presented by solid particle coatings,[57] the γ_{BET} values we report here represent lower limits for the ambient reactivity of volcanic dust toward ozone.

3.3.1.2 Influence of ozone concentration

As illustrated in Figure 3.2, γ_{BET} decreases exponentially with increasing ozone concentrations (10–200 ppb; 30% RH) under both dark and light conditions. These results are consistent with a Langmuir–Hinshelwood reaction mechanism, in which ozone loss at higher ozone mixing ratios is limited by saturation of available surface sites and k values are correspondingly lower.[58] This behavior has previously been observed for metal oxides,[59–62] clays,[42] and Saharan dust deposited in Cape Verde.[32]

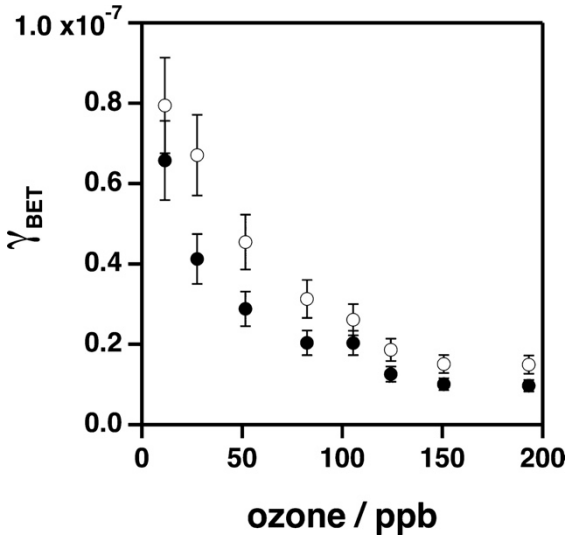

Figure 3.2: BET uptake coefficients (γ_{BET}) for ozone at the surface of Mýrdalssandur dust as a function of ozone mixing ratio (30% RH). Filled and open circles represent γ_{BET} values under dark and illuminated conditions, respectively. Error bars are estimated as 15% of calculated values, as described in Section 3.2.4.

3.3.1.3 Influence of relative humidity

As shown in Figure 3.3, the highest γ_{BET} values (50 ppb ozone) were found under dry conditions, whereas the lowest value was observed at 50% RH. This trend, previously observed for clays[42,57] and mineral dust proxies,[31,48,61] has been attributed to competition by water vapor for reactive surface sites. This explanation is consistent with our results, and in particular our observation that γ_{BET} values for ozone determined under dry conditions were highly variable, as under these conditions, any variation in the amount of sorbed water remaining in the dust films after overnight drying would not be mitigated by contributions from the humidified air flow.

Although previous investigations of water uptake by clays,[57,63] dust,[51,64] and volcanic ash[51] have demonstrated the equivalent of monolayer water coverage at <30% RH, we find that the reactivity of our sample toward ozone persists even at 50% RH. This observation, which again agrees with previous studies of ozone uptake by mineral dust and mineral dust

proxies,[31,42,48,57,61] may reflect uneven surface water coverage, which would leave surface sites available for ozone uptake at RH values higher than those associated with apparent monolayer coverage.[65] Alternatively, it may reflect the reaction of ozone with soluble species (e.g., chloride and bromide) present in a surface water film under elevated RH conditions.[66]

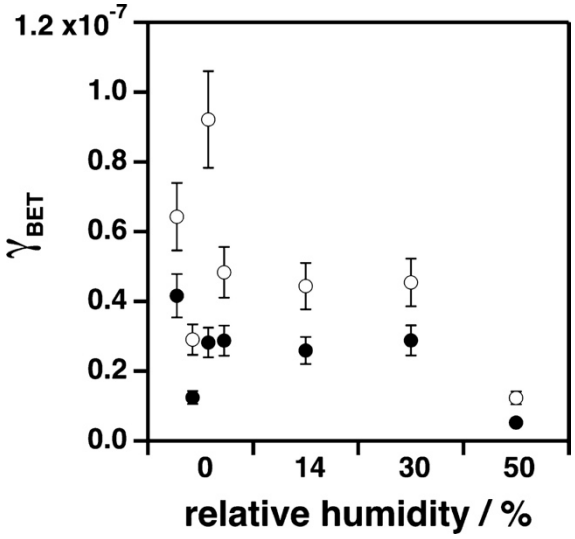

Figure 3.3: BET uptake coefficients (γ_{BET}) for ozone at the surface of Mýrdalssandur dust as a function of RH (50 ppb ozone). Filled and open circles represent γ_{BET} values under dark and illuminated conditions, respectively. Error bars are estimated as 15% of calculated values, as described in Section 3.2.4.

Finally, we note that the uptake of ozone by this sample also decreases with increasing RH under illuminated conditions (Figure 3.3). However, since γ_{BET} values obtained under illumination also include contributions from processes occurring under dark conditions, this observation most likely reflects the aforementioned decrease in dark ozone uptake observed at elevated RH, rather than a major change in the magnitude of light-mediated ozone loss.

3.3.2 Ozone uptake by Mýrdalssandur dust under dark conditions: Mechanistic discussion and comparison to previous literature

3.3.2.1 Mechanistic discussion

The reactivity of the Mýrdalssandur dust sample toward ozone decreased with time over the course of the experiment (Figure 3.1); however, it was never fully diminished. Similar sustained ozone uptake has previously been observed for metal oxides,[59–62] clays,[42] and natural desert dusts.[31,32]

Although the mechanism of ozone loss on the surface of volcanic dust is not currently known, ozone uptake by metal oxides has been suggested to proceed via the following set of reactions, where SS represents a Lewis acid surface site needed for the decomposition of ozone[62,67]

$$O_3 + SS \rightarrow SS{-}O + O_2 \quad (3.1)$$

$$SS{-}{-}{-}O + O_3 \rightarrow SS{-}{-}O_2 + O_2 \quad (3.2)$$

$$SS{-}{-}O_2 \rightarrow SS + O_2 \quad (3.3)$$

$$SS{-}O + SS{-}O \rightarrow 2\,SS + O_2 \quad (3.4)$$

According to this mechanism, the saturation of available surface sites via Reaction 3.1 and 3.2 would result in decreasing ozone uptake with increasing ozone exposure time; at the same time, however, regeneration of surface sites via Reaction 3.3 and 3.4 could counteract this effect. This competition between saturation and regeneration processes has been previously used to explain observations of time-dependent ozone uptake by natural mineral dusts,[31,32,59] mineral dust proxies,[59,61,68] and clays,[42] and is also consistent with the results reported here.

Ozone has previously been used to probe for Lewis acid sites at the surface of volcanic ash;[37] to date, however, these sites have not been explicitly characterized. In the case of metal oxides, Lewis acid sites consist of surface oxygen vacancies (i.e., natural deformations) in the crystal lattice structure.[48,69,70] Similar sites surely exist within the mineral fraction of Mýrdalssandur dust; however, because volcanic PM also contains noncrystalline material (i.e., glass)[71] and

undergoes plume processing upon emission,[66] ozone uptake by this sample may also occur via other mechanisms.

Interestingly, our results contrast with those reported by Maters et al., who saw no evidence of sustained decomposition of ozone by volcanic ash and glass.[36] As shown in Table B.1, the Fe content of Mýrdalssandur dust is ~12 wt %, whereas the Fe contents of the volcanic ash and glass samples employed in Maters et al. are much lower.[36] If the Fe in the Mýrdalssandur sample were present as Fe_2O_3, which is known to exhibit catalytic ozone uptake over long timescales,[61] this could explain our results; however, Baldo et al. have recently shown that the Fe in Mýrdalssandur dust is primarily present in its glass fraction.[35] Here, we suggest several alternative explanations for this difference. First, since these two sample sets were obtained from different locations, the strength of their reductive sites may be different.[37] Second, surface weathering processes[72] could change the abundance of reactive surface sites capable of facilitating sustained destruction of ozone. Third, the Knudsen cell system employed in Maters et al.[36] may not be sensitive enough to detect minor, but sustained, ozone uptake by volcanic PM.[46]

3.3.2.2 Comparison to previous literature

As shown in Figure 3.3, γ_{BET} for ozone at the surface of Mýrdalssandur dust is $(2.9 \pm 0.4) \times 10^{-8}$ at 30% RH, which is orders of magnitude lower than uptake values reported by Maters et al. ($\gamma = 10^{-2}$ to 10^{-3}).[36] This discrepancy is unsurprising, as Maters et al. reported initial γ values and did not scale to the specific BET area of their samples. Interestingly, these values are also at the lower end of those reported for mineral phases commonly found in volcanic PM, including ilmenite, augite (a type of pyroxene), and phlogopite.[31,71] However, Mýrdalssandur dust is predominantly composed of glass, with only minor amounts of ilmenite and pyroxene (see Section 3.3.3), and the majority of the mineral components that are present are engulfed by glass (Figure 3.5). Since ozone uptake by both SiO_2 powder[31,73] and planar glass surfaces[74] is minimal, this may explain the modest reactivity observed here.

3.3.3 Ozone uptake by Mýrdalssandur dust under illuminated conditions: Magnitude and mechanism

As shown in Figures 3.1–3, Mýrdalssandur dust exhibits photoenhanced uptake of ozone under all experimental conditions explored here. This behavior has previously been observed for TiO_2, a semiconductor photocatalyst that is commonly employed as a proxy for the photoactive component of mineral dust.[31,48,73,75] Here, the photoenhanced uptake of ozone by TiO_2 is initiated via the absorption of light with energy greater than or equal to its band gap, which results in the formation of an electron–hole pair and initiates a chain of reactions that ultimately results in the reduction of ozone.[73,76]

If the Ti in the Mýrdalssandur dust sample (Table B.1) were present as TiO_2, we would expect γ_{BET} to increase by several orders of magnitude upon illumination;[31,48,73] however, as illustrated in Figure 3.2, the light enhancement for the dust sample was only ~20–60%. This discrepancy suggests that the Ti in Mýrdalssandur dust may not exist in its highly photoactive TiO_2 form and that the observed photochemistry may be driven instead by other dust components. We have recently demonstrated that natural Ti-containing minerals and mineral dusts also exhibit photoenhanced ozone uptake, although to a lesser degree than TiO_2.[31] In fact, γ_{BET} values reported by our group for ozone on the surface of Ti-containing minerals found in volcanic PM[71] are similar to those obtained here, which is consistent with this interpretation.

In order to further explore this possibility, we used polarized light microscopy and EMPA to determine the location and predicted phase of Ti in the Mýrdalssandur dust sample. As shown in Figure 3.4, the sample is primarily composed of glass fragments internally mixed with minerals, with the latter present as individual crystals, lithic fragments, or microlites and phenocrysts within the glass fraction. This internal mixing is also reflected in the EMPA data, which show both glass and mineral components in the majority of individual particles, even after density separation (Figure 3.5). These components and mixing states have been previously observed for Icelandic aeolian samples.[5]

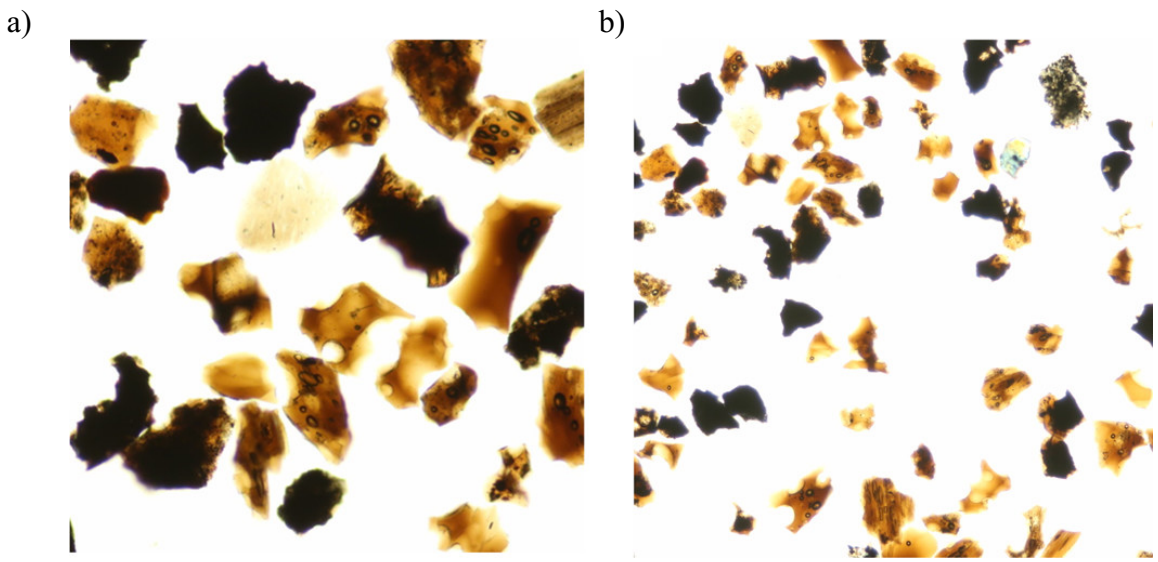

Figure 3.4: Light microscopy images of the 150–75 μm size fraction of Mýrdalssandur dust. Opaque pieces are minerals or lithics. Transparent and partially transparent shards, which often contain vesicles, are glass with varying amounts of microlites.

Although density fractionation could not fully separate the mineral and glass components of the dust sample, the electron beam in the microprobe was narrow enough to spot-select points for elemental analysis on the internally mixed mineral and glass components within both density-separated fractions. As shown in Table B.7, the sample is predominantly composed of basaltic (low-silica) glass,[77] which is enriched with Ti (4.5 ± 0.5 wt %). We therefore conclude that most of the elemental Ti in this sample is contained in its glass fraction. Our results agree with those reported by Dagsson-Waldhauserova et al., who used X-ray diffraction and optical microscopy to show that aeolian deposits collected during a dust storm in Reykjavík primarily consisted of metal-rich volcanic glass.[78]

As illustrated in Tables B.2–6, elemental Ti is also present in the mineral component of Mýrdalssandur dust. We used the elemental abundance ratios from EMPA to predict the following Ti-containing mineral phases in the sample: pyroxene, plagioclase, ilmenite, titanomagnetite, and olivine. However, we note that these minerals exist mostly as micron-sized grains (i.e., microlites) and are much less abundant than particles composed of glass. The

predicted mineral phases identified in this work have previously been identified in Icelandic aeolian samples[5] and in Icelandic volcanic ash.[71,79]

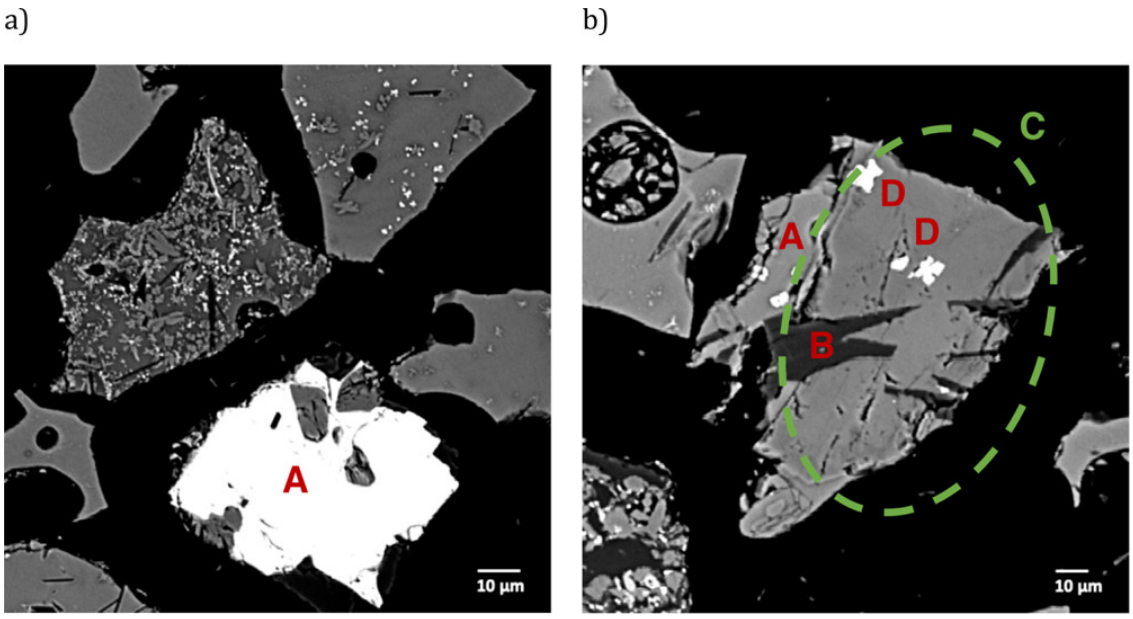

Figure 3.5: Back-scattered electron images obtained via electron microprobe analysis of the heavy fraction of the 75–45 µm size fraction of Mýrdalssandur dust. The brighter shades represent the portion of the sample with higher atomic numbers, and the darker shades represent the portion of the sample with lower atomic numbers. Components identified here include: (a) ilmenite phenocryst (A; large bright particle), (b) basaltic glass (A), plagioclase (B; dark crystal), pyroxene (C; large grain), and ilmenite microlites (D; small bright regions).

In summary, the analyses described here show that the majority of the Ti in Mýrdalssandur dust is present in its glassy fraction, and the Ti in its mineral fraction is present not as highly photoreactive anatase and/or rutile but rather in a range of other mineral phases not known for their photochemical activity. However, the band gaps of two predicted mineral phases identified here, ilmenite and augite, can lie within the range of the UV-A lamps used in this study,[31] which implies that they may also reduce ozone via the mechanism described above for TiO_2. If the other predicted mineral phases have similar band gaps, they may also contribute to the observed ozone loss under illuminated conditions. Finally, we note that we have

previously suggested that the photoenhanced uptake of ozone by Ti-containing minerals may also occur via the photocleavage of the SS–O bond shown in R3, which would regenerate the surface sites required for sustained ozone uptake;[31] this ozone loss pathway may also be active here.

3.4 Atmospheric implications

In this study, we present observations of ozone uptake by Icelandic volcanic dust as a function of ozone mixing ratio and RH under dark and illuminated conditions. To assess the overall influence of volcanic PM on ozone concentrations in Iceland, we consider the following two equations, which allow us to compare the ozone flux to the ground surface (F_{grd}, mol m^{-2} s^{-1}) with the ozone flux to volcanic PM (F_{PM}, mol m^{-2} s^{-1}) present in a well-mixed overlying atmospheric volume[80]

$$F_{grd} = -V_d[O_3] \times 10^{-2} \quad (3.5)$$

$$F_{aer} = \frac{< c > \gamma_{BET}}{4} Ah[O_3] \times 10^{-6} \quad (3.6)$$

Here, V_d is the deposition velocity of ozone (cm s^{-1}), [O_3] is the mixing ratio of ozone (mol m^{-3}), $<c>$ is the mean thermal velocity of ozone (m s^{-1}), γ_{BET} is the steady-state surface area-scaled uptake coefficient for ozone obtained in this study, A is the total surface area of volcanic PM (μm^2 cm^{-3}), and h is the atmospheric mixing height (m).

Using these equations, we apply a similar approach to Li et al.[80] to determine the volcanic PM loading required for the PM-mediated ozone loss to equal 10% of its loss to the ground surface (i.e., $F_{PM} = 0.1F_{grd}$). Assuming an ozone deposition velocity of 0.15 cm s^{-1}; a γ_{BET} value of 5×10^{-8}, which is similar to the value we report at an ozone mixing ratio of 50 ppb; a mixing height of 2000 m; and volcanic PM with diameter = 1 μm and density = 2.7 g cm^{-3}, this condition is only satisfied at volcanic PM loadings of nearly 1 mg m^{-3}. We note that these

calculations may underestimate the required PM loadings, since Icelandic dust is often larger than 1 μm in diameter[81] and since we would expect even lower γ_{BET} values for volcanic PM under typical Icelandic weather conditions (~60–80% RH).[82]

Although these results suggest that volcanic dust chemistry likely only influences ozone mixing ratios during extreme dust events, several caveats remain. First, as discussed previously, because the surface area presented by the dust film in the coated-wall flow tube employed here is most likely lower than the surface area of the equivalent mass of the powdered sample, the γ_{BET} values reported here represent lower limits for the magnitude of ozone uptake by Mýrdalssandur dust. Second, during periods when wind speeds are elevated substantially above those required for saltation, the atmospheric transit time between dust source regions and populated areas may be short enough such that a γ_{BET} value intermediate between initial and steady-state conditions may more appropriately reflect the reactivity of the transported PM.[20] Third, the Mýrdalssandur dust sample had certainly been exposed to ambient ozone levels prior to its collection, yet still exhibited substantial ozone uptake, which implies that it—like mineral dust[32,83]—may be "reactivated" during periods of low ozone exposure. Fourth, the mineralogy of volcanic PM is source-dependent,[35,84] so the reactivity of this PM class in other volcanically active regions may differ from that reported here. Fifth, as climate change is projected to lead to glacial retreat[85] and corresponding increases in dust source areas[19] and dust production,[5] the importance of dust–pollutant gas interactions will likely increase in the future.

Finally, we note that the scavenging of halogen species during volcanic eruptions and subsequent enrichment of halides on the surface of volcanic PM[86] may lead to air quality consequences beyond those explored here. For example, the uptake of ozone by sodium chloride in the presence of soluble ferric iron can release Cl_2 gas,[87] a strong atmospheric oxidant. Although the solubility of iron in Mýrdalssandur dust is relatively low (~0.2%), dust samples obtained from other Icelandic source regions exhibit higher solubilities.[35] In this context, we hypothesize that ozone uptake by halide-rich volcanic ash and dust may lead to

halogen activation, with concomitant impacts for local oxidative capacities in volcanically active regions.

3.5 References

(1) Goudie, A. S.; Middleton, N. J.*Desert Dust in the Global System*; Springer, Berlin: Heidelberg, 2006.

(2) Bullard, J. E.; Baddock, M.; Bradwell, T.; Crusius, J.; Darlington, E.; Gaiero, D.; Gassó, S.; Gisladottir, G.; Hodgkins, R.; McCulloch, R.; McKenna-Neuman, C.; Mockford, T.; Stewart, H.; Thorsteinsson, T. High-Latitude Dust in the Earth System. *Rev. Geophys.* 2016, *54*, 447−485.

(3) Groot Zwaaftink, C. D.; Grythe, H.; Skov, H.; Stohl, A. Substantial Contribution of Northern High-Latitude Sources to Mineral Dust in the Arctic. *J. Geophys. Res.: Atmos.* 2016, *121*, 13,678−13,697.

(4) Bullard, J. E. The Distribution and Biogeochemical Importance of High-Latitude Dust in the Arctic and Southern Ocean-Antarctic Regions. *J. Geophys. Res.: Atmos.* 2017, *122*, 3098−3103.

(5) Arnalds, O.; Dagsson-Waldhauserova, P.; Olafsson, H. The Icelandic Volcanic Aeolian Environment: Processes and Impacts A Review. *Aeolian Res.* 2016, *20*, 176−195.

(6) Björnsson, H.; Pálsson, F. Icelandic Glaciers. *Jökull* 2008, *58*, 365−386.

(7) Gíslason, S. R.; Arnórsson, S.; Ármannsson, H. Chemical Weathering of Basalt in Southwest Iceland: Effects of Runoff, Age of Rocks and Vegetative/Glacial Cover. *Am. J. Sci.* 1996, *296*, 837−907.

(8) Arnalds, O.; Gisladottir, F. O.; Sigurjonsson, H. Sandy Deserts of Iceland: An Overview. *J. Arid Environ.* 2001, *47*, 359–371.

(9) Arnalds, O. Dust Sources and Deposition of Aeolian Materials in Iceland. *Icel. Agric. Sci.* 2010, *23*, 3–21.

(10) Butwin, M. K.; von Löwis, S.; Pfeffer, M. A.; Thorsteinsson, T. The Effects of Volcanic Eruptions on the Frequency of Particulate Matter Suspension Events in Iceland. *J. Aerosol Sci.* 2019, *128*, 99– 113.

(11) Beckett, F.; Kylling, A.; Sigurðardóttir, G.; von Löwis, S.; Witham, C. Quantifying the Mass Loading of Particles in an Ash Cloud Remobilized from Tephra Deposits on Iceland. *Atmos. Chem. Phys.* 2017, *17*, 4401–4418.

(12) Leadbetter, S. J.; Hort, M. C.; von Löwis, S.; Weber, K.; Witham, C. S. Modeling the Resuspension of Ash Deposited during the Eruption of Eyjafjallajökull in Spring 2010. *J. Geophys. Res.: Atmos.* 2012, *117*, D00U10.

(13) Gudmundsson, M. T.; Thordarson, T.; Höskuldsson, A .; Larsen, G.; Björnsson, H.; Prata, F. J.; Oddsson, B.; Magnusson, E.; Högnadóttir, T.; Petersen, G. N.; Hayward, C. L.; Stevenson, J. A.; Jónsdóttir, I. Ash Generation and Distribution from the April–May 2010 Eruption of Eyjafjallajökull, Iceland. *Sci. Rep.* 2012, *2*, 572.

(14) Liu, E. J.; Cashman, K. V.; Beckett, F. M.; Witham, C. S.; Leadbetter, S. J.; Hort, M. C.; Guðmundsson, S. Ash Mists and Brown Snow: Remobilization of Volcanic Ash from Recent Icelandic Eruptions. *J. Geophys. Res.: Atmos.* 2014, *119*, 9463–9480.

(15) Thorsteinsson, T.; Jóhannsson, T.; Stohl, A.; Kristiansen, N. I. High Levels of Particulate Matter in Iceland Due to Direct Ash Emissions by the Eyjafjallajökull Eruption and Resuspension of Deposited Ash. *J. Geophys. Res.: Solid Earth* 2012, *117*, B00C05.

(16) Dagsson-Waldhauserova, P.; Arnalds, O.; Olafsson, H. Long- Term Variability of Dust Events in Iceland (1949–2011). *Atmos. Chem. Phys.* 2014, *14*, 13411–13422.

(17) Dagsson-Waldhauserova, P.; Arnalds, O.; Olafsson, H. Long-Term Frequency and Characteristics of Dust Storm Events in Northeast Iceland (1949–2011). *Atmos. Environ.* 2013, *77*, 117–127.

(18) Butwin, M. K.; von Löwis, S.; Pfeffer, M. A.; Dagsson- Waldhauserova, P.; Thorsson, J.; Thorsteinsson, T. Influence of Weather Conditions on Particulate Matter Suspension Following the 2010 Eyjafjallajökull Volcanic Eruption. *Earth Interact.* 2020, *24*, 1–16.

(19) Gisladottir, F. O.; Arnalds, O.; Gisladottir, G. The Effect of Landscape and Retreating Glaciers on Wind Erosion in South Iceland. *Land Degrad. Dev.* 2005, *16*, 177–187.

(20) Thorsteinsson, T.; Gísladóttir, G.; Bullard, J.; McTainsh, G. Dust Storm Contributions to Airborne Particulate Matter in Reykjavik, Iceland. *Atmos. Environ.* 2011, *45*, 5924–5933.

(21) Carlsen, H.; Gislason, T.; Forsberg, B.; Meister, K.; Thorsteinsson, T.; Jóhannsson, T.; Finnbjornsdottir, R.; Oudin, A. Emergency Hospital Visits in Association with Volcanic Ash, Dust Storms and Other Sources of Ambient Particles: A Time Series Study in Reykjavik, Iceland. *Int. J. Environ. Res. Public Health* 2015, *12*, 4047–4059.

(22) Mueller, W.; Cowie, H.; Horwell, C. J.; Hurley, F.; Baxter, P. J. Health Impact Assessment of Volcanic Ash Inhalation: A Comparison With Outdoor Air Pollution Methods. *GeoHealth* 2020, *4*, No. e2020GH000256.

(23) Gudmundsson, G. Respiratory Health Effects of Volcanic Ash with Special Reference to Iceland. A Review. *Clin. Respir. J.* 2011, *5*, 2–9.

(24) Urupina, D.; Lasne, J.; Romanias, M. N.; Thiery, V.; Dagsson-Waldhauserova, P.; Thevenet, F. Uptake and Surface Chemistry of SO_2 on Natural Volcanic Dusts. *Atmos. Environ.* 2019, *217*, 116942.

(25) Romanias, M. N.; Ren, Y.; Grosselin, B.; Daële, V.; Mellouki, A.; Dagsson-Waldhauserova, P.; Thevenet, F. Reactive Uptake of NO_2 on Volcanic Particles: A Possible Source of HONO in the Atmosphere. *J. Environ. Sci.* 2020, *95*, 155–164.

(26) Vance, A.; McGonigle, A. J. S.; Aiuppa, A.; Stith, J. L.; Turnbull, K.; von Glasow, R. Ozone Depletion in Tropospheric Volcanic Plumes. *Geophys. Res. Lett.* 2010, *37*, L22802.

(27) Surl, L.; Donohoue, D.; Aiuppa, A.; Bobrowski, N.; von Glasow, R. Quantification of the Depletion of Ozone in the Plume of Mount Etna. *Atmos. Chem. Phys.* 2015, *15*, 2613–2628.

(28) Roberts, T. J.; Braban, C. F.; Martin, R. S.; Oppenheimer, C.; Adams, J. W.; Cox, R. A.; Jones, R. L.; Griffiths, P. T. Modelling Reactive Halogen Formation and Ozone Depletion in Volcanic Plumes. *Chem. Geol.* 2009, *263*, 151–163.

(29) Andrey, J.; Cuevas, E.; Parrondo, M. C.; Alonso-Pérez, S.; Redondas, A.; Gil-Ojeda, M. Quantification of Ozone Reductions within the Saharan Air Layer through a 13-Year Climatologic Analysis of Ozone Profiles. *Atmos. Environ.* 2014, *84*, 28–34.

(30) Nan, Y.; Wang, Y. Observational Evidence for Direct Uptake of Ozone in China by Asian Dust in Springtime. *Atmos. Environ.* 2018, *186*, 45–55.

(31) Abou-Ghanem, M.; Oliynyk, A. O.; Chen, Z.; Matchett, L. C.; McGrath, D. T.; Katz, M. J.; Locock, A. J.; Styler, S. A. Significant Variability in the Photocatalytic Activity of Natural Titanium- Containing Minerals: Implications for Understanding and Predicting Atmospheric Mineral Dust Photochemistry. *Environ. Sci. Technol.* 2020, *54*, 13509–13516.

(32) Hanisch, F.; Crowley, J. N. Ozone Decomposition on Saharan Dust: An Experimental Investigation. *Atmos. Chem. Phys.* 2003, *3*, 119–130.

(33) Wang, X.; Romanias, M.; Thévenet, F.; Rousseau, A. Geocatalytic Uptake of Ozone onto Natural Mineral Dust. *Catalysts* 2018, *8*, 263.

(34) de Reus, M.; Dentener, F.; Thomas, A.; Borrmann, S.; Ström, J.; Lelieveld, J. Airborne Observations of Dust Aerosol over the North Atlantic Ocean during ACE 2: Indications for Heterogeneous Ozone Destruction. *J. Geophys. Res.: Atmos.* 2000, *105*(D12), 15263–15275.

(35) Baldo, C.; Formenti, P.; Nowak, S.; Chevaillier, S.; Cazaunau, M.; Pangui, E.; Di Biagio, C.; Doussin, J.-F.; Ignatyev, K.; Dagsson- Waldhauserova, P.; Arnalds, O.; MacKenzie, A. R.; Shi, Z. Distinct Chemical and Mineralogical Composition of Icelandic Dust Compared to Northern African and Asian Dust. *Atmos. Chem. Phys.* 2020, *20*, 13521–13539.

(36) Maters, E. C.; Delmelle, P.; Rossi, M. J.; Ayris, P. M. Reactive Uptake of Sulfur Dioxide and Ozone on Volcanic Glass and Ash at Ambient Temperature. *J. Geophys. Res.: Atmos.* 2017, *122*, 10077–10088.

(37) Maters, E. C.; Delmelle, P.; Rossi, M. J.; Ayris, P. M.; Bernard, A. Controls on the Surface Chemical Reactivity of Volcanic Ash Investigated with Probe Gases. *Earth Planet. Sci. Lett.* 2016, *450*, 254– 262.

(38) Tang, M.; Cziczo, D. J.; Grassian, V. H. Interactions of Water with Mineral Dust Aerosol: Water Adsorption, Hygroscopicity, Cloud Condensation, and Ice Nucleation. *Chem. Rev.* 2016, *116*, 4205–4259.

(39) Styler, S. A.; Donaldson, D. J. Heterogeneous Photochemistry of Oxalic Acid on Mauritanian Sand and Icelandic Volcanic Ash. *Environ. Sci. Technol.* 2012, *46*, 8756–8763.

(40) Styler, S. A.; Myers, A. L.; Donaldson, D. J. Heterogeneous Photooxidation of Fluorotelomer Alcohols: A New Source of Aerosol- Phase Perfluorinated Carboxylic Acids. *Environ. Sci. Technol.* 2013, *47*, 6358–6367.

(41) Ndour, M.; Nicolas, M.; D'Anna, B.; Ka, O.; George, C. Photoreactivity of NO_2 on Mineral Dusts Originating from Different Locations of the Sahara Desert. *Phys. Chem. Chem. Phys.* 2009, *11*, 1312–1319.

(42) Lasne, J.; Romanias, M. N.; Thevenet, F. Ozone Uptake by Clay Dusts under Environmental Conditions. *ACS Earth Space Chem.* 2018, *2*, 904–914.

(43) Hofzumahaus, A. Measurement of Photolysis Frequencies in the Atmosphere. In *Analytical Techniques for Atmospheric Measurement*; Heard, D. E., Ed.; Blackwell Publishing, 2006.

(44) Bohn, B.; Rohrer, F.; Brauers, T.; Wahner, A. Actinometric Measurements of NO_2 Photolysis Frequencies in the Atmosphere Simulation Chamber SAPHIR. *Atmos. Chem. Phys.* 2005, *5*, 493–503.

(45) Pöschl, U.; Rudich, Y.; Ammann, M. Kinetic Model Framework for Aerosol and Cloud Surface Chemistry and Gas-Particle Interactions–Part 1: General Equations, Parameters, and Terminol- ogy. *Atmos. Chem. Phys.* 2007, *7*, 5989–6023.

(46) Kolb, C. E.; Cox, R. A.; Abbatt, J. P. D.; Ammann, M.; Davis, E. J.; Donaldson, D. J.; Garrett, B. C.; George, C.; Griffiths, P. T.; Hanson, D. R.; Kulmala, M.; McFiggans, G.; Pöschl, U.; Riipinen, I.; Rossi, M. J.; Rudich, Y.; Wagner, P. E.; Winkler, P. M.; Worsnop, D. R.; O' Dowd, C. D. An Overview of Current Issues in the Uptake of Atmospheric Trace Gases by Aerosols and Clouds. *Atmos. Chem. Phys.* 2010, *10*, 10561–10605.

(47) Knopf, D. A.; Pöschl, U.; Shiraiwa, M. Radial Diffusion and Penetration of Gas Molecules and Aerosol Particles through Laminar Flow Reactors, Denuders, and Sampling Tubes. *Anal. Chem.* 2015, *87*, 3746–3754.

(48) Chen, H.; Stanier, C. O.; Young, M. A.; Grassian, V. H. A Kinetic Study of Ozone Decomposition on Illuminated Oxide Surfaces. *J. Phys. Chem. A* 2011, *115*, 11979–11987.

(49) George, C.; Ammann, M.; D'Anna, B.; Donaldson, D. J.; Nizkorodov, S. A. Heterogeneous Photochemistry in the Atmosphere. *Chem. Rev.* 2015, *115*, 4218–4258.

(50) Butwin, M. K.; Pfeffer, M. A.; von Löwis, S.; Støren, E. W. N.; Bali, E.; Thorsteinsson, T. Properties of Dust Source Material and Volcanic Ash in Iceland. *Sedimentology* 2020, *67*, 3067–3087.

(51) Joshi, N.; Romanias, M. N.; Riffault, V.; Thevenet, F. Investigating Water Adsorption onto Natural Mineral Dust Particles: Linking DRIFTS Experiments and BET Theory. *Aeolian Res.* 2017, *27*, 35–45.

(52) van der Heide, P. *X-ray Photoelectron Spectroscopy: An Introduction to Principles and Practices*; John Wiley & Sons, 2011.

(53) Jensen, B. J. L.; Beaudoin, A. B.; Clynne, M. A.; Harvey, J.; Vallance, J. W. A Re-Examination of the Three Most Prominent Holocene Tephra Deposits in Western Canada: Bridge River, Mount St. Helens Yn and Mazama. *Quat. Int.* 2019, *500*, 83–95.

(54) Stringer, M. E. Separation of Pumice from Soil Mixtures. *Soils Found.* 2019, *59*, 1073–1084.

(55) Barthelmy, D. Mineralogy Database http://www.webmineral.com/ (accessed March 1, 2021).

(56) Reed, S. J. B. *Electron Microprobe Analysis and Scanning Electron Microscopy in Geology*; Cambridge University Press, 2005.

(57) Coates Fuentes, Z. L.; Kucinski, T. M.; Hinrichs, R. Z. Ozone Decomposition on Kaolinite as a Function of Monoterpene Exposure and Relative Humidity. *ACS Earth Space Chem.* 2018, *2*, 21–30.

(58) Adamson, A. W. *Physical Chemistry of Surfaces*; John Wiley andSons, 1990.

(59) Michel, A. E.; Usher, C. R.; Grassian, V. H. Reactive Uptake of Ozone on Mineral Oxides and Mineral Dusts. *Atmos. Environ.* 2003, *37*, 3201–3211.

(60) Michel, A. E.; Usher, C. R.; Grassian, V. H. Heterogeneous and Catalytic Uptake of Ozone on Mineral Oxides and Dusts: A Knudsen Cell Investigation. *Geophys. Res. Lett.* 2002, *29*, 10-1–10-4.

(61) Mogili, P. K.; Kleiber, P. D.; Young, M. A.; Grassian, V. H. Heterogeneous Uptake of Ozone on Reactive Components of Mineral Dust Aerosol: An Environmental Aerosol Reaction Chamber Study. *J. Phys. Chem. A* 2006, *110*, 13799–13807.

(62) Sullivan, R. C.; Thornberry, T.; Abbatt, J. P. D. Ozone Decomposition Kinetics on Alumina: Effects of Ozone Partial Pressure, Relative Humidity and Repeated Oxidation Cycles. *Atmos. Chem. Phys.* 2004, *4*, 1301–1310.

(63) Hatch, C. D.; Wiese, J. S.; Crane, C. C.; Harris, K. J.; Kloss, H. G.; Baltrusaitis, J. Water Adsorption on Clay Minerals As a Function of Relative Humidity: Application of BET and Freundlich Adsorption Models. *Langmuir* 2012, *28*, 1790–1803.

(64) Ibrahim, S.; Romanias, M. N.; Alleman, L. Y.; Zeineddine, M. N.; Angeli, G. K.; Trikalitis, P. N.; Thevenet, F. Water Interaction with Mineral Dust Aerosol: Particle Size and Hygroscopic Properties of Dust. *ACS Earth Space Chem.* 2018, *2*, 376–386.

(65) Rubasinghege, G.; Grassian, V. H. Role(s) of Adsorbed Water in the Surface Chemistry of Environmental Interfaces. *Chem. Commun.* 2013, *49*, 3071–3094.

(66) Delmelle, P.; Wadsworth, F. B.; Maters, E. C.; Ayris, P. M. High Temperature Reactions Between Gases and Ash Particles in Volcanic Eruption Plumes. *Rev. Mineral. Geochem.* 2018, *84*, 285–308.

(67) Li, W.; Gibbs, G. V.; Oyama, S. T. Mechanism of Ozone Decomposition on a Manganese Oxide Catalyst. 1. In Situ Raman Spectroscopy and Ab Initio Molecular Orbital Calculations. *J. Am. Chem. Soc.* 1998, *120*, 9041–9046.

(68) Usher, C. R.; Michel, A. E.; Grassian, V. H. Reactions on Mineral Dust. *Chem. Rev.* 2003, *103*, 4883–4940.

(69) Thomas, K.; Hoggan, P. E.; Mariey, L.; Lamotte, J.; Lavalley, J. C. Experimental and Theoretical Study of Ozone Adsorption on Alumina. *Catal. Lett.* 1997, *46*, 77–82.

(70) Jia, J.; Zhang, P.; Chen, L. Catalytic Decomposition of Gaseous Ozone over Manganese Dioxides with Different Crystal Structures. *Appl. Catal., B* 2016, *189*, 210–218.

(71) Durant, A. J.; Bonadonna, C.; Horwell, C. J. Atmospheric and Environmental Impacts of Volcanic Particulates. *Elements* 2010, *6*, 235–240.

(72) Gíslason, S. R. Weathering in Iceland. *Jökull* 2008, *58*, 387–408.

(73) Nicolas, M.; Ndour, M.; Ka, O.; D'Anna, B.; George, C. Photochemistry of Atmospheric Dust: Ozone Decomposition on Illuminated Titanium Dioxide. *Environ. Sci. Technol.* 2009, *43*, 7437–7442.

(74) Cano-Ruiz, J. A.; Kong, D.; Balas, R. B.; Nazaroff, W. W. Removal of Reactive Gases at Indoor Surfaces: Combining Mass Transport and Surface Kinetics. *Atmos. Environ., Part A* 1993, *27*, 2039–2050.

(75) Chen, H.; Nanayakkara, C. E.; Grassian, V. H. Titanium Dioxide Photocatalysis in Atmospheric Chemistry. *Chem. Rev.* 2012, *112*, 5919–5948.

(76) Hoffmann, M. R.; Martin, S. T.; Choi, W.; Bahnemann, D. W. Environmental Applications of Semiconductor Photocatalysis. *Chem. Rev.* 1995, *95*, 69–96.

(77) Carroll, D. *Rock Weathering*; Springer: Boston, 1970.

(78) Dagsson-Waldhauserova, P.; Arnalds, O.; Olafsson, H.; Hladil, J.; Skala, R.; Navratil, T.; Chadimova, L.; Meinander, O. Snow–Dust Storm: Unique Case Study from Iceland, March 6–7, 2013. *Aeolian Res.* 2015, *16*, 69–74.

(79) Ivleva, N. P.; Huckele, S.; Weinzierl, B.; Niessner, R.; Haisch, C.; Baumann, T. Identification and Characterization of Individual Airborne Volcanic Ash Particles by Raman Microspectroscopy. *Anal. Bioanal. Chem.* 2013, *405*, 9071–9084.

(80) Li, M.; Su, H.; Li, G.; Ma, N.; Pöschl, U.; Cheng, Y. Relative Importance of Gas Uptake on Aerosol and Ground Surfaces Characterized by Equivalent Uptake Coefficients. *Atmos. Chem. Phys.* 2019, *19*, 10981–11011.

(81) Dagsson-Waldhauserova, P.; Renard, J.-B.; Olafsson, H.; Vignelles, D.; Berthet, G.; Verdier, N.; Duverger, V. Vertical Distribution of Aerosols in Dust Storms during the Arctic Winter. *Sci. Rep.* 2019, *9*, 16122.

(82) https://en.vedur.is/weather/observations/areas/ (accessed Dec 30, 2020).

(83) Chang, R. Y.-W.; Sullivan, R. C.; Abbatt, J. P. D. Initial Uptake of Ozone on Saharan Dust at Atmospheric Relative Humidities. *Geophys. Res. Lett.* 2005, *32*, L14815.

(84) Nakagawa, M.; Ohba, T. Minerals in Volcanic Ash 1: Primary Minerals and Volcanic Glass. *Global Environ. Res.* 2002, *6*, 41–51.

(85) Aðalgeirsdóttir, G.; Jóhannesson, T.; Björnsson, H.; Pálsson, F.; Sigurðsson, O. Response of Hofsjökull and Southern Vatnajökull, Iceland, to Climate Change. *J. Geophys. Res.: Earth Surf.* 2006, *111*, F03001.

(86) Ayris, P. M.; Delmelle, P.; Cimarelli, C.; Maters, E. C.; Suzuki, Y. J.; Dingwell, D. B. HCl Uptake by Volcanic Ash in the High Temperature Eruption Plume: Mechanistic Insights. *Geochim. Cosmochim. Acta* 2014, *144*, 188–201.

(87) Sadanaga, Y.; Hirokawa, J.; Akimoto, H. Formation of Molecular Chlorine in Dark Condition: Heterogeneous Reaction of Ozone with Sea Salt in the Presence of Ferric Ion. *Geophys. Res. Lett.* 2001, *28*, 4433–4436.

Chapter 4

Ozone Uptake and Halogen Activation by Road Dust and Anti-icing Solution: Implications for Wintertime Air Quality in High-Latitude Urban Environments

Maya Abou-Ghanem, Danial Nodeh-Farahani, Devon T. McGrath, Trevor C. VandenBoer, and Sarah A. Styler

Submitted. *Environmental Science: Processes & Impacts,* 2021.

4.1 Introduction

Road dust is a complex mixture of road wear, salts, crustal material, plant debris, and non-exhaust emissions (*e.g.*, tire and brake wear).[1–3] Its emission into the atmosphere is associated with major reductions in urban air quality:[4–6] in Canada, for example, road dust suspension from both paved and unpaved roads contributes nearly half of total annual primary emissions of anthropogenic fine particulate matter ($PM_{2.5}$).[7] As countries move toward zero-emission public and private fleets to combat the climate crisis,[8,9] it is increasingly important to understand the air quality and health impacts of road dust and other non-exhaust emission sources.

Our group has previously shown that road dust is a photochemical source of singlet oxygen ($^1O_2$),[10] an important environmental oxidant,[11] and can catalyze organosulfate ($ROSO_3^-$) production.[12] These results suggest that road dust photochemistry can alter both the lifetime of individual pollutant species and the overall chemical composition of the road dust organic fraction. Although these studies have provided insight into the atmospheric reactivity of road dust, its heterogeneous chemistry with trace pollutant gases[13] is still unknown.

Many of road dust's individual components are known to react with ozone,[14–18] an important atmospheric oxidant, air quality indicator, and regulated pollutant.[19] For example, laboratory studies have reported uptake of ozone by natural mineral dusts,[14–16] humic[20] and humic-like[17] material, and PAHs[18]. In many cases, substrate reactivity toward ozone is higher upon illumination; for example, ozone uptake coefficients increase by up to two orders of magnitude for humic material[20] and ~2× for mineral dust in the presence of light.[15] Evidence for this reactivity has also been provided by field studies, which have reported substantial reductions in ozone mixing ratios during major dust events in northern China[21] and in the Canary Islands.[22] In summary, these results and observations suggest that road dust may represent a substantial sink for ozone, and thereby influence its abundance in the urban atmosphere.

Recently, road salts in cold-climate regions have been shown to facilitate heterogeneous chemistry pathways previously thought to be important only in marine environments.[23] For example, dinitrogen pentaoxide (N_2O_5) uptake and subsequent reaction on road salt has been used to explain the higher-than-expected mixing ratios for nitryl chloride ($ClNO_2$), an important chlorine atom precursor,[24] observed at several inland locations during winter and spring.[23,25–27] Ozone uptake by halide-containing surfaces (*e.g.*, aerosol, snow, ice) has also been shown to lead to halogen activation,[28] although this pathway is generally thought to be less important for chloride compared to bromide and iodide due to its slow reaction with ozone.[29] However, chlorine activation during ozone uptake by chloride-containing surfaces may be possible at inland urban locations, where surfaces contain not only salts but also organics, heavy metals, and crustal material.[1–3]

The application of road salts can be harmful to roadside vegetation,[30] contaminate groundwater[31] and freshwater,[32] and cost billions of dollars in vehicle and transportation structure corrosion repairs in the U.S. alone.[33] In an effort to reduce these negative environmental and economic impacts, many municipalities are turning to agro-based anti-icer alternatives, including molasses-based anti-icer,[34–36] which has several beneficial effects: first, it can sequester salts on the road surface, thereby reducing salt content in urban runoff;[37] second, it reduces the dissolution of metals in steel, thereby mitigating the corrosion effects of salts;[38] third, it depresses the freezing point of brine, thereby improving anti-icer efficacy in especially cold climates.[39,40] Despite these benefits, agro-based anti-icers also have negative environmental impacts: for example, as a result of their high biochemical oxygen demand,[41] their presence in surface runoff can be harmful for aquatic life.[42] Chemical interactions at the air–anti-icer surface could lead to additional environmental impacts; however, this possibility has neither been explored nor considered.

To assess the air quality impacts of chemistry at the surface of road dust and winter road maintenance materials, we explore the uptake of ozone by urban road dust and a commercial anti-icing solution. First, we use a custom-built coated-wall flow tube to quantify ozone uptake

by road dust as a function of relative humidity (RH) and ozone mixing ratio under dark and illuminated conditions. Second, we use a combination of inline trapping and offline analysis to quantify halogen release from anti-icer upon exposure to ozone. Together, these results show that road dust and anti-icer can serve as an oxidant sink and source, respectively, and highlight the need for municipalities to consider the potential indirect air quality impacts of road maintenance decisions.

4.2 Methods

4.2.1 Photochemical coated-wall flow tube reactor

Experiments were conducted in a custom-built photochemical coated-wall flow tube reactor, which we have previously used to investigate the photochemical uptake of ozone by Ti-containing minerals[15] and commercial brake pad materials.[43] In brief, the flow tube consists of a water-jacketed Pyrex tube (34.4 cm length, 1.6 cm id, 0.7 cm thickness water jacket), which houses a Pyrex insert tube (20.0 cm length, 1.05 cm id) coated with the sample of interest. A movable injector, also made of Pyrex (0.6 cm od), is used to control the interaction time of ozone and the sample; in this study, all ozone exposure experiments were conducted with the injector fully retracted, which corresponds to a gas–surface interaction time of ~1.7 s. The flow tube is surrounded by 4 Sylvania 25W BL UV-A lamps (300–410 nm, λ max: 356 nm); to remove interference from ambient light, the entire assembly is enclosed in an opaque box. The photon flux inside the empty flow tube was previously estimated using the photolysis frequency of NO_2, (J_{NO_2}),[15] which was determined to be (0.0045 ± 0.0001) s^{-1}; this value is similar to wintertime J_{NO_2} values reported for a mid-latitude site.[44]

Experiments were performed in a flow of purified air, which was provided by a zero air generator (747-30 reactor type A, Aadco Instruments). The output of the zero air generator was delivered to three mass flow controllers (MFCs; MC-2SLPM-D/5M, Alicat), which were placed upstream of the movable injector and used to control the flows of dry air, ozone (created by passing dry air through a UV ozone generator [97-0066-01, UVP]), and wet air (created by

passing dry air through a bubbler filled with deionized water). The total combined volumetric flow of these MFCs was held constant at 400 sccm. The RH and ozone mixing ratios in the flow tube were adjusted by altering the fractions of the total flow from the dry, wet, and ozone MFCs. The temperature inside the flow tube was controlled using a recirculating chiller (RTE-140, Neslab), which was held at 296.5 K; RH was measured in three locations (directly after the zero air generator, prior to the flow tube, and at the exit of the flow tube) using in-line RH sensors (SHT75, Sensirion). A fourth MFC, which was located at the exit of the flow tube, delivered 500 sccm of zero air to provide sufficient flow for the requirements of the ozone analyzer (T400, Teledyne).

4.2.2 Experimental procedure

4.2.2.1 Sample preparation for coated-wall flow tube experiments

Road dust-coated Pyrex insert tubes were prepared using a modified version of that reported in Abou-Ghanem et al.[15] First, ~50 mg of road dust was weighed into a Pyrex insert tube and several drops of deionized water were added to form a slurry. Then, a rubber stopper was inserted into each end of the insert tube, which was rotated and shaken until all inner surfaces were coated with the road dust slurry. Coatings were dried in a uniform manner by placing the coated tubes on a hot dog roller (RHD800 Retro Series Hot Dog Roller, Nostalgia Electrics). To ensure sufficient time for laminar flow development prior to ozone–surface interaction,[45] the first 5 cm of the dust film was removed with a damp laboratory wipe (Kimberly-Clark Professional™); to avoid areas of uneven coating, the last 1 cm was removed as well. Finally, tubes were placed in a gravity oven (100 L, Fisherbrand™) at 324 ± 5 K overnight prior to use. The mass of each sample coating was determined by weighing by difference on an analytical balance (AB265-S/FACT, Mettler Toledo).

4.2.2.2 Experimental protocol for coated-wall flow tube experiments

At the beginning of each experiment, a sample-coated Pyrex insert tube was placed inside the reactor and the movable injector was fully pulled back; then, zero air (at the RH to be employed in the experiment) was passed over the sample for 30 min. At this point, the injector

was pushed in past the sample coating and the ozone generator was turned on. After the ozone mixing ratio reached a constant value (+/- ~0.5 ppb; typically 45 min), the injector was fully retracted to expose the entire sample coating to ozone. After 3 h, the sample was exposed to both ozone and light for 2 h; then, it was exposed to ozone for an additional 1 h in the dark. Finally, to verify that the initial ozone mixing ratio was maintained over the course of the experiment (i.e., that the ozone generator output was constant), the injector was pushed past the sample coating and the ozone mixing ratio was measured for 30 min. At the end of each experiment, the ozone generator was turned off and data were recorded for an additional 5 min.

4.2.2.3 Chlorine activation experiments

Chlorine activation experiments were conducted by passing a flow of ozone (~250 ppb in zero air, 25% RH) over the sample of interest (*i.e.*, road dust, anti-icer, salt; see Table C.6) and into reducing media to convert any inorganic Cl vapor (*e.g.*, Cl_2 and HCl) to chloride.[46] Chloride was then quantified via offline ion chromatography (IC), as described in Appendix C.3.1.

The experimental apparatus consisted of a Pyrex insert tube with custom-built Teflon inlet/outlet inserts, which was placed on a 3D-printed holder. For most experiments, the Pyrex tube was wrapped in aluminum foil to avoid any photochemistry induced by ambient light; in one experiment using road dust, the dust-coated tube was illuminated using a solar simulator (SunLite, Abet Technologies). Since the solar simulator output beam size is smaller than the length of the road dust coating, only a portion of the coating was illuminated in this experiment; the non-illuminated sections of the tube were wrapped in aluminum foil. To remove the small region of the solar simulator spectrum that extends into the blue of the actinic region[10] and reflect the majority of incoming IR light and thereby minimize sample heating, a 295 nm long-pass optical filter (Edmund Optics) and an ultraviolet (UV) hot mirror (Edmund Optics) were placed in the solar simulator light path, respectively. Similar to the flow tube reactor set-up described in Section 4.2.1, three MFCs were used to control gas flow upstream of the tube and a fourth MFC was used to deliver supplementary zero air to meet the

volumetric flow requirements of the ozone analyzer, which we used to verify the stability of the ozone mixing ratio prior to beginning each set of experiments. Here, to ensure that the post-dilution ozone mixing ratio was within the calibrated range of the ozone analyzer, the total gas flow through the tube was set to 200 sccm.

During each experiment, the gas flow from the exit of the tube was directed through an aluminum foil-wrapped impinger containing 20 mL of 30 mM sodium bicarbonate ($NaHCO_3$) and 0.408 mM of sodium bisulfite ($NaHSO_3$).[46] To minimize any sample cross-contamination from the experimental system, we thoroughly rinsed the impinger between collection periods and analyzed impinger solutions for both coated (sample) and clean (control) tubes. Specifically, for each sample/control, we analyzed aliquots (10 mL) of impinger solutions collected for each of the following, in order: clean tube (1 h collection), sample-coated tube (3 h collection), clean tube (1 h collection; ×3). All aliquots were stored at 277 K prior to IC analysis. We note that the chloride present in all blank samples (Figure 4.5) is likely from trace contamination of sodium bisulfite contained in the impinger solution.

4.2.3 Determination of uptake coefficients for ozone by road dust

To quantify the reactivity of each sample with ozone, we used the average ozone mixing ratios during the last 5 min of each experimental step (light, dark, and movable injector pushed in; see Section 4.2.2.2) to calculate a parameter known as an uptake coefficient (γ), which is defined as the number of ozone molecules lost from the gas phase divided by the total number of ozone collisions with the surface.[16] As trace gas uptake by environmental surfaces often decreases with increasing exposure time,[47] reports of initial and steady-state uptake coefficients are both common in the literature.[48] Here, to capture the atmospheric reactivity of road dust over its entire atmospheric lifetime, we report steady-state values (γ_{SS}). However, we note that because road dust (like mineral dust[14]) may undergo reactivation under low-ozone conditions, γ_{SS} likely represents a lower limit for its environmental reactivity.

To determine γ_{SS} for each sample, we first calculate the pseudo-first-order rate constant (k_{obs}) for ozone loss using the following equation:[47]

$$k_{obs} = \frac{ln\left(\frac{[O_3]_t}{[O_3]_0}\right)}{-t} \quad (4.1)$$

Here, $[O_3]_t$ is the average steady-state ozone mixing ratio (ppb) at the exit of the flow tube with the movable injector fully retracted under either dark or light conditions, $[O_3]_0$ is the average ozone mixing ratio (ppb) with the movable injector fully pushed in (*i.e.*, with no exposure to the road dust coating), and t is the ozone–road dust interaction time (s).

From k_{obs}, we use the following equation to obtain an effective uptake coefficient (γ_{eff}) for ozone:[47]

$$\gamma_{eff} = \frac{k_{obs} D_{tube}}{< c >} \quad (4.2)$$

Here, D_{tube} is the diameter of the Pyrex insert tube (m) and $<c>$ is the mean molecular speed of ozone (m s^{-1}) under our experimental conditions.[15] To correct for radial diffusion limitations, which occur at high γ_{eff} values as a result of ozone depletion near the sample coating surface, we apply the KPS method to γ_{eff} as follows:[18]

$$\gamma_{corr} = \frac{\gamma_{eff}}{1 - \gamma_{eff} \frac{3}{N_{Shw}^{eff} Kn}} \quad (4.3)$$

Here, γ_{corr} is the diffusion-corrected uptake coefficient, N_{Shw}^{eff} is the effective Sherwood number, and Kn is the Knudsen number. N_{Shw}^{eff} and Kn were estimated using the parameters and experimental conditions in Abou-Ghanem et al.[15]

The calculations described thus far assume that the surface area of the road dust that is available for reaction with ozone can be approximated by the geometric surface area of the coated section of the Pyrex insert tube. To include contributions from multiple dust layers, as well as the internal surface area of dust particles, we scale all γ_{corr} values as follows:[49]

$$\gamma_{BET} = \gamma_{corr} \times \frac{S_{geo}}{S_{BET} \times m} \quad (4.4)$$

Here, S_{geo} is the geometric surface area of the sample-coated section of the Pyrex reaction tube (m^2); S_{BET} is the Brunauer–Emmett–Teller (BET) specific surface area of our sample (BET; $m^2\ g^{-1}$), determined as described in Appendix C.3.4; and m is the sample mass (g) in a given experiment. We note that the γ_{BET} values calculated as described here likely represent lower limits with respect to suspended road dust, as the addition of water during film preparation (see Section 4.2.2.1) leads to particle agglomeration, which would reduce the specific surface area of particles in the coated tubes as compared to that obtained from nitrogen adsorption analysis of the powdered sample.[50]

4.2.4 Sample collection, preparation, and characterization

Road dust samples were collected at a high-traffic location in Treaty 6 territory, the traditional lands of First Nations and Métis people (Edmonton, Alberta, Canada; 53°33′6.5″ N, 113°29′22.0″ W) on April 15th, 2019. We have previously demonstrated the photochemical production of $^1O_2$ by dust collected from this location.[14] All experiments were conducted using the <40 μm sample fraction, which we isolated as described in Appendix C.1.

We report the elemental composition (via inductively coupled plasma mass spectrometry; Table C.1); total carbon (TC), total organic carbon (TOC), and total nitrogen content (via dry combustion; Table C.3); and BET specific surface areas (via nitrogen adsorption analysis; Table C.4) of both road dust and rinsed road dust samples. The anion content (see Table C.2) of road dust leachates was quantified using ion chromatography (IC). Detailed procedures for all techniques are presented in the Appendix C.

4.2.5 Chemicals

Deionized water (18 MΩ.cm) was obtained from a Millipore Synergy UV ultrapure water system. Potassium hydroxide (pellets; ACS reagent, 85%), calcium chloride dihydrate (BioReagent, ≥99.0%), iron(III) chloride (≥99.99% trace metals basis), and sulfuric acid (99.9999% trace metals basis) were obtained from Sigma Aldrich. Methanol (Optima grade,

99.9%), 2-propanol (certified ACS Plus), and sodium bisulfite (certified ACS powder) were obtained from Fisher Chemicals. Sodium hydrogen carbonate (Puratronic, 99.998% metals basis) was obtained from Alfa Aesar. Concentrated sulfuric acid (reagent grade) was obtained from Caledon Laboratory Chemicals. Sparkleen™ was obtained from Fisherbrand. Road Guard Plus™ was donated by Tiger Calcium.

4.3 Results and discussion

4.3.1 Sample characterization

Elemental analysis (Table C.1) shows that the largest contributor by mass to the road dust sample is Si (~33%) which is consistent with the the application of sand (SiO_2) and gravel (aluminosilicate minerals) as part of the City of Edmonton's winter road maintenance plan.[51] These results agree with X-ray diffraction (XRD) data collected by the City in 2015, which found the pan fines fraction (<80 μm) of winter street sweepings to consist primarily of quartz (SiO_2), with minor amounts of dolomite ($CaMg(CO_3)_2$), potassium feldspar ($K(SiAl_3O_8)$), plagioclase feldspar ($Na(AlSi_3O_8)$), calcite ($CaCO_3$), illite ($KAl_2(OH)_2(AlSi_3(O,OH)_{10})$, and kaolinite ($Al_4Si_4O_{10}(OH)_8$).[52]

As shown in Table C.2, the chloride content in combined road dust aqueous leachates contributes to ~3% of bulk road dust sample mass, which is orders of magnitude higher than those reported for lower-latitude urban areas.[6,53] The enrichment of chloride in the road dust sample used in this study likely reflects the influence of road salt, which is also applied in Edmonton as part of winter road maintenance.[51] We also determined the chloride content of individual leachate samples (*i.e.*, rinses 1–7; see Figure C.1). Interestingly, as shown in Figure C.2, the chloride content of each of these samples was higher than expected based on our rinsing protocol (see Appendix C.2.1). These results imply that small amounts of residual chloride can remain in road dust despite its aqueous solubility, even after instances of heavy precipitation.

The Edmonton winters of 2018 and 2019 were unique because Road Guard Plus™, an anti-icer solution containing $CaCl_2$, $MgCl_2$, NaCl, KCl, and a proprietary salt dissolution inhibitor,[54] was also used for road maintenance.[55] As of Winter 2020, Edmonton has limited anti-icer use to specific purposes;[56] however, its application remains common worldwide.[57] As the primary salt in Road Guard Plus™ is $CaCl_2$ (25–27%),[54] we hypothesized that the Ca content of the road dust sample would decrease with rinsing. However, as shown in Table C.1, whereas Na in the rinsed sample is significantly lower than in the unrinsed sample, the Ca content of both samples is similar. This result suggests that residual road salt remained the dominant source of chloride in springtime Edmonton road dust, even during years when both anti-icer and road salt were applied.

As shown in Table C.3, road dust carbon (TC; 5.6%) is primarily present as organic carbon (TOC; 4.2%). These TC and TOC values are similar to those obtained for road dust collected in September 2016 from the same location,[10] and generally in line with observations in other urban locations.[3] Extensive rinsing (7×) leads to only a small decrease (~0.4%) in the TOC content of the sample, which means that most of the organic carbon fraction is only slightly soluble in water. Although characterization of the road dust organic fraction is beyond the scope of this work, results from previous studies suggest that it likely includes humic-like material from soil[58] and organic material (*e.g.*, microplastics and fibre binders) from non-exhaust emissions (*e.g.*, tire and brake wear debris).[2,59]

4.3.2 Heterogeneous reactivity of road dust with ozone

As shown in Figure 4.1, the retraction of the movable injector is accompanied by an immediate drop in the ozone mixing ratio measured at the exit of the flow tube, followed by a slow increase toward a steady-state (*i.e.*, plateau) value lower than the ozone mixing ratio in the absence of dust. The observed sustained ozone uptake persists for the entire time ozone is exposed to road dust. Illumination of the flow tube results in a further decrease in the ozone mixing ratio, which indicates that road dust contains photoactive materials.

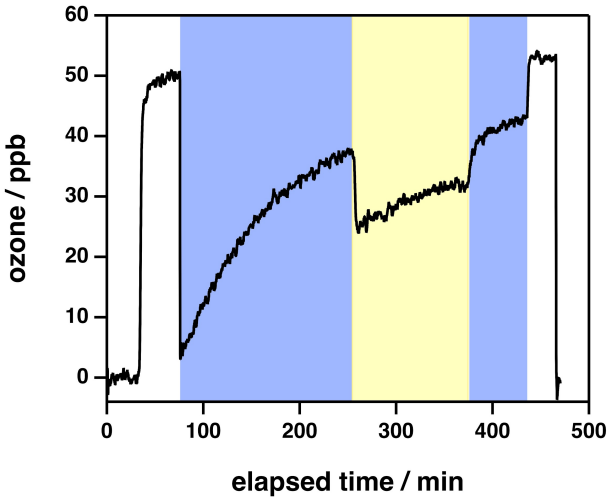

Figure 4.1: Reaction profile of ozone with road dust at 25% RH. The blue and yellow regions of the plot indicate periods during which road dust was exposed to ozone under dark and illuminated conditions, respectively.

4.3.2.1 Influence of road dust mass

As shown in Figure 4.2, γ_{corr} increases with increasing road dust mass (~12–85 mg) under both dark and light conditions. Previous studies of trace gas uptake by dust have demonstrated that γ_{corr} will increase linearly with increasing sample mass until the point at which the dust coating becomes too thick for gases to access the total surface area available for uptake, after which γ_{corr} remains constant.[49,60] Interestingly, for the 85 mg sample, we observe a positive deviation from linearity (Figure 4.2a). This observation likely arises from the fact that higher road dust mass loadings provide a larger number of available non-regenerative surface sites, which require longer ozone exposure times for deactivation; as a result, our use of the same experimental time intervals for all samples likely results in overestimates of ozone loss at steady-state and, by extension, positive biases in γ_{corr} for higher sample masses. Further evidence for the importance of coating thickness is provided by the decrease in $\gamma_{corr_{light}}/\gamma_{corr_{dark}}$ with increasing sample mass (Figure 4.2b), which indicates that light transmission through the sample is limited at higher masses. Given these results, we conducted

the remainder of our experiments with masses between 20–40 mg, which are within the linear range of our mass dependence experiments.

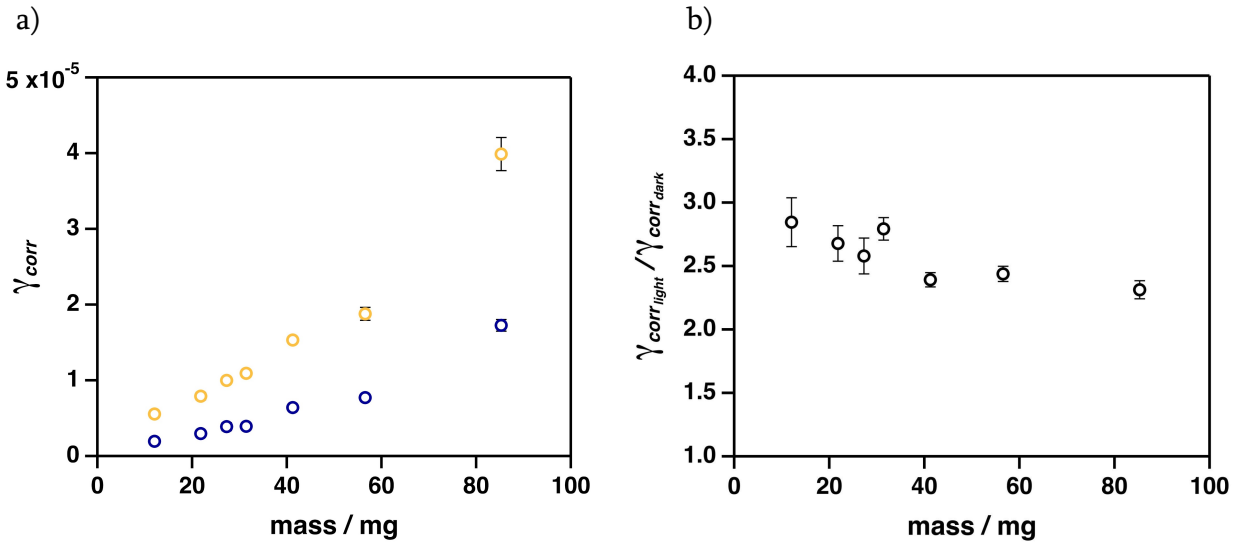

Figure 4.2: a) γ_{corr} for ozone uptake by road dust (50 ppb ozone, 25% RH) as a function of sample mass (n = 7) under dark (open blue circles) and illuminated (open yellow circles) conditions. The error bars represent the experimental error for each individual experiment, which includes uncertainties from the ozone analyzer and sample mass (in most cases, the error bars are too small to be seen); and b) $\gamma_{corr_{light}}/\gamma_{corr_{dark}}$ for ozone uptake by road dust (25% RH) as a function of sample mass. The error bars represent the experimental error for each individual experiment, which includes uncertainties from the ozone analyzer and sample mass.

4.3.2.2 Influence of ozone mixing ratios

As illustrated in Figure 4.3, γ_{BET} decays exponentially as a function of ozone mixing ratio under both dark and illuminated conditions. This relationship implies that ozone uptake by road dust follows a Langmuir–Hinshelwood mechanism, in which saturation of surface sites at higher ozone mixing ratios results in lower k_{obs} values.[61] This mechanism has previously been reported for major components of road dust including metal oxides,[49,62–64] natural mineral dust,[14] clays,[65] humic material,[20,66] and aqueous salts.[67]

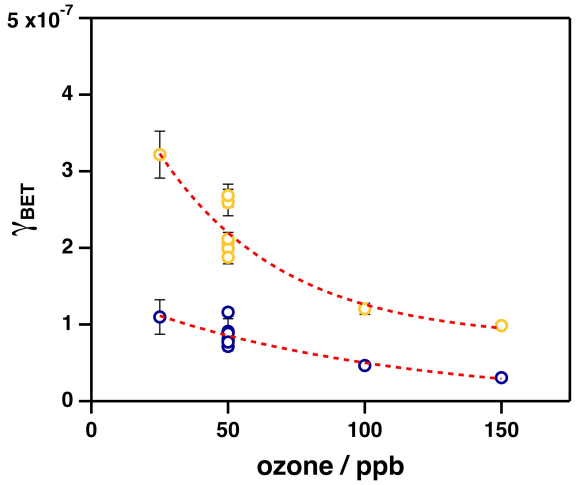

Figure 4.3: γ_{BET} for ozone uptake by road dust (25% RH) as a function of ozone mixing ratio under dark (open blue circles) and illuminated (open yellow circles) conditions. The error bars represent the experimental error for each individual experiment, which includes uncertainties from the ozone analyzer and sample mass. The dashed lines indicate an exponential fit to the plotted points.

4.3.3 Sustained uptake of ozone by road dust under dark conditions

4.3.3.1 Mechanistic discussion

As shown in Figure 4.1, ozone uptake by road dust is sustained for several hours. This observation is consistent with the mechanism suggested by other authors for ozone uptake by crustal material (*e.g.*, metal oxides);[64,68] in the following equations, SS represents a Lewis acid surface site for ozone adsorption:

$$O_3 + SS \rightarrow SS{-}O + O_2 \quad (4.1)$$

$$SS{-}{-}{-}O + O_3 \rightarrow SS{-}{-}O_2 + O_2 \quad (4.2)$$

$$SS{-}{-}O_2 \rightarrow SS + O_2 \quad (4.3)$$

$$2(SS{-}O) \rightarrow 2\,SS + O_2 \quad (4.4)$$

Here, Reaction 4.1 and 4.2 lead to the loss of ozone from the gas-phase and Reactions 4.3 and 4.4 lead to the regeneration of active surface sites, which is needed for sustained ozone uptake.

As road dust is more chemically complex than mineral dust, its interactions with ozone likely reflect contributions from additional constituents. For example, road dust contains humic-like material,[58] polycyclic aromatic hydrocarbons (PAHs),[69,70] and soot,[71] all of which demonstrate sustained ozone uptake.[17,18,72,73] In addition, as discussed in Section 4.3.1, the road dust sample studied here is abundant in salt; although ozone uptake by NaCl alone is negligible,[74] it is significantly enhanced in the presence of water-soluble Fe^{3+}.[75] This enhancement may also occur with salt-rich road dust, as vehicular exhaust[76] and crustal material[77] can both contain water-soluble Fe^{3+}. Finally, road dust contains a variety of anthropogenic metals (Table C.1), which may also facilitate ozone uptake; to date, however, the reactivity of these substrates has not been explored.

4.3.3.2 Comparison to previous literature

As illustrated in Figure 4.4, γ_{BET} for ozone uptake by road dust is $(8.6 \pm 1.5) \times 10^{-8}$ at 25% RH and 50 ppb of ozone. This value is between those previously reported for road dust-relevant substrates; for example, the γ_{BET} reported here is 2.4 and 3.9× larger than those obtained by our group for natural mineral dust samples collected from Cape Verde and the Gobi Desert, respectively,[13] and generally lower than γ values obtained for other individual components of road dust, including humic material ($\gamma \sim 10^{-6}$),[20] humic-like material ($\gamma \sim 10^{-6}$),[17] NaCl and sea spray aerosol mixed with water-soluble Fe^{3+} ($\gamma \sim 10^{-6}$),[75] and soot ($\gamma_{BET} \sim 10^{-7}$).[73]

4.3.4 Photoenhanced uptake of ozone by road dust

As illustrated in Figure 4.4, γ_{BET} for ozone uptake by road dust at 25% RH increases from $(8.6 \pm 1.5) \times 10^{-8}$ to $(2.2 \pm 0.3) \times 10^{-7}$ upon illumination. As was the case for road dust under dark conditions, this observation likely reflects contributions from multiple reactive components. For example, if the Fe and Ti in road dust (see Table C.1) were present in their semi-conducting oxide forms, they could promote the photochemical uptake of ozone.[15,43,60,78] In this mechanism, the absorption of light at wavelengths greater than or equal to the band gaps of Fe and Ti oxides results in the formation of an electron–hole pair,[79] which initiates a chain of reactions that leads to the reduction of ozone.[60,78] These oxides have been suggested

to be responsible for the photochemistry of mineral dust[80] and vehicular brake wear particles.[43] In addition, our group has previously reported photoenhanced uptake of ozone by a broad range of Ti-containing minerals, which suggests that other photoactive minerals in the crustal fraction of road dust could also contribute to its photoreactivity.[15]

The photoreactivity of road dust may also be mediated by photosensitizers in the organic fraction of the sample. For example, humic acids,[20] humic-like material,[17] soot,[73] PAHs,[18,72] and benzophenone (an atmospheric aromatic proxy)[81] have all been shown to exhibit light-enhanced ozone uptake. In these cases, ozone decomposition is believed to occur via reaction with $^1O_2$ formed by energy transfer from the electronically excited organic substrate to molecular oxygen.[81]

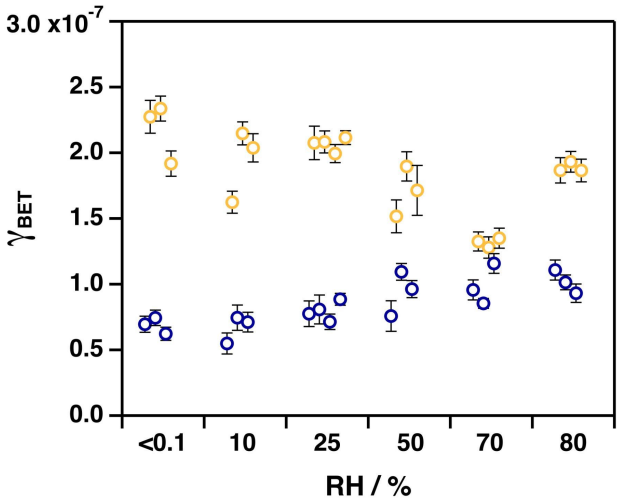

Figure 4.4: γ_{BET} values for ozone (50 ppb) uptake by road dust as a function of RH under dark (open blue circles) and illuminated (open yellow circles) conditions. The error bars represent the experimental error for each individual experiment, which include the uncertainty from the ozone analyzer and sample mass.

4.3.5 Influence of relative humidity on ozone uptake by road dust

Water is an important factor in many atmospheric surface reactions.[82] In this context, we investigated ozone uptake by road dust as a function of RH. As shown in Figure 4.4, γ_{BET} increases with increasing RH under dark conditions. These results contrast with previous

studies of ozone uptake by mineral dust,[83] mineral dust proxies,[15,63–65] volcanic dust,[84] and PAHs,[18,85] which found ozone uptake to decrease or remain unchanged with increasing RH, with the former being attributed to competitive adsorption between ozone and water vapour. Instead, the observed RH dependence agrees with those reported for humic acid[20] and humic-like material,[17] which have been attributed to the exposure of additional surface sites for ozone uptake via the molecular expansion of humic acid at higher RH.[86]

Under illumination, γ_{BET} decreases with increasing RH (Figure 4.4). Although studies of photoenhanced ozone uptake by mineral dust and mineral dust proxies have reported a variety of RH trends, decreases in γ with increasing RH have consistently been observed for organic films;[18,20,81] here, researchers have proposed that $^1O_2$ quenching by surface-sorbed water at higher RH reduces the likelihood of ozone reacting with $^1O_2$. Although the chemical complexity of the road dust sample makes it challenging to identify which components are mediating its reactivity under elevated RH conditions, its behaviour is most consistent with that of humic material, which suggests that organics play a key role in ozone uptake by road dust.

4.3.6 Influence of water-soluble material on ozone uptake by road dust

To explore the contribution of water-soluble material to ozone uptake by road dust, we also investigated the reactivity of rinsed road dust (rinsing details provided in Appendix C.2.1). As demonstrated in Figure C.3, the photoreactivity of rinsed road dust is less than that of the parent dust at 25% RH, which could reflect the removal of photoactive humic and humic-like material.[10,58] In addition, whereas the photoreactivity of the parent sample decreases substantially with increasing RH, the photoreactivity of the rinsed sample is only slightly lower at 75% RH than at 25% RH. This result is also consistent with the removal of organic material, provided that this material—like the humic photosensitizers discussed in the previous section—is subject to $^1O_2$ quenching at elevated RH.[20,81] At the same time, the weak RH dependence for rinsed road dust may also be related to the substantial decrease in salt content as a result of rinsing (Table C.1 and Figure C.1), which could reduce the hygroscopicity

of the sample[87] and potentially suppress these RH effects for any remaining photoactive organic material.

Given these interesting but somewhat inconclusive results, we also explored the role of road salts and organic material more directly through examining the uptake of ozone by the following samples, all under elevated RH conditions: a) $CaCl_2 \cdot 2H_2O$, the main component of the anti-icer solution studied here; b) anti-icer itself; c) road dust doped with $CaCl_2 \cdot 2H_2O$; and d) road dust doped with anti-icer. As $CaCl_2 \cdot 2H_2O$ and anti-icer are both hygroscopic, it was not possible to obtain uniform coatings at 70% RH; instead, these samples existed as aqueous films at the bottom of the Pyrex insert tubes. In addition, the specific surface areas of $CaCl_2 \cdot 2H_2O$ or anti-icer coated road dust are likely different from that of road dust itself, which precludes the accurate determination of γ_{BET} values. Consequently, we did not calculate γ for these samples, but instead qualitatively compared their individual reaction profiles with ozone.

As shown in Figure C.4, minimal loss of ozone is observed upon exposure to $CaCl_2 \cdot 2H_2O$, which agrees with results previously reported for NaCl.[74] In contrast, significant ozone loss occurs in the presence of anti-icer, which suggests that the reactivity of the anti-icing solution is driven not by its salt content but instead by its organic fraction. According to the manufacturer SDS, the organic fraction of the anti-icer studied here contains 0–10% molasses (CAS #: 68476-78-8),[54] a viscous, brown liquid produced during the refinement of sugarcane or sugar beets that consists of a complex chemical mixture of sugars (>60%), protein, organic acids, and lesser quantities of metals, phosphates, sulfates, and chlorides.[88] The brown colour of molasses largely stems from melanoidins,[89] which are high-molecular weight species formed by the Maillard reaction between sugars and amino acids.[90] Although ozone uptake by molasses itself has not been investigated in an atmospheric context, ozone is commonly used to remove melanoidins in wastewater from molasses distillation.[91] In addition, ozone reacts with many of the component classes of molasses, including proteins,[92–94] unsaturated organic acids,[95,96] metal oxides,[49,62,64,68] and metals.[43] Together, these components are likely responsible for the substantial loss of ozone observed with anti-icer.

We also examined the influence of $CaCl_2 \cdot 2H_2O$ and anti-icer on road dust reactivity toward ozone. As demonstrated in Figure C.4, ozone loss at the surface of road dust doped with 5% (w/w) chloride is less than ozone loss at the surface of road dust doped with 50 ppb (w/w) chloride. This observation, which most likely reflects blockage by salt of road dust surface sites required for ozone uptake,[97] provides further confirmation that salts do not contribute to road dust reactivity toward ozone. Finally, road dust doped with anti-icer displays a much larger ozone loss compared to anti-icer alone, which may reflect an increase in the surface area of anti-icer in the mixed road dust–anti-icer coatings.

4.3.7 Chlorine activation during ozone uptake by road dust and winter road maintenance materials

To assess whether ozone uptake by road dust and winter road maintenance materials can lead to chlorine activation, we used an offline analysis technique (see Section 4.2.2.3) to quantify inorganic chlorine release from road dust, winter road maintenance materials, and mixtures of the two. To avoid contributions from any photochemical processes, we conducted these experiments under dark conditions. Detailed descriptions of all samples studied here, as well as the motivation for their selection, is provided in Appendix C.2.2 and in Table C.6. We used $CaCl_2 \cdot 2H_2O$ mixed with $FeCl_3$ as a positive control in these experiments, based on previous observations of gas-phase chlorine formation during ozone uptake by NaCl mixed with water-soluble Fe^{3+}.[75]

As demonstrated in Figure 4.5, impinger chloride concentrations were not elevated above the blank values for any road dust samples—whether unmodified or subject to any of the sample treatment conditions explored here (*i.e.*, acidification, illumination, rinsing). The same is true for $CaCl_2 \cdot 2H_2O$, the primary salt component in anti-icer. Interestingly, however, in the case of anti-icer (and, to a lesser extent, road dust mixed with anti-icer), impinger chloride concentrations were elevated substantially above the blank values. These results imply that anti-icer can participate in chlorine activation, and that the observed reactivity reflects contributions from materials other than salt.

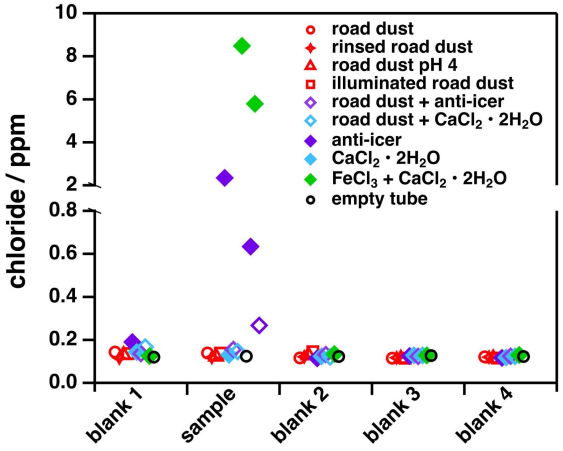

Figure 4.5: Chloride content in impinger solutions, as determined by IC analysis. Experiments were run in duplicate; each point represents the average value of two experiments, except for samples that demonstrated chlorine activation (*i.e.*, anti-icer, $CaCl_2 \cdot 2H_2O$, and road dust mixed with anti-icer), for which we report the chloride content for each individual trial.

We observe the highest impinger chloride concentrations for $CaCl_2 \cdot 2H_2O$ mixed with $FeCl_3$, which we used as a positive control.[75] Although the original report by Sadanaga et al. did not provide a mechanism for chlorine activation, a more recent study attributed enhanced gas-phase iodine emissions during ozone oxidation of iron-containing aqueous iodide solutions to a pH buffering effect, in which scavenging of hydroxide ion by Fe^{3+} promotes formation of HOI and, ultimately, I_2.[98] The authors of this latter study suggested that chlorine production in mixed chloride–iron systems could also be initiated by trace levels of iodide, which may have been the case in our experiments.

Although molasses can contain high levels of Fe (0.1–0.2 mg g^{-1}),[99] Fe was not detected in our sample (Table C.5), which suggests that chlorine activation via anti-icer proceeds via a different mechanism. Given the organic composition of molasses, we propose the following pathway: first, ozonolysis of unsaturated species (*e.g.*, melanoidins,[91] proteins,[92–94] organic acids[95,96]) leads to the formation of primary ozonides, which decompose to produce unstable

Criegee intermediates,[100] an important source of OH radicals;[101–103] second, chloride oxidation by OH radicals ultimately leads to the formation of gas-phase chlorine:[104]

$$OH^{\bullet}_{(g)} + Cl^{-} \rightarrow OHCl^{\bullet-} \quad (4.5)$$

$$2OHCl^{\bullet-} \rightarrow Cl_{2(g)} + 2OH^{-}_{(aq)} \quad (4.6)$$

Although not the primary focus of their study, we note that Faxon and colleagues observed an increase in chlorine production during dark ozone uptake by deliquescent NH_4Cl in the presence of secondary organic aerosol,[105] which further supports our proposed chlorine activation pathway.

4.4 Atmospheric significance and conclusion

In this study, we show for the first time that road dust provides a surface for uptake of trace pollutant gases; in particular, we find road dust to be more reactive toward ozone than natural dusts (*i.e.*, mineral and volcanic).[15,84] This higher reactivity, which likely reflects contributions from the road dust organic fraction, suggests the need for road dust to be considered as distinct from dust emitted from crustal sources. To predict the overall impact of suspended road dust on urban ozone mixing ratios, we compare ozone fluxes to road dust and ground surfaces using the following equations:[106]

$$F_{grd} = -V_d[X_g] \times 10^{-2} \quad (4.5)$$

$$F_{aer} = \frac{\omega \gamma_{BET}}{4} Ah[X_g] \times 10^{-6} \quad (4.6)$$

Here, V_d is the deposition velocity of ozone (cm s^{-1}), $[X_g]$ is the mixing ratio of ozone (mol m^{-3}), ω is the mean thermal velocity of ozone (m s^{-1}), γ_{BET} is the steady-state surface area-scaled uptake coefficient for ozone with road dust, A is the total surface area of road dust PM (μm^2 cm^{-3}), and h is the atmospheric mixing height (m).

Assuming an ozone deposition velocity of 0.15 cm s^{-1}, a 50 ppb ozone mixing ratio; a γ_{BET} value of 2×10^{-7}, a mixing height of 300 m, and road dust PM with diameter = 1 μm and density = 2.0 g cm^{-3},[107] a road dust mass loading of ~9.6 mg m^{-3} would be required for the ozone flux to suspended road dust to equal 10% of its flux to the ground (*i.e.*, $F_{aer} = 0.1F_{grd}$). However, there are several caveats to this conclusion: first, we use the steady-state γ_{BET} value here, which underestimates the reactivity of road dust at shorter ozone exposure times; second, since the composition of road dust varies with both season (*e.g.*, via loss of water-soluble material during spring melt, changes in contributions of individual components) and location,[108] ozone uptake by road dust may also vary. Nonetheless, as road dust mass loadings are typically orders of magnitude lower than this value,[109] we conclude that suspended road dust is not reactive enough to influence ozone mixing ratios in the urban atmosphere. Of course, since the deposition velocity of ozone at the road surface also in part reflects its reactivity with road dust, this comparison inherently underestimates this substrate's overall impact.

Interestingly, ozone exhibits substantial and sustained loss to the surface of anti-icer; although our specific experimental set-up limited our ability to determine reliable uptake coefficients for this substrate, our qualitative results indicate that road surface uptake may be an important ozone loss pathway in wintertime urban environments. Furthermore, ozone uptake by anti-icer leads to the release of inorganic chlorine, which we collected using impinger solutions containing a reductive trapping agent and detected as chloride via offline IC analysis. We propose that this chlorine activation proceeds via ozone oxidation of unsaturated organic molecules in anti-icer, which yields reactive radicals (*i.e.*, OH) that can mobilize chloride. As our analytical approach does not allow for determination of chlorine speciation, we cannot exclude the formation of chlorine-containing species other than Cl_2. However, as bromide was

below the limit of detection in all impinger solutions analyzed, we can conclude that the detected chloride did not originate from the release of mixed halides (*e.g.* BrCl), which are the dominant form of chlorine produced during ozone uptake by snow surfaces.[110]

To explore the atmospheric impacts of chlorine activation by anti-icer, we first use measured impinger chloride concentrations to determine chlorine mixing ratios in the reactor outflow; here, we assume that chlorine is present as Cl_2. Using background-subtracted values for each individual anti-icer trial presented in Figure 4.5, and assuming constant chlorine release over the duration of each experiment, we calculate Cl_2 mixing ratios of ~98 and ~425 ppb of Cl_2 in the gas flow at the exit of the sample-coated Pyrex insert tube. As all experiments were conducted in a gas flow containing ~250 ppb ozone, these results imply the possibility of a greater-than-unity chlorine yield for this chlorine activation pathway. Finally, we use the corresponding surface fluxes from our experiments (0.6 and 2.6 mg m^{-2} h^{-1}, assuming uniform coatings in the Pyrex insert tubes) to obtain a preliminary estimate of chlorine emissions from anti-icer treated roads; assuming an ozone mixing ratio of 50 ppb (and that the chlorine yield is invariant with ozone concentration, which may not be the case) and a mixing height of 300 m, these fluxes imply an atmospheric input of 0.2 and 0.9 ppb h^{-1}.

Finally, chlorine activation has also been observed during N_2O_5 uptake by by winter road maintenance materials (here, road salts); this pathway results in the formation of $ClNO_2$, a precursor of reactive atomic chlorine.[23] However, this pathway may be suppressed in regions where agro-based anti-icers are used, as N_2O_5 uptake by aqueous PM decreases with increasing organic content.[111,112] Studies have also shown that organics can reduce $ClNO_2$ yield;[113] this suppression, which is believed to involve the scavenging of intermediate nitronium ion prior to its reaction with chloride,[119] is likely especially important for molasses-containing anti-icer, as it is both rich in unsaturated organics[114] and highly viscous. In addition, N_2O_5 is depleted near the ground surface[115] due to reaction of NO_3, its precursor, with NO and volatile organic compounds emitted from soils and roadways,[116,117] which also reduces the likelihood of N_2O_5 reacting with anti-icer at the road surface.

In summary, we show here for the first time that road dust and winter road maintenance materials can serve as both oxidant sinks (via ozone uptake) and sources (via chlorine activation). These conclusions highlight the need for cold-climate urban municipalities to consider the potential indirect air quality impacts of winter road maintenance strategies. In future, we suggest studies to explore chlorine activation by agro-based anti-icing solutions using more sensitive, online measurement techniques (*e.g.*, chemical ionization mass spectrometry), which will provide a better understanding of emission rates, chlorine speciation, and atmospheric fate. Finally, as the organic fraction of anti-icers can also contain glycols, formates, acetates, and agro-based products other than molasses,[118] a full understanding of the air quality impacts of anti-icing solutions will require a comprehensive experimental approach.

4.5 References

(1) Loganathan, P.; Vigneswaran, S.; Kandasamy, J. Road-Deposited Sediment Pollutants: A Critical Review of Their Characteristics, Source Apportionment, and Management. *Crit. Rev. Environ. Sci. Technol.* **2013**, *43* (13), 1315–1348.

(2) Thorpe, A.; Harrison, R. M. Sources and Properties of Non-Exhaust Particulate Matter from Road Traffic: A Review. *Sci. Total Environ.* **2008**, *400* (1–3), 270–282.

(3) Gunawardana, C.; Goonetilleke, A.; Egodawatta, P.; Dawes, L.; Kokot, S. Source Characterisation of Road Dust Based on Chemical and Mineralogical Composition. *Chemosphere* **2012**, *87* (2), 163–170.

(4) Bukowiecki, N.; Lienemann, P.; Hill, M.; Furger, M.; Richard, A.; Amato, F.; Prévôt, A. S. H.; Baltensperger, U.; Buchmann, B.; Gehrig, R. PM10 Emission Factors for Non-Exhaust Particles Generated by Road Traffic in an Urban Street Canyon and along a Freeway in Switzerland. *Atmos. Environ.* **2010**, *44* (19), 2330–2340.

(5) Zhang, J.; Peng, J.; Song, C.; Ma, C.; Men, Z.; Wu, J.; Wu, L.; Wang, T.; Zhang, X.; Tao, S.; Gao, S.; Hopke, P. K.; Mao, H. Vehicular Non-Exhaust Particulate Emissions in Chinese Megacities: Source Profiles, Real-World Emission Factors, and Inventories. *Environ. Pollut.* **2020**, *266*, 115268.

(6) Han, L.; Zhuang, G.; Cheng, S.; Wang, Y.; Li, J. Characteristics of Re-Suspended Road Dust and Its Impact on the Atmospheric Environment in Beijing. *Atmos. Environ.* **2007**, *41* (35), 7485–7499.

(7) Environment Canada and Health Canada. Canadian Smog Science Assessment: Highlights and Key Messages. 2011.

(8) Canada, T. Building a green economy: Government of Canada to require 100% of car and

passenger truck sales be zero-emission by 2035 in Canada https://www.canada.ca/en/transport-canada/news/2021/06/building-a-green-economy-government-of-canada-to-require-100-of-car-and-passenger-truck-sales-be-zero-emission-by-2035-in-canada.html (accessed 2021 -09 -13).

(9) Zero Emission Fleet vehicles For European Roll-out - TRIMIS - European Commission https://trimis.ec.europa.eu/project/zero-emission-fleet-vehicles-european-roll-out (accessed 2021 -09 -13).

(10) Cote, C. D.; Schneider, S. R.; Lyu, M.; Gao, S.; Gan, L.; Holod, A. J.; Chou, T. H. H.; Styler, S. A. Photochemical Production of Singlet Oxygen by Urban Road Dust. *Environ. Sci. Technol. Lett.* **2018**, *5* (2), 92–97.

(11) Pitts, J. N.; Khan, A. U.; Smith, E. B.; Wayne, R. P. Singlet Oxygen in the Environmental Sciences. Singlet Molecular Oxygen and Photochemical Air Pollution. *Environ. Sci. Technol.* **1969**, *3* (3), 241–247.

(12) Schmidt, M.; Jansen van Beek, S. M.; Abou-Ghanem, M.; Oliynyk, A. O.; Locock, A. J.; Styler, S. A. Production of Atmospheric Organosulfates via Mineral-Mediated Photochemistry. *ACS Earth Space Chem.* **2019**, *3* (3), 424–431.

(13) D. Abbatt, J. P.; Y. Lee, A. K.; A. Thornton, J. Quantifying Trace Gas Uptake to Tropospheric Aerosol: Recent Advances and Remaining Challenges. *Chem. Soc. Rev.* **2012**, *41* (19), 6555–6581.

(14) Hanisch, F.; Crowley, J. N. Ozone Decomposition on Saharan Dust: An Experimental Investigation. *Atmos Chem Phys* **2003**, *3* (1), 119–130.

(15) Abou-Ghanem, M.; Oliynyk, A. O.; Chen, Z.; Matchett, L. C.; McGrath, D. T.; Katz, M. J.; Locock, A. J.; Styler, S. A. Significant Variability in the Photocatalytic Activity of Natural Titanium-Containing Minerals: Implications for Understanding and Predicting Atmospheric Mineral Dust Photochemistry. *Environ. Sci. Technol.* **2020**, *54* (21), 13509–13516.

(16) Wang, X.; Romanias, M. N.; Thévenet, F.; Rousseau, A. Geocatalytic Uptake of Ozone onto Natural Mineral Dust. *Catalysts* **2018**, *8* (7), 263.

(17) Baduel, C.; Monge, M. E.; Voisin, D.; Jaffrezo, J.-L.; George, C.; Haddad, I. E.; Marchand, N.; D'Anna, B. Oxidation of Atmospheric Humic Like Substances by Ozone: A Kinetic and Structural Analysis Approach. *Environ. Sci. Technol.* **2011**, *45* (12), 5238–5244.

(18) Styler, S. A.; Brigante, M.; D'Anna, B.; George, C.; Donaldson, D. J. Photoenhanced Ozone Loss on Solid Pyrene Films. *Phys. Chem. Chem. Phys.* **2009**, *11* (36), 7876–7884.

(19) Seinfeld, J. H.; Pandis, S. N. *Atmospheric Chemistry and Physics: From Air Pollution to Climate Change*; John Wiley & Sons, 2016.

(20) D'Anna, B.; Jammoul, A.; George, C.; Stemmler, K.; Fahrni, S.; Ammann, M.; Wisthaler, A. Light-Induced Ozone Depletion by Humic Acid Films and Submicron Aerosol Particles. *J. Geophys. Res. Atmos.* **2009**, *114* (D12), D12301.

(21) Nan, Y.; Wang, Y. Observational Evidence for Direct Uptake of Ozone in China by Asian Dust in Springtime. *Atmos. Environ.* **2018**, *186*, 45–55.

(22) de Reus, M.; Fischer, H.; Sander, R.; Gros, V.; Kormann, R.; Salisbury, G.; Van Dingenen,

R.; Williams, J.; Zöllner, M.; Lelieveld, J. Observations and Model Calculations of Trace Gas Scavenging in a Dense Saharan Dust Plume during MINATROC. *Atmos. Chem. Phys.* **2005**, *5* (7), 1787–1803.

(23) McNamara, S. M.; Kolesar, K. R.; Wang, S.; Kirpes, R. M.; May, N. W.; Gunsch, M. J.; Cook, R. D.; Fuentes, J. D.; Hornbrook, R. S.; Apel, E. C.; China, S.; Laskin, A.; Pratt, K. A. Observation of Road Salt Aerosol Driving Inland Wintertime Atmospheric Chlorine Chemistry. *ACS Cent. Sci.* **2020**, *6* (5), 684–694.

(24) Finlayson-Pitts, B. J.; Ezell, M. J.; Pitts, J. N. Formation of Chemically Active Chlorine Compounds by Reactions of Atmospheric NaCl Particles with Gaseous N2O5 and ClONO2. *Nature* **1989**, *337* (6204), 241–244.

(25) Thornton, J. A.; Kercher, J. P.; Riedel, T. P.; Wagner, N. L.; Cozic, J.; Holloway, J. S.; Dubé, W. P.; Wolfe, G. M.; Quinn, P. K.; Middlebrook, A. M.; Alexander, B.; Brown, S. S. A Large Atomic Chlorine Source Inferred from Mid-Continental Reactive Nitrogen Chemistry. *Nature* **2010**, *464* (7286), 271–274.

(26) Mielke, L. H.; Furgeson, A.; Odame-Ankrah, C. A.; Osthoff, H. D. Ubiquity of ClNO2 in the Urban Boundary Layer of Calgary, Alberta, Canada. *Can. J. Chem.* **2015**, *94* (4), 414–423.

(27) Mielke, L. H.; Furgeson, A.; Osthoff, H. D. Observation of ClNO2 in a Mid-Continental Urban Environment. *Environ. Sci. Technol.* **2011**, *45* (20), 8889–8896.

(28) Rossi, M. J. Heterogeneous Reactions on Salts. *Chem. Rev.* **2003**, *103* (12), 4823–4882.

(29) Finlayson-Pitts, B. J. The Tropospheric Chemistry of Sea Salt: A Molecular-Level View of the Chemistry of NaCl and NaBr. *Chem. Rev.* **2003**, *103* (12), 4801–4822.

(30) Equiza, M. A.; Calvo-Polanco, M.; Cirelli, D.; Señorans, J.; Wartenbe, M.; Saunders, C.; Zwiazek, J. J. Long-Term Impact of Road Salt (NaCl) on Soil and Urban Trees in Edmonton, Canada. *Urban For. Urban Green.* **2017**, *21*, 16–28.

(31) Howard, K. W. F.; Beck, P. J. Hydrogeochemical Implications of Groundwater Contamination by Road De-Icing Chemicals. *J. Contam. Hydrol.* **1993**, *12* (3), 245–268.

(32) Kaushal, S. S.; Groffman, P. M.; Likens, G. E.; Belt, K. T.; Stack, W. P.; Kelly, V. R.; Band, L. E.; Fisher, G. T. Increased Salinization of Fresh Water in the Northeastern United States. *Proc. Natl. Acad. Sci.* **2005**, *102* (38), 13517–13520.

(33) Shi, X.; Veneziano, D.; Xie, N.; Gong, J. Use of Chloride-Based Ice Control Products for Sustainable Winter Maintenance: A Balanced Perspective. *Cold Reg. Sci. Technol.* **2013**, *86*, 104–112.

(34) Rhodan, M.; Sanburn, J. How Beet Juice Is Helping Keep Roads Safe This Winter https://time.com/5761/salt-shortage-triggers-beet-juice-cheese-brine-alternatives/ (accessed 2021 -09 -07).

(35) Daily, P. B. / V. Beet juice, molasses and mag: Colorado's search for the right highway de-icing mixture https://www.skyhinews.com/news/beet-juice-molasses-and-mag-colorados-search-for-the-right-highway-de-icing-mixture/ (accessed 2021 -09 -07).

(36) Berke, J. Cities are starting to put beet juice, beer waste, and pickle brine on icy winter roads to cut down on salt https://www.businessinsider.com/why-cities-put-beet-juice-

beer-waste-molasses-on-roads-2018-1 (accessed 2021 -09 -07).

(37) Fu, L.; Omer, R.; Jiang, C. Field Test of Organic Deicers as Prewetting and Anti-Icing Agents for Winter Road Maintenance. *Transp. Res. Rec.* **2012**, *2272* (1), 130–135.

(38) Petkuviene, J.; Paliulis, D. Experimental Research of Road Maintenance Salts and Molasses ("safecote") Corrosive Impact on Metals. *J. Environ. Eng. Landsc. Manag.* **2009**, *17* (4), 236–243.

(39) Honarvar Nazari, M.; Havens, E. A.; Shi, X.; Muthumani, A.; Washington State University. Department of Civil and Environmental Engineering; Western Transportation Institute. *Bio-Based Renewable Additives for Anti-Icing Applications (Phase One)*; INE/CESTiCC 101406; 2016.

(40) Honarvar Nazari, M.; Havens, E. A.; Muthumani, A.; Shi, X. Effects of Processed Agro-Residues on the Performance of Sodium Chloride Brine Anti-Icer. *ACS Sustain. Chem. Eng.* **2019**, *7* (16), 13655–13667.

(41) Shi, X.; Quilty, S. M.; Long, T.; Jayakaran, A.; Fay, L.; Xu, G. Managing Airport Stormwater Containing Deicers: Challenges and Opportunities. *Front. Struct. Civ. Eng.* **2017**, *11* (1), 35–46.

(42) Koryak, M.; Stafford, L. J.; Reilly, R. J.; Hoskin, R. H.; Haberman, M. H. The Impact of Airport Deicing Runoff on Water Quality and Aquatic Life in a Pennsylvania Stream. *J. Freshw. Ecol.* **1998**, *13* (3), 287–298.

(43) Matchett, L. C.; Abou-Ghanem, M.; Stix, K. A. R.; McGrath, D. T.; Styler, S. A. Submitted. Ozone Uptake by Commercial Brake Pads: Assessing the Potential Indirect Air Quality Impacts of Non-Exhaust Emissions. *Submitt. Environ. Sci. Atmos.* **2018**.

(44) Michoud, V.; Colomb, A.; Borbon, A.; Miet, K.; Beekmann, M.; Camredon, M.; Aumont, B.; Perrier, S.; Zapf, P.; Siour, G.; Ait-Helal, W.; Afif, C.; Kukui, A.; Furger, M.; Dupont, J. C.; Haeffelin, M.; Doussin, J. F. Study of the Unknown HONO Daytime Source at a European Suburban Site during the MEGAPOLI Summer and Winter Field Campaigns. *Atmos. Chem. Phys.* **2014**, *14* (6), 2805–2822.

(45) Knopf, D. A.; Pöschl, U.; Shiraiwa, M. Radial Diffusion and Penetration of Gas Molecules and Aerosol Particles through Laminar Flow Reactors, Denuders, and Sampling Tubes. *Anal. Chem.* **2015**, *87* (7), 3746–3754.

(46) Keene, W. C.; Maben, J. R.; Pszenny, A. A. P.; Galloway, J. N. Measurement Technique for Inorganic Chlorine Gases in the Marine Boundary Layer. *Environ. Sci. Technol.* **1993**, *27* (5), 866–874.

(47) Pöschl, U.; Rudich, Y.; Ammann, M. Kinetic Model Framework for Aerosol and Cloud Surface Chemistry and Gas-Particle Interactions–Part 1: General Equations, Parameters, and Terminology. *Atmos. Chem. Phys.* **2007**, *7* (23), 5989–6023.

(48) Kolb, C. E.; Cox, R. A.; Abbatt, J. P. D.; Ammann, M.; Davis, E. J.; Donaldson, D. J.; Garrett, B. C.; George, C.; Griffiths, P. T.; Hanson, D. R.; Kulmala, M.; McFiggans, G.; Pöschl, U.; Riipinen, I.; Rossi, M. J.; Rudich, Y.; Wagner, P. E.; Winkler, P. M.; Worsnop, D. R.; O' Dowd, C. D. An Overview of Current Issues in the Uptake of Atmospheric Trace Gases by Aerosols and Clouds. *Atmos. Chem. Phys.* **2010**, *10* (21), 10561–10605.

(49) Michel, A. E.; Usher, C. R.; Grassian, V. H. Reactive Uptake of Ozone on Mineral Oxides and Mineral Dusts. *Atmos. Environ.* **2003**, *37* (23), 3201–3211.
(50) Coates Fuentes, Z. L.; Kucinski, T. M.; Hinrichs, R. Z. Ozone Decomposition on Kaolinite as a Function of Monoterpene Exposure and Relative Humidity. *ACS Earth Space Chem.* **2017**.
(51) Edmonton Winter Road Maintenance.
(52) City of Edmonton. Shape, Angularity and Petrography of Seven Sucessively Fractioned Street Sweeping Samples. October 2015.
(53) Othman, M.; Latif, M. T. Pollution Characteristics, Sources, and Health Risk Assessments of Urban Road Dust in Kuala Lumpur City. *Environ. Sci. Pollut. Res.* **2020**, *27* (10), 11227–11245.
(54) Tiger Calcium. *Road Guard Plus™ SDS*.
(55) News ·, M. D. · C. First round of city's new salt brine hits Edmonton streets | CBC News https://www.cbc.ca/news/canada/edmonton/salt-brine-roads-edmonton-rust-1.4403846 (accessed 2021 -08 -05).
(56) City of Edmonton. Winter Roads - Frequently Asked Questions https://www.edmonton.ca/transportation/on_your_streets/snow-faq (accessed 2021 -08 -05).
(57) Terry, L. G.; Conaway, K.; Rebar, J.; Graettinger, A. J. Alternative Deicers for Winter Road Maintenance—A Review. *Water. Air. Soil Pollut.* **2020**, *231* (8), 394.
(58) Aryal, R.; Lee, B.-K.; Beecham, S.; Kandasamy, J.; Aryal, N.; Parajuli, K. Characterisation of Road Dust Organic Matter as a Function of Particle Size: A PARAFAC Approach. *Water. Air. Soil Pollut.* **2015**, *226* (2), 24.
(59) Sommer, F.; Dietze, V.; Baum, A.; Sauer, J.; Gilge, S.; Maschowski, C.; Gieré, R. Tire Abrasion as a Major Source of Microplastics in the Environment. *Aerosol Air Qual. Res.* **2018**, *18* (8), 2014–2028.
(60) Nicolas, M.; Ndour, M.; Ka, O.; D'Anna, B.; George, C. Photochemistry of Atmospheric Dust: Ozone Decomposition on Illuminated Titanium Dioxide. *Environ. Sci. Technol.* **2009**, *43* (19), 7437–7442.
(61) Arthur W Adamson; Alice Petry Gast. *Physical Chemistry of Surfaces*; New York: Interscience publishers, 1967; Vol. 15.
(62) Michel A. E.; Usher C. R.; Grassian V. H. Heterogeneous and Catalytic Uptake of Ozone on Mineral Oxides and Dusts: A Knudsen Cell Investigation. *Geophys. Res. Lett.* **2002**, *29* (14), 10–11.
(63) Mogili, P. K.; Kleiber, P. D.; Young, M. A.; Grassian, V. H. Heterogeneous Uptake of Ozone on Reactive Components of Mineral Dust Aerosol: An Environmental Aerosol Reaction Chamber Study. *J. Phys. Chem. A* **2006**, *110* (51), 13799–13807.
(64) Sullivan, R. C.; Thornberry, T.; Abbatt, J. P. D. Ozone Decomposition Kinetics on Alumina: Effects of Ozone Partial Pressure, Relative Humidity and Repeated Oxidation Cycles. *Atmos Chem Phys* **2004**, *4* (5), 1301–1310.
(65) Lasne, J.; Romanias, M. N.; Thevenet, F. Ozone Uptake by Clay Dusts under

Environmental Conditions. *ACS Earth Space Chem.* **2018**, *2* (9), 904–914.
(66) Brigante, M.; D'Anna, B.; Conchon, P.; George, C. Multiphase Chemistry of Ozone on Fulvic Acids Solutions. *Environ. Sci. Technol.* **2008**, *42* (24), 9165–9170.
(67) Moreno, C.; Teresa Baeza-Romero, M. A Kinetic Model for Ozone Uptake by Solutions and Aqueous Particles Containing I – and Br – , Including Seawater and Sea-Salt Aerosol. *Phys. Chem. Chem. Phys.* **2019**, *21* (36), 19835–19856.
(68) Li, W.; Oyama, S. T. Mechanism of Ozone Decomposition on a Manganese Oxide Catalyst. 2. Steady-State and Transient Kinetic Studies. *J. Am. Chem. Soc.* **1998**, *120* (35), 9047–9052.
(69) Dong, T. T. T.; Lee, B.-K. Characteristics, Toxicity, and Source Apportionment of Polycylic Aromatic Hydrocarbons (PAHs) in Road Dust of Ulsan, Korea. *Chemosphere* **2009**, *74* (9), 1245–1253.
(70) Murakami, M.; Nakajima, F.; Furumai, H. Size- and Density-Distributions and Sources of Polycyclic Aromatic Hydrocarbons in Urban Road Dust. *Chemosphere* **2005**, *61* (6), 783–791.
(71) Han, Y. M.; Cao, J. J.; Chow, J. C.; Watson, J. G.; An, Z. S.; Liu, S. X. Elemental Carbon in Urban Soils and Road Dusts in Xi'an, China and Its Implication for Air Pollution. *Atmos. Environ.* **2009**, *43* (15), 2464–2470.
(72) Cope, V. W.; Kalkwarf, D. R. Photooxidation of Selected Polycyclic Aromatic Hydrocarbons and Pyrenequinones Coated on Glass Surfaces. *Environ. Sci. Technol.* **1987**, *21* (7), 643–648.
(73) Zelenay, V.; Monge, M. E.; D'Anna, B.; George, C.; Styler, S. A.; Huthwelker, T.; Ammann, M. Increased Steady State Uptake of Ozone on Soot Due to UV/Vis Radiation. *J. Geophys. Res. Atmos.* **2011**, *116* (D11), D11301.
(74) Abbatt, J. P. D.; Waschewsky, G. C. G. Heterogeneous Interactions of HOBr, HNO3, O3, and NO2 with Deliquescent NaCl Aerosols at Room Temperature. *J. Phys. Chem. A* **1998**, *102* (21), 3719–3725.
(75) Sadanaga, Y.; Hirokawa, J.; Akimoto, H. Formation of Molecular Chlorine in Dark Condition: Heterogeneous Reaction of Ozone with Sea Salt in the Presence of Ferric Ion. *Geophys. Res. Lett.* **2001**, *28* (23), 4433–4436.
(76) Salazar, J. R.; Cartledge, B. T.; Haynes, J. P.; York-Marini, R.; Robinson, A. L.; Drozd, G. T.; Goldstein, A. H.; Fakra, S. C.; Majestic, B. J. Water-Soluble Iron Emitted from Vehicle Exhaust Is Linked to Primary Speciated Organic Compounds. *Atmos. Chem. Phys.* **2020**, *20* (3), 1849–1860.
(77) Marcotte, A. R.; Anbar, A. D.; Majestic, B. J.; Herckes, P. Mineral Dust and Iron Solubility: Effects of Composition, Particle Size, and Surface Area. *Atmos.* **2020**, *11* (5), 533.
(78) Chen, H.; Stanier, C. O.; Young, M. A.; Grassian, V. H. A Kinetic Study of Ozone Decomposition on Illuminated Oxide Surfaces. *J. Phys. Chem. A* **2011**, *115* (43), 11979–11987.
(79) Hoffmann, M. R.; Martin, S. T.; Choi, W.; Bahnemann, D. W. Environmental Applications of Semiconductor Photocatalysis. *Chem. Rev.* **1995**, *95* (1), 69–96.

(80) George, C.; D'Anna, B.; Herrmann, H.; Weller, C.; Vaida, V.; Donaldson, D. J.; Bartels-Rausch, T.; Ammann, M. Emerging Areas in Atmospheric Photochemistry. In *Atmospheric and Aerosol Chemistry*; Topics in Current Chemistry; Springer, Berlin, Heidelberg, 2012; pp 1–53.

(81) Jammoul, A.; Gligorovski, S.; George, C.; D'Anna, B. Photosensitized Heterogeneous Chemistry of Ozone on Organic Films. *J. Phys. Chem. A* **2008**, *112* (6), 1268–1276.

(82) Rubasinghege, G.; H. Grassian, V. Role(s) of Adsorbed Water in the Surface Chemistry of Environmental Interfaces. *Chem. Commun.* **2013**, *49* (30), 3071–3094.

(83) Chang, R. Y.-W.; Sullivan, R. C.; Abbatt, J. P. D. Initial Uptake of Ozone on Saharan Dust at Atmospheric Relative Humidities. *Geophys. Res. Lett.* **2005**, *32* (14), L14815.

(84) Abou-Ghanem, M.; Jensen, B. J. L.; Styler, S. A.; Romanias, M. N. Ozone Chemistry and Photochemistry at the Surface of Icelandic Volcanic Dust: Insights from Elemental Speciation Analysis. *Accepted. ACS Earth Space Chem.* **2021**.

(85) Pöschl, U.; Letzel, T.; Schauer, C.; Niessner, R. Interaction of Ozone and Water Vapor with Spark Discharge Soot Aerosol Particles Coated with Benzo[a]Pyrene: O3 and H2O Adsorption, Benzo[a]Pyrene Degradation, and Atmospheric Implications. *J. Phys. Chem. A* **2001**, *105* (16), 4029–4041.

(86) Redwood, P. S.; Lead, J. R.; Harrison, R. M.; Jones, I. P.; Stoll, S. Characterization of Humic Substances by Environmental Scanning Electron Microscopy. *Environ. Sci. Technol.* **2005**, *39* (7), 1962–1966.

(87) Tang, I. N.; Tridico, A. C.; Fung, K. H. Thermodynamic and Optical Properties of Sea Salt Aerosols. *J. Geophys. Res. Atmos.* **1997**, *102* (D19), 23269–23275.

(88) Palmonari, A.; Cavallini, D.; Sniffen, C. J.; Fernandes, L.; Holder, P.; Fagioli, L.; Fusaro, I.; Biagi, G.; Formigoni, A.; Mammi, L. Short Communication: Characterization of Molasses Chemical Composition. *J. Dairy Sci.* **2020**, *103* (7), 6244–6249.

(89) Chandra, R.; Bharagava, R. N.; Rai, V. Melanoidins as Major Colourant in Sugarcane Molasses Based Distillery Effluent and Its Degradation. *Bioresour. Technol.* **2008**, *99* (11), 4648–4660.

(90) Hodge, J. E. Dehydrated Foods, Chemistry of Browning Reactions in Model Systems. *J. Agric. Food Chem.* **1953**, *1* (15), 928–943.

(91) Peña, M.; Coca, M.; González, G.; Rioja, R.; García, M. T. Chemical Oxidation of Wastewater from Molasses Fermentation with Ozone. *Chemosphere* **2003**, *51* (9), 893–900.

(92) Shiraiwa, M.; Sosedova, Y.; Rouvière, A.; Yang, H.; Zhang, Y.; Abbatt, J. P. D.; Ammann, M.; Pöschl, U. The Role of Long-Lived Reactive Oxygen Intermediates in the Reaction of Ozone with Aerosol Particles. *Nat. Chem.* **2011**, *3* (4), 291–295.

(93) Liu, F.; Lakey, P. S. J.; Berkemeier, T.; Tong, H.; Kunert, A. T.; Meusel, H.; Cheng, Y.; Su, H.; Fröhlich-Nowoisky, J.; Lai, S.; Weller, M. G.; Shiraiwa, M.; Pöschl, U.; Kampf, C. J. Atmospheric Protein Chemistry Influenced by Anthropogenic Air Pollutants: Nitration and Oligomerization upon Exposure to Ozone and Nitrogen Dioxide. *Faraday Discuss.* **2017**, *200* (0), 413–427.

(94) Shiraiwa, M.; Selzle, K.; Yang, H.; Sosedova, Y.; Ammann, M.; Pöschl, U. Multiphase Chemical Kinetics of the Nitration of Aerosolized Protein by Ozone and Nitrogen Dioxide. *Environ. Sci. Technol.* **2012**, *46* (12), 6672–6680.

(95) Moise, T.; Rudich, Y. Reactive Uptake of Ozone by Aerosol-Associated Unsaturated Fatty Acids: Kinetics, Mechanism, and Products. *J. Phys. Chem. A* **2002**, *106* (27), 6469–6476.

(96) Eliason, T. L.; Aloisio, S.; Donaldson, D. J.; Cziczo, D. J.; Vaida, V. Processing of Unsaturated Organic Acid Films and Aerosols by Ozone. *Atmos. Environ.* **2003**, *37* (16), 2207–2219.

(97) Usher, C. R.; Michel, A. E.; Stec, D.; Grassian, V. H. Laboratory Studies of Ozone Uptake on Processed Mineral Dust. *Atmos. Environ.* **2003**, *37* (38), 5337–5347.

(98) Sakamoto, Y.; Enami, S.; Tonokura, K. Enhancement of Gaseous Iodine Emission by Aqueous Ferrous Ions during the Heterogeneous Reaction of Gaseous Ozone with Aqueous Iodide. *J. Phys. Chem. A* **2013**, *117* (14), 2980–2986.

(99) Jain, R.; Venkatasubramanian, P. Sugarcane Molasses – A Potential Dietary Supplement in the Management of Iron Deficiency Anemia. *J. Diet. Suppl.* **2017**, *14* (5), 589–598.

(100) Criegee, R. Mechanism of Ozonolysis. *Angew. Chem. Int. Ed. Engl.* **1975**, *14* (11), 745–752.

(101) Kroll, J. H.; Sahay, S. R.; Anderson, J. G.; Demerjian, K. L.; Donahue, N. M. Mechanism of HOx Formation in the Gas-Phase Ozone-Alkene Reaction. 2. Prompt versus Thermal Dissociation of Carbonyl Oxides to Form OH. *J. Phys. Chem. A* **2001**, *105* (18), 4446–4457.

(102) Kroll, J. H.; Donahue, N. M.; Cee, V. J.; Demerjian, K. L.; Anderson, J. G. Gas-Phase Ozonolysis of Alkenes: Formation of OH from Anti Carbonyl Oxides. *J. Am. Chem. Soc.* **2002**, *124* (29), 8518–8519.

(103) Siese, M.; Becker, K. H.; Brockmann, K. J.; Geiger, H.; Hofzumahaus, A.; Holland, F.; Mihelcic, D.; Wirtz, K. Direct Measurement of OH Radicals from Ozonolysis of Selected Alkenes: A EUPHORE Simulation Chamber Study. *Environ. Sci. Technol.* **2001**, *35* (23), 4660–4667.

(104) Knipping, E. M.; Dabdub, D. Modeling Cl2 Formation from Aqueous NaCl Particles: Evidence for Interfacial Reactions and Importance of Cl2 Decomposition in Alkaline Solution. *J. Geophys. Res. Atmos.* **2002**, *107* (D18), ACH 8-1-ACH 8-30.

(105) Faxon, C. B.; Dhulipala, S. V.; Allen, D. T.; Ruiz, L. H. Heterogeneous Production of Cl2 from Particulate Chloride: Effects of Composition and Relative Humidity. *AIChE J.* **2018**, *64* (8), 3151–3158.

(106) Li, M.; Su, H.; Li, G.; Ma, N.; Pöschl, U.; Cheng, Y. Relative Importance of Gas Uptake on Aerosol and Ground Surfaces Characterized by Equivalent Uptake Coefficients. *Atmos. Chem. Phys.* **2019**, *19* (16), 10981–11011.

(107) McNamara, S. M.; Kolesar, K. R.; Wang, S.; Kirpes, R. M.; May, N. W.; Gunsch, M. J.; Cook, R. D.; Fuentes, J. D.; Hornbrook, R. S.; Apel, E. C.; China, S.; Laskin, A.; Pratt, K. A. Observation of Road Salt Aerosol Driving Inland Wintertime Atmospheric Chlorine Chemistry. *ACS Cent. Sci.* **2020**, *6* (5), 684–694.

(108) Casotti Rienda, I.; Alves, C. A. Road Dust Resuspension: A Review. *Atmos. Res.* **2021**, *261*, 105740.

(109) Amato, F.; Pandolfi, M.; Escrig, A.; Querol, X.; Alastuey, A.; Pey, J.; Perez, N.; Hopke, P. K. Quantifying Road Dust Resuspension in Urban Environment by Multilinear Engine: A Comparison with PMF2. *Atmos. Environ.* **2009**, No. 43, 2770–2780.

(110) Wren, S. N.; Donaldson, D. J.; Abbatt, J. P. D. Photochemical Chlorine and Bromine Activation from Artificial Saline Snow. *Atmos. Chem. Phys.* **2013**, *13* (19), 9789–9800.

(111) Thornton, J. A.; Abbatt, J. P. D. N2O5 Reaction on Submicron Sea Salt Aerosol: Kinetics, Products, and the Effect of Surface Active Organics. *J. Phys. Chem. A* **2005**, *109* (44), 10004–10012.

(112) McNeill, V. F.; Patterson, J.; Wolfe, G. M.; Thornton, J. A. The Effect of Varying Levels of Surfactant on the Reactive Uptake of N_2O_5 to Aqueous Aerosol. *Atmos. Chem. Phys.* **2006**, *6* (6), 1635–1644.

(113) Ryder, O. S.; Campbell, N. R.; Shaloski, M.; Al-Mashat, H.; Nathanson, G. M.; Bertram, T. H. Role of Organics in Regulating ClNO2 Production at the Air–Sea Interface. *J. Phys. Chem. A* **2015**, *119* (31), 8519–8526.

(114) Feuer, H. *The Nitro Group in Organic Synthesis*, 1st ed.; John Wiley & Sons, Ltd, 2001.

(115) Stutz, J.; Alicke, B.; Ackermann, R.; Geyer, A.; White, A.; Williams, E. Vertical Profiles of NO3, N2O5, O3, and NOx in the Nocturnal Boundary Layer: 1. Observations during the Texas Air Quality Study 2000. *J. Geophys. Res. Atmos.* **2004**, *109* (D12).

(116) Slemr, F.; Seiler, W. Field Study of Environmental Variables Controlling the NO Emissions from Soil and the NO Compensation Point. *J. Geophys. Res. Atmos.* **1991**, *96* (D7), 13017–13031.

(117) Li, N.; Jiang, Q.; Wang, F.; Cui, P.; Xie, J.; Li, J.; Wu, S.; Barbieri, D. M. Comparative Assessment of Asphalt Volatile Organic Compounds Emission from Field to Laboratory. *J. Clean. Prod.* **2021**, *278*, 123479.

(118) Fay, L.; Shi, X. Environmental Impacts of Chemicals for Snow and Ice Control: State of the Knowledge. *Water. Air. Soil Pollut.* **2012**, *223* (5), 2751–2770.

(119) Herrmann, H.; Schaefer, T.; Tilgner, A.; Styler, S. A.; Weller, C.; Teich, M.; Otto, T. Tropospheric Aqueous-Phase Chemistry: Kinetics, Mechanisms, and Its Coupling to a Changing Gas Phase. *Chem. Rev.* **2015**, *115* (10), 4259–4334.

Chapter 5

Design and First Application of a Photochemical Aerosol Flow Tube Reactor to Explore the Influence of Atmospheric Aging on Dust Photochemistry

Contributions:
This manuscript was written by Maya Abou-Ghanem with critical comments from Dr. Sarah A. Styler.

5.1 Introduction

In this chapter, the design and construction of a custom-built photochemical aerosol flow tube is discussed. In addition, this chapter contains preliminary work on the photochemical uptake of ozone by organic-coated commercial TiO_2 aerosol, which I use as a simple photoactive model system for aged mineral dust. I note that the use of commercial TiO_2 cannot provide quantitative uptake coefficient values suitable for inclusion in atmospheric models, as I have shown in Chapter 2 of this thesis that the photoreactivity of commercial TiO_2 is larger than that of natural Ti-containing minerals. Instead, the goal of this final thesis chapter is to explore the influence of organic viscosity and coating thickness on the photochemistry of semi-conducting materials relevant to mineral dust,[1] which can provide insight on the chemical evolution of mineral dust photochemistry during atmospheric transport.

To date, the influence of organic aging on the heterogenous chemistry of dust has only been investigated in a few studies. For example, Usher and colleagues demonstrated that functionalization of SiO_2 particles with C_8-alkanes and alkenes can suppress and enhance the uptake of ozone, respectively.[2] Similarly, Coates Fuentes used a coated-wall flow tube to show that ozone uptake by kaolinite increases by nearly two orders of magnitude in the presence of monoterpene coatings.[3] However, both of these studies investigated ozone uptake under dark conditions, which limits our ability to understand the influence of these coatings on dust photochemistry. To my best knowledge, this work is the first to investigate the influence of organic coatings on mineral dust photochemistry.

5.2 Experimental

5.2.1 Photochemical aerosol flow tube reactor

The custom-built aerosol flow tube photochemical reactor (Figure 5.1) is constructed of Pyrex 7740 (120 cm length, 4 cm i.d) and vertically mounted in a black plastic box surrounded by eight UV-A lamps (21625 F15T8/BLB, Sylvania; 300–410 nm, λ_{max}: 356 nm). The flow tube is equipped with a water jacket layer connected to a recirculating chiller (RTE-140, Neslab),

which is used to control the temperature inside the reactor. A biocide (chloriamine-T) was added to the chiller water to prevent any microbial growth that could absorb UV radiation inside the water jacket layer. The absorbance of the chiller water was monitored often to ensure that its spectrum in the UV-A region was similar to that of deionized water.

Dry, purified air generated from a commercial zero air generator (747-30 reactor type A, Aadco Instruments) was used for all experiments. Ozone was produced by a UV ozone generator (97-0066-01, UVP) and measured at the exit of the aerosol flow tube using a photometric ozone analyzer (T400, Teledyne). An analogue-to-digital converter (U6, LabJack) was connected to the ozone analyzer to collect ozone mixing ratio data (at 5 s intervals) using a custom-built LabVIEW program. The aerosol flow tube set-up consists of three MFC's (MC-2SLPM-D/5M, Alicat), which control the flow of ozone in dry air (100 sccm), dry air (300 sscm), and dry air through a nebulizer (1000 sccm). The ozone and dry air flow were combined and introduced into the flow tube through a ¼ inch stainless steel movable injector.

A Laskin nebulizer[4] was used to aerosolize a TiO_2 and deionized water mixture, which was continuously stirred with a Teflon-coated stir bar. After, the generated TiO_2 aerosol was passed through a silica bead diffusion drier to remove any water vapor prior to entering a coating apparatus containing an organic coating material of choice (*i.e.*, eicosane or decylcyclohexane; selected for their environmental relevance in diesel exhaust emissions[5] and minimal reactivity with ozone[6]). The coating apparatus was placed in a water bath, the temperature of which was varied from 23–75°C to increase the volatilization of the organic species, and ultimately the coating thickness. At the exit of the aerosol flow tube, organic-coated TiO_2 aerosol were neutralized by a soft X-ray charger (XRC-05, HCT) prior to obtaining their particle size and number using a scanning electrical mobility spectrometer ([SEMS]; Brechtel). In all experiments, the aerosol flow tube reactor was operated under ambient temperature and pressure.

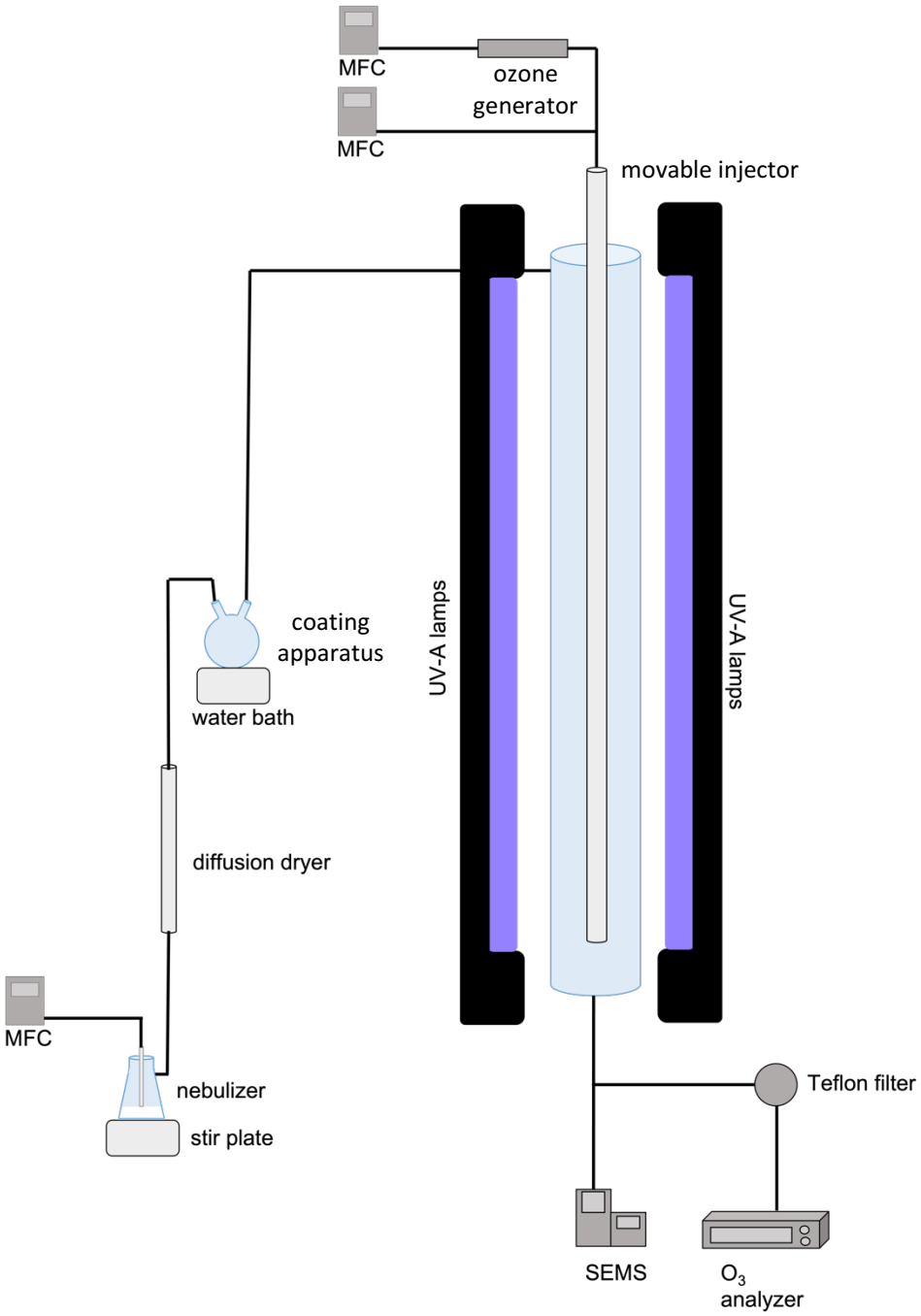

Figure 5.1: Schematic of the photochemical aerosol flow tube reactor.

5.2.2 Experimental protocol

At the beginning of each experiment, the gas flow through the nebulizer was by-passed and 70 mg of eicosane or 0.5 mL of decylcyclohexane was transferred to the coating apparatus. During this time, the movable injector was fully retracted, and the ozone generator was turned on until a stable ozone signal was reached (~45 min). Afterward, the dry air flow was directed through the nebulizer and the water bath temperature was adjusted to 23°C. Then, ozone was exposed to organic-coated TiO_2 for 30 min in the dark followed by 30 min in the light. This exposure procedure was repeated with the water bath held at 50°C and 75°C. Finally, ozone uptake by uncoated TiO_2 was used as an experimental control. Ozone mixing ratios were averaged over the last 2 min in the dark, light, and in the absence of TiO_2 aerosol, which are used in the calculations described below.

5.2.3 Data analysis

To quantify the photochemical uptake of ozone by TiO_2, we calculate a steady-state pseudo-first-order rate constant (k_{obs}) for ozone loss using the following equation:

$$k_{obs} = \frac{ln\left(\frac{[O_3]_t}{[O_3]_0}\right)}{-t} \qquad 5.1$$

Here, $[O_3]_t$ is the average steady-state ozone mixing ratio (ppb) at the exit of the flow tube under illuminated conditions, $[O_3]_0$ is the average steady-state ozone mixing ratio (ppb) in the absence of TiO_2 aerosol under dark conditions, and t is the residence time of ozone in the flow tube (s).

The obtained k_{obs} value can be used to calculate an uptake coefficient (γ) using the following equation:[7]

5.2

$$\gamma = \frac{4k_{obs}}{< c > S_a}$$

Here $< c >$ is the mean molecular speed of ozone (cm s^{-1}) and S_a is the total surface area of TiO_2 particles per unit volume (cm^2 cm^{-3}), as determined by SEMS using spherical particle assumptions.

5.3 Results and discussion

5.3.1 Particle size distribution determined by SEMS

The particle size distribution of TiO_2 aerosol was determining using a SEMS, which uses a DMA to classify charged particles based on their electrical mobility and a condensation particle counter (CPC) to count the number of particles for a select size bin. As shown in Figure 5.3, an increase in the total particle number was observed during periods of illumination, which suggests effects from thermophoresis.[10] Here, a temperature gradient formed inside the flow tube by the cooler wall temperatures generated by the recirculating chiller (20°C) can lead to greater migration of TiO_2 toward the walls under dark conditions and suggests that the temperature of the walls slowly increased during illumination periods, despite use of the chiller. To obtain constant TiO_2 aerosol loadings throughout the experiment and reduce wall loss effects, the chiller water temperature was increased from 20 to 30°C, which was successful at reducing thermophoresis effects, as shown by the stable TiO_2 aerosol loadings presented in Figure 5.3. Finally, generated TiO_2 aerosol appear to display a bimodal size distribution of ~700 and 1500 nm diameter particles, which may be a result of multiply charged particles that can be corrected for in future work.

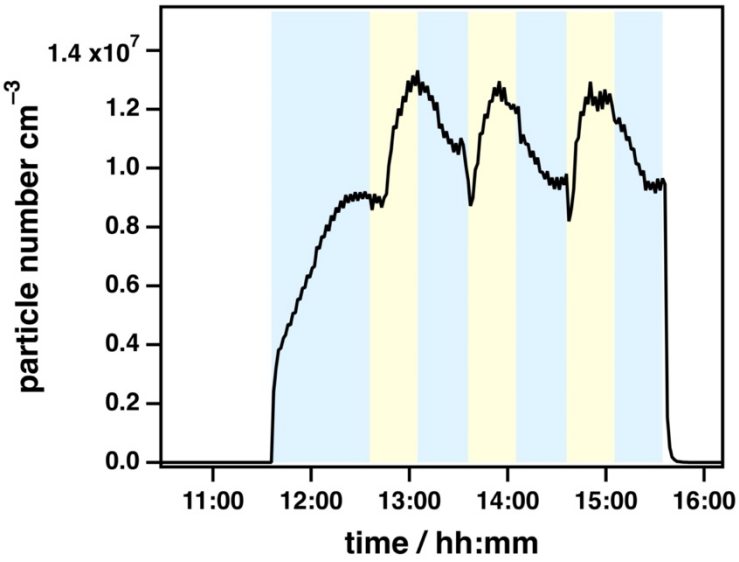

Figure 5.2: Total number of TiO_2 particles as a function of time. The blue and yellow shaded regions indicate periods under dark and illuminated conditions.

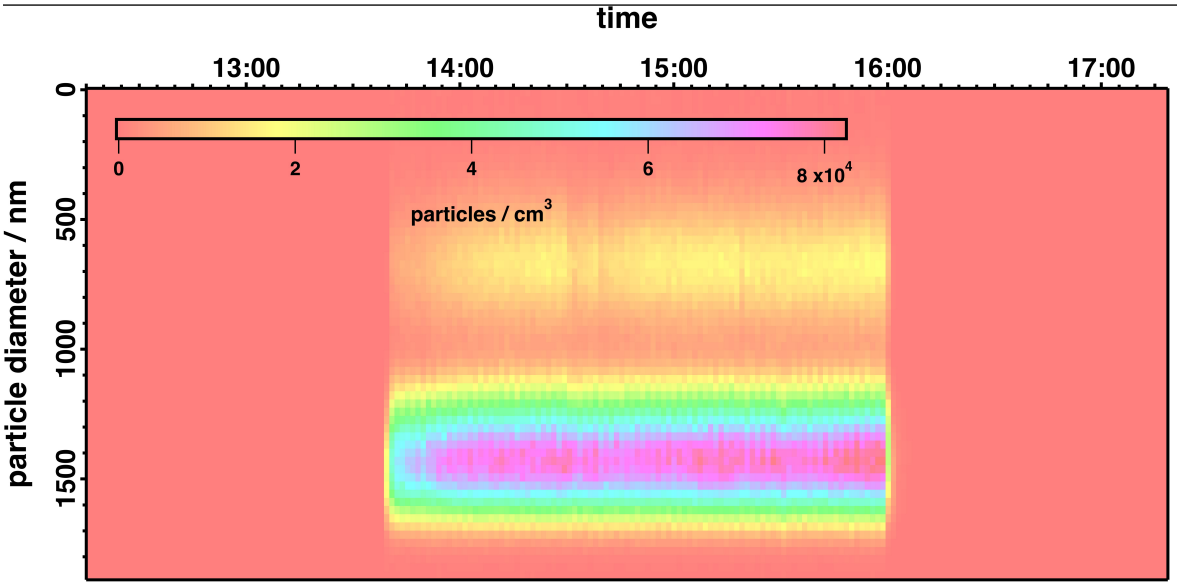

Figure 5.3: Size distribution of uncoated TiO_2 aerosol detected at the exit of the aerosol flow tube, as determined using SEMS.

5.3.2 Reaction profile of ozone with TiO_2

As shown in Figure 5.2, the ozone mixing ratio under illuminated conditions decreases upon exposure to TiO_2 aerosol, which has previously been demonstrated in laboratory studies.[8,9] This decrease in ozone mixing ratio returns back to its original value after the UV-A lamps are turned off. Finally, the loss of ozone appears to decrease slightly with increasing coating apparatus temperature, which may be a result of cross-contamination from organic material used in the alkane-coated TiO_2 experiments.

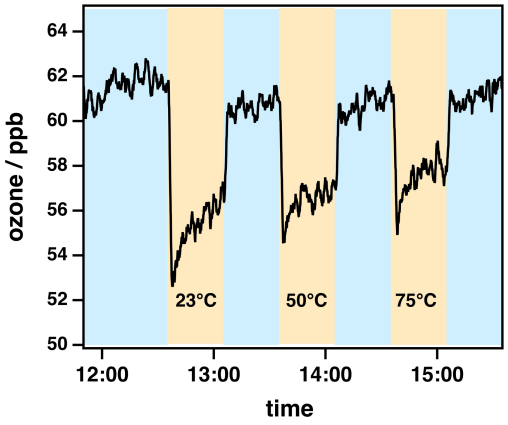

Figure 5.4: Reaction profile of ozone with uncoated TiO_2 as a function of coating apparatus temperature. The blue and yellow shaded regions indicate time periods of ozone interaction with TiO_2 under dark and light conditions, respectively.

5.3.3 Suppression of the photochemical uptake of ozone by organic-coated TiO_2

As demonstrated in Figure 5.5, the obtained photochemical uptake coefficients for ozone at 23°C are similar for uncoated and organic-coated TiO_2. These results are likely attributed to inefficient volatilization of organic material at lower temperatures; however, as the coating apparatus temperature is increased, the uptake of ozone decreases for organic-coated TiO_2, which suggests that alkane coatings can limit the diffusion of ozone to the photoactive TiO_2 surface. These results agree those obtained by Usher and coworkers, who observed a decrease in ozone uptake by C_8-alkane functionalized SiO_2 compared to untreated SiO_2 under dark conditions.[2] Finally, photoenhanced ozone uptake is most suppressed with decylcyclohexane-

coated TiO_2 (Figure 5.5) and is likely attributed to its higher vapor pressure, which can lead to the generation of thicker coatings.

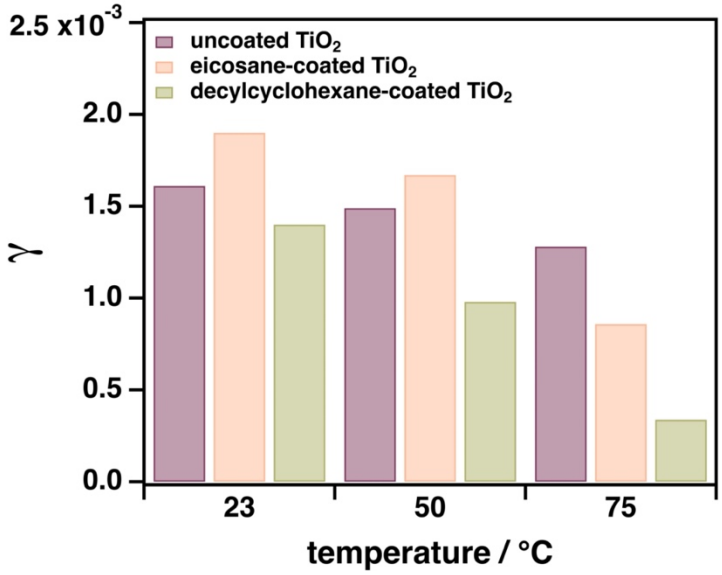

Figure 5.5: Uptake coefficients (γ) determined for uncoated, eicosane-coated, and decylcyclohexane-coated TiO_2 as a function of coating apparatus temperature.

5.4 Conclusions and future work

This work provides first evidence for the photochemical suppression of TiO_2 aerosol photochemistry by alkane coatings. Moving forward, this may require researchers to consider the implications of organic aging on the inherent photochemistry of atmospheric dust. The next steps for this project will include the transformation of preliminary data to more quantitative data through the following considerations and applications:

- Consideration for TiO_2 wall loss effects in the uptake coefficient calculations, which are evident due to the observed loss of ozone in the absence of TiO_2 aerosol during periods of illumination
- The addition of an in-line radioactive particle neutralizer prior to the aerosol flow tube to apply a known charge distribution to reduce TiO_2 particle wall loss[11]

- The replacement of the water bath for a more accurate temperature-controlled coating apparatus, which I recently constructed with the help of the Department of Chemistry machine shop (Figure 5.6)
- Approximate determination of organic coating thickness by analyzing SEMS data for size distribution changes between organic-coated and uncoated TiO_2 aerosol

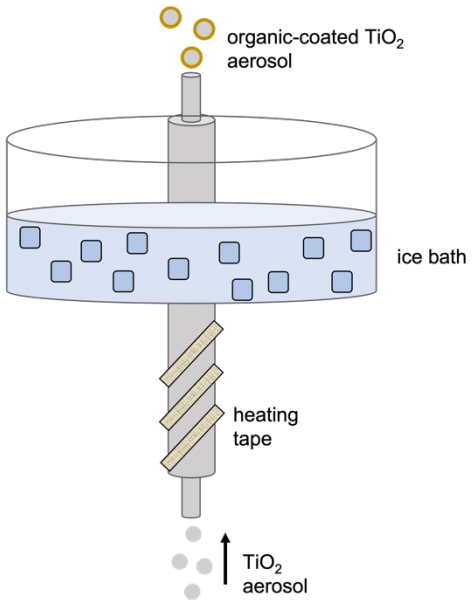

Figure 5.6: The custom-built coating apparatus to be employed in future experiments.

This project will also include the exploration of a shorter chain alkane (*i.e.*, heptadecane) coating in the future to determine which coating viscosities can suppress the diffusion of ozone to the photoactive TiO_2 surface. Finally, it would be of interest to also explore a hygroscopic coating to investigate the influence of RH on coating viscosity, and ultimately the photochemical uptake of ozone.

5.5 References

(1) Sakata, K.; Takahashi, Y.; Takano, S.; Matsuki, A.; Sakaguchi, A.; Tanimoto, H. First X-Ray Spectroscopic Observations of Atmospheric Titanium Species: Size Dependence and the Emission Source. *Environ. Sci. Technol.* **2021**, *55* (16), 10975–10986.

(2) Usher, C. R.; Michel, A. E.; Stec, D.; Grassian, V. H. Laboratory Studies of Ozone Uptake on Processed Mineral Dust. *Atmos. Environ.* **2003**, *37* (38), 5337–5347.

(3) Coates Fuentes, Z. L.; Kucinski, T. M.; Hinrichs, R. Z. Ozone Decomposition on Kaolinite as a Function of Monoterpene Exposure and Relative Humidity. *ACS Earth Space Chem.* **2018**, *2* (1), 21–30.

(4) Drew, R. T.; Bernstein, D. M.; Laskin, S. The Laskin Aerosol Generator. *J. Toxicol. Environ. Health* **1978**, *4* (4), 661–670.

(5) Alam, M. S.; Zeraati-Rezaei, S.; Liang, Z.; Stark, C.; Xu, H.; MacKenzie, A. R.; Harrison, R. M. Mapping and Quantifying Isomer Sets of Hydrocarbons (≥ C₁₂) in Diesel Exhaust, Lubricating Oil and Diesel Fuel Samples Using GC × GC-ToF-MS. *Atmospheric Meas. Tech.* **2018**, *11* (5), 3047–3058.

(6) Thomas, E. R.; Frost, G. J.; Rudich, Y. Reactive Uptake of Ozone by Proxies for Organic Aerosols: Surface-Bound and Gas-Phase Products. *J. Geophys. Res. Atmospheres* **2001**, *106* (D3), 3045–3056.

(7) Kolb, C. E.; Cox, R. A.; Abbatt, J. P. D.; Ammann, M.; Davis, E. J.; Donaldson, D. J.; Garrett, B. C.; George, C.; Griffiths, P. T.; Hanson, D. R.; Kulmala, M.; McFiggans, G.; Pöschl, U.; Riipinen, I.; Rossi, M. J.; Rudich, Y.; Wagner, P. E.; Winkler, P. M.; Worsnop, D. R.; O' Dowd, C. D. An Overview of Current Issues in the Uptake of Atmospheric Trace Gases by Aerosols and Clouds. *Atmospheric Chem. Phys.* **2010**, *10* (21), 10561–10605.

(8) Nicolas, M.; Ndour, M.; Ka, O.; D'Anna, B.; George, C. Photochemistry of Atmospheric Dust: Ozone Decomposition on Illuminated Titanium Dioxide. *Environ. Sci. Technol.* **2009**, *43* (19), 7437–7442.

(9) Abou-Ghanem, M.; Oliynyk, A. O.; Chen, Z.; Matchett, L. C.; McGrath, D. T.; Katz, M. J.; Locock, A. J.; Styler, S. A. Significant Variability in the Photocatalytic Activity of Natural Titanium-Containing Minerals: Implications for Understanding and Predicting Atmospheric Mineral Dust Photochemistry. *Environ. Sci. Technol.* **2020**, *54* (21), 13509–13516.

(10) Romay, F. J.; Takagaki, S. S.; Pui, D. Y. H.; Liu, B. Y. H. Thermophoretic Deposition of Aerosol Particles in Turbulent Pipe Flow. *J. Aerosol Sci.* **1998**, *29* (8), 943–959.

(11) Dyson, J. E.; Boustead, G. A.; Fleming, L. T.; Blitz, M.; Stone, D.; Arnold, S. R.; Whalley, L. K.; Heard, D. E. Production of HONO from NO_2 Uptake on Illuminated TiO_2 Aerosol Particles and Following the Illumination of Mixed TiO_2/ammonium Nitrate Particles. *Atmospheric Chem. Phys.* **2021**, *21* (7), 5755–5775.

Chapter 6

Conclusions and future directions

Contributions:
This manuscript was written by Maya Abou-Ghanem with critical comments from Dr. Sarah A. Styler.

6.1 Summary of thesis results

The work presented in this thesis advances our current understanding of dust heterogeneous chemistry by exploring the reactivity of more atmospherically relevant dust substrates. For example, in Chapter 2, I demonstrated that the photoreactivity of a suite of 10 natural Ti-containing minerals varies between and within mineral phases. In addition, I showed that the photoreactivity of commercial TiO_2 is orders of magnitude greater than that of naturally sourced TiO_2. Motivated by these results, in Chapter 3 I focused on the application of elemental speciation to infer about the photoactivity of Ti-rich volcanic dust from the Mýrdalssandur source region in Iceland. In this chapter, I highlighted that Ti is predominantly contained in the non-photoactive glass fraction of the volcanic dust sample, with lesser amounts in pyroxene, plagioclase, ilmenite, titanomagnetite, and olivine mineral phases, which explains its modest photoreactivity with ozone. Together, these chapters highlight that the elemental and mineralogical composition of natural dust cannot be used to accurately predict its atmospheric reactivity and consequently, its impacts on AQ.

In Chapter 4, I investigated the heterogeneous chemistry of urban road dust and anti-icer for the first time. Here, I demonstrated that ozone is 3–4× more reactive with road dust than desert dust and that road dust reactivity is likely driven by its organic components, which suggests that road dust should be considered as its own dust entity. Furthermore, I demonstrated the production of inorganic chlorine gas during ozone uptake by commercial anti-icer, which I proposed was driven by the reaction of chloride with OH radicals produced from ozone oxidation of organic compounds in the molasses fraction of anti-icer. Overall, this chapter demonstrates that road dust and winter road maintenance materials in high-latitude regions can influence urban AQ by serving as an atmospheric oxidant sink and source, respectively.

In Chapter 5, I presented the design and construction of a photochemical aerosol flow tube reactor used to investigate the influence of atmospheric aging on mineral dust photochemistry.

In this work, I showed that ozone uptake by TiO_2 is suppressed in the presence of organic coatings. These results suggest that atmospheric aging can influence the inherent photochemistry of mineral dust, which may require us to re-evaluate the AQ impacts of dust–pollutant interactions.

6.2 Future research directions

6.2.1 Heterogeneous chemistry of natural dust

Moving forward, it will become increasingly important to have a comprehensive understanding of dust heterogeneous chemistry, as low-latitude dust emissions are predicted to increase in future as a result of desertification from both climate change and land use change.[1] To accurately capture the AQ implications of these increasing emissions, it will be important to move away from using uptake coefficients obtained for mineral dust proxies in atmospheric models. Instead, uptake coefficients should be obtained from a wide range of dust source regions to include the unique elemental and mineralogical compositional factors responsible for each dust substrate reactivity.

High-latitude dust emissions are also expected to increase in the future due to increasing glacial retreat,[2] which leads to the exposure of fresh sediments that can be transported into the atmosphere by strong winds.[3] For example, recent glacial retreat in Ä'äy Chù Valley, Yukon, Canada has resulted in 24 hr average PM_{10} loadings of up 4000 μg m^{-3} during spring,[4] which is almost 100× greater than the World Health Organization AQ guidelines.[5] However, only the heterogeneous chemistry of Icelandic volcanic dust, which is rich in glass, has been explored to date.[6,7] This leads to major knowledge gaps in the reactivity of other high-latitude dusts, especially those that are not volcanic in origin. Not only should these dusts be investigated in heterogeneous chemistry laboratory studies, but high-latitude dust source regions also present unique opportunities for field work. For example, direct correlations between pollutant gas mixing ratios and dust events are easier to elucidate in these regions due to their relatively pristine atmospheric conditions.

6.2.2 Heterogeneous chemistry of anthropogenic dust

The contributions of non-exhaust emissions to traffic-related PM are also expected to increase in the future as countries move towards zero-emission vehicles.[8,9] Although the transition to net-zero fleet is aimed to reduce total vehicular PM emissions, the use of electric vehicles, which are heavier than conventional vehicles, can increase road abrasion and consequently, road dust resuspension.[10] As a result, the heterogeneous chemistry of non-exhaust PM will become increasingly important in the future. However, to date, the reactivity of this PM class has only been studied by our research group; for example, Matchett and coworkers investigated the heterogeneous uptake of ozone by ground brake pad material[11] and I explored the reactivity of road dust in Chapter 4 of this thesis. Therefore, future research should focus on the investigation of road dust interactions with different pollutant gases and from various urban locations to gain a more comprehensive understanding on the atmospheric reactivity of road dust. Finally, no studies have investigated the heterogeneous chemistry of industrial dust, which may have specific and local AQ implications based on both the location and type of industry.

6.2.3 Heterogeneous chemistry at the road surface

The results presented in Chapter 4 can also serve as motivation for future studies of chlorine activation during heterogeneous chemistry at the road surface. For example, online chemical ionization mass spectrometry (CIMS) could be used to identify and quantify halogen species emitted during ozone uptake by anti-icer. In addition, this technique could be used to compare the speciation and production rates of halogen gases released during ozone uptake by different types of commercially available anti-icer. Finally, chlorine activation at the road surface may not be limited to studies of pollutant gas uptake but also from interactions between individual components of road material. For example, TiO_2, which is commonly used in road marking paints[12] and as a road coating material for the photochemical removal of pollutant gases emitted from vehicular exhaust,[13–15] may also initiate the photochemical release of inorganic chlorine gas in the presence of anti-icer.[16]

6.2.4 Atmospheric aging implications on dust photochemistry

In Chapter 5, I presented preliminary results that suggest alkane coatings can suppress TiO_2 photochemistry with ozone. In future, more quantitative results can be achieved by the following: 1) considerations of both ozone and TiO_2 wall loss effects on the observed ozone mixing ratios at the exit of the flow tube, 2) generating more consistent organic coatings by using a custom-built temperature-controlled coating apparatus, 3) using SEMS data to estimate organic coating thicknesses by looking for changes in particle size distributions of uncoated and organic-coated TiO_2 aerosol, and 4) the addition of a radioactive particle neutralizer prior to the aerosol flow tube to reduce TiO_2 wall loss. In addition, experimental expansion of this project will include the exploration of shorter chain alkanes coatings (*i.e.*, heptadecane) to assess the coating viscosity required to shut-off TiO_2 heterogeneous photochemistry. Finally, a hygroscopic organic coating could be investigated to explore the influence of RH on TiO_2 photochemistry.

Aside from this work, future studies should also explore the photochemical uptake of ozone by organic-coated naturally sourced mineral dusts to obtain more atmospherically relevant uptake coefficients for ozone. In addition, it would be of interest to investigate the influence of organic coatings on the photochemical production of HONO during NO_2 uptake by TiO_2 and natural mineral dusts.[17,18] Suppression of HONO, which is an important precursor for the OH radical, may have important influences on the local oxidative capacity of the atmosphere.

6.2.5 Exploration of halogen activation by halide-rich dust

Future studies should also move towards exploring halogen activation during halide-rich dust–pollutant interactions. These substrates may include:

- Volcanic PM, which can be rich in chloride from in-plume processing with co-emitted halogen gases[19]
- Playas[20] or transoceanic mineral dust,[21] which are often found internally mixed with sea salt

- High-latitude road dust, which contains road salt[22,23]

Recently, studies have shown that the uptake of N_2O_5 by road salt[22] and playas dust[24] can lead to the production of $ClNO_2$ gas; however, other heterogeneous chemistry pathways may also result in halogen activation. For example, the formation of Br_2 and Cl_2 gas during ozone uptake by mixed soluble ferric and salt particles[25] has remained largely unexplored in the context of halide-rich dusts. This pathway may be especially important for atmospherically aged mineral dust, which undergo acidic processing by SO_2 gas that enhances ferric iron mobilization.[26]

Although chlorine activation was not observed for Edmonton road dust (see Chapter 4), the offline technique used to measure inorganic chlorine gas in this study may not be sensitive enough to detect the production of Cl_2 from this pathway; therefore, future work can include the use of more sensitive, mass spectrometry techniques (*e.g.*, CIMS) to measure halogen activation. The results from these studies can help identify potential sources for halogen gases and ultimately provide a better understanding of the oxidative capacity of the atmosphere.

6.3 References

(1) Woodward, S.; Roberts, D. L.; Betts, R. A. A Simulation of the Effect of Climate Change–Induced Desertification on Mineral Dust Aerosol. *Geophys. Res. Lett.* **2005**, *32* (18).

(2) Bliss, A.; Hock, R.; Radić, V. Global Response of Glacier Runoff to Twenty-First Century Climate Change. *J. Geophys. Res. Earth Surf.* **2014**, *119* (4), 717–730.

(3) Bullard, J. E.; Baddock, M.; Bradwell, T.; Crusius, J.; Darlington, E.; Gaiero, D.; Gassó, S.; Gisladottir, G.; Hodgkins, R.; McCulloch, R.; McKenna-Neuman, C.; Mockford, T.; Stewart, H.; Thorsteinsson, T. High-Latitude Dust in the Earth System. *Rev. Geophys.* **2016**, *54* (2), 447–485.

(4) Bachelder, J.; Cadieux, M.; Liu-Kang, C.; Lambert, P.; Filoche, A.; Galhardi, J. A.; Hadioui, M.; Chaput, A.; Bastien-Thibault, M.-P.; Wilkinson, K. J.; King, J.; Hayes, P. L. Chemical and Microphysical Properties of Wind-Blown Dust near an Actively Retreating Glacier in Yukon, Canada. *Aerosol Sci. Technol.* **2020**, *54* (1), 2–20.

(5) World Health Organization. Ambient (outdoor) air pollution https://www.who.int/news-room/fact-sheets/detail/ambient-(outdoor)-air-quality-and-health (accessed 2021 -10 -14).

(6) Urupina, D.; Lasne, J.; Romanias, M. N.; Thiery, V.; Dagsson-Waldhauserova, P.; Thevenet, F. Uptake and Surface Chemistry of SO2 on Natural Volcanic Dusts. *Atmos. Environ.* **2019**, *217*, 116942.

(7) Abou-Ghanem, M.; Jensen, B. J. L.; Styler, S. A.; Romanias, M. N. Accepted. Ozone Chemistry and Photochemistry at the Surface of Icelandic Volcanic Dust: Insights from Elemental Speciation Analysis. *ACS Earth Space Chem.* **2021**.

(8) Zero Emission Fleet vehicles For European Roll-out - TRIMIS - European Commission https://trimis.ec.europa.eu/project/zero-emission-fleet-vehicles-european-roll-out (accessed 2021 -09 -13).

(9) Canada, T. Building a green economy: Government of Canada to require 100% of car and passenger truck sales be zero-emission by 2035 in Canada https://www.canada.ca/en/transport-canada/news/2021/06/building-a-green-economy-government-of-canada-to-require-100-of-car-and-passenger-truck-sales-be-zero-emission-by-2035-in-canada.html (accessed 2021 -09 -13).

(10) Beddows, D. C. S.; Harrison, R. M. PM_{10} and $PM_{2.5}$ Emission Factors for Non-Exhaust Particles from Road Vehicles: Dependence upon Vehicle Mass and Implications for Battery Electric Vehicles. *Atmos. Environ.* **2021**, *244*, 117886.

(11) Matchett, L. C.; Abou-Ghanem, M.; Stix, K. A. R.; McGrath, D. T.; Styler, S. A. Accepted. Ozone Uptake by Commercial Brake Pads: Assessing the Potential Indirect Air Quality Impacts of Non-Exhaust Emissions. *Environ. Sci. Atmospheres* **2021**.

(12) Burghardt, T. E.; Pashkevich, A. Green Public Procurement Criteria for Road Marking Materials from Insiders' Perspective. *J. Clean. Prod.* **2021**, *298*, 126521.

(13) Toro, C.; Jobson, B. T.; Haselbach, L.; Shen, S.; Chung, S. H. Photoactive Roadways: Determination of CO, NO and VOC Uptake Coefficients and Photolabile Side Product Yields on TiO_2 Treated Asphalt and Concrete. *Atmos. Environ.* **2016**, *139*, 37–45.

(14) Xie, X.; Hao, C.; Huang, Y.; Huang, Z. Influence of TiO_2-Based Photocatalytic Coating Road on Traffic-Related NO_x Pollutants in Urban Street Canyon by CFD Modeling. *Sci. Total Environ.* **2020**, *724*, 138059.

(15) Fujishima, A.; Zhang, X.; Tryk, D. A. TiO_2 Photocatalysis and Related Surface Phenomena. *Surf. Sci. Rep.* **2008**, *63* (12), 515–582.

(16) Li, Y.; Nie, W.; Liu, Y.; Huang, D.; Xu, Z.; Peng, X.; George, C.; Yan, C.; Tham, Y. J.; Yu, C.; Xia, M.; Fu, X.; Wang, X.; Xue, L.; Wang, Z.; Xu, Z.; Chi, X.; Wang, T.; Ding, A. Photoinduced Production of Chlorine Molecules from Titanium Dioxide Surfaces Containing Chloride. *Environ. Sci. Technol. Lett.* **2020**, *7* (2), 70–75.

(17) Ndour, M.; D'Anna, B.; George, C.; Ka, O.; Balkanski, Y.; Kleffmann, J.; Stemmler, K.; Ammann, M. Photoenhanced Uptake of NO₂ on mineral dust: Laboratory experiments and model simulations. *Geophys. Res. Lett.* **2008**, *35* (5), L05812.

(18) Dyson, J. E.; Boustead, G. A.; Fleming, L. T.; Blitz, M.; Stone, D.; Arnold, S. R.; Whalley, L. K.; Heard, D. E. Production of HONO from NO_2 Uptake on Illuminated TiO_2 Aerosol Particles and Following the Illumination of Mixed TiO_2/ammonium Nitrate Particles. *Atmospheric Chem. Phys.* **2021**, *21* (7), 5755–5775.

(19) Ayris, P. M.; Delmelle, P.; Cimarelli, C.; Maters, E. C.; Suzuki, Y. J.; Dingwell, D. B. HCl Uptake by Volcanic Ash in the High Temperature Eruption Plume: Mechanistic Insights. *Geochim. Cosmochim. Acta* **2014**, *144*, 188–201.

(20) Buck, B. J.; King, J.; Etyemezian, V. Effects of Salt Mineralogy on Dust Emissions, Salton Sea, California. *Soil Sci. Soc. Am. J.* **2011**, *75* (5), 1971–1985.

(21) Groß, S.; Tesche, M.; Freudenthaler, V.; Toledano, C.; Wiegner, M.; Ansmann, A.; Althausen, D.; Seefeldner, M. Characterization of Saharan Dust, Marine Aerosols and Mixtures of Biomass-Burning Aerosols and Dust by Means of Multi-Wavelength Depolarization and Raman Lidar Measurements during SAMUM 2. *Tellus B Chem. Phys. Meteorol.* **2011**, *63* (4), 706–724.

(22) McNamara, S. M.; Kolesar, K. R.; Wang, S.; Kirpes, R. M.; May, N. W.; Gunsch, M. J.; Cook, R. D.; Fuentes, J. D.; Hornbrook, R. S.; Apel, E. C.; China, S.; Laskin, A.; Pratt, K. A. Observation of Road Salt Aerosol Driving Inland Wintertime Atmospheric Chlorine Chemistry. *ACS Cent. Sci.* **2020**, *6* (5), 684–694.

(23) Abou-Ghanem, M.; Nodeh-Farahani, D.; McGrath, D. T.; VandenBoer, T. C.; Styler, S. A. Submitted. Ozone Uptake and Halogen Activation by Road Dust and Anti-Icing Solution: Implications for Wintertime Air Quality in High-Latitude Urban Environments. *Environ. Sci. Process. Impacts* **2021**.

(24) Mitroo, D.; Gill, T. E.; Haas, S.; Pratt, K. A.; Gaston, C. J. $ClNO_2$ Production from N_2O_5 Uptake on Saline Playa Dusts: New Insights into Potential Inland Sources of $ClNO_2$. *Environ. Sci. Technol.* **2019**, *53* (13), 7442–7452.

(25) Sadanaga, Y.; Hirokawa, J.; Akimoto, H. Formation of Molecular Chlorine in Dark Condition: Heterogeneous Reaction of Ozone with Sea Salt in the Presence of Ferric Ion. *Geophys. Res. Lett.* **2001**, *28* (23), 4433–4436.

(26) Shi, Z.; Krom, M. D.; Bonneville, S.; Baker, A. R.; Bristow, C.; Drake, N.; Mann, G.; Carslaw, K.; McQuaid, J. B.; Jickells, T.; Benning, L. G. Influence of Chemical Weathering and Aging of Iron Oxides on the Potential Iron Solubility of Saharan Dust during Simulated Atmospheric Processing. *Glob. Biogeochem. Cycles* **2011**, *25* (2).

References

Chapter 1

(1) Huneeus, N.; Schulz, M.; Balkanski, Y.; Griesfeller, J.; Prospero, J.; Kinne, S.; Bauer, S.; Boucher, O.; Chin, M.; Dentener, F.; Diehl, T.; Easter, R.; Fillmore, D.; Ghan, S.; Ginoux, P.; Grini, A.; Horowitz, L.; Koch, D.; Krol, M. C.; Landing, W.; Liu, X.; Mahowald, N.; Miller, R.; Morcrette, J.-J.; Myhre, G.; Penner, J.; Perlwitz, J.; Stier, P.; Takemura, T.; Zender, C. S. Global Dust Model Intercomparison in AeroCom Phase I. *Atmospheric Chem. Phys.* **2011**, *11* (15), 7781–7816.
(2) Perry, K. D.; Cahill, T. A.; Eldred, R. A.; Dutcher, D. D.; Gill, T. E. Long-Range Transport of North African Dust to the Eastern United States. *J. Geophys. Res. Atmospheres* **1997**, *102* (D10), 11225–11238.
(3) Choobari, O. A.; Zawar-Reza, P.; Sturman, A. The Global Distribution of Mineral Dust and Its Impacts on the Climate System: A Review. *Atmospheric Res.* **2014**, *138*, 152–165.
(4) Betzer, P. R.; Carder, K. L.; Duce, R. A.; Merrill, J. T.; Tindale, N. W.; Uematsu, M.; Costello, D. K.; Young, R. W.; Feely, R. A.; Breland, J. A.; Bernstein, R. E.; Greco, A. M. Long–Range Transport of Giant Mineral Aerosol Particles. *Nature* **1988**, *336* (6199), 568–571.
(5) Jaenicke, R.; Schütz, L. Comprehensive Study of Physical and Chemical Properties of the Surface Aerosols in the Cape Verde Islands Region. *J. Geophys. Res. Oceans* **1978**, *83* (C7), 3585–3599.
(6) Cook, A. G.; Weinstein, P.; Centeno, J. A. Health Effects of Natural Dust: Role of Trace Elements and Compounds. *Biol. Trace Elem. Res.* **2005**, *103* (1), 001–016.
(7) Tang, M.; Huang, X.; Lu, K.; Ge, M.; Li, Y.; Cheng, P.; Zhu, T.; Ding, A.; Zhang, Y.; Gligorovski, S.; Song, W.; Ding, X.; Bi, X.; Wang, X. Heterogeneous Reactions of Mineral Dust Aerosol: Implications for Tropospheric Oxidation Capacity. *Atmospheric Chem. Phys.* **2017**, *17* (19), 11727–11777.
(8) Usher, C. R.; Michel, A. E.; Grassian, V. H. Reactions on Mineral Dust. *Chem. Rev.* **2003**, *103* (12), 4883–4940.
(9) Nan, Y.; Wang, Y. Observational Evidence for Direct Uptake of Ozone in China by Asian Dust in Springtime. *Atmos. Environ.* **2018**, *186*, 45–55.
(10) Sullivan, R. C.; Guazzotti, S. A.; Sodeman, D. A.; Prather, K. A. Direct Observations of the Atmospheric Processing of Asian Mineral Dust. *Atmospheric Chem. Phys.* **2007**, *7* (5), 1213–1236.
(11) Journet, E.; Balkanski, Y.; Harrison, S. P. A New Data Set of Soil Mineralogy for Dust-Cycle Modeling. *Atmospheric Chem. Phys.* **2014**, *14* (8), 3801–3816.
(12) Amato, F.; Pandolfi, M.; Moreno, T.; Furger, M.; Pey, J.; Alastuey, A.; Bukowiecki, N.; Prevot, A. S. H.; Baltensperger, U.; Querol, X. Sources and Variability of Inhalable Road Dust Particles in Three European Cities. *Atmos. Environ.* **2011**, *45* (37), 6777–6787.
(13) Haynes, W. M. *CRC Handbook of Chemistry and Physics*; CRC Press, 2016.

(14) Christiansen, E. H.; Hamblin, W. K. *Dynamic Earth: An Introduction to Physical Geology*; Jones & Bartlett Publishers, 2014.
(15) Nicol, A. *Physicochemical Methods of Mineral Analysis*; Springer Science & Business Media, 2012.
(16) Deer, W. A.; Howie, R. A.; Zussman, J. *An Introduction to the Rock-Forming Minerals*; Mineralogical Society, 2013.
(17) Hefferan, K.; O'Brien, J. *Earth Materials*; John Wiley & Sons, 2010.
(18) Bowles, J. F. W.; Howie, R. A.; Vaughan, D. J.; Zussman, J. *Rock-Forming Minerals*; Geological Society of London, 2011.
(19) Chang, L. L. Y.; Deer, W. A.; Howie, R. A.; Zussman, J. *Rock-Forming Minerals*; Geological Society of London, 1998.
(20) Tegen, I.; Fung, I. Modeling of Mineral Dust in the Atmosphere: Sources, Transport, and Optical Thickness. *J. Geophys. Res. Atmospheres* **1994**, *99* (D11), 22897–22914.
(21) Stokes, G. G. On the Effect of Internal Friction of Fluids on the Motion of Pendulums. *Trans. Camb. Philos. Soc.* **1850**, *9*, 8–106.
(22) Maring, H.; Savoie, D. L.; Izaguirre, M. A.; Custals, L.; Reid, J. S. Mineral Dust Aerosol Size Distribution Change during Atmospheric Transport. *J. Geophys. Res. Atmospheres* **2003**, *108* (D19).
(23) Ryder, C. L.; Highwood, E. J.; Lai, T. M.; Sodemann, H.; Marsham, J. H. Impact of Atmospheric Transport on the Evolution of Microphysical and Optical Properties of Saharan Dust. *Geophys. Res. Lett.* **2013**, *40* (10), 2433–2438.
(24) Denjean, C.; Cassola, F.; Mazzino, A.; Triquet, S.; Chevaillier, S.; Grand, N.; Bourrianne, T.; Momboisse, G.; Sellegri, K.; Schwarzenbock, A.; Freney, E.; Mallet, M.; Formenti, P. Size Distribution and Optical Properties of Mineral Dust Aerosols Transported in the Western Mediterranean. *Atmospheric Chem. Phys.* **2016**, *16* (2), 1081–1104.
(25) Does, M. van der; Knippertz, P.; Zschenderlein, P.; Harrison, R. G.; Stuut, J.-B. W. The Mysterious Long-Range Transport of Giant Mineral Dust Particles. *Sci. Adv.* **2018**, *4* (12), eaau2768.
(26) Glaccum, R. A.; Prospero, J. M. Saharan Aerosols over the Tropical North Atlantic — Mineralogy. *Mar. Geol.* **1980**, *37* (3), 295–321.
(27) Reid, J. S.; Jonsson, H. H.; Maring, H. B.; Smirnov, A.; Savoie, D. L.; Cliff, S. S.; Reid, E. A.; Livingston, J. M.; Meier, M. M.; Dubovik, O.; Tsay, S.-C. Comparison of Size and Morphological Measurements of Coarse Mode Dust Particles from Africa. *J. Geophys. Res. Atmospheres* **2003**, *108* (D19).
(28) Tsamalis, C.; Chédin, A.; Pelon, J.; Capelle, V. The Seasonal Vertical Distribution of the Saharan Air Layer and Its Modulation by the Wind. *Atmospheric Chem. Phys.* **2013**, *13* (22), 11235–11257.
(29) Jickells, T. D.; An, Z. S.; Andersen, K. K.; Baker, A. R.; Bergametti, G.; Brooks, N.; Cao, J. J.; Boyd, P. W.; Duce, R. A.; Hunter, K. A.; Kawahata, H.; Kubilay, N.; laRoche, J.; Liss, P. S.; Mahowald, N.; Prospero, J. M.; Ridgwell, A. J.; Tegen, I.; Torres, R. Global Iron

Connections Between Desert Dust, Ocean Biogeochemistry, and Climate. *Science* **2005**, *308* (5718), 67–71.
(30) Bristow, C. S.; Hudson-Edwards, K. A.; Chappell, A. Fertilizing the Amazon and Equatorial Atlantic with West African Dust. *Geophys. Res. Lett.* **2010**, *37* (14).
(31) Onishi, K.; Otani, S.; Yoshida, A.; Mu, H.; Kurozawa, Y. Adverse Health Effects of Asian Dust Particles and Heavy Metals in Japan. *Asia Pac. J. Public Health* **2015**, *27* (2), NP1719–NP1726.
(32) Liu, C.-M.; Young, C.-Y.; Lee, Y.-C. Influence of Asian Dust Storms on Air Quality in Taiwan. *Sci. Total Environ.* **2006**, *368* (2), 884–897.
(33) Kok, J. F.; Adebiyi, A. A.; Albani, S.; Balkanski, Y.; Checa-Garcia, R.; Chin, M.; Colarco, P. R.; Hamilton, D. S.; Huang, Y.; Ito, A.; Klose, M.; Li, L.; Mahowald, N. M.; Miller, R. L.; Obiso, V.; Pérez García-Pando, C.; Rocha-Lima, A.; Wan, J. S. Contribution of the World's Main Dust Source Regions to the Global Cycle of Desert Dust. *Atmospheric Chem. Phys.* **2021**, *21* (10), 8169–8193.
(34) NASA Worldview https://worldview.earthdata.nasa.gov (accessed 2021 -06 -23).
(35) Claquin, T.; Schulz, M.; Balkanski, Y. J. Modeling the Mineralogy of Atmospheric Dust Sources. *J. Geophys. Res. Atmospheres* **1999**, *104* (D18), 22243–22256.
(36) Formenti, P.; Schütz, L.; Balkanski, Y.; Desboeufs, K.; Ebert, M.; Kandler, K.; Petzold, A.; Scheuvens, D.; Weinbruch, S.; Zhang, D. Recent Progress in Understanding Physical and Chemical Properties of African and Asian Mineral Dust. *Atmospheric Chem. Phys.* **2011**, *11* (16), 8231–8256.
(37) Caquineau, S.; Gaudichet, A.; Gomes, L.; Legrand, M. Mineralogy of Saharan Dust Transported over Northwestern Tropical Atlantic Ocean in Relation to Source Regions. *J. Geophys. Res. Atmospheres* **2002**, *107* (D15), AAC 4-1-AAC 4-12.
(38) Caquineau, S.; Gaudichet, A.; Gomes, L.; Magonthier, M.-C.; Chatenet, B. Saharan Dust: Clay Ratio as a Relevant Tracer to Assess the Origin of Soil-Derived Aerosols. *Geophys. Res. Lett.* **1998**, *25* (7), 983–986.
(39) Muhs, D. R.; Prospero, J. M.; Baddock, M. C.; Gill, T. E. Identifying Sources of Aeolian Mineral Dust: Present and Past. In *Mineral Dust: A Key Player in the Earth System*; Knippertz, P., Stuut, J.-B. W., Eds.; Springer Netherlands: Dordrecht, 2014; pp 51–74.
(40) Bullard, J. E.; Baddock, M.; Bradwell, T.; Crusius, J.; Darlington, E.; Gaiero, D.; Gasso, S.; Gisladottir, G.; Hodgkins, R.; McCulloch, R.; McKenna-Neuman, C.; Mockford, T.; Stewart, H.; Thorsteinsson, T. High-Latitude Dust in the Earth System. *Rev. Geophys.* **2016**, *54* (2), 447–485.
(41) Zwaaftink, C. D. G.; Grythe, H.; Skov, H.; Stohl, A. Substantial Contribution of Northern High-Latitude Sources to Mineral Dust in the Arctic. *J. Geophys. Res. Atmospheres* **2016**, *121* (22), 13,678-13,697.
(42) Bullard, J. E. Contemporary Glacigenic Inputs to the Dust Cycle. *Earth Surf. Process. Landf.* **2013**, *38* (1), 71–89.
(43) McKenna Neuman, C. A Review of Aeolian Transport Processes in Cold Environments. *Prog. Phys. Geogr. Earth Environ.* **1993**, *17* (2), 137–155.

(44) Mckenna Neuman, C. Effects of Temperature and Humidity upon the Entrainment of Sedimentary Particles by Wind. *Bound.-Layer Meteorol.* **2003**, *108* (1), 61–89.
(45) Bachelder, J.; Cadieux, M.; Liu-Kang, C.; Lambert, P.; Filoche, A.; Galhardi, J. A.; Hadioui, M.; Chaput, A.; Bastien-Thibault, M.-P.; Wilkinson, K. J.; King, J.; Hayes, P. L. Chemical and Microphysical Properties of Wind-Blown Dust near an Actively Retreating Glacier in Yukon, Canada. *Aerosol Sci. Technol.* **2020**, *54* (1), 2–20.
(46) Gaiero, D. M.; Depetris, P. J.; Probst, J.-L.; Bidart, S. M.; Leleyter, L. The Signature of River- and Wind-Borne Materials Exported from Patagonia to the Southern Latitudes: A View from REEs and Implications for Paleoclimatic Interpretations. *Earth Planet. Sci. Lett.* **2004**, *219* (3), 357–376.
(47) Ramsperger, B.; Peinemann, N.; Stahr, K. Deposition Rates and Characteristics of Aeolian Dust in the Semi-Arid and Sub-Humid Regions of the Argentinean Pampa. *J. Arid Environ.* **1998**, *39* (3), 467–476.
(48) Friedman, I.; Long, W. Volcanic Glasses, Their Origins and Alteration Processes. *J. Non-Cryst. Solids* **1984**, *67* (1), 127–133.
(49) Baldo, C.; Formenti, P.; Nowak, S.; Chevaillier, S.; Cazaunau, M.; Pangui, E.; Di Biagio, C.; Doussin, J.-F.; Ignatyev, K.; Dagsson-Waldhauserova, P.; Arnalds, O.; MacKenzie, A. R.; Shi, Z. Distinct Chemical and Mineralogical Composition of Icelandic Dust Compared to Northern African and Asian Dust. *Atmospheric Chem. Phys.* **2020**, *20* (21), 13521–13539.
(50) Arnalds, O.; Gisladottir, F.; Sigurjonsson, H. Sandy Deserts of Iceland: An Overview. *J. Arid Environ.* **2001**, *47* (3), 359–371.
(51) Jeong, G. Y. Bulk and Single-Particle Mineralogy of Asian Dust and a Comparison with Its Source Soils. *J. Geophys. Res. Atmospheres* **2008**, *113* (D2).
(52) Shi, Z.; Krom, M. D.; Bonneville, S.; Baker, A. R.; Bristow, C.; Drake, N.; Mann, G.; Carslaw, K.; McQuaid, J. B.; Jickells, T.; Benning, L. G. Influence of Chemical Weathering and Aging of Iron Oxides on the Potential Iron Solubility of Saharan Dust during Simulated Atmospheric Processing. *Glob. Biogeochem. Cycles* **2011**, *25* (2).
(53) Hooper, J.; Marx, S. A Global Doubling of Dust Emissions during the Anthropocene? *Glob. Planet. Change* **2018**, *169*, 70–91.
(54) Tegen, I.; Fung, I. Contribution to the Atmospheric Mineral Aerosol Load from Land Surface Modification. *J. Geophys. Res. Atmospheres* **1995**, *100* (D9), 18707–18726.
(55) Chen, S.; Jiang, N.; Huang, J.; Zang, Z.; Guan, X.; Ma, X.; Luo, Y.; Li, J.; Zhang, X.; Zhang, Y. Estimations of Indirect and Direct Anthropogenic Dust Emission at the Global Scale. *Atmos. Environ.* **2019**, *200*, 50–60.
(56) Casotti Rienda, I.; Alves, C. A. Road Dust Resuspension: A Review. *Atmospheric Res.* **2021**, *261*, 105740.
(57) Csavina, J.; Field, J.; Taylor, M. P.; Gao, S.; Landázuri, A.; Betterton, E. A.; Sáez, A. E. A Review on the Importance of Metals and Metalloids in Atmospheric Dust and Aerosol from Mining Operations. *Sci. Total Environ.* **2012**, *433*, 58–73.
(58) Hiscox, A. L.; Miller, D. R.; Holmén, B. A.; Yang, W.; Wang, J. Near-Field Dust Exposure from Cotton Field Tilling and Harvesting. *J. Environ. Qual.* **2008**, *37* (2), 551–556.

(59) Wang, X.; Chow, J. C.; Kohl, S. D.; Percy, K. E.; Legge, A. H.; Watson, J. G. Characterization of PM2.5 and PM10 Fugitive Dust Source Profiles in the Athabasca Oil Sands Region. *J. Air Waste Manag. Assoc.* **2015**, *65* (12), 1421–1433.
(60) Flanagan, M. E.; Seixas, N.; Majar, M.; Camp, J.; Morgan, M. Silica Dust Exposures During Selected Construction Activities. *AIHA J.* **2003**, *64* (3), 319–328.
(61) Thorpe, A.; Harrison, R. M. Sources and Properties of Non-Exhaust Particulate Matter from Road Traffic: A Review. *Sci. Total Environ.* **2008**, *400* (1–3), 270–282.
(62) Kok, J. F.; Adebiyi, A. A.; Albani, S.; Balkanski, Y.; Checa-Garcia, R.; Chin, M.; Colarco, P. R.; Hamilton, D. S.; Huang, Y.; Ito, A.; Klose, M.; Leung, D. M.; Li, L.; Mahowald, N. M.; Miller, R. L.; Obiso, V.; Pérez García-Pando, C.; Rocha-Lima, A.; Wan, J. S.; Whicker, C. A. Improved Representation of the Global Dust Cycle Using Observational Constraints on Dust Properties and Abundance. *Atmospheric Chem. Phys.* **2021**, *21* (10), 8127–8167.
(63) Ginoux, P.; Prospero, J. M.; Gill, T. E.; Hsu, N. C.; Zhao, M. Global-Scale Attribution of Anthropogenic and Natural Dust Sources and Their Emission Rates Based on MODIS Deep Blue Aerosol Products. *Rev. Geophys.* **2012**, *50* (3).
(64) Wang, X.; Chow, J. C.; Kohl, S. D.; Yatavelli, L. N. R.; Percy, K. E.; Legge, A. H.; Watson, J. G. Wind Erosion Potential for Fugitive Dust Sources in the Athabasca Oil Sands Region. *Aeolian Res.* **2015**, *18*, 121–134.
(65) Brotons, J. M.; Díaz, A. R.; Sarría, F. A.; Serrato, F. B. Wind Erosion on Mining Waste in Southeast Spain. *Land Degrad. Dev.* **2010**, *21* (2), 196–209.
(66) Chakraborty, M. K.; Ahmad, M.; Singh, R. S.; Pal, D.; Bandopadhyay, C.; Chaulya, S. K. Determination of the Emission Rate from Various Opencast Mining Operations. *Environ. Model. Softw.* **2002**, *17* (5), 467–480.
(67) Al-Khashman, Omar. A. Heavy Metal Distribution in Dust, Street Dust and Soils from the Work Place in Karak Industrial Estate, Jordan. *Atmos. Environ.* **2004**, *38* (39), 6803–6812.
(68) Xu, G.; Chen, Y.; Eksteen, J.; Xu, J. Surfactant-Aided Coal Dust Suppression: A Review of Evaluation Methods and Influencing Factors. *Sci. Total Environ.* **2018**, *639*, 1060–1076.
(69) Parvej, S.; Naik, D. L.; Sajid, H. U.; Kiran, R.; Huang, Y.; Thanki, N. Fugitive Dust Suppression in Unpaved Roads: State of the Art Research Review. *Sustainability* **2021**, *13* (4), 2399.
(70) Wu, Z.; Zhang, X.; Wu, M. Mitigating Construction Dust Pollution: State of the Art and the Way Forward. *J. Clean. Prod.* **2016**, *112*, 1658–1666.
(71) Belton, D. N.; Taylor, K. C. Automobile Exhaust Emission Control by Catalysts. *Curr. Opin. Solid State Mater. Sci.* **1999**, *4* (1), 97–102.
(72) Kolesar, K. R.; Mattson, C. N.; Peterson, P. K.; May, N. W.; Prendergast, R. K.; Pratt, K. A. Increases in Wintertime PM2.5 Sodium and Chloride Linked to Snowfall and Road Salt Application. *Atmos. Environ.* **2018**, *177*, 195–202.
(73) Harrison, R. M.; Jones, A. M.; Gietl, J.; Yin, J.; Green, D. C. Estimation of the Contributions of Brake Dust, Tire Wear, and Resuspension to Nonexhaust Traffic Particles Derived from Atmospheric Measurements. *Environ. Sci. Technol.* **2012**, *46* (12), 6523–6529.

(74) Lin, C.-C.; Chen, S.-J.; Huang, K.-L.; Hwang, W.-I.; Chang-Chien, G.-P.; Lin, W.-Y. Characteristics of Metals in Nano/Ultrafine/Fine/Coarse Particles Collected Beside a Heavily Trafficked Road. *Environ. Sci. Technol.* **2005**, *39* (21), 8113–8122.
(75) Kupiainen, K. J.; Tervahattu, H.; Räisänen, M.; Mäkelä, T.; Aurela, M.; Hillamo, R. Size and Composition of Airborne Particles from Pavement Wear, Tires, and Traction Sanding. *Environ. Sci. Technol.* **2005**, *39* (3), 699–706.
(76) Equiza, M. A.; Calvo-Polanco, M.; Cirelli, D.; Señorans, J.; Wartenbe, M.; Saunders, C.; Zwiazek, J. J. Long-Term Impact of Road Salt (NaCl) on Soil and Urban Trees in Edmonton, Canada. *Urban For. Urban Green.* **2017**, *21*, 16–28.
(77) Khan, R. K.; Strand, M. A. Road Dust and Its Effect on Human Health: A Literature Review. *Epidemiol. Health* **2018**, *40*, e2018013.
(78) Shi, G.; Chen, Z.; Bi, C.; Wang, L.; Teng, J.; Li, Y.; Xu, S. A Comparative Study of Health Risk of Potentially Toxic Metals in Urban and Suburban Road Dust in the Most Populated City of China. *Atmos. Environ.* **2011**, *45* (3), 764–771.
(79) Yu, B.; Xie, X.; Ma, L. Q.; Kan, H.; Zhou, Q. Source, Distribution, and Health Risk Assessment of Polycyclic Aromatic Hydrocarbons in Urban Street Dust from Tianjin, China. *Environ. Sci. Pollut. Res.* **2014**, *21* (4), 2817–2825.
(80) Evangeliou, N.; Grythe, H.; Klimont, Z.; Heyes, C.; Eckhardt, S.; Lopez-Aparicio, S.; Stohl, A. Atmospheric Transport Is a Major Pathway of Microplastics to Remote Regions. *Nat. Commun.* **2020**, *11* (1), 3381.
(81) Brahney, J.; Mahowald, N.; Prank, M.; Cornwell, G.; Klimont, Z.; Matsui, H.; Prather, K. A. Constraining the Atmospheric Limb of the Plastic Cycle. *Proc. Natl. Acad. Sci.* **2021**, *118* (16).
(82) Rodríguez, S.; Alastuey, A.; Querol, X. A Review of Methods for Long Term in Situ Characterization of Aerosol Dust. *Aeolian Res.* **2012**, *6*, 55–74.
(83) Waza, A.; Schneiders, K.; May, J.; Rodríguez, S.; Epple, B.; Kandler, K. Field Comparison of Dry Deposition Samplers for Collection of Atmospheric Mineral Dust: Results from Single-Particle Characterization. *Atmospheric Meas. Tech.* **2019**, *12* (12), 6647–6665.
(84) Engelbrecht, J. P.; Moosmüller, H.; Pincock, S.; Jayanty, R. K. M.; Lersch, T.; Casuccio, G. Technical Note: Mineralogical, Chemical, Morphological, and Opticalinterrelationships of Mineral Dust Re-Suspensions. *Atmospheric Chem. Phys.* **2016**, *16* (17), 10809–10830.
(85) May, K. R. The Cascade Impactor: An Instrument for Sampling Coarse Aerosols. *J. Sci. Instrum.* **1945**, *22* (10), 187–195.
(86) Adachi, K.; Tainosho, Y. Characterization of Heavy Metal Particles Embedded in Tire Dust. *Environ. Int.* **2004**, *30* (8), 1009–1017.
(87) Falkovich, A. H.; Schkolnik, G.; Ganor, E.; Rudich, Y. Adsorption of Organic Compounds Pertinent to Urban Environments onto Mineral Dust Particles. *J. Geophys. Res. Atmospheres* **2004**, *109* (D2), D02208.

(88) Manno, E.; Varrica, D.; Dongarrà, G. Metal Distribution in Road Dust Samples Collected in an Urban Area Close to a Petrochemical Plant at Gela, Sicily. *Atmos. Environ.* **2006**, *40* (30), 5929–5941.
(89) Urupina, D.; Lasne, J.; Romanias, M. N.; Thiery, V.; Dagsson-Waldhauserova, P.; Thevenet, F. Uptake and Surface Chemistry of SO2 on Natural Volcanic Dusts. *Atmos. Environ.* **2019**, *217*, 116942.
(90) Ahmady-Birgani, H.; McQueen, K. G.; Mirnejad, H. Characteristics of Mineral Dust Impacting the Persian Gulf. *Aeolian Res.* **2018**, *30*, 11–19.
(91) Maters, E. C.; Delmelle, P.; Rossi, M. J.; Ayris, P. M. Reactive Uptake of Sulfur Dioxide and Ozone on Volcanic Glass and Ash at Ambient Temperature. *J. Geophys. Res. Atmospheres* **2017**, *122* (18), 10,077-10,088.
(92) Guieu, C.; Loÿe-Pilot, M.-D.; Ridame, C.; Thomas, C. Chemical Characterization of the Saharan Dust End-Member: Some Biogeochemical Implications for the Western Mediterranean Sea. *J. Geophys. Res. Atmospheres* **2002**, *107* (D15), ACH 5-1-ACH 5-11.
(93) Rajaram, B. S.; Suryawanshi, P. V.; Bhanarkar, A. D.; Rao, C. V. C. Heavy Metals Contamination in Road Dust in Delhi City, India. *Environ. Earth Sci.* **2014**, *72* (10), 3929–3938.
(94) Khairy, M. A.; Barakat, A. O.; Mostafa, A. R.; Wade, T. L. Multielement Determination by Flame Atomic Absorption of Road Dust Samples in Delta Region, Egypt. *Microchem. J.* **2011**, *97* (2), 234–242.
(95) Harris, D. C.; Lucy, C. A. *Quantitative Chemical Analysis*; W. H. Freeman, 2019.
(96) Cote, C. D.; Schneider, S. R.; Lyu, M.; Gao, S.; Gan, L.; Holod, A. J.; Chou, T. H. H.; Styler, S. A. Photochemical Production of Singlet Oxygen by Urban Road Dust. *Environ. Sci. Technol. Lett.* **2018**, *5* (2), 92–97.
(97) Styler, S. A.; Donaldson, D. J. Heterogeneous Photochemistry of Oxalic Acid on Mauritanian Sand and Icelandic Volcanic Ash. *Environ. Sci. Technol.* **2012**, *46* (16), 8756–8763.
(98) Margui, E.; Grieken, R. V. *X-Ray Fluorescence Spectrometry and Related Techniques: An Introduction*; Momentum Press, 2013.
(99) Beckhoff, B.; Kanngießer, B.; Langhoff, N.; Wedell, R.; Wolff, H. *Handbook of Practical X-Ray Fluorescence Analysis*; Springer Science & Business Media: Berlin Heidelberg, 2007.
(100) Formenti, P.; Rajot, J. L.; Desboeufs, K.; Caquineau, S.; Chevaillier, S.; Nava, S.; Gaudichet, A.; Journet, E.; Triquet, S.; Alfaro, S.; Chiari, M.; Haywood, J.; Coe, H.; Highwood, E. Regional Variability of the Composition of Mineral Dust from Western Africa: Results from the AMMA SOP0/DABEX and DODO Field Campaigns. *J. Geophys. Res. Atmospheres* **2008**, *113* (D23).
(101) Formenti, P.; Nava, S.; Prati, P.; Chevaillier, S.; Klaver, A.; Lafon, S.; Mazzei, F.; Calzolai, G.; Chiari, M. Self-Attenuation Artifacts and Correction Factors of Light Element Measurements by X-Ray Analysis: Implication for Mineral Dust Composition Studies. *J. Geophys. Res. Atmospheres* **2010**, *115* (D1).

(102) Formenti, P.; Elbert, W.; Maenhaut, W.; Haywood, J.; Andreae, M. O. Chemical Composition of Mineral Dust Aerosol during the Saharan Dust Experiment (SHADE) Airborne Campaign in the Cape Verde Region, September 2000. *J. Geophys. Res. Atmospheres* **2003**, *108* (D18).
(103) Zhang, R.; Han, Z.; Cheng, T.; Tao, J. Chemical Properties and Origin of Dust Aerosols in Beijing during Springtime. *Particuology* **2009**, *7* (1), 61–67.
(104) Faiz, Y.; Siddique, N.; Tufail, M. Pollution Level and Health Risk Assessment of Road Dust from an Expressway. *J. Environ. Sci. Health Part A* **2012**, *47* (6), 818–829.
(105) Guinn, V. P.; Wagner, C. D. Instrumental Neutron Activation Analysis. *Anal. Chem.* **1960**, *32* (3), 317–323.
(106) Abou-Ghanem, M.; Oliynyk, A. O.; Chen, Z.; Matchett, L. C.; McGrath, D. T.; Katz, M. J.; Locock, A. J.; Styler, S. A. Significant Variability in the Photocatalytic Activity of Natural Titanium-Containing Minerals: Implications for Understanding and Predicting Atmospheric Mineral Dust Photochemistry. *Environ. Sci. Technol.* **2020**, *54* (21), 13509–13516.
(107) Falkovich, A. H.; Ganor, E.; Levin, Z.; Formenti, P.; Rudich, Y. Chemical and Mineralogical Analysis of Individual Mineral Dust Particles. *J. Geophys. Res. Atmospheres* **2001**, *106* (D16), 18029–18036.
(108) Egerton, R. F. *Physical Principles of Electron Microscopy: An Introduction to TEM, SEM, and AEM*; Springer: Germany, 2016.
(109) Jabłońska, M.; Janeczek, J. Identification of Industrial Point Sources of Airborne Dust Particles in an Urban Environment by a Combined Mineralogical and Meteorological Analyses: A Case Study from the Upper Silesian Conurbation, Poland. *Atmospheric Pollut. Res.* **2019**, *10* (3), 980–988.
(110) Abou-Ghanem, M.; Jensen, B. J. L.; Styler, S. A.; Romanias, M. N. Accepted. Ozone Chemistry and Photochemistry at the Surface of Icelandic Volcanic Dust: Insights from Elemental Speciation Analysis. *ACS Earth Space Chem.* **2021**.
(111) Coz, E.; Gómez-Moreno, F. J.; Casuccio, G. S.; Artíñano, B. Variations on Morphology and Elemental Composition of Mineral Dust Particles from Local, Regional, and Long-Range Transport Meteorological Scenarios. *J. Geophys. Res. Atmospheres* **2010**, *115* (D12).
(112) Caggiano, R.; Fiore, S.; Lettino, A.; Macchiato, M.; Sabia, S.; Trippetta, S. PM2.5 Measurements in a Mediterranean Site: Two Typical Cases. *Atmospheric Res.* **2011**, *102* (1), 157–166.
(113) Pöschl, U.; Rudich, Y.; Ammann, M. Kinetic Model Framework for Aerosol and Cloud Surface Chemistry and Gas-Particle Interactions–Part 1: General Equations, Parameters, and Terminology. *Atmospheric Chem. Phys.* **2007**, *7* (23), 5989–6023.
(114) Goel, V.; Mishra, S. K.; Pal, P.; Ahlawat, A.; Vijayan, N.; Jain, S.; Sharma, C. Influence of Chemical Aging on Physico-Chemical Properties of Mineral Dust Particles: A Case Study of 2016 Dust Storms over Delhi. *Environ. Pollut.* **2020**, *267*, 115338.
(115) Huertas, J. I.; Huertas, M. E.; Solís, D. A. Characterization of Airborne Particles in an Open Pit Mining Region. *Sci. Total Environ.* **2012**, *423*, 39–46.

(116) Lin, H.; Zhu, X.; Feng, Q.; Guo, J.; Sun, X.; Liang, Y. Pollution, Sources, and Bonding Mechanism of Mercury in Street Dust of a Subtropical City, Southern China. *Hum. Ecol. Risk Assess. Int. J.* **2019**, *25* (1–2), 393–409.
(117) Heide, P. van der. *X-Ray Photoelectron Spectroscopy: An Introduction to Principles and Practices*; John Wiley & Sons: Hoboken, New Jersey, 2011.
(118) Chang, L. W. Neurotoxic Effects of Mercury—A Review. *Environ. Res.* **1977**, *14* (3), 329–373.
(119) Liu, Y.; Liu, G.; Yousaf, B.; Zhou, C.; Shen, X. Identification of the Featured-Element in Fine Road Dust of Cities with Coal Contamination by Geochemical Investigation and Isotopic Monitoring. *Environ. Int.* **2021**, *152*, 106499.
(120) Waseda, Y.; Matsubara, E.; Shinoda, K. *X-Ray Diffraction Crystallography: Introduction, Examples and Solved Problems*; Springer Science & Business Media: Germany, 2011.
(121) Fujiwara, F.; Rebagliati, R. J.; Dawidowski, L.; Gómez, D.; Polla, G.; Pereyra, V.; Smichowski, P. Spatial and Chemical Patterns of Size Fractionated Road Dust Collected in a Megacitiy. *Atmos. Environ.* **2011**, *45* (8), 1497–1505.
(122) Matchett, L. C.; Abou-Ghanem, M.; Stix, K. A. R.; McGrath, D. T.; Styler, S. A. Accepted. Ozone Uptake by Commercial Brake Pads: Assessing the Potential Indirect Air Quality Impacts of Non-Exhaust Emissions. *Environ. Sci. Atmospheres* **2021**.
(123) Rietveld, H. M. Line Profiles of Neutron Powder-Diffraction Peaks for Structure Refinement. *Acta Crystallogr.* **1967**, *22* (1), 151–152.
(124) Nowak, S.; Lafon, S.; Caquineau, S.; Journet, E.; Laurent, B. Quantitative Study of the Mineralogical Composition of Mineral Dust Aerosols by X-Ray Diffraction. *Talanta* **2018**, *186*, 133–139.
(125) Soleimani, Z.; Teymouri, P.; Darvishi Boloorani, A.; Mesdaghinia, A.; Middleton, N.; Griffin, D. W. An Overview of Bioaerosol Load and Health Impacts Associated with Dust Storms: A Focus on the Middle East. *Atmos. Environ.* **2020**, *223*, 117187.
(126) Hallar, A. G.; Chirokova, G.; McCubbin, I.; Painter, T. H.; Wiedinmyer, C.; Dodson, C. Atmospheric Bioaerosols Transported via Dust Storms in the Western United States. *Geophys. Res. Lett.* **2011**, *38* (17).
(127) Prospero, J. M.; Blades, E.; Mathison, G.; Naidu, R. Interhemispheric Transport of Viable Fungi and Bacteria from Africa to the Caribbean with Soil Dust. *Aerobiologia* **2005**, *21* (1), 1–19.
(128) Chen, P.-S.; Tsai, F. T.; Lin, C. K.; Yang, C.-Y.; Chan, C.-C.; Young, C.-Y.; Lee, C.-H. Ambient Influenza and Avian Influenza Virus during Dust Storm Days and Background Days. *Environ. Health Perspect.* **2010**, *118* (9), 1211–1216.
(129) Conen, F.; Morris, C. E.; Leifeld, J.; Yakutin, M. V.; Alewell, C. Biological Residues Define the Ice Nucleation Properties of Soil Dust. *Atmospheric Chem. Phys.* **2011**, *11* (18), 9643–9648.

(130) Jeon, E. M.; Kim, H. J.; Jung, K.; Kim, J. H.; Kim, M. Y.; Kim, Y. P.; Ka, J.-O. Impact of Asian Dust Events on Airborne Bacterial Community Assessed by Molecular Analyses. *Atmos. Environ.* **2011**, *45* (25), 4313–4321.
(131) Tang, K.; Huang, Z.; Huang, J.; Maki, T.; Zhang, S.; Shimizu, A.; Ma, X.; Shi, J.; Bi, J.; Zhou, T.; Wang, G.; Zhang, L. Characterization of Atmospheric Bioaerosols along the Transport Pathway of Asian Dust during the Dust-Bioaerosol 2016 Campaign. *Atmospheric Chem. Phys.* **2018**, *18* (10), 7131–7148.
(132) Bora, J.; Deka, P.; Bhuyan, P.; Sarma, K. P.; Hoque, R. R. Morphology and Mineralogy of Ambient Particulate Matter over Mid-Brahmaputra Valley: Application of SEM–EDX, XRD, and FTIR Techniques. *SN Appl. Sci.* **2021**, *3* (1), 137.
(133) Müller, K.; Lehmann, S.; van Pinxteren, D.; Gnauk, T.; Niedermeier, N.; Wiedensohler, A.; Herrmann, H. Particle Characterization at the Cape Verde Atmospheric Observatory during the 2007 RHaMBLe Intensive. *Atmospheric Chem. Phys.* **2010**, *10* (6), 2709–2721.
(134) Paris, R.; Desboeufs, K. V.; Formenti, P.; Nava, S.; Chou, C. Chemical Characterisation of Iron in Dust and Biomass Burning Aerosols during AMMA-SOP0/DABEX: Implication for Iron Solubility. *Atmospheric Chem. Phys.* **2010**, *10* (9), 4273–4282.
(135) Song, Y.-C.; Eom, H.-J.; Jung, H.-J.; Malek, M. A.; Kim, H. K.; Geng, H.; Ro, C.-U. Investigation of Aged Asian Dust Particles by the Combined Use of Quantitative ED-EPMA and ATR-FTIR Imaging. *Atmospheric Chem. Phys.* **2013**, *13* (6), 3463–3480.
(136) Abou-Ghanem, M.; Nodeh-Farahani, D.; McGrath, D. T.; VandenBoer, T. C.; Styler, S. A. Submitted. Ozone Uptake and Halogen Activation by Road Dust and Anti-Icing Solution: Implications for Wintertime Air Quality in High-Latitude Urban Environments. *Environ. Sci. Process. Impacts* **2021**.
(137) Lee, Y.-N.; Weber, R.; Ma, Y.; Orsini, D.; Maxwell-Meier, K.; Blake, D.; Meinardi, S.; Sachse, G.; Harward, C.; Chen, T.-Y.; Thornton, D.; Tu, F.-H.; Bandy, A. Airborne Measurement of Inorganic Ionic Components of Fine Aerosol Particles Using the Particle-into-Liquid Sampler Coupled to Ion Chromatography Technique during ACE-Asia and TRACE-P. *J. Geophys. Res. Atmospheres* **2003**, *108* (D23).
(138) Witham, C. S.; Oppenheimer, C.; Horwell, C. J. Volcanic Ash-Leachates: A Review and Recommendations for Sampling Methods. *J. Volcanol. Geotherm. Res.* **2005**, *141* (3), 299–326.
(139) Aryal, R.; Lee, B.-K.; Beecham, S.; Kandasamy, J.; Aryal, N.; Parajuli, K. Characterisation of Road Dust Organic Matter as a Function of Particle Size: A PARAFAC Approach. *Water. Air. Soil Pollut.* **2015**, *226* (2), 24.
(140) Laskina, O.; Young, M. A.; Kleiber, P. D.; Grassian, V. H. Infrared Extinction Spectroscopy and Micro-Raman Spectroscopy of Select Components of Mineral Dust Mixed with Organic Compounds. *J. Geophys. Res. Atmospheres* **2013**, *118* (12), 6593–6606.
(141) Youn, J.-S.; Kim, Y.-M.; Siddiqui, M. Z.; Watanabe, A.; Han, S.; Jeong, S.; Jung, Y.-W.; Jeon, K.-J. Quantification of Tire Wear Particles in Road Dust from Industrial and Residential Areas in Seoul, Korea. *Sci. Total Environ.* **2021**, *784*, 147177.

(142) Xu, J.; Bergin, M. H.; Greenwald, R.; Schauer, J. J.; Shafer, M. M.; Jaffrezo, J. L.; Aymoz, G. Aerosol Chemical, Physical, and Radiative Characteristics near a Desert Source Region of Northwest China during ACE-Asia. *J. Geophys. Res. Atmospheres* **2004**, *109* (D19).
(143) Froyd, K. D.; Murphy, D. M.; Brock, C. A.; Campuzano-Jost, P.; Dibb, J. E.; Jimenez, J.-L.; Kupc, A.; Middlebrook, A. M.; Schill, G. P.; Thornhill, K. L.; Williamson, C. J.; Wilson, J. C.; Ziemba, L. D. A New Method to Quantify Mineral Dust and Other Aerosol Species from Aircraft Platforms Using Single-Particle Mass Spectrometry. *Atmospheric Meas. Tech.* **2019**, *12* (11), 6209–6239.
(144) Lee, S.-H.; Murphy, D. M.; Thomson, D. S.; Middlebrook, A. M. Chemical Components of Single Particles Measured with Particle Analysis by Laser Mass Spectrometry (PALMS) during the Atlanta SuperSite Project: Focus on Organic/Sulfate, Lead, Soot, and Mineral Particles. *J. Geophys. Res. Atmospheres* **2002**, *107* (D1), AAC 1-1-AAC 1-13.
(145) Li, W.; Shao, L.; Zhang, D.; Ro, C.-U.; Hu, M.; Bi, X.; Geng, H.; Matsuki, A.; Niu, H.; Chen, J. A Review of Single Aerosol Particle Studies in the Atmosphere of East Asia: Morphology, Mixing State, Source, and Heterogeneous Reactions. *J. Clean. Prod.* **2016**, *112, Part 2*, 1330–1349.
(146) Dall'Osto, M.; Beddows, D. C. S.; McGillicuddy, E. J.; Esser-Gietl, J. K.; Harrison, R. M.; Wenger, J. C. On the Simultaneous Deployment of Two Single-Particle Mass Spectrometers Atan Urban Background and a Roadside Site during SAPUSS. *Atmospheric Chem. Phys.* **2016**, *16* (15), 9693–9710.
(147) Beddows, D. C. S.; Dall'Osto, M.; Olatunbosun, O. A.; Harrison, R. M. Detection of Brake Wear Aerosols by Aerosol Time-of-Flight Mass Spectrometry. *Atmos. Environ.* **2016**, *129*, 167–175.
(148) Dall'Osto, M.; Beddows, D. C. S.; Gietl, J. K.; Olatunbosun, O. A.; Yang, X.; Harrison, R. M. Characteristics of Tyre Dust in Polluted Air: Studies by Single Particle Mass Spectrometry (ATOFMS). *Atmos. Environ.* **2014**, *94*, 224–230.
(149) Möhler, O.; Benz, S.; Saathoff, H.; Schnaiter, M.; Wagner, R.; Schneider, J.; Walter, S.; Ebert, V.; Wagner, S. The Effect of Organic Coating on the Heterogeneous Ice Nucleation Efficiency of Mineral Dust Aerosols. *Environ. Res. Lett.* **2008**, *3* (2), 025007.
(150) Reitz, P.; Spindler, C.; Mentel, T. F.; Poulain, L.; Wex, H.; Mildenberger, K.; Niedermeier, D.; Hartmann, S.; Clauss, T.; Stratmann, F.; Sullivan, R. C.; DeMott, P. J.; Petters, M. D.; Sierau, B.; Schneider, J. Surface Modification of Mineral Dust Particles by Sulphuric Acid Processing: Implications for Ice Nucleation Abilities. *Atmospheric Chem. Phys.* **2011**, *11* (15), 7839–7858.
(151) Marsden, N. A.; Ullrich, R.; Möhler, O.; Eriksen Hammer, S.; Kandler, K.; Cui, Z.; Williams, P. I.; Flynn, M. J.; Liu, D.; Allan, J. D.; Coe, H. Mineralogy and Mixing State of North African Mineral Dust by Online Single-Particle Mass Spectrometry. *Atmospheric Chem. Phys.* **2019**, *19* (4), 2259–2281.
(152) Jayne, J. T.; Leard, D. C.; Zhang, X.; Davidovits, P.; Smith, K. A.; Kolb, C. E.; Worsnop, D. R. Development of an Aerosol Mass Spectrometer for Size and Composition Analysis of Submicron Particles. *Aerosol Sci. Technol.* **2000**, *33* (1–2), 49–70.

(153) Murphy, D. M.; Thomson, D. S. Laser Ionization Mass Spectroscopy of Single Aerosol Particles. *Aerosol Sci. Technol.* **1995**, *22* (3), 237–249.
(154) Gard, E.; Mayer, J. E.; Morrical, B. D.; Dienes, T.; Fergenson, D. P.; Prather, K. A. Real-Time Analysis of Individual Atmospheric Aerosol Particles: Design and Performance of a Portable ATOFMS. *Anal. Chem.* **1997**, *69* (20), 4083–4091.
(155) Dentener, F. J.; Carmichael, G. R.; Zhang, Y.; Lelieveld, J.; Crutzen, P. J. Role of Mineral Aerosol as a Reactive Surface in the Global Troposphere. *J. Geophys. Res. Atmospheres* **1996**, *101* (D17), 22869–22889.
(156) de Reus, M.; Dentener, F.; Thomas, A.; Borrmann, S.; Ström, J.; Lelieveld, J. Airborne Observations of Dust Aerosol over the North Atlantic Ocean during ACE 2: Indications for Heterogeneous Ozone Destruction. *J. Geophys. Res. Atmospheres* **2000**, *105* (D12), 15263–15275.
(157) Fairlie, T. D.; Jacob, D. J.; Dibb, J. E.; Alexander, B.; Avery, M. A.; van Donkelaar, A.; Zhang, L. Impact of Mineral Dust on Nitrate, Sulfate, and Ozone in Transpacific Asian Pollution Plumes. *Atmospheric Chem. Phys.* **2010**, *10* (8), 3999–4012.
(158) Umann, B.; Arnold, F.; Schaal, C.; Hanke, M.; Uecker, J.; Aufmhoff, H.; Balkanski, Y.; Dingenen, R. V. Interaction of Mineral Dust with Gas Phase Nitric Acid and Sulfur Dioxide during the MINATROC II Field Campaign: First Estimate of the Uptake Coefficient from Atmospheric Data. *J. Geophys. Res. Atmospheres* **2005**, *110* (D22).
(159) Matsumoto, J.; Takahashi, K.; Matsumi, Y.; Yabushita, A.; Shimizu, A.; Matsui, I.; Sugimoto, N. Scavenging of Pollutant Acid Substances by Asian Mineral Dust Particles. *Geophys. Res. Lett.* **2006**, *33* (7).
(160) Bonasoni, P.; Cristofanelli, P.; Calzolari, F.; Bonafè, U.; Evangelisti, F.; Stohl, A.; Zauli Sajani, S.; van Dingenen, R.; Colombo, T.; Balkanski, Y. Aerosol-Ozone Correlations during Dust Transport Episodes. *Atmospheric Chem. Phys.* **2004**, *4* (5), 1201–1215.
(161) Kandler, K.; Lieke, K.; Benker, N.; Emmel, C.; Küpper, M.; Müller-Ebert, D.; Ebert, M.; Scheuvens, D.; Schladitz, A.; Schütz, L.; Weinbruch, S. Electron Microscopy of Particles Collected at Praia, Cape Verde, during the Saharan Mineral Dust Experiment: Particle Chemistry, Shape, Mixing State and Complex Refractive Index. *Tellus B Chem. Phys. Meteorol.* **2011**, *63* (4), 475–496.
(162) Scarnato, B. V.; China, S.; Nielsen, K.; Mazzoleni, C. Perturbations of the Optical Properties of Mineral Dust Particles by Mixing with Black Carbon: A Numerical Simulation Study. *Atmospheric Chem. Phys.* **2015**, *15* (12), 6913–6928.
(163) Gibson, E. R.; Gierlus, K. M.; Hudson, P. K.; Grassian, V. H. Generation of Internally Mixed Insoluble and Soluble Aerosol Particles to Investigate the Impact of Atmospheric Aging and Heterogeneous Processing on the CCN Activity of Mineral Dust Aerosol. *Aerosol Sci. Technol.* **2007**, *41* (10), 914–924.
(164) Lederer, M. R.; Staniec, A. R.; Coates Fuentes, Z. L.; Van Ry, D. A.; Hinrichs, R. Z. Heterogeneous Reactions of Limonene on Mineral Dust: Impacts of Adsorbed Water and Nitric Acid. *J. Phys. Chem. A* **2016**, *120* (48), 9545–9556.

(165) Coates Fuentes, Z. L.; Kucinski, T. M.; Hinrichs, R. Z. Ozone Decomposition on Kaolinite as a Function of Monoterpene Exposure and Relative Humidity. *ACS Earth Space Chem.* **2018**, *2* (1), 21–30.
(166) Kameda, T.; Azumi, E.; Fukushima, A.; Tang, N.; Matsuki, A.; Kamiya, Y.; Toriba, A.; Hayakawa, K. Mineral Dust Aerosols Promote the Formation of Toxic Nitropolycyclic Aromatic Compounds. *Sci. Rep.* **2016**, *6*, 24427.
(167) Bian, H.; Zender, C. S. Mineral Dust and Global Tropospheric Chemistry: Relative Roles of Photolysis and Heterogeneous Uptake. *J. Geophys. Res. Atmospheres* **2003**, *108* (D21).
(168) Li, G.; Bei, N.; Tie, X.; Molina, L. T. Aerosol Effects on the Photochemistry in Mexico City during MCMA-2006/MILAGRO Campaign. *Atmospheric Chem. Phys.* **2011**, *11* (11), 5169–5182.
(169) McNamara, S. M.; Kolesar, K. R.; Wang, S.; Kirpes, R. M.; May, N. W.; Gunsch, M. J.; Cook, R. D.; Fuentes, J. D.; Hornbrook, R. S.; Apel, E. C.; China, S.; Laskin, A.; Pratt, K. A. Observation of Road Salt Aerosol Driving Inland Wintertime Atmospheric Chlorine Chemistry. *ACS Cent. Sci.* **2020**, *6* (5), 684–694.
(170) Schmidt, M.; Jansen van Beek, S. M.; Abou-Ghanem, M.; Oliynyk, A. O.; Locock, A. J.; Styler, S. A. Production of Atmospheric Organosulfates via Mineral-Mediated Photochemistry. *ACS Earth Space Chem.* **2019**, *3* (3), 424–431.
(171) Finlayson-Pitts, B. J.; Jr, J. N. P. *Chemistry of the Upper and Lower Atmosphere: Theory, Experiments, and Applications*; Academic Press, 1999.
(172) Mielke, L. H.; Furgeson, A.; Odame-Ankrah, C. A.; Osthoff, H. D. Ubiquity of ClNO2 in the Urban Boundary Layer of Calgary, Alberta, Canada. *Can. J. Chem.* **2015**, *94* (4), 414–423.
(173) Mielke, L. H.; Furgeson, A.; Osthoff, H. D. Observation of ClNO2 in a Mid-Continental Urban Environment. *Environ. Sci. Technol.* **2011**, *45* (20), 8889–8896.
(174) Ullerstam, M.; Johnson, M. S.; Vogt, R.; Ljungström, E. DRIFTS and Knudsen Cell Study of the Heterogeneous Reactivity of SO_2 and NO_2 on Mineral Dust. *Atmospheric Chem. Phys.* **2003**, *3* (6), 2043–2051.
(175) Underwood, G. M.; Song, C. H.; Phadnis, M.; Carmichael, G. R.; Grassian, V. H. Heterogeneous Reactions of NO_2 and HNO_3 on Oxides and Mineral Dust: A Combined Laboratory and Modeling Study. *J. Geophys. Res. Atmospheres* **2001**, *106* (D16), 18055–18066.
(176) J. Tang, M.; Thieser, J.; Schuster, G.; N. Crowley, J. Kinetics and Mechanism of the Heterogeneous Reaction of N_2O_5 with Mineral Dust Particles. *Phys. Chem. Chem. Phys.* **2012**, *14* (24), 8551–8561.
(177) Usher, C. R.; Al-Hosney, H.; Carlos-Cuellar, S.; Grassian, V. H. A Laboratory Study of the Heterogeneous Uptake and Oxidation of Sulfur Dioxide on Mineral Dust Particles. *J. Geophys. Res. Atmospheres* **2002**, *107* (D23), 4713.

(178) Sullivan, R. C.; Guazzotti, S. A.; Sodeman, D. A.; Tang, Y.; Carmichael, G. R.; Prather, K. A. Mineral Dust Is a Sink for Chlorine in the Marine Boundary Layer. *Atmos. Environ.* **2007**, *41* (34), 7166–7179.
(179) Koulouri, E.; Saarikoski, S.; Theodosi, C.; Markaki, Z.; Gerasopoulos, E.; Kouvarakis, G.; Mäkelä, T.; Hillamo, R.; Mihalopoulos, N. Chemical Composition and Sources of Fine and Coarse Aerosol Particles in the Eastern Mediterranean. *Atmos. Environ.* **2008**, *42* (26), 6542–6550.
(180) Collaud Coen, M.; Weingartner, E.; Schaub, D.; Hueglin, C.; Corrigan, C.; Henning, S.; Schwikowski, M.; Baltensperger, U. Saharan Dust Events at the Jungfraujoch: Detection by Wavelength Dependence of the Single Scattering Albedo and First Climatology Analysis. *Atmospheric Chem. Phys.* **2004**, *4* (11/12), 2465–2480.
(181) Aymoz, G.; Jaffrezo, J.-L.; Jacob, V.; Colomb, A.; George, C. Evolution of Organic and Inorganic Components of Aerosol during a Saharan Dust Episode Observed in the French Alps. *Atmospheric Chem. Phys.* **2004**, *4* (11/12), 2499–2512.
(182) Wang, Y.; Zhou, L.; Wang, W.; Ge, M. Heterogeneous Uptake of Formic Acid and Acetic Acid on Mineral Dust and Coal Fly Ash. *ACS Earth Space Chem.* **2020**, *4* (2), 202–210.
(183) Bates, T. S.; Quinn, P. K.; Coffman, D. J.; Covert, D. S.; Miller, T. L.; Johnson, J. E.; Carmichael, G. R.; Uno, I.; Guazzotti, S. A.; Sodeman, D. A.; Prather, K. A.; Rivera, M.; Russell, L. M.; Merrill, J. T. Marine Boundary Layer Dust and Pollutant Transport Associated with the Passage of a Frontal System over Eastern Asia. *J. Geophys. Res. Atmospheres* **2004**, *109* (D19).
(184) Groß, S.; Tesche, M.; Freudenthaler, V.; Toledano, C.; Wiegner, M.; Ansmann, A.; Althausen, D.; Seefeldner, M. Characterization of Saharan Dust, Marine Aerosols and Mixtures of Biomass-Burning Aerosols and Dust by Means of Multi-Wavelength Depolarization and Raman Lidar Measurements during SAMUM 2. *Tellus B Chem. Phys. Meteorol.* **2011**, *63* (4), 706–724.
(185) Smith, D. J.; Timonen, H. J.; Jaffe, D. A.; Griffin, D. W.; Birmele, M. N.; Perry, K. D.; Ward, P. D.; Roberts, M. S. Intercontinental Dispersal of Bacteria and Archaea by Transpacific Winds. *Appl. Environ. Microbiol.* **2013**, *79* (4), 1134–1139.
(186) Li, M.; Su, H.; Li, G.; Ma, N.; Pöschl, U.; Cheng, Y. Relative Importance of Gas Uptake on Aerosol and Ground Surfaces Characterized by Equivalent Uptake Coefficients. *Atmospheric Chem. Phys.* **2019**, *19* (16), 10981–11011.
(187) Wang, X.; Romanias, M. N.; Thévenet, F.; Rousseau, A. Geocatalytic Uptake of Ozone onto Natural Mineral Dust. *Catalysts* **2018**, *8* (7), 263.
(188) Ndour, M.; Nicolas, M.; D'Anna, B.; Ka, O.; George, C. Photoreactivity of NO 2 on Mineral Dusts Originating from Different Locations of the Sahara Desert. *Phys. Chem. Chem. Phys.* **2009**, *11* (9), 1312–1319.
(189) Hanisch, F.; Crowley, J. N. Ozone Decomposition on Saharan Dust: An Experimental Investigation. *Atmos Chem Phys* **2003**, *3* (1), 119–130.
(190) Chang, R. Y.-W.; Sullivan, R. C.; Abbatt, J. P. D. Initial Uptake of Ozone on Saharan Dust at Atmospheric Relative Humidities. *Geophys. Res. Lett.* **2005**, *32* (14).

(191) Adams, J. W.; Rodriguez, D.; Cox, R. A. The Uptake of SO2 on Saharan Dust: A Flow Tube Study. *Atmospheric Chem. Phys.* **2005**, *5* (10), 2679–2689.
(192) Ndour, M.; D'Anna, B.; George, C.; Ka, O.; Balkanski, Y.; Kleffmann, J.; Stemmler, K.; Ammann, M. Photoenhanced Uptake of NO_2 on Mineral Dust: Laboratory Experiments and Model Simulations. *Geophys. Res. Lett.* **2008**, *35* (5).
(193) Kolb, C. E.; Cox, R. A.; Abbatt, J. P. D.; Ammann, M.; Davis, E. J.; Donaldson, D. J.; Garrett, B. C.; George, C.; Griffiths, P. T.; Hanson, D. R.; Kulmala, M.; McFiggans, G.; Pöschl, U.; Riipinen, I.; Rossi, M. J.; Rudich, Y.; Wagner, P. E.; Winkler, P. M.; Worsnop, D. R.; O' Dowd, C. D. An Overview of Current Issues in the Uptake of Atmospheric Trace Gases by Aerosols and Clouds. *Atmospheric Chem. Phys.* **2010**, *10* (21), 10561–10605.
(194) Crowley, J. N.; Ammann, M.; Cox, R. A.; Hynes, R. G.; Jenkin, M. E.; Mellouki, A.; Rossi, M. J.; Troe, J.; Wallington, T. J. Evaluated Kinetic and Photochemical Data for Atmospheric Chemistry: Volume V – Heterogeneous Reactions on Solid Substrates. *Atmospheric Chem. Phys.* **2010**, *10* (18), 9059–9223.
(195) Golden, D. M.; Spokes, G. N.; Benson, S. W. Very Low-Pressure Pyrolysis (VLPP); A Versatile Kinetic Tool. *Angew. Chem. Int. Ed. Engl.* **1973**, *12* (7), 534–546.
(196) Michel A. E.; Usher C. R.; Grassian V. H. Heterogeneous and Catalytic Uptake of Ozone on Mineral Oxides and Dusts: A Knudsen Cell Investigation. *Geophys. Res. Lett.* **2002**, *29* (14), 10–11.
(197) Usher, C. R.; Michel, A. E.; Stec, D.; Grassian, V. H. Laboratory Studies of Ozone Uptake on Processed Mineral Dust. *Atmos. Environ.* **2003**, *37* (38), 5337–5347.
(198) Styler, S. A.; Donaldson, D. J. Photooxidation of Atmospheric Alcohols on Laboratory Proxies for Mineral Dust. *Environ. Sci. Technol.* **2011**, *45* (23), 10004–10012.
(199) Seisel, S.; Börensen, C.; Vogt, R.; Zellner, R. Kinetics and Mechanism of the Uptake of N_2O_5 on Mineral Dust at 298 K. *Atmospheric Chem. Phys.* **2005**, *5* (12), 3423–3432.
(200) Michel, A. E.; Usher, C. R.; Grassian, V. H. Reactive Uptake of Ozone on Mineral Oxides and Mineral Dusts. *Atmos. Environ.* **2003**, *37* (23), 3201–3211.
(201) Al-Hosney, H. A.; Carlos-Cuellar, S.; Baltrusaitis, J.; Grassian, V. H. Heterogeneous Uptake and Reactivity of Formic Acid on Calcium Carbonate Particles: A Knudsen Cell Reactor, FTIR and SEM Study. *Phys. Chem. Chem. Phys.* **2005**, *7* (20), 3587–3595.
(202) Lasne, J.; Romanias, M. N.; Thevenet, F. Ozone Uptake by Clay Dusts under Environmental Conditions. *ACS Earth Space Chem.* **2018**, *2* (9), 904–914.
(203) Bedjanian, Y.; Romanias, M. N.; El Zein, A. Interaction of OH Radicals with Arizona Test Dust: Uptake and Products. *J. Phys. Chem. A* **2013**, *117* (2), 393–400.
(204) Wang, X.; Romanias, M. N.; Pei, Z.; Rousseau, A.; Thévenet, F. Uptake Mechanism of Acetic Acid onto Natural Gobi Dust. *ACS Earth Space Chem.* **2020**, *4* (9), 1650–1662.
(205) Romanias, M. N.; Zeineddine, M. N.; Gaudion, V.; Lun, X.; Thevenet, F.; Riffault, V. Heterogeneous Interaction of Isopropanol with Natural Gobi Dust. *Environ. Sci. Technol.* **2016**, *50* (21), 11714–11722.

(206) Zeineddine, M. N.; Romanias, M. N.; Gaudion, V.; Riffault, V.; Thévenet, F. Heterogeneous Interaction of Isoprene with Natural Gobi Dust. *ACS Earth Space Chem.* **2017**, *1* (5), 236–243.
(207) Cooney, D. O.; Kim, S.-S.; James Davis, E. Analyses of Mass Transfer in Hemodialyzers for Laminar Blood Flow and Homogeneous Dialysate. *Chem. Eng. Sci.* **1974**, *29* (8), 1731–1738.
(208) Knopf, D. A.; Pöschl, U.; Shiraiwa, M. Radial Diffusion and Penetration of Gas Molecules and Aerosol Particles through Laminar Flow Reactors, Denuders, and Sampling Tubes. *Anal. Chem.* **2015**, *87* (7), 3746–3754.
(209) Wagner, C.; Hanisch, F.; Holmes, N.; de Coninck, H.; Schuster, G.; Crowley, J. N. The Interaction of N_2O_5 with Mineral Dust: Aerosol Flow Tube and Knudsen Reactor Studies. *Atmospheric Chem. Phys.* **2008**, *8* (1), 91–109.
(210) Dupart, Y.; Fine, L.; D'Anna, B.; George, C. Heterogeneous Uptake of NO2 on Arizona Test Dust under UV-A Irradiation: An Aerosol Flow Tube Study. *Aeolian Res.* **2014**, *15*, 45–51.
(211) Matthews, P. S. J.; Baeza-Romero, M. T.; Whalley, L. K.; Heard, D. E. Uptake of HO_2 Radicals onto Arizona Test Dust Particles Using an Aerosol Flow Tube. *Atmospheric Chem. Phys.* **2014**, *14* (14), 7397–7408.
(212) Sullivan, R. C.; Miñambres, L.; DeMott, P. J.; Prenni, A. J.; Carrico, C. M.; Levin, E. J. T.; Kreidenweis, S. M. Chemical Processing Does Not Always Impair Heterogeneous Ice Nucleation of Mineral Dust Particles. *Geophys. Res. Lett.* **2010**, *37* (24).
(213) Moon, D. R.; Taverna, G. S.; Anduix-Canto, C.; Ingham, T.; Chipperfield, M. P.; Seakins, P. W.; Baeza-Romero, M.-T.; Heard, D. E. Heterogeneous Reaction of HO_2 with Airborne TiO_2 Particles and Its Implication for Climate Change Mitigation Strategies. *Atmospheric Chem. Phys.* **2018**, *18* (1), 327–338.
(214) C. Sullivan, R.; K. Moore, M. J.; D. Petters, M.; M. Kreidenweis, S.; C. Roberts, G.; A. Prather, K. Timescale for Hygroscopic Conversion of Calcite Mineral Particles through Heterogeneous Reaction with Nitric Acid. *Phys. Chem. Chem. Phys.* **2009**, *11* (36), 7826–7837.
(215) Mogili, P. K.; Kleiber, P. D.; Young, M. A.; Grassian, V. H. N_2O_5 Hydrolysis on the Components of Mineral Dust and Sea Salt Aerosol: Comparison Study in an Environmental Aerosol Reaction Chamber. *Atmos. Environ.* **2006**, *40* (38), 7401–7408.
(216) Mogili, P. K.; Kleiber, P. D.; Young, M. A.; Grassian, V. H. Heterogeneous Uptake of Ozone on Reactive Components of Mineral Dust Aerosol: An Environmental Aerosol Reaction Chamber Study. *J. Phys. Chem. A* **2006**, *110* (51), 13799–13807.
(217) Chen, H.; Stanier, C. O.; Young, M. A.; Grassian, V. H. A Kinetic Study of Ozone Decomposition on Illuminated Oxide Surfaces. *J. Phys. Chem. A* **2011**, *115* (43), 11979–11987.
(218) Romanías, M. N.; Ourrad, H.; Thévenet, F.; Riffault, V. Investigating the Heterogeneous Interaction of VOCs with Natural Atmospheric Particles: Adsorption of

Limonene and Toluene on Saharan Mineral Dusts. *J. Phys. Chem. A* **2016**, *120* (8), 1197–1212.
(219) Börensen, C.; Kirchner, U.; Scheer, V.; Vogt, R.; Zellner, R. Mechanism and Kinetics of the Reactions of NO_2 or HNO_3 with Alumina as a Mineral Dust Model Compound. *J. Phys. Chem. A* **2000**, *104* (21), 5036–5045.
(220) Roscoe, J. M.; Abbatt, J. P. D. Diffuse Reflectance FTIR Study of the Interaction of Alumina Surfaces with Ozone and Water Vapor. *J. Phys. Chem. A* **2005**, *109* (40), 9028–9034.
(221) Armaroli, T.; Bécue, T.; Gautier, S. Diffuse Reflection Infrared Spectroscopy (Drifts): Application to the in Situ Analysis of Catalysts. *Oil Gas Sci. Technol.* **2004**, *59* (2), 215–237.
(222) Kortüm, G. *Reflectance Spectroscopy: Principles, Methods, Applications*; Springer Science & Business Media, 2012.
(223) Rubasinghege, G.; H. Grassian, V. Role(s) of Adsorbed Water in the Surface Chemistry of Environmental Interfaces. *Chem. Commun.* **2013**, *49* (30), 3071–3094.
(224) Newberg, J. T.; Starr, D. E.; Yamamoto, S.; Kaya, S.; Kendelewicz, T.; Mysak, E. R.; Porsgaard, S.; Salmeron, M. B.; Brown, G. E.; Nilsson, A.; Bluhm, H. Formation of Hydroxyl and Water Layers on MgO Films Studied with Ambient Pressure XPS. *Surf. Sci.* **2011**, *605* (1), 89–94.
(225) Ketteler, G.; Yamamoto, S.; Bluhm, H.; Andersson, K.; Starr, D. E.; Ogletree, D. F.; Ogasawara, H.; Nilsson, A.; Salmeron, M. The Nature of Water Nucleation Sites on TiO2(110) Surfaces Revealed by Ambient Pressure X-Ray Photoelectron Spectroscopy. *J. Phys. Chem. C* **2007**, *111* (23), 8278–8282.
(226) Joshi, N.; Romanias, M. N.; Riffault, V.; Thevenet, F. Investigating Water Adsorption onto Natural Mineral Dust Particles: Linking DRIFTS Experiments and BET Theory. *Aeolian Res.* **2017**, *27*, 35–45.
(227) Wang, L.; Wang, W.; Ge, M. Heterogeneous Uptake of NO_2 on Soils under Variable Temperature and Relative Humidity Conditions. *J. Environ. Sci.* **2012**, *24* (10), 1759–1766.
(228) Liu, Y.; Han, C.; Ma, J.; Bao, X.; He, H. Influence of Relative Humidity on Heterogeneous Kinetics of NO_2 on Kaolin and Hematite. *Phys. Chem. Chem. Phys.* **2015**, *17* (29), 19424–19431.
(229) D'Anna, B.; Jammoul, A.; George, C.; Stemmler, K.; Fahrni, S.; Ammann, M.; Wisthaler, A. Light-Induced Ozone Depletion by Humic Acid Films and Submicron Aerosol Particles. *J. Geophys. Res. Atmospheres* **2009**, *114* (D12), D12301.
(230) Abbatt, J. P. D.; Lee, A. K. Y.; Thornton, J. A. Quantifying Trace Gas Uptake to Tropospheric Aerosol: Recent Advances and Remaining Challenges. *Chem. Soc. Rev.* **2012**, *41* (19), 6555–6581.
(231) Aubin, D. G.; Abbatt, J. P. Adsorption of Gas-Phase Nitric Acid to n-Hexane Soot: Thermodynamics and Mechanism. *J. Phys. Chem. A* **2003**, *107* (50), 11030–11037.
(232) Aubin, D. G.; Abbatt, J. P. D. Interaction of NO_2 with Hydrocarbon Soot: Focus on HONO Yield, Surface Modification, and Mechanism. *J. Phys. Chem. A* **2007**, *111* (28), 6263–6273.

(233) Lelièvre, S.; Bedjanian, Y.; Pouvesle, N.; Delfau, J.-L.; Vovelle, C.; Bras, G. L. Heterogeneous Reaction of Ozone with Hydrocarbon Flame Soot. *Phys. Chem. Chem. Phys.* **2004**, *6* (6), 1181–1191.
(234) Underwood, G. M.; Li, P.; Usher, C. R.; Grassian, V. H. Determining Accurate Kinetic Parameters of Potentially Important Heterogeneous Atmospheric Reactions on Solid Particle Surfaces with a Knudsen Cell Reactor. *J. Phys. Chem. A* **2000**, *104* (4), 819–829.
(235) Park, J.; Jang, M.; Yu, Z. Heterogeneous Photo-Oxidation of SO_2 in the Presence of Two Different Mineral Dust Particles: Gobi and Arizona Dust. *Environ. Sci. Technol.* **2017**, *51* (17), 9605–9613.
(236) Di Biagio, C.; Formenti, P.; Balkanski, Y.; Caponi, L.; Cazaunau, M.; Pangui, E.; Journet, E.; Nowak, S.; Andreae, M. O.; Kandler, K.; Saeed, T.; Piketh, S.; Seibert, D.; Williams, E.; Doussin, J.-F. Complex Refractive Indices and Single-Scattering Albedo of Global Dust Aerosols in the Shortwave Spectrum and Relationship to Size and Iron Content. *Atmospheric Chem. Phys.* **2019**, *19* (24), 15503–15531.
(237) Wagner, C.; Schuster, G.; Crowley, J. N. An Aerosol Flow Tube Study of the Interaction of N_2O_5 with Calcite, Arizona Dust and Quartz. *Atmos. Environ.* **2009**, *43* (32), 5001–5008.
(238) Tang, M. J.; Camp, J. C. J.; Rkiouak, L.; McGregor, J.; Watson, I. M.; Cox, R. A.; Kalberer, M.; Ward, A. D.; Pope, F. D. Heterogeneous Interaction of SiO_2 with N_2O_5: Aerosol Flow Tube and Single Particle Optical Levitation–Raman Spectroscopy Studies. *J. Phys. Chem. A* **2014**, *118* (38), 8817–8827.
(239) Vlasenko, A.; Huthwelker, T.; W. Gäggeler, H.; Ammann, M. Kinetics of the Heterogeneous Reaction of Nitric Acid with Mineral Dust Particles: An Aerosol Flowtube Study. *Phys. Chem. Chem. Phys.* **2009**, *11* (36), 7921–7930.
(240) Santschi, Ch.; Rossi, M. J. Uptake of CO_2, SO_2, HNO_3 and HCl on Calcite ($CaCO_3$) at 300 K: Mechanism and the Role of Adsorbed Water. *J. Phys. Chem. A* **2006**, *110* (21), 6789–6802.
(241) Tang, M. J.; Schuster, G.; Crowley, J. N. Heterogeneous Reaction of N_2O_5 with Illite and Arizona Test Dust Particles. *Atmospheric Chem. Phys.* **2014**, *14* (1), 245–254.
(242) Li, W.; Oyama, S. T. Mechanism of Ozone Decomposition on a Manganese Oxide Catalyst. 2. Steady-State and Transient Kinetic Studies. *J. Am. Chem. Soc.* **1998**, *120* (35), 9047–9052.
(243) Jia, X.; Gu, W.; Peng, C.; Li, R.; Chen, L.; Wang, H.; Wang, H.; Wang, X.; Tang, M. Heterogeneous Reaction of $CaCO_3$ With NO_2 at Different Relative Humidities: Kinetics, Mechanisms, and Impacts on Aerosol Hygroscopicity. *J. Geophys. Res. Atmospheres* **2021**, *126* (11), e2021JD034826.
(244) Seisel, S.; Börensen, C.; Vogt, R.; Zellner, R. The Heterogeneous Reaction of HNO_3 on Mineral Dust and γ-Alumina Surfaces: A Combined Knudsen Cell and DRIFTS Study. *Phys. Chem. Chem. Phys.* **2004**, *6* (24), 5498–5508.

(245) Tang, M.; Larish, W. A.; Fang, Y.; Gankanda, A.; Grassian, V. H. Heterogeneous Reactions of Acetic Acid with Oxide Surfaces: Effects of Mineralogy and Relative Humidity. *J. Phys. Chem. A* **2016**, *120* (28), 5609–5616.
(246) Xu, B.; Shang, J.; Zhu, T.; Tang, X. Heterogeneous Reaction of Formaldehyde on the Surface of γ-Al_2O_3 Particles. *Atmos. Environ.* **2011**, *45* (21), 3569–3575.
(247) Carlos-Cuellar, S.; Li, P.; Christensen, A. P.; Krueger, B. J.; Burrichter, C.; Grassian, V. H. Heterogeneous Uptake Kinetics of Volatile Organic Compounds on Oxide Surfaces Using a Knudsen Cell Reactor: Adsorption of Acetic Acid, Formaldehyde, and Methanol on α-Fe_2O_3, α-Al_2O_3, and SiO_2. *J. Phys. Chem. A* **2003**, *107* (21), 4250–4261.
(248) Chen, H.; Nanayakkara, C. E.; Grassian, V. H. Titanium Dioxide Photocatalysis in Atmospheric Chemistry. *Chem. Rev.* **2012**, *112* (11), 5919–5948.
(249) George, C.; D'Anna, B.; Herrmann, H.; Weller, C.; Vaida, V.; Donaldson, D. J.; Bartels-Rausch, T.; Ammann, M. Emerging Areas in Atmospheric Photochemistry. In *Atmospheric and Aerosol Chemistry*; Topics in Current Chemistry; Springer, Berlin, Heidelberg, 2012; pp 1–53.
(250) Hoffmann, M. R.; Martin, S. T.; Choi, W.; Bahnemann, D. W. Environmental Applications of Semiconductor Photocatalysis. *Chem. Rev.* **1995**, *95* (1), 69–96.
(251) Nicolas, M.; Ndour, M.; Ka, O.; D'Anna, B.; George, C. Photochemistry of Atmospheric Dust: Ozone Decomposition on Illuminated Titanium Dioxide. *Environ. Sci. Technol.* **2009**, *43* (19), 7437–7442.
(252) Wang, H.; Li, K.; Li, J.; Sun, Y.; Dong, F. Photochemical Transformation Pathways of Nitrates from Photocatalytic NO_x Oxidation: Implications for Controlling Secondary Pollutants. *Environ. Sci. Technol. Lett.* **2021**.
(253) Ma, Q.; Wang, L.; Chu, B.; Ma, J.; He, H. Contrary Role of H_2O and O_2 in the Kinetics of Heterogeneous Photochemical Reactions of SO_2 on TiO_2. *J. Phys. Chem. A* **2019**, *123* (7), 1311–1318.

Chapter 2

(1) Hand, J. L.; Gill, T. E.; Schichtel, B. A. Urban and Rural Coarse Aerosol Mass across the United States: Spatial and Seasonal Variability and Long-Term Trends. *Atmospheric Environment* **2019**, *218*, 117025. https://doi.org/10.1016/j.atmosenv.2019.117025.
(2) IPCC. AR5 Climate Change 2013: The Physical Science Basis.
(3) World Health Organization. *Ambient Air Pollution: A Global Assessment of Exposure and Burden of Disease*; World Health Organization, 2016.
(4) Tanaka, T. Y.; Chiba, M. A Numerical Study of the Contributions of Dust Source Regions to the Global Dust Budget. *Global Planet. Change* **2006**, *52* (1), 88–104. https://doi.org/10.1016/j.gloplacha.2006.02.002.
(5) Pan, X.; Uno, I.; Wang, Z.; Nishizawa, T.; Sugimoto, N.; Yamamoto, S.; Kobayashi, H.; Sun, Y.; Fu, P.; Tang, X.; Wang, Z. Real-Time Observational Evidence of Changing Asian Dust Morphology with the Mixing of Heavy Anthropogenic Pollution. *Sci. Rep.* **2017**, *7* (1), 335. https://doi.org/10.1038/s41598-017-00444-w.

(6) Sillman, S. *"Tropospheric Ozone and Photochemical Smog" Environmental Geochemistry*; Elsevier, 2003; Vol. 9.

(7) de Reus, M.; Dentener, F.; Thomas, A.; Borrmann, S.; Ström, J.; Lelieveld, J. Airborne Observations of Dust Aerosol over the North Atlantic Ocean during ACE 2: Indications for Heterogeneous Ozone Destruction. *J. Geophys. Res. Atmos.* **2000**, *105* (D12), 15263–15275. https://doi.org/10.1029/2000JD900164.

(8) Kameda, T.; Azumi, E.; Fukushima, A.; Tang, N.; Matsuki, A.; Kamiya, Y.; Toriba, A.; Hayakawa, K. Mineral Dust Aerosols Promote the Formation of Toxic Nitropolycyclic Aromatic Compounds. *Sci. Rep.* **2016**, *6*, 24427. https://doi.org/10.1038/srep24427.

(9) Alexander, J. M.; Grassian, V. H.; Young, M. A.; Kleiber, P. D. Optical Properties of Selected Components of Mineral Dust Aerosol Processed with Organic Acids and Humic Material. *J. Geophys. Res. Atmos.* **2015**, *120* (6). https://doi.org/10.1002/2014JD022782.

(10) Sullivan, R. C.; Moore, M. J. K.; Petters, M. D.; Kreidenweis, S. M.; Roberts, G. C.; Prather, K. A. Effect of Chemical Mixing State on the Hygroscopicity and Cloud Nucleation Properties of Calcium Mineral Dust Particles. *Atmos. Chem. Phys.* **2009**, *9* (10), 3303–3316. https://doi.org/10.5194/acp-9-3303-2009.

(11) Möhler, O.; Benz, S.; Saathoff, H.; Schnaiter, M.; Wagner, R.; Schneider, J.; Walter, S.; Ebert, V.; Wagner, S. The Effect of Organic Coating on the Heterogeneous Ice Nucleation Efficiency of Mineral Dust Aerosols. *Environ. Res. Lett.* **2008**, *3* (2), 025007. https://doi.org/10.1088/1748-9326/3/2/025007.

(12) Shi, Z.; Krom, M. D.; Jickells, T. D.; Bonneville, S.; Carslaw, K. S.; Mihalopoulos, N.; Baker, A. R.; Benning, L. G. Impacts on Iron Solubility in the Mineral Dust by Processes in the Source Region and the Atmosphere: A Review. *Aeolian Res.* **2012**, *5*, 21–42. https://doi.org/10.1016/j.aeolia.2012.03.001.

(13) Tang, M.; Huang, X.; Lu, K.; Ge, M.; Li, Y.; Cheng, P.; Zhu, T.; Ding, A.; Zhang, Y.; Gligorovski, S.; Song, W.; Ding, X.; Bi, X.; Wang, X. Heterogeneous Reactions of Mineral Dust Aerosol: Implications for Tropospheric Oxidation Capacity. *Atmos. Chem. Phys.* **2017**, *17* (19), 11727–11777. https://doi.org/10.5194/acp-17-11727-2017.

(14) Romanías, M. N.; Ourrad, H.; Thévenet, F.; Riffault, V. Investigating the Heterogeneous Interaction of VOCs with Natural Atmospheric Particles: Adsorption of Limonene and Toluene on Saharan Mineral Dusts. *J. Phys. Chem. A* **2016**, *120* (8), 1197–1212. https://doi.org/10.1021/acs.jpca.5b10323.

(15) Carlos-Cuellar, S.; Li, P.; Christensen, A. P.; Krueger, B. J.; Burrichter, C.; Grassian, V. H. Heterogeneous Uptake Kinetics of Volatile Organic Compounds on Oxide Surfaces Using a Knudsen Cell Reactor: Adsorption of Acetic Acid, Formaldehyde, and Methanol on α-Fe_2O_3, α-Al_2O_3, and SiO_2. *J. Phys. Chem. A* **2003**, *107* (21), 4250–4261. https://doi.org/10.1021/jp0267609.

(16) George, C.; Ammann, M.; D'Anna, B.; Donaldson, D. J.; Nizkorodov, S. A. Heterogeneous Photochemistry in the Atmosphere. *Chem. Rev.* **2015**, *115* (10), 4218–4258. https://doi.org/10.1021/cr500648z.

(17) Hoffmann, M. R.; Martin, S. T.; Choi, W.; Bahnemann, D. W. Environmental Applications of Semiconductor Photocatalysis. *Chem. Rev.* **1995**, *95* (1), 69–96. https://doi.org/10.1021/cr00033a004.

(18) Chen, H.; Nanayakkara, C. E.; Grassian, V. H. Titanium Dioxide Photocatalysis in Atmospheric Chemistry. *Chem. Rev.* **2012**, *112* (11), 5919–5948. https://doi.org/10.1021/cr3002092.

(19) Guthrie, G. D.; Mossman, B. T. *Health Effects of Mineral Dusts*; Reviews in Mineralogy; Walter de Gruyter GmbH & Co KG, 2018; Vol. 28.

(20) Fitzpatrick, R. W.; Chittleborough, D. J. Titanium and Zirconium Minerals. In *Soil Mineralogy with Environmental Applications*; John Wiley & Sons, Ltd, 2002; pp 667–690. https://doi.org/10.2136/sssabookser7.c22.

(21) Engelbrecht, J. P.; McDonald, E. V.; Gillies, J. A.; Jayanty, R. K. M. "Jay"; Casuccio, G.; Gertler, A. W. Characterizing Mineral Dusts and Other Aerosols from the Middle East—Part 2: Grab Samples and Re-Suspensions. *Inhal. Toxicol.* **2009**, *21* (4), 327–336. https://doi.org/10.1080/08958370802464299.

(22) Zhang, J.; Zhou, P.; Liu, J.; Yu, J. New Understanding of the Difference of Photocatalytic Activity among Anatase, Rutile and Brookite TiO_2. *Phys. Chem. Chem. Phys.* **2014**, *16* (38), 20382–20386. https://doi.org/10.1039/C4CP02201G.

(23) Folli, A.; Campbell, S. B.; Anderson, J. A.; Macphee, D. E. Role of TiO2 Surface Hydration on NO Oxidation Photo-Activity. *J .Photoch. Photobio. A* **2011**, *220* (2), 85–93. https://doi.org/10.1016/j.jphotochem.2011.03.017.

(24) Kumar, S. G.; Devi, L. G. Review on Modified TiO_2 Photocatalysis under UV/Visible Light: Selected Results and Related Mechanisms on Interfacial Charge Carrier Transfer Dynamics. *J. Phys. Chem. A* **2011**, *115* (46), 13211–13241. https://doi.org/10.1021/jp204364a.

(25) Sieland, F.; Schneider, J.; W. Bahnemann, D. Photocatalytic Activity and Charge Carrier Dynamics of TiO_2 Powders with a Binary Particle Size Distribution. *Phys. Chem. Chem. Phys.* **2018**, *20* (12), 8119–8132. https://doi.org/10.1039/C8CP00398J.

(26) Zafonte, L.; Rieger, P. L.; Holmes, J. R. Nitrogen Dioxide Photolysis in the Los Angeles Atmosphere. *Environ. Sci. Technol.* **1977**, *11* (5), 483–487.

(27) Michoud, V.; Colomb, A.; Borbon, A.; Miet, K.; Beekmann, M.; Camredon, M.; Aumont, B.; Perrier, S.; Zapf, P.; Siour, G.; Ait-Helal, W.; Afif, C.; Kukui, A.; Furger, M.; Dupont, J. C.; Haeffelin, M.; Doussin, J. F. Study of the Unknown HONO Daytime Source at a European Suburban Site during the MEGAPOLI Summer and Winter Field Campaigns. *Atmos. Chem. Phys.* **2014**, *14* (6), 2805–2822. https://doi.org/10.5194/acp-14-2805-2014.

(28) Pöschl, U.; Rudich, Y.; Ammann, M. Kinetic Model Framework for Aerosol and Cloud Surface Chemistry and Gas-Particle Interactions–Part 1: General Equations, Parameters, and Terminology. *Atmos. Chem. Phys.* **2007**, *7* (23), 5989–6023.

(29) Knopf, D. A.; Pöschl, U.; Shiraiwa, M. Radial Diffusion and Penetration of Gas Molecules and Aerosol Particles through Laminar Flow Reactors, Denuders, and Sampling Tubes. *Analytical Chemistry* **2015**, *87* (7), 3746–3754. https://doi.org/10.1021/ac5042395.

(30) Michel, A. E.; Usher, C. R.; Grassian, V. H. Reactive Uptake of Ozone on Mineral Oxides and Mineral Dusts. *Atmos. Environ.* **2003**, *37* (23), 3201–3211. https://doi.org/10.1016/S1352-2310(03)00319-4.

(31) Jaffe, H. W. *Crystal Chemistry and Refractivity*; Courier Corporation, 1996.

(32) Bowles, J. F. W.; Howie, R. A.; Vaughan, D. J.; Zussman, J. *Rock-Forming Minerals*; Geological Society of London, 2011.

(33) Clarke, F. W.; Washington, H. S. *The Composition of the Earth's Crust*; U.S. Government Printing Office, 1924.

(34) Franz, G.; Liebscher, A. Physical and Chemical Properties of the Epidote Minerals–an Introduction. *Rev. Mineral Geochem.* **2004**, *56* (1), 1–81. https://doi.org/10.2138/gsrmg.56.1.1.

(35) Reyes-Coronado, D.; Rodríguez-Gattorno, G.; Espinosa-Pesqueira, M. E.; Cab, C.; Coss, R. de; Oskam, G. Phase-Pure TiO_2 Nanoparticles: Anatase, Brookite and Rutile. *Nanotechnology* **2008**, *19* (14), 145605. https://doi.org/10.1088/0957-4484/19/14/145605.

(36) Staehelin, J.; Hoigne, J. Decomposition of Ozone in Water in the Presence of Organic Solutes Acting as Promoters and Inhibitors of Radical Chain Reactions. *Environ. Sci. Technol.* **1985**, *19* (12), 1206–1213. https://doi.org/10.1021/es00142a012.

(37) Nicolas, M.; Ndour, M.; Ka, O.; D'Anna, B.; George, C. Photochemistry of Atmospheric Dust: Ozone Decomposition on Illuminated Titanium Dioxide. *Environ. Sci. Technol.* **2009**, *43* (19), 7437–7442. https://doi.org/10.1021/es901569d.

(38) Xu, Y.; Schoonen, M. A. A. The Absolute Energy Positions of Conduction and Valence Bands of Selected Semiconducting Minerals. *Am. Mineral.* **2000**, *85* (3–4), 543–556. https://doi.org/10.2138/am-2000-0416.

(39) Bulanin, K. M.; Lavalley, J. C.; Tsyganenko, A. A. IR Spectra of Adsorbed Ozone. *Colloids Surf. A Physicochem. Eng. Asp.* **1995**, *101* (2), 153–158. https://doi.org/10.1016/0927-7757(95)03130-6.

(40) Li, W.; Gibbs, G. V.; Oyama, S. T. Mechanism of Ozone Decomposition on a Manganese Oxide Catalyst. 1. In Situ Raman Spectroscopy and Ab Initio Molecular Orbital Calculations. *J. Am. Chem. Soc.* **1998**, *120* (35), 9041–9046. https://doi.org/10.1021/ja981441+.

(41) Li, W.; Oyama, S. T. Mechanism of Ozone Decomposition on a Manganese Oxide Catalyst. 2. Steady-State and Transient Kinetic Studies. *J. Am. Chem. Soc.* **1998**, *120* (35), 9047–9052. https://doi.org/10.1021/ja9814422.

(42) Bulanin, K. M.; Lavalley, J. C.; Tsyganenko, A. A. Infrared Study of Ozone Adsorption on TiO2 (Anatase). *The Journal of Physical Chemistry* **1995**, *99* (25), 10294–10298. https://doi.org/10.1021/j100025a034.

(43) Ostaszewski, C. J.; Stuart, N. M.; Lesko, D. M. B.; Kim, D.; Lueckheide, M. J.; Navea, J. G. Effects of Coadsorbed Water on the Heterogeneous Photochemistry of Nitrates Adsorbed on TiO2. *J. Phys. Chem. A* **2018**, *122* (31), 6360–6371. https://doi.org/10.1021/acs.jpca.8b04979.

(44) George, S.; Pokhrel, S.; Ji, Z.; Henderson, B. L.; Xia, T.; Li, L.; Zink, J. I.; Nel, A. E.; Mädler, L. Role of Fe Doping in Tuning the Band Gap of TiO_2 for the Photo-Oxidation-Induced Cytotoxicity Paradigm. *J. Am. Chem. Soc.* **2011**, *133* (29), 11270–11278. https://doi.org/10.1021/ja202836s.

(45) Zhou, M.; Yu, J.; Cheng, B. Effects of Fe-Doping on the Photocatalytic Activity of Mesoporous TiO_2 Powders Prepared by an Ultrasonic Method. *J. Hazard. Mater.* **2006**, *137* (3), 1838–1847. https://doi.org/10.1016/j.jhazmat.2006.05.028.

(46) Hurum, D. C.; Agrios, A. G.; Gray, K. A.; Rajh, T.; Thurnauer, M. C. Explaining the Enhanced Photocatalytic Activity of Degussa P25 Mixed-Phase TiO_2 Using EPR. *J. Phys. Chem. B* **2003**, *107* (19), 4545–4549. https://doi.org/10.1021/jp0273934.

(47) Zaki, M. I.; Fouad, N. E.; Mekhemer, G. A. H.; Jagadale, T. C.; Ogale, S. B. TiO2 Nanoparticle Size Dependence of Porosity, Adsorption and Catalytic Activity. *Colloids and Surfaces A: Physicochemical and Engineering Aspects* **2011**, *385* (1), 195–200. https://doi.org/10.1016/j.colsurfa.2011.06.010.

(48) Schneider, J.; Matsuoka, M.; Takeuchi, M.; Zhang, J.; Horiuchi, Y.; Anpo, M.; Bahnemann, D. W. Understanding TiO_2 Photocatalysis: Mechanisms and Materials. *Chem. Rev.* **2014**, *114* (19), 9919–9986. https://doi.org/10.1021/cr5001892.

(49) Pan, J.; Liu, G.; Lu, G. Q. (Max); Cheng, H.-M. On the True Photoreactivity Order of 001, 010, and 101 Facets of Anatase TiO_2 Crystals. *Angew. Chem. Int. Ed.* **2011**, *50* (9), 2133–2137. https://doi.org/10.1002/anie.201006057.

(50) Luttrell, T.; Halpegamage, S.; Tao, J.; Kramer, A.; Sutter, E.; Batzill, M. Why Is Anatase a Better Photocatalyst than Rutile? - Model Studies on Epitaxial TiO_2 Films. *Sci. Rep.* **2014**, *4* (1), 1–8. https://doi.org/10.1038/srep04043.

(51) Gao, L.; Zhang, Q. Effects of Amorphous Contents and Particle Size on the Photocatalytic Properties of TiO_2 Nanoparticles. *Scr. Mater.* **2001**, *44* (8), 1195–1198. https://doi.org/10.1016/S1359-6462(01)00681-9.

(52) Miao, J.; Zhang, R.; Zhang, L. Photocatalytic Degradations of Three Dyes with Different Chemical Structures Using Ball-Milled TiO_2. *Mater. Res. Bull.* **2018**, *97*, 109–114. https://doi.org/10.1016/j.materresbull.2017.08.032.

(53) Ohtani, B.; Mahaney, O. O. P.; Amano, F.; Murakami, N.; Abe, R. What Are Titania Photocatalysts?—An Exploratory Correlation of Photocatalytic Activity with Structural and Physical Properties. *J. Adv. Oxid. Technol.* **2016**, *13* (3), 247–261. https://doi.org/10.1515/jaots-2010-0303.

(54) Ndour, M.; D'Anna, B.; George, C.; Ka, O.; Balkanski, Y.; Kleffmann, J.; Stemmler, K.; Ammann, M. Photoenhanced Uptake of NO_2 on Mineral Dust: Laboratory Experiments and Model Simulations. *Geophys. Res. Lett.* **2008**, *35* (5), L05812. https://doi.org/10.1029/2007GL032006.

(55) Hanisch, F.; Crowley, J. N. Ozone Decomposition on Saharan Dust: An Experimental Investigation. *Atmos. Chem. Phys.* **2003**, *3* (1), 119–130. https://doi.org/10.5194/acp-3-119-2003.

(56) Ji, Z.; Wang, G.; Yu, M.; Pal, J. S. Potential Climate Effect of Mineral Aerosols over West Africa: Part II—Contribution of Dust and Land Cover to Future Climate Change. *Clim. Dyn.* **2018**, *50* (7), 2335–2353. https://doi.org/10.1007/s00382-015-2792-x.

(57) Journet, E.; Desboeufs, K. V.; Caquineau, S.; Colin, J.-L. Mineralogy as a Critical Factor of Dust Iron Solubility. *Geophys. Res. Lett.* **2008**, *35* (7), L07805. https://doi.org/10.1029/2007GL031589.

(58) Caquineau, S.; Gaudichet, A.; Gomes, L.; Magonthier, M.-C.; Chatenet, B. Saharan Dust: Clay Ratio as a Relevant Tracer to Assess the Origin of Soil-Derived Aerosols. *Geophys. Res. Lett.* **1998**, *25* (7), 983–986. https://doi.org/10.1029/98GL00569.

(59) Atkinson, J. D.; Murray, B. J.; Woodhouse, M. T.; Whale, T. F.; Baustian, K. J.; Carslaw, K. S.; Dobbie, S.; O'Sullivan, D.; Malkin, T. L. The Importance of Feldspar for Ice Nucleation by Mineral Dust in Mixed-Phase Clouds. *Nature* **2013**, *498* (7454), 355–358. https://doi.org/10.1038/nature12278.

(60) Kebede, M. A.; Bish, D. L.; Losovyj, Y.; Engelhard, M. H.; Raff, J. D. The Role of Iron-Bearing Minerals in NO_2 to HONO Conversion on Soil Surfaces. *Environ. Sci. Technol.* **2016**, *50* (16), 8649–8660. https://doi.org/10.1021/acs.est.6b01915.

(61) Engelbrecht, J. P.; Moosmüller, H.; Pincock, S.; Jayanty, R. K. M.; Lersch, T.; Casuccio, G. Technical Note: Mineralogical, Chemical, Morphological, and Optical Interrelationships of Mineral Dust Re-Suspensions. *Atmos. Chem. Phys.* **2016**, *16* (17), 10809–10830. https://doi.org/10.5194/acp-16-10809-2016.

(62) Mishra, M.; Chun, D.-M. α-Fe_2O_3 as a Photocatalytic Material: A Review. *Appl. Catal. A Gen.* **2015**, *498*, 126–141. https://doi.org/10.1016/j.apcata.2015.03.023.

(63) Chen, H.; Navea, J. G.; Young, M. A.; Grassian, V. H. Heterogeneous Photochemistry of Trace Atmospheric Gases with Components of Mineral Dust Aerosol. *J. Phys. Chem. A* **2011**, *115* (4), 490–499. https://doi.org/10.1021/jp110164j.

Chapter 3

(1) Goudie, A. S.; Middleton, N. J.*Desert Dust in the Global System*; Springer, Berlin: Heidelberg, 2006.

(2) Bullard, J. E.; Baddock, M.; Bradwell, T.; Crusius, J.; Darlington, E.; Gaiero, D.; Gassó, S.; Gisladottir, G.; Hodgkins, R.; McCulloch, R.; McKenna-Neuman, C.; Mockford, T.; Stewart, H.; Thorsteinsson, T. High-Latitude Dust in the Earth System. *Rev. Geophys.* 2016, *54*, 447–485.

(3) Groot Zwaaftink, C. D.; Grythe, H.; Skov, H.; Stohl, A. Substantial Contribution of Northern High-Latitude Sources to Mineral Dust in the Arctic. *J. Geophys. Res.: Atmos.* 2016, *121*, 13,678–13,697.

(4) Bullard, J. E. The Distribution and Biogeochemical Importance of High-Latitude Dust in the Arctic and Southern Ocean-Antarctic Regions. *J. Geophys. Res.: Atmos.* 2017, *122*, 3098–3103.

(5) Arnalds, O.; Dagsson-Waldhauserova, P.; Olafsson, H. The Icelandic Volcanic Aeolian Environment: Processes and Impacts A Review. *Aeolian Res.* 2016, *20*, 176–195.

(6) Björnsson, H.; Pálsson, F. Icelandic Glaciers. *Jökull* 2008, *58*, 365–386.
(7) Gíslason, S. R.; Arnórsson, S.; Ármannsson, H. Chemical Weathering of Basalt in Southwest Iceland: Effects of Runoff, Age of Rocks and Vegetative/Glacial Cover. *Am. J. Sci.* 1996, *296*, 837–907.
(8) Arnalds, O.; Gisladottir, F. O.; Sigurjonsson, H. Sandy Deserts of Iceland: An Overview. *J. Arid Environ.* 2001, *47*, 359–371.
(9) Arnalds, O. Dust Sources and Deposition of Aeolian Materials in Iceland. *Icel. Agric. Sci.* 2010, *23*, 3–21.
(10) Butwin, M. K.; von Löwis, S.; Pfeffer, M. A.; Thorsteinsson, T. The Effects of Volcanic Eruptions on the Frequency of Particulate Matter Suspension Events in Iceland. *J. Aerosol Sci.* 2019, *128*, 99– 113.
(11) Beckett, F.; Kylling, A.; Sigurðardóttir, G.; von Löwis, S.; Witham, C. Quantifying the Mass Loading of Particles in an Ash Cloud Remobilized from Tephra Deposits on Iceland. *Atmos. Chem. Phys.* 2017, *17*, 4401–4418.
(12) Leadbetter, S. J.; Hort, M. C.; von Löwis, S.; Weber, K.; Witham, C. S. Modeling the Resuspension of Ash Deposited during the Eruption of Eyjafjallajökull in Spring 2010. *J. Geophys. Res.: Atmos.* 2012, *117*, D00U10.
(13) Gudmundsson, M. T.; Thordarson, T.; Höskuldsson, A .; Larsen, G.; Björnsson, H.; Prata, F. J.; Oddsson, B.; Magnusson, E.; Högnadóttir, T.; Petersen, G. N.; Hayward, C. L.; Stevenson, J. A.; Jónsdóttir, I. Ash Generation and Distribution from the April–May 2010 Eruption of Eyjafjallajökull, Iceland. *Sci. Rep.* 2012, *2*, 572.
(14) Liu, E. J.; Cashman, K. V.; Beckett, F. M.; Witham, C. S.; Leadbetter, S. J.; Hort, M. C.; Guðmundsson, S. Ash Mists and Brown Snow: Remobilization of Volcanic Ash from Recent Icelandic Eruptions. *J. Geophys. Res.: Atmos.* 2014, *119*, 9463–9480.
(15) Thorsteinsson, T.; Jóhannsson, T.; Stohl, A.; Kristiansen, N. I. High Levels of Particulate Matter in Iceland Due to Direct Ash Emissions by the Eyjafjallajökull Eruption and Resuspension of Deposited Ash. *J. Geophys. Res.: Solid Earth* 2012, *117*, B00C05.
(16) Dagsson-Waldhauserova, P.; Arnalds, O.; Olafsson, H. Long- Term Variability of Dust Events in Iceland (1949–2011). *Atmos. Chem. Phys.* 2014, *14*, 13411–13422.
(17) Dagsson-Waldhauserova, P.; Arnalds, O.; Olafsson, H. Long-Term Frequency and Characteristics of Dust Storm Events in Northeast Iceland (1949–2011). *Atmos. Environ.* 2013, *77*, 117–127.
(18) Butwin, M. K.; von Löwis, S.; Pfeffer, M. A.; Dagsson- Waldhauserova, P.; Thorsson, J.; Thorsteinsson, T. Influence of Weather Conditions on Particulate Matter Suspension Following the 2010 Eyjafjallajökull Volcanic Eruption. *Earth Interact.* 2020, *24*, 1–16.
(19) Gisladottir, F. O.; Arnalds, O.; Gisladottir, G. The Effect of Landscape and Retreating Glaciers on Wind Erosion in South Iceland. *Land Degrad. Dev.* 2005, *16*, 177–187.
(20) Thorsteinsson, T.; Gísladóttir, G.; Bullard, J.; McTainsh, G. Dust Storm Contributions to Airborne Particulate Matter in Reykjavik, Iceland. *Atmos. Environ.* 2011, *45*, 5924–5933.

(21) Carlsen, H.; Gislason, T.; Forsberg, B.; Meister, K.; Thorsteinsson, T.; Jóhannsson, T.; Finnbjornsdottir, R.; Oudin, A. Emergency Hospital Visits in Association with Volcanic Ash, Dust Storms and Other Sources of Ambient Particles: A Time Series Study in Reykjavik, Iceland. *Int. J. Environ. Res. Public Health* 2015, *12*, 4047–4059.

(22) Mueller, W.; Cowie, H.; Horwell, C. J.; Hurley, F.; Baxter, P. J. Health Impact Assessment of Volcanic Ash Inhalation: A Comparison With Outdoor Air Pollution Methods. *GeoHealth* 2020, *4*, No. e2020GH000256.

(23) Gudmundsson, G. Respiratory Health Effects of Volcanic Ash with Special Reference to Iceland. A Review. *Clin. Respir. J.* 2011, *5*, 2–9.

(24) Urupina, D.; Lasne, J.; Romanias, M. N.; Thiery, V.; Dagsson-Waldhauserova, P.; Thevenet, F. Uptake and Surface Chemistry of SO_2 on Natural Volcanic Dusts. *Atmos. Environ.* 2019, *217*, 116942.

(25) Romanias, M. N.; Ren, Y.; Grosselin, B.; Daële, V.; Mellouki, A.; Dagsson-Waldhauserova, P.; Thevenet, F. Reactive Uptake of NO_2 on Volcanic Particles: A Possible Source of HONO in the Atmosphere. *J. Environ. Sci.* 2020, *95*, 155–164.

(26) Vance, A.; McGonigle, A. J. S.; Aiuppa, A.; Stith, J. L.; Turnbull, K.; von Glasow, R. Ozone Depletion in Tropospheric Volcanic Plumes. *Geophys. Res. Lett.* 2010, *37*, L22802.

(27) Surl, L.; Donohoue, D.; Aiuppa, A.; Bobrowski, N.; von Glasow, R. Quantification of the Depletion of Ozone in the Plume of Mount Etna. *Atmos. Chem. Phys.* 2015, *15*, 2613–2628.

(28) Roberts, T. J.; Braban, C. F.; Martin, R. S.; Oppenheimer, C.; Adams, J. W.; Cox, R. A.; Jones, R. L.; Griffiths, P. T. Modelling Reactive Halogen Formation and Ozone Depletion in Volcanic Plumes. *Chem. Geol.* 2009, *263*, 151–163.

(29) Andrey, J.; Cuevas, E.; Parrondo, M. C.; Alonso-Pérez, S.; Redondas, A.; Gil-Ojeda, M. Quantification of Ozone Reductions within the Saharan Air Layer through a 13-Year Climatologic Analysis of Ozone Profiles. *Atmos. Environ.* 2014, *84*, 28–34.

(30) Nan, Y.; Wang, Y. Observational Evidence for Direct Uptake of Ozone in China by Asian Dust in Springtime. *Atmos. Environ.* 2018, *186*, 45–55.

(31) Abou-Ghanem, M.; Oliynyk, A. O.; Chen, Z.; Matchett, L. C.; McGrath, D. T.; Katz, M. J.; Locock, A. J.; Styler, S. A. Significant Variability in the Photocatalytic Activity of Natural Titanium- Containing Minerals: Implications for Understanding and Predicting Atmospheric Mineral Dust Photochemistry. *Environ. Sci. Technol.* 2020, *54*, 13509–13516.

(32) Hanisch, F.; Crowley, J. N. Ozone Decomposition on Saharan Dust: An Experimental Investigation. *Atmos. Chem. Phys.* 2003, *3*, 119–130.

(33) Wang, X.; Romanias, M.; Thévenet, F.; Rousseau, A. Geocatalytic Uptake of Ozone onto Natural Mineral Dust. *Catalysts* 2018, *8*, 263.

(34) de Reus, M.; Dentener, F.; Thomas, A.; Borrmann, S.; Ström, J.; Lelieveld, J. Airborne Observations of Dust Aerosol over the North Atlantic Ocean during ACE 2: Indications for Heterogeneous Ozone Destruction. *J. Geophys. Res.: Atmos.* 2000, *105*(D12), 15263–15275.

(35) Baldo, C.; Formenti, P.; Nowak, S.; Chevaillier, S.; Cazaunau, M.; Pangui, E.; Di Biagio, C.; Doussin, J.-F.; Ignatyev, K.; Dagsson- Waldhauserova, P.; Arnalds, O.; MacKenzie, A.

R.; Shi, Z. Distinct Chemical and Mineralogical Composition of Icelandic Dust Compared to Northern African and Asian Dust. *Atmos. Chem. Phys.* 2020, *20*, 13521–13539.

(36) Maters, E. C.; Delmelle, P.; Rossi, M. J.; Ayris, P. M. Reactive Uptake of Sulfur Dioxide and Ozone on Volcanic Glass and Ash at Ambient Temperature. *J. Geophys. Res.: Atmos.* 2017, *122*, 10077–10088.

(37) Maters, E. C.; Delmelle, P.; Rossi, M. J.; Ayris, P. M.; Bernard, A. Controls on the Surface Chemical Reactivity of Volcanic Ash Investigated with Probe Gases. *Earth Planet. Sci. Lett.* 2016, *450*, 254– 262.

(38) Tang, M.; Cziczo, D. J.; Grassian, V. H. Interactions of Water with Mineral Dust Aerosol: Water Adsorption, Hygroscopicity, Cloud Condensation, and Ice Nucleation. *Chem. Rev.* 2016, *116*, 4205–4259.

(39) Styler, S. A.; Donaldson, D. J. Heterogeneous Photochemistry of Oxalic Acid on Mauritanian Sand and Icelandic Volcanic Ash. *Environ. Sci. Technol.* 2012, *46*, 8756–8763.

(40) Styler, S. A.; Myers, A. L.; Donaldson, D. J. Heterogeneous Photooxidation of Fluorotelomer Alcohols: A New Source of Aerosol- Phase Perfluorinated Carboxylic Acids. *Environ. Sci. Technol.* 2013, *47*, 6358–6367.

(41) Ndour, M.; Nicolas, M.; D'Anna, B.; Ka, O.; George, C. Photoreactivity of NO_2 on Mineral Dusts Originating from Different Locations of the Sahara Desert. *Phys. Chem. Chem. Phys.* 2009, *11*, 1312–1319.

(42) Lasne, J.; Romanias, M. N.; Thevenet, F. Ozone Uptake by Clay Dusts under Environmental Conditions. *ACS Earth Space Chem.* 2018, *2*, 904–914.

(43) Hofzumahaus, A. Measurement of Photolysis Frequencies in the Atmosphere. In *Analytical Techniques for Atmospheric Measurement*; Heard, D. E., Ed.; Blackwell Publishing, 2006.

(44) Bohn, B.; Rohrer, F.; Brauers, T.; Wahner, A. Actinometric Measurements of NO_2 Photolysis Frequencies in the Atmosphere Simulation Chamber SAPHIR. *Atmos. Chem. Phys.* 2005, *5*, 493–503.

(45) Pöschl, U.; Rudich, Y.; Ammann, M. Kinetic Model Framework for Aerosol and Cloud Surface Chemistry and Gas-Particle Interactions–Part 1: General Equations, Parameters, and Terminol- ogy. *Atmos. Chem. Phys.* 2007, *7*, 5989–6023.

(46) Kolb, C. E.; Cox, R. A.; Abbatt, J. P. D.; Ammann, M.; Davis, E. J.; Donaldson, D. J.; Garrett, B. C.; George, C.; Griffiths, P. T.; Hanson, D. R.; Kulmala, M.; McFiggans, G.; Pöschl, U.; Riipinen, I.; Rossi, M. J.; Rudich, Y.; Wagner, P. E.; Winkler, P. M.; Worsnop, D. R.; O' Dowd, C. D. An Overview of Current Issues in the Uptake of Atmospheric Trace Gases by Aerosols and Clouds. *Atmos. Chem. Phys.* 2010, *10*, 10561–10605.

(47) Knopf, D. A.; Pöschl, U.; Shiraiwa, M. Radial Diffusion and Penetration of Gas Molecules and Aerosol Particles through Laminar Flow Reactors, Denuders, and Sampling Tubes. *Anal. Chem.* 2015, *87*, 3746–3754.

(48) Chen, H.; Stanier, C. O.; Young, M. A.; Grassian, V. H. A Kinetic Study of Ozone Decomposition on Illuminated Oxide Surfaces. *J. Phys. Chem. A* 2011, *115*, 11979–11987.

(49) George, C.; Ammann, M.; D'Anna, B.; Donaldson, D. J.; Nizkorodov, S. A. Heterogeneous Photochemistry in the Atmosphere. *Chem. Rev.* 2015, *115*, 4218–4258.

(50) Butwin, M. K.; Pfeffer, M. A.; von Löwis, S.; Støren, E. W. N.; Bali, E.; Thorsteinsson, T. Properties of Dust Source Material and Volcanic Ash in Iceland. *Sedimentology* 2020, *67*, 3067–3087.

(51) Joshi, N.; Romanias, M. N.; Riffault, V.; Thevenet, F. Investigating Water Adsorption onto Natural Mineral Dust Particles: Linking DRIFTS Experiments and BET Theory. *Aeolian Res.* 2017, *27*, 35–45.

(52) van der Heide, P. *X-ray Photoelectron Spectroscopy: An Introduction to Principles and Practices*; John Wiley & Sons, 2011.

(53) Jensen, B. J. L.; Beaudoin, A. B.; Clynne, M. A.; Harvey, J.; Vallance, J. W. A Re-Examination of the Three Most Prominent Holocene Tephra Deposits in Western Canada: Bridge River, Mount St. Helens Yn and Mazama. *Quat. Int.* 2019, *500*, 83–95.

(54) Stringer, M. E. Separation of Pumice from Soil Mixtures. *Soils Found.* 2019, *59*, 1073–1084.

(55) Barthelmy, D. Mineralogy Database http://www.webmineral.com/ (accessed March 1, 2021).

(56) Reed, S. J. B. *Electron Microprobe Analysis and Scanning Electron Microscopy in Geology*; Cambridge University Press, 2005.

(57) Coates Fuentes, Z. L.; Kucinski, T. M.; Hinrichs, R. Z. Ozone Decomposition on Kaolinite as a Function of Monoterpene Exposure and Relative Humidity. *ACS Earth Space Chem.* 2018, *2*, 21–30.

(58) Adamson, A. W. *Physical Chemistry of Surfaces*; John Wiley andSons, 1990.

(59) Michel, A. E.; Usher, C. R.; Grassian, V. H. Reactive Uptake of Ozone on Mineral Oxides and Mineral Dusts. *Atmos. Environ.* 2003, *37*, 3201–3211.

(60) Michel, A. E.; Usher, C. R.; Grassian, V. H. Heterogeneous and Catalytic Uptake of Ozone on Mineral Oxides and Dusts: A Knudsen Cell Investigation. *Geophys. Res. Lett.* 2002, *29*, 10-1–10-4.

(61) Mogili, P. K.; Kleiber, P. D.; Young, M. A.; Grassian, V. H. Heterogeneous Uptake of Ozone on Reactive Components of Mineral Dust Aerosol: An Environmental Aerosol Reaction Chamber Study. *J. Phys. Chem. A* 2006, *110*, 13799–13807.

(62) Sullivan, R. C.; Thornberry, T.; Abbatt, J. P. D. Ozone Decomposition Kinetics on Alumina: Effects of Ozone Partial Pressure, Relative Humidity and Repeated Oxidation Cycles. *Atmos. Chem. Phys.* 2004, *4*, 1301–1310.

(63) Hatch, C. D.; Wiese, J. S.; Crane, C. C.; Harris, K. J.; Kloss, H. G.; Baltrusaitis, J. Water Adsorption on Clay Minerals As a Function of Relative Humidity: Application of BET and Freundlich Adsorption Models. *Langmuir* 2012, *28*, 1790–1803.

(64) Ibrahim, S.; Romanias, M. N.; Alleman, L. Y.; Zeineddine, M. N.; Angeli, G. K.; Trikalitis, P. N.; Thevenet, F. Water Interaction with Mineral Dust Aerosol: Particle Size and Hygroscopic Properties of Dust. *ACS Earth Space Chem.* 2018, *2*, 376–386.

(65) Rubasinghege, G.; Grassian, V. H. Role(s) of Adsorbed Water in the Surface Chemistry of Environmental Interfaces. *Chem. Commun.* 2013, *49*, 3071–3094.

(66) Delmelle, P.; Wadsworth, F. B.; Maters, E. C.; Ayris, P. M. High Temperature Reactions Between Gases and Ash Particles in Volcanic Eruption Plumes. *Rev. Mineral. Geochem.* 2018, *84*, 285–308.

(67) Li, W.; Gibbs, G. V.; Oyama, S. T. Mechanism of Ozone Decomposition on a Manganese Oxide Catalyst. 1. In Situ Raman Spectroscopy and Ab Initio Molecular Orbital Calculations. *J. Am. Chem. Soc.* 1998, *120*, 9041–9046.

(68) Usher, C. R.; Michel, A. E.; Grassian, V. H. Reactions on Mineral Dust. *Chem. Rev.* 2003, *103*, 4883–4940.

(69) Thomas, K.; Hoggan, P. E.; Mariey, L.; Lamotte, J.; Lavalley, J. C. Experimental and Theoretical Study of Ozone Adsorption on Alumina. *Catal. Lett.* 1997, *46*, 77–82.

(70) Jia, J.; Zhang, P.; Chen, L. Catalytic Decomposition of Gaseous Ozone over Manganese Dioxides with Different Crystal Structures. *Appl. Catal., B* 2016, *189*, 210–218.

(71) Durant, A. J.; Bonadonna, C.; Horwell, C. J. Atmospheric and Environmental Impacts of Volcanic Particulates. *Elements* 2010, *6*, 235–240.

(72) Gíslason, S. R. Weathering in Iceland. *Jökull* 2008, *58*, 387–408.

(73) Nicolas, M.; Ndour, M.; Ka, O.; D'Anna, B.; George, C. Photochemistry of Atmospheric Dust: Ozone Decomposition on Illuminated Titanium Dioxide. *Environ. Sci. Technol.* 2009, *43*, 7437–7442.

(74) Cano-Ruiz, J. A.; Kong, D.; Balas, R. B.; Nazaroff, W. W. Removal of Reactive Gases at Indoor Surfaces: Combining Mass Transport and Surface Kinetics. *Atmos. Environ., Part A* 1993, *27*, 2039–2050.

(75) Chen, H.; Nanayakkara, C. E.; Grassian, V. H. Titanium Dioxide Photocatalysis in Atmospheric Chemistry. *Chem. Rev.* 2012, *112*, 5919–5948.

(76) Hoffmann, M. R.; Martin, S. T.; Choi, W.; Bahnemann, D. W. Environmental Applications of Semiconductor Photocatalysis. *Chem. Rev.* 1995, *95*, 69–96.

(77) Carroll, D. *Rock Weathering*; Springer: Boston, 1970.

(78) Dagsson-Waldhauserova, P.; Arnalds, O.; Olafsson, H.; Hladil, J.; Skala, R.; Navratil, T.; Chadimova, L.; Meinander, O. Snow–Dust Storm: Unique Case Study from Iceland, March 6–7, 2013. *Aeolian Res.* 2015, *16*, 69–74.

(79) Ivleva, N. P.; Huckele, S.; Weinzierl, B.; Niessner, R.; Haisch, C.; Baumann, T. Identification and Characterization of Individual Airborne Volcanic Ash Particles by Raman Microspectroscopy. *Anal. Bioanal. Chem.* 2013, *405*, 9071–9084.

(80) Li, M.; Su, H.; Li, G.; Ma, N.; Pöschl, U.; Cheng, Y. Relative Importance of Gas Uptake on Aerosol and Ground Surfaces Characterized by Equivalent Uptake Coefficients. *Atmos. Chem. Phys.* 2019, *19*, 10981–11011.

(81) Dagsson-Waldhauserova, P.; Renard, J.-B.; Olafsson, H.; Vignelles, D.; Berthet, G.; Verdier, N.; Duverger, V. Vertical Distribution of Aerosols in Dust Storms during the Arctic Winter. *Sci. Rep.* 2019, *9*, 16122.

(82) https://en.vedur.is/weather/observations/areas/ (accessed Dec 30, 2020).
(83) Chang, R. Y.-W.; Sullivan, R. C.; Abbatt, J. P. D. Initial Uptake of Ozone on Saharan Dust at Atmospheric Relative Humidities. *Geophys. Res. Lett.* 2005, *32*, L14815.
(84) Nakagawa, M.; Ohba, T. Minerals in Volcanic Ash 1: Primary Minerals and Volcanic Glass. *Global Environ. Res.* 2002, *6*, 41–51.
(85) Aðalgeirsdóttir, G.; Jóhannesson, T.; Björnsson, H.; Pálsson, F.; Sigurðsson, O. Response of Hofsjökull and Southern Vatnajökull, Iceland, to Climate Change. *J. Geophys. Res.: Earth Surf.* 2006, *111*, F03001.
(86) Ayris, P. M.; Delmelle, P.; Cimarelli, C.; Maters, E. C.; Suzuki, Y. J.; Dingwell, D. B. HCl Uptake by Volcanic Ash in the High Temperature Eruption Plume: Mechanistic Insights. *Geochim. Cosmochim. Acta* 2014, *144*, 188–201.
(87) Sadanaga, Y.; Hirokawa, J.; Akimoto, H. Formation of Molecular Chlorine in Dark Condition: Heterogeneous Reaction of Ozone with Sea Salt in the Presence of Ferric Ion. *Geophys. Res. Lett.* 2001, *28*, 4433–4436.

Chapter 4

(1) Loganathan, P.; Vigneswaran, S.; Kandasamy, J. Road-Deposited Sediment Pollutants: A Critical Review of Their Characteristics, Source Apportionment, and Management. *Crit. Rev. Environ. Sci. Technol.* **2013**, *43* (13), 1315–1348.
(2) Thorpe, A.; Harrison, R. M. Sources and Properties of Non-Exhaust Particulate Matter from Road Traffic: A Review. *Sci. Total Environ.* **2008**, *400* (1–3), 270–282.
(3) Gunawardana, C.; Goonetilleke, A.; Egodawatta, P.; Dawes, L.; Kokot, S. Source Characterisation of Road Dust Based on Chemical and Mineralogical Composition. *Chemosphere* **2012**, *87* (2), 163–170.
(4) Bukowiecki, N.; Lienemann, P.; Hill, M.; Furger, M.; Richard, A.; Amato, F.; Prévôt, A. S. H.; Baltensperger, U.; Buchmann, B.; Gehrig, R. PM10 Emission Factors for Non-Exhaust Particles Generated by Road Traffic in an Urban Street Canyon and along a Freeway in Switzerland. *Atmos. Environ.* **2010**, *44* (19), 2330–2340.
(5) Zhang, J.; Peng, J.; Song, C.; Ma, C.; Men, Z.; Wu, J.; Wu, L.; Wang, T.; Zhang, X.; Tao, S.; Gao, S.; Hopke, P. K.; Mao, H. Vehicular Non-Exhaust Particulate Emissions in Chinese Megacities: Source Profiles, Real-World Emission Factors, and Inventories. *Environ. Pollut.* **2020**, *266*, 115268.
(6) Han, L.; Zhuang, G.; Cheng, S.; Wang, Y.; Li, J. Characteristics of Re-Suspended Road Dust and Its Impact on the Atmospheric Environment in Beijing. *Atmos. Environ.* **2007**, *41* (35), 7485–7499.
(7) Environment Canada and Health Canada. Canadian Smog Science Assessment: Highlights and Key Messages. 2011.
(8) Canada, T. Building a green economy: Government of Canada to require 100% of car and passenger truck sales be zero-emission by 2035 in Canada https://www.canada.ca/en/transport-canada/news/2021/06/building-a-green-economy-government-of-canada-to-require-100-of-car-and-passenger-truck-sales-be-zero-

emission-by-2035-in-canada.html (accessed 2021 -09 -13).
(9) Zero Emission Fleet vehicles For European Roll-out - TRIMIS - European Commission https://trimis.ec.europa.eu/project/zero-emission-fleet-vehicles-european-roll-out (accessed 2021 -09 -13).
(10) Cote, C. D.; Schneider, S. R.; Lyu, M.; Gao, S.; Gan, L.; Holod, A. J.; Chou, T. H. H.; Styler, S. A. Photochemical Production of Singlet Oxygen by Urban Road Dust. *Environ. Sci. Technol. Lett.* **2018**, *5* (2), 92–97.
(11) Pitts, J. N.; Khan, A. U.; Smith, E. B.; Wayne, R. P. Singlet Oxygen in the Environmental Sciences. Singlet Molecular Oxygen and Photochemical Air Pollution. *Environ. Sci. Technol.* **1969**, *3* (3), 241–247.
(12) Schmidt, M.; Jansen van Beek, S. M.; Abou-Ghanem, M.; Oliynyk, A. O.; Locock, A. J.; Styler, S. A. Production of Atmospheric Organosulfates via Mineral-Mediated Photochemistry. *ACS Earth Space Chem.* **2019**, *3* (3), 424–431.
(13) D. Abbatt, J. P.; Y. Lee, A. K.; A. Thornton, J. Quantifying Trace Gas Uptake to Tropospheric Aerosol: Recent Advances and Remaining Challenges. *Chem. Soc. Rev.* **2012**, *41* (19), 6555–6581.
(14) Hanisch, F.; Crowley, J. N. Ozone Decomposition on Saharan Dust: An Experimental Investigation. *Atmos Chem Phys* **2003**, *3* (1), 119–130.
(15) Abou-Ghanem, M.; Oliynyk, A. O.; Chen, Z.; Matchett, L. C.; McGrath, D. T.; Katz, M. J.; Locock, A. J.; Styler, S. A. Significant Variability in the Photocatalytic Activity of Natural Titanium-Containing Minerals: Implications for Understanding and Predicting Atmospheric Mineral Dust Photochemistry. *Environ. Sci. Technol.* **2020**, *54* (21), 13509–13516.
(16) Wang, X.; Romanias, M. N.; Thévenet, F.; Rousseau, A. Geocatalytic Uptake of Ozone onto Natural Mineral Dust. *Catalysts* **2018**, *8* (7), 263.
(17) Baduel, C.; Monge, M. E.; Voisin, D.; Jaffrezo, J.-L.; George, C.; Haddad, I. E.; Marchand, N.; D'Anna, B. Oxidation of Atmospheric Humic Like Substances by Ozone: A Kinetic and Structural Analysis Approach. *Environ. Sci. Technol.* **2011**, *45* (12), 5238–5244.
(18) Styler, S. A.; Brigante, M.; D'Anna, B.; George, C.; Donaldson, D. J. Photoenhanced Ozone Loss on Solid Pyrene Films. *Phys. Chem. Chem. Phys.* **2009**, *11* (36), 7876–7884.
(19) Seinfeld, J. H.; Pandis, S. N. *Atmospheric Chemistry and Physics: From Air Pollution to Climate Change*; John Wiley & Sons, 2016.
(20) D'Anna, B.; Jammoul, A.; George, C.; Stemmler, K.; Fahrni, S.; Ammann, M.; Wisthaler, A. Light-Induced Ozone Depletion by Humic Acid Films and Submicron Aerosol Particles. *J. Geophys. Res. Atmos.* **2009**, *114* (D12), D12301.
(21) Nan, Y.; Wang, Y. Observational Evidence for Direct Uptake of Ozone in China by Asian Dust in Springtime. *Atmos. Environ.* **2018**, *186*, 45–55.
(22) de Reus, M.; Fischer, H.; Sander, R.; Gros, V.; Kormann, R.; Salisbury, G.; Van Dingenen, R.; Williams, J.; Zöllner, M.; Lelieveld, J. Observations and Model Calculations of Trace Gas Scavenging in a Dense Saharan Dust Plume during MINATROC. *Atmos. Chem. Phys.* **2005**, *5* (7), 1787–1803.

(23) McNamara, S. M.; Kolesar, K. R.; Wang, S.; Kirpes, R. M.; May, N. W.; Gunsch, M. J.; Cook, R. D.; Fuentes, J. D.; Hornbrook, R. S.; Apel, E. C.; China, S.; Laskin, A.; Pratt, K. A. Observation of Road Salt Aerosol Driving Inland Wintertime Atmospheric Chlorine Chemistry. *ACS Cent. Sci.* **2020**, *6* (5), 684–694.
(24) Finlayson-Pitts, B. J.; Ezell, M. J.; Pitts, J. N. Formation of Chemically Active Chlorine Compounds by Reactions of Atmospheric NaCl Particles with Gaseous N2O5 and ClONO2. *Nature* **1989**, *337* (6204), 241–244.
(25) Thornton, J. A.; Kercher, J. P.; Riedel, T. P.; Wagner, N. L.; Cozic, J.; Holloway, J. S.; Dubé, W. P.; Wolfe, G. M.; Quinn, P. K.; Middlebrook, A. M.; Alexander, B.; Brown, S. S. A Large Atomic Chlorine Source Inferred from Mid-Continental Reactive Nitrogen Chemistry. *Nature* **2010**, *464* (7286), 271–274.
(26) Mielke, L. H.; Furgeson, A.; Odame-Ankrah, C. A.; Osthoff, H. D. Ubiquity of ClNO2 in the Urban Boundary Layer of Calgary, Alberta, Canada. *Can. J. Chem.* **2015**, *94* (4), 414–423.
(27) Mielke, L. H.; Furgeson, A.; Osthoff, H. D. Observation of ClNO2 in a Mid-Continental Urban Environment. *Environ. Sci. Technol.* **2011**, *45* (20), 8889–8896.
(28) Rossi, M. J. Heterogeneous Reactions on Salts. *Chem. Rev.* **2003**, *103* (12), 4823–4882.
(29) Finlayson-Pitts, B. J. The Tropospheric Chemistry of Sea Salt: A Molecular-Level View of the Chemistry of NaCl and NaBr. *Chem. Rev.* **2003**, *103* (12), 4801–4822.
(30) Equiza, M. A.; Calvo-Polanco, M.; Cirelli, D.; Señorans, J.; Wartenbe, M.; Saunders, C.; Zwiazek, J. J. Long-Term Impact of Road Salt (NaCl) on Soil and Urban Trees in Edmonton, Canada. *Urban For. Urban Green.* **2017**, *21*, 16–28.
(31) Howard, K. W. F.; Beck, P. J. Hydrogeochemical Implications of Groundwater Contamination by Road De-Icing Chemicals. *J. Contam. Hydrol.* **1993**, *12* (3), 245–268.
(32) Kaushal, S. S.; Groffman, P. M.; Likens, G. E.; Belt, K. T.; Stack, W. P.; Kelly, V. R.; Band, L. E.; Fisher, G. T. Increased Salinization of Fresh Water in the Northeastern United States. *Proc. Natl. Acad. Sci.* **2005**, *102* (38), 13517–13520.
(33) Shi, X.; Veneziano, D.; Xie, N.; Gong, J. Use of Chloride-Based Ice Control Products for Sustainable Winter Maintenance: A Balanced Perspective. *Cold Reg. Sci. Technol.* **2013**, *86*, 104–112.
(34) Rhodan, M.; Sanburn, J. How Beet Juice Is Helping Keep Roads Safe This Winter https://time.com/5761/salt-shortage-triggers-beet-juice-cheese-brine-alternatives/ (accessed 2021 -09 -07).
(35) Daily, P. B. / V. Beet juice, molasses and mag: Colorado's search for the right highway de-icing mixture https://www.skyhinews.com/news/beet-juice-molasses-and-mag-colorados-search-for-the-right-highway-de-icing-mixture/ (accessed 2021 -09 -07).
(36) Berke, J. Cities are starting to put beet juice, beer waste, and pickle brine on icy winter roads to cut down on salt https://www.businessinsider.com/why-cities-put-beet-juice-beer-waste-molasses-on-roads-2018-1 (accessed 2021 -09 -07).
(37) Fu, L.; Omer, R.; Jiang, C. Field Test of Organic Deicers as Prewetting and Anti-Icing Agents for Winter Road Maintenance. *Transp. Res. Rec.* **2012**, *2272* (1), 130–135.

(38) Petkuviene, J.; Paliulis, D. Experimental Research of Road Maintenance Salts and Molasses ("safecote") Corrosive Impact on Metals. *J. Environ. Eng. Landsc. Manag.* **2009**, *17* (4), 236–243.
(39) Honarvar Nazari, M.; Havens, E. A.; Shi, X.; Muthumani, A.; Washington State University. Department of Civil and Environmental Engineering; Western Transportation Institute. *Bio-Based Renewable Additives for Anti-Icing Applications (Phase One)*; INE/CESTiCC 101406; 2016.
(40) Honarvar Nazari, M.; Havens, E. A.; Muthumani, A.; Shi, X. Effects of Processed Agro-Residues on the Performance of Sodium Chloride Brine Anti-Icer. *ACS Sustain. Chem. Eng.* **2019**, *7* (16), 13655–13667.
(41) Shi, X.; Quilty, S. M.; Long, T.; Jayakaran, A.; Fay, L.; Xu, G. Managing Airport Stormwater Containing Deicers: Challenges and Opportunities. *Front. Struct. Civ. Eng.* **2017**, *11* (1), 35–46.
(42) Koryak, M.; Stafford, L. J.; Reilly, R. J.; Hoskin, R. H.; Haberman, M. H. The Impact of Airport Deicing Runoff on Water Quality and Aquatic Life in a Pennsylvania Stream. *J. Freshw. Ecol.* **1998**, *13* (3), 287–298.
(43) Matchett, L. C.; Abou-Ghanem, M.; Stix, K. A. R.; McGrath, D. T.; Styler, S. A. Submitted. Ozone Uptake by Commercial Brake Pads: Assessing the Potential Indirect Air Quality Impacts of Non-Exhaust Emissions. *Submitt. Environ. Sci. Atmos.* **2018**.
(44) Michoud, V.; Colomb, A.; Borbon, A.; Miet, K.; Beekmann, M.; Camredon, M.; Aumont, B.; Perrier, S.; Zapf, P.; Siour, G.; Ait-Helal, W.; Afif, C.; Kukui, A.; Furger, M.; Dupont, J. C.; Haeffelin, M.; Doussin, J. F. Study of the Unknown HONO Daytime Source at a European Suburban Site during the MEGAPOLI Summer and Winter Field Campaigns. *Atmos. Chem. Phys.* **2014**, *14* (6), 2805–2822.
(45) Knopf, D. A.; Pöschl, U.; Shiraiwa, M. Radial Diffusion and Penetration of Gas Molecules and Aerosol Particles through Laminar Flow Reactors, Denuders, and Sampling Tubes. *Anal. Chem.* **2015**, *87* (7), 3746–3754.
(46) Keene, W. C.; Maben, J. R.; Pszenny, A. A. P.; Galloway, J. N. Measurement Technique for Inorganic Chlorine Gases in the Marine Boundary Layer. *Environ. Sci. Technol.* **1993**, *27* (5), 866–874.
(47) Pöschl, U.; Rudich, Y.; Ammann, M. Kinetic Model Framework for Aerosol and Cloud Surface Chemistry and Gas-Particle Interactions–Part 1: General Equations, Parameters, and Terminology. *Atmos. Chem. Phys.* **2007**, *7* (23), 5989–6023.
(48) Kolb, C. E.; Cox, R. A.; Abbatt, J. P. D.; Ammann, M.; Davis, E. J.; Donaldson, D. J.; Garrett, B. C.; George, C.; Griffiths, P. T.; Hanson, D. R.; Kulmala, M.; McFiggans, G.; Pöschl, U.; Riipinen, I.; Rossi, M. J.; Rudich, Y.; Wagner, P. E.; Winkler, P. M.; Worsnop, D. R.; O' Dowd, C. D. An Overview of Current Issues in the Uptake of Atmospheric Trace Gases by Aerosols and Clouds. *Atmos. Chem. Phys.* **2010**, *10* (21), 10561–10605.
(49) Michel, A. E.; Usher, C. R.; Grassian, V. H. Reactive Uptake of Ozone on Mineral Oxides and Mineral Dusts. *Atmos. Environ.* **2003**, *37* (23), 3201–3211.

(50) Coates Fuentes, Z. L.; Kucinski, T. M.; Hinrichs, R. Z. Ozone Decomposition on Kaolinite as a Function of Monoterpene Exposure and Relative Humidity. *ACS Earth Space Chem.* **2017**.
(51) Edmonton Winter Road Maintenance.
(52) City of Edmonton. Shape, Angularity and Petrography of Seven Sucessively Fractioned Street Sweeping Samples. October 2015.
(53) Othman, M.; Latif, M. T. Pollution Characteristics, Sources, and Health Risk Assessments of Urban Road Dust in Kuala Lumpur City. *Environ. Sci. Pollut. Res.* **2020**, *27* (10), 11227–11245.
(54) Tiger Calcium. *Road Guard Plus™ SDS*.
(55) News ·, M. D. · C. First round of city's new salt brine hits Edmonton streets | CBC News https://www.cbc.ca/news/canada/edmonton/salt-brine-roads-edmonton-rust-1.4403846 (accessed 2021 -08 -05).
(56) City of Edmonton. Winter Roads - Frequently Asked Questions https://www.edmonton.ca/transportation/on_your_streets/snow-faq (accessed 2021 -08 -05).
(57) Terry, L. G.; Conaway, K.; Rebar, J.; Graettinger, A. J. Alternative Deicers for Winter Road Maintenance—A Review. *Water. Air. Soil Pollut.* **2020**, *231* (8), 394.
(58) Aryal, R.; Lee, B.-K.; Beecham, S.; Kandasamy, J.; Aryal, N.; Parajuli, K. Characterisation of Road Dust Organic Matter as a Function of Particle Size: A PARAFAC Approach. *Water. Air. Soil Pollut.* **2015**, *226* (2), 24.
(59) Sommer, F.; Dietze, V.; Baum, A.; Sauer, J.; Gilge, S.; Maschowski, C.; Gieré, R. Tire Abrasion as a Major Source of Microplastics in the Environment. *Aerosol Air Qual. Res.* **2018**, *18* (8), 2014–2028.
(60) Nicolas, M.; Ndour, M.; Ka, O.; D'Anna, B.; George, C. Photochemistry of Atmospheric Dust: Ozone Decomposition on Illuminated Titanium Dioxide. *Environ. Sci. Technol.* **2009**, *43* (19), 7437–7442.
(61) Arthur W Adamson; Alice Petry Gast. *Physical Chemistry of Surfaces*; New York: Interscience publishers, 1967; Vol. 15.
(62) Michel A. E.; Usher C. R.; Grassian V. H. Heterogeneous and Catalytic Uptake of Ozone on Mineral Oxides and Dusts: A Knudsen Cell Investigation. *Geophys. Res. Lett.* **2002**, *29* (14), 10–11.
(63) Mogili, P. K.; Kleiber, P. D.; Young, M. A.; Grassian, V. H. Heterogeneous Uptake of Ozone on Reactive Components of Mineral Dust Aerosol: An Environmental Aerosol Reaction Chamber Study. *J. Phys. Chem. A* **2006**, *110* (51), 13799–13807.
(64) Sullivan, R. C.; Thornberry, T.; Abbatt, J. P. D. Ozone Decomposition Kinetics on Alumina: Effects of Ozone Partial Pressure, Relative Humidity and Repeated Oxidation Cycles. *Atmos Chem Phys* **2004**, *4* (5), 1301–1310.
(65) Lasne, J.; Romanias, M. N.; Thevenet, F. Ozone Uptake by Clay Dusts under Environmental Conditions. *ACS Earth Space Chem.* **2018**, *2* (9), 904–914.
(66) Brigante, M.; D'Anna, B.; Conchon, P.; George, C. Multiphase Chemistry of Ozone on

Fulvic Acids Solutions. *Environ. Sci. Technol.* **2008**, *42* (24), 9165–9170.
(67) Moreno, C.; Teresa Baeza-Romero, M. A Kinetic Model for Ozone Uptake by Solutions and Aqueous Particles Containing I – and Br – , Including Seawater and Sea-Salt Aerosol. *Phys. Chem. Chem. Phys.* **2019**, *21* (36), 19835–19856.
(68) Li, W.; Oyama, S. T. Mechanism of Ozone Decomposition on a Manganese Oxide Catalyst. 2. Steady-State and Transient Kinetic Studies. *J. Am. Chem. Soc.* **1998**, *120* (35), 9047–9052.
(69) Dong, T. T. T.; Lee, B.-K. Characteristics, Toxicity, and Source Apportionment of Polycylic Aromatic Hydrocarbons (PAHs) in Road Dust of Ulsan, Korea. *Chemosphere* **2009**, *74* (9), 1245–1253.
(70) Murakami, M.; Nakajima, F.; Furumai, H. Size- and Density-Distributions and Sources of Polycyclic Aromatic Hydrocarbons in Urban Road Dust. *Chemosphere* **2005**, *61* (6), 783–791.
(71) Han, Y. M.; Cao, J. J.; Chow, J. C.; Watson, J. G.; An, Z. S.; Liu, S. X. Elemental Carbon in Urban Soils and Road Dusts in Xi'an, China and Its Implication for Air Pollution. *Atmos. Environ.* **2009**, *43* (15), 2464–2470.
(72) Cope, V. W.; Kalkwarf, D. R. Photooxidation of Selected Polycyclic Aromatic Hydrocarbons and Pyrenequinones Coated on Glass Surfaces. *Environ. Sci. Technol.* **1987**, *21* (7), 643–648.
(73) Zelenay, V.; Monge, M. E.; D'Anna, B.; George, C.; Styler, S. A.; Huthwelker, T.; Ammann, M. Increased Steady State Uptake of Ozone on Soot Due to UV/Vis Radiation. *J. Geophys. Res. Atmos.* **2011**, *116* (D11), D11301.
(74) Abbatt, J. P. D.; Waschewsky, G. C. G. Heterogeneous Interactions of HOBr, HNO3, O3, and NO2 with Deliquescent NaCl Aerosols at Room Temperature. *J. Phys. Chem. A* **1998**, *102* (21), 3719–3725.
(75) Sadanaga, Y.; Hirokawa, J.; Akimoto, H. Formation of Molecular Chlorine in Dark Condition: Heterogeneous Reaction of Ozone with Sea Salt in the Presence of Ferric Ion. *Geophys. Res. Lett.* **2001**, *28* (23), 4433–4436.
(76) Salazar, J. R.; Cartledge, B. T.; Haynes, J. P.; York-Marini, R.; Robinson, A. L.; Drozd, G. T.; Goldstein, A. H.; Fakra, S. C.; Majestic, B. J. Water-Soluble Iron Emitted from Vehicle Exhaust Is Linked to Primary Speciated Organic Compounds. *Atmos. Chem. Phys.* **2020**, *20* (3), 1849–1860.
(77) Marcotte, A. R.; Anbar, A. D.; Majestic, B. J.; Herckes, P. Mineral Dust and Iron Solubility: Effects of Composition, Particle Size, and Surface Area. *Atmos.* **2020**, *11* (5), 533.
(78) Chen, H.; Stanier, C. O.; Young, M. A.; Grassian, V. H. A Kinetic Study of Ozone Decomposition on Illuminated Oxide Surfaces. *J. Phys. Chem. A* **2011**, *115* (43), 11979–11987.
(79) Hoffmann, M. R.; Martin, S. T.; Choi, W.; Bahnemann, D. W. Environmental Applications of Semiconductor Photocatalysis. *Chem. Rev.* **1995**, *95* (1), 69–96.
(80) George, C.; D'Anna, B.; Herrmann, H.; Weller, C.; Vaida, V.; Donaldson, D. J.; Bartels-

Rausch, T.; Ammann, M. Emerging Areas in Atmospheric Photochemistry. In *Atmospheric and Aerosol Chemistry*; Topics in Current Chemistry; Springer, Berlin, Heidelberg, 2012; pp 1–53.

(81) Jammoul, A.; Gligorovski, S.; George, C.; D'Anna, B. Photosensitized Heterogeneous Chemistry of Ozone on Organic Films. *J. Phys. Chem. A* **2008**, *112* (6), 1268–1276.

(82) Rubasinghege, G.; H. Grassian, V. Role(s) of Adsorbed Water in the Surface Chemistry of Environmental Interfaces. *Chem. Commun.* **2013**, *49* (30), 3071–3094.

(83) Chang, R. Y.-W.; Sullivan, R. C.; Abbatt, J. P. D. Initial Uptake of Ozone on Saharan Dust at Atmospheric Relative Humidities. *Geophys. Res. Lett.* **2005**, *32* (14), L14815.

(84) Abou-Ghanem, M.; Jensen, B. J. L.; Styler, S. A.; Romanias, M. N. Ozone Chemistry and Photochemistry at the Surface of Icelandic Volcanic Dust: Insights from Elemental Speciation Analysis. *Accepted. ACS Earth Space Chem.* **2021**.

(85) Pöschl, U.; Letzel, T.; Schauer, C.; Niessner, R. Interaction of Ozone and Water Vapor with Spark Discharge Soot Aerosol Particles Coated with Benzo[a]Pyrene: O3 and H2O Adsorption, Benzo[a]Pyrene Degradation, and Atmospheric Implications. *J. Phys. Chem. A* **2001**, *105* (16), 4029–4041.

(86) Redwood, P. S.; Lead, J. R.; Harrison, R. M.; Jones, I. P.; Stoll, S. Characterization of Humic Substances by Environmental Scanning Electron Microscopy. *Environ. Sci. Technol.* **2005**, *39* (7), 1962–1966.

(87) Tang, I. N.; Tridico, A. C.; Fung, K. H. Thermodynamic and Optical Properties of Sea Salt Aerosols. *J. Geophys. Res. Atmos.* **1997**, *102* (D19), 23269–23275.

(88) Palmonari, A.; Cavallini, D.; Sniffen, C. J.; Fernandes, L.; Holder, P.; Fagioli, L.; Fusaro, I.; Biagi, G.; Formigoni, A.; Mammi, L. Short Communication: Characterization of Molasses Chemical Composition. *J. Dairy Sci.* **2020**, *103* (7), 6244–6249.

(89) Chandra, R.; Bharagava, R. N.; Rai, V. Melanoidins as Major Colourant in Sugarcane Molasses Based Distillery Effluent and Its Degradation. *Bioresour. Technol.* **2008**, *99* (11), 4648–4660.

(90) Hodge, J. E. Dehydrated Foods, Chemistry of Browning Reactions in Model Systems. *J. Agric. Food Chem.* **1953**, *1* (15), 928–943.

(91) Peña, M.; Coca, M.; González, G.; Rioja, R.; García, M. T. Chemical Oxidation of Wastewater from Molasses Fermentation with Ozone. *Chemosphere* **2003**, *51* (9), 893–900.

(92) Shiraiwa, M.; Sosedova, Y.; Rouvière, A.; Yang, H.; Zhang, Y.; Abbatt, J. P. D.; Ammann, M.; Pöschl, U. The Role of Long-Lived Reactive Oxygen Intermediates in the Reaction of Ozone with Aerosol Particles. *Nat. Chem.* **2011**, *3* (4), 291–295.

(93) Liu, F.; Lakey, P. S. J.; Berkemeier, T.; Tong, H.; Kunert, A. T.; Meusel, H.; Cheng, Y.; Su, H.; Fröhlich-Nowoisky, J.; Lai, S.; Weller, M. G.; Shiraiwa, M.; Pöschl, U.; Kampf, C. J. Atmospheric Protein Chemistry Influenced by Anthropogenic Air Pollutants: Nitration and Oligomerization upon Exposure to Ozone and Nitrogen Dioxide. *Faraday Discuss.* **2017**, *200* (0), 413–427.

(94) Shiraiwa, M.; Selzle, K.; Yang, H.; Sosedova, Y.; Ammann, M.; Pöschl, U. Multiphase

Chemical Kinetics of the Nitration of Aerosolized Protein by Ozone and Nitrogen Dioxide. *Environ. Sci. Technol.* **2012**, *46* (12), 6672–6680.

(95) Moise, T.; Rudich, Y. Reactive Uptake of Ozone by Aerosol-Associated Unsaturated Fatty Acids: Kinetics, Mechanism, and Products. *J. Phys. Chem. A* **2002**, *106* (27), 6469–6476.

(96) Eliason, T. L.; Aloisio, S.; Donaldson, D. J.; Cziczo, D. J.; Vaida, V. Processing of Unsaturated Organic Acid Films and Aerosols by Ozone. *Atmos. Environ.* **2003**, *37* (16), 2207–2219.

(97) Usher, C. R.; Michel, A. E.; Stec, D.; Grassian, V. H. Laboratory Studies of Ozone Uptake on Processed Mineral Dust. *Atmos. Environ.* **2003**, *37* (38), 5337–5347.

(98) Sakamoto, Y.; Enami, S.; Tonokura, K. Enhancement of Gaseous Iodine Emission by Aqueous Ferrous Ions during the Heterogeneous Reaction of Gaseous Ozone with Aqueous Iodide. *J. Phys. Chem. A* **2013**, *117* (14), 2980–2986.

(99) Jain, R.; Venkatasubramanian, P. Sugarcane Molasses – A Potential Dietary Supplement in the Management of Iron Deficiency Anemia. *J. Diet. Suppl.* **2017**, *14* (5), 589–598.

(100) Criegee, R. Mechanism of Ozonolysis. *Angew. Chem. Int. Ed. Engl.* **1975**, *14* (11), 745–752.

(101) Kroll, J. H.; Sahay, S. R.; Anderson, J. G.; Demerjian, K. L.; Donahue, N. M. Mechanism of HOx Formation in the Gas-Phase Ozone-Alkene Reaction. 2. Prompt versus Thermal Dissociation of Carbonyl Oxides to Form OH. *J. Phys. Chem. A* **2001**, *105* (18), 4446–4457.

(102) Kroll, J. H.; Donahue, N. M.; Cee, V. J.; Demerjian, K. L.; Anderson, J. G. Gas-Phase Ozonolysis of Alkenes: Formation of OH from Anti Carbonyl Oxides. *J. Am. Chem. Soc.* **2002**, *124* (29), 8518–8519.

(103) Siese, M.; Becker, K. H.; Brockmann, K. J.; Geiger, H.; Hofzumahaus, A.; Holland, F.; Mihelcic, D.; Wirtz, K. Direct Measurement of OH Radicals from Ozonolysis of Selected Alkenes: A EUPHORE Simulation Chamber Study. *Environ. Sci. Technol.* **2001**, *35* (23), 4660–4667.

(104) Knipping, E. M.; Dabdub, D. Modeling Cl2 Formation from Aqueous NaCl Particles: Evidence for Interfacial Reactions and Importance of Cl2 Decomposition in Alkaline Solution. *J. Geophys. Res. Atmos.* **2002**, *107* (D18), ACH 8-1-ACH 8-30.

(105) Faxon, C. B.; Dhulipala, S. V.; Allen, D. T.; Ruiz, L. H. Heterogeneous Production of Cl2 from Particulate Chloride: Effects of Composition and Relative Humidity. *AIChE J.* **2018**, *64* (8), 3151–3158.

(106) Li, M.; Su, H.; Li, G.; Ma, N.; Pöschl, U.; Cheng, Y. Relative Importance of Gas Uptake on Aerosol and Ground Surfaces Characterized by Equivalent Uptake Coefficients. *Atmos. Chem. Phys.* **2019**, *19* (16), 10981–11011.

(107) McNamara, S. M.; Kolesar, K. R.; Wang, S.; Kirpes, R. M.; May, N. W.; Gunsch, M. J.; Cook, R. D.; Fuentes, J. D.; Hornbrook, R. S.; Apel, E. C.; China, S.; Laskin, A.; Pratt, K. A. Observation of Road Salt Aerosol Driving Inland Wintertime Atmospheric Chlorine Chemistry. *ACS Cent. Sci.* **2020**, *6* (5), 684–694.

(108) Casotti Rienda, I.; Alves, C. A. Road Dust Resuspension: A Review. *Atmos. Res.* **2021**, *261*, 105740.
(109) Amato, F.; Pandolfi, M.; Escrig, A.; Querol, X.; Alastuey, A.; Pey, J.; Perez, N.; Hopke, P. K. Quantifying Road Dust Resuspension in Urban Environment by Multilinear Engine: A Comparison with PMF2. *Atmos. Environ.* **2009**, No. 43, 2770–2780.
(110) Wren, S. N.; Donaldson, D. J.; Abbatt, J. P. D. Photochemical Chlorine and Bromine Activation from Artificial Saline Snow. *Atmos. Chem. Phys.* **2013**, *13* (19), 9789–9800.
(111) Thornton, J. A.; Abbatt, J. P. D. N2O5 Reaction on Submicron Sea Salt Aerosol: Kinetics, Products, and the Effect of Surface Active Organics. *J. Phys. Chem. A* **2005**, *109* (44), 10004–10012.
(112) McNeill, V. F.; Patterson, J.; Wolfe, G. M.; Thornton, J. A. The Effect of Varying Levels of Surfactant on the Reactive Uptake of N_2O_5 to Aqueous Aerosol. *Atmos. Chem. Phys.* **2006**, *6* (6), 1635–1644.
(113) Ryder, O. S.; Campbell, N. R.; Shaloski, M.; Al-Mashat, H.; Nathanson, G. M.; Bertram, T. H. Role of Organics in Regulating ClNO2 Production at the Air–Sea Interface. *J. Phys. Chem. A* **2015**, *119* (31), 8519–8526.
(114) Feuer, H. *The Nitro Group in Organic Synthesis*, 1st ed.; John Wiley & Sons, Ltd, 2001.
(115) Stutz, J.; Alicke, B.; Ackermann, R.; Geyer, A.; White, A.; Williams, E. Vertical Profiles of NO3, N2O5, O3, and NOx in the Nocturnal Boundary Layer: 1. Observations during the Texas Air Quality Study 2000. *J. Geophys. Res. Atmos.* **2004**, *109* (D12).
(116) Slemr, F.; Seiler, W. Field Study of Environmental Variables Controlling the NO Emissions from Soil and the NO Compensation Point. *J. Geophys. Res. Atmos.* **1991**, *96* (D7), 13017–13031.
(117) Li, N.; Jiang, Q.; Wang, F.; Cui, P.; Xie, J.; Li, J.; Wu, S.; Barbieri, D. M. Comparative Assessment of Asphalt Volatile Organic Compounds Emission from Field to Laboratory. *J. Clean. Prod.* **2021**, *278*, 123479.
(118) Fay, L.; Shi, X. Environmental Impacts of Chemicals for Snow and Ice Control: State of the Knowledge. *Water. Air. Soil Pollut.* **2012**, *223* (5), 2751–2770.
(119) Herrmann, H.; Schaefer, T.; Tilgner, A.; Styler, S. A.; Weller, C.; Teich, M.; Otto, T. Tropospheric Aqueous-Phase Chemistry: Kinetics, Mechanisms, and Its Coupling to a Changing Gas Phase. *Chem. Rev.* **2015**, *115* (10), 4259–4334.

Chapter 5

(1) Sakata, K.; Takahashi, Y.; Takano, S.; Matsuki, A.; Sakaguchi, A.; Tanimoto, H. First X-Ray Spectroscopic Observations of Atmospheric Titanium Species: Size Dependence and the Emission Source. *Environ. Sci. Technol.* **2021**, *55* (16), 10975–10986.
(2) Usher, C. R.; Michel, A. E.; Stec, D.; Grassian, V. H. Laboratory Studies of Ozone Uptake on Processed Mineral Dust. *Atmos. Environ.* **2003**, *37* (38), 5337–5347.

(3) Coates Fuentes, Z. L.; Kucinski, T. M.; Hinrichs, R. Z. Ozone Decomposition on Kaolinite as a Function of Monoterpene Exposure and Relative Humidity. *ACS Earth Space Chem.* **2018**, *2* (1), 21–30.
(4) Drew, R. T.; Bernstein, D. M.; Laskin, S. The Laskin Aerosol Generator. *J. Toxicol. Environ. Health* **1978**, *4* (4), 661–670.
(5) Alam, M. S.; Zeraati-Rezaei, S.; Liang, Z.; Stark, C.; Xu, H.; MacKenzie, A. R.; Harrison, R. M. Mapping and Quantifying Isomer Sets of Hydrocarbons (≥ C₁₂) in Diesel Exhaust, Lubricating Oil and Diesel Fuel Samples Using GC × GC-ToF-MS. *Atmospheric Meas. Tech.* **2018**, *11* (5), 3047–3058.
(6) Thomas, E. R.; Frost, G. J.; Rudich, Y. Reactive Uptake of Ozone by Proxies for Organic Aerosols: Surface-Bound and Gas-Phase Products. *J. Geophys. Res. Atmospheres* **2001**, *106* (D3), 3045–3056.
(7) Kolb, C. E.; Cox, R. A.; Abbatt, J. P. D.; Ammann, M.; Davis, E. J.; Donaldson, D. J.; Garrett, B. C.; George, C.; Griffiths, P. T.; Hanson, D. R.; Kulmala, M.; McFiggans, G.; Pöschl, U.; Riipinen, I.; Rossi, M. J.; Rudich, Y.; Wagner, P. E.; Winkler, P. M.; Worsnop, D. R.; O' Dowd, C. D. An Overview of Current Issues in the Uptake of Atmospheric Trace Gases by Aerosols and Clouds. *Atmospheric Chem. Phys.* **2010**, *10* (21), 10561–10605.
(8) Nicolas, M.; Ndour, M.; Ka, O.; D'Anna, B.; George, C. Photochemistry of Atmospheric Dust: Ozone Decomposition on Illuminated Titanium Dioxide. *Environ. Sci. Technol.* **2009**, *43* (19), 7437–7442.
(9) Abou-Ghanem, M.; Oliynyk, A. O.; Chen, Z.; Matchett, L. C.; McGrath, D. T.; Katz, M. J.; Locock, A. J.; Styler, S. A. Significant Variability in the Photocatalytic Activity of Natural Titanium-Containing Minerals: Implications for Understanding and Predicting Atmospheric Mineral Dust Photochemistry. *Environ. Sci. Technol.* **2020**, *54* (21), 13509–13516.
(10) Romay, F. J.; Takagaki, S. S.; Pui, D. Y. H.; Liu, B. Y. H. Thermophoretic Deposition of Aerosol Particles in Turbulent Pipe Flow. *J. Aerosol Sci.* **1998**, *29* (8), 943–959.
(11) Dyson, J. E.; Boustead, G. A.; Fleming, L. T.; Blitz, M.; Stone, D.; Arnold, S. R.; Whalley, L. K.; Heard, D. E. Production of HONO from NO_2 Uptake on Illuminated TiO_2 Aerosol Particles and Following the Illumination of Mixed TiO_2/ammonium Nitrate Particles. *Atmospheric Chem. Phys.* **2021**, *21* (7), 5755–5775.

Chapter 6

(1) Woodward, S.; Roberts, D. L.; Betts, R. A. A Simulation of the Effect of Climate Change–Induced Desertification on Mineral Dust Aerosol. *Geophys. Res. Lett.* **2005**, *32* (18).
(2) Bliss, A.; Hock, R.; Radić, V. Global Response of Glacier Runoff to Twenty-First Century Climate Change. *J. Geophys. Res. Earth Surf.* **2014**, *119* (4), 717–730.
(3) Bullard, J. E.; Baddock, M.; Bradwell, T.; Crusius, J.; Darlington, E.; Gaiero, D.; Gassó, S.; Gisladottir, G.; Hodgkins, R.; McCulloch, R.; McKenna-Neuman, C.; Mockford, T.; Stewart, H.; Thorsteinsson, T. High-Latitude Dust in the Earth System. *Rev. Geophys.* **2016**, *54* (2), 447–485.

(4) Bachelder, J.; Cadieux, M.; Liu-Kang, C.; Lambert, P.; Filoche, A.; Galhardi, J. A.; Hadioui, M.; Chaput, A.; Bastien-Thibault, M.-P.; Wilkinson, K. J.; King, J.; Hayes, P. L. Chemical and Microphysical Properties of Wind-Blown Dust near an Actively Retreating Glacier in Yukon, Canada. *Aerosol Sci. Technol.* **2020**, *54* (1), 2–20.
(5) World Health Organization. Ambient (outdoor) air pollution https://www.who.int/news-room/fact-sheets/detail/ambient-(outdoor)-air-quality-and-health (accessed 2021 -10 -14).
(6) Urupina, D.; Lasne, J.; Romanias, M. N.; Thiery, V.; Dagsson-Waldhauserova, P.; Thevenet, F. Uptake and Surface Chemistry of SO2 on Natural Volcanic Dusts. *Atmos. Environ.* **2019**, *217*, 116942.
(7) Abou-Ghanem, M.; Jensen, B. J. L.; Styler, S. A.; Romanias, M. N. Accepted. Ozone Chemistry and Photochemistry at the Surface of Icelandic Volcanic Dust: Insights from Elemental Speciation Analysis. *ACS Earth Space Chem.* **2021**.
(8) Zero Emission Fleet vehicles For European Roll-out - TRIMIS - European Commission https://trimis.ec.europa.eu/project/zero-emission-fleet-vehicles-european-roll-out (accessed 2021 -09 -13).
(9) Canada, T. Building a green economy: Government of Canada to require 100% of car and passenger truck sales be zero-emission by 2035 in Canada https://www.canada.ca/en/transport-canada/news/2021/06/building-a-green-economy-government-of-canada-to-require-100-of-car-and-passenger-truck-sales-be-zero-emission-by-2035-in-canada.html (accessed 2021 -09 -13).
(10) Beddows, D. C. S.; Harrison, R. M. PM_{10} and $PM_{2.5}$ Emission Factors for Non-Exhaust Particles from Road Vehicles: Dependence upon Vehicle Mass and Implications for Battery Electric Vehicles. *Atmos. Environ.* **2021**, *244*, 117886.
(11) Matchett, L. C.; Abou-Ghanem, M.; Stix, K. A. R.; McGrath, D. T.; Styler, S. A. Accepted. Ozone Uptake by Commercial Brake Pads: Assessing the Potential Indirect Air Quality Impacts of Non-Exhaust Emissions. *Environ. Sci. Atmospheres* **2021**.
(12) Burghardt, T. E.; Pashkevich, A. Green Public Procurement Criteria for Road Marking Materials from Insiders' Perspective. *J. Clean. Prod.* **2021**, *298*, 126521.
(13) Toro, C.; Jobson, B. T.; Haselbach, L.; Shen, S.; Chung, S. H. Photoactive Roadways: Determination of CO, NO and VOC Uptake Coefficients and Photolabile Side Product Yields on TiO_2 Treated Asphalt and Concrete. *Atmos. Environ.* **2016**, *139*, 37–45.
(14) Xie, X.; Hao, C.; Huang, Y.; Huang, Z. Influence of TiO_2-Based Photocatalytic Coating Road on Traffic-Related NO_x Pollutants in Urban Street Canyon by CFD Modeling. *Sci. Total Environ.* **2020**, *724*, 138059.
(15) Fujishima, A.; Zhang, X.; Tryk, D. A. TiO_2 Photocatalysis and Related Surface Phenomena. *Surf. Sci. Rep.* **2008**, *63* (12), 515–582.
(16) Li, Y.; Nie, W.; Liu, Y.; Huang, D.; Xu, Z.; Peng, X.; George, C.; Yan, C.; Tham, Y. J.; Yu, C.; Xia, M.; Fu, X.; Wang, X.; Xue, L.; Wang, Z.; Xu, Z.; Chi, X.; Wang, T.; Ding, A. Photoinduced Production of Chlorine Molecules from Titanium Dioxide Surfaces Containing Chloride. *Environ. Sci. Technol. Lett.* **2020**, *7* (2), 70–75.

(17) Ndour, M.; D'Anna, B.; George, C.; Ka, O.; Balkanski, Y.; Kleffmann, J.; Stemmler, K.; Ammann, M. Photoenhanced Uptake of NO<sub>2<sub> on mineral dust: Laboratory experiments and model simulations. *Geophys. Res. Lett.* **2008**, *35* (5), L05812.
(18) Dyson, J. E.; Boustead, G. A.; Fleming, L. T.; Blitz, M.; Stone, D.; Arnold, S. R.; Whalley, L. K.; Heard, D. E. Production of HONO from NO_2 Uptake on Illuminated TiO_2 Aerosol Particles and Following the Illumination of Mixed TiO_2/ammonium Nitrate Particles. *Atmospheric Chem. Phys.* **2021**, *21* (7), 5755–5775.
(19) Ayris, P. M.; Delmelle, P.; Cimarelli, C.; Maters, E. C.; Suzuki, Y. J.; Dingwell, D. B. HCl Uptake by Volcanic Ash in the High Temperature Eruption Plume: Mechanistic Insights. *Geochim. Cosmochim. Acta* **2014**, *144*, 188–201.
(20) Buck, B. J.; King, J.; Etyemezian, V. Effects of Salt Mineralogy on Dust Emissions, Salton Sea, California. *Soil Sci. Soc. Am. J.* **2011**, *75* (5), 1971–1985.
(21) Groß, S.; Tesche, M.; Freudenthaler, V.; Toledano, C.; Wiegner, M.; Ansmann, A.; Althausen, D.; Seefeldner, M. Characterization of Saharan Dust, Marine Aerosols and Mixtures of Biomass-Burning Aerosols and Dust by Means of Multi-Wavelength Depolarization and Raman Lidar Measurements during SAMUM 2. *Tellus B Chem. Phys. Meteorol.* **2011**, *63* (4), 706–724.
(22) McNamara, S. M.; Kolesar, K. R.; Wang, S.; Kirpes, R. M.; May, N. W.; Gunsch, M. J.; Cook, R. D.; Fuentes, J. D.; Hornbrook, R. S.; Apel, E. C.; China, S.; Laskin, A.; Pratt, K. A. Observation of Road Salt Aerosol Driving Inland Wintertime Atmospheric Chlorine Chemistry. *ACS Cent. Sci.* **2020**, *6* (5), 684–694.
(23) Abou-Ghanem, M.; Nodeh-Farahani, D.; McGrath, D. T.; VandenBoer, T. C.; Styler, S. A. Submitted. Ozone Uptake and Halogen Activation by Road Dust and Anti-Icing Solution: Implications for Wintertime Air Quality in High-Latitude Urban Environments. *Environ. Sci. Process. Impacts* **2021**.
(24) Mitroo, D.; Gill, T. E.; Haas, S.; Pratt, K. A.; Gaston, C. J. $ClNO_2$ Production from N_2O_5 Uptake on Saline Playa Dusts: New Insights into Potential Inland Sources of $ClNO_2$. *Environ. Sci. Technol.* **2019**, *53* (13), 7442–7452.
(25) Sadanaga, Y.; Hirokawa, J.; Akimoto, H. Formation of Molecular Chlorine in Dark Condition: Heterogeneous Reaction of Ozone with Sea Salt in the Presence of Ferric Ion. *Geophys. Res. Lett.* **2001**, *28* (23), 4433–4436.
(26) Shi, Z.; Krom, M. D.; Bonneville, S.; Baker, A. R.; Bristow, C.; Drake, N.; Mann, G.; Carslaw, K.; McQuaid, J. B.; Jickells, T.; Benning, L. G. Influence of Chemical Weathering and Aging of Iron Oxides on the Potential Iron Solubility of Saharan Dust during Simulated Atmospheric Processing. *Glob. Biogeochem. Cycles* **2011**, *25* (2).

Appendix A

(1) Parrish, D. D.; Murphy, P. C.; Albritton, D. L.; Fehsenfeld, F. C. The Measurement of the Photodissociation Rate of NO2 in the Atmosphere. *Atmos. Environ.* **1983**, *17* (7), 1365–1379. https://doi.org/10.1016/0004-6981(83)90411-0.

(2) Zafonte, L.; Rieger, P. L.; Holmes, J. R. Nitrogen Dioxide Photolysis in the Los Angeles Atmosphere. *Environ. Sci. Technol.* **1977**, *11* (5), 483–487.
(3) Nicolas, M.; Ndour, M.; Ka, O.; D'Anna, B.; George, C. Photochemistry of Atmospheric Dust: Ozone Decomposition on Illuminated Titanium Dioxide. *Environ. Sci. Technol.* **2009**, *43* (19), 7437–7442. https://doi.org/10.1021/es901569d.
(4) Pöschl, U.; Rudich, Y.; Ammann, M. Kinetic Model Framework for Aerosol and Cloud Surface Chemistry and Gas-Particle Interactions–Part 1: General Equations, Parameters, and Terminology. *Atmos. Chem. Phys.* **2007**, *7* (23), 5989–6023.
(5) Michel, A. E.; Usher, C. R.; Grassian, V. H. Reactive Uptake of Ozone on Mineral Oxides and Mineral Dusts. *Atmos. Environ.* **2003**, *37* (23), 3201–3211. https://doi.org/10.1016/S1352-2310(03)00319-4.
(6) Adams, J. W.; Rodriguez, D.; Cox, R. A. The Uptake of SO2 on Saharan Dust: A Flow Tube Study. *Atmos. Chem. Phys.* **2005**, *5* (10), 2679–2689.
(7) El Zein, A.; Bedjanian, Y. Interaction of NO2 with TiO2 Surface under UV Irradiation: Measurements of the Uptake Coefficient. *Atmos. Chem. Phys.* **2012**, *12* (2), 1013–1020. https://doi.org/10.5194/acp-12-1013-2012.
(8) Lasne, J.; Romanias, M. N.; Thevenet, F. Ozone Uptake by Clay Dusts under Environmental Conditions. *ACS Earth Space Chem.* **2018**, *2* (9), 904–914. https://doi.org/10.1021/acsearthspacechem.8b00057.
(9) Wang, X.; Romanias, M. N.; Thévenet, F.; Rousseau, A. Geocatalytic Uptake of Ozone onto Natural Mineral Dust. *Catalysts* **2018**, *8* (7), 263. https://doi.org/10.3390/catal8070263.
(10) Knopf, D. A.; Pöschl, U.; Shiraiwa, M. Radial Diffusion and Penetration of Gas Molecules and Aerosol Particles through Laminar Flow Reactors, Denuders, and Sampling Tubes. *Anal. Chem.* **2015**, *87* (7), 3746–3754. https://doi.org/10.1021/ac5042395.
(11) Sing, K. S. W. Adsorption by Powders and Porous Solids. In *Adsorption by Powders and Porous Solids (Second Edition)*; Rouquerol, F., Rouquerol, J., Sing, K. S. W., Llewellyn, P., Maurin, G., Eds.; Academic Press: Oxford, 2014; pp 237–268. https://doi.org/10.1016/B978-0-08-097035-6.00007-3.
(12) Donovan, J. J.; Kremser, D.; Fournelle, J. H.; Goemann, K. *Probe for EPMA: Acquisition, Automation and Analysis, Version 11*; Eugene, Oregon, Probe Software, Inc., 2015.
(13) Donovan, J. J.; Snyder, D. A.; Rivers, M. L. *An Improved Interference Correction for Trace Element Analysis*, 2nd ed.; Microbeam Analysis, 1993.
(14) Armstrong, J. T. *CITZAF: A Package of Correction Programs for the Quantitative Electron Microbeam X-Ray-Analysis of Thick Polished Materials, Thin-Films, and Particles*; Microbeam Analysis 4, 1995.
(15) Jarosewich, E.; Nelen, J. A.; Norberg, J. A. *Reference Samples for Electron Microprobe Analysis*, 4th ed.; Geostand. Geoanal. Res, 1980.
(16) Gates-Rector, S.; Blanton, T. The Powder Diffraction File: A Quality Materials Characterization Database. *Powder Diffraction* **2019**, *34* (4), 352–360. https://doi.org/10.1017/S0885715619000812.
(17) Jade 9.5; Materials Data: Livermore, CA. 2019.
(18) TOPAS V4: General Profile and Structure Analysis Software for Powder Diffraction Data. - User's Manual, Bruker AXS, Karlsruhe, Germany. Bruker AXS (2008).
(19) Pawley, G. S. Unit-Cell Refinement from Powder Diffraction Scans. *J. Appl. Cryst.* **1981**, *14* (6), 357–361. https://doi.org/10.1107/S0021889881009618.
(20) Bruker AXS Inc. *Version, S. A. D. A. B. S.*; Madison WI, USA, 2001.

(21) Sheldrick, G. M. SHELXTL, Version 6.12. Bruker AXS Inc.: Madison, WI 2001.
(22) Kortüm, G. *Reflectance Spectroscopy: Principles, Methods, Applications*; Springer Science & Business Media, 2012.
(23) Murphy, A. B. Band-Gap Determination from Diffuse Reflectance Measurements of Semiconductor Films, and Application to Photoelectrochemical Water-Splitting. *Sol. Energy Mater. Sol. Cell* **2007**, *91* (14), 1326–1337. https://doi.org/10.1016/j.solmat.2007.05.005.
(24) Jenkins, R.; Snyder, R. *Introduction to X-Ray Powder Diffractometry*; Wiley: New York, 1996.
(25) Sullivan, R. C.; Thornberry, T.; Abbatt, J. P. D. Ozone Decomposition Kinetics on Alumina: Effects of Ozone Partial Pressure, Relative Humidity and Repeated Oxidation Cycles. *Atmos. Chem. Phys.* **2004**, *4* (5), 1301–1310. https://doi.org/10.5194/acp-4-1301-2004.
(26) Li, W.; Gibbs, G. V.; Oyama, S. T. Mechanism of Ozone Decomposition on a Manganese Oxide Catalyst. 1. In Situ Raman Spectroscopy and Ab Initio Molecular Orbital Calculations. *J. Am. Chem. Soc.* **1998**, *120* (35), 9041–9046. https://doi.org/10.1021/ja981441+.
(27) Hanisch, F.; Crowley, J. N. Ozone Decomposition on Saharan Dust: An Experimental Investigation. *Atmos. Chem. Phys.* **2003**, *3* (1), 119–130. https://doi.org/10.5194/acp-3-119-2003.
(28) Michel A. E.; Usher C. R.; Grassian V. H. Heterogeneous and Catalytic Uptake of Ozone on Mineral Oxides and Dusts: A Knudsen Cell Investigation. *Geophys. Res. Lett.* **2002**, *29* (14), 10–11. https://doi.org/10.1029/2002GL014896.
(29) Coates Fuentes, Z. L.; Kucinski, T. M.; Hinrichs, R. Z. Ozone Decomposition on Kaolinite as a Function of Monoterpene Exposure and Relative Humidity. *ACS Earth Space Chem.* **2017**. https://doi.org/10.1021/acsearthspacechem.7b00107.
(30) Mogili, P. K.; Kleiber, P. D.; Young, M. A.; Grassian, V. H. Heterogeneous Uptake of Ozone on Reactive Components of Mineral Dust Aerosol: An Environmental Aerosol Reaction Chamber Study. *J. Phys. Chem. A* **2006**, *110* (51), 13799–13807. https://doi.org/10.1021/jp063620g.
(31) Chen, H.; Stanier, C. O.; Young, M. A.; Grassian, V. H. A Kinetic Study of Ozone Decomposition on Illuminated Oxide Surfaces. *J. Phys. Chem. A* **2011**, *115* (43), 11979–11987. https://doi.org/10.1021/jp208164v.
(32) Maters, E. C.; Delmelle, P.; Rossi, M. J.; Ayris, P. M.; Bernard, A. Controls on the Surface Chemical Reactivity of Volcanic Ash Investigated with Probe Gases. *Earth Planet. Sci. Lett.* **2016**, *450*, 254–262. https://doi.org/10.1016/j.epsl.2016.06.044.
(33) Bulanin, K. M.; Lavalley, J. C.; Tsyganenko, A. A. IR Spectra of Adsorbed Ozone. *Colloids Surf. A Physicochem. Eng. Asp.* **1995**, *101* (2), 153–158. https://doi.org/10.1016/0927-7757(95)03130-6.
(34) Lampimäki, M.; Zelenay, V.; Křepelová, A.; Liu, Z.; Chang, R.; Bluhm, H.; Ammann, M. Ozone-Induced Band Bending on Metal-Oxide Surfaces Studied under Environmental Conditions. *ChemPhysChem* **2013**, *14* (11), 2419–2425. https://doi.org/10.1002/cphc.201300418.
(35) Li, W.; Oyama, S. T. Mechanism of Ozone Decomposition on a Manganese Oxide Catalyst. 2. Steady-State and Transient Kinetic Studies. *J. Am. Chem. Soc.* **1998**, *120* (35), 9047–9052. https://doi.org/10.1021/ja9814422.
(36) Radhakrishnan, R.; Oyama, S. T. Ozone Decomposition over Manganese Oxide Supported on ZrO2 and TiO2: A Kinetic Study Using in Situ Laser Raman Spectroscopy. *J. Catal.* **2001**, *199* (2), 282–290. https://doi.org/10.1006/jcat.2001.3167.
(37) Roscoe, J. M.; Abbatt, J. P. D. Diffuse Reflectance FTIR Study of the Interaction of Alumina Surfaces with Ozone and Water Vapor. *J. Phys. Chem. A* **2005**, *109* (40), 9028–9034. https://doi.org/10.1021/jp050766r.

(38) Fitzpatrick, R. W.; Chittleborough, D. J. Titanium and Zirconium Minerals. In *Soil Mineralogy with Environmental Applications*; John Wiley & Sons, Ltd, 2002; pp 667–690. https://doi.org/10.2136/sssabookser7.c22.
(39) Chang, R. Y.-W.; Sullivan, R. C.; Abbatt, J. P. D. Initial Uptake of Ozone on Saharan Dust at Atmospheric Relative Humidities. *Geophys. Res. Lett.* **2005**, *32* (14), L14815. https://doi.org/10.1029/2005GL023317.
(40) Kolb, C. E.; Cox, R. A.; Abbatt, J. P. D.; Ammann, M.; Davis, E. J.; Donaldson, D. J.; Garrett, B. C.; George, C.; Griffiths, P. T.; Hanson, D. R.; Kulmala, M.; McFiggans, G.; Pöschl, U.; Riipinen, I.; Rossi, M. J.; Rudich, Y.; Wagner, P. E.; Winkler, P. M.; Worsnop, D. R.; O' Dowd, C. D. An Overview of Current Issues in the Uptake of Atmospheric Trace Gases by Aerosols and Clouds. *Atmospheric Chemistry and Physics* **2010**, *10* (21), 10561–10605. https://doi.org/10.5194/acp-10-10561-2010.
(41) Hanisch, F.; Crowley, J. N. Ozone Decomposition on Saharan Dust: An Experimental Investigation. *Atmos. Chem. Phys.* **2003**, *3* (1), 119–130. https://doi.org/10.5194/acp-3-119-2003.
(42) Aubin, D. G.; Abbatt, J. P. D. Interaction of NO2 with Hydrocarbon Soot: Focus on HONO Yield, Surface Modification, and Mechanism. *J Phys Chem A* **2007**, *111* (28), 6263–6273. https://doi.org/10.1021/jp068884h.
(43) Wu, L. Impact of Saharan Air Layer on Hurricane Peak Intensity. *Geophys. Res. Lett.* **2007**, *34* (9). https://doi.org/10.1029/2007GL029564.
(44) Perry, K. D.; Cahill, T. A.; Eldred, R. A.; Dutcher, D. D.; Gill, T. E. Long-Range Transport of North African Dust to the Eastern United States. *J. Geophys. Res.* **1997**, *102* (D10), 11225–11238. https://doi.org/10.1029/97JD00260.
(45) Xie, C.; Nishizawa, T.; Sugimoto, N.; Matsui, I.; Wang, Z. Characteristics of Aerosol Optical Properties in Pollution and Asian Dust Episodes over Beijing, China. *Appl. Opt.* **2008**, *47* (27), 4945–4951. https://doi.org/10.1364/AO.47.004945.
(46) Rubasinghege, G.; H. Grassian, V. Role(s) of Adsorbed Water in the Surface Chemistry of Environmental Interfaces. *Chem. Commun.* **2013**, *49* (30), 3071–3094. https://doi.org/10.1039/C3CC38872G.
(47) Nicolas, M.; Ndour, M.; Ka, O.; D'Anna, B.; George, C. Photochemistry of Atmospheric Dust: Ozone Decomposition on Illuminated Titanium Dioxide. *Environ. Sci. Technol.* **2009**, *43* (19), 7437–7442. https://doi.org/10.1021/es901569d.
(48) Hoffmann, M. R.; Martin, S. T.; Choi, W.; Bahnemann, D. W. Environmental Applications of Semiconductor Photocatalysis. *Chem. Rev.* **1995**, *95* (1), 69–96. https://doi.org/10.1021/cr00033a004.
(49) Hurum, D. C.; Agrios, A. G.; Gray, K. A.; Rajh, T.; Thurnauer, M. C. Explaining the Enhanced Photocatalytic Activity of Degussa P25 Mixed-Phase TiO_2 Using EPR. *J. Phys. Chem. B* **2003**, *107* (19), 4545–4549. https://doi.org/10.1021/jp0273934.
(50) Bickley, R. I.; Gonzalez-Carreno, T.; Lees, J. S.; Palmisano, L.; Tilley, R. J. D. A Structural Investigation of Titanium Dioxide Photocatalysts. *J. Solid State Chem.* **1991**, *92* (1), 178–190. https://doi.org/10.1016/0022-4596(91)90255-G.
(51) Folli, A.; Campbell, S. B.; Anderson, J. A.; Macphee, D. E. Role of TiO2 Surface Hydration on NO Oxidation Photo-Activity. *J .Photoch. Photobio. A* **2011**, *220* (2), 85–93. https://doi.org/10.1016/j.jphotochem.2011.03.017.
(52) Styler, S. A.; Donaldson, D. J. Photooxidation of Atmospheric Alcohols on Laboratory Proxies for Mineral Dust. *Environ. Sci. Technol.* **2011**, *45* (23), 10004–10012. https://doi.org/10.1021/es202263q.

(53) Brown, G. E.; Henrich, V. E.; Casey, W. H.; Clark, D. L.; Eggleston, C.; Felmy, A.; Goodman, D. W.; Grätzel, M.; Maciel, G.; McCarthy, M. I.; Nealson, K. H.; Sverjensky, D. A.; Toney, M. F.; Zachara, J. M. Metal Oxide Surfaces and Their Interactions with Aqueous Solutions and Microbial Organisms. *Chem. Rev.* **1999**, *99* (1), 77–174. https://doi.org/10.1021/cr980011z.
(54) Ivanov, A. V.; Trakhtenberg, S.; Bertram, A. K.; Gershenzon, Y. M.; Molina, M. J. OH, HO2, and Ozone Gaseous Diffusion Coefficients. *J. Phys. Chem. A* **2007**, *111* (9), 1632–1637. https://doi.org/10.1021/jp066558w.
(55) Jennings, S. G. The Mean Free Path in Air. *J. Aerosol Sci* **1988**, *19* (2), 159–166. https://doi.org/10.1016/0021-8502(88)90219-4.

Appendix C

(1) ASTM C136 / C136M-19, Standard Test Method for Sieve Analysis of Fine and Coarse Aggregates. ASTM International, West Conshohocken, PA 2019.
(2) Casotti Rienda, I.; Alves, C. A. Road Dust Resuspension: A Review. *Atmos. Res.* **2021**, *261*, 105740.
(3) Sadanaga, Y.; Hirokawa, J.; Akimoto, H. Formation of Molecular Chlorine in Dark Condition: Heterogeneous Reaction of Ozone with Sea Salt in the Presence of Ferric Ion. *Geophys. Res. Lett.* **2001**, *28* (23), 4433–4436.
(4) Shi, Z.; Krom, M. D.; Jickells, T. D.; Bonneville, S.; Carslaw, K. S.; Mihalopoulos, N.; Baker, A. R.; Benning, L. G. Impacts on Iron Solubility in the Mineral Dust by Processes in the Source Region and the Atmosphere: A Review. *Aeolian Res.* **2012**, *5*, 21–42.
(5) Pekney, N. J.; Davidson, C. I. Determination of Trace Elements in Ambient Aerosol Samples. *Anal. Chim. Acta* **2005**, *540* (2), 269–277.
(6) Sing, K. S. W. Adsorption by Powders and Porous Solids. In *Adsorption by Powders and Porous Solids (Second Edition)*; Rouquerol, F., Rouquerol, J., Sing, K. S. W., Llewellyn, P., Maurin, G., Eds.; Academic Press: Oxford, **2014**, 237–268.

Appendix A

Supplementary Information for Chapter 2

Maya Abou-Ghanem, Anton O. Oliynyk, Zhihao Chen, Laura C. Matchett, Devon T. McGrath, Michael J. Katz, Andrew J. Locock, and Sarah A. Styler

As published in *Environmental Science & Technology*, 2020, 54 (21), 13509-13516, DOI: 10.1021/acs.est.0c05861.

A.1 Experimental details and sample characterization

A.1.1 Photochemical coated-wall flow tube reactor

All experiments were conducted in a newly constructed photochemical coated-wall flow tube reactor system under ambient temperature and pressure conditions. A schematic of the system is provided in Figure A.1 and the parameters of the flow tube are shown in Table A.1.

The flow tube itself is constructed of Pyrex 7740 (34.4 cm length, 1.6 cm id, 0.7 cm thickness water jacket). Insert tubes, also constructed from Pyrex 7740 (20.0 cm length, 1.05 cm id), were coated with the mineral sample of interest and placed inside the flow tube. Mounted in the center of a black plastic box, the flow tube is surrounded by four Sylvania 25W BL UV-A lamps (300–410 nm, λ_{max}: 356 nm). To verify that the light intensity inside the flow tube was atmospherically relevant, the photolysis frequency of NO_2 (J_{NO_2}) was investigated and found to be 0.0045 ± 0.0001 s^{-1} (see Section A.1.2), which is in the range of the photolysis rate constants found in the atmosphere[1,2].

The temperature inside the reactor was controlled by a recirculating chiller (RTE-140, Neslab), which was set to 296.5 K. To avoid any microbial growth inside the chiller that could potentially absorb UV radiation in the water jacket layer, the common biocide chloramine-T was added to the chiller water. The chiller water was frequently monitored to verify that its absorbance spectrum in the UV-A range matched that of deionized water.

Dry, purified zero air for experiments was produced using a commercial zero air generator (747-30 reactor type A, Aadco Instruments). Ozone was generated in the dry air flow using a commercial ozone generator (97-0066-01, UVP) and monitored at the exit of the flow tube using a photometric ozone analyzer (T400, Teledyne). Acquisition of the ozone data was accomplished by connecting the ozone analyzer to an analog-to-digital converter (U6, LabJack) and collecting the data using a custom-built LabVIEW program at 5 s intervals.

The flow tube system contains 4 mass flow controllers (MFCs; MC-2SLPM-D/5M, Alicat), 3 of which were used to control the flows of ozone in dry air, dry air, and wet air prior to the flow

tube. The flow of dry air through the ozone generator was held constant at 100 sccm, and the relative humidity (RH) in the flow tube was varied by changing the flow ratio between the dry and wet MFCs. Wet air was generated by passing dry air through a water bubbler. RH in the system was monitored by 3 in-line humidity/temperature sensors (SHT75, Sensirion), which were placed directly after the zero air generator in order to make sure the zero air was dry (RH reading of 0.1%), prior to the flow tube, and at the exit of the flow tube; RH values prior to and at the exit of the flow tube were always ± 1% of the values reported in our figures and text. A customized Arduino was employed to convert RH analog signals into a digital output that was collected using a custom-built LabVIEW program at 5 s intervals.

The total flow upstream of the flow tube was set equal to 400 sccm for all experiments. Since the ozone analyzer requires a flow rate of 750 sccm, a fourth MFC was placed at the outlet of the flow tube to add an additional mass flow of 500 sccm, with excess flow directed to exhaust; all reported ozone concentrations were corrected for this dilution.

When experiments were not being conducted, the coated-wall flow tube reactor was continuously flushed with zero air (400 sccm); in addition, the RH of the zero air flow was adjusted as described above at the end of each day to reflect the desired RH for the subsequent day's experiments.

A.1.2 Determination of NO_2 photolysis frequency (J_{NO_2}) for the flow tube reactor

Irradiance inside the flow tube was quantified using NO_2 actinometry[1,2], in which the magnitude of production of NO from NO_2 upon illumination is used to determine the photolysis frequency for NO_2, J_{NO_2}.

In these experiments, which were conducted at ambient temperature and pressure, NO_2 (4.93 ppm ± 5% in N_2, Certified Standard, Praxair) was diluted with N_2 (5.0 grade, Praxair) upstream of the flow tube to lead to a final concentration of ~370 ppb. A Na_2CO_3 denuder was placed upstream of the flow tube to remove any HONO formed in the cylinder regulator or wetted parts of the MFCs. The denuder consisted of a sandblasted Pyrex tube (37.5 cm length, 0.635

cm outer diameter), the interior surface of which was coated with Na_2CO_3 solution previously prepared by adding 1 g of glycerol and 1 g of Na_2CO_3 to 50 mL of methanol. The coating solution was dripped into the Pyrex tube, which was then dried with N_2 (5.0 grade, Praxair) prior to use.

Upon illumination, the increase in NO and decrease in NO_2 were measured using a chemiluminescence NO_x (NO + NO_2) analyzer (T200U, Teledyne). To prevent the photolysis of NO_2 in undesired areas and control the illuminated volume inside the flow tube, all but 8.5 cm of the length of the flow tube was covered with aluminum foil; in order to ensure the light intensity within the reactor was identical to that in our dust photochemistry experiments, these experiments were conducted with a Pyrex insert tube placed inside the flow tube. From these data, J_{NO_2} was obtained as follows[2]:

$$[NO_2]_{avg} = [NO_2]_{final} + \frac{1}{2}\Delta[NO] \quad \text{(A.1)}$$

$$J_{NO_2} = \frac{\Delta[NO]}{[NO_2]_{avg}} \times \frac{F}{V} \times \frac{1}{\phi} \times \frac{1}{T} \quad \text{(A.2)}$$

Here, $[NO_2]_{final}$ is the concentration of NO_2 at the exit of the illuminated flow tube, $\Delta[NO]$ is the increase in NO concentration upon illumination, F is the volumetric flow rate in L s^{-1}, V is the illuminated volume of the reactor in L, ϕ represents the quantum yield of NO production, and T represents the transmission factor of the lamps through the reactor walls.

The quantum yield of NO from the photolysis of NO_2 in N_2 depends on several subsequent reactions induced by the formation of NO. Using the principal reactions described in Zafonte et al.[2], we derive a quantum yield of 1.63 for NO for our experimental conditions, which is in good agreement with the values reported by these authors. Finally, we note that we set the value of T as unity, because we are interested in measuring the irradiance within the flow tube rather than the inherent emission profile of the lamps.

Experimental protocol for J_{NO_2} determination involved first establishing a steady concentration of NO_2 in the dark (~360 ppb) followed by the following illumination protocol:

20 min light (1 lamp), 20 min dark, 20 min light (2 lamps), 20 min dark, 20 min light (3 lamps), 20 min dark, 20 min light (4 lamps), and 20 min dark. This procedure was conducted in triplicate, with results shown in Figure A.2. A maximum photolysis frequency of 0.0045 ± 0.0001 s^{-1} was obtained for NO_2 when all 4 lamps were turned on inside the reactor, which is similar to the photolysis frequency of NO_2 in the atmosphere and indicates an atmospherically relevant irradiance inside the flow tube[1,2].

A.1.3 Experimental details

A.1.3.1 Pyrex insert tube preparation

Pyrex insert tubes were cleaned prior to use by first placing each tube in a 1% H_2SO_4 bath for 1 min followed by a concentrated base bath for 1 h. After the base bath, the tubes were thoroughly rinsed with deionized water and dried in a gravity oven (100L, Fisherbrand™) at 324 ± 5 K.

The acid bath was prepared by adding 10 mL of concentrated H_2SO_4 to 990 mL of deionized water. The base bath was prepared by adding 1 L of 2-propanol to 166 mL of deionized water, followed by adding 41.7 g of solid KOH pellets and mixing until fully dissolved.

A.1.3.1.1 Tube coating procedure for natural minerals

Each coated tube was prepared by adding ~50 mg of Ti-containing mineral to a Pyrex insert tube, followed by several drops of deionized water to form a slurry. The tube was then stoppered with rubber stoppers (No. 00), rotated until the slurry covered the entire inner surface of the tube, and placed on a hot dog roller (RHD800 Retro Series Hot Dog Roller, Nostalgia Electrics) at maximum temperature to allow the mineral sample to dry in an even layer. After drying, the first 5 cm of one end of the tube and the first 1 cm of the other end were wiped clean using moistened laboratory wipes (Kimberly-Clark ProfessionalTM). The first 5 cm was wiped to allow the ozone-containing gas flow to achieve laminar flow prior to its interaction with the mineral surface (see Table A.1); the last 1 cm was wiped due to the

formation of an uneven coating at the tube ends from the use of the stoppers. The coated tubes were placed in a gravity oven (100L, FisherbrandTM) at 324 ± 5 K overnight prior to use.

The mass of mineral inside each Pyrex insert tube was determined by weighing by difference on an analytical balance (AB265-S/FACT, Mettler Toledo). Coated tubes were weighed after each experiment; then, they were rinsed with a tap water/Sparkleen™ mixture, distilled water, methanol, and deionized water, placed in a gravity oven (100L, FisherbrandTM) at 324 ± 5 K overnight to dry, and weighed again.

A.1.3.1.2 Tube coating procedure for TiO_2 minerals (commercial and natural)

For both the commercial and natural TiO_2 samples, almost complete depletion of ozone was observed upon illumination, which resulted in a diffusion correction of several orders of magnitude for γ (as discussed in main text of the manuscript). Mixing of TiO_2 with photochemically inert SiO_2 has been previously used to mitigate the effect of significant depletion of ozone from the gas-phase reservoir upon exposure to illuminated TiO_2[3]; in this study, a similar strategy was employed.

TiO_2/SiO_2 mixed films were prepared by first sonicating SiO_2 in 30 mL of deionized water for 1 h (2.8 L Ultrasonic Bath, Fisher Scientific) to reduce the agglomeration of SiO_2 in the coating procedure, then transferring TiO_2 powder to the SiO_2 suspension. To ensure quantitative TiO_2 transfer, 1 mL of water was used to rinse the weighing tray that contained the TiO_2. The resultant mixture was stirred with a PTFE stir bar (1 inch, Fisherbrand™) to ensure homogeneous mixing of TiO_2 and SiO_2 particles; after 10 min, 1 mL was pipetted into a Pyrex insert tube and the same coating procedure described in Section A.1.3.1.1 was applied. Because each TiO_2 sample type displayed significantly different reactivity, different TiO_2 loadings were employed for each TiO_2 sample; the masses of both TiO_2 and SiO_2 used for each sample type are shown in Table A.2.

A.1.3.2 Experimental protocol

At the beginning of each experiment, a Pyrex insert tube coated with the mineral substrate of interest was placed in the coated-wall flow tube reactor, the movable injector was retracted, and the coating was exposed for 30 min to zero air at the experimental RH. Then, the injector was pushed in past the mineral coating, preventing exposure of the sample to the gas flow, and the ozone generator was turned on. After 45 min, at which point a stable ozone concentration was achieved, the injector was pulled back and samples were exposed to ozone. After 1 h of dark exposure, samples were illuminated for 1 h; after an additional 30 min of dark exposure, the injector was again pushed in in order to verify that there was no drift in ozone concentrations throughout the experiment; after 30 min, the ozone generator was turned off and ozone concentrations were recorded for an additional 5 min. The average ozone concentrations over the last 5 min in the light, dark, and with the injector pushed in were used in the calculations described in main text of the manuscript.

Experiments were performed in triplicate for all minerals at 25% RH; selected reaction profiles for each mineral sample are shown in Figures A.3–4. For some minerals, experiments were also performed as a function of RH (here, experiments were only performed once at each RH value); representative reaction profiles are shown in Figure A.5.

A.1.3.3 Considerations in calculations of uptake coefficients

In this work, we quantify the reactivity of ozone with Ti-containing minerals using a quantity known as an uptake coefficient (γ)[4], which is defined as the number of ozone molecules taken up by the surface divided by the total number of collisions of ozone molecules with the surface. Previous studies of trace gas–dust interactions have reported both initial[5–7] and steady-state[5,7–9] uptake coefficients; because the latter is most relevant for the behavior of dust over extended timescales in the atmosphere, we report it here.

In our system, laminar flow conditions (Reynolds number < 2000) and continuum flow regimes (Knudsen number << 1) are applicable (see Table A.1); therefore, at high values of γ, where

significant depletion of ozone occurs near the sample surface, γ_{eff} can be limited by the diffusion of ozone from the centre of the flow tube to the sample surface. In order to correct for underestimations in γ_{eff} as a result of these radial diffusion limitations, a correction factor is applied using the CKD method[10] as described in the main text of the manuscript. We note that we chose mineral sample masses such that reported uptake coefficients had a maximum correction for radial diffusion of 30% from γ_{eff}.

A.1.3.3.1 Additional considerations for TiO_2 samples

As described in Section A.1.3.1.2, in order to minimize the need for excessive corrections for gas-phase diffusion limitations, we employed TiO_2/SiO_2 mixed films for all TiO_2 samples. Because SiO_2 itself exhibited non-negligible photochemistry in our experiments, calculations were slightly more involved for these mixed films.

In order to correct for SiO_2 reactivity, we calculated γ_{BET} (25% RH) for 3 SiO_2 samples with similar masses and used the average γ_{BET} value to back-calculate a γ_{eff} value for the mass of SiO_2 employed in a given TiO_2/SiO_2 experiment. From the γ_{eff} thus obtained, we back-calculated k_{obs} (s^{-1}) for this mass of SiO_2 and subtracted this value from the overall k_{obs} value for the TiO_2/SiO_2 mixed film. In this way, we were able to obtain a k_{obs} value for TiO_2 alone, which we then used to calculate γ_{eff} and γ_{BET} for TiO_2 as described in the previous section. Importantly, we used the total surface area of TiO_2 alone in these calculations, rather than the total surface area of the mixed film. We note that these calculations led to negligible values for k_{obs} of TiO_2 alone under dark conditions; as a result, we do not report dark uptake values for TiO_2.

We note that since radial diffusion limitations are independent of sample type and only depend on overall loss of ozone onto the surface, γ_{eff} values for the TiO_2/SiO_2 mixed films were multiplied by the correction factor ratio associated with γ_{eff} values calculated for the original mixed films (*i.e.*, not for the TiO_2 fraction alone).

A.1.4 Sample treatment, preparation, and characterization

A.1.4.1 Sample treatment and preparation

Minerals were analyzed for their purity via visual inspection, electron microprobe analysis (EMPA), and X-ray diffraction (XRD). Impurities were identified for each mineral and purification treatments were selected accordingly; a summary of all treatments is presented in Table A.3. Pictures of mineral samples prior to treatment and preparation are provided in Figure A.6.

Obvious impurities on the outside of mineral samples and impurities that could not be removed via chemical treatment (*vide infra*) were removed using a Dremel® tool. Rust was removed by submersing minerals in a 40 g L^{-1} solution of SUPER IRON out® (active ingredients sodium hydrosulfite, sodium metabisulfite, and sodium sulfite) for 30 min. $CaCO_3$ was removed by placing minerals in 1 M HCl (phlogopite, 1.5 hours; titanite 1, 1 day). After the removal of impurities, minerals were rinsed with methanol once and with deionized water 3 times. Minerals that were not subjected to these treatments were also rinsed in this manner.

After minerals underwent purification treatments, they were first broken down using a steel percussion mortar and pestle. To remove any steel contamination from use of the percussion mortar, a rare earth magnet wrapped in weighing paper was then passed over each broken-down sample (this was not possible for ilmenite and hastingsite samples, as they also displayed magnetic properties). Minerals were then ground using an agate mortar and pestle until they had a fine, powder-like appearance. To prevent cross contamination, pure gem-quality Brazilian quartz (from Corinto, Brazil) was used to clean the steel percussion and agate mortar and pestle between samples by grinding the quartz into a fine powder; afterward, grinding equipment was rinsed with ethanol.

A.1.4.2 Surface area determination

Prior to gas adsorption analysis, samples were degassed (activated) on a gas adsorption sample preparation instrument (Smart VacPrep, Micromeritics); in order to ensure that the measured

surface area is reflective of the surface area presented under our experimental conditions, degassing was performed in the absence of heat. For activation, each sample was weighed into a pre-weighed glass sample tube equipped with filler rod and steel frit ball valve. Samples were subsequently activated by evacuating the sample holder at 5.00 mmHg s^{-1} until a pressure level of 1.00 mmHg or lower was achieved; the Smart VacPrep instrument has a needle on the vacuum port to open the ball valve. Subsequently the samples were held under unrestricted vacuum for 24 h. The sample holders were then backfilled with nitrogen gas, removed from the Smart VacPrep instrument, and reweighed. Gas adsorption isotherm data were collected at 77 K using nitrogen gas as the probe molecule (3Flex, Micromeritics). Using the MicroActive software suite, the data obtained were used to determine the Brunauer–Emmett–Teller (BET) accessible surface area by fitting the linear BET equation and ensuring that the 4-point criterion was met[11].

A.1.4.3 Electron microprobe analysis

Electron microprobe analysis was conducted on 2 separate dates because minerals were purchased in 2 groups. The first set of minerals analyzed consisted of anatase 1, rutile, ilmenite, titanite 1, phlogopite, hastingsite, augite, and epidote. The second set, which was purchased to enable us to study the reactivity of samples of the same mineral obtained from different locations, consisted of anatase 2 and titanite 2. All EMPA data can be found in Tables A.5–14.

A.1.4.3.1 Analysis of anatase 1, rutile, ilmenite, titanite 1, phlogopite, hastingsite, augite, and epidote

An electron microprobe (JXA-8900R, JEOL) was used to examine grains of anatase 1, rutile, ilmenite, titanite 1, phlogopite, hastingsite, augite, and epidote, which had been mounted in epoxy, polished, and carbon-coated (25 nm thickness) prior to analysis. In addition to back-scattered electron images, quantitative compositional data were acquired from spot analyses of the minerals using wavelength-dispersive spectrometry and Probe for EPMA software[12]. Thirteen elements were measured (Na, Mg, Al, Si, K, Ca, Ti, V, Cr, Mn, Fe, Zn, and Nb) with the following conditions: 20 kV accelerating voltage, 20 nA probe current, and a

1 μm beam diameter for all minerals except pholgopite, for which a 5 μm beam was used. Total count times of 20 s were used for both peaks and backgrounds for all elements except V, Zn, and Nb, for which 30 s was used. The X-ray lines and diffraction crystals were: Na *K*α, TAP (thallium hydrogen phthalate); Mg *K*α, TAP; Al *K*α, TAP; Si *K*α, TAP; K *K*α, PET (pentaerythritol); Ca *K*α, PET; Ti *K*α, PET; V *K*α, PET; Cr *K*α, PET; Mn *K*α, LIF (lithium fluoride); Fe *K*α, LIF; Zn *K*α, LIF; and Nb *L*α, PET. Corrections were applied to V for interference by Ti, to Cr for interference by V, and to Mn for interference by Cr[13]. X-ray intensity data were reduced following Armstrong (1995)[14]. The reference standards consisted of metals, synthetic inorganic materials, and natural minerals[15].

A.1.4.3.2 Analysis of anatase 2 and titanite 2

An electron microprobe (SX100, Cameca) was used to examine grains of anatase 2 and titanite 2, which had been mounted in epoxy, polished, and carbon-coated (25 nm thickness) prior to analysis. In addition to back-scattered electron images, quantitative compositional data were acquired from spot analyses of the minerals using wavelength-dispersive spectrometry and Probe for EPMA software[12]. Thirteen elements were measured (Na, Mg, Al, Si, K, Ca, Ti, V, Cr, Mn, Fe, Zn, and Nb) with the following conditions: 20 kV accelerating voltage, 20 nA probe current, and a 1 μm beam diameter. Total count times of 30 s were used for both peaks and backgrounds for all elements. The X-ray lines and diffraction crystals were: Na *K*α, TAP; Mg *K*α, TAP; Al *K*α, TAP; Si *K*α, TAP; K *K*α, PET; Ca *K*α, PET; Ti *K*α, PET; V *K*α, PET; Cr *K*α, PET; Mn *K*α, LIF; Fe *K*α, LIF; Zn *K*α, LIF; and Nb *L*α, PET. Corrections were applied to V for interference by Ti, to Cr for interference by V, and to Mn for interference by Cr[13]. However, the correction to V was found to be insufficient, based on analysis of reference rutile, and so the V data were discarded. The X-ray intensity data were reduced following Armstrong (1995)[14]. The reference standards consisted of metals, synthetic inorganic materials, and natural minerals[15].

A.1.4.4 X-ray diffraction analysis

Powder X-ray diffraction (XRD) patterns of the ground mineral samples were collected on a Rigaku Ultima IV diffractometer with a Co *K*α radiation source operated at 38 kV and 38 mA. Phase identification was performed using JADE 9.6 software with the 2019 ICDD Database PDF 4+ and 2018-1 ICSD databases[16,17]. The patterns were analyzed with the TOPAS academic software package[18]. All phases were analyzed with Pawley refinement method[19]. X-Ray diffraction data and refinement fits are shown in Figures A.9–10. The phases and their statistics from refinement fits are presented in Table A.15, which also summarizes the results and lists the cell parameters of the refined phases from the powder XRD data.

The refinements in Figures A.9–10 show good visual fits and excellent refinement statistics (Table A.15). Ilmenite had no observed impurity peaks in its diffraction pattern (Figure A.10). For the rest of the samples, asterisks indicate the most intense impurities observed with the X-ray diffraction technique. The phlogopite sample exhibited a strong preferred orientation in the 0 0 2*n* direction, which resulted in a strong intensity of the 0 0 2*n* peaks in the powder pattern (Figure A.10). The samples with major impurity contents (hastingsite and epidote) were also analyzed with Pawley fit to identify the presence of secondary phases (see Figure A.10).

Powder diffraction of all anatase (TiO_2) samples revealed minor (< 5%) unidentified impurities based on a relative intensity comparison (Figure A.7). The peak at ~32° 2θ could theoretically be assigned to rutile; the absence of other rutile phase peaks likely reflects the low abundance of this phase. The commercial anatase sample was purchased from a batch with a claimed anatase purity of 99.8%; a minor rutile peak was apparent in a quality check diffraction pattern collected in 2014 (see Figure A.8). However, Figure A.7 shows multiple other unidentified peaks in the powder diffraction pattern for this sample. Since most of the impurities found in all 3 anatase samples gave reflections at the same diffraction angles, a single crystal was picked from one of the samples (anatase 2) for analysis to check whether these peaks reflected impurities within the phase itself or the existence of additional impurity phases. Similarly,

titanite 2 (Figure A.10) features 2 unassigned peaks in its diffraction pattern that were not present in the diffraction pattern for titanite 1 (Figure A.10). In order to check if these peaks originated from the structure of this particular sample of titanite, a single crystal was picked from the mineral sample and analyzed via single crystal diffraction.

Single crystal diffraction measurements were accomplished using a Bruker PLATFORM diffractometer equipped with a SMART APEX II CCD area detector and a graphite-monochromated Mo Kα radiation source, using ω scans at 8 different ϕ angles with a frame width of 0.3° and an exposure time of 10 s per frame. Face-indexed absorption corrections were applied[20]. Structure solution and refinement were carried out using the SHELXTL (version 6.12) program package[21]. The results of these analyses are displayed in Tables A.16–20.

Atomic coordinates and crystallographic details are comparable to other crystallographic reports of anatase and titanite crystals; no structural anomalies were observed. Atomic distances from the crystallographic analysis are similar to multiple single crystal diffraction reports of these minerals. In the case of anatase 2, a small excess of electron density on Ti atom (0.4 $e^-/Å^3$) is in a good agreement with the atomic composition (0.92 Ti + 0.08 Fe) suggested by microprobe analysis (Table A.6). Additionally, atomic displacement parameters are slightly higher than what would be expected, suggesting negligible mixing in the metal site, which is in a good agreement with the microprobe data. The extra peaks (observed on powder patterns) were absent in the single crystal diffraction data, which suggests that these peaks indeed belonged to impurity phase(s) and/or Kβ diffraction from the anatase phase rather than to structural imperfections of the main phase.

A.1.4.5 UV-Vis diffuse reflectance spectroscopy

In order to determine the extent to which each Ti-containing mineral sample absorbs light within the transmission range of the UV-A lamps in the photoreactor and to obtain their band gaps, diffuse reflectance spectra were collected using a UV-Vis-NIR spectrophotometer (Cary, 5000) equipped with a diffuse reflectance accessory. Spectralon® was used as 100% reflectance

standard and spectra were measured from 200–800 nm for all minerals except ilmenite, the spectrum of which was measured to 1200 nm, as its absorbance extended into the NIR region. Diffuse reflectance data were transformed using the Kubelka–Munk function[22]:

$$\frac{K}{S} = \frac{(1-R)^2}{2R} \tag{A.3}$$

Here, K is the absorption coefficient, S is the scattering coefficient, and R is the reflectance. Band gaps for Ti-containing minerals were determined by plotting the Kubelka–Munk function (K/S) against eV, where eV corresponds to the kinetic energy of a single electron at a given wavelength, and then taking the intersection between a linear fit of the reflectance dip and a horizontal line along the baseline of K/S[23]. The Kubelka–Munk plots for a selection of minerals (with associated band gaps, when possible) are presented in Figure 2.4; the remainder of the minerals are shown in Figure A.11.

A.1.4.6 Scanning electron microscopy

The size and morphology of a select set of mineral samples—commercial anatase, anatase 1, anatase 2, rutile, titanite 1, and titanite 2—were assessed using a field emission scanning electron microscope (FESEM, Zeiss Sigma). In order to prepare samples for SEM analysis, a small amount (several mg) of each mineral was sprinkled onto carbon tape, which was then mounted on an aluminum stub. To reduce the influence of surface charging from the electron beam, samples were carbon coated using a sputter coater (EM SCD005, Leica).

Secondary electron images were collected using in-lens mode at 10 kV at 1000× magnification, except in the case of commercial anatase, which was obtained at 10,000× magnification due to its significantly smaller particle sizes compared to the natural ground minerals. All secondary electron images are presented in Figure A.12.

A.1.5 Chemicals

Natural minerals were sourced from www.minfind.com and through contact with individual vendors. Deionized water (18 MΩ) was obtained from a Millipore Synergy UV ultrapure water system. TiO_2 (anatase, 99.8% trace metal basis), KOH (ACS reagent ≥ 85%, pellets), and

chloramine T trihydrate (Reag. Ph. Eur. grade) were obtained from Sigma Aldrich. SiO_2 (amorphous fumed, reported surface area 85–115 $m^2\ g^{-1}$) was obtained from Alfa Aesar. Methanol (Optima grade, 99.9%), 2-propanol (certified ACS Plus), Na_2CO_3 (anhydrous, certified ACS powder), and glycerol (certified ACS) were obtained from Fisher Chemicals. Concentrated H_2SO_4 (reagent grade) and concentrated HCl (reagent grade) were obtained from Caledon Laboratory Chemicals. SUPER IRON out® (Summit Brands) was purchased from Canadian Tire®. Sparkleen™ was purchased from Fisherbrand™. Ethanol (95%) was obtained from Commercial Alcohols. Except for the natural mineral samples, which were treated as described in Section A.1.4.1, all chemicals were used as received.

A.2 Supporting results and discussion

A.2.1 Ozone uptake by Ti-containing minerals under dark conditions

Although the primary focus of this study was the photochemistry of Ti-containing minerals, we also investigated ozone uptake by these minerals under dark conditions. As illustrated in Figures A.3–4, ozone exhibited time-dependent uptake to most Ti-containing mineral samples under dark conditions. In particular, for most samples, the magnitude of ozone loss decreased with increasing sample exposure and eventually reached a plateau value; in other words, the concentration of ozone at the exit of the flow tube increased with increasing sample exposure and eventually reached a steady state. We note that in some cases, steady-state conditions were not reached *(e.g.*, phlogopite, titanite 1, anatase 1, and anatase 2; Figures A.3–4), as we wanted to keep the total reaction time similar between experiments; for these minerals, therefore, γ_{BET} values represent an upper limit.

As shown in Figure A.14, γ_{BET} values for our samples under dark conditions were significantly lower than values obtained under illumination. Under dark conditions, γ_{BET} values spanned almost an order of magnitude, with the highest values calculated for ilmenite (7.6×10^{-7}) and the lowest for epidote ($(7.5 \pm 1.8) \times 10^{-8}$). We note that ilmenite displayed 2 distinct types of reaction profiles with associated uptake coefficients ($(6.9 \pm 1.3) \times 10^{-7}$, $n = 3$; $(2.4 \pm 0.6) \times 10^{-7}$,

$n = 3$); although we are not currently able to definitively explain this behavior, we tentatively suggest that it may reflect variable contributions from additional minor mineral phases within the sample. If present, these additional mineral phases may have gone undetected during our sample characterization procedures, as EMPA results only reflect the elemental abundances in spot-selected areas of mineral samples and XRD is not always able to detect minor phases in multi-phase samples[24]. To compare the reactivity of our minerals to natural dust samples, we also measured ozone uptake by Cape Verde dust and Gobi dust; for these samples, γ_{BET} values of $(2.2 \pm 0.2) \times 10^{-8}$ and $(3.6 \pm 0.6) \times 10^{-8}$ were obtained, respectively.

Ozone uptake by TiO_2/SiO_2 mixed films under dark conditions was indistinguishable from that by SiO_2 films, which was itself small. These results agree with the coated-wall flow tube study of Nicolas et al., which reported minimal uptake of ozone by TiO_2/SiO_2 films under dark conditions[3]. As noted in Section A.1.3.3.1, because of the substantial photoreactivity of TiO_2 samples, our films were prepared using low Ti mass fractions (see Table A.2), which implies that TiO_2 minerals themselves may be measurably reactive toward ozone under dark conditions; however, this was not the focus of the present study and is not explored/discussed here.

A.2.1.1 Suggested mechanism for ozone uptake by Ti and Ti-bearing minerals

The following mechanism has been proposed for the interaction of ozone with metal oxide surfaces, where SS represents an active surface site (we note that the importance of Reaction A.4 is debated)[25,26]:

$$O_3 + SS \rightarrow SS{-}O + O_2 \quad (A.1)$$

$$SS{-}O + O_3 \rightarrow SS{-}O_2 + O_2 \quad (A.2)$$

$$SS{-}O_2 \rightarrow SS + O_2 \quad (A.3)$$

$$2(SS{-}O) \rightarrow 2\,SS + O_2 \quad (A.4)$$

The saturation of active surface sites via Reactions A.1 and A.2 implies that ozone uptake by these samples will eventually become negligible; however, the mechanism also allows for regeneration of these sites via Reactions A.3 and A.4, which would lead to sustained (*i.e.* catalytic) ozone loss. Our steady-state ozone concentrations do not return back to their initial values prior to sample exposure (see Figures A.3–4), which implies that destruction of ozone is catalytic in nature to some degree for all of our samples. This catalytic behavior has been previously observed for several natural mineral dusts[5,9,27] , clays[5,8,29], and metal oxides[3,5,28,30,31], the latter two of which are commonly used as mineral dust proxies.

The surface sites (SS) presented in Reactions A.1–4 represent active Lewis acid sites (*i.e.* surface defects in the form of oxygen vacancies) that can promote ozone dissociation and resultant formation of surface-bound oxygen atoms; in fact, in the case of volcanic ash, ozone has been used as a molecular probe for Lewis acid sites[32]. The adsorption of ozone at these Lewis acid sites has been studied using many surface spectroscopic techniques, including FT-IR[33], XPS[34], Raman[26,35,36], and DRIFTS[37]. The degree to which the catalytic destruction of ozone occurs depends greatly on the strength of these Lewis acid sites. For example, previous studies have found that the catalytic uptake of ozone by Fe_2O_3 is greater than by Al_2O_3, which is in turn greater than by SiO_2[5]. This trend has been attributed to Fe_2O_3 having the weakest Lewis acid sites—and, by extension, the weakest SS–O_2 bonds—which allows for greater regeneration of SS[30].

We suggest that similar considerations may be relevant for our sample set, which includes minerals with different chemical compositions and crystal structures (*i.e.*, that observed reactivity differences may arise from differences in strength of Lewis acid sites). For example, ilmenite's elevated dark reactivity compared to other samples may reflect its elevated Fe content (~45%, Table A.8) and consequent availability of Fe cations at its surface. In addition, titanite 1's reactivity (γ_{BET} = (1.29 ± 0.02) × 10^{-7}) compared to titanite 2 (uptake negligible compared to controls, and therefore not reported) may reflect the 4× larger amount of Fe detected in the former sample (Tables A.9–10).

Fe can easily substitute for Ti in mineral structures due to its similar cation size and charge[38]. Depending on formation processes and conditions (*e.g.,* crystallization environment), therefore, we expect titanium-containing minerals in the environment to have different abundances of these elements in their crystal structures, and ultimately exhibit different reactivities; in other words, we anticipate that the results obtained here are not specific for titanite but rather reflective of broader variability in environmental samples.

A.2.1.2 Comparison of uptake coefficients to previous literature

Previous laboratory studies investigating the uptake of ozone by natural mineral dusts and mineral dust proxies have been conducted using coated-wall flow tubes[8,25,29,39], environmental chambers[30,31], and Knudsen cells[5,27,28]. Detailed descriptions of these systems are provided in a review by Kolb et al.[40], but the most significant difference between them is that whereas Knudsen cells are operated under molecular flow conditions (*i.e.*, under vacuum), coated-wall flow tubes and environmental chambers can be operated at atmospheric pressures.

Uptake coefficients reported in Knudsen cell studies of dust–ozone interactions are significantly larger than those obtained in this work. For example, Hanisch and Crowley reported a steady-state BET uptake coefficient of 7×10^{-6} for the uptake of ozone by Saharan Desert dust[41], which is ~9–90× larger than the values obtained in our experiments for our natural Ti-containing mineral samples and 200–300× larger than our Gobi and Saharan dust samples, respectively. In the following paragraph, we suggest three possibilities to explain this discrepancy.

First, as recently discussed by Lasne et al., the larger ozone uptake coefficients obtained in Knudsen cell experiments could potentially be explained by more favorable regeneration of surface sites via decomposition of SS–O_2 (Reaction A.3) at lower operating pressures[8]. Second, as noted by Coates Fuentes et al., who reported smaller ozone uptake coefficients for clays in their coated-wall flow tube experiments as compared to previous values from Knudsen cell experiments, the *in situ* BET surface area of samples may differ from that measured when

samples are present in powder form[29]. A reduction in the actual BET surface area of our coated tubes with respect to the values determined for dry samples would also lead to an underestimation in our calculated γ_{BET} values. In the case of ozone uptake by hydrocarbon soot, *in situ* gas adsorption analysis[42] has previously been used to address these issues; however, this approach would be challenging for our samples, which have significantly lower specific surface areas. Third, we show in Section A.2.1.3 for a subset of our mineral samples that the uptake of ozone decreases with increasing RH. By extension, we might expect uptake coefficients to be higher in low-pressure reactors, where adsorbed water may be more thoroughly removed from samples and the number of available surface sites for ozone adsorption may be correspondingly increased.

Uptake coefficients derived from studies conducted at atmospheric pressure are in better agreement with our values[3,8,25,29–31]. For example, Mogili et al. investigated ozone uptake onto α-Al_2O_3 and α-Fe_2O_3 as a function of RH and ozone partial pressure in an atmospheric chamber and obtained γ_{BET} values ranging from 1.9×10^{-9} to 1.3×10^{-7} for these samples[30]. In addition, Coates Fuentes et al. studied ozone uptake onto kaolinite, a clay used as a mineral dust proxy, using a coated-wall flow tube and found a γ_{BET} value of 1.9×10^{-8} at RH <1%[29]; similar results were obtained by Lasne et al.[8]. Finally, our results for Gobi dust are similar to those reported in a previous study of the catalytic uptake of ozone by this substrate in a U-shape fixed-bed reactor[9].

A.2.1.3 Influence of relative humidity on ozone uptake

Although mineral dust is emitted primarily in arid regions, it can be exposed to environments of differing RH during atmospheric transport. For example, mineral dust is primarily transported across the Atlantic Ocean in the Saharan Air Layer, a dry, warm, air mass; during transport, however, tropical disturbances can lead to vertical mixing of this layer with underlying cool, moist, tropical Atlantic air and ultimately expose dust to more humid environmental conditions[43,44]. In addition, the mixing between dry, dust-laden air flows and more humid air can also occur during dust storm episodes that occur at lower altitudes[45]. In

this context, it is important to understand the influence of water vapour on the reactivity of our samples toward ozone.

Here, we investigated the RH dependence of ozone uptake for all TiO_2 minerals studied (commercial anatase, anatase 1, anatase 2, and rutile) and for 4 Ti-containing minerals (titanite 1, titanite 2, phlogopite, and ilmenite). Because we observed minimal loss of ozone for all TiO_2/SiO_2 samples under dark conditions, discussion of the influence of RH on ozone uptake by these samples is presented in Section A.2.2.3 (illuminated conditions). In the case of titanite 2, dark reactivity was small at all RH values (results not shown), so trends in uptake were difficult to discern. In the case of ilmenite, the bimodal reactivity described in Chapter 2.1 precluded reliable interpretation of RH trends. For these reasons, we limit our discussion to the influence of RH on ozone uptake by titanite 1 and phlogopite.

As illustrated in Figure A.5, the loss of ozone at the surface of both titanite 1 and phlogopite increased with decreasing RH. At lower RH values, the correction factor for radial diffusion of ozone inside the coated-wall flow tube becomes very large; for this reason, we did not calculate γ_{BET} values for these experiments. These results agree qualitatively with those obtained in previous studies of ozone uptake by metal oxides[25,25,31] and clays[8,29], and most likely reflect competition by water vapour for available surface sites for ozone adsorption[46].

A.2.2 Ozone uptake by TiO2 under illuminated conditions

A.2.2.1 Mechanistic discussion for photoenhanced ozone uptake by TiO2

Here, we elaborate on the mechanism proposed by Nicolas et al. for the TiO_2-catalyzed uptake of ozone (Reactions A.5–13)[47]:

$$TiO_2 + h\nu \rightarrow TiO_2(e^- + h^+) \quad \text{(A.5)}$$

$$O_3 + e^- \rightarrow O_3^{\bullet-} \quad \text{(A.6)}$$

$$O_2 + e^- \rightarrow O_2^{\bullet-} \quad \text{(A.7)}$$

$$O_2^{\bullet-} + O_3 \rightarrow O_3^{\bullet-} + O_2 \quad \text{(A.8)}$$

$$O_3^{\bullet-} + H^+ \rightarrow HO_3^{\bullet} \quad \text{(A.9)}$$

$$HO_3^{\bullet} \rightarrow O_2 + {}^{\bullet}OH \quad \text{(A.10)}$$

$${}^{\bullet}OH + O_3 \rightarrow O_2 + HO_2^{\bullet} \quad \text{(A.11)}$$

$$H_2O_{(ads)} + h^+ \rightarrow 2\ {}^{\bullet}OH \quad \text{(A.12)}$$

$$>TiOH + h^+ \rightarrow \{>TiOH^{\bullet}\}^+ \quad \text{(A.13)}$$

In this mechanism, absorption of light with energy equal to or greater than the band gap of TiO_2 leads to the formation of an electron–hole pair (Reaction A.5) and initiates a chain of reactions that reduce ozone and ultimately result in the release of molecular oxygen (Reactions A.6–R11). In this proposed mechanism, ozone can be reduced directly by photogenerated electrons (Reaction A.6) or indirectly by superoxide radicals produced from the reduction of molecular oxygen by photogenerated electrons (Reactions A.7–8). In both cases, the ozonide radical thus produced can decompose to yield hydroxyl radicals (Reactions A.9–10), which can in turn lead to further ozone decomposition (Reaction A.11). Under our experimental conditions, additional mechanisms for hydroxyl radical production include the reaction of photogenerated holes with molecularly adsorbed water (Reaction A.12) and/or the hydrated surface of TiO_2 (Reaction A.13)[48].

A.2.2.2 Comparison of uptake coefficients to previous literature

Although this work is the first to study the photochemical uptake of ozone by natural Ti-containing minerals, several other studies have explored the photochemical uptake of ozone by commercial TiO_2. Using a coated-wall flow tube, Nicolas et al. obtained a γ_{BET} value of $(2.6 \pm 0.4) \times 10^{-6}$ for TiO_2/SiO_2 mixed films at similar ozone concentrations, RH values, and film masses to those employed in our experiments[47]. This value is much lower than the value we obtain in this work (*i.e.* $(1.8 \pm 0.3) \times 10^{-4}$). We suggest that this difference may reflect different approaches used to calculate γ_{BET}: specifically, because these authors were interested in the reactivity of the composite film rather than the reactivity of TiO_2 itself, they reported γ_{BET} values corrected for the entire surface area of their TiO_2/SiO_2 mixed films. By contrast, in this

work, because we were interested in obtaining γ_{BET} for the TiO_2 fraction, we used the surface area of TiO_2 alone in our calculations (see Section A.1.3.3.1). In another study, Chen et al.[31] used an environmental reaction chamber to obtain a γ_{BET} value of $(2.4 \pm 0.1) \times 10^{-7}$, which is lower than both the values obtained in this study and those reported by Nicolas et al.[31]. We suggest that this discrepancy likely reflects the use of significantly higher ozone concentrations in the reaction chamber than in the flow tube studies, as calculated γ_{BET} values for surface-mediated reactions display a negative dependence on gas-phase ozone concentrations[47]. Finally, whereas our commercial TiO_2 was primarily anatase, the two previous studies used Degussa TiO_2, which contains both anatase and rutile. Since studies have shown that the photoreactivity of mixed TiO_2 phases can differ from that of individual TiO_2 phases[49], it is also possible that the inherent photoreactivity of our TiO_2 sample differs from those employed in these previous studies.

A.2.2.3 Influence of relative humidity on ozone uptake

In order to assess the influence of adsorbed water on the photochemical uptake of ozone by our TiO_2 samples, we performed experiments at several RH values. As illustrated in Figure A.13, anatase 1 exhibits the highest photoreactivity at RH 10%. These results agree with those of Nicolas et al., who observed the highest photoreactivity values for TiO_2 with ozone at intermediate RH values[47]. They attributed lower photoreactivities under wet conditions to competitive adsorption by water vapour, and lower photoreactivities under dry conditions to reductions in the quantity of adsorbed water available to generate radical species ((Reaction A.12) in the mechanism described in Section A.2.2.1) at the illuminated TiO_2 surface[47,51]. The fact that photochemistry still occurs under dry conditions in both of our studies implies that the hydrated TiO_2 surface itself may also participate in photochemistry (Reaction A.13); additional evidence for photochemistry in the absence of water vapour is also provided by observations of TiO_2-mediated photochemistry under vacuum conditions (*i.e.* in a photochemical Knudsen cell)[52].

Figure A.13 also shows that the trends in γ_{BET} as a function of RH are mineral-dependent for our sample set: specifically, commercial anatase and anatase 2 display the highest photoreactivity at RH <0.1%, whereas the photoreactivity of rutile is relatively invariant with RH. If the two competing mechanisms described by Nicolas et al.[47] are also in operation for our samples, these discrepancies imply that our samples may differ in their degree of inherent hydration and/or their ability to retain residual water during our (relatively mild) sample drying process[53]. These results again highlight the complexities associated with photochemistry at the surface of natural samples, and that observations obtained for model systems may not be directly applicable to all environmental substrates.

a)

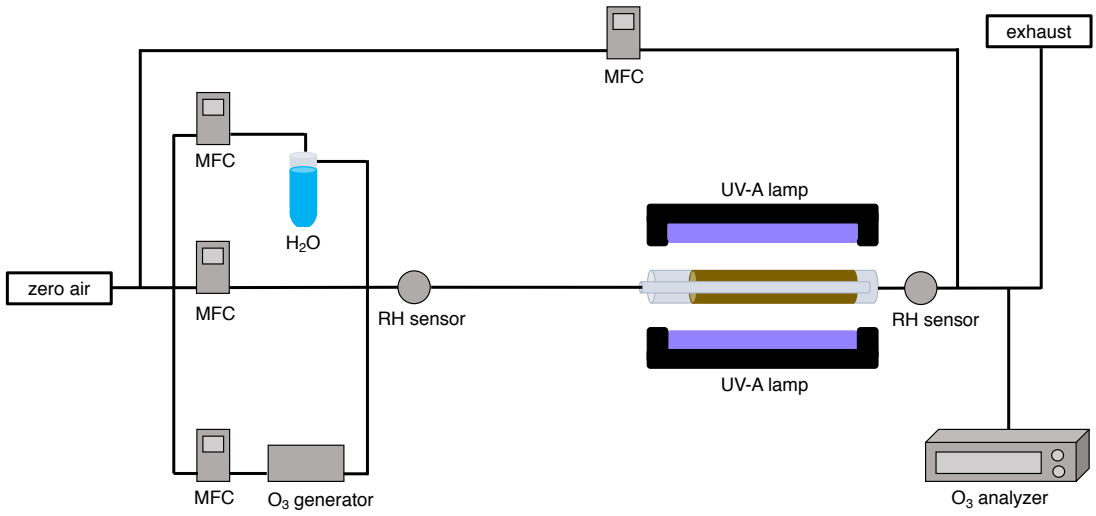

b)

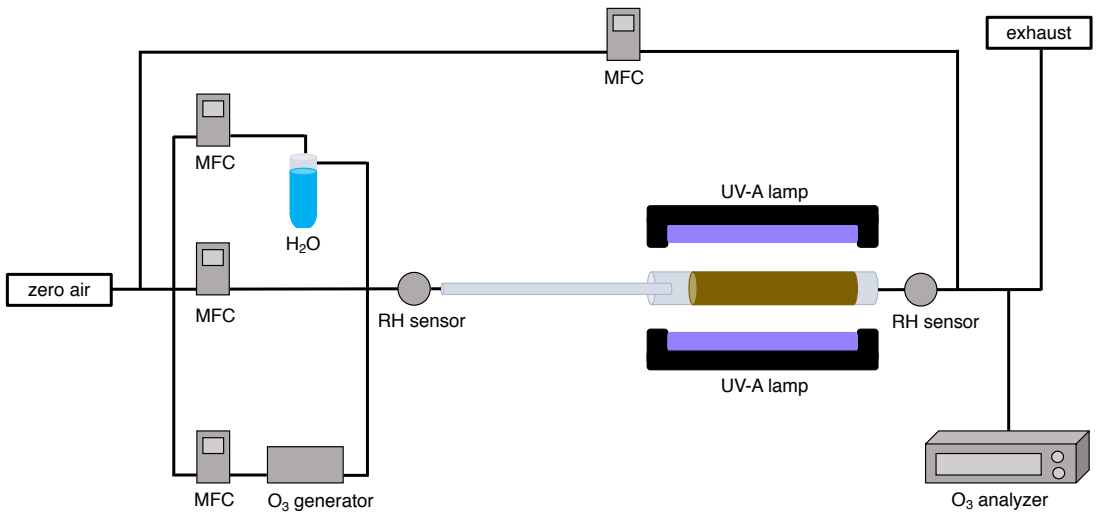

Figure A.1: Schematic of the photochemical coated-wall flow tube reactor, with a) the movable injector pushed in, which prevents the interaction of ozone with mineral samples and b) the movable injector pulled back, which allows for interaction between ozone and mineral samples. For clarity, only 2 of the 4 UV-A lamps in the apparatus are shown here.

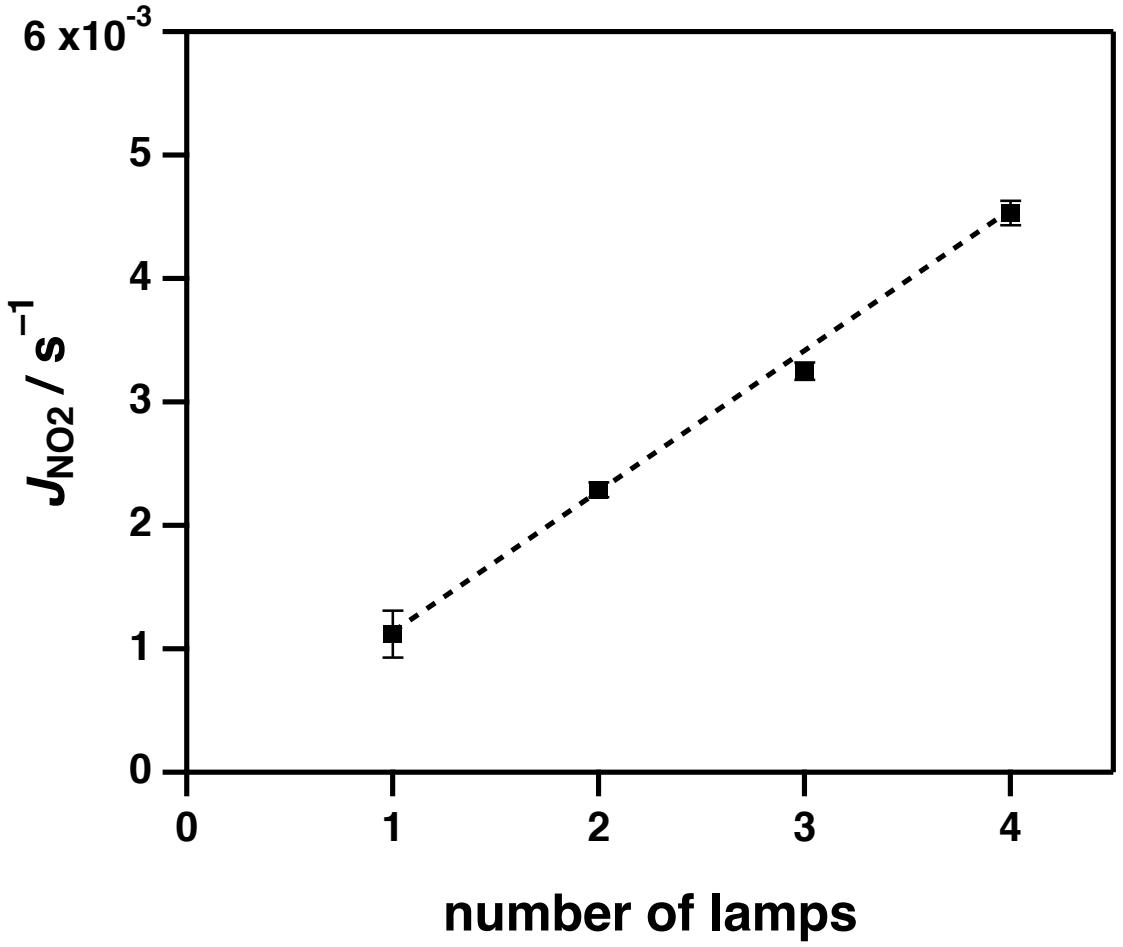

Figure A.2: Photolysis frequencies for NO_2 (J_{NO_2}) inside the flow tube versus the number of lamps turned on. Each data point represents the mean of 3 experimental trials, with 1σ error bars; in some cases, error bars are too small to be seen. The dashed line is a linear fit to the experimental data.

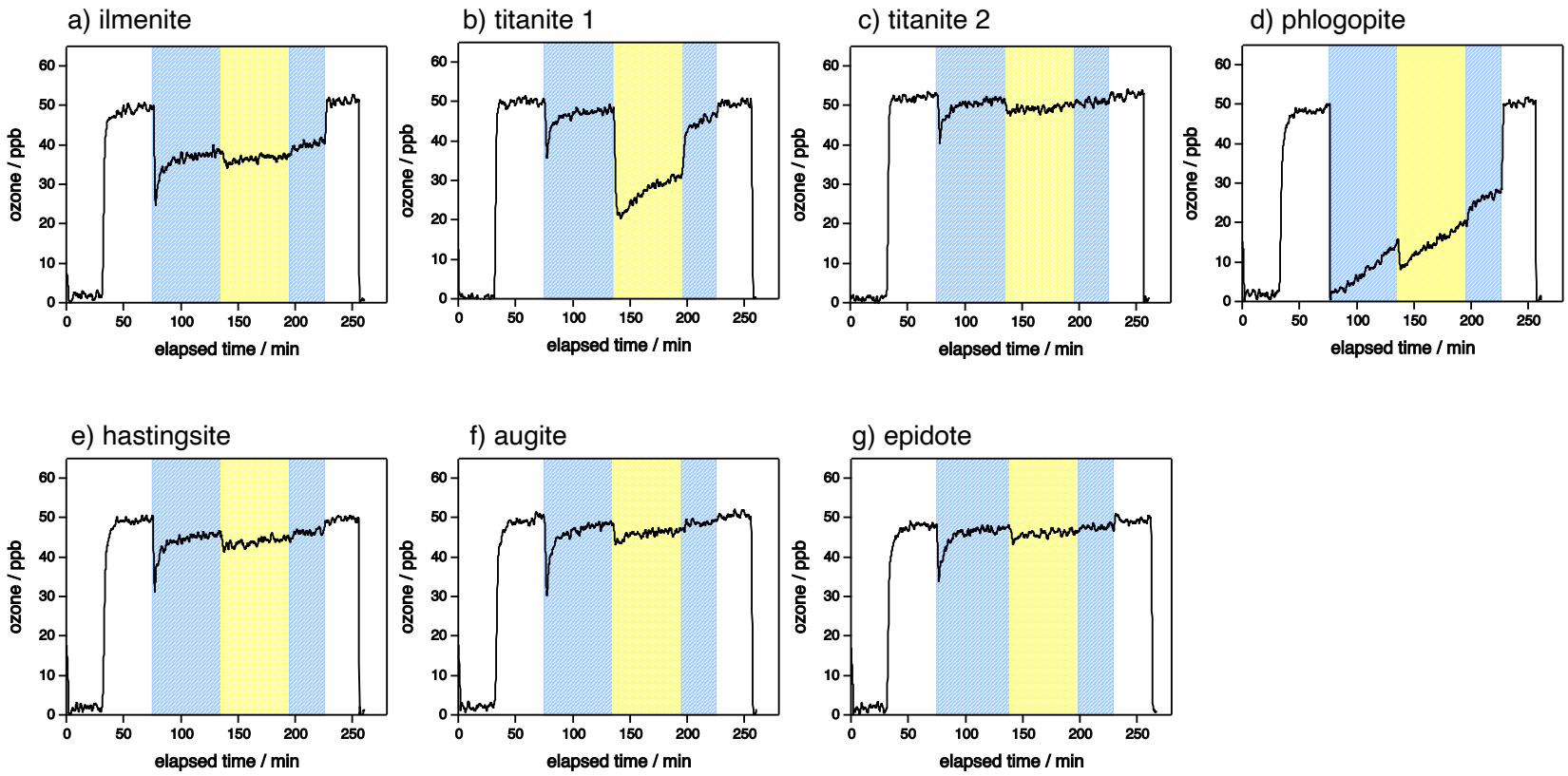

Figure A.3: Representative reaction profiles of Ti-containing minerals with ozone at 25% RH. The unshaded regions of the profile show time periods in which ozone was not exposed to our Ti-containing mineral. The blue and yellow regions of the profile show the exposure of ozone to our Ti-containing mineral under dark and illuminated conditions, respectively: a) ilmenite, b) titanite 1, c) titanite 2, d) phlogopite, e) hastingsite, f) augite, and g) epidote.

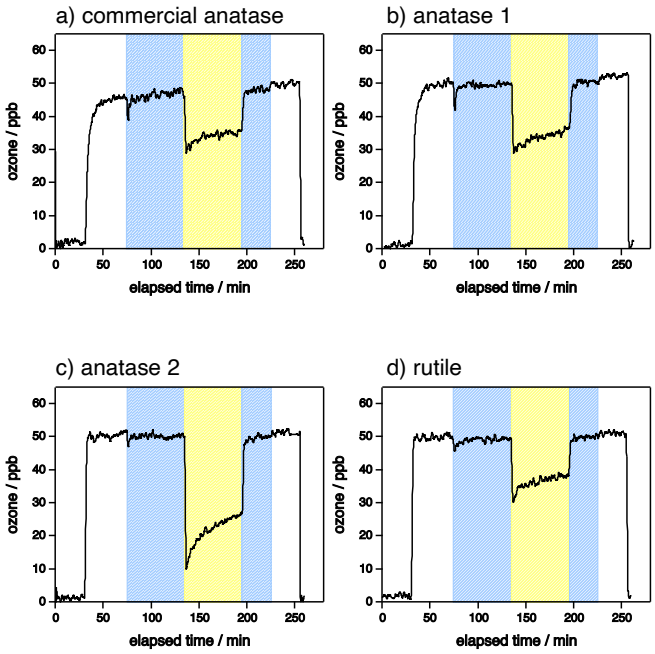

Figure A.4: Representative reaction profiles of TiO_2/SiO_2 mixtures with ozone at 25% RH. The unshaded regions of the profile show time periods in which ozone was not exposed to our Ti-containing mineral. The blue and yellow regions of the profile show the exposure of ozone to our Ti-containing mineral under dark and illuminated conditions, respectively: a) commercial anatase (0.1 wt. %), b) anatase 1 (1 wt. %), c) anatase 2 (20 wt. %), and d) rutile (10 wt. %).

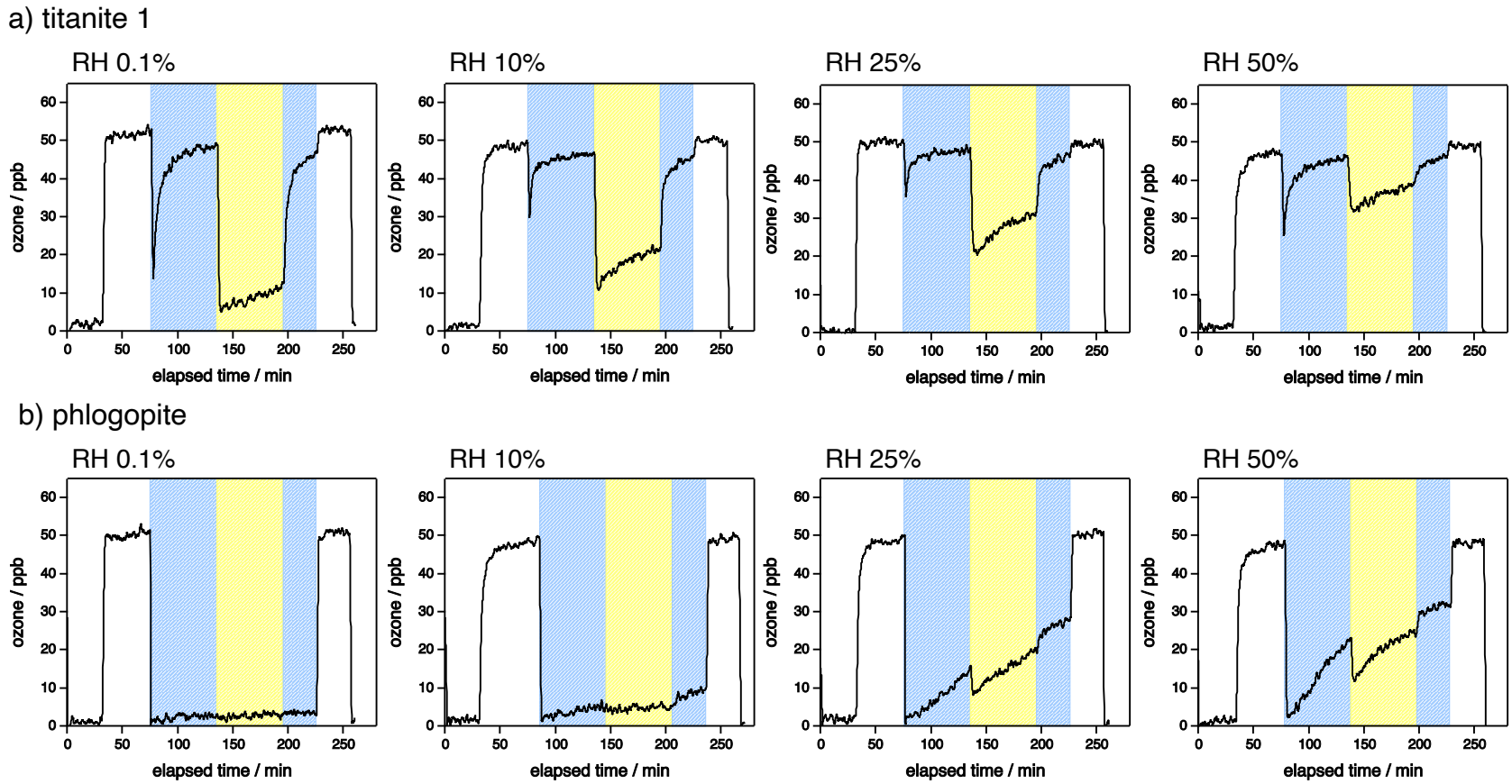

Figure A.5: Reaction profiles of selected Ti-containing minerals with ozone as a function of RH. The unshaded regions of the profile show time periods in which ozone was not exposed to our Ti-containing mineral. The blue and yellow regions of the profile show the exposure of ozone to our Ti-containing mineral under dark and illuminated conditions, respectively: a) titanite 1 and b) phlogopite.

Figure A.6: Photographs of natural Ti-containing minerals prior to grinding, with countries of origin listed in parentheses.

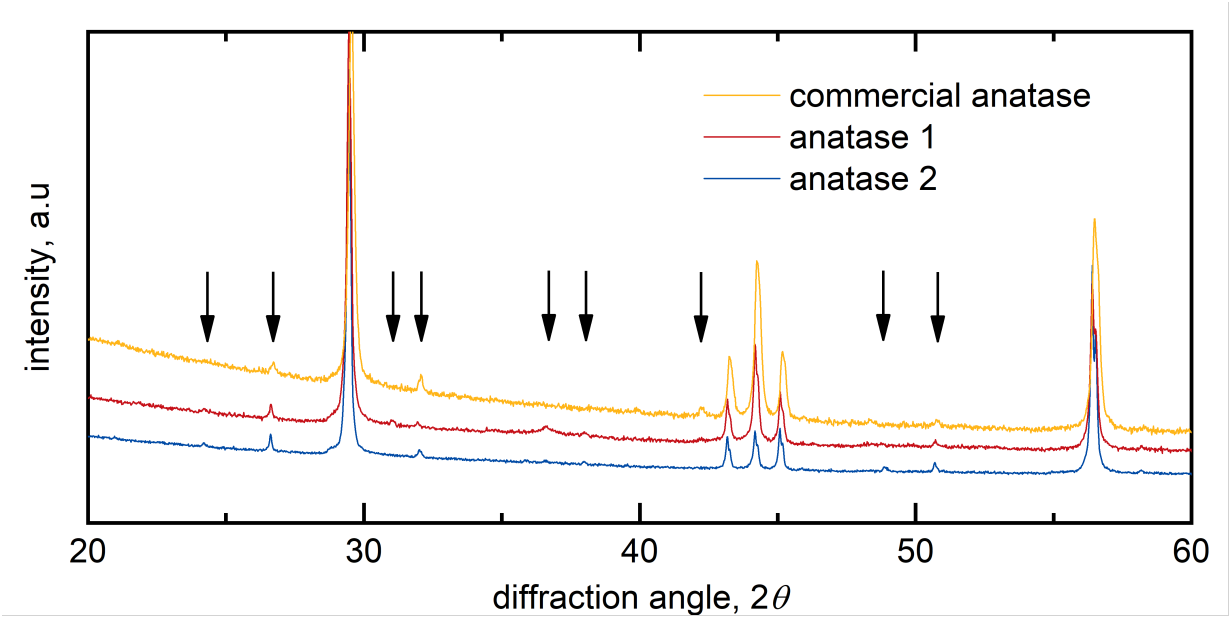

Figure A.7: Comparison of powder diffraction data of commercial anatase, anatase 1, and anatase 2. Impurity peaks and/or peaks from Kβ radiation are indicated with arrows.

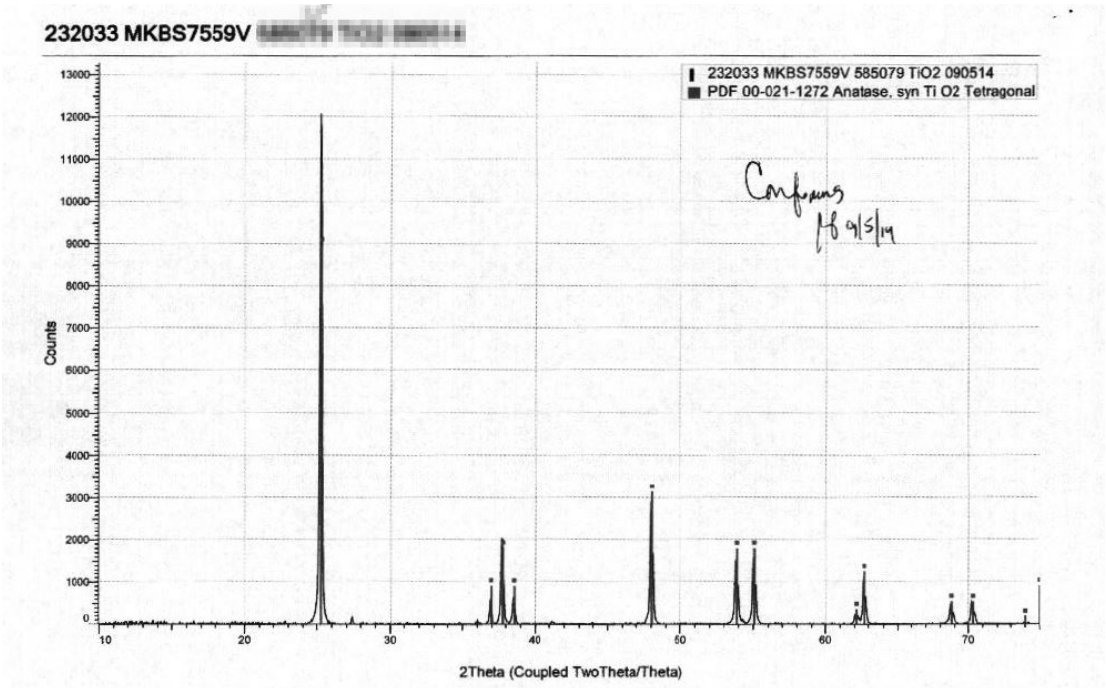

Figure A.8: Anatase purity check from Sigma Aldrich. The pattern is from the same batch as our commercial anatase sample. Cu radiation source was used for this measurement. Minor rutile peak is at 27.3° 2θ angle.

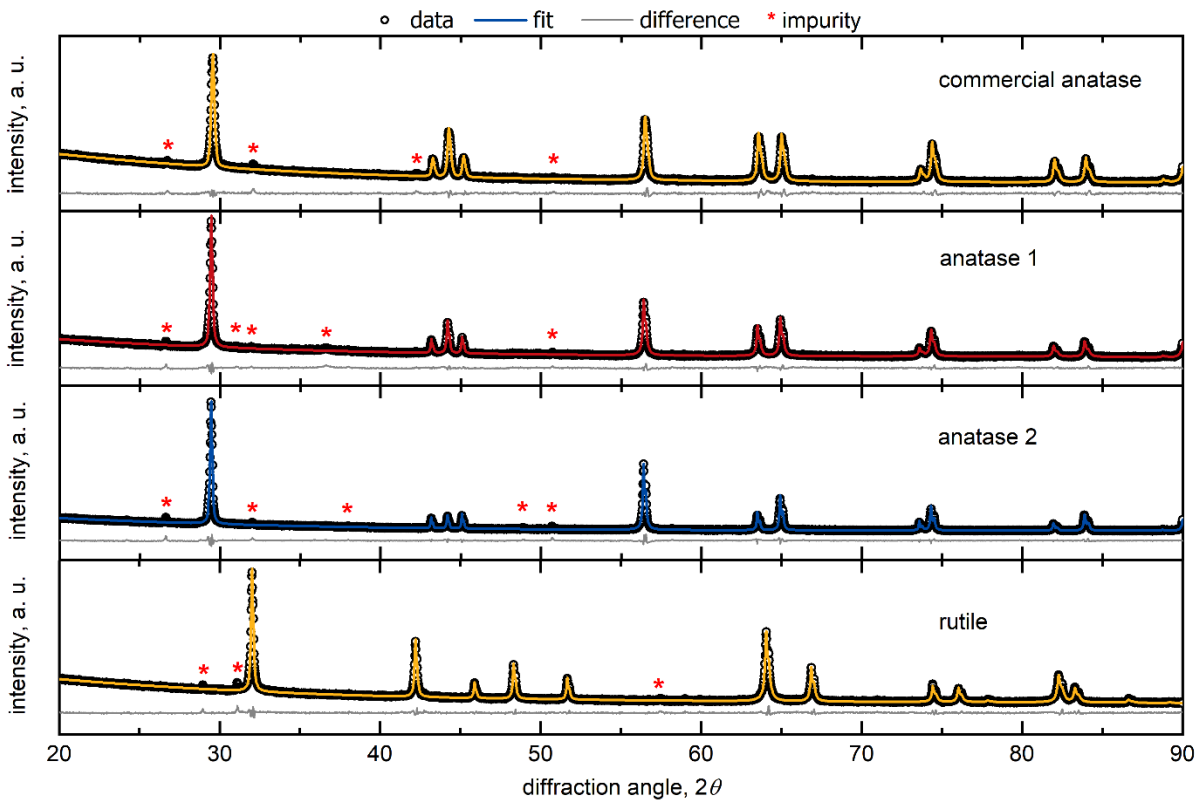

Figure A.9: Pawley refinement fit for TiO_2 minerals: commercial anatase, anatase 1, anatase 2, and rutile.

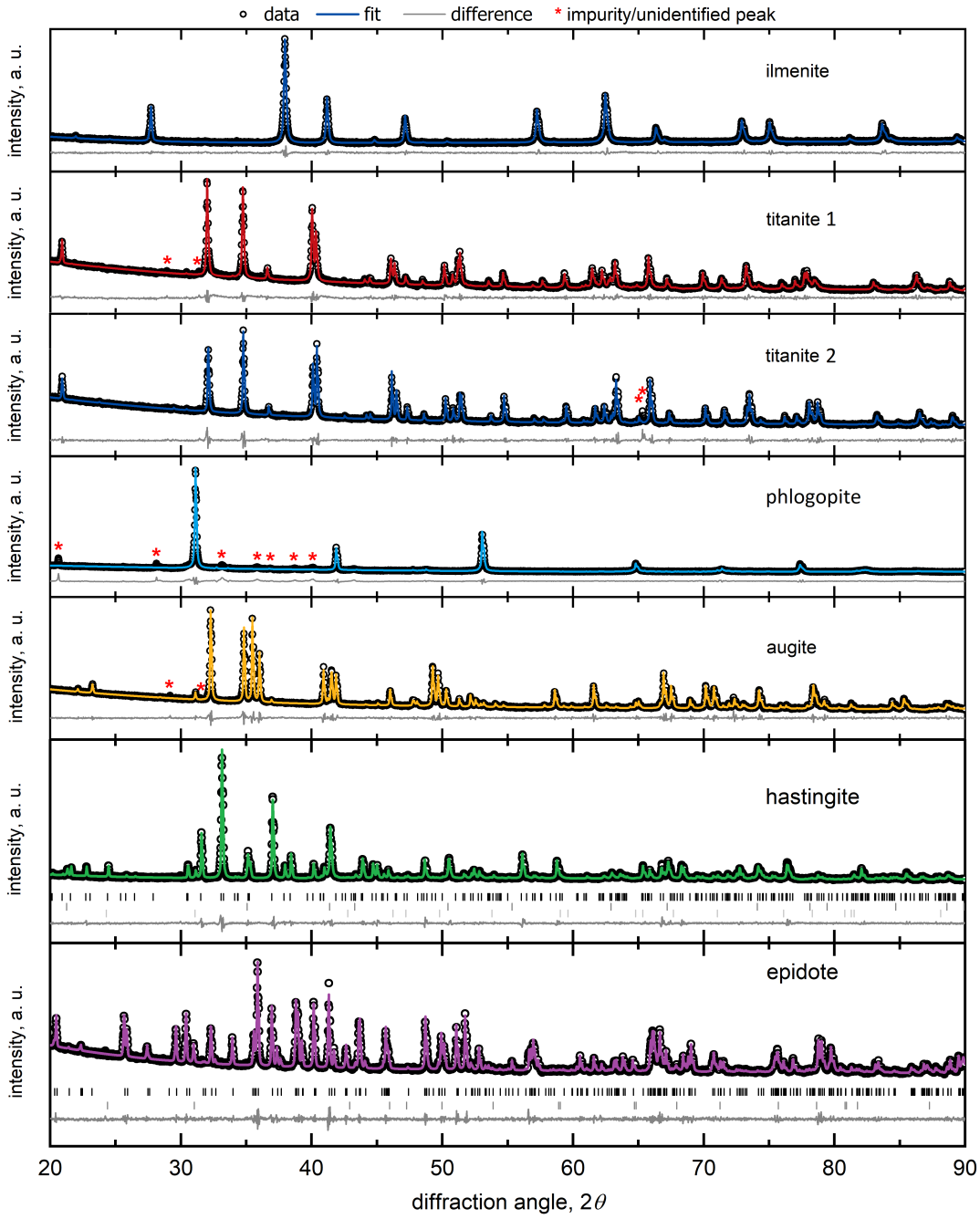

Figure A.10: Pawley refinement fit for remaining minerals. Ilmenite, titanite 1, titanite 2, phlogopite, and augite are fit with only one phase, whereas the hastingsite sample has diffraction peaks from hastingsite (black ticks), magnetite (dark grey ticks), and quartz (light grey ticks), and the epidote sample has diffraction peaks from epidote (black ticks) and quartz (dark grey ticks).

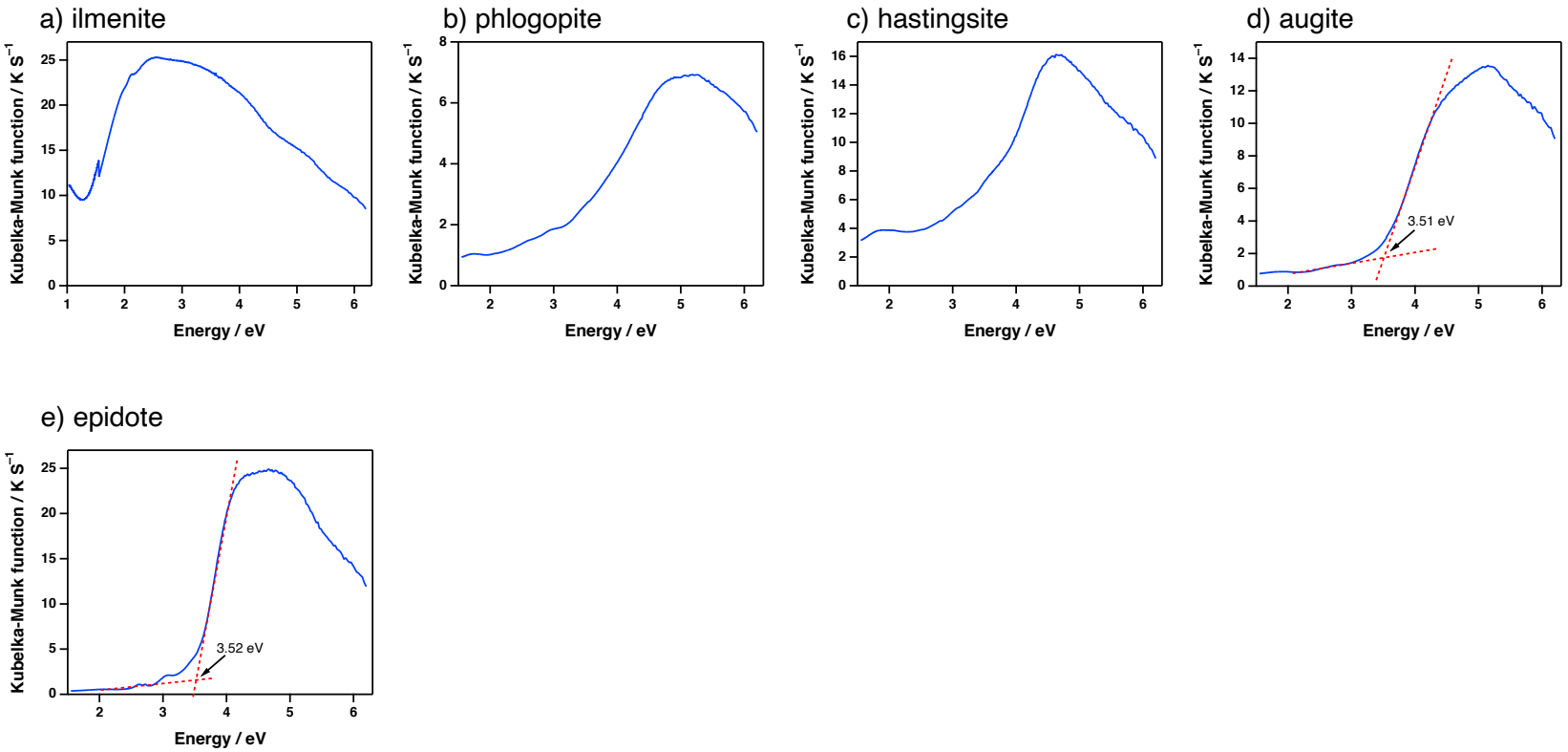

Figure A.11: Kubelka–Munk plots for Ti-containing minerals, in some cases with associated band gaps: a) ilmenite, b) phlogopite, c) hastingsite, d) augite, and e) epidote.

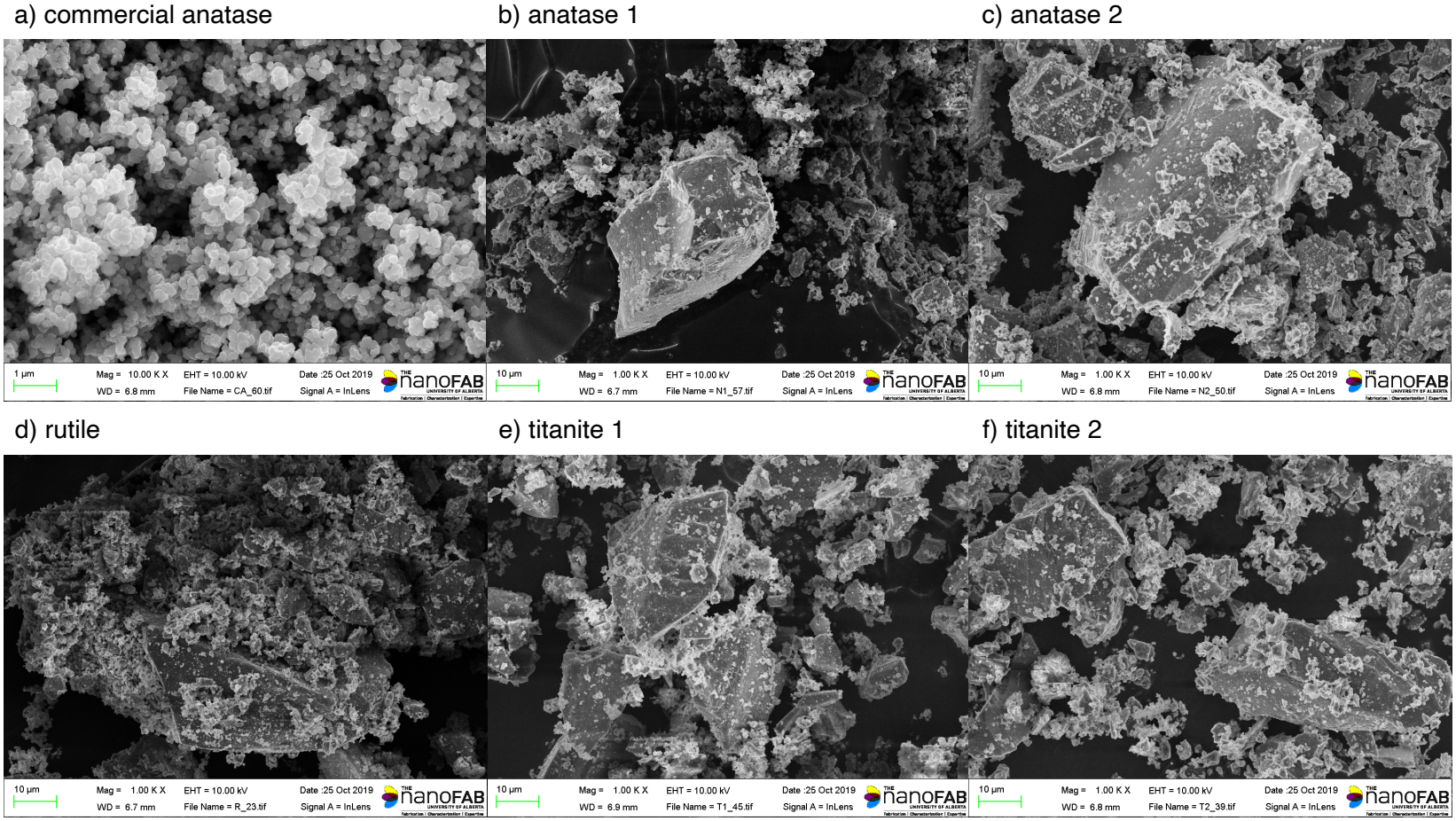

Figure A.12: Secondary electron images collected by FESEM of: a) commercial anatase, b) anatase 1, c) anatase 2, d) rutile, e) titanite 1, and f) titanite 2.

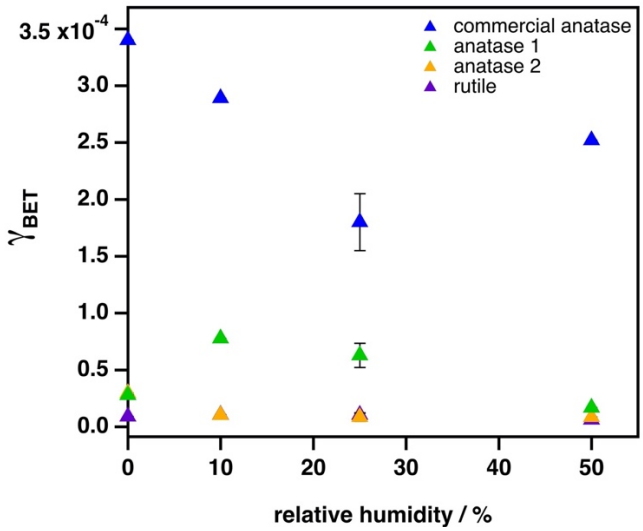

Figure A.13: Influence of relative humidity on light ozone BET uptake coefficients (γ_{BET}) for TiO_2 minerals. Each data point represents 1 trial, except for RH 25%, in which each data point represents the mean of 3 trials with 1σ error bars.

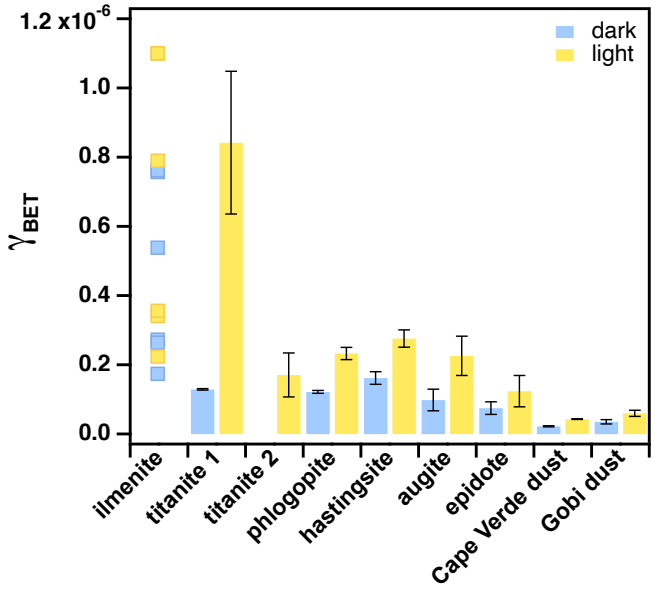

Figure A.14: BET uptake coefficients (γ_{BET}) under dark and illuminated conditions for ozone at RH 25% at the surface of Ti minerals, Ti-bearing minerals, and desert dust samples (Cape Verde dust and Gobi dust). Titanite 2 dark uptake was not significantly larger than the blank experiments (as discussed in main text of the manuscript). Each data point represents the mean of 3 trials with 1σ error bars, except for ilmenite, in which each trial (n = 6) is displayed individually as this sample appeared to display bimodal reactivity (see Chapter 2.1).

Parameter	Experimental	Equation
Temperature (T)	296.5 K	
Pressure (P)	1 atm	
Flow tube reactor diameter ($D_{reactor}$)	1.6 cm	
Flow tube reactor length ($L_{reactor}$)	34.4 cm	
Pyrex insert tube diameter (D_{tube})	1.05 cm	
Pyrex insert tube length (L_{tube})	20 cm	
Flow reactor cross-sectional area (A)	0.865 cm^2	$A = \pi r^2$
Volumetric flow (F)	0.440 L min^{-1}	
Linear velocity (v)	8.47 cm s^{-1}	$v = \frac{F}{A}$
Length of coated tube (L)	14.0 cm	
Residence time (t)	1.6 s	$t = \frac{v}{L}$
Reynolds number (Re)*	59.3	$Re = \frac{\rho \times D_{tube} \times v}{\eta}$
Length to laminar flow (l)[10]	2.18 cm	$l = 0.035 \times Re \times D_{tube}$
Mean molecular velocity (ω)**	361.6 m s^{-1}	$w = \sqrt{\frac{8RT}{\pi M}}$
Ozone diffusion coefficient (D)[54]	0.13 cm^2 s^{-2}	
Mean free path (λ)	105.7 nm	$\lambda = \frac{D}{w}$
Knudsen number (Kn)	2.00×10^{-5}	$Kn = \frac{2 \times \lambda}{D_{tube}}$
Dimensionless axial distance (z^*)[10]	0.38	$z^* = z\frac{\pi D}{2F}$ z = axial distance of tube (L)

Effective Sherwood number (N_{Shw}^{eff})[10]	3.97	$N_{Shw}^{eff} = 3.6568 + \frac{A}{(z^* + B)}\ 55$ A = 0.0978 and B = 0.0154

Table A.1: Photochemical coated-wall flow tube parameters.
*Re calculations require density (ρ) and viscosity (η) of air, which are taken to be 1.2 kg m^{-3} and 1.8 x 10^{-5} Pa s, respectively at 296.5 K[55]
**ω calculations require the ideal gas constant (R) and the molar mass of ozone (M), which are 8.3145 J K^{-1} mol^{-1} and 48 x 10^{-3} kg mol^{-1}

Sample	**Mass of SiO_2 (mg)**	**Mass of TiO_2 (mg)**	**TiO_2 wt. %**
Commercial anatase	899.2	0.87	0.1
Anatase 1	891.0	9.00	1.0
Anatase 2	720	180.08	20.0
Rutile	809.7	90.37	10.0

Table A.2: TiO_2/SiO_2 mixtures prepared for each TiO_2 sample.

Sample	Dremel®	SUPER IRON out® (0.04 g mL^{-1})	HCl (1 M)
Anatase 1	✓		
Anatase 2			
Rutile			
Ilmenite			
Titanite 1	✓		✓
Titanite 2			
Phlogopite	✓	✓	✓
Hastingsite		✓	
Augite		✓	
Epidote	✓	✓	

Table A.3: Summary of mineral sample pretreatments.

Sample	**BET surface area ($m^2\ g^{-1}$)**
Commercial anatase	9.6791
Anatase 1	3.7258
Anatase 2	1.5205
Rutile	1.9323
Ilmenite	2.0914
Titanite 1	1.9616
Titanite 2	1.0077
Phlogopite	18.7799
Hastingsite	1.7424
Augite	1.6235
Epidote	1.3855
Silicon dioxide	94.5500

Table A.4: Specific surface areas (BET; $m^2\ g^{-1}$) of each mineral sample under study.

	Nb_2O_5	SiO_2	TiO_2	ZnO	Al_2O_3	V_2O_3	Cr_2O_3	Fe_2O_3	MnO	MgO	CaO	Na_2O	K_2O	Total
	0.09	0.00	99.63	0.00	0.00	0.03	0.00	0.00	0.00	0.00	0.00	0.00	0.00	99.75
	0.07	0.00	100.12	0.00	0.00	0.08	0.00	0.00	0.00	0.00	0.00	0.00	0.00	100.27
	0.08	0.00	99.19	0.00	0.00	0.10	0.00	0.09	0.00	0.00	0.00	0.00	0.00	99.46
	0.07	0.00	99.70	0.00	0.00	0.00	0.00	0.00	0.00	0.00	0.00	0.00	0.00	99.77
	0.12	0.02	99.51	0.00	0.01	0.04	0.00	0.03	0.00	0.00	0.00	0.00	0.00	99.73
	0.00	0.00	99.30	0.00	0.02	0.06	0.00	0.03	0.00	0.00	0.00	0.00	0.00	99.41
	0.00	0.00	99.14	0.00	0.00	0.11	0.00	0.00	0.00	0.00	0.01	0.00	0.00	99.26
	0.10	0.00	99.14	0.00	0.00	0.10	0.00	0.05	0.00	0.00	0.00	0.00	0.00	99.39
Average	0.07	0.00	99.47	0.00	0.00	0.07	0.00	0.03	0.00	0.00	0.00	0.00	0.00	99.63
Std Dev.	0.04	0.01	0.34	0.00	0.01	0.04	0.00	0.03	0.00	0.00	0.00	0.00	0.00	0.32
Min	0.00	0.00	99.14	0.00	0.00	0.00	0.00	0.00	0.00	0.00	0.00	0.00	0.00	99.26
Max	0.12	0.02	100.12	0.00	0.02	0.11	0.00	0.09	0.00	0.00	0.01	0.00	0.00	100.27

Table A.5: Elemental composition of anatase 1 as obtained via electron microprobe analysis. In all cases, results less than the estimated limit of detection are reported as zero.

	Nb_2O_5	SiO_2	TiO_2	ZnO	Al_2O_3	Cr_2O_3	Fe_2O_3	MnO	MgO	CaO	Na_2O	K_2O	Total
	0.00	0.00	100.08	0.00	0.00	0.00	0.03	0.00	0.00	0.00	0.00	0.00	100.11
	0.00	0.00	100.02	0.00	0.00	0.00	0.10	0.00	0.00	0.00	0.00	0.00	100.12
	0.00	0.00	99.89	0.03	0.00	0.00	0.09	0.00	0.00	0.00	0.00	0.00	100.01
	0.00	0.00	99.80	0.00	0.00	0.00	0.06	0.00	0.00	0.00	0.00	0.00	99.86
	0.00	0.00	99.68	0.03	0.00	0.00	0.11	0.00	0.00	0.00	0.00	0.00	99.82
	0.00	0.00	99.67	0.00	0.03	0.00	0.05	0.00	0.00	0.00	0.00	0.00	99.75
	0.00	0.00	100.20	0.00	0.00	0.00	0.05	0.00	0.00	0.00	0.00	0.00	100.25
	0.00	0.00	99.81	0.00	0.00	0.00	0.08	0.00	0.00	0.00	0.00	0.00	99.89
	0.00	0.00	99.63	0.00	0.00	0.00	0.03	0.00	0.00	0.00	0.00	0.00	99.66
	0.00	0.00	99.78	0.00	0.00	0.00	0.03	0.00	0.00	0.00	0.00	0.00	99.81
	0.04	0.00	99.81	0.00	0.00	0.00	0.06	0.00	0.00	0.00	0.00	0.00	99.91
	0.00	0.00	99.89	0.00	0.00	0.00	0.08	0.00	0.00	0.00	0.00	0.00	99.97
	0.00	0.00	99.79	0.00	0.00	0.00	0.08	0.00	0.00	0.00	0.00	0.00	99.87
	0.00	0.00	99.78	0.00	0.03	0.00	0.08	0.00	0.00	0.00	0.00	0.01	99.90
	0.00	0.00	99.72	0.00	0.00	0.00	0.07	0.00	0.00	0.00	0.00	0.00	99.79
	0.00	0.00	99.79	0.00	0.02	0.00	0.06	0.00	0.00	0.00	0.00	0.00	99.87
Average	0.00	0.00	99.83	0.00	0.01	0.00	0.07	0.00	0.00	0.00	0.00	0.00	99.91
Std Dev.	0.01	0.00	0.15	0.01	0.01	0.00	0.02	0.00	0.00	0.00	0.00	0.00	0.15
Min	0.00	0.00	99.63	0.00	0.00	0.00	0.03	0.00	0.00	0.00	0.00	0.00	99.66
Max	0.04	0.00	100.20	0.03	0.03	0.00	0.11	0.00	0.00	0.00	0.00	0.01	100.25

Table A.6: Elemental composition of anatase 2 as obtained via electron microprobe analysis. In all cases, results less than the estimated limit of detection are reported as zero.

	Nb_2O_5	SiO_2	TiO_2	ZnO	Al_2O_3	V_2O_3	Cr_2O_3	Fe_2O_3	MnO	MgO	CaO	Na_2O	K_2O	Total
	0.49	0.00	98.73	0.00	0.04	0.00	0.00	0.68	0.00	0.00	0.00	0.00	0.00	99.94
	0.50	0.00	98.74	0.00	0.04	0.05	0.00	0.67	0.00	0.00	0.00	0.00	0.00	100.00
	0.54	0.01	98.72	0.00	0.03	0.12	0.00	0.67	0.00	0.00	0.00	0.00	0.00	100.09
	0.48	0.00	98.63	0.00	0.03	0.19	0.00	0.66	0.00	0.00	0.00	0.00	0.00	99.99
	0.60	0.02	98.74	0.00	0.02	0.12	0.00	0.66	0.00	0.00	0.00	0.00	0.00	100.16
	0.52	0.00	98.93	0.00	0.03	0.14	0.00	0.68	0.00	0.00	0.00	0.00	0.00	100.30
	0.49	0.00	98.90	0.00	0.04	0.13	0.00	0.68	0.00	0.00	0.00	0.00	0.00	100.24
	0.51	0.00	98.86	0.00	0.02	0.14	0.00	0.64	0.00	0.00	0.00	0.00	0.00	100.17
Average	0.52	0.00	98.78	0.00	0.03	0.11	0.00	0.67	0.00	0.00	0.00	0.00	0.00	100.11
Std Dev.	0.04	0.01	0.10	0.00	0.01	0.06	0.00	0.01	0.00	0.00	0.00	0.00	0.00	0.13
Min	0.48	0.00	98.63	0.00	0.02	0.00	0.00	0.64	0.00	0.00	0.00	0.00	0.00	99.94
Max	0.60	0.02	98.93	0.00	0.04	0.19	0.00	0.68	0.00	0.00	0.00	0.00	0.00	100.30

Table A.7: Elemental composition of rutile as obtained via electron microprobe analysis. In all cases, results less than the estimated limit of detection are reported as zero.

	Nb_2O_5	SiO_2	TiO_2	ZnO	Al_2O_3	V_2O_3	Cr_2O_3	FeO	MnO	MgO	CaO	Na_2O	K_2O	Total
	0.00	0.02	50.01	0.04	0.00	0.00	0.00	46.09	0.66	0.00	0.00	0.00	0.00	96.82
	0.00	0.00	50.73	0.00	0.00	0.00	0.00	46.03	0.71	0.00	0.00	0.00	0.00	97.47
	0.00	0.00	50.94	0.04	0.00	0.00	0.00	45.86	0.69	0.00	0.00	0.00	0.00	97.53
	0.00	0.01	50.10	0.03	0.00	0.00	0.00	46.43	0.69	0.00	0.00	0.00	0.00	97.26
	0.47	0.00	51.44	0.00	0.00	0.00	0.00	44.53	0.71	0.00	0.00	0.00	0.00	97.15
	0.00	0.00	50.49	0.03	0.00	0.00	0.00	45.87	0.71	0.00	0.00	0.00	0.00	97.1
	4.48	0.00	53.50	0.00	0.02	0.06	0.00	38.96	0.60	0.03	0.00	0.00	0.00	97.65
Average	0.71	0.00	51.03	0.02	0.00	0.01	0.00	44.82	0.68	0.00	0.00	0.00	0.00	97.28
Std Dev.	1.67	0.01	1.19	0.02	0.01	0.02	0.00	2.65	0.04	0.01	0.00	0.00	0.00	0.29
Min	0.00	0.00	50.01	0.00	0.00	0.00	0.00	38.96	0.60	0.00	0.00	0.00	0.00	96.82
Max	4.48	0.02	53.50	0.04	0.02	0.06	0.00	46.43	0.71	0.03	0.00	0.00	0.00	97.65
Impurity	0.00	3.47	14.82	0.00	1.53	0.04	0.00	66.95	0.39	0.14	0.00	0.00	0.00	87.42

Table A.8: Elemental composition of ilmenite as obtained via electron microprobe analysis. In all cases, results less than the estimated limit of detection are reported as zero. We note that the impurity in the ilmenite sample was not used in the overall average for the elemental composition.

	Nb_2O_5	SiO_2	TiO_2	ZnO	Al_2O_3	V_2O_3	Cr_2O_3	Fe_2O_3	MnO	MgO	CaO	Na_2O	K_2O	Total
	1.14	30.35	34.98	0.00	1.23	0.00	0.00	2.33	0.08	0.06	27.22	0.30	0.00	97.69
	1.08	30.50	34.98	0.00	1.20	0.04	0.00	2.29	0.08	0.04	27.34	0.32	0.00	97.87
	1.13	30.12	34.72	0.00	1.23	0.06	0.00	2.30	0.09	0.05	27.22	0.32	0.00	97.24
	1.16	30.23	34.86	0.00	1.19	0.04	0.00	2.31	0.09	0.08	27.08	0.29	0.00	97.33
	1.11	30.04	34.70	0.00	1.17	0.06	0.00	2.29	0.08	0.06	27.14	0.33	0.00	96.98
	0.93	30.23	34.39	0.00	1.27	0.00	0.00	2.38	0.08	0.08	27.24	0.30	0.00	96.90
	0.91	30.10	34.51	0.00	1.33	0.06	0.00	2.42	0.08	0.08	27.12	0.29	0.00	96.90
	0.98	30.32	34.59	0.00	1.29	0.00	0.00	2.40	0.08	0.07	27.26	0.29	0.00	97.28
Average	1.06	30.24	34.72	0.00	1.24	0.03	0.00	2.34	0.08	0.07	27.20	0.31	0.00	97.27
Std Dev.	0.10	0.15	0.22	0.00	0.05	0.03	0.00	0.05	0.00	0.02	0.08	0.02	0.00	0.36
Min	0.91	30.04	34.39	0.00	1.17	0.00	0.00	2.29	0.08	0.04	27.08	0.29	0.00	96.90
Max	1.16	30.50	34.98	0.00	1.33	0.06	0.00	2.42	0.09	0.08	27.34	0.33	0.00	97.87

Table A.9: Elemental composition of titanite 1 as obtained via electron microprobe analysis. In all cases, results less than the estimated limit of detection are reported as zero.

	Nb_2O_5	SiO_2	TiO_2	ZnO	Al_2O_3	Cr_2O_3	Fe_2O_3	MnO	MgO	CaO	Na_2O	K_2O	Total
	0.00	30.81	38.44	0.00	0.86	0.00	0.57	0.00	0.03	28.25	0.00	0.00	98.96
	0.00	30.78	38.68	0.00	0.82	0.00	0.53	0.00	0.03	28.22	0.00	0.00	99.06
	0.00	30.72	38.16	0.00	0.86	0.00	0.57	0.00	0.04	28.30	0.12	0.00	98.77
	0.00	30.78	38.17	0.00	0.86	0.00	0.57	0.00	0.02	28.30	0.00	0.00	98.70
	0.00	30.74	38.26	0.00	0.90	0.00	0.57	0.00	0.02	28.33	0.00	0.00	98.82
	0.00	30.76	38.33	0.00	0.88	0.00	0.57	0.03	0.03	28.35	0.00	0.00	98.95
	0.00	30.75	38.42	0.00	0.96	0.00	0.62	0.00	0.02	28.31	0.00	0.00	99.08
	0.00	30.75	38.64	0.00	0.83	0.00	0.52	0.00	0.03	28.42	0.00	0.00	99.19
	0.00	30.70	38.76	0.00	0.71	0.00	0.50	0.02	0.04	28.26	0.00	0.00	98.99
	0.00	30.77	38.46	0.00	0.90	0.00	0.57	0.02	0.03	28.29	0.00	0.00	99.04
	0.00	30.77	38.31	0.00	0.88	0.00	0.58	0.02	0.03	28.28	0.03	0.00	98.90
	0.00	30.85	38.44	0.00	0.90	0.00	0.58	0.00	0.02	28.39	0.00	0.00	99.18
	0.00	30.76	38.51	0.00	0.85	0.00	0.61	0.00	0.03	28.27	0.00	0.00	99.03
	0.00	30.78	38.51	0.00	0.87	0.00	0.58	0.00	0.03	28.37	0.00	0.00	99.14
	0.00	30.79	38.64	0.00	0.86	0.00	0.59	0.02	0.02	28.29	0.00	0.00	99.21
	0.00	30.73	38.83	0.00	0.70	0.00	0.49	0.00	0.02	28.38	0.00	0.00	99.15
Average	0.00	30.77	38.47	0.00	0.85	0.00	0.56	0.01	0.03	28.31	0.01	0.00	99.01
Std Dev.	0.00	0.04	0.20	0.00	0.07	0.00	0.04	0.01	0.01	0.06	0.03	0.00	0.15
Min	0.00	30.70	38.16	0.00	0.70	0.00	0.49	0.00	0.02	28.22	0.00	0.00	98.70
Max	0.00	30.85	38.83	0.00	0.96	0.00	0.62	0.03	0.04	28.42	0.12	0.00	99.21

Table A.10: Elemental composition of titanite 2 as obtained via electron microprobe analysis. In all cases, results less than the estimated limit of detection are reported as zero.

	Nb_2O_5	SiO_2	TiO_2	ZnO	Al_2O_3	V_2O_3	Cr_2O_3	FeO	MnO	MgO	CaO	Na_2O	K_2O	Total
	0.00	42.82	0.92	0.08	11.08	0.00	0.00	6.66	0.13	22.43	0.00	0.43	10.07	94.62
	0.00	42.80	0.98	0.08	11.02	0.00	0.00	6.60	0.13	22.23	0.00	0.18	10.51	94.53
	0.00	42.85	1.05	0.07	11.20	0.00	0.00	6.80	0.13	22.05	0.00	0.25	10.31	94.71
	0.00	42.53	1.02	0.09	11.19	0.00	0.00	6.79	0.12	22.26	0.00	0.34	10.17	94.51
	0.00	42.83	1.04	0.07	11.10	0.00	0.00	6.68	0.12	22.13	0.00	0.25	10.39	94.61
	0.00	42.68	1.05	0.08	10.95	0.00	0.00	6.79	0.12	22.05	0.00	0.33	10.25	94.30
	0.00	42.23	1.07	0.06	11.17	0.00	0.00	6.88	0.14	22.15	0.00	0.36	10.17	94.23
Average	0.00	42.68	1.02	0.08	11.10	0.00	0.00	6.74	0.13	22.19	0.00	0.31	10.27	94.50
Std Dev.	0.00	0.23	0.05	0.01	0.09	0.00	0.00	0.10	0.01	0.13	0.00	0.08	0.15	0.18
Min	0.00	42.23	0.92	0.06	10.95	0.00	0.00	6.60	0.12	22.05	0.00	0.18	10.07	94.23
Max	0.00	42.85	1.07	0.09	11.20	0.00	0.00	6.88	0.14	22.43	0.00	0.43	10.51	94.71

Table A.11: Elemental composition of phlogopite as obtained via electron microprobe analysis. In all cases, results less than the estimated limit of detection are reported as zero.

	Nb_2O_5	SiO_2	TiO_2	ZnO	Al_2O_3	V_2O_3	Cr_2O_3	FeO	MnO	MgO	CaO	Na_2O	K_2O	Total
	0.00	40.95	0.80	0.00	10.59	0.00	0.00	21.01	0.21	8.76	11.17	1.68	2.07	97.24
	0.00	40.79	0.77	0.00	10.58	0.00	0.00	20.96	0.23	8.66	11.14	1.63	2.02	96.78
	0.00	40.86	0.76	0.03	10.42	0.00	0.00	20.96	0.20	8.64	11.16	1.63	2.02	96.68
	0.00	40.72	0.78	0.03	10.43	0.00	0.00	20.98	0.20	8.59	11.08	1.63	2.02	96.46
	0.00	40.58	0.76	0.00	10.53	0.00	0.00	21.02	0.21	8.73	11.14	1.67	2.02	96.66
	0.00	40.63	0.84	0.03	10.46	0.00	0.00	20.91	0.20	8.62	11.12	1.64	2.07	96.52
	0.00	40.75	0.76	0.00	10.37	0.00	0.00	21.00	0.19	8.66	11.11	1.69	2.03	96.56
	0.00	40.79	0.81	0.00	10.44	0.00	0.00	21.00	0.22	8.68	11.11	1.64	2.02	96.71
Average	0.00	40.76	0.79	0.01	10.48	0.00	0.00	20.98	0.21	8.67	11.13	1.65	2.03	96.70
Std Dev.	0.00	0.12	0.03	0.02	0.08	0.00	0.00	0.04	0.01	0.06	0.03	0.02	0.02	0.24
Min	0.00	40.58	0.76	0.00	10.37	0.00	0.00	20.91	0.19	8.59	11.08	1.63	2.02	96.46
Max	0.00	40.95	0.84	0.03	10.59	0.00	0.00	21.02	0.23	8.76	11.17	1.69	2.07	97.24

Table A.12: Elemental composition of hastingsite as obtained via electron microprobe analysis. In all cases, results less than the estimated limit of detection are reported as zero.

	Nb_2O_5	SiO_2	TiO_2	ZnO	Al_2O_3	V_2O_3	Cr_2O_3	FeO	MnO	MgO	CaO	Na_2O	K_2O	Total
	0.00	50.90	0.76	0.00	3.39	0.00	0.58	5.81	0.11	16.41	19.70	0.33	0.00	97.99
	0.00	51.55	0.64	0.00	2.88	0.00	0.55	5.69	0.13	16.94	19.57	0.34	0.00	98.29
	0.00	51.96	0.55	0.00	2.49	0.00	0.67	5.41	0.11	17.32	19.72	0.32	0.00	98.55
	0.00	51.55	0.73	0.00	2.98	0.03	0.69	5.45	0.12	16.51	20.15	0.33	0.00	98.54
	0.00	51.31	0.77	0.00	3.09	0.06	0.60	5.54	0.12	16.56	20.19	0.37	0.00	98.61
	0.00	51.46	0.76	0.00	3.18	0.00	0.61	5.61	0.13	16.61	20.12	0.35	0.00	98.83
	0.00	51.74	0.75	0.00	3.38	0.03	0.61	5.70	0.11	16.68	20.20	0.33	0.00	99.53
	0.00	52.26	0.75	0.00	3.41	0.00	0.59	5.80	0.13	16.80	20.25	0.37	0.00	100.36
Average	0.00	51.59	0.71	0.00	3.10	0.02	0.61	5.63	0.12	16.73	19.99	0.34	0.00	98.84
Std Dev.	0.00	0.41	0.08	0.00	0.32	0.02	0.05	0.15	0.01	0.29	0.27	0.02	0.00	0.76
Min	0.00	50.90	0.55	0.00	2.49	0.00	0.55	5.41	0.11	16.41	19.57	0.32	0.00	97.99
Max	0.00	52.26	0.77	0.00	3.41	0.06	0.69	5.81	0.13	17.32	20.25	0.37	0.00	100.36

Table A.13: Elemental composition of augite as obtained via electron microprobe analysis. In all cases, results less than the estimated limit of detection are reported as zero.

	Nb_2O_5	SiO_2	TiO_2	ZnO	Al_2O_3	V_2O_3	Cr_2O_3	Fe_2O_3	MnO	MgO	CaO	Na_2O	K_2O	Total
	0.00	37.19	0.22	0.00	22.39	0.05	0.00	14.18	0.14	0.03	23.03	0.00	0.00	97.23
	0.00	37.03	0.23	0.00	22.62	0.04	0.00	14.13	0.14	0.03	23.16	0.00	0.00	97.38
	0.00	37.31	0.17	0.00	22.66	0.05	0.00	14.24	0.14	0.03	23.01	0.00	0.00	97.61
	0.00	37.02	0.23	0.00	22.60	0.04	0.00	14.15	0.13	0.04	23.02	0.00	0.00	97.23
	0.00	37.20	0.20	0.00	22.63	0.05	0.00	14.18	0.12	0.03	23.03	0.00	0.00	97.44
	0.00	37.13	0.20	0.00	22.49	0.04	0.00	14.18	0.11	0.05	23.07	0.00	0.00	97.27
	0.00	37.20	0.20	0.00	22.53	0.04	0.00	14.23	0.12	0.03	23.13	0.00	0.00	97.48
	0.00	37.19	0.22	0.00	22.38	0.05	0.00	14.34	0.12	0.02	23.13	0.00	0.00	97.45
Average	0.00	37.16	0.21	0.00	22.54	0.05	0.00	14.20	0.13	0.03	23.07	0.00	0.00	97.39
Std Dev.	0.00	0.10	0.02	0.00	0.11	0.01	0.00	0.07	0.01	0.01	0.06	0.00	0.00	0.14
Min	0.00	37.02	0.17	0.00	22.38	0.04	0.00	14.13	0.11	0.02	23.01	0.00	0.00	97.23
Max	0.00	37.31	0.23	0.00	22.66	0.05	0.00	14.34	0.14	0.05	23.16	0.00	0.00	97.61

Table A.14: Elemental composition of epidote as obtained via electron microprobe analysis. In all cases, results less than the estimated limit of detection are reported as zero.

sample	**Commercial anatase**	**Anatase 1**	**Anatase 2**	**Rutile**
space group	$I4_1/amd$ (No. 136)	$I4_1/amd$ (No. 136)	$I4_1/amd$ (No. 136)	$P4_2/mnm$ (No. 136)
a (Å)	3.78645(5)	3.78514(4)	3.78489(3)	4.59572(6)
b(Å)	3.78645(5)	3.78514(4)	3.78489(3)	4.59572(6)
c (Å)	9.5179(1)	9.5120(1)	9.5119(1)	2.95966(4)
α,°	90	90	90	90
β,°	90	90	90	90
γ,°	90	90	90	90
T (K)	296	296	296	296
radiation	Co Kα,	Co Kα,	Co Kα,	Co Kα,
	Kα1 λ=1.78900 Å	Kα1 λ=1.78900 Å	Kα1 λ=1.78900 Å	Kα1 λ=1.78900 Å
	Kα2 λ=1.79283 Å	Kα2 λ=1.79283 Å	Kα2 λ=1.79283 Å	Kα2 λ=1.79283 Å
2θ limits	20.00–90.00°	20.00–90.00°	20.00–90.00°	20.00–90.00°
refinement method	Pawley	Pawley	Pawley	Pawley
no. of data collected	3500 data points	3500 data points	3500 data points	3500 data points
no. of Bragg reflections	14	14	14	13
no. of variables	27	27	27	27
residuals	R_{wp} = 0.0472	R_{wp} = 0.0492	R_{wp} = 0.0657	R_{wp} = 0.0482

sample	Titanite 1	Titanite 2	Phlogopite	Augite	Hastingsite	Epidote	ilmenite
space group	$C2/c$ (No. 15)	$C2/c$ (No. 15)	$C2/m$ (No. 12)	$C2/c$ (No. 15)	$C2/m$ (No. 12)	$P2_1/m$ (No. 11)	$R\bar{3}$ (No. 148)
a (Å)	6.5529(1)	6.5735(1)	5.1635(2)	9.7361(2)	9.9076(1)	8.8986(1)	5.08769(7)
b(Å)	8.7022(2)	8.7278(1)	9.0833(6)	8.8989(1)	18.1624(4)	5.63531(8)	5.08769(7)
c (Å)	7.0569(1)	7.0851(1)	20.086(2)	5.2686(1)	5.3283(3)	10.1623(1)	4.0820(2)
α,°	90	90	90	90	90	90	90
β,°	113.849(1)	113.962(1)	95.685(3)	106.327(1)	104.992(3)	115.4145(8)	90
γ,°	90	90	90	90	90	90	120
T (K)	296	296	296	296	296	296	296
radiation	Co Kα,	Co Kα,	Co Kα,	Co Kα,	Co Kα,	Co Kα,	Co Kα,
	Kα1 λ=1.78900 Å	Kα1 λ=1.78900 Å	Kα1 λ=1.78900 Å	Kα1 λ=1.78900 Å	Kα1 λ=1.78900 Å	Kα1 λ=1.78900 Å	Kα1 λ=1.78900 Å
	Kα2 λ=1.79283 Å	Kα2 λ=1.79283 Å	Kα2 λ=1.79283 Å	Kα2 λ=1.79283 Å	Kα2 λ=1.79283 Å	Kα2 λ=1.79283 Å	Kα2 λ=1.79283 Å
2θ limits	20.00–90.00°	20.00–90.00°	20.00–90.00°	20.00–90.00°	20.00–90.00°	20.00–90.00°	20.00–90.00°
refinement method	Pawley	Pawley	Pawley	Pawley	Pawley	Pawley	Pawley
no. of data collected	3500 data points	3500 data points	3500 data points	3500 data points	3500 data points	3500 data points	3500 data points
no. of Bragg reflections	189	189	257	14	258	281	36
no. of variables	205	205	273	27	330	333	50
residuals	R_{wp} = 0.0731	R_{wp} = 0.0482	R_{wp} = 0.0923	R_{wp} = 0.0526	R_{wp} = 0.0347	R_{wp} = 0.0358	R_{wp} = 0.0201

Table A.15. Crystallographic data for Ti-containing sample refinement.

Formula	**TiO_2**	**$CaTiSiO_5$**
Formula mass (amu)	79.90	196.07
Space group	$I4_1/amd$ (No. 136)	$C2/c$ (No. 15)
a (Å)	3.806(4)	6.572(3)
b (Å)	3.806(4)	8.731(3)
c (Å)	9.576(9)	7.084(4)
α, °	90	90
β, °	90	113.922(4)
γ, °	90	90
V (Å^3)	138.7(2)	371.6(3)
Z	4	4
ρ_{calcd} (g cm^{-3})	3.825	3.505
T (K)	296(2)	296(2)
Crystal dimensions (mm)	0.01 × 0.08 × 0.20	0.05 × 0.12 × 0.14
Radiation	Graphite monochromated Mo $K\alpha$, λ = 0.71073 Å	
μ (Mo $K\alpha$) (mm^{-1})	5.55	3.900
Transmission factors	0.3958– 0.9313	0.6191–0.8441
2θ limits	11.54 – 95.74 °	8.24 – 66.44 °
Data collected	$-5 \le h \le 5$, $-5 \le k \le 5$, $-14 \le l \le 14$	$-9 \le h \le 10$, $-13 \le k \le 13$, $-10 \le l \le 10$
No. of data collected	917	2164
No. of unique data, including $F_o^2 < 0$	84 (R_{int} = 0.0370)	706 (R_{int} = 0.0285)
No. of unique data, with $F_o^2 > 2\sigma(F_o^2)$	72	560
No. of variables	8	41
$R(F)$ for $F_o^2 > 2\sigma(F_o^2)$ [a]	0.0127	0.0373
$R_w(F_o^2)$ [b]	0.0144	0.0481
Goodness of fit	1.231	1.084
$(\Delta\rho)_{max}$, $(\Delta\rho)_{min}$ (e Å^{-3})	0.362, – 0.448	0.644, – 1.262

[a] $R(F) = \sum||F_o| - |F_c|| / \sum|F_o|$. [b] $R_w(F_o^2) = [\sum[w(F_o^2 - F_c^2)^2] / \sum wF_o^4]^{1/2}$; $w^{-1} = [\sigma^2(F_o^2) + (Ap)^2 + Bp]$, where $p = [\max(F_o^2,0) + 2F_c^2] / 3$.

Table A.16: Crystallographic data for anatase 2 and titanite 1 single crystals.

Position	Wyckoff position	*x*	*y*	*z*	U_{11} (Å²)	U_{22} (Å²)	U_{33} (Å²)
Ti	4*b*	0	1/4	3/8	0.0081(3)	0.0081(3)	0.0059(3)
O	8*e*	0	1/4	0.1668(2)	0.0069(6)	0.0134(6)	0.0064(6)

Table A.17: Atomic coordinates and displacement parameters for anatase 2.

Ti – O (×4)	1.945(2)
Ti – O (×2)	1.993(2)
Ti –Ti (×4)	3.058(2)

Table A.18: Selected interatomic distances (Å) for anatase 2.

Position	Wyckoff position	*x*	*y*	*z*	U_{11} (Å²)	U_{22} (Å²)	U_{33} (Å²)
Ti	4*a*	0	0	0	0.0102(3)	0.0118(3)	0.0225(4)
Si	4*e*	0	0.68280(9)	1/4	0.0090(4)	0.0091(4)	0.0111(4)
Ca	4*e*	0	0.33202(7)	1/4	0.0120(3)	0.0103(3)	0.0361(5)
O1	4*e*	0	0.0721(3)	1/4	0.0174(10)	0.0122(9)	0.0123(10)
O2	8*f*	0.3976(2)	0.28987(16)	0.3819(2)	0.0144(7)	0.0121(7)	0.0183(8)
O3	8*f*	0.3141(2)	0.06639(19)	0.0897(2)	0.0141(7)	0.0147(8)	0.0177(8)

Table A.19: Atomic coordinates and displacement parameters for titanite 1.

A.3 References

(1) Parrish, D. D.; Murphy, P. C.; Albritton, D. L.; Fehsenfeld, F. C. The Measurement of the Photodissociation Rate of NO2 in the Atmosphere. *Atmos. Environ.* **1983**, *17* (7), 1365–1379. https://doi.org/10.1016/0004-6981(83)90411-0.

(2) Zafonte, L.; Rieger, P. L.; Holmes, J. R. Nitrogen Dioxide Photolysis in the Los Angeles Atmosphere. *Environ. Sci. Technol.* **1977**, *11* (5), 483–487.

(3) Nicolas, M.; Ndour, M.; Ka, O.; D'Anna, B.; George, C. Photochemistry of Atmospheric Dust: Ozone Decomposition on Illuminated Titanium Dioxide. *Environ. Sci. Technol.* **2009**, *43* (19), 7437–7442. https://doi.org/10.1021/es901569d.

(4) Pöschl, U.; Rudich, Y.; Ammann, M. Kinetic Model Framework for Aerosol and Cloud Surface Chemistry and Gas-Particle Interactions–Part 1: General Equations, Parameters, and Terminology. *Atmos. Chem. Phys.* **2007**, *7* (23), 5989–6023.

(5) Michel, A. E.; Usher, C. R.; Grassian, V. H. Reactive Uptake of Ozone on Mineral Oxides and Mineral Dusts. *Atmos. Environ.* **2003**, *37* (23), 3201–3211. https://doi.org/10.1016/S1352-2310(03)00319-4.

(6) Adams, J. W.; Rodriguez, D.; Cox, R. A. The Uptake of SO2 on Saharan Dust: A Flow Tube Study. *Atmos. Chem. Phys.* **2005**, *5* (10), 2679–2689.

(7) El Zein, A.; Bedjanian, Y. Interaction of NO2 with TiO2 Surface under UV Irradiation: Measurements of the Uptake Coefficient. *Atmos. Chem. Phys.* **2012**, *12* (2), 1013–1020. https://doi.org/10.5194/acp-12-1013-2012.

(8) Lasne, J.; Romanias, M. N.; Thevenet, F. Ozone Uptake by Clay Dusts under Environmental Conditions. *ACS Earth Space Chem.* **2018**, *2* (9), 904–914. https://doi.org/10.1021/acsearthspacechem.8b00057.

(9) Wang, X.; Romanias, M. N.; Thévenet, F.; Rousseau, A. Geocatalytic Uptake of Ozone onto Natural Mineral Dust. *Catalysts* **2018**, *8* (7), 263. https://doi.org/10.3390/catal8070263.

(10) Knopf, D. A.; Pöschl, U.; Shiraiwa, M. Radial Diffusion and Penetration of Gas Molecules and Aerosol Particles through Laminar Flow Reactors, Denuders, and Sampling Tubes. *Anal. Chem.* **2015**, *87* (7), 3746–3754. https://doi.org/10.1021/ac5042395.

(11) Sing, K. S. W. Adsorption by Powders and Porous Solids. In *Adsorption by Powders and Porous Solids (Second Edition)*; Rouquerol, F., Rouquerol, J., Sing, K. S. W., Llewellyn, P., Maurin, G., Eds.; Academic Press: Oxford, 2014; pp 237–268. https://doi.org/10.1016/B978-0-08-097035-6.00007-3.

(12) Donovan, J. J.; Kremser, D.; Fournelle, J. H.; Goemann, K. *Probe for EPMA: Acquisition, Automation and Analysis, Version 11*; Eugene, Oregon, Probe Software, Inc., 2015.

(13) Donovan, J. J.; Snyder, D. A.; Rivers, M. L. *An Improved Interference Correction for Trace Element Analysis*, 2nd ed.; Microbeam Analysis, 1993.

(14) Armstrong, J. T. *CITZAF: A Package of Correction Programs for the Quantitative Electron Microbeam X-Ray-Analysis of Thick Polished Materials, Thin-Films, and Particles*; Microbeam Analysis 4, 1995.

(15) Jarosewich, E.; Nelen, J. A.; Norberg, J. A. *Reference Samples for Electron Microprobe Analysis*, 4th ed.; Geostand. Geoanal. Res, 1980.

(16) Gates-Rector, S.; Blanton, T. The Powder Diffraction File: A Quality Materials Characterization Database. *Powder Diffraction* **2019**, *34* (4), 352–360. https://doi.org/10.1017/S0885715619000812.

(17) Jade 9.5; Materials Data: Livermore, CA. 2019.

(18) TOPAS V4: General Profile and Structure Analysis Software for Powder Diffraction Data. - User's Manual, Bruker AXS, Karlsruhe, Germany. Bruker AXS (2008).
(19) Pawley, G. S. Unit-Cell Refinement from Powder Diffraction Scans. *J. Appl. Cryst.* **1981**, *14* (6), 357–361. https://doi.org/10.1107/S0021889881009618.
(20) Bruker AXS Inc. *Version, S. A. D. A. B. S.*; Madison WI, USA, 2001.
(21) Sheldrick, G. M. SHELXTL, Version 6.12. Bruker AXS Inc.: Madison, WI 2001.
(22) Kortüm, G. *Reflectance Spectroscopy: Principles, Methods, Applications*; Springer Science & Business Media, 2012.
(23) Murphy, A. B. Band-Gap Determination from Diffuse Reflectance Measurements of Semiconductor Films, and Application to Photoelectrochemical Water-Splitting. *Sol. Energy Mater. Sol. Cell* **2007**, *91* (14), 1326–1337. https://doi.org/10.1016/j.solmat.2007.05.005.
(24) Jenkins, R.; Snyder, R. *Introduction to X-Ray Powder Diffractometry*; Wiley: New York, 1996.
(25) Sullivan, R. C.; Thornberry, T.; Abbatt, J. P. D. Ozone Decomposition Kinetics on Alumina: Effects of Ozone Partial Pressure, Relative Humidity and Repeated Oxidation Cycles. *Atmos. Chem. Phys.* **2004**, *4* (5), 1301–1310. https://doi.org/10.5194/acp-4-1301-2004.
(26) Li, W.; Gibbs, G. V.; Oyama, S. T. Mechanism of Ozone Decomposition on a Manganese Oxide Catalyst. 1. In Situ Raman Spectroscopy and Ab Initio Molecular Orbital Calculations. *J. Am. Chem. Soc.* **1998**, *120* (35), 9041–9046. https://doi.org/10.1021/ja981441+.
(27) Hanisch, F.; Crowley, J. N. Ozone Decomposition on Saharan Dust: An Experimental Investigation. *Atmos. Chem. Phys.* **2003**, *3* (1), 119–130. https://doi.org/10.5194/acp-3-119-2003.
(28) Michel A. E.; Usher C. R.; Grassian V. H. Heterogeneous and Catalytic Uptake of Ozone on Mineral Oxides and Dusts: A Knudsen Cell Investigation. *Geophys. Res. Lett.* **2002**, *29* (14), 10–11. https://doi.org/10.1029/2002GL014896.
(29) Coates Fuentes, Z. L.; Kucinski, T. M.; Hinrichs, R. Z. Ozone Decomposition on Kaolinite as a Function of Monoterpene Exposure and Relative Humidity. *ACS Earth Space Chem.* **2017**. https://doi.org/10.1021/acsearthspacechem.7b00107.
(30) Mogili, P. K.; Kleiber, P. D.; Young, M. A.; Grassian, V. H. Heterogeneous Uptake of Ozone on Reactive Components of Mineral Dust Aerosol: An Environmental Aerosol Reaction Chamber Study. *J. Phys. Chem. A* **2006**, *110* (51), 13799–13807. https://doi.org/10.1021/jp063620g.
(31) Chen, H.; Stanier, C. O.; Young, M. A.; Grassian, V. H. A Kinetic Study of Ozone Decomposition on Illuminated Oxide Surfaces. *J. Phys. Chem. A* **2011**, *115* (43), 11979–11987. https://doi.org/10.1021/jp208164v.
(32) Maters, E. C.; Delmelle, P.; Rossi, M. J.; Ayris, P. M.; Bernard, A. Controls on the Surface Chemical Reactivity of Volcanic Ash Investigated with Probe Gases. *Earth Planet. Sci. Lett.* **2016**, *450*, 254–262. https://doi.org/10.1016/j.epsl.2016.06.044.
(33) Bulanin, K. M.; Lavalley, J. C.; Tsyganenko, A. A. IR Spectra of Adsorbed Ozone. *Colloids Surf. A Physicochem. Eng. Asp.* **1995**, *101* (2), 153–158. https://doi.org/10.1016/0927-7757(95)03130-6.
(34) Lampimäki, M.; Zelenay, V.; Křepelová, A.; Liu, Z.; Chang, R.; Bluhm, H.; Ammann, M. Ozone-Induced Band Bending on Metal-Oxide Surfaces Studied under Environmental Conditions. *ChemPhysChem* **2013**, *14* (11), 2419–2425. https://doi.org/10.1002/cphc.201300418.
(35) Li, W.; Oyama, S. T. Mechanism of Ozone Decomposition on a Manganese Oxide Catalyst. 2. Steady-State and Transient Kinetic Studies. *J. Am. Chem. Soc.* **1998**, *120* (35), 9047–9052. https://doi.org/10.1021/ja9814422.

(36) Radhakrishnan, R.; Oyama, S. T. Ozone Decomposition over Manganese Oxide Supported on ZrO2 and TiO2: A Kinetic Study Using in Situ Laser Raman Spectroscopy. *J. Catal.* **2001**, *199* (2), 282–290. https://doi.org/10.1006/jcat.2001.3167.
(37) Roscoe, J. M.; Abbatt, J. P. D. Diffuse Reflectance FTIR Study of the Interaction of Alumina Surfaces with Ozone and Water Vapor. *J. Phys. Chem. A* **2005**, *109* (40), 9028–9034. https://doi.org/10.1021/jp050766r.
(38) Fitzpatrick, R. W.; Chittleborough, D. J. Titanium and Zirconium Minerals. In *Soil Mineralogy with Environmental Applications*; John Wiley & Sons, Ltd, 2002; pp 667–690. https://doi.org/10.2136/sssabookser7.c22.
(39) Chang, R. Y.-W.; Sullivan, R. C.; Abbatt, J. P. D. Initial Uptake of Ozone on Saharan Dust at Atmospheric Relative Humidities. *Geophys. Res. Lett.* **2005**, *32* (14), L14815. https://doi.org/10.1029/2005GL023317.
(40) Kolb, C. E.; Cox, R. A.; Abbatt, J. P. D.; Ammann, M.; Davis, E. J.; Donaldson, D. J.; Garrett, B. C.; George, C.; Griffiths, P. T.; Hanson, D. R.; Kulmala, M.; McFiggans, G.; Pöschl, U.; Riipinen, I.; Rossi, M. J.; Rudich, Y.; Wagner, P. E.; Winkler, P. M.; Worsnop, D. R.; O' Dowd, C. D. An Overview of Current Issues in the Uptake of Atmospheric Trace Gases by Aerosols and Clouds. *Atmospheric Chemistry and Physics* **2010**, *10* (21), 10561–10605. https://doi.org/10.5194/acp-10-10561-2010.
(41) Hanisch, F.; Crowley, J. N. Ozone Decomposition on Saharan Dust: An Experimental Investigation. *Atmos. Chem. Phys.* **2003**, *3* (1), 119–130. https://doi.org/10.5194/acp-3-119-2003.
(42) Aubin, D. G.; Abbatt, J. P. D. Interaction of NO2 with Hydrocarbon Soot: Focus on HONO Yield, Surface Modification, and Mechanism. *J Phys Chem A* **2007**, *111* (28), 6263–6273. https://doi.org/10.1021/jp068884h.
(43) Wu, L. Impact of Saharan Air Layer on Hurricane Peak Intensity. *Geophys. Res. Lett.* **2007**, *34* (9). https://doi.org/10.1029/2007GL029564.
(44) Perry, K. D.; Cahill, T. A.; Eldred, R. A.; Dutcher, D. D.; Gill, T. E. Long-Range Transport of North African Dust to the Eastern United States. *J. Geophys. Res.* **1997**, *102* (D10), 11225–11238. https://doi.org/10.1029/97JD00260.
(45) Xie, C.; Nishizawa, T.; Sugimoto, N.; Matsui, I.; Wang, Z. Characteristics of Aerosol Optical Properties in Pollution and Asian Dust Episodes over Beijing, China. *Appl. Opt.* **2008**, *47* (27), 4945–4951. https://doi.org/10.1364/AO.47.004945.
(46) Rubasinghege, G.; H. Grassian, V. Role(s) of Adsorbed Water in the Surface Chemistry of Environmental Interfaces. *Chem. Commun.* **2013**, *49* (30), 3071–3094. https://doi.org/10.1039/C3CC38872G.
(47) Nicolas, M.; Ndour, M.; Ka, O.; D'Anna, B.; George, C. Photochemistry of Atmospheric Dust: Ozone Decomposition on Illuminated Titanium Dioxide. *Environ. Sci. Technol.* **2009**, *43* (19), 7437–7442. https://doi.org/10.1021/es901569d.
(48) Hoffmann, M. R.; Martin, S. T.; Choi, W.; Bahnemann, D. W. Environmental Applications of Semiconductor Photocatalysis. *Chem. Rev.* **1995**, *95* (1), 69–96. https://doi.org/10.1021/cr00033a004.
(49) Hurum, D. C.; Agrios, A. G.; Gray, K. A.; Rajh, T.; Thurnauer, M. C. Explaining the Enhanced Photocatalytic Activity of Degussa P25 Mixed-Phase TiO_2 Using EPR. *J. Phys. Chem. B* **2003**, *107* (19), 4545–4549. https://doi.org/10.1021/jp0273934.
(50) Bickley, R. I.; Gonzalez-Carreno, T.; Lees, J. S.; Palmisano, L.; Tilley, R. J. D. A Structural Investigation of Titanium Dioxide Photocatalysts. *J. Solid State Chem.* **1991**, *92* (1), 178–190. https://doi.org/10.1016/0022-4596(91)90255-G.

(51) Folli, A.; Campbell, S. B.; Anderson, J. A.; Macphee, D. E. Role of TiO2 Surface Hydration on NO Oxidation Photo-Activity. *J .Photoch. Photobio. A* **2011**, *220* (2), 85–93. https://doi.org/10.1016/j.jphotochem.2011.03.017.
(52) Styler, S. A.; Donaldson, D. J. Photooxidation of Atmospheric Alcohols on Laboratory Proxies for Mineral Dust. *Environ. Sci. Technol.* **2011**, *45* (23), 10004–10012. https://doi.org/10.1021/es202263q.
(53) Brown, G. E.; Henrich, V. E.; Casey, W. H.; Clark, D. L.; Eggleston, C.; Felmy, A.; Goodman, D. W.; Grätzel, M.; Maciel, G.; McCarthy, M. I.; Nealson, K. H.; Sverjensky, D. A.; Toney, M. F.; Zachara, J. M. Metal Oxide Surfaces and Their Interactions with Aqueous Solutions and Microbial Organisms. *Chem. Rev.* **1999**, *99* (1), 77–174. https://doi.org/10.1021/cr980011z.
(54) Ivanov, A. V.; Trakhtenberg, S.; Bertram, A. K.; Gershenzon, Y. M.; Molina, M. J. OH, HO2, and Ozone Gaseous Diffusion Coefficients. *J. Phys. Chem. A* **2007**, *111* (9), 1632–1637. https://doi.org/10.1021/jp066558w.
(55) Jennings, S. G. The Mean Free Path in Air. *J. Aerosol Sci* **1988**, *19* (2), 159–166. https://doi.org/10.1016/0021-8502(88)90219-4.

Date	Experiment	mass (g)	length of tube (m)	[O3] Initial
March 25 2019	Titanite1 30mg RH25 O350	0.02266	0.14	52.3
March 25 2019	Titanite2 30mg RH25 O350	0.03495	0.141	53.2
March 26 2019	Ilmenite 30mg RH25 O350	0.02331	0.14	52.1
March 27 2019	Augite 30mg RH25 O350	0.02433	0.14	53.1
March 27 2019	Magnesioamphibole 30mg RH25 O350	0.03329	0.141	54
March 29 2019	Hastingsite 30mg RH25 O350	0.02212	0.14	52
April 2 2019	Titanite1 30mg RH25 O350	0.02168	0.141	49.8
April 4 2019	Mica 30mg RH25 O350	0.02562	0.142	50.8
April 5 2019	Hastingsite 30mg RH25 O350	0.01842	0.141	49.7
April 5 2019	Ilmenite 30mg RH25 O350	0.02054	0.142	50.4
April 8 2019	Titanite2 30mg RH25 O350	0.03297	0.141	49.9
April 8 2019	Mica 30mg RH25 O350	0.02341	0.141	51
April 9 2019	Augite 30mg RH25 O350	0.02136	0.141	50.6
April 10 2019	Magnesioamphibole 30mg RH25 O350	0.02064	0.141	49.2
April 10 2019	Titanite1 30mg RH25 O350	0.01967	0.141	50.5
April 11 2019	Hastingsite 30mg RH25 O350	0.02441	0.14	49.5
April 12 2019	Ilmenite 30mg RH25 O350	0.04002	0.14	48.4
April 15 2019	Augite 30mg RH25 O350	0.01994	0.14	50.8
April 15 2019	Titanite2 30mg RH25 O350	0.01989	0.139	50.4
April 16 2019	Magnesioamphibole 30mg RH25 O350	0.02443	0.14	49.6
April 17 2019	Mica 30mg RH25 O350	0.02816	0.141	49.3
April 17 2019	Ilmenite 30mg RH25 O350	0.01834	0.14	47.9
April 18 2019	Hastingsite 30mg RH25 O350	0.01879	0.14	49.3
April 24 2019	Titanite1 30mg RH0 O350	0.02912	0.14	50.1
April 24 2019	Titanite2 RH0 O350	0.0196	0.14	50.9
April 25 2019	Ilmenite 30mg RH0 O350	0.00657	0.14	51
April 25 2019	Mica 30mg RH0 O350	0.01794	0.139	50.8
April 26 2019	Titanite 1 RH10	0.01697	0.139	49.4
April 26 2019	Titanite 2 RH10	0.0206	0.14	51.8
April 29 2019	Mica RH10	0.02249	0.139	50
April 29 2019	Ilmenite RH10	0.01483	0.14	51
April 30 2019	Titanite 1 RH50	0.02295	0.141	50
April 30 2019	Titanite 2 Rh50	0.2768	0.138	49.6
May 1 2019	Mica RH50	0.02226	0.14	48.5
May 1 2019	Ilmenite RH50	0.0173	0.139	47.7
May 2 2019	Ilmenite RH25	0.01289	0.139	51.9
May 2 2019	SDCV RH25	0.01713	0.141	51.1
May 3 2019	Gobi RH25	0.01488	0.14	49.9
May 7 2019	Ilmenite RH25	0.01406	0.14	50.2
May 7 2019	Fumed SiO2 Trial 1 RH25	0.02197	0.14	51.1
May 8 2019	Commericial Anatase Trial 1 (5%)	0.0009749	0.141	49.9
May 8 2019	Commericial Anatase Trial 2 (5%)	0.000822433	0.14	48.8
May 9 2019	Natural Anatase 1 Trial 1 (5%)	0.000930394	0.14	49.4
May 9 2019	Natural Anatase 1 Trial 2 (5%)	0.001094757	0.14	51.4
May 10 2019	Commericial Anatase Trial 1 (2%)	0.000381542	0.14	49.7
May 10 2019	Commericial Anatase Trial 2 (2%)	0.000370126	0.139	51.2
May 17 2019	Commercial Antase Trial 1 (0.5%)	9.29819E-05	0.14	49.6
May 17 2019	Commericial Anatase Trial 2 (0.5%)	8.88561E-05	0.14	50.8
May 21 2019	Commercial Antase Trial 1 (0.1%)	1.33E-05	0.139	50.1
May 21 2019	Commercial Antase Trial 2 (0.1%)	1.89839E-05	0.141	50.5
May 22 2019	Natural Anatase 1 Trial 1 (0.1%)	1.76024E-05	0.141	50.8
May 22 2019	Natural Anatase 1 Trial 2 (0.1%)	1.56642E-05	0.141	50.7
May 23 2019	Rutile Trial 1 (10%)	0.001134557	0.139	50.4
May 24 2019	Natural Anatase 2 Trial 1 (20%)	0.003399208	0.141	48.5
May 24 2019	Natural Anatase 2 Trial 2 (20%)	0.003191134	0.14	
May 25 2016	Rutile Trial 2 (10%)	0.001345404	0.141	50.7
May 25 2016	Rutile Trial 3 (10%)	0.00098596	0.139	51.1
May 26 2019	Natural Anatase 2 Trial 2 (20%)	0.003487239	0.14	50.2
May 26 2019	Natural Anatase 2 Trial 3 (20%)	0.003137115	0.141	50.8
May 27 2019	Natural Anatase 1 Trial 3 (0.1%)	1.14E-05	0.139	50.5
May 27 2019	Commericial Anatase Trial 3 (0.1%)	1.47792E-05	0.14	51.8
May 28 2019	Fumed SiO2 Trial 2 RH25	0.0181	0.14	49.9
May 28 2019	Fumed SiO2 Trial 3 RH25	0.02073	0.141	51.9
May 29 2019	Nat Ana 1 (0.1%) RH0	2.12218E-05	0.139	50.3
May 29 2019	Com Ana (0.1%) RH0	2.16613E-05	0.14	51.4
May 30 2019	Rutile (10%) RH0	0.001481953	0.139	50.4
May 30 2019	Nat Ana 2 (20%) RH0	0.00213876	0.14	50.4
May 31 2019	Nat Ana 1 (0.1%) RH10	1.79485E-05	0.139	49.7
May 31 2019	Com Ana (0.1%) RH10	1.76403E-05	0.141	51
June 3 2019	Rutile (10%) RH10	0.001527134	0.141	50.6
June 3 2019	Nat Ana 2 (20%) RH10	0.003551262	0.14	48.4
June 4 2019	Nat Ana 1 (0.1%) RH 50	1.33996E-05	0.141	47.3
June 4 2019	Com Ana (0.1%) RH50	2.10137E-05	0.141	47.2
June 5 2019	Rutile (10%) RH50	0.001644606	0.14	47.1
June 5 2019	Nat Ana 2 (20%) RH50	0.003647296	0.139	47.6
June 6 2019	SDCV 2 RH25	0.02092	0.14	47
June 6 2019	SDCV 3 RH25	0.02153	0.137	48.5
June 7 2019	Gobi 2 RH25	0.02634	0.14	47.9
June 7 2019	Gobi 3 RH25	0.02346	0.14	48.5
June 10 2019	Fumed SiO2 RH0	0.02258	0.139	48
June 10 2019	Mica RH0	0.01106	0.137	47.6
June 11 2019	Fumed SiO2 RH10	0.01861	0.139	47.4
June 11 2019	Mica RH10	0.00609	0.139	48.5
June 12 2019	Fumed SiO2 RH50	0.01776	0.14	53
June 12 2019	BLK RH50	0	0.2	53.2
June 20 2019	BLK RH25	0	0.2	52.4
June 20 2019	Nat Ana (0.5%) Trial 1	6.36834E-05	0.141	54.4
June 24 2019	BLK RH10	0	0.2	52.3
June 24 2019	Titanite 1 RH10	0.0157	0.14	54.1
June 25 2019	BLK RH0	0	0.2	52.1
June 25 2019	Titanite 1 RH0	0.02395	0.14	52.4
June 27 2019	Nat Ana (1%) Trial 1	0.0001253	0.141	52.7
July 3 2019	Nat Ana (1%) Trial 2	0.0001518	0.141	52.3
July 3 2019	Nat Ana (1%) Trial 3	0.0001409	0.141	54
July 4 2019	Nat Ana (1%) RH10	0.0001148	0.142	52.9
July 6 2019	Nat Ana (1%) RH50	0.0002166	0.14	51.2
July 7 2019	Nat Ana (1%) RH0	0.0001098	0.139	53.4
July 8 2019	Blk 2 RH25	0	0.2	52.7
July 8 2019	Blk 3 RH25	0	0.2	52.7
July 9 2019	Nat Ana (1%) RH0	0.0001844	0.141	54.4
June 20 2019	BLK RH25	0	0.2	52.4
July 8 2019	Blk 2 RH25	0	0.2	52.7
July 8 2019	Blk 3 RH25	0	0.2	52.7

Date	Residence Time (s)	BET (m^2/g)	z*	S geo (cm^2)	Sherwood #	[O3] final dark (ppb)	[O3] final light (ppb)	k (dark)	k light
March 25 2019	1.652246591	1.9616	0.379786005	46.158	3.9042784	48.7	37.5	0.04316386	0.201335224
March 25 2019	1.664048352	1.0077	0.382498762	46.4877	3.902591164	51	50.2	0.025379529	0.034880819
March 26 2019	1.652246591	2.0914	0.379786005	46.158	3.9042784	47.1	45.8	0.061063493	0.078003404
March 27 2019	1.652246591	1.6235	0.379786005	46.158	3.9042784	50.6	46.4	0.029187745	0.081632772
March 27 2019	1.664048352	1.3855	0.382498762	46.4877	3.902591164	51.9	51.3	0.023836601	0.030824401
March 29 2019	1.652246591	1.7424	0.379786005	46.158	3.9042784	47.8	45.3	0.050971858	0.083484322
April 2 2019	1.664048352	1.9616	0.382498762	46.4877	3.902591164	46.6	31	0.039911366	0.284864186
April 4 2019	1.675850114	18.7799	0.385211519	46.8174	3.90092678	28	19.9	0.355456517	0.559224608
April 5 2019	1.664048352	1.7424	0.382498762	46.4877	3.902591164	46.8	45	0.036129798	0.059699253
April 5 2019	1.675850114	2.0914	0.385211519	46.8174	3.90092678	43.9	42.5	0.082392127	0.101731711
April 8 2019	1.664048352	1.0077	0.382498762	46.4877	3.902591164	49.5	47.3	0.004836598	0.032156943
April 8 2019	1.664048352	18.7799	0.382498762	46.4877	3.902591164	29.5	20	0.328978042	0.562539759
April 9 2019	1.664048352	1.6235	0.382498762	46.4877	3.902591164	49.2	46.9	0.016861261	0.045632028
April 10 2019	1.664048352	1.3855	0.382498762	46.4877	3.902591164	47.6	46.3	0.019867729	0.036508352
April 10 2019	1.664048352	1.9616	0.382498762	46.4877	3.902591164	47.5	36.5	0.036803994	0.19510315
April 11 2019	1.652246591	1.7424	0.379786005	46.158	3.9042784	45.9	43.4	0.045699929	0.079596611
April 12 2019	1.652246591	2.0914	0.379786005	46.158	3.9042784	37.7	34.9	0.151212126	0.197920205
April 15 2019	1.652246591	1.6235	0.379786005	46.158	3.9042784	48.3	46.9	0.030543137	0.048345495
April 15 2019	1.64044483	1.0077	0.377073248	45.8283	3.905988959	48.5	47.5	0.023424974	0.036125241
April 16 2019	1.652246591	1.3855	0.379786005	46.158	3.9042784	48.4	47.5	0.01482286	0.026183212
April 17 2019	1.664048352	18.7799	0.382498762	46.4877	3.902591164	26.8	18.9	0.366288752	0.57616244
April 17 2019	1.652246591	2.0914	0.379786005	46.158	3.9042784	34.8	31.1	0.193371933	0.26140631
April 18 2019	1.652246591	1.7424	0.379786005	46.158	3.9042784	46	42.2	0.041932412	0.094116617
April 24 2019	1.652246591	1.9616	0.379786005	46.158	3.9042784	39.8	5.7	0.139297667	1.315514794
April 24 2019	1.652246591	1.0077	0.379786005	46.158	3.9042784	50	49.8	0.01079737	0.013223171
April 25 2019	1.652246591	2.0914	0.379786005	46.158	3.9042784	44.7	35.8	0.079801727	0.214179736
April 25 2019	1.64044483	18.7799	0.377073248	45.8283	3.905988959	3.5	2.7	1.630736577	1.788932202
April 26 2019	1.64044483	1.9616	0.377073248	45.8283	3.905988959	45.4	21.3	0.051472819	0.512814169
April 26 2019	1.652246591	1.0077	0.379786005	46.158	3.9042784	51	48	0.009420214	0.04611245
April 29 2019	1.64044483	18.7799	0.377073248	45.8283	3.905988959	9.6	4.7	1.00598318	1.441353256
April 29 2019	1.652246591	2.0914	0.379786005	46.158	3.9042784	36.1	28.6	0.209129055	0.350080259
April 30 2019	1.664048352	1.9616	0.382498762	46.4877	3.902591164	46.4	38.9	0.044904672	0.150854243
April 30 2019	1.628643068	1.0077	0.37436049	45.4986	3.90772333	48.1	47	0.018855363	0.033060179
May 1 2019	1.652246591	18.7799	0.379786005	46.158	3.9042784	44.6	24.5	0.050736942	0.413310389
May 1 2019	1.64044483	2.0914	0.377073248	45.8283	3.905988959	46.2	44.9	0.0194774	0.036876341
May 2 2019	1.64044483	2.0914	0.377073248	45.8283	3.905988959	41.1	37.3	0.142224026	0.201363348
May 2 2019	1.664048352	39.6	0.382498762	46.4877	3.902591164	43.5	36.8	0.096766154	0.197281919
May 3 2019	1.652246591	10.5	0.379786005	46.158	3.9042784	46.3	43.9	0.045319532	0.077534845
May 7 2019	1.652246591	2.0914	0.379786005	46.158	3.9042784	41.8	38.7	0.11083012	0.157467673
May 7 2019	1.652246591	94.55	0.379786005	46.158	3.9042784	49.3	47.2	0.021704034	0.048050094
May 8 2019	1.664048352	9.6791	0.382498762	46.4877	3.902591164	49.4	9.9	0.006051855	0.972018778
May 8 2019	1.652246591	9.6791	0.379786005	46.158	3.9042784	48.4	6.7	0.004981399	1.201771453
May 9 2019	1.652246591	3.7258	0.379786005	46.158	3.9042784	47.7	15	0.021194794	0.72138156
May 9 2019	1.652246591	3.7258	0.379786005	46.158	3.9042784	49	16.3	0.028941125	0.695097857
May 10 2019	1.652246591	9.6791	0.379786005	46.158	3.9042784	48.6	9.9	0.013546042	0.976531097
May 10 2019	1.64044483	9.6791	0.377073248	45.8283	3.905988959	51.7	14.9	-0.005924155	0.75246561
May 17 2019	1.652246591	9.6791	0.379786005	46.158	3.9042784	47.7	14.3	0.023640198	0.752751619
May 17 2019	1.652246591	9.6791	0.379786005	46.158	3.9042784	48.8	16.7	0.024309956	0.67331816
May 21 2019	1.64044483	9.6791	0.377073248	45.8283	3.905988959	48.4	35.6	0.021043801	0.208282146
May 21 2019	1.664048352	9.6791	0.382498762	46.4877	3.902591164	49.6	32.5	0.010806478	0.264856034
May 22 2019	1.664048352	3.7258	0.382498762	46.4877	3.902591164	49.1	43.6	0.020454526	0.091847814
May 22 2019	1.664048352	3.7258	0.382498762	46.4877	3.902591164	50.5	45.2	0.002375276	0.069005701
May 23 2019	1.64044483	1.9323	0.377073248	45.8283	3.905988959	48.9	38.3	0.01841804	0.167357825
May 24 2019	1.664048352	1.5205	0.382498762	46.4877	3.902591164	48	32.6	0.006227455	0.238725941
May 24 2019	1.652246591	1.5205	0.379786005	46.158	3.9042784			#DIV/0!	#DIV/0!
May 25 2016	1.664048352	1.9323	0.382498762	46.4877	3.902591164	49.7	36.4	0.011971393	0.199127108
May 25 2016	1.64044483	1.9323	0.377073248	45.8283	3.905988959	50.2	38.1	0.010832105	0.178957689
May 26 2019	1.652246591	1.5205	0.379786005	46.158	3.9042784	49.7	32.8	0.006058474	0.257580505
May 26 2019	1.664048352	1.5205	0.382498762	46.4877	3.902591164	50	26.4	0.009538995	0.393337335
May 27 2019	1.64044483	3.7258	0.377073248	45.8283	3.905988959	50.1	46.3	0.004847666	0.052931603
May 27 2019	1.652246591	9.6791	0.379786005	46.158	3.9042784	50.7	38.2	0.012990941	0.184327591
May 28 2019	1.652246591	94.55	0.379786005	46.158	3.9042784	48.8	46	0.01349114	0.049253911
May 28 2019	1.664048352	94.55	0.382498762	46.4877	3.902591164	50.9	47	0.011691888	0.059596338
May 29 2019	1.64044483	3.7258	0.377073248	45.8283	3.905988959	49.6	46	0.008542953	0.054475273
May 29 2019	1.652246591	9.6791	0.379786005	46.158	3.9042784	49.8	23.4	0.019139509	0.47626193
May 30 2019	1.64044483	1.9323	0.377073248	45.8283	3.905988959	50.3	35.3	0.001210707	0.217080273
May 30 2019	1.652246591	1.5205	0.379786005	46.158	3.9042784	48.9	20.5	0.018286483	0.544450383
May 31 2019	1.64044483	3.7258	0.377073248	45.8283	3.905988959	48	44	0.021216149	0.07425748
May 31 2019	1.664048352	9.6791	0.382498762	46.4877	3.902591164	49.6	28.5	0.016727158	0.349702306
June 3 2019	1.664048352	1.9323	0.382498762	46.4877	3.902591164	48.8	33.8	0.021766954	0.24247539
June 3 2019	1.652246591	1.5205	0.379786005	46.158	3.9042784	47.7	26	0.008817338	0.376095965
June 4 2019	1.664048352	3.7258	0.382498762	46.4877	3.902591164	44	41.2	0.043460673	0.082973574
June 4 2019	1.664048352	9.6791	0.382498762	46.4877	3.902591164	43.4	25.4	0.050439911	0.372371823
June 5 2019	1.652246591	1.9323	0.379786005	46.158	3.9042784	45.6	34.9	0.019588653	0.181441544
June 5 2019	1.64044483	1.5205	0.377073248	45.8283	3.905988959	46	27.2	0.02084274	0.34113661
June 6 2019	1.652246591	39.6	0.379786005	46.158	3.9042784	37.9	32.4	0.130244778	0.225141441
June 6 2019	1.616841307	39.6	0.371647733	45.1689	3.909482012	38.6	32.7	0.141208368	0.243801738
June 7 2019	1.652246591	10.5	0.379786005	46.158	3.9042784	43.6	40.4	0.056927552	0.103063139
June 7 2019	1.652246591	10.5	0.379786005	46.158	3.9042784	43.4	41.2	0.067244416	0.098729537
June 10 2019	1.64044483	94.55	0.377073248	45.8283	3.905988959	44.9	42	0.040698239	0.081399502
June 10 2019	1.616841307	18.7799	0.371647733	45.1689	3.909482012	10.6	5.3	0.928958676	1.357663199
June 11 2019	1.64044483	94.55	0.377073248	45.8283	3.905988959	45.7	43.2	0.022264651	0.056558887
June 11 2019	1.64044483	18.7799	0.377073248	45.8283	3.905988959	31.9	23	0.255392794	0.454797119
June 12 2019	1.652246591	94.55	0.379786005	46.158	3.9042784	51.1	48.1	0.022095622	0.058713837
June 12 2019	2.360352273	0	0.542551435	65.94	3.832084073	51.1	49.1	0.017062665	0.033977709
June 20 2019	2.360352273	0	0.542551435	65.94	3.832084073	50.9	50.1	0.012304802	0.019016476
June 20 2019	1.664048352	3.7258	0.382498762	46.4877	3.902591164	52.1	43.9	0.025960306	0.128872357
June 24 2019	2.360352273	0	0.542551435	65.94	3.832084073	51.4	50.7	0.007354071	0.013163484
June 24 2019	1.652246591	1.9616	0.379786005	46.158	3.9042784	48.8	26.3	0.062402231	0.436536078
June 25 2019	2.360352273	0	0.542551435	65.94	3.832084073	51.4	49.4	0.005730829	0.022545162
June 25 2019	1.652246591	1.9616	0.379786005	46.158	3.9042784	46.2	11.5	0.076215496	0.917877249
June 27 2019	1.664048352	3.7258	0.382498762	46.4877	3.902591164	50.5	36.5	0.025625529	0.220728679
July 3 2019	1.664048352	3.7258	0.382498762	46.4877	3.902591164	50.8	31.9	0.017487483	0.297100959
July 3 2019	1.664048352	3.7258	0.382498762	46.4877	3.902591164	52.6	37.8	0.015785555	0.214341695
July 4 2019	1.675850114	3.7258	0.385211519	46.8174	3.90092678	52.8	35.1	0.001129068	0.244772611
July 6 2019	1.652246591	3.7258	0.379786005	46.158	3.9042784	49.1	38.5	0.025347607	0.172541612
July 7 2019	1.64044483	3.7258	0.377073248	45.8283	3.905988959	51.2	44.5	0.025646223	0.111141535
July 8 2019	2.360352273	0	0.542551435	65.94	3.832084073	51.6	50.1	0.00893671	0.021435126
July 8 2019	2.360352273	0	0.542551435	65.94	3.832084073	52.4	50.3	0.002418649	0.019747213
July 9 2019	1.664048352	3.7258	0.382498762	46.4877	3.902591164	51.9	38.7	0.028271633	0.204636213
	0		0	0	10.00744935			#DIV/0!	#DIV/0!
June 20 2019	2.360352273	0	0.542551435	65.94	3.832084073	50.9	50.1	0.012304802	0.019016476
July 8 2019	2.360352273	0	0.542551435	65.94	3.832084073	51.6	50.1	0.00893671	0.021435126
July 8 2019	2.360352273	0	0.542551435	65.94	3.832084073	52.4	50.3	0.002418649	0.019747213

Date	γ geo dark	γ geo light	γ BET dark	γ BET light	γ eff dark	γ eff light	γ corr	γ corr	γ BET dark corr	γ BET light corr
March 25 2019	1.25338E-06	5.84629E-06	1.30154E-07	6.07096E-07	1.25338E-06	5.84629E-06	1.28426E-06	6.58494E-06	1.33361E-07	6.83799E-07
March 25 2019	7.36961E-07	1.01286E-06	9.72756E-08	1.33693E-07	7.36961E-07	1.01286E-06	7.47536E-07	1.03294E-06	9.86714E-08	1.36343E-07
March 26 2019	1.77314E-06	2.26503E-06	1.67884E-07	2.14458E-07	1.77314E-06	2.26503E-06	1.83559E-06	2.36794E-06	1.73797E-07	2.24201E-07
March 27 2019	8.47542E-07	2.37042E-06	9.90408E-08	2.76999E-07	8.47542E-07	2.37042E-06	8.61553E-07	2.48337E-06	1.00678E-07	2.90197E-07
March 27 2019	6.92158E-07	8.95067E-07	6.97626E-08	9.02139E-08	6.92158E-07	8.95067E-07	7.01478E-07	9.10714E-07	7.0702E-08	9.17909E-08
March 29 2019	1.4801E-06	2.42419e-06	1.77258E-07	2.90322E-07	1.4801E-06	2.42419e-06	1.52336E-06	2.54244e-06	1.82439e-07	3.04484e-07
April 2 2019	1.15893E-06	8.27178E-06	1.26685E-07	9.04205E-07	1.15893E-06	8.27178E-06	1.1853E-06	9.83305E-06	1.29568E-07	1.07487E-06
April 4 2019	1.03216E-05	1.62385E-05	1.00434E-07	1.58009E-07	1.03216E-05	1.62385E-05	1.28732E-05	2.35969E-05	1.25263E-07	2.29609E-07
April 5 2019	1.04912E-06	1.73352E-06	1.51959E-07	2.51091E-07	1.04912E-06	1.73352E-06	1.07068E-06	1.79319E-06	1.55082E-07	2.59733E-07
April 5 2019	2.39247E-06	2.95405E-06	2.60745E-07	3.21949E-07	2.39247E-06	2.95405E-06	2.50768E-06	3.1317E-06	2.73302E-07	3.41311E-07
April 8 2019	1.40443E-07	9.33761E-07	1.96512E-08	1.30654E-07	1.40443E-07	9.33761E-07	1.40823E-07	9.50803E-07	1.97043E-08	1.33039E-07
April 8 2019	9.55274E-06	1.63348E-05	1.01012E-07	1.72726E-07	9.55274E-06	1.63348E-05	1.16977E-05	2.3796E-05	1.23693E-07	2.51622E-07
April 9 2019	4.89611E-07	1.32505e-06	6.5635E-08	1.7763E-07	4.89611E-07	1.32505e-06	4.94256E-07	1.35963E-06	6.62577E-08	1.82265E-07
April 10 2019	5.76911E-07	1.06012E-06	9.37845E-08	1.72336E-07	5.76911E-07	1.06012E-06	5.83372E-07	1.08214E-06	9.48347E-08	1.75915E-07
April 10 2019	1.0687E-06	5.66533e-06	1.28759E-07	6.82572E-07	1.0687E-06	5.66533e-06	1.09108E-06	6.35659e-06	1.31456E-07	7.65856E-07
April 11 2019	1.32702E-06	2.3113E-06	1.44015E-07	2.50834E-07	1.32702E-06	2.3113E-06	1.36169E-06	2.41855E-06	1.47778E-07	2.62474E-07
April 12 2019	4.39084E-06	5.74713E-06	2.42148E-07	3.16945E-07	4.39084E-06	5.74713E-06	4.79478E-06	6.4594E-06	2.64425E-07	3.56226E-07
April 15 2019	8.869E-07	1.40384E-06	1.26457E-07	2.00164E-07	8.869E-07	1.40384E-06	9.02253E-07	1.4427E-06	1.28646E-07	2.05705E-07
April 15 2019	6.80205E-07	1.04899E-06	1.55528E-07	2.3985E-07	6.80205E-07	1.04899E-06	6.89196E-07	1.07053E-06	1.57583E-07	2.44774E-07
April 16 2019	4.3042E-07	7.60298E-07	5.86962E-08	1.03681E-07	4.3042E-07	7.60298E-07	4.34005E-07	7.71553E-07	5.9185E-08	1.05216E-07
April 17 2019	1.06362E-05	1.67304E-05	9.34968E-08	1.47068E-07	1.06362E-05	1.67304E-05	1.33647E-05	2.46449E-05	1.17482E-07	2.1664E-07
April 17 2019	5.61506E-06	7.59061E-06	6.75717E-07	9.13456E-07	5.61506E-06	7.59061E-06	6.29304E-06	8.88456E-06	7.57306E-07	1.06917E-06
April 18 2019	1.21762e-06	2.73292e-06	1.71666E-07	3.853E-07	1.21762e-06	2.73292e-06	1.24674e-06	2.88416e-06	1.75772e-07	4.06622E-07
April 24 2019	4.04487E-06	3.81994E-05	3.26851E-07	3.08675E-06	4.04487E-06	3.81994E-05	4.3852E-06	0.00014303	3.54352E-07	1.15577E-05
April 24 2019	3.1353E-07	3.83969E-07	7.32721E-08	8.97338E-08	3.1353E-07	3.83969E-07	3.15427E-07	3.86819E-07	7.37155E-08	9.03998E-08
April 25 2019	2.31725E-06	6.21927E-06	7.78427E-07	2.08922E-06	2.31725E-06	6.21927E-06	2.42507E-06	7.06196E-06	8.14646E-07	2.3723E-06
April 25 2019	4.73527E-05	5.19463E-05	6.44114E-07	7.06599E-07	4.73527E-05	5.19463E-05	0.000515557	0.013856149	7.01285E-06	0.000188478
April 26 2019	1.49465E-06	1.48909E-05	2.05769E-07	2.05004E-06	1.49465E-06	1.48909E-05	1.53876E-06	2.08435E-05	2.11842E-07	2.86954E-06
April 26 2019	2.73541E-07	1.339E-06	6.08233E-08	2.97733E-07	2.73541E-07	1.339E-06	2.74984E-07	1.3743E-06	6.11442E-08	3.05584E-07
April 29 2019	2.92113E-05	4.18535E-05	3.16959E-07	4.54132E-07	2.92113E-05	4.18535E-05	6.6424E-05	0.000212115	7.20736E-07	2.30156E-06
April 29 2019	6.07261E-06	1.01655E-05	9.03741E-07	1.51285E-06	6.07261E-06	1.01655E-05	6.87347E-06	1.26286E-05	1.02293E-06	1.87943E-06
April 30 2019	1.30392E-06	4.38045E-06	1.34647E-07	4.52338E-07	1.30392E-06	4.38045E-06	1.3374E-06	4.78258E-06	1.38104E-07	4.93864E-07
April 30 2019	5.47515E-07	9.59989E-07	8.93093E-09	1.56591E-08	5.47515E-07	9.59989E-07	5.53322E-07	9.77986E-07	9.02566E-09	1.59527E-08
May 1 2019	1.47328E-06	1.20015E-05	1.62672E-08	1.32515E-07	1.47328E-06	1.20015E-05	1.51614E-06	1.55919E-05	1.67404E-08	1.72159E-07
May 1 2019	5.65577E-07	1.0708E-06	7.16378E-08	1.35631E-07	5.65577E-07	1.0708E-06	5.71779E-07	1.09325E-06	7.24234E-08	1.38475E-07
May 2 2019	4.12985E-06	5.84711E-06	7.02065E-07	9.93997E-07	4.12985E-06	5.84711E-06	4.48508E-06	6.58561E-06	7.62455E-07	1.11954E-06
May 2 2019	2.80986E-06	5.7286E-06	1.92562E-08	3.92585E-08	2.80986E-06	5.7286E-06	2.97005E-06	6.43634E-06	2.0354E-08	4.41088E-08
May 3 2019	1.31597E-06	2.25143E-06	3.88777E-08	6.65139E-08	1.31597E-06	2.25143E-06	1.35006E-06	2.35307E-06	3.98848E-08	6.95169E-08
May 7 2019	3.21824E-06	4.57248E-06	5.05177E-07	7.17756E-07	3.21824E-06	4.57248E-06	3.43004E-06	5.01222E-06	5.38423E-07	7.86782E-07
May 7 2019	6.30233E-07	1.39526E-06	1.40041E-09	3.10035E-09	6.30233E-07	1.39526E-06	6.37947E-07	1.43364E-06	1.41756E-09	3.18563E-09
May 8 2019	1.75731E-07	2.82251E-05	8.65749E-08	1.39052E-05	1.75731E-07	2.82251E-05	1.76326E-07	6.1598E-05	8.6868E-08	3.03466E-05
May 8 2019	1.44648E-07	3.48966E-05	8.38733E-08	2.02346E-05	1.44648E-07	3.48966E-05	1.4505E-07	0.000105605	8.41068E-08	6.12346E-05
May 9 2019	6.15446E-07	2.09472E-05	8.19503E-07	2.78924E-05	6.15446E-07	2.09472E-05	6.22801E-07	3.50236E-05	8.29296E-07	4.66359E-05
May 9 2019	8.40381E-07	2.0184E-05	9.51012E-07	2.28411E-05	8.40381E-07	2.0184E-05	8.54154E-07	3.29409E-05	9.66597E-07	3.72774E-05
May 10 2019	3.93345E-07	2.83561E-05	4.91635E-07	3.54419E-05	3.93345E-07	2.83561E-05	3.96336E-07	6.21934E-05	4.95374E-07	7.77346E-05
May 10 2019	-1.72023E-07	2.18498E-05	-2.20058E-07	2.7951E-05	-1.72023E-07	2.18498E-05	-1.71458E-07	3.76102E-05	-2.19334E-07	4.81122E-05
May 17 2019	6.86455E-07	2.18581E-05	3.52067E-06	0.000112105	6.86455E-07	2.18581E-05	6.95617E-07	3.76467E-05	3.56766E-06	0.000193082
May 17 2019	7.05903E-07	1.95516E-05	3.78852E-06	0.000104932	7.05903E-07	1.95516E-05	7.15595E-07	3.12891E-05	3.84054E-06	0.000167926
May 21 2019	6.11062E-07	6.04802E-06	2.16901E-05	0.000214679	6.11062E-07	6.04802E-06	6.18308E-07	6.84158E-06	2.19473E-05	0.000242847
May 21 2019	3.13794E-07	7.69079E-06	7.93896E-06	0.000194576	3.13794E-07	7.69079E-06	3.15696E-07	9.02278E-06	7.98707E-06	0.000228275
May 22 2019	5.93951E-07	2.66704E-06	4.21014E-05	0.00018905	5.93951E-07	2.66704E-06	6.008E-07	2.81095E-06	4.25869E-05	0.00019925
May 22 2019	6.89723e-08	2.00376e-06	5.49397E-06	0.000159609	6.89723e-08	2.00376e-06	6.90638e-08	2.08391E-06	5.50125E-06	0.000165993
May 23 2019	5.34816E-07	4.85967E-06	1.11799E-06	1.01587E-05	5.34816E-07	4.85967E-06	5.40358E-07	5.35915E-06	1.12957E-06	1.12029E-05
May 24 2019	1.8083E-07	6.93203e-06	1.62647E-07	6.23497E-06	1.8083E-07	6.93203e-06	1.8146E-07	7.99599E-06	1.63213E-07	7.19194E-06
May 24 2019	#DIV/0!	#DIV/0!	#DIV/0!	#DIV/0!	#DIV/0!	#DIV/0!	#DIV/0!	#DIV/0!	#DIV/0!	#DIV/0!
May 25 2016	3.47621E-07	5.78218E-06	6.21608E-07	1.03396E-05	3.47621E-07	5.78218E-06	3.49956E-07	6.50406E-06	6.25783E-07	1.16304E-05
May 25 2016	3.14538E-07	5.1965E-06	7.56612E-07	1.25E-05	3.14538E-07	5.1965E-06	3.16447E-07	5.77172E-06	7.61204E-07	1.38837E-05
May 26 2019	1.75924E-07	7.47952E-06	1.53145E-07	6.51107E-06	1.75924E-07	7.47952E-06	1.76519E-07	8.73275E-06	1.53664E-07	7.60203E-06
May 26 2019	2.7699E-07	1.14216E-05	2.69951E-07	1.11313E-05	2.7699E-07	1.14216E-05	2.7847E-07	1.46288E-05	2.71394E-07	1.4257E-05
May 27 2019	1.40765E-07	1.53701E-06	1.51329E-05	0.000165236	1.40765E-07	1.53701E-06	1.41146E-07	1.58369E-06	1.51739E-05	0.000170255
May 27 2019	3.77226E-07	5.35243e-06	1.2172E-05	0.000172708	3.77226E-07	5.35243e-06	3.79976E-07	5.96502E-06	1.22608E-05	0.000192475
May 28 2019	3.9175E-07	1.43022E-06	1.05661E-09	3.85752E-09	3.9175E-07	1.43022E-06	3.94717E-07	1.47057E-06	1.06462E-09	3.96637E-09
May 28 2019	3.39504E-07	1.73054E-06	8.05235E-10	4.10448E-09	3.39504E-07	1.73054E-06	3.41731E-07	1.79E-06	8.10517E-10	4.2455E-09
May 29 2019	2.48067E-07	1.58183E-06	1.43781E-05	9.16838E-05	2.48067E-07	1.58183E-06	2.49253E-07	1.63132E-06	1.44468E-05	9.45522E-05
May 29 2019	5.55766E-07	1.38295E-05	1.22354E-05	0.000304463	5.55766E-07	1.38295E-05	5.61756E-07	1.88245E-05	1.23673E-05	0.000414429
May 30 2019	3.5156E-08	6.30349E-06	5.62632E-08	1.0088E-05	3.5156E-08	6.30349E-06	3.51798E-08	7.17032E-06	5.63012E-08	1.14753E-05
May 30 2019	5.30996E-07	1.58095E-05	7.53684E-07	2.24397E-05	5.30996E-07	1.58095E-05	5.36461E-07	2.26932E-05	7.61442E-07	3.22102E-05
May 31 2019	6.16066E-07	2.15626E-06	4.22195E-05	0.00014777	6.16066E-07	2.15626E-06	6.23432E-07	2.24928E-06	4.27243E-05	0.000154144
May 31 2019	4.85717E-07	1.01545E-05	1.32245E-05	0.000276475	4.85717E-07	1.01545E-05	4.90288E-07	1.2613E-05	1.3349E-05	0.000343413
June 3 2019	6.3206E-07	7.04091E-06	9.95737E-07	1.10921E-05	6.3206E-07	7.04091E-06	6.39823E-07	8.1412E-06	1.00797E-06	1.28255E-05
June 3 2019	2.56034e-07	1.09209e-05	2.18865e-07	9.3355E-06	2.56034e-07	1.09209e-05	2.57298e-07	1.38159e-05	2.19945e-07	1.18102e-05
June 4 2019	1.26199E-06	2.40935e-06	0.000117513	0.000224351	1.26199E-06	2.40935e-06	1.29332E-06	2.52619E-06	0.00012043	0.00023523
June 4 2019	1.46465e-06	1.08128E-05	3.34762E-05	0.000247137	1.46465e-06	1.08128E-05	1.50702E-06	1.36448E-05	3.44446E-05	0.000311866
June 5 2019	5.68808E-07	5.26863E-06	8.26182E-07	7.65258E-06	5.68808E-07	5.26863E-06	5.75084E-07	5.86112E-06	8.35299E-07	8.51317E-06
June 5 2019	6.05223E-07	9.90579E-06	5.0014E-07	8.18588E-06	6.05223E-07	9.90579E-06	6.12331E-07	1.2229E-05	5.06014E-07	1.01058E-05
June 6 2019	3.782E-06	6.53757E-06	2.10723E-08	3.64256E-08	3.782E-06	6.53757E-06	4.07791E-06	7.47523E-06	2.2721E-08	4.165E-08
June 6 2019	4.10035E-06	7.07942E-06	2.17231E-08	3.75058E-08	4.10035E-06	7.07942E-06	4.44998E-06	8.19047E-06	2.35754E-08	4.33919E-08
June 7 2019	1.65304E-06	2.99271E-06	2.75883E-08	4.99466E-08	1.65304E-06	2.99271E-06	1.70719E-06	3.17502E-06	2.8492E-08	5.29893E-08
June 7 2019	1.95262E-06	2.86687E-06	3.65887E-08	5.37202E-08	1.95262E-06	2.86687E-06	2.02862E-06	3.03374E-06	3.80128E-08	5.68472E-08
June 10 2019	1.18178E-06	2.36365E-06	2.53679E-09	5.07377E-09	1.18178E-06	2.36365E-06	1.20919E-06	2.47588E-06	2.59562E-09	5.31469E-09
June 10 2019	2.69747E-05	3.94233e-05	5.86609E-07	8.57322E-07	2.69747E-05	3.94233e-05	5.58335E-05	0.000161177	1.21419e-06	3.50504E-06
June 11 2019	6.46512E-07	1.64233E-06	1.68385E-09	4.27748E-09	6.46512E-07	1.64233E-06	6.54629E-07	1.69575E-06	1.70499E-09	4.41659E-09
June 11 2019	7.416E-06	1.32062E-05	2.97162E-07	5.29178E-07	7.416E-06	1.32062E-05	8.64564E-06	1.76855E-05	3.46434E-07	7.08665E-07
June 12 2019	6.41604E-07	1.70491E-06	1.76364E-09	4.68645E-09	6.41604E-07	1.70491E-06	6.49601E-07	1.76257E-06	1.78562E-09	4.84494E-09
June 12 2019	4.95459E-07	9.86631E-07	#DIV/0!	#DIV/0!	4.95459E-07	9.86631E-07	5.00305E-07	1.00603E-06	#DIV/0!	#DIV/0!
June 20 2019	3.57302E-07	5.52193e-07	#DIV/0!	#DIV/0!	3.57302E-07	5.52193e-07	3.59815E-07	5.58219e-07	#DIV/0!	#DIV/0!
June 20 2019	7.53825E-07	3.74215E-06	1.47694E-05	7.33183E-05	7.53825E-07	3.74215E-06	7.64893E-07	4.03175E-06	1.49862E-05	7.89925E-05
June 24 2019	2.13545E-07	3.82236E-07	#DIV/0!	#DIV/0!	2.13545E-07	3.82236E-07	2.1444E-07	3.85114E-07	#DIV/0!	#DIV/0!
June 24 2019	1.81201E-06	1.2676E-05	2.7158E-07	1.89984E-06	1.81201E-06	1.2676E-05	1.87728E-06	1.67497E-05	2.81362E-07	2.5104E-06
June 25 2019	1.6641E-07	6.54658E-07	#DIV/0!	#DIV/0!	1.6641E-07	6.54658E-07	1.66953E-07	6.63144E-07	#DIV/0!	#DIV/0!
June 25 2019	2.21312E-06	2.6653E-05	2.17438E-07	2.61864E-06	2.21312E-06	2.6653E-05	2.31126E-06	5.45482E-05	2.2708E-07	5.35934E-06
June 27 2019	7.44104E-07	6.40943E-06	7.40971E-06	6.38245E-05	7.44104E-07	6.40943E-06	7.54886E-07	7.30861E-06	7.51708E-06	7.27784E-05
July 3 2019	5.07795E-07	8.6271E-06	4.17383E-06	7.09107E-05	5.07795E-07	8.6271E-06	5.12793E-07	1.03393E-05	4.21492E-06	8.49839E-05
July 3 2019	4.58375E-07	6.22397E-06	4.05909E-06	5.51157E-05	4.58375E-07	6.22397E-06	4.62444E-07	7.06844E-06	4.09512E-06	6.25938E-05
July 4 2019	3.27854E-08	7.10761E-06	3.58861E-07	7.77982E-05	3.27854E-08	7.10761E-06	3.28061E-08	8.23107E-06	3.59087E-07	9.00953E-05
July 6 2019	7.36034E-07	5.0102E-06	4.20985E-06	2.86565E-05	7.36034E-07	5.0102E-06	7.46577E-07	5.54305E-06	4.27016E-06	3.17043E-05
July 7 2019	7.44705E-07	3.22728E-06	8.3425E-06	3.61534E-05	7.44705E-07	3.22728E-06	7.55495E-07	3.44021E-06	8.46338E-06	3.85387E-05
July 8 2019	2.59501E-07	6.22425e-07	#DIV/0!	#DIV/0!	2.59501E-07	6.22425e-07	2.60824E-07	6.30091E-07	#DIV/0!	#DIV/0!
July 8 2019	7.02318E-08	5.73412E-07	#DIV/0!	#DIV/0!	7.02318E-08	5.73412E-07	7.03283E-08	5.79912E-07	#DIV/0!	#DIV/0!
July 9 2019	8.20941E-07	5.94215E-06	5.55481E-06	4.02069E-05	8.20941E-07	5.94215E-06	8.34084E-07	6.70717E-06	5.64375E-06	4.53834E-05
	#DIV/0!	#DIV/0!	#DIV/0!	#DIV/0!	#DIV/0!	#DIV/0!	#DIV/0!	#DIV/0!	#DIV/0!	#DIV/0!
June 20 2019	3.57302E-07	5.52193e-07	#DIV/0!	#DIV/0!	3.57302E-07	5.52193e-07	3.59815E-07	5.58219e-07	#DIV/0!	#DIV/0!
July 8 2019	2.59501E-07	6.22425e-07	#DIV/0!	#DIV/0!	2.59501E-07	6.22425e-07	2.60824E-07	6.30091E-07	#DIV/0!	#DIV/0!
July 8 2019	7.02318E-08	5.73412E-07	#DIV/0!	#DIV/0!	7.02318E-08	5.73412E-07	7.03283E-08	5.79912E-07	#DIV/0!	#DIV/0!

Date	Experiment	mass (g)	length of tube (m)	[O3] Initial
May 7 2019	Fumed SiO2 Trial 1 RH25	0.02197	0.14	51.1
May 28 2019	Fumed SiO2 Trial 2 RH25	0.0181	0.14	49.9
May 28 2019	Fumed SiO2 Trial 3 RH25	0.02073	0.141	51.9
June 10 2019	Fumed SiO2 RH0	0.02258	0.139	48
June 11 2019	Fumed SiO2 RH10	0.01861	0.139	47.4
June 12 2019	Fumed SiO2 RH50	0.01776	0.14	53
May 21 2019	Commercial Antase Trial 1 (0.1%)	0.013786661		
May 21 2019	Commercial Antase Trial 2 (0.1%)	0.019621016		
May 22 2019	Natural Anatase 1 Trial 1 (0.1%)	0.017782398		
May 22 2019	Natural Anatase 1 Trial 2 (0.1%)	0.015824336		
May 23 2019	Rutile Trial 1 (10%)	0.010165443		
May 24 2019	Natural Anatase 2 Trial 1 (20%)	0.013590792		
May 25 2016	Rutile Trial 2 (10%)	0.012054596		
May 25 2016	Rutile Trial 3 (10%)	0.00883404		
May 26 2019	Natural Anatase 2 Trial 2 (20%)	0.013942761		
May 26 2019	Natural Anatase 2 Trial 3 (20%)	0.012542885		
May 27 2019	Natural Anatase 1 Trial 3 (0.1%)	0.011558558		
May 27 2019	Commericial Anatase Trial 3 (0.1%)	0.015275221		
May 29 2019	Nat Ana 1 (0.1%) RH0	0.021438778		
May 29 2019	Com Ana (0.1%) RH0	0.022388339		
May 30 2019	Rutile (10%) RH0	0.013278047		
May 30 2019	Nat Ana 2 (20%) RH0	0.00855124		
May 31 2019	Nat Ana 1 (0.1%) RH10	0.018132051		
May 31 2019	Com Ana (0.1%) RH10	0.01823236		
June 3 2019	Rutile (10%) RH10	0.013682866		
June 3 2019	Nat Ana 2 (20%) RH10	0.014198738		
June 4 2019	Nat Ana 1 (0.1%) RH 50	0.0135366		
June 4 2019	Com Ana (0.1%) RH50	0.021718986		
June 5 2019	Rutile (10%) RH50	0.014735394		
June 5 2019	Nat Ana 2 (20%) RH50	0.014582704		
June 20 2019	Nat Ana (0.5%) Trial 1	0.012646317		
June 27 2019	Nat Ana (1%) Trial 1	0.0124047		
July 3 2019	Nat Ana (1%) Trial 2	0.0150282		
July 3 2019	Nat Ana (1%) Trial 3	0.0139491		
July 4 2019	Nat Ana (1%) RH10	0.0113652		
July 6 2019	Nat Ana (1%) RH50	0.0214434		
July 7 2019	Nat Ana (1%) RH0	0.0108702		
July 9 2019	Nat Ana (1%) RH0	0.0182556		

Date	Residence Time (s)	BET (m^2/g)	z*	S geo (cm^2)	Sherwood #	[O3] final dark (ppb)	[O3] final light (ppb)
May 7 2019	1.81747125	94.55	0.41776461	46.158	3.88258022	49.3	47.2
May 28 2019	1.81747125	94.55	0.41776461	46.158	3.88258022	48.8	46
May 28 2019	1.830453188	94.55	0.42074864	46.4877	3.881035482	50.9	47
June 10 2019	1.804489313	94.55	0.41478057	45.8283	3.88414639	44.9	42
June 11 2019	1.804489313	94.55	0.41478057	45.8283	3.88414639	45.7	43.2
June 12 2019	1.81747125	94.55	0.41776461	46.158	3.88258022	51.1	48.1
May 21 2019		94.55		45.8283			
May 21 2019		94.55		46.4877			
May 22 2019		94.55		46.4877			
May 22 2019		94.55		46.4877			
May 23 2019		94.55		45.8283			
May 24 2019		94.55		46.4877			
May 25 2016		94.55		46.4877			
May 25 2016		94.55		45.8283			
May 26 2019		94.55		46.158			
May 26 2019		94.55		46.4877			
May 27 2019		94.55		45.8283			
May 27 2019		94.55		46.158			
May 29 2019		94.55		45.8283			
May 29 2019		94.55		46.158			
May 30 2019		94.55		45.8283			
May 30 2019		94.55		46.158			
May 31 2019		94.55		45.8283			
May 31 2019		94.55		46.4877			
June 3 2019		94.55		46.4877			
June 3 2019		94.55		46.158			
June 4 2019		94.55		46.4877			
June 4 2019		94.55		46.4877			
June 5 2019		94.55		46.158			
June 5 2019		94.55		45.8283			
June 20 2019		94.55		46.4877			
June 27 2019		94.55		46.4877			
July 3 2019		94.55		46.4877			
July 3 2019		94.55		46.4877			
July 4 2019		94.55		46.8174			
July 6 2019		94.55		46.158			
July 7 2019		94.55		45.8283			
July 9 2019		94.55		46.4877			

Date	k (dark)	k light	γ geo dark	γ geo light	γ BET dark	γ BET light	Experiment		
May 7 2019	0.019731	0.043682	5.76446E-07	1.27618E-06	1.2809E-09	2.83575E-09	Fumed SiO2 Trial 1 RH25		
May 28 2019	0.012265	0.044776	3.58317E-07	1.30816E-06	9.66438E-10	3.52831E-09	Fumed SiO2 Trial 2 RH25		
May 28 2019	0.010629	0.054178	3.1053E-07	1.58284E-06	7.36513E-10	3.75418E-09	Fumed SiO2 Trial 3 RH25		
June 10 2019	0.036998	0.074000	1.08092E-06	2.16192E-06	2.32029E-09	4.64075E-09	Fumed SiO2 RH0		
June 11 2019	0.020241	0.051417	5.91336E-07	1.50217E-06	1.54014E-09	3.91242E-09	Fumed SiO2 RH10		
June 12 2019	0.020087	0.053376	5.86847E-07	1.55941E-06	1.61312E-09	4.28649E-09	Fumed SiO2 RH50		
May 21 2019	0.009683	0.032837	2.82906E-07	9.59336E-07	**BET avg dark**	**BET avg light**			
May 21 2019	0.013586	0.046070	3.96918E-07	1.34595E-06	9.94616E-10	3.37275E-09			
May 22 2019	0.012313	0.041753	3.59724E-07	1.21982E-06					
May 22 2019	0.010957	0.037155	3.20114E-07	1.08551E-06					
May 23 2019	0.007140	0.024212	2.08598E-07	7.07356E-07					
May 24 2019	0.009410	0.031911	2.74931E-07	9.32292E-07					
May 25 2016	0.008347	0.028304	2.43855E-07	8.26913E-07					
May 25 2016	0.006205	0.021041	1.81277E-07	6.14711E-07					
May 26 2019	0.009723	0.032971	2.84066E-07	9.63268E-07					
May 26 2019	0.008685	0.029451	2.53733E-07	8.60408E-07					
May 27 2019	0.008118	0.027530	2.37185E-07	8.04295E-07					
May 27 2019	0.010652	0.036122	3.11213E-07	1.05532E-06					
May 29 2019	0.035128	0.070260	1.02629E-06	2.05266E-06					
May 29 2019	0.036422	0.072847	1.06409E-06	2.12826E-06					
May 30 2019	0.021757	0.043515	6.3563E-07	1.27131E-06					
May 30 2019	0.013912	0.027824	4.0643E-07	8.12891E-07					
May 31 2019	0.019721	0.050097	5.76149E-07	1.46359E-06					
May 31 2019	0.019549	0.049659	5.71119E-07	1.45081E-06					
June 3 2019	0.014671	0.037268	4.28609E-07	1.08879E-06					
June 3 2019	0.015333	0.038949	4.47945E-07	1.13791E-06					
June 4 2019	0.015202	0.040395	4.4412E-07	1.18014E-06					
June 4 2019	0.024390	0.064812	7.12575E-07	1.8935E-06					
June 5 2019	0.016666	0.044286	4.86904E-07	1.29383E-06					
June 5 2019	0.016612	0.044142	4.85325E-07	1.28964E-06					
June 20 2019	0.008757	0.029693	2.55825E-07	8.67503E-07					
June 27 2019	0.008589	0.029126	2.50937E-07	8.50929E-07					
July 3 2019	0.010406	0.035286	3.04009E-07	1.03089E-06					
July 3 2019	0.009659	0.032752	2.82179E-07	9.56871E-07					
July 4 2019	0.012100	0.030737	3.53502E-07	8.98E-07					
July 6 2019	0.024253	0.064446	7.08558E-07	1.88282E-06					
July 7 2019	0.017811	0.035624	5.20365E-07	1.04077E-06					
July 9 2019	0.029488	0.058979	8.61513E-07	1.72309E-06					

Date	Experiment	mass (g)	length of tube (m)
May 21 2019	Commercial Antase Trial 1 (0.1%)	1.33E-05	0.139
May 21 2019	Commercial Antase Trial 2 (0.1%)	1.89839E-05	0.141
May 22 2019	Natural Anatase 1 Trial 1 (0.1%)	1.76024E-05	0.141
May 22 2019	Natural Anatase 1 Trial 2 (0.1%)	1.56642E-05	0.141
May 23 2019	Rutile Trial 1 (10%)	0.001134557	0.139
May 24 2019	Natural Anatase 2 Trial 1 (20%)	0.003399208	0.141
May 25 2016	Rutile Trial 2 (10%)	0.001345404	0.141
May 25 2016	Rutile Trial 3 (10%)	0.00098596	0.139
May 26 2019	Natural Anatase 2 Trial 2 (20%)	0.003487239	0.14
May 26 2019	Natural Anatase 2 Trial 3 (20%)	0.003137115	0.141
May 27 2019	Natural Anatase 1 Trial 3 (0.1%)	1.14E-05	0.139
May 27 2019	Commericial Anatase Trial 3 (0.1%)	1.47792E-05	0.14
May 29 2019	Nat Ana 1 (0.1%) RH0	2.12218E-05	0.139
May 29 2019	Com Ana (0.1%) RH0	2.16613E-05	0.14
May 30 2019	Rutile (10%) RH0	0.001481953	0.139
May 30 2019	Nat Ana 2 (20%) RH0	0.00213876	0.14
May 31 2019	Nat Ana 1 (0.1%) RH10	1.79485E-05	0.139
May 31 2019	Com Ana (0.1%) RH10	1.76403E-05	0.141
June 3 2019	Rutile (10%) RH10	0.001527134	0.141
June 3 2019	Nat Ana 2 (20%) RH10	0.003551262	0.14
June 4 2019	Nat Ana 1 (0.1%) RH 50	1.33996E-05	0.141
June 4 2019	Com Ana (0.1%) RH50	2.10137E-05	0.141
June 5 2019	Rutile (10%) RH50	0.001644606	0.14
June 5 2019	Nat Ana 2 (20%) RH50	0.003647296	0.139
June 20 2019	Nat Ana (0.5%) Trial 1	6.36834E-05	0.141
June 27 2019	Nat Ana (1%) Trial 1	0.0001253	0.141
July 3 2019	Nat Ana (1%) Trial 2	0.0001518	0.141
July 3 2019	Nat Ana (1%) Trial 3	0.0001409	0.141
July 4 2019	Nat Ana (1%) RH10	0.0001148	0.142
July 6 2019	Nat Ana (1%) RH50	0.0002166	0.14
July 7 2019	Nat Ana (1%) RH0	0.0001098	0.139
July 9 2019	Nat Ana (1%) RH0	0.0001844	0.141

Date	[O3] Initial	Residence Time (s)	BET (m^2/g)	z*	S geo (cm^2)	Sherwood #
May 21 2019	50.1	1.64044483	9.6791	0.377073248	45.8283	3.905988959
May 21 2019	50.5	1.664048352	9.6791	0.382498762	46.4877	3.902591164
May 22 2019	50.8	1.664048352	3.7258	0.382498762	46.4877	3.902591164
May 22 2019	50.7	1.664048352	3.7258	0.382498762	46.4877	3.902591164
May 23 2019	50.4	1.64044483	1.9323	0.377073248	45.8283	3.905988959
May 24 2019	48.5	1.664048352	1.5205	0.382498762	46.4877	3.902591164
May 25 2016	50.7	1.664048352	1.9323	0.382498762	46.4877	3.902591164
May 25 2016	51.1	1.64044483	1.9323	0.377073248	45.8283	3.905988959
May 26 2019	50.2	1.652246591	1.5205	0.379786005	46.158	3.9042784
May 26 2019	50.8	1.664048352	1.5205	0.382498762	46.4877	3.902591164
May 27 2019	50.5	1.64044483	3.7258	0.377073248	45.8283	3.905988959
May 27 2019	51.8	1.652246591	9.6791	0.379786005	46.158	3.9042784
May 29 2019	50.3	1.64044483	3.7258	0.377073248	45.8283	3.905988959
May 29 2019	51.4	1.652246591	9.6791	0.379786005	46.158	3.9042784
May 30 2019	50.4	1.64044483	1.9323	0.377073248	45.8283	3.905988959
May 30 2019	50.4	1.652246591	1.5205	0.379786005	46.158	3.9042784
May 31 2019	49.7	1.64044483	3.7258	0.377073248	45.8283	3.905988959
May 31 2019	51	1.664048352	9.6791	0.382498762	46.4877	3.902591164
June 3 2019	50.6	1.664048352	1.9323	0.382498762	46.4877	3.902591164
June 3 2019	48.4	1.652246591	1.5205	0.379786005	46.158	3.9042784
June 4 2019	47.3	1.664048352	3.7258	0.382498762	46.4877	3.902591164
June 4 2019	47.2	1.664048352	9.6791	0.382498762	46.4877	3.902591164
June 5 2019	47.1	1.652246591	1.9323	0.379786005	46.158	3.9042784
June 5 2019	47.6	1.64044483	1.5205	0.377073248	45.8283	3.905988959
June 20 2019	54.4	1.664048352	3.7258	0.382498762	46.4877	3.902591164
June 27 2019	52.7	1.664048352	3.7258	0.382498762	46.4877	3.902591164
July 3 2019	52.3	1.664048352	3.7258	0.382498762	46.4877	3.902591164
July 3 2019	54	1.664048352	3.7258	0.382498762	46.4877	3.902591164
July 4 2019	52.9	1.675850114	3.7258	0.385211519	46.8174	3.90092678
July 6 2019	51.2	1.81747125	3.7258	0.417764605	46.158	3.88258022
July 7 2019	53.4	1.804489313	3.7258	0.414780572	45.8283	3.88414639
July 9 2019	54.4	1.830453188	3.7258	0.420748638	46.4877	3.881035482

Date	[O3] final dark (ppb)	[O3] final light (ppb)	k (dark)	k light	SiO2 ratio	γ geo dark
May 21 2019	48.4	35.6	0.021044	0.208282	6.342971	3.30E-07
May 21 2019	49.6	32.5	0.010806	0.264856	5.749002	-8.07E-08
May 22 2019	49.1	43.6	0.020455	0.091848	2.199797	2.36E-07
May 22 2019	50.5	45.2	0.002375	0.069006	1.857221	-2.49E-07
May 23 2019	48.9	38.3	0.018418	0.167358	6.912251	3.27E-07
May 24 2019	48	32.6	0.006227	0.238726	7.480988	-9.24E-08
May 25 2016	49.7	36.4	0.011971	0.199127	7.035287	1.05E-07
May 25 2016	50.2	38.1	0.010832	0.178958	8.505323	1.34E-07
May 26 2019	49.7	32.8	0.006058	0.257581	7.812270	-1.06E-07
May 26 2019	50	26.4	0.009539	0.393337	13.355858	2.48E-08
May 27 2019	50.1	46.3	0.004848	0.052932	1.922698	-9.50E-08
May 27 2019	50.7	38.2	0.012991	0.184328	5.102886	6.79E-08
May 29 2019	49.6	46	0.008543	0.054475	0.775344	-7.72E-07
May 29 2019	49.8	23.4	0.019140	0.476262	6.537807	-5.02E-07
May 30 2019	50.3	35.3	0.001211	0.217080	4.988627	-5.97E-07
May 30 2019	48.9	20.5	0.018286	0.544450	19.567589	1.27E-07
May 31 2019	48	44	0.021216	0.074257	1.482284	4.34E-08
May 31 2019	49.6	28.5	0.016727	0.349702	7.042034	-8.19E-08
June 3 2019	48.8	33.8	0.021767	0.242475	6.506286	2.06E-07
June 3 2019	47.7	26	0.008817	0.376096	9.656069	-1.89E-07
June 4 2019	44	41.2	0.043461	0.082974	2.054076	8.21E-07
June 4 2019	43.4	25.4	0.050440	0.372372	5.745443	7.56E-07
June 5 2019	45.6	34.9	0.019589	0.181442	4.097040	8.49E-08
June 5 2019	46	27.2	0.020843	0.341137	7.728091	1.23E-07
June 20 2019	52.1	43.9	0.025960	0.128872	4.340101	5.00E-07
June 27 2019	50.5	36.5	0.025626	0.220729	7.578384	4.95E-07
July 3 2019	50.8	31.9	0.017487	0.297101	8.419788	2.06E-07
July 3 2019	52.6	37.8	0.015786	0.214342	6.544320	1.78E-07
July 4 2019	52.8	35.1	0.001129	0.244773	7.963381	-3.19E-07
July 6 2019	49.1	38.5	0.023043	0.156856	2.433900	-3.51E-08
July 7 2019	51.2	44.5	0.023315	0.101038	2.836227	1.60E-07
July 9 2019	51.9	38.7	0.025701	0.186033	3.154227	-1.10E-07

Date	γ geo light	k corr dark	k corr light	γ BET dark	γ BET light	γ corr dark
May 21 2019	5.09E-06	1.14E-02	1.75E-01	1.17E-05	1.81E-04	0.99
May 21 2019	6.35E-06	-2.78E-03	2.19E-01	-2.04E-06	1.61E-04	0.99
May 22 2019	1.45E-06	8.14E-03	5.01E-02	1.68E-05	1.03E-04	0.99
May 22 2019	9.25E-07	-8.58E-03	3.19E-02	-1.98E-05	7.37E-05	1.00
May 23 2019	4.16E-06	1.13E-02	1.43E-01	6.85E-07	8.69E-06	0.99
May 24 2019	6.01E-06	-3.18E-03	2.07E-01	-8.31E-08	5.40E-06	1.00
May 25 2016	4.96E-06	3.62E-03	1.71E-01	1.88E-07	8.87E-06	0.99
May 25 2016	4.59E-06	4.63E-03	1.58E-01	3.23E-07	1.10E-05	0.99
May 26 2019	6.52E-06	-3.66E-03	2.25E-01	-9.26E-08	5.68E-06	1.00
May 26 2019	1.06E-05	8.54E-04	3.64E-01	2.42E-08	1.03E-05	1.00
May 27 2019	7.38E-07	-3.27E-03	2.54E-02	-1.02E-05	7.93E-05	1.00
May 27 2019	4.30E-06	2.34E-03	1.48E-01	2.19E-06	1.39E-04	0.99
May 29 2019	-4.58E-07	-2.66E-02	-1.58E-02	-4.47E-05	-2.66E-05	1.00
May 29 2019	1.17E-05	-1.73E-02	4.03E-01	-1.10E-05	2.58E-04	0.99
May 30 2019	5.04E-06	-2.05E-02	1.74E-01	-9.55E-07	8.07E-06	1.00
May 30 2019	1.50E-05	4.37E-03	5.17E-01	1.80E-07	2.13E-05	0.99
May 31 2019	7.02E-07	1.50E-03	2.42E-02	2.98E-06	4.81E-05	0.99
May 31 2019	8.71E-06	-2.82E-03	3.00E-01	-2.23E-06	2.37E-04	0.99
June 3 2019	5.96E-06	7.10E-03	2.05E-01	3.25E-07	9.39E-06	0.99
June 3 2019	9.79E-06	-6.52E-03	3.37E-01	-1.62E-07	8.37E-06	1.00
June 4 2019	1.24E-06	2.83E-02	4.26E-02	7.64E-05	1.15E-04	0.98
June 4 2019	8.93E-06	2.60E-02	3.08E-01	1.73E-05	2.04E-04	0.97
June 5 2019	3.98E-06	2.92E-03	1.37E-01	1.23E-07	5.78E-06	0.99
June 5 2019	8.62E-06	4.23E-03	2.97E-01	1.02E-07	7.13E-06	0.99
June 20 2019	2.88E-06	1.72E-02	9.92E-02	9.79E-06	5.64E-05	0.99
June 27 2019	5.56E-06	1.70E-02	1.92E-01	4.93E-06	5.54E-05	0.99
July 3 2019	7.60E-06	7.08E-03	2.62E-01	1.69E-06	6.25E-05	0.99
July 3 2019	5.27E-06	6.13E-03	1.82E-01	1.58E-06	4.67E-05	0.99
July 4 2019	6.22E-06	-1.10E-02	2.14E-01	-3.49E-06	6.80E-05	1.00
July 6 2019	2.68E-06	-1.21E-03	9.24E-02	-2.01E-07	1.53E-05	0.99
July 7 2019	1.90E-06	5.50E-03	6.54E-02	1.79E-06	2.13E-05	0.99
July 9 2019	3.69E-06	-3.79E-03	1.27E-01	-7.44E-07	2.50E-05	0.99

Date	γ corr light	γ BET dark corr	γ BET light corr	Experiment
May 21 2019	1.12	1.16E-05	2.02E-04	Commercial Antase Trial 1 (0.1%)
May 21 2019	1.16	-2.03E-06	1.86E-04	Commercial Antase Trial 2 (0.1%)
May 22 2019	1.05	1.66E-05	1.08E-04	Natural Anatase 1 Trial 1 (0.1%)
May 22 2019	1.04	-1.98E-05	7.64E-05	Natural Anatase 1 Trial 2 (0.1%)
May 23 2019	1.09	6.78E-07	9.50E-06	Rutile Trial 1 (10%)
May 24 2019	1.14	-8.29E-08	6.15E-06	Natural Anatase 2 Trial 1 (20%)
May 25 2016	1.11	1.87E-07	9.87E-06	Rutile Trial 2 (10%)
May 25 2016	1.10	3.21E-07	1.21E-05	Rutile Trial 3 (10%)
May 26 2019	1.15	-9.23E-08	6.53E-06	Natural Anatase 2 Trial 2 (20%)
May 26 2019	1.25	2.41E-08	1.29E-05	Natural Anatase 2 Trial 3 (20%)
May 27 2019	1.03	-1.02E-05	8.15E-05	Natural Anatase 1 Trial 3 (0.1%)
May 27 2019	1.10	2.18E-06	1.53E-04	Commericial Anatase Trial 3 (0.1%)
May 29 2019	1.03	-4.45E-05	-2.73E-05	Nat Ana 1 (0.1%) RH0
May 29 2019	1.32	-1.09E-05	3.40E-04	Com Ana (0.1%) RH0
May 30 2019	1.12	-9.54E-07	9.07E-06	Rutile (10%) RH0
May 30 2019	1.38	1.79E-07	2.95E-05	Nat Ana 2 (20%) RH0
May 31 2019	1.04	2.94E-06	5.00E-05	Nat Ana 1 (0.1%) RH10
May 31 2019	1.22	-2.21E-06	2.89E-04	Com Ana (0.1%) RH10
June 3 2019	1.14	3.21E-07	1.07E-05	Rutile (10%) RH10
June 3 2019	1.24	-1.61E-07	1.04E-05	Nat Ana 2 (20%) RH10
June 4 2019	1.04	7.47E-05	1.20E-04	Nat Ana 1 (0.1%) RH 50
June 4 2019	1.23	1.68E-05	2.52E-04	Com Ana (0.1%) RH50
June 5 2019	1.10	1.22E-07	6.37E-06	Rutile (10%) RH50
June 5 2019	1.21	1.00E-07	8.62E-06	Nat Ana 2 (20%) RH50
June 20 2019	1.07	9.66E-06	6.04E-05	Nat Ana (0.5%) Trial 1
June 27 2019	1.13	4.86E-06	6.24E-05	Nat Ana (1%) Trial 1
July 3 2019	1.18	1.68E-06	7.36E-05	Nat Ana (1%) Trial 2
July 3 2019	1.12	1.56E-06	5.24E-05	Nat Ana (1%) Trial 3
July 4 2019	1.14	-3.48E-06	7.77E-05	Nat Ana (1%) RH10
July 6 2019	1.10	-1.98E-07	1.68E-05	Nat Ana (1%) RH50
July 7 2019	1.06	1.77E-06	2.26E-05	Nat Ana (1%) RH0
July 9 2019	1.12	-7.33E-07	2.79E-05	Nat Ana (1%) RH0

Raw data and calculations for uptake coefficients for Chapter 2.

Appendix B

Supplementary Information for Chapter 3

Maya Abou-Ghanem, Britta J. L. Jensen, Sarah A. Styler, and Manolis N. Romanias

As published in *Earth and Space Chemistry*, 2021.
doi-org./10.1021/acsearthspacechem.0c00363

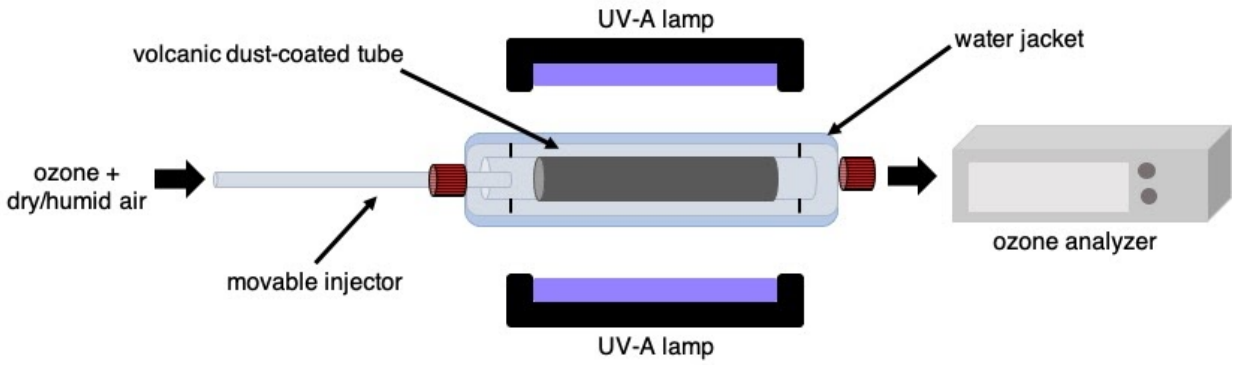

Figure B.1: Schematic of coated-wall flow tube reactor.

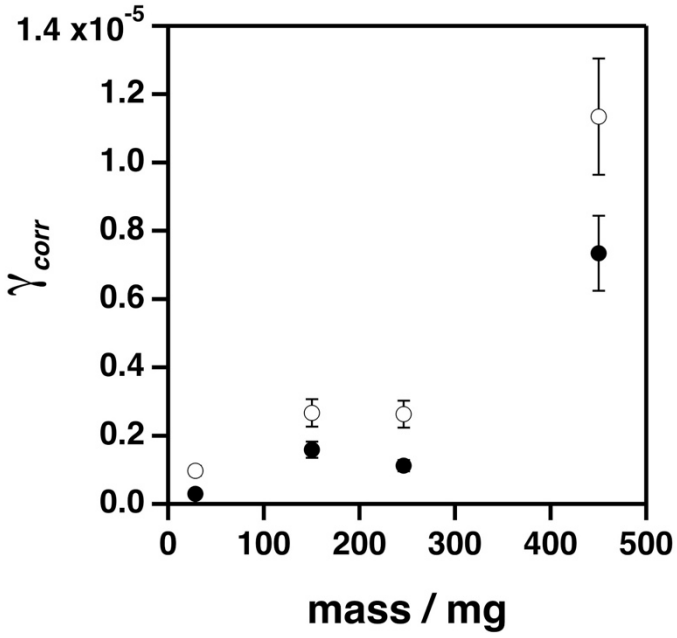

Figure B.2: Diffusion-corrected uptake coefficients (γ_{corr}) for ozone at the surface of Mýrdalssandur dust as a function of sample mass (dry conditions, 50 ppb ozone). Filled and open circles represent γ_{corr} values under dark and illuminated conditions, respectively. Error bars are estimated as 15% of calculated values, as described in Chapter 3.

	Al	Ca	Fe	K	Mg	Mn	Na	Si	Ti
Bulk	6.3	7.0	11.7	0.7	2.6	0.2	2.4	15.9	3.9
Surface	17.6	6.6	11.7	0.7	4.4	<0.1	3.3	53.1	2.6

Table B.1: Elemental bulk and surface composition of Mýrdalssandur dust as determined by ICP-MS (wt %) and XPS (at. %), respectively. ICP-MS values represent the average of six measurements and are only reported for elements >0.1%. The uncertainties on the quantification of major elements are below 10%. At. % for XPS are normalized to elements identified and exclude O and C.

	SiO_2	TiO_2	Al_2O_3	Cr_2O_3	FeO	MnO	MgO	CaO	Na_2O	K_2O	Total
	47.23	1.52	2.49	0.00	16.41	0.37	10.03	17.63	0.35	0.02	96.04
	46.71	2.06	3.54	0.00	14.86	0.34	10.79	18.06	0.41	0.00	96.77
	49.65	1.14	1.41	0.00	18.17	0.54	11.76	14.13	0.25	0.04	97.08
	47.99	1.50	2.31	0.00	13.21	0.37	13.59	16.81	0.32	0.02	96.12
	49.57	0.81	1.49	0.00	20.82	0.52	12.62	12.03	0.19	0.02	98.06
	45.15	3.77	5.08	0.00	13.43	0.28	11.55	17.06	0.62	0.02	96.98
	48.96	1.36	2.01	0.00	12.18	0.27	13.42	17.43	0.31	0.04	96.00

	49.76	1.74	2.73	0.00	12.21	0.30	13.39	16.73	0.34	0.07	97.27
	49.86	1.91	3.49	0.04	14.59	0.39	11.96	16.02	0.59	0.14	99.00
	48.02	1.94	2.82	0.00	13.48	0.36	13.04	16.49	0.35	0.03	96.53
	49.91	0.69	1.46	0.00	13.55	0.68	11.29	18.78	0.39	0.02	96.77
	50.13	0.92	1.45	0.00	13.90	0.42	12.60	17.49	0.28	0.02	97.20
	49.10	0.31	0.25	0.00	30.69	0.79	12.02	3.57	0.10	0.00	96.84
Average	48.62	1.51	2.35	0.00	15.96	0.43	12.16	15.56	0.35	0.03	96.97
SD	1.51	0.86	1.24	0.01	5.06	0.16	1.08	4.01	0.14	0.04	0.83

Table B.2: Oxide abundances (wt %) for the predicted mineral phase pyroxene, as determined by EMPA for the 75–45 μm density fractionated Mýrdalssandur sample.

	SiO_2	TiO_2	Al_2O_3	Cr_2O_3	FeO	MnO	MgO	CaO	Na_2O	K_2O	Total
	51.39	0.13	29.58	0.00	0.90	0.00	0.16	12.76	4.01	0.14	99.11
	64.64	0.04	21.67	0.00	0.41	0.00	0.00	2.33	9.12	1.17	99.39
	52.81	0.15	28.55	0.00	0.97	0.00	0.14	11.67	4.72	0.19	99.20

	54.22	0.21	27.48	0.00	0.86	0.00	0.09	10.07	5.62	0.36	98.92
	55.52	0.24	26.64	0.00	1.13	0.00	0.12	9.66	5.71	0.40	99.43
	52.86	0.26	27.99	0.00	1.23	0.02	0.22	11.42	4.78	0.21	98.99
	51.47	0.15	29.39	0.00	1.15	0.00	0.09	12.74	3.96	0.27	99.25
	50.49	0.14	29.93	0.00	0.92	0.00	0.14	13.27	3.83	0.14	98.85
	51.00	0.15	29.75	0.00	1.01	0.00	0.15	12.71	4.04	0.15	98.98
	52.60	0.18	28.44	0.00	0.93	0.00	0.14	11.38	4.79	0.20	98.68
	54.27	0.20	27.81	0.00	0.87	0.00	0.13	10.53	5.19	0.30	99.31
	54.20	0.20	26.61	0.00	1.05	0.00	0.08	9.42	5.76	0.54	97.84
	53.71	0.20	27.70	0.00	0.85	0.00	0.11	10.67	5.47	0.30	99.01
	51.97	0.18	28.92	0.00	1.17	0.00	0.18	11.99	4.43	0.18	99.03
	56.17	0.15	26.39	0.00	0.89	0.00	0.08	8.97	6.05	0.43	99.15
	53.43	0.18	28.45	0.00	0.98	0.00	0.16	11.32	4.83	0.26	99.62
	58.40	0.08	25.19	0.00	0.82	0.02	0.06	7.25	7.05	0.47	99.36

	51.84	0.15	28.42	0.00	0.96	0.00	0.14	12.03	4.35	0.17	98.08
	55.41	0.10	26.87	0.00	0.86	0.00	0.04	9.42	5.72	0.51	98.93
Average	54.02	0.16	27.67	0.00	0.95	0.00	0.12	10.51	5.23	0.34	99.01
SD	3.25	0.05	1.93	0.00	0.18	0.01	0.05	2.51	1.26	0.24	0.44

Table B.3: Oxide abundances (wt %) for the predicted mineral phase plagioclase, as determined by EMPA for the 75–45 μm density fractionated Mýrdalssandur sample.

	SiO_2	TiO_2	Al_2O_3	Cr_2O_3	FeO	Fe_2O_3	MnO	MgO	CaO	Na_2O	K_2O	Total
	0.00	48.15	0.08	0.00	39.86	6.48	0.50	1.64	0.04	0.00	0.00	96.75
	0.12	45.78	0.38	0.00	32.70	11.77	0.51	4.28	0.30	0.00	0.03	95.87
	0.19	46.21	0.09	0.00	37.87	8.08	0.61	1.51	0.46	0.00	0.01	95.03
	0.69	43.79	0.79	0.00	28.82	15.83	0.32	5.66	0.44	0.08	0.02	96.44
Average	0.25	45.98	0.34	0.00	34.81	10.54	0.49	3.27	0.31	0.02	0.02	96.02

SD	0.30	1.79	0.33	0.00	5.01	4.16	0.12	2.04	0.19	0.04	0.01	0.75

Table B.4: Oxide abundances (wt %) for the predicted mineral phase ilmenite, as determined by EMPA for the 75–45 μm density fractionated Mýrdalssandur sample.

	SiO_2	TiO_2	Al_2O_3	Cr_2O_3	FeO	Fe_2O_3	MnO	MgO	CaO	Na_2O	K_2O	Total
	0.14	14.32	1.47	0.00	41.70	37.36	0.82	0.62	0.02	0.05	0.00	96.50
	0.14	23.30	1.94	0.04	49.10	19.70	0.46	1.41	0.09	0.05	0.00	96.23
	2.85	17.03	2.44	0.00	47.61	25.93	0.40	0.44	0.33	0.24	0.06	97.33
	0.11	18.44	3.64	0.07	39.76	29.32	0.37	4.93	0.15	0.00	0.00	96.79
Average	0.81	18.27	2.37	0.03	44.54	28.08	0.51	1.85	0.15	0.09	0.02	96.71
SD	1.36	3.76	0.93	0.03	4.52	7.36	0.21	2.10	0.13	0.11	0.03	0.47

Table B.5: Oxide abundances (wt %) for the predicted mineral phase titanomagnetite, as determined by EMPA for the 75–45 μm density fractionated Mýrdalssandur sample.

	SiO_2	TiO_2	Al_2O_3	Cr_2O_3	FeO	MnO	MgO	CaO	Na_2O	K_2O	Total
	37.22	0.15	0.33	0.00	25.21	0.36	33.66	0.57	0.06	0.02	97.57
	35.93	0.11	0.00	0.00	33.07	0.48	28.24	0.33	0.00	0.00	98.19
	37.21	0.15	0.04	0.00	24.86	0.37	34.85	0.35	0.00	0.00	97.83
	32.97	0.34	0.00	0.00	48.92	0.73	15.27	0.39	0.00	0.00	98.66
	37.60	0.71	1.10	0.00	27.85	0.45	28.61	1.49	0.20	0.13	98.13
	30.26	5.70	0.21	0.00	47.54	0.90	13.97	0.52	0.07	0.02	99.19
	36.99	0.12	0.02	0.00	27.45	0.43	32.06	0.35	0.00	0.00	97.44
	33.91	0.20	0.07	0.00	42.06	0.66	19.83	0.53	0.04	0.00	97.32
Average	35.26	0.94	0.22	0.00	34.62	0.55	25.81	0.57	0.05	0.02	98.04
SD	2.64	1.94	0.37	0.00	10.07	0.19	8.31	0.38	0.07	0.04	0.64

Table B.6: Oxide abundances (wt %) for the predicted mineral phase olivine, as determined by EMPA for the 75–45 μm density fractionated Mýrdalssandur sample.

	SiO_2	TiO_2	Al_2O_3	FeOt	MnO	MgO	CaO	Na_2O	K_2O	Cl	P_2O_5	Total
	46.68	4.67	12.94	15.16	0.22	5.15	9.94	3.30	0.74	0.56	0.03	99.37
	46.82	4.47	12.72	15.27	0.24	5.15	9.98	3.31	0.74	0.64	0.02	99.37
	47.11	4.66	12.53	15.24	0.25	4.86	9.61	3.51	0.82	0.76	0.03	99.38
	47.13	4.47	12.69	15.21	0.20	5.17	9.78	3.33	0.75	0.59	0.06	99.38
	47.22	4.74	12.70	15.36	0.30	4.72	9.45	3.32	0.77	0.76	0.04	99.38
	47.25	4.58	12.52	15.37	0.22	4.96	9.49	3.34	0.84	0.78	0.05	99.39
	47.26	4.66	12.59	15.01	0.29	4.89	9.60	3.45	0.80	0.79	0.04	99.39
	47.27	4.55	12.65	15.31	0.20	5.12	9.67	3.18	0.75	0.62	0.05	99.38
	47.39	4.52	12.66	15.08	0.23	5.16	9.68	3.20	0.76	0.65	0.04	99.38
	47.41	4.68	12.64	14.97	0.18	4.96	9.40	3.57	0.86	0.68	0.05	99.39
	47.41	4.77	12.61	14.80	0.25	4.90	9.46	3.45	0.87	0.80	0.07	99.40
	47.41	4.70	12.60	15.05	0.27	4.85	9.47	3.32	0.83	0.84	0.04	99.39
	47.48	4.88	12.54	14.97	0.26	4.88	9.33	3.45	0.78	0.76	0.06	99.40

	47.56	4.67	12.79	14.78	0.27	4.96	9.34	3.34	0.87	0.80	0.04	99.40
	47.87	4.61	12.57	15.05	0.23	4.76	9.27	3.39	0.84	0.77	0.02	99.39
	47.12	4.77	12.32	15.36	0.22	4.98	9.60	3.37	0.79	0.79	0.05	99.37
	47.20	4.49	12.46	15.20	0.29	5.04	9.36	3.68	0.91	0.73	0.01	99.38
	47.21	4.53	12.67	15.14	0.24	5.01	9.67	3.49	0.73	0.65	0.03	99.37
	47.24	4.52	12.68	15.11	0.27	5.02	9.54	3.49	0.75	0.70	0.06	99.38
	47.28	4.66	12.86	15.11	0.20	5.08	9.57	3.31	0.75	0.53	0.03	99.38
	47.34	4.48	12.65	14.95	0.26	5.06	9.79	3.33	0.73	0.71	0.07	99.38
	47.35	4.55	12.46	15.47	0.20	4.54	9.52	3.63	0.82	0.75	0.08	99.37
	47.37	4.64	12.45	15.09	0.29	4.90	9.42	3.63	0.80	0.72	0.07	99.38
	47.40	4.52	12.76	14.94	0.19	5.18	9.69	3.31	0.73	0.61	0.04	99.37
	47.40	4.57	12.67	14.95	0.26	5.09	9.56	3.32	0.76	0.75	0.05	99.38
	47.54	4.74	12.51	14.92	0.22	4.92	9.38	3.50	0.84	0.76	0.04	99.38
	47.54	4.62	12.73	14.95	0.20	5.05	9.52	3.29	0.75	0.66	0.07	99.38

	47.91	4.38	12.56	14.79	0.21	5.16	9.51	3.43	0.77	0.61	0.05	99.38
	50.17	2.85	13.21	13.82	0.2	5.22	9.63	3.48	0.52	0.28	0.02	99.40
	50.76	2.65	13.41	13.21	0.22	5.54	9.69	3.16	0.49	0.24	0.03	99.40
Average	47.54	4.49	12.67	14.99	0.24	5.01	9.56	3.40	0.77	0.68	0.04	99.38
SD	0.84	0.49	0.22	0.45	0.03	0.18	0.17	0.13	0.09	0.14	0.02	0.01

Table B.7: Oxide abundances (wt %) for the glass fraction, as determined by EMPA for the 75–45 μm density fractionated Mýrdalssandur sample. As is standard in volcanic ash studies, the values are normalized to 100% on a volatile and anhydrous basis, although the original totals are reported. Total Fe reported as FeOt.

Date	Experiment	Flow rate (m3/s)	Velocity (m/s)	mass (g)	length of tube (m)	[O3] Initial	Residence Time (s)
July 25 2018 (Sarah)	Mass Dependence 250mg	1.50E-05	2.01E-01	0.2463	0.16	53.1	0.79599
July 31 2018 (Manolis)	Mass Dependence 28 mg	1.42E-05	1.91E-01	0.0286	0.16	54.8	0.83886534
August 1 2018 (Manolis)	Mass Dependence 150	1.45E-05	1.94E-01	0.1504	0.16	52	0.823437931
August 2 2018 (Manolis)	Mass Dependence 450	1.40E-05	1.88E-01	0.4503	0.15	51.7	0.799543527
August 9 2018 (Manolis)	Ozone concentration 10	1.45E-05	1.94E-01	0.055	0.16	9.8	0.823437931
August 16 2018 (Manolis)	Ozone concentration 11	1.45E-05	1.95E-01	0.2555	0.16	11.5	0.821549312
July 21 2018 (Sarah)	Ozone concentration 25	1.50E-05	2.01E-01	0.2657	0.16	27.6	0.794225055
July 19 2018 (Sarah)	Ozone concentration 50	1.51E-05	2.02E-01	0.2846	0.16	49.5	0.79246792
August 14 2018 (Manolis)	Ozone concentration 82	1.44E-05	1.93E-01	0.252	0.16	82.4	0.828197688
July 20 2018 (Sarah)	Ozone concentration 100	1.50E-05	2.01E-01	0.2805	0.16	105.4	0.794225055
August 10 2018 (Manolis)	Ozone concentration 124	1.42E-05	1.90E-01	0.2008	0.16	124.2	0.842812941
July 20 2018 (Sarah)	Ozone concentration 150	OMIT			0.16		#VALUE!
August 7 2018 (Manolis)	Ozone concentration 150	1.47E-05	1.97E-01	0.2706	0.16	150.7	0.814080682
August 11 2018 (Manolis)	Ozone concentration 200	1.42E-05	1.90E-01	0.22	0.16	193	0.842812941
July 25 2018 (Sarah)	RH 0	1.50E-05	2.01E-01	0.2463	0.16	53.1	0.79599
July 19 2018 (Sarah)	RH 30	1.51E-05	2.02E-01	0.2846	0.16	49.5	0.79246792
July 26 2018 (Sarah)	RH 50	1.50E-05	2.01E-01	0.2618	0.16	47.6	0.79599
July 31 2018 (Manolis)	RH 0	1.42E-05	1.91E-01	0.0286	0.16	54.8	0.83886534
August 1 2018 (Manolis)	RH 0	1.45E-05	1.94E-01	0.1504	0.16	52	0.823437931
August 2 2018 (Manolis)	RH 0	1.40E-05	1.88E-01	0.4503	0.15	51.7	0.799543527
August 17 2018 (Manolis)	RH 14	1.46E-05	1.95E-01	0.2027	0.16	50.7	0.819669336

BET (m^2/g)	z*	S geo (cm^2)	Sherwood #	[O3] final dark (ppb)	[O3] final light (ppb)	k (dark)	k light	γ geo dark	γ geo light
1.8	0.2121979	48.984	4.086505205	51.4	49.3	0.04087835	0.09328364	1.10192E-06	2.51456E-06
1.8	0.2236278	48.984	4.065957501	54.3	53.2	0.01092663	0.03532366	2.94539E-07	9.52186E-07
1.8	0.2195151	48.984	4.073120684	49.6	48.1	0.05738488	0.0946781	1.54687E-06	2.55215E-06
1.8	0.2131452	45.9225	4.084724092	42.6	39	0.24214257	0.35257134	6.52721E-06	9.50393E-06
1.8	0.2195151	48.984	4.073120684	9.4	8.8	0.05060818	0.1307089	1.3642E-06	3.52339E-06
1.8	0.2190116	48.984	4.074014868	9.7	9.4	0.20719529	0.24543548	5.58516E-06	6.61597E-06
1.8	0.2117274	48.984	4.08739536	24.7	23.2	0.13977465	0.21865779	3.76777E-06	5.89415E-06
1.8	0.211259	48.984	4.088285247	45.5	43.5	0.1063265	0.16304979	2.86614E-06	4.39518E-06
1.8	0.2207839	48.984	4.070884046	77.9	75.7	0.06780927	0.1023998	1.82787E-06	2.76029E-06
1.8	0.2117274	48.984	4.08739536	99.3	97.7	0.07506319	0.09551584	2.02341E-06	2.57473E-06
1.8	0.2246801	48.984	4.064164002	120.7	119.1	0.03391623	0.0497497	9.14247E-07	1.34106E-06
1.8	#REF!	48.984	#REF!			#DIV/0!	#DIV/0!	#DIV/0!	#DIV/0!
1.8	0.2170206	48.984	4.07758891	146.3	144.2	0.03639909	0.0541591	9.81175E-07	1.45992E-06
1.8	0.2246801	48.984	4.064164002	188.4	186	0.0286218	0.04383359	7.71531E-07	1.18158E-06
1.8	0.2121979	48.984	4.086505205	51.4	49.3	0.04087835	0.09328364	1.10192E-06	2.51456E-06
1.8	0.211259	48.984	4.088285247	45.5	43.5	0.1063265	0.16304979	2.86614E-06	4.39518E-06
1.8	0.2121979	48.984	4.086505205	46.9	46	0.01861215	0.04295452	5.0171E-07	1.15788E-06
1.8	0.2236278	48.984	4.065957501	54.3	53.2	0.01092663	0.03532366	2.94539E-07	9.52186E-07
1.8	0.2195151	48.984	4.073120684	49.6	48.1	0.05738488	0.0946781	1.54687E-06	2.55215E-06
1.8	0.2131452	45.9225	4.084724092	42.6	39	0.24214257	0.35257134	6.52721E-06	9.50393E-06
1.8	0.2185104	48.984	4.074908782	47.9	46.1	0.06930893	0.11603821	1.86829E-06	3.12793E-06
1.8	#DIV/0!	48.984	#DIV/0!			#DIV/0!	#DIV/0!	#DIV/0!	#DIV/0!

γ BET dark	γ BET light	γ eff dark	γ eff light	γ corr	γ corr	γ BET dark corr	γ BET light corr
1.21749E-08	2.7783E-08	1.10192E-06	2.5146E-06	1.123E-06	2.627E-06	1.24077E-08	2.90257E-08
2.80258E-08	9.0602E-08	2.94539E-07	9.5219E-07	2.9603E-07	9.6796E-07	2.81678E-08	9.21027E-08
2.7989E-08	4.61785E-08	1.54687E-06	2.5521E-06	1.5889E-06	2.6685E-06	2.87487E-08	4.82835E-08
3.6981E-08	5.38461E-08	6.52721E-06	9.5039E-06	7.3437E-06	1.134E-05	4.1607E-08	6.42471E-08
6.74988E-08	1.74333E-07	1.3642E-06	3.5234E-06	1.3967E-06	3.749E-06	6.91093E-08	1.85498E-07
5.94877E-08	7.04668E-08	5.58516E-06	6.616E-06	6.1741E-06	7.4588E-06	6.57604E-08	7.94433E-08
3.859E-08	6.03686E-08	3.76777E-06	5.8941E-06	4.026E-06	6.5515E-06	4.12347E-08	6.71013E-08
2.74059E-08	4.20265E-08	2.86614E-06	4.3952E-06	3.0131E-06	4.7505E-06	2.88113E-08	4.54243E-08
1.97391E-08	2.98082E-08	1.82787E-06	2.7603E-06	1.8868E-06	2.897E-06	2.03756E-08	3.12842E-08
1.96305E-08	2.49793E-08	2.02341E-06	2.5747E-06	2.0956E-06	2.6928E-06	2.03308E-08	2.61243E-08
1.23903E-08	1.81746E-08	9.14247E-07	1.3411E-06	9.2878E-07	1.3726E-06	1.25873E-08	1.86017E-08
#DIV/0!	#DIV/0!	#VALUE!	#VALUE!	#VALUE!	#VALUE!	#VALUE!	#VALUE!
9.86735E-09	1.46819E-08	9.81175E-07	1.4599E-06	9.9788E-07	1.4972E-06	1.00354E-08	1.5057E-08
9.5436E-09	1.46158E-08	7.71531E-07	1.1816E-06	7.8186E-07	1.206E-06	9.67135E-09	1.49176E-08
1.21749E-08	2.7783E-08	1.10192E-06	2.5146E-06	1.123E-06	2.627E-06	1.24077E-08	2.90257E-08
2.74059E-08	4.20265E-08	2.86614E-06	4.3952E-06	3.0131E-06	4.7505E-06	2.88113E-08	4.54243E-08
5.21513E-09	1.20359E-08	5.0171E-07	1.1579E-06	5.0603E-07	1.1812E-06	5.26006E-09	1.22779E-08
2.80258E-08	9.0602E-08	2.94539E-07	9.5219E-07	2.9603E-07	9.6796E-07	2.81678E-08	9.21027E-08
2.7989E-08	4.61785E-08	1.54687E-06	2.5521E-06	1.5889E-06	2.6685E-06	2.87487E-08	4.82835E-08
3.6981E-08	5.38461E-08	6.52721E-06	9.5039E-06	7.3437E-06	1.134E-05	4.1607E-08	6.42471E-08
2.50826E-08	4.19938E-08	1.86829E-06	3.1279E-06	1.9299E-06	3.3044E-06	2.59092E-08	4.43632E-08
#DIV/0!	#DIV/0!	#DIV/0!	#DIV/0!	#DIV/0!	#DIV/0!	#DIV/0!	#DIV/0!

Raw data and calculations for uptake coefficients for Chapter 3.

Appendix C

Supplementary Information for Chapter 4

Maya Abou-Ghanem, Danial Nodeh-Farahani, Devon T. McGrath, Trevor C. VandenBoer, and Sarah A. Styler

Submitted. *Environmental Science: Processes & Impacts,* 2021.

C.1 Sieving procedures

The road dust sample used in this study was collected using a dustpan and brush, and therefore contained particles ranging from >500 to <20 μm. To isolate the resuspendable fraction, we used a two-stage sieving method. First, to separate the fine dust from larger particles, the latter of which comprised the bulk of the sample, ~150 g of road dust was placed onto an 8 inch stainless steel and brass sieve stack (W. S. Tyler) and the >500, 500–212, 212–125, and <125 μm size fractions were collected using a sieve shaker (AS 200 basic, Retsch). Second, to separate the finer fractions, ~23 g of road dust collected from the <125 μm size fraction was placed into a 3 inch stainless steel sieve stack (Hoskin Scientific) and the 125–75, 75–45, 45–20, and <20 μm subfractions were collected using the same sieve shaker.

Sieving was conducted as described in the American Society for Testing and Materials (ASTM) standard sieve method: in particular, the mass of road dust used during both sieving stages was 7 kg/m^2 or less and sieving times were selected based on tap test results.[1] To prevent the loss of water-soluble material, which we hypothesized would contribute to road dust reactivity, all samples were dry sieved.

Although the <20 μm fraction is most representative of airborne road dust, we used the 45–20 μm fraction for all experiments conducted in this study, since the <20 μm fraction contained insufficient mass. The small relative contribution from the <20 μm fraction likely reflects a combination of several factors: first, the known bias against small particle collection for the dustpan and brush method;[2] second, the road dust particle size in Edmonton being generally larger than in lower-latitude sites, owing to the wintertime application of gravel; and third, the prior depletion of smaller particles via wind suspension and/or meltwater runoff.

C.2 Sample preparation

C.2.1 Sample preparation for rinsed road dust and road dust leachate

To prepare the rinsed road dust sample, 1.00 g (± 1%) of road dust was weighed into three 50 mL centrifuge tubes; then, 40 mL of deionized water was added to each tube. Centrifuge tubes

containing sample suspensions were shaken on a table-top shaker (Multi-Platform Shaker, Fisherbrand™) at 450 rpm for 10 min and then ultracentrifuged (Avanti® J-26 XPI, Beckman Coulter) at 7000 rpm for 10 min. A pipette was used to carefully remove 30 mL of the supernatant from the centrifuge tube while avoiding disruption of the road dust pellet; then, 30 mL of fresh deionized water was added to the tube. This shaking and rinsing procedure was repeated 7 times. After the last rinse, the road dust slurries were transferred into a Pyrex sample jar, and each centrifuge tube was rinsed several times with a small quantity of deionized water to ensure quantitative transfer. This jar was placed in a gravity oven (100L, Fisherbrand™) at 324 ± 5 K until the sample was dry.

The collection of road dust leachate followed the same procedure described above, except in this case, ~10 mL of the supernatant was filtered using 0.2 μm nylon filters (VWR) into 15 mL centrifuge tubes. These filtered solutions were then analyzed for F^-, Cl^-, NO_2^-, Br^-, NO_3^-, SO_4^{2-}, PO_4^{3-}, and I^- using ion chromatography, as described in Section C.3.1.

C.2.2 Sample preparation and experimental details for chlorine activation experiments

Chlorine activation experiments were performed with the following coated tubes: road dust, rinsed road dust, road dust coatings prepared with deionized water adjusted to pH 4 by H_2SO_4, illuminated road dust, road dust mixed with $CaCl_2 \cdot 2H_2O$, road dust mixed with anti-icer, $CaCl_2 \cdot 2H_2O$, anti-icer, and $FeCl_3$ mixed with $CaCl_2 \cdot 2H_2O$. A summary of experimental details and motivation for each experiment is presented in Table C.6. For these experiments, Pyrex insert tubes were prepared as described in Chapter 4.2.2.1, except with a higher mass (200 mg) and a different wiping protocol (the first 2 cm and last 1 cm of the Pyrex insert tubes were wiped) as an attempt to maximize the total chlorine production. All experiments were performed in the dark, unless otherwise stated, and in duplicate.

C.2.2.1 Road dust doped with anti-icer or $CaCl_2 \cdot 2H_2O$

To explore the role of salts in chlorine activation, we conducted experiments with mixed anti-icer/road dust and $CaCl_2 \cdot 2H_2O$/road dust coatings. To ensure samples contained equal amounts

of chloride, either 750 μL of Road Guard Plus™ (4.3 mmol chloride, as estimated from the manufacturer SDS) or ~320 mg of $CaCl_2 \cdot 2H_2O$ (4.3 mmol chloride) was added to the road dust during the coating process.

C.2.2.2 Acidified conditions

To explore the potential for chlorine activation by water-soluble Fe^{3+} in road dust, we prepared road dust coatings using deionized water adjusted to pH 4 using concentrated H_2SO_4, which has been shown to result in the mobilization of Fe^{3+} in mineral dust.[4]

C.2.2.3 $FeCl_3$ and $CaCl_2 \cdot 2H_2O$

Mixed $FeCl_3$ and $CaCl_2 \cdot 2H_2O$ coated tubes were used as a positive control for chlorine activation, based on published results from Sadanaga and coworkers, who observed Cl_2 formation during ozone uptake by acidified (via H_2SO_4 addition; pH ~4) $FeCl_3$ and NaCl mixed particles.[3] Since the authors observed increasing Cl_2 yield with increasing Fe content,[3] we performed experiments using a 1:1 wt ratio of Fe:Ca to optimize our ability to observe chlorine activation. Here, coated tubes were prepared by adding deionized water, adjusted to pH 4 using concentrated H_2SO_4, to a mixture of ~88 mg of $FeCl_3$ and ~111 mg of $CaCl_2 \cdot 2H_2O$.

C.3 Sample characterization

C.3.1 Ion chromatography (IC) analysis

C.3.1.1 Instrumentation

Road dust leachate and impinger samples collected from chlorine activation experiments were analyzed using ion chromatography (Thermo Scientific Dionex™ ICS-6000 IC) coupled with suppressed conductivity detection. Samples were injected using an autosampler (Thermo Scientific Dionex™ AS-DV) into a 250 μL sample loop and separated with a Dionex IonPac AS23 analytical column (4 x 250 mm; P/N: 064149) at 25 °C column temperature; a Dionex IonPac AG23 guard column (4 x 50 mm; P/N: 064147) was used to avoid analytical column contamination. After separation, a dynamically regenerated suppressor (Dionex™ ADRS 600, 4 mm; P/N: 088666) held at a compartment temperature of 20 °C was used to suppress the eluent

before it entered the conductivity cell, which was held at 35 °C. Analyte quantification was performed using Thermo Scientific™ Chromeleon 7 software.

C.3.1.2 Anion quantification

100 mM sodium hydroxide (NaOH) eluent was prepared by dissolving 9.8 mL of aqueous NaOH (certified, Fisher Chemicals, CAT#SS254-500, 50% w/w) in 1800 mL of deionized water. The eluent was purged with nitrogen gas for 5 min prior to use and kept under nitrogen (4 psi) during use.

Samples were separated using a gradient elution method designed to resolve F^-, Cl^-, NO_2^-, Br^-, NO_3^-, SO_4^{2-}, PO_4^{3-} , and I^-. The gradient program starts by holding at 10 mM NaOH for the first 15 min, followed by a linear increase over 5 min to 60 mM NaOH. The mobile phase composition is held at 60 mM for 5 min; then, the NaOH concentration is stepped back to 10 mM and held for 5 min to re-equilibrate the system prior to injection of the next sample, yielding a total separation time of 30 min. The mobile phase flow rate employed for all analyses was 1 mL min^{-1}.

Instrument response was calibrated using a six-point external calibration curve spanning 8.7 ng mL^{-1}–1.38 μg mL^{-1} for F^-, 87 ng mL^{-1}–13.8 μg mL^{-1} for PO_4^{3-}, and 43 ng mL^{-1}–6.9 μg mL^{-1} for the remaining analytes. All standards were prepared by serial dilution of commercially available stock solutions (Dionex™ Combined Seven Anion Standard II; P/N: 057590, VeriSpec™iodide standard; CAT# RV010920-100N). Samples with analyte concentrations that fell outside of this calibration range were diluted prior to quantification.

As shown in Table C.2, all anions were present in road dust leachate above their detection limits except for NO_2^- and I^-. For chlorine activation experiments, only Cl^- and also F^- were present above its detection limit.

C.3.1.3 Quality assurance and control

To monitor the reproducibility of the instrument's response over each period of analysis, a check standard was injected regularly (at least every 10 injections). DI water obtained from a

Milli-Q™ Direct 8 water purification system was used as an instrument blank for IC measurements. As a result of ion competition effects for analytes and eluent in IC separations, peak shape and maxima are both sensitive to the identity of an ion pair and their relative concentrations. Therefore, to robustly identify the target analytes across the working range of the instrument, a three-sigma retention time window was defined for each ion using the standard deviation of the retention times observed across the calibrated range for each analyte. This strategy allowed the ions to be reliably quantified and in particular, ensured that Br^- was not co-eluting with the CO_3^{2-} in the matrix.

We tested our approach through the analysis of a randomly selected sample. From the commercially available Combined Seven Anion Standard II (which contains Br^-), 100 µL was added to i) 5 mL of the random sample and ii) 5 mL of deionized water and each was analyzed. An increase was observed in the peak areas corresponding to the ions quantified in each of the defined windows. We did not observe an increase in the number of peaks in each window, confirming that the ions corresponding to each window are correctly identified for quantitative analysis. Br^- was also found to be baseline-resolved from CO_3^{2-}, demonstrating no co-elution or matrix effects for Br^- quantification.

C.3.2 Elemental analysis by inductively coupled plasma mass spectrometry (ICP-MS) for road dust samples

C.3.2.1 Instrumentation

ICP-MS analysis was performed using a Perkin Elmer Elan 6000, which was operated at 1300 W in dual-detector mode, with auto lens on, and at a flow rate of 1 mL min^{-1}. Sample measurements for each replicate were collected over 35 sweeps; three replicates were conducted for each sample. Dwell times were 10 ms for Na, Al, K, Cu, Zn, and Sr and 20 ms for all other elements, except Se (150 ms); the integration time for each element is the dwell time multiplied by the number of sweeps (*e.g.*, 350 ms for Na).

Quantification was accomplished using four-point calibration curves (0, 0.25, 0.50, 1.00 ppm for Na, Ca, Mg, Fe, K, and P; 0, 0.005, 0.010, 0.020 ppm for the rest of the elements), which were obtained using Bi, Sc, and In as internal standards and measured in cps (counts per second). Blank subtractions were applied after internal standard corrections. The final results of these analyses are presented in Table C.1.

C.3.2.2 Sample preparation

Road dust samples (~0.2 g) were acid digested in a beaker at 130 °C using a three-step process: first, samples were heated overnight in a mixture of HF (8 mL) and HNO_3 (2 mL); second, HCl (5 mL) and HNO_3 (5 mL) were added and the mixture was heated until completely dry; third, 8 M HNO_3 (10 mL) was added and the mixture was heated for 2 h.

After the digestion process, the resultant solution was transferred to a 15 mL test tube; to ensure quantitative transfer, the beaker was rinsed several times with DI water until a total of 15 mL of water was added to the test tube. 1 mL of this solution was added to HNO_3 (0.1 mL), internal standards (0.1 mL), and deionized water (8.8 mL); the final analysis solution was shaken well. All acids used were trace metal grade.

Since HF acid digestion results in the formation of stable SiF_4,[5] a different digestion method was required for Si analysis. First, road dust (~0.2 g) and Na_2O_2 (~0.8 g) were placed into a Ni crucible and heated at 480 °C for 1 h. Second, deionized water (5 mL) was added to the crucible and the mixture was transferred to a test tube and centrifuged; the supernatant was decanted into a 50 mL centrifuge tube.

To determine Si in the sample rinse, the solid pellet remaining in the centrifuge tube was rinsed twice (5 mL deionized water for each rinse) and the combined supernatants were adjusted to a total volume of 20 mL using deionized water. Finally, 0.1 mL of this solution was added to HNO_3 (0.1 mL), internal standards (0.1 mL), and deionized water (9.7 mL); the resultant solution was then analyzed.

To determine Si in the sample itself, 8 M HNO_3 (10 mL) was added to the test tube to dissolve the solid road dust pellet and the solution was transferred to a 125 mL bottle; then, deionized water was added (90 mL). Finally, 1 mL of this solution was added to HNO_3 (0.1 mL), internal standards (0.1 mL), and deionized water (8.8 mL); the resultant solution was then analyzed.

C.3.3 Total nitrogen, carbon, and organic carbon determination by dry combustion

Complete combustion of the sample was achieved by transferring a known mass of road dust into a combustion quartz tube containing Cr(III) oxide and cobaltous/ic oxide silver catalysts. A flow of purified oxygen is added to the quartz tube and its reaction with the Sb or Ag weigh boat results in a flash combustion reaction which increases the temperature from 1020°C to 1800–2000°C. During flash combustion, the carbon in the sample is converted to CO_2 and the nitrogen in the sample is converted to N_2 and NO_x. These combustion gases are carried via a stream of ultra high purity (UHP) He through a reduction furnace filled with copper wires that reduce NO_x to N_2. The CO_2/N_2 gas stream then passes through a $MgCl_2$ sorbent trap to remove water and is separated on a 2 m × 6 mm OD stainless steel Porapak QS 80/100 mesh packed chromatographic column. Finally, total nitrogen and carbon are detected quantitatively by a thermal conductivity detector (Thermo FLASH 2000 Organic Elemental Analyzer, Thermo Fisher Scientific Inc., Bremen, Germany 2016.).

For TOC analysis, road dust samples were weighed in open Ag boats and acidified with sequential 50 μL additions of 1 M HCl until no further reaction was observed. Using this method, samples will bubble in the presence of inorganic carbon. The samples are then oven dried at 40 °C overnight and crushed before analyzing using the Thermo FLASH 2000 system described above.

Acetanilide (C_8H_9NO; >99+%, ACROS) was used as a calibration standard; the theoretical values of 71.09 and 10.36 wt % for C and N, respectively, was used for a five-point calibration. Continuing calibration verifications of acetanilide were routinely performed, with required recoveries of 95–105% of its theoretical value. Atropine ($C_{17}H_{23}NO_3$; Costech) was used as an

external reference standard. A known mass of this standard was analyzed and the recovery was calculated based on theoretical values of 70.56 and 4.84 wt % for C and N, respectively.

C.3.4 Brunauer–Emmett–Teller (BET) surface area by nitrogen adsorption analysis

Prior to gas adsorption analysis, samples were degassed (activated) in the absence of heat on a gas adsorption sample preparation instrument (Smart VacPrep, Micromeritics) in order to ensure that the measured–surface area is reflective of the surface area presented under our experimental conditions. For activation, each sample was weighed into a pre-weighed glass sample tube/holder equipped with a filler rod (for the reduction of unoccupied volume) and a steel frit ball valve (to prevent the sample from interacting with the atmosphere during transfer from the activation instrument to the measurement instrument). Samples were activated by evacuating the sample holder at 5.00 mmHg s^{-1} until 1.00 mmHg was reached. Subsequently, the samples were held under an unrestricted vacuum for 24 h. The sample holders were then filled with N_2 gas, removed from the Smart VacPrep instrument, and reweighed prior to gas adsorption analysis. Gas adsorption isotherm data were collected at 77 K using N_2 gas as the probe molecule on a 3Flex Surface Characterization Analyzer (Micromeritics). The data obtained was used to determine the Brunauer–Emmett–Teller (BET) surface area by fitting the linear BET equation to the data and ensuring that the 4-point criterion was met.[6]

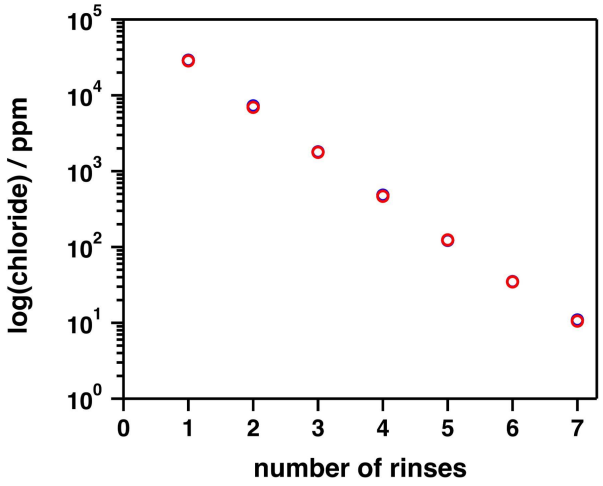

Figure C.1: Total leachable chloride in road dust ($n = 3$) as a function of rinses. Black, blue, and red open circles represent each individual trial; in most cases, variation between trials was minimal.

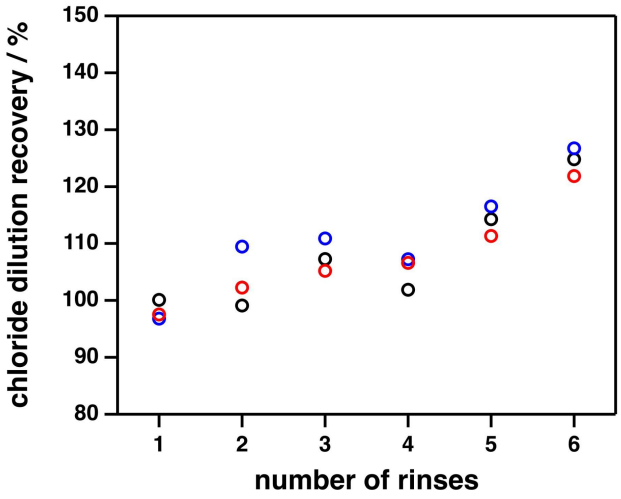

Figure C.2: Apparent "recovery" of chloride after leachate ($n = 3$) dilution as a function of rinses. Black, blue, and red open circles represent each individual trial.

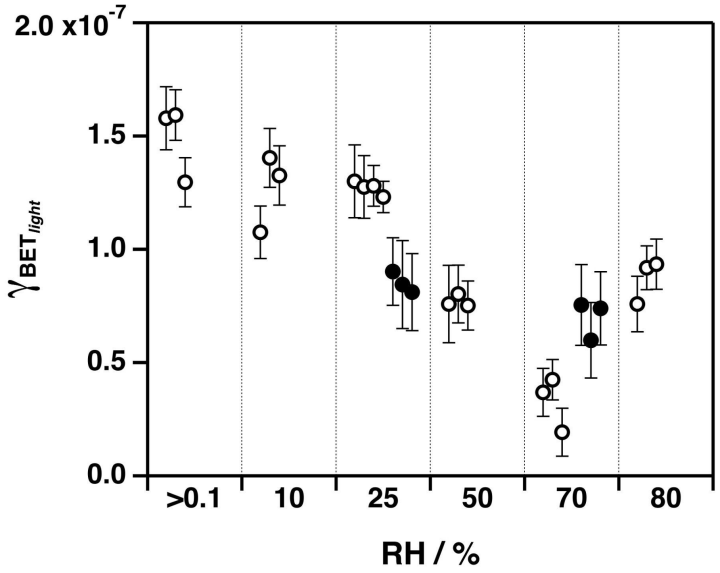

Figure C.3: Reaction profiles of ozone with a) road dust and anti icer, b) road dust with 500 ppm added chloride (w/w), c) road dust with 5% added chloride (w/w), d) anti-icer, and e) $CaCl_2 \cdot 2H_2O$ at 70% RH. The blue and yellow regions of the plot indicate periods of ozone interaction with the samples under dark and light conditions, respectively.

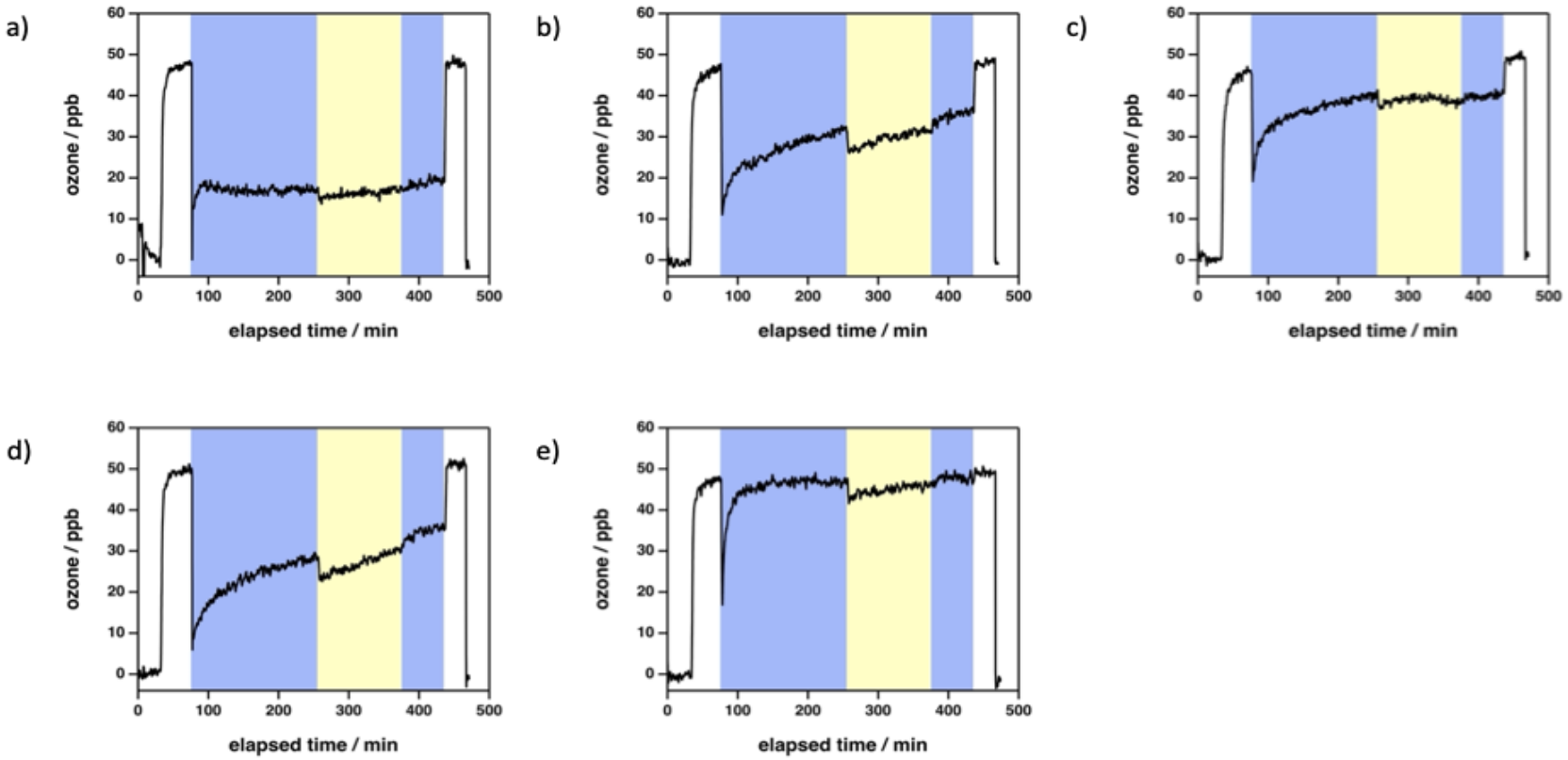

Figure C.4: Reaction profiles of ozone with a) road dust and anti icer, b) road dust with 500 ppm added chloride (w/w), c) road dust with 5% added chloride (w/w), d) anti-icer, and e) $CaCl_2 \cdot 2H_2O$ at 70% RH. The blue and yellow regions of the plot indicate periods of ozone interaction with the samples under dark and light conditions, respectively.

	road dust	rinsed road dust
element	wt %	
Si	33.2	32.6
Ca	3.3	3.6
Al	2.5	2.7
Fe	2.4	2.7
K	1.0	1.1
Mg	0.8	0.9
Na	2.1	0.6
Ti	0.1	0.1
element	ppm	
P	976.7	980.0
Mn	585.0	649.1
Ba	477.1	507.9
Zn	228.7	241.5
Sr	132.1	138.4
Cr	66.0	76.0
Cu	67.3	72.5
Pb	49.5	49.1
V	46.5	49.0
Ce	38.4	41.2
Rb	36.3	40.1
Ni	30.3	28.9
La	18.1	20.2
Nd	16.3	16.9
Li	16.1	16.8
Y	10.6	11.7
Sn	8.5	10.3
Co	7.8	8.1

W	14.2	7.9
Ga	6.2	6.8
Th	4.3	5.3
Pr	4.3	4.5
Sb	4.6	4.5
As	4.4	4.4
Nb	4.0	4.1
Sm	3.1	3.2
Mo	3.9	3.1
Gd	3.0	3.0
Dy	1.9	2.0
Cs	1.5	1.5
U	1.4	1.5
Er	1.2	1.2
Yb	1.0	1.1
Eu	0.7	0.7
Be	0.9	0.4
Ho	0.3	0.4
Tb	0.4	0.4
Se	0.5	0.3
Cd	0.2	0.3
Ag	0.2	0.3
Tl	0.3	0.3
Tm	0.2	0.2
Lu	0.2	0.2
Ru	0.1	0.1

Table C.1: Elemental composition of road and rinsed road dust samples, as determined using ICP-MS.

ion	wt %
Cl^-	2.9
	2.9
	2.8
ion	**ppm**
SO_4^{2-}	576.8
	560.4
	552.5
NO_3^-	82.1
	82.5
	83.6
F^-	21.3
	35.7
	34.6
PO_4^{3-}	6.3
	18.4
	10.0
Br^-	8.2
	8.5
	9.3
NO_2^-	undetected
	undetected
	undetected
I^-	undetected
	undetected
	undetected

Table C.2: Leachable anion content of road dust, as determined by IC analysis ($n = 3$).

	total nitrogen (TN)	total carbon (TC)	total organic carbon (TOC)	total inorganic carbon (TIC)
road dust	0.16	5.58	4.23	1.35
rinsed road dust	0.12	4.80	3.88	0.92

Table C.3: Total nitrogen, carbon, organic carbon, and inorganic carbon (all reported as % w/w) content of road dust and rinsed road dust, as determined by dry combustion analysis.

sample	BET surface area ($m^2\ g^{-1}$)
road dust	8.10
rinsed road dust	7.02

Table C.4: Specific surface areas (BET; $m^2\ g^{-1}$) of road dust and rinsed road dust, as determined by nitrogen adsorption analysis.

element	wt %
Ca	13.1
Mg	1.3
K	1.0
Na	0.7
Sr	0.3
element	**ppm**
Zn	655.6
Al	46.5
Mn	15.8
Ba	6.2
Sn	5.7
Cu	2.3
Be	0.8
Cr	0.6
Pb	0.5
V	0.2
Ag	undetected
As	undetected
Cd	undetected
Co	undetected
Fe	undetected
Mo	undetected

Ni	undetected
Sb	undetected
Se	undetected
Ti	undetected
Tl	undetected

Table C.5: Elemental composition of Road Guard Plus™, as determined by ICP-MS.

sample	illuminated	acidified	motivation
road dust			to explore chlorine activation by road dust
rinsed road dust			to explore chlorine activation by road dust with reduced chloride content
road dust + light	✓		to determine if chlorine activation is driven by light
road dust + anti-icer			to determine if anti-icer enhances chloride activation in road dust
road dust + $CaCl_2 \cdot 2H_2O$			to determine if salts enhance chloride activation by road dust
road dust (pH adjusted)		✓	to explore whether mobilized Fe^{3+} enhances chloride activation in road dust, as demonstrated by Sadanaga et al.[3]
anti-icer			to determine if anti-icer is driving chlorine activation
$CaCl_2 \cdot 2H_2O$			control experiment; to verify chlorine activation is not driven by salt alone
$FeCl_3$ + $CaCl_2 \cdot 2H_2O$ (pH adjusted)		✓	positive control, as demonstrated by Sadanaga et al.[3]
empty tube			blank control

Table C.6: Summary of sample-coated tubes for chlorine activation experiments. Further details regarding sample preparation are provided in Section C.1.2.

C.4 References

(1) ASTM C136 / C136M-19, Standard Test Method for Sieve Analysis of Fine and Coarse Aggregates. ASTM International, West Conshohocken, PA 2019.

(2) Casotti Rienda, I.; Alves, C. A. Road Dust Resuspension: A Review. *Atmos. Res.* **2021**, *261*, 105740.

(3) Sadanaga, Y.; Hirokawa, J.; Akimoto, H. Formation of Molecular Chlorine in Dark Condition: Heterogeneous Reaction of Ozone with Sea Salt in the Presence of Ferric Ion. *Geophys. Res. Lett.* **2001**, *28* (23), 4433–4436.

(4) Shi, Z.; Krom, M. D.; Jickells, T. D.; Bonneville, S.; Carslaw, K. S.; Mihalopoulos, N.; Baker, A. R.; Benning, L. G. Impacts on Iron Solubility in the Mineral Dust by Processes in the Source Region and the Atmosphere: A Review. *Aeolian Res.* **2012**, *5*, 21–42.

(5) Pekney, N. J.; Davidson, C. I. Determination of Trace Elements in Ambient Aerosol Samples. *Anal. Chim. Acta* **2005**, *540* (2), 269–277.

(6) Sing, K. S. W. Adsorption by Powders and Porous Solids. In *Adsorption by Powders and Porous Solids (Second Edition)*; Rouquerol, F., Rouquerol, J., Sing, K. S. W., Llewellyn, P., Maurin, G., Eds.; Academic Press: Oxford, **2014**, 237–268.

Date	Experiment	mass std dev before (g)	mass std dev after (g)	mass error (g)
July 22 2019	Road Dust RH25 (1)	0.07	0.06	9.39858E-05
July 23 2019	Road Dust RH50 (1)	0.01	0.19	0.000190263
August 21 2019	Road Dust RH70 (1)	0.14	0.06	0.000152315
August 22 2019	Road Dust RH0 (1)	0.03	0.05	5.83095E-05
August 23 2019	Road Dust RH70 (2)	0.05	0.09	0.000102956
August 26 2019	Road Dust RH0 (2)	0.12	0.07	0.000138924
August 28 2019	Road Dust RH70 (3)	0.04	0.05	6.40312E-05
August 29 2019	Road Dust RH0 (3)	0.17	0.15	0.000226716
August 30 2019	Road Dust RH80 (1)	0.49	0.07	0.000494975
Sept 3 2019	Road Dust RH50 (2)	0.09	0.05	0.000102956
Sept 4 2019	Road Dust RH80 (2)	0.07	0.11	0.000130384
Sept 5 2019	Road Dust RH80 (3)	0.04	0.11	0.000117047
Sept 6 2019	Road Dust RH50 (3)	0.17	0.08	0.000187883
Sept 9 2019	Road Dust RH10 (1)	0.24	0.05	0.000245153
Sept 10 2019	Road Dust RH10 (2)	0.07	0.14	0.000156525
Sept 11 2019	Road Dust RH10 (3)	0.16	0.04	0.000164924
Sept 12 2019	Road Dust RH25 15 mg	0.13	0.02	0.000131529
September 13 2019	Road Dust RH25 50mg	0.06	0.16	0.00017088
September 16 2019	Road Dust RH25 75mg	0.21	0.08	0.000224722
September 17 2019	Road Dust RH25 30mg	0.14	0.05	0.000148661
September 18 2019	Road Dust RH25 100mg	0.13	0.08	0.000152643
September 19 2019	Road Dust RH25 O3100	0.29	0.1	0.000306757
September 20 2019	Road Dust RH25 O3150	0.22	0.21	0.000304138
September 23 2019	Road Dust RH25 O3 25	0.03	0.09	9.48683E-05
September 24 2019	Road Dust Baked RH25	0.14	0.12	0.000184391
September 25 2019	Road Dust Baked RH70	0.19	0.19	0.000268701
September 26 2019	Road Dust RH25 20mg	0.11	0.08	0.000136015
October 1 2019	Road Dust Baked RH25	0.1	0.07	0.000122066
October 2 2010	SiO2 50ppm Chloride RH25			0
October 3 2019	RD 500 ppm Chloride RH70			0
October 4 2019	SiO2 500 ppm Chloride RH70			0
October 7 2019	RD 5% Chloride RH70			0
October 8 2019	Road Dust Rinsed RH70	0.07	0.14	0.000156525
October 9 2019	Road Dust Rinsed RH25	0.18	0.03	0.000182483
October 10 2019	Road Dust RH70	0.17	0.13	0.000214009
October 11 2019	Road Dust Rinsed RH25 (2)	0.03	0.25	0.000251794
October 15 2019	Road Dust Rinsed RH25 (3)	0.06	0.24	0.000247386
October 21 2019	Road Dust Rinsed RH70 (2)	0.12	0.17	0.000208087
October 22 2019	Road Dust Rinsed RH70 (3)	0.15	0.12	0.000192094
October 30 2019	Anti Icer RD RH70			0
October 31 2019	Anti Icer RH70			0
November 1 2019	CaICl2 RH70 (1)			0
November 4 2019	Anti Icer RH25			0
November 5 2019	Fumed SiO2 + Anti Icer RH70			0
November 6 2019	Anti Icer RH70 (2)			0
November 7 2019	Anti Icer RH25 (2)			0
November 8 2019	CaCl2 RH25 (1)			0
November 12 2019	CaCl2 RH25 (2)			0
November 13 2019	CaCl2 RH70 (2)			0

Date	mass (g)	length of tube (m)	O3 flow (sccm)	Dry air flow (sccm)	Wet air flow (sccm)
July 22 2019	0.0273	0.14	111	226	102
July 23 2019	0.02818	0.14	111	107	218
August 21 2019	0.01766	0.149	111	16	305
August 22 2019	0.02789	0.15	111	336	0
August 23 2019	0.02598	0.149	111	16	307
August 26 2019	0.03091	0.141	111	334	0
August 28 2019	0.02887	0.141	111	14	305
August 29 2019	0.02782	0.14	53	332	0
August 30 2019	0.028	0.141	55	0	372
Sept 3 2019	0.02921	0.14	111	107	218
Sept 4 2019	0.02521	0.14	56	0	376
Sept 5 2019	0.02732	0.138	55	371	0
Sept 6 2019	0.02872	0.138	110	96	217
Sept 9 2019	0.02495	0.14	111	296	37
Sept 10 2019	0.02496	0.139	110	295	36
Sept 11 2019	0.02524	0.139	110	295	36
Sept 12 2019	0.01208	0.139	110	226	102
September 13 2019	0.04126	0.14	111	230	102
September 16 2019	0.05658	0.139	111	232	102
September 17 2019	0.03142	0.141	111	231	102
September 18 2019	0.08529	0.141	111	231	102
September 19 2019	0.03168	0.141	55	286	101
September 20 2019	0.02635	0.14	56	286	101
September 23 2019	0.02485	0.14	55	286	102
September 24 2019	0.02958	0.14	111	232	102
September 25 2019	0.02616	0.14	111	16	307
September 26 2019	0.02184	0.141	112	233	103
October 1 2019	0.03049	0.14	110	228	101
October 2 2010	0.02873	0.14			
October 3 2019	0.02875	0.14			
October 4 2019	0.03508	0.141			
October 7 2019	0.03313	0.141			
October 8 2019	0.029	0.139	111	16	307
October 9 2019	0.03025	0.141	109	224	96
October 10 2019	0.02823	0.141	111	16	307
October 11 2019	0.02802	0.14	109	224	96
October 15 2019	0.02301	0.141	110	230	100
October 21 2019	0.02976	0.14	111	16	306
October 22 2019	0.02422	0.139	112	18	307
October 30 2019	0.12369	0.141			
October 31 2019	0.1166	0.141			
November 1 2019	0.09486	0.141			
November 4 2019	0.10729	0.141			
November 5 2019	0.1526	0.141			
November 6 2019	0.08636	0.14			
November 7 2019	0.13609	0.141			
November 8 2019	0.05341	0.14			
November 12 2019	0.03093	0.139			
November 13 2019	0.04612	0.138			

Date	Total flow (lpm)	flow rate (m^3/s)	linear velocity (m/s)	[O3] Initial	[O3] Initial err
July 22 2019	0.439	7.32E-06	0.084540539	53.69	0.56
July 23 2019	0.436	7.27E-06	0.083962814	52.09	0.85
August 21 2019	0.432	7.20E-06	0.083192513	51.80	0.49
August 22 2019	0.447	7.45E-06	0.086081142	55.99	0.54
August 23 2019	0.434	7.23E-06	0.083577663	51.76	0.34
August 26 2019	0.445	7.42E-06	0.085695991	55.41	0.54
August 28 2019	0.43	7.17E-06	0.082807362	55.40	0.23
August 29 2019	0.385	6.42E-06	0.074141475	56.31	0.39
August 30 2019	0.427	7.12E-06	0.082229636	53.90	0.45
Sept 3 2019	0.436	7.27E-06	0.083962814	56.83	0.54
Sept 4 2019	0.432	7.20E-06	0.083192513	54.03	0.27
Sept 5 2019	0.426	7.10E-06	0.082037061	54.77	0.30
Sept 6 2019	0.423	7.05E-06	0.081459335	51.75	0.33
Sept 9 2019	0.444	7.40E-06	0.085503416	51.09	0.47
Sept 10 2019	0.441	7.35E-06	0.08492569	53.28	0.58
Sept 11 2019	0.441	7.35E-06	0.08492569	52.76	0.57
Sept 12 2019	0.438	7.30E-06	0.084347964	52.08	0.55
September 13 2019	0.443	7.38E-06	0.085310841	53.11	0.46
September 16 2019	0.445	7.42E-06	0.085695991	52.97	0.27
September 17 2019	0.444	7.40E-06	0.085503416	52.77	0.20
September 18 2019	0.444	7.40E-06	0.085503416	53.39	0.72
September 19 2019	0.442	7.37E-06	0.085118265	101.61	0.57
September 20 2019	0.443	7.38E-06	0.085310841	153.32	0.25
September 23 2019	0.443	7.38E-06	0.085310841	24.47	0.47
September 24 2019	0.445	7.42E-06	0.085695991	51.02	0.37
September 25 2019	0.434	7.23E-06	0.083577663	50.86	0.33
September 26 2019	0.448	7.47E-06	0.086273717	50.90	0.47
October 1 2019	0.439	7.32E-06	0.084540539	50.79	0.68
October 2 2010	0	0.00E+00	0	52.00	
October 3 2019	0	0.00E+00	0	48.60	
October 4 2019	0	0.00E+00	0	48.70	
October 7 2019	0	0.00E+00	0	49.50	
October 8 2019	0.434	7.23E-06	0.083577663	49.65	0.53
October 9 2019	0.429	7.15E-06	0.082614787	52.42	0.63
October 10 2019	0.434	7.23E-06	0.083577663	50.17	0.41
October 11 2019	0.429	7.15E-06	0.082614787	51.11	0.68
October 15 2019	0.44	7.33E-06	0.084733115	51.31	0.39
October 21 2019	0.433	7.22E-06	0.083385088	47.59	0.58
October 22 2019	0.437	7.28E-06	0.084155389	49.03	0.50
October 30 2019	0	0.00E+00	0	47.60	
October 31 2019	0	0.00E+00	0	48.40	
November 1 2019	0	0.00E+00	0	49.00	
November 4 2019	0	0.00E+00	0	51.80	
November 5 2019	0	0.00E+00	0	50.00	
November 6 2019	0	0.00E+00	0	51.30	
November 7 2019	0	0.00E+00	0	51.80	
November 8 2019	0	0.00E+00	0		
November 12 2019	0	0.00E+00	0		
November 13 2019	0	0.00E+00	0		

Date	[O3]err/[O3]	Residence Time (s)	BET (m^2/g)	z*	S geo (cm^2)	Sherwood #	[O3] final dark (ppb)
July 22 2019	0.010430248	1.656010251	8.1011	0.379786005	46.158	3.9042784	43.72
July 23 2019	0.016317911	1.667404817	8.1011	0.379786005	46.158	3.9042784	42.62
August 21 2019	0.009459459	1.791026563	8.1011	0.404200819	49.1253	3.889878668	41.22
August 22 2019	0.009644579	1.742541946	8.1011	0.406913577	49.455	3.888381473	46.78
August 23 2019	0.006568779	1.782772984	8.1011	0.404200819	49.1253	3.889878668	40.99
August 26 2019	0.009745533	1.64535118	8.1011	0.382498762	46.4877	3.902591164	44.88
August 28 2019	0.004151625	1.702747151	8.1011	0.382498762	46.4877	3.902591164	43.89
August 29 2019	0.006925946	1.888281818	8.1011	0.379786005	46.158	3.9042784	46.72
August 30 2019	0.008348794	1.714710246	8.1011	0.382498762	46.4877	3.902591164	40.36
Sept 3 2019	0.009502024	1.667404817	8.1011	0.379786005	46.158	3.9042784	42.49
Sept 4 2019	0.004997224	1.68284375	8.1011	0.379786005	46.158	3.9042784	42.53
Sept 5 2019	0.005477451	1.682166549	8.1011	0.37436049	45.4986	3.90772333	43.02
Sept 6 2019	0.006376812	1.694096809	8.1011	0.37436049	45.4986	3.90772333	39.81
Sept 9 2019	0.009199452	1.637361486	8.1011	0.379786005	46.158	3.9042784	44.88
Sept 10 2019	0.010885886	1.636725	8.1011	0.377073248	45.8283	3.905988959	44.76
Sept 11 2019	0.010803639	1.636725	8.1011	0.377073248	45.8283	3.905988959	44.57
Sept 12 2019	0.010560676	1.647935445	8.1011	0.377073248	45.8283	3.905988959	46.82
September 13 2019	0.008661269	1.641057562	8.1011	0.379786005	46.158	3.9042784	38.47
September 16 2019	0.005097225	1.622012865	8.1011	0.377073248	45.8283	3.905988959	36.41
September 17 2019	0.003790032	1.649056926	8.1011	0.382498762	46.4877	3.902591164	42.92
September 18 2019	0.013485671	1.649056926	8.1011	0.382498762	46.4877	3.902591164	25.58
September 19 2019	0.005609684	1.656518722	8.1011	0.382498762	46.4877	3.902591164	88.40
September 20 2019	0.001630577	1.641057562	8.1011	0.379786005	46.158	3.9042784	141.80
September 23 2019	0.019207192	1.641057562	8.1011	0.379786005	46.158	3.9042784	19.10
September 24 2019	0.007252058	1.633682022	9.3024	0.379786005	46.158	3.9042784	29.20
September 25 2019	0.0064884	1.67508871	9.3024	0.379786005	46.158	3.9042784	38.90
September 26 2019	0.009233792	1.634333203	8.1011	0.382498762	46.4877	3.902591164	43.50
October 1 2019	0.013388462	1.656010251	9.3024	0.379786005	46.158	3.9042784	30.71
October 2 2010	0	#DIV/0!	94.55	0.379786005	46.158	3.9042784	51.00
October 3 2019	0	#DIV/0!	8.1011	0.379786005	46.158	3.9042784	36.50
October 4 2019	0	#DIV/0!	94.55	0.382498762	46.4877	3.902591164	47.00
October 7 2019	0	#DIV/0!	8.1011	0.382498762	46.4877	3.902591164	40.60
October 8 2019	0.010674723	1.66312379	7.0233	0.377073248	45.8283	3.905988959	37.41
October 9 2019	0.012018314	1.706716259	7.0233	0.382498762	46.4877	3.902591164	44.35
October 10 2019	0.008172214	1.687053629	8.1011	0.382498762	46.4877	3.902591164	37.23
October 11 2019	0.013304637	1.694611888	7.0233	0.379786005	46.158	3.9042784	43.65
October 15 2019	0.007600858	1.664048352	7.0233	0.382498762	46.4877	3.902591164	44.64
October 21 2019	0.012187434	1.678957275	7.0233	0.379786005	46.158	3.9042784	35.25
October 22 2019	0.010197838	1.651706465	7.0233	0.377073248	45.8283	3.905988959	37.92
October 30 2019	0	#DIV/0!	8.1011	0.382498762	46.4877	3.902591164	19.10
October 31 2019	0	#DIV/0!		0.382498762	46.4877	3.902591164	32.70
November 1 2019	0	#DIV/0!		0.382498762	46.4877	3.902591164	48.00
November 4 2019	0	#DIV/0!		0.382498762	46.4877	3.902591164	44.00
November 5 2019	0	#DIV/0!	94.55	0.382498762	46.4877	3.902591164	24.50
November 6 2019	0	#DIV/0!		0.379786005	46.158	3.9042784	35.90
November 7 2019	0	#DIV/0!		0.382498762	46.4877	3.902591164	45.00
November 8 2019	#DIV/0!	#DIV/0!		0.379786005	46.158	3.9042784	
November 12 2019	#DIV/0!	#DIV/0!		0.377073248	45.8283	3.905988959	
November 13 2019	#DIV/0!	#DIV/0!		0.37436049	45.4986	3.90772333	

Date	[O3] dark std dev	[O3]err/[O3]	total O3 error	total error kdark	[O3] final light (ppb)	[O3] light std dev
July 22 2019	0.73	0.016697164	0.019687187	0.011888325	33.30	0.29
July 23 2019	0.62	0.014547161	0.02186079	0.013110667	35.75	0.52
August 21 2019	0.61	0.014798641	0.017563632	0.009806461	34.60	0.74
August 22 2019	0.26	0.005557931	0.01113142	0.006388035	33.30	0.59
August 23 2019	0.47	0.011466211	0.013214494	0.007412326	37.80	0.39
August 26 2019	0.30	0.006684492	0.011817692	0.007182474	31.20	0.41
August 28 2019	0.26	0.005923901	0.00723385	0.004248341	39.60	0.57
August 29 2019	0.38	0.008133562	0.010682862	0.005657451	33.60	0.56
August 30 2019	0.43	0.010654113	0.013535601	0.007893812	34.10	0.45
Sept 3 2019	0.31	0.007295834	0.011979885	0.007184749	35.50	0.60
Sept 4 2019	0.34	0.007994357	0.009427724	0.005602258	35.30	0.39
Sept 5 2019	0.50	0.011622501	0.012848541	0.007638091	35.00	0.47
Sept 6 2019	0.43	0.010801306	0.012543203	0.007404065	33.40	0.47
Sept 9 2019	0.43	0.009581105	0.013282601	0.008112198	35.90	0.31
Sept 10 2019	0.52	0.011617516	0.015920715	0.009727178	33.90	0.23
Sept 11 2019	0.28	0.006282253	0.012497412	0.007635621	34.10	0.41
Sept 12 2019	0.40	0.008543358	0.013583697	0.008242858	39.20	0.31
September 13 2019	0.30	0.007798284	0.011654648	0.007101913	27.20	0.21
September 16 2019	0.33	0.009063444	0.010398448	0.00641083	24.50	0.60
September 17 2019	0.49	0.011416589	0.01202925	0.007294624	31.60	0.37
September 18 2019	0.48	0.01876466	0.023107916	0.014012807	14.80	0.71
September 19 2019	0.72	0.008144796	0.009889705	0.005970174	72.60	0.94
September 20 2019	0.69	0.004866008	0.005131941	0.003127216	121.00	0.55
September 23 2019	0.58	0.030366492	0.035931046	0.021895055	13.10	0.49
September 24 2019	0.32	0.010958904	0.013141154	0.008043887	16.70	0.44
September 25 2019	0.58	0.014910026	0.016260633	0.009707327	36.40	0.25
September 26 2019	0.46	0.010574713	0.014038784	0.008589915	34.60	0.48
October 1 2019	0.33	0.010745685	0.017167431	0.010366742	19.67	0.63
October 2 2010	0.00	0	0	#DIV/0!	46.50	
October 3 2019	0.00	0	0	#DIV/0!	31.30	
October 4 2019	0.00	0	0	#DIV/0!	43.40	
October 7 2019	0.00	0	0	#DIV/0!	38.30	
October 8 2019	0.35	0.009355787	0.014194382	0.008534772	32.24	0.69
October 9 2019	0.56	0.012626832	0.017432061	0.010213801	36.26	0.53
October 10 2019	0.40	0.010744024	0.013498857	0.008001439	35.63	0.38
October 11 2019	0.35	0.008018328	0.015534058	0.009166735	36.56	0.84
October 15 2019	0.71	0.015905018	0.017627894	0.010593378	38.82	0.44
October 21 2019	0.63	0.01787234	0.021632247	0.012884334	31.22	0.35
October 22 2019	0.49	0.012921941	0.016461241	0.009966202	33.49	0.31
October 30 2019	0.00	0	0	#DIV/0!	17.20	
October 31 2019	0.00	0	0	#DIV/0!	27.90	
November 1 2019	0.00	0	0	#DIV/0!	46.10	
November 4 2019	0.00	0	0	#DIV/0!	43.00	
November 5 2019	0.00	0	0	#DIV/0!	23.20	
November 6 2019	0.00	0	0	#DIV/0!	30.10	
November 7 2019	0.00	0	0	#DIV/0!	41.30	
November 8 2019						
November 12 2019						
November 13 2019						

Date	[O3]err/[O3]	O3 error	total error klight	k (dark)	k light	γ geo dark	γ geo light	γ BET dark	γ BET light	γ eff dark	γ eff dark err
July 22 2019	0.008708709	0.013587924	0.008205217	0.12404579	0.28845	3.601E-06	8.37346E-06	7.51559E-08	1.74761E-07	3.601E-06	3.45113E-07
July 23 2019	0.014545455	0.021859654	0.013109986	0.12033632	0.22575	3.49331E-06	6.55353E-06	7.06317E-08	1.32507E-07	3.49331E-06	3.80597E-07
August 21 2019	0.021387283	0.023385835	0.013057224	0.1275618	0.22531	3.70307E-06	6.54066E-06	1.27155E-07	2.24591E-07	3.70307E-06	2.84677E-07
August 22 2019	0.017717718	0.020172641	0.01157656	0.10313516	0.29819	2.99397E-06	8.65645E-06	6.55338E-08	1.89477E-07	2.99397E-06	1.85442E-07
August 23 2019	0.01031746	0.012231061	0.006860694	0.13085767	0.1763	3.79874E-06	5.11801E-06	8.8667E-08	1.1946E-07	3.79874E-06	2.15177E-07
August 26 2019	0.013141026	0.016360378	0.009943396	0.12809899	0.34907	3.71866E-06	1.01333E-05	6.90369E-08	1.88126E-07	3.71866E-06	2.08504E-07
August 28 2019	0.014393939	0.014980704	0.008797961	0.13677491	0.19718	3.97052E-06	5.7241E-06	7.89214E-08	1.13777E-07	3.97052E-06	1.23328E-07
August 29 2019	0.016666667	0.018048449	0.009558133	0.09887285	0.27345	2.87024E-06	7.93807E-06	5.87846E-08	1.62578E-07	2.87024E-06	1.64233E-07
August 30 2019	0.013196481	0.01561568	0.009106892	0.16871147	0.267	4.89762E-06	7.75099E-06	1.00374E-07	1.58852E-07	4.89762E-06	2.29154E-07
Sept 3 2019	0.016901408	0.019389329	0.011628447	0.17440012	0.28219	5.06276E-06	8.19197E-06	9.8755E-08	1.59794E-07	5.06276E-06	2.0857E-07
Sept 4 2019	0.011048159	0.01212576	0.007205517	0.14221745	0.25294	4.12851E-06	7.34271E-06	9.33091E-08	1.65953E-07	4.12851E-06	1.62631E-07
Sept 5 2019	0.013428571	0.014502724	0.008621455	0.14355147	0.2662	4.16724E-06	7.72771E-06	8.56686E-08	1.58863E-07	4.16724E-06	2.21731E-07
Sept 6 2019	0.014071856	0.0154493	0.009119491	0.15483548	0.25847	4.49481E-06	7.5032E-06	8.78984E-08	1.46729E-07	4.49481E-06	2.14937E-07
Sept 9 2019	0.008635097	0.012617243	0.007705838	0.07914961	0.2155	2.29768E-06	6.25588E-06	5.24713E-08	1.42863E-07	2.29768E-06	2.35494E-07
Sept 10 2019	0.006784661	0.012827086	0.007837044	0.10646024	0.27625	3.0905E-06	8.01944E-06	7.00444E-08	1.81756E-07	3.0905E-06	2.82376E-07
Sept 11 2019	0.01202346	0.016164227	0.009875957	0.103067	0.26666	2.99199E-06	7.74115E-06	6.70596E-08	1.73503E-07	2.99199E-06	2.21659E-07
Sept 12 2019	0.007908163	0.013193442	0.008006043	0.06460844	0.1724	1.87556E-06	5.0047E-06	8.7832E-08	2.3437E-07	1.87556E-06	2.39287E-07
September 13 2019	0.007720588	0.011602804	0.007070321	0.1965114	0.40775	5.70464E-06	1.18369E-05	7.87775E-08	1.63461E-07	5.70464E-06	2.06166E-07
September 16 2019	0.024489796	0.025014632	0.015421969	0.23112163	0.47537	6.70936E-06	1.37997E-05	6.70823E-08	1.37974E-07	6.70936E-06	1.86104E-07
September 17 2019	0.011708861	0.01230698	0.007463042	0.12528672	0.31096	3.63702E-06	9.02695E-06	6.64253E-08	1.64865E-07	3.63702E-06	2.1176E-07
September 18 2019	0.047972973	0.049832414	0.030218735	0.4462021	0.77802	1.29531E-05	2.25855E-05	8.71502E-08	1.51959E-07	1.29531E-05	4.06786E-07
September 19 2019	0.012947658	0.014110649	0.008518255	0.0840739	0.20294	2.44063E-06	5.89132E-06	4.4209E-08	1.06714E-07	2.44063E-06	1.73312E-07
September 20 2019	0.004545455	0.004829072	0.002942659	0.04759713	0.14426	1.38172E-06	4.18777E-06	2.98775E-08	9.05534E-08	1.38172E-06	9.07818E-08
September 23 2019	0.03740458	0.042047816	0.02562239	0.15097553	0.38075	4.38276E-06	1.10531E-05	1.0049E-07	2.53431E-07	4.38276E-06	6.35604E-07
September 24 2019	0.026347305	0.027327145	0.016727334	0.34158973	0.68361	9.91621E-06	1.9845E-05	1.66341E-07	3.32894E-07	9.91621E-06	2.33511E-07
September 25 2019	0.006868132	0.00944831	0.005640483	0.16004078	0.1997	4.64592E-06	5.79708E-06	8.81223E-08	1.09957E-07	4.64592E-06	2.818E-07
September 26 2019	0.013872832	0.016664885	0.010196749	0.09612604	0.23619	2.7905E-06	6.85643E-06	7.33201E-08	1.80152E-07	2.7905E-06	2.49362E-07
October 1 2019	0.03202847	0.034714173	0.020962535	0.3038092	0.57283	8.81945E-06	1.66289E-05	1.43528E-07	2.70619E-07	8.81945E-06	3.00942E-07
October 2 2010	0	0	#DIV/0!	#DIV/0!	#DIV/0!	#DIV/0!	#DIV/0!	#DIV/0!	#DIV/0!	#DIV/0!	#DIV/0!
October 3 2019	0	0	#DIV/0!	#DIV/0!	#DIV/0!	#DIV/0!	#DIV/0!	#DIV/0!	#DIV/0!	#DIV/0!	#DIV/0!
October 4 2019	0	0	#DIV/0!	#DIV/0!	#DIV/0!	#DIV/0!	#DIV/0!	#DIV/0!	#DIV/0!	#DIV/0!	#DIV/0!
October 7 2019	0	0	#DIV/0!	#DIV/0!	#DIV/0!	#DIV/0!	#DIV/0!	#DIV/0!	#DIV/0!	#DIV/0!	#DIV/0!
October 8 2019	0.021401985	0.02391641	0.014380415	0.170198	0.25963	4.94078E-06	7.53684E-06	1.11171E-07	1.69584E-07	4.94078E-06	2.47761E-07
October 9 2019	0.014616657	0.018923175	0.011087475	0.09795154	0.21595	2.84349E-06	6.26907E-06	6.22191E-08	1.37175E-07	2.84349E-06	2.96502E-07
October 10 2019	0.01066517	0.01343618	0.007964287	0.17681853	0.20286	5.13297E-06	5.88883E-06	1.0434E-07	1.19705E-07	5.13297E-06	2.32278E-07
October 11 2019	0.02297593	0.02655008	0.015667351	0.09310503	0.1977	2.7028E-06	5.73916E-06	6.33945E-08	1.34613E-07	2.7028E-06	2.66106E-07
October 15 2019	0.011334364	0.013647008	0.008201089	0.08368468	0.16763	2.42933E-06	4.86633E-06	6.98823E-08	1.39985E-07	2.42933E-06	3.07521E-07
October 21 2019	0.011210762	0.016559431	0.009862926	0.17877592	0.25109	5.18979E-06	7.28894E-06	1.1461E-07	1.60967E-07	5.18979E-06	3.74027E-07
October 22 2019	0.009256494	0.013772385	0.008338276	0.15556861	0.23078	4.51609E-06	6.69953E-06	1.21669E-07	1.80494E-07	4.51609E-06	2.89315E-07
October 30 2019	0	0	#DIV/0!	#DIV/0!	#DIV/0!	#DIV/0!	#DIV/0!	#DIV/0!	#DIV/0!	#DIV/0!	#DIV/0!
October 31 2019	0	0	#DIV/0!	#DIV/0!	#DIV/0!	#DIV/0!	#DIV/0!	#DIV/0!	#DIV/0!	#DIV/0!	#DIV/0!
November 1 2019	0	0	#DIV/0!	#DIV/0!	#DIV/0!	#DIV/0!	#DIV/0!	#DIV/0!	#DIV/0!	#DIV/0!	#DIV/0!
November 4 2019	0	0	#DIV/0!	#DIV/0!	#DIV/0!	#DIV/0!	#DIV/0!	#DIV/0!	#DIV/0!	#DIV/0!	#DIV/0!
November 5 2019	0	0	#DIV/0!	#DIV/0!	#DIV/0!	#DIV/0!	#DIV/0!	#DIV/0!	#DIV/0!	#DIV/0!	#DIV/0!
November 6 2019	0	0	#DIV/0!	#DIV/0!	#DIV/0!	#DIV/0!	#DIV/0!	#DIV/0!	#DIV/0!	#DIV/0!	#DIV/0!
November 7 2019	0	0	#DIV/0!	#DIV/0!	#DIV/0!	#DIV/0!	#DIV/0!	#DIV/0!	#DIV/0!	#DIV/0!	#DIV/0!
November 8 2019		#DIV/0!	#DIV/0!	#DIV/0!	#DIV/0!	#DIV/0!	#DIV/0!	#DIV/0!	#DIV/0!	#DIV/0!	0
November 12 2019		#DIV/0!	#DIV/0!	#DIV/0!	#DIV/0!	#DIV/0!	#DIV/0!	#DIV/0!	#DIV/0!	#DIV/0!	0
November 13 2019		#DIV/0!	#DIV/0!	#DIV/0!	#DIV/0!	#DIV/0!	#DIV/0!	#DIV/0!	#DIV/0!	#DIV/0!	0

Date	γ eff light	γ eff light error	γ corr	γ corr denominator err	γ corr denominator	γ corr err	γ corr	γ corr denominator err
July 22 2019	8.37346E-06	2.38194E-07	3.86834E-06	0.006623473	0.069110998	5.24298E-07	9.97678E-06	0.004571463
July 23 2019	6.55353E-06	3.80577E-07	3.74435E-06	0.00730449	0.067044302	5.76925E-07	7.49641E-06	0.007304111
August 21 2019	6.54066E-06	3.79046E-07	3.98751E-06	0.005483807	0.071333002	4.33519E-07	7.48354E-06	0.007301645
August 22 2019	8.65645E-06	3.36063E-07	3.17729E-06	0.003573587	0.057695746	2.78312E-07	1.03896E-05	0.006476145
August 23 2019	5.11801E-06	1.99163E-07	4.09867E-06	0.004144998	0.073176062	3.28332E-07	5.67778E-06	0.003836524
August 26 2019	1.01333E-05	2.88653E-07	4.00459E-06	0.004003381	0.071400056	3.17542E-07	1.25812E-05	0.005542269
August 28 2019	5.7241E-06	2.55401E-07	4.2982E-06	0.002367948	0.076235859	1.88805E-07	6.43089E-06	0.004903824
August 29 2019	7.93807E-06	2.77469E-07	3.03757E-06	0.003151998	0.055086119	2.45801E-07	9.36478E-06	0.005325228
August 30 2019	7.75099E-06	2.64369E-07	5.40598E-06	0.004399868	0.094036717	3.57711E-07	9.1062E-06	0.005076016
Sept 3 2019	8.19197E-06	3.37569E-07	5.60763E-06	0.004002918	0.097165461	3.26708E-07	9.7202E-06	0.006478685
Sept 4 2019	7.34271E-06	2.09173E-07	4.48379E-06	0.003121248	0.079235172	2.49787E-07	8.5472E-06	0.004014489
Sept 5 2019	7.72771E-06	2.50277E-07	4.52915E-06	0.004251742	0.079907904	3.40808E-07	9.072E-06	0.004799132
Sept 6 2019	7.5032E-06	2.64735E-07	4.91875E-06	0.004121472	0.086189149	3.32636E-07	8.76414E-06	0.005076363
Sept 9 2019	6.25588E-06	2.23697E-07	2.40368E-06	0.004519638	0.044097494	3.48402E-07	7.10947E-06	0.004293239
Sept 10 2019	8.01944E-06	2.27506E-07	3.28527E-06	0.005417037	0.059287394	4.24508E-07	9.47748E-06	0.004364427
Sept 11 2019	7.74115E-06	2.86695E-07	3.17418E-06	0.004252255	0.057397708	3.32561E-07	9.09124E-06	0.005499891
Sept 12 2019	5.0047E-06	2.32412E-07	1.94556E-06	0.004590423	0.035980247	3.51033E-07	5.53623E-06	0.004458542
September 13 2019	1.18369E-05	2.05248E-07	6.406E-06	0.003956767	0.109484561	3.27408E-07	1.53165E-05	0.003939166
September 16 2019	1.37997E-05	4.47693E-07	7.7005E-06	0.003570172	0.128710948	3.0207E-07	1.87683E-05	0.008588449
September 17 2019	9.02695E-06	2.16649E-07	3.91007E-06	0.004065891	0.069832548	3.21957E-07	1.09195E-05	0.004159764
September 18 2019	2.25855E-05	8.77237E-07	1.7241E-05	0.007810485	0.248704972	7.65721E-07	3.98794E-05	0.016843376
September 19 2019	5.89132E-06	2.47281E-07	2.56062E-06	0.003327667	0.046861268	2.5715E-07	6.64272E-06	0.004747921
September 20 2019	4.18777E-06	8.54241E-08	1.41936E-06	0.0017423	0.026518312	1.31882E-07	4.55376E-06	0.001639476
September 23 2019	1.10531E-05	7.43807E-07	4.78527E-06	0.012198633	0.084114663	9.81433E-07	1.40291E-05	0.014275284
September 24 2019	1.9845E-05	4.85588E-07	1.2247E-05	0.004481579	0.190313651	4.07854E-07	3.20531E-05	0.009319484
September 25 2019	5.79708E-06	1.63741E-07	5.10072E-06	0.00540835	0.089165285	4.37538E-07	6.5228E-06	0.003142545
September 26 2019	6.85643E-06	2.96007E-07	2.94848E-06	0.004787863	0.053578916	3.72615E-07	7.8959E-06	0.005683483
October 1 2019	1.66289E-05	6.08534E-07	1.06164E-05	0.005775737	0.169264567	5.12313E-07	2.44235E-05	0.011679088
October 2 2010	#DIV/0!	#DIV/0!	#DIV/0!	#DIV/0!	#DIV/0!	#DIV/0!	#DIV/0!	#DIV/0!
October 3 2019	#DIV/0!	#DIV/0!	#DIV/0!	#DIV/0!	#DIV/0!	#DIV/0!	#DIV/0!	#DIV/0!
October 4 2019	#DIV/0!	#DIV/0!	#DIV/0!	#DIV/0!	#DIV/0!	#DIV/0!	#DIV/0!	#DIV/0!
October 7 2019	#DIV/0!	#DIV/0!	#DIV/0!	#DIV/0!	#DIV/0!	#DIV/0!	#DIV/0!	#DIV/0!
October 8 2019	7.53684E-06	4.17457E-07	5.45811E-06	0.004752989	0.09478276	3.87075E-07	8.81074E-06	0.00800841
October 9 2019	6.26907E-06	3.21865E-07	3.0077E-06	0.005692988	0.054596416	4.43533E-07	7.12693E-06	0.006179958
October 10 2019	5.88883E-06	2.312E-07	5.69416E-06	0.004459857	0.098555449	3.64405E-07	6.63955E-06	0.00443915
October 11 2019	5.73916E-06	4.54817E-07	2.85067E-06	0.005107164	0.051872631	3.96921E-07	6.44956E-06	0.008728924
October 15 2019	4.86633E-06	2.38074E-07	2.54819E-06	0.005904557	0.046644323	4.56179E-07	5.36788E-06	0.004571138
October 21 2019	7.28894E-06	2.86317E-07	5.76389E-06	0.007178391	0.099603396	5.87468E-07	8.47443E-06	0.00549504
October 22 2019	6.69953E-06	2.42057E-07	4.94446E-06	0.005550149	0.086635696	4.47962E-07	7.68755E-06	0.004643561
October 30 2019	#DIV/0!	#DIV/0!	#DIV/0!	#DIV/0!	#DIV/0!	#DIV/0!	#DIV/0!	#DIV/0!
October 31 2019	#DIV/0!	#DIV/0!	#DIV/0!	#DIV/0!	#DIV/0!	#DIV/0!	#DIV/0!	#DIV/0!
November 1 2019	#DIV/0!	#DIV/0!	#DIV/0!	#DIV/0!	#DIV/0!	#DIV/0!	#DIV/0!	#DIV/0!
November 4 2019	#DIV/0!	#DIV/0!	#DIV/0!	#DIV/0!	#DIV/0!	#DIV/0!	#DIV/0!	#DIV/0!
November 5 2019	#DIV/0!	#DIV/0!	#DIV/0!	#DIV/0!	#DIV/0!	#DIV/0!	#DIV/0!	#DIV/0!
November 6 2019	#DIV/0!	#DIV/0!	#DIV/0!	#DIV/0!	#DIV/0!	#DIV/0!	#DIV/0!	#DIV/0!
November 7 2019	#DIV/0!	#DIV/0!	#DIV/0!	#DIV/0!	#DIV/0!	#DIV/0!	#DIV/0!	#DIV/0!
November 8 2019	#DIV/0!	#DIV/0!	#DIV/0!	0	#DIV/0!	#DIV/0!	#DIV/0!	#DIV/0!
November 12 2019	#DIV/0!	#DIV/0!	#DIV/0!	0	#DIV/0!	#DIV/0!	#DIV/0!	#DIV/0!
November 13 2019	#DIV/0!	#DIV/0!	#DIV/0!	0	#DIV/0!	#DIV/0!	#DIV/0!	#DIV/0!

Date	γ corr denominator	γ corr err	γ BET dark corr	γ BET dark corr err	γ BET light corr	γ BET light corr err	Experiment
July 22 2019	0.160705043	4.01357E-07	8.07356E-08	1.09461E-08	2.08224E-07	8.40729E-09	Road Dust RH25 (1)
July 23 2019	0.125776618	6.15652E-07	7.57074E-08	1.16761E-08	1.51571E-07	1.24899E-08	Road Dust RH50 (1)
August 21 2019	0.125994219	6.13327E-07	1.36922E-07	1.49328E-08	2.56967E-07	2.11765E-08	Road Dust RH70 (1)
August 22 2019	0.166815375	5.70419E-07	6.95463E-08	6.09359E-09	2.27414E-07	1.24947E-08	Road Dust RH0 (1)
August 23 2019	0.09858935	3.12465E-07	9.56676E-08	7.67301E-09	1.32526E-07	7.31217E-09	Road Dust RH70 (2)
August 26 2019	0.194565043	5.06827E-07	7.43452E-08	5.90463E-09	2.3357E-07	9.46763E-09	Road Dust RH0 (2)
August 28 2019	0.109905475	4.0579E-07	8.54345E-08	3.75763E-09	1.27826E-07	8.07081E-09	Road Dust RH70 (3)
August 29 2019	0.152348857	4.62926E-07	6.22116E-08	5.05966E-09	1.91798E-07	9.60905E-09	Road Dust RH0 (3)
August 30 2019	0.148822739	4.39244E-07	1.10793E-07	7.58819E-09	1.86626E-07	9.58756E-09	Road Dust RH80 (1)
Sept 3 2019	0.157221861	5.66453E-07	1.09383E-07	6.38446E-09	1.89604E-07	1.10695E-08	Road Dust RH50 (2)
Sept 4 2019	0.140922582	3.44341E-07	1.01339E-07	5.66975E-09	1.93176E-07	7.84636E-09	Road Dust RH80 (2)
Sept 5 2019	0.148180789	4.15517E-07	9.31087E-08	7.01755E-09	1.86499E-07	8.57934E-09	Road Dust RH80 (3)
Sept 6 2019	0.143875755	4.3731E-07	9.61888E-08	6.53525E-09	1.71387E-07	8.62502E-09	Road Dust RH50 (3)
Sept 9 2019	0.120063919	3.59521E-07	5.48919E-08	7.9746E-09	1.62356E-07	8.36381E-09	Road Dust RH10 (1)
Sept 10 2019	0.153843053	3.80239E-07	7.44589E-08	9.63256E-09	2.14802E-07	8.72256E-09	Road Dust RH10 (2)
Sept 11 2019	0.148504494	4.7616E-07	7.1143E-08	7.46819E-09	2.03762E-07	1.07549E-08	Road Dust RH10 (3)
Sept 12 2019	0.096009109	3.63588E-07	9.11102E-08	1.64687E-08	2.59261E-07	1.72592E-08	Road Dust RH25 15 mg
September 13 2019	0.227176641	3.75591E-07	8.84628E-08	4.53612E-09	2.11511E-07	5.26012E-09	Road Dust RH25 50mg
September 16 2019	0.264730885	8.61091E-07	7.69921E-08	3.03563E-09	1.87651E-07	8.64166E-09	Road Dust RH25 75mg
September 17 2019	0.173321778	3.70625E-07	7.14122E-08	5.88981E-09	1.99431E-07	6.83443E-09	Road Dust RH25 30mg
September 18 2019	0.433653249	2.19053E-06	1.16E-07	5.15607E-09	2.68314E-07	1.47461E-08	Road Dust RH25 100mg
September 19 2019	0.113116132	3.94312E-07	4.63826E-08	4.67956E-09	1.20325E-07	7.23688E-09	Road Dust RH25 O3100
September 20 2019	0.080372393	1.31366E-07	3.06914E-08	2.87365E-09	9.84675E-08	3.05951E-09	Road Dust RH25 O3150
September 23 2019	0.212132455	1.33513E-06	1.09719E-07	2.25067E-08	3.21667E-07	3.06371E-08	Road Dust RH25 O3 25
September 24 2019	0.380869772	1.10918E-06	2.05439E-07	6.96044E-09	5.3768E-07	1.89055E-08	Road Dust Baked RH25
September 25 2019	0.111258657	2.60553E-07	9.67489E-08	8.35837E-09	1.23722E-07	5.10287E-09	Road Dust Baked RH70
September 26 2019	0.131646693	4.82082E-07	7.7471E-08	9.80231E-09	2.07464E-07	1.27324E-08	Road Dust RH25 20mg
October 1 2019	0.319144567	1.26399E-06	1.72772E-07	8.36603E-09	3.97469E-07	2.06317E-08	Road Dust Baked RH25
October 2 2010	#DIV/0!	#DIV/0!	#DIV/0!	#DIV/0!	#DIV/0!	#DIV/0!	SiO2 50ppm Chloride RH25
October 3 2019	#DIV/0!	#DIV/0!	#DIV/0!	#DIV/0!	#DIV/0!	#DIV/0!	RD 500 ppm Chloride RH70
October 4 2019	#DIV/0!	#DIV/0!	#DIV/0!	#DIV/0!	#DIV/0!	#DIV/0!	SiO2 500 ppm Chloride RH70
October 7 2019	#DIV/0!	#DIV/0!	#DIV/0!	#DIV/0!	#DIV/0!	#DIV/0!	RD 5% Chloride RH70
October 8 2019	0.144585047	6.90161E-07	1.22811E-07	8.73461E-09	1.98247E-07	1.55659E-08	Road Dust Rinsed RH70
October 9 2019	0.120369107	5.17473E-07	6.58122E-08	9.71316E-09	1.55946E-07	1.1362E-08	Road Dust Rinsed RH25
October 10 2019	0.113068363	3.68649E-07	1.15748E-07	7.45923E-09	1.34965E-07	7.56322E-09	Road Dust RH70
October 11 2019	0.110146995	7.22825E-07	6.68628E-08	9.32919E-09	1.51275E-07	1.70084E-08	Road Dust Rinsed RH25 (2)
October 15 2019	0.093435823	3.71389E-07	7.33014E-08	1.31461E-08	1.54413E-07	1.08116E-08	Road Dust Rinsed RH25 (3)
October 21 2019	0.139890666	4.70769E-07	1.27288E-07	1.3004E-08	1.87147E-07	1.04784E-08	Road Dust Rinsed RH70 (2)
October 22 2019	0.128522264	3.92804E-07	1.3321E-07	1.21148E-08	2.07113E-07	1.07094E-08	Road Dust Rinsed RH70 (3)
October 30 2019	#DIV/0!	#DIV/0!	#DIV/0!	#DIV/0!	#DIV/0!	#DIV/0!	Anti Icer RD RH70
October 31 2019	#DIV/0!	#DIV/0!	#DIV/0!	#DIV/0!	#DIV/0!	#DIV/0!	Anti Icer RH70
November 1 2019	#DIV/0!	#DIV/0!	#DIV/0!	#DIV/0!	#DIV/0!	#DIV/0!	CaCl2 RH70 (1)
November 4 2019	#DIV/0!	#DIV/0!	#DIV/0!	#DIV/0!	#DIV/0!	#DIV/0!	Anti Icer RH25
November 5 2019	#DIV/0!	#DIV/0!	#DIV/0!	#DIV/0!	#DIV/0!	#DIV/0!	Fumed SiO2 + Anti Icer RH70
November 6 2019	#DIV/0!	#DIV/0!	#DIV/0!	#DIV/0!	#DIV/0!	#DIV/0!	Anti Icer RH70 (2)
November 7 2019	#DIV/0!	#DIV/0!	#DIV/0!	#DIV/0!	#DIV/0!	#DIV/0!	Anti Icer RH25 (2)
November 8 2019	#DIV/0!	#DIV/0!	#DIV/0!	#DIV/0!	#DIV/0!	#DIV/0!	CaCl2 RH25 (1)
November 12 2019	#DIV/0!	#DIV/0!	#DIV/0!	#DIV/0!	#DIV/0!	#DIV/0!	CaCl2 RH25 (2)
November 13 2019	#DIV/0!	#DIV/0!	#DIV/0!	#DIV/0!	#DIV/0!	#DIV/0!	CaCl2 RH70 (2)

Raw data and calculations for uptake coefficients for Chapter 4.